A structural understanding of interleukin-11 signalling

Riley Dunstan Metcalfe
(ORCID: 0000-0002-7154-780X)

Submitted in total fulfillment of the requirements of the degree of Doctor of Philosophy

January 2020

Department of Biochemistry and Molecular Biology, Bio21 Molecular Science and Biotechnology Institute, The University of Melbourne

Abstract

Interleukin (IL)-11 is an IL-6 family cytokine with several described roles in normal human physiology, haematopoiesis and disease. IL-11 signals by forming a hexameric signalling complex with its two receptors, the IL-11 specific receptor IL-11Rα, and the receptor glycoprotein (gp) 130, which is also utilised by approximately 15 other cytokines. IL-11 signalling has been shown to have roles in several diseases, including gastrointestinal cancer and cardiovascular fibrosis. Despite the growing importance that has been assigned to IL-11 signalling in disease, little is known about the structure of IL-11, the structural mechanisms of IL-11 signalling, or the structural basis of existing IL-11 signalling inhibitors. Overall, this thesis aims to develop a structural and mechanistic understanding of the formation of the IL-11 signalling complex, and the mechanism of action of an existing IL-11 signalling inhibitor.

Here, we present the structures of IL-11 and IL-11Rα. The new high-resolution structure of IL-11 uncovers details not resolved in previous structures, including in a loop which has previously been directly implicated in binding to IL-11Rα. The structure of IL-11Rα shows structural differences to related cytokine receptors. Combined with biophysical analysis of the interaction between IL-11 and IL-11Rα, our structures allow us to propose a model for the recruitment of IL-11 by IL-11Rα. We also used our structure to investigate the mechanism of action of known disease mutations in IL-11Rα. These mutations were distal to cytokine-binding regions in IL-11Rα and appear to act through destabilisation of IL-11Rα.

We also solved the structure of the IL-11 signalling complex using cryo-electron microscopy and X-ray crystallography. The complex is a hexameric complex consisting of two copies each of IL-11, IL-11Rα and gp130. The resolution of the map is sufficiently high to define in detail of the binding sites on IL-11 and the receptors and uncovers mechanistic differences in complex formation by IL-11 and the related cytokines IL-6 and viral IL-6. Using solution methods, we also showed that the IL-11 signalling complex is hexameric in solution, and forms in three high-affinity steps, combined with our knowledge of the IL-11/IL-11Rα interaction, this

allows us a detailed, mechanistic understanding of the formation of the IL-11 signalling complex.

We also studied the lead IL-11 signalling inhibitor, IL-11 Mutein. IL-11 Mutein was developed from an existing antagonistic mutant of IL-11, IL-11 W147A, which removed a key residue required for hexameric complex formation. IL-11 Mutein was developed from IL-11 W147A using phage display, to identify novel mutations which increased the potency of IL-11 W147A. We solved structures of IL-11 Mutein and the IL-11 W147A mutant, showing that the mutations in IL-11 Mutein disrupt a loop in proximity to the IL-11Rα binding site. We showed that IL-11 Mutein is an effective IL-11 antagonist and prevents the assembly of the IL-11 signalling complex. Supported with extensive biochemical and biophysical analysis, we propose a model for the antagonistic action of IL-11 Mutein, which will guide the development of novel cytokine-like inhibitors.

Overall, the work presented here allows a detailed understanding of the structural mechanisms underpinning IL-11 signalling. The results will allow the development of novel antagonists targeting the IL-11 signalling complex, which we hope will be of therapeutic benefit in cancers and other diseases.

Declaration

This is to certify that:

1. This thesis comprises only my original work towards this PhD, except where indicated in the preface.
2. Due acknowledgement has been made of other sources used.
3. This thesis is less than 100,000 words, exclusive of figures, tables, maps, bibliography and appendices.

Riley Metcalfe

January 2020

Preface

The following components of the work were carried out in collaboration with others:

1. The IL-11Rα crystal structure presented in Chapter 3 was a collaborative work between myself, Dr. Kahenia Aizel and A/Prof. Michael Griffin. Dr. Aizel obtained the crystals. Dr. Aizel and myself collected X-ray diffraction data. A/Prof. Griffin built and refined the structure, with significant input from Dr. Aizel and myself. All presented analysis of the structure is my own.
2. The cryo-EM reconstruction of the IL-11 signalling complex presented in Chapter 4 was a collaborative work between myself, Dr. Andrew Leis, A/Prof. Eric Hanssen and A/Prof. Michael Griffin. Dr. Leis and A/Prof. Hannsen prepared EM grids, acquired data and obtained the reconstruction, with input from myself and A/Prof. Griffin. Solution and refinement of the structure were conducted by myself. All presented analysis of the structure is my own.
3. The crystal structure of the IL-11 signalling complex presented in Chapter 4 was a collaborative work between myself, Dr. Kahenia Aizel and A/Prof. Michael Griffin. Initial crystal screening was undertaken by Dr. Aizel. Subsequent optimisation of crystallisation conditions and X-ray diffraction data collection were conducted by myself and A/Prof. Griffin. Solution and refinement of the crystal structure were conducted by myself. All presented analysis of the structure is my own.
4. The SPR data presented in Chapter 5 was acquired in collaboration with Dr. Larissa Doughty. The deuterated IL-11 samples used for the NMR experiments in Chapter 5 were expressed by Karyn Wilde at the National Deuteration Facility, part of the Australian Nuclear Science and Technology Organisation. Protein purification and subsequent characterisation was done by myself.

Chapter 1 is a literature review. Chapter 2 is a detailed description of the protein expression and purification methods developed to enable the results presented in the remainder of this thesis. Chapter 3 is presented as a manuscript, which is currently under review. Chapters 4 and 5 are presented as manuscripts which have not been submitted for publication. Chapter 6 is a general discussion of the results

in chapters 2-5. Appendix A is a publication that I co-first authored during my PhD, along with Dr. Stanley Xie and A/Prof. Eric Hannsen. A/Prof. Michael Griffin and Prof. Leann Tilley are the corresponding authors on the publication.

Awards, presentations and publications

Publications:

Metcalfe, R.D., Aizel, K., Zlatic, C.O., Nguyen, P.M., Morton, C.J., Lio, D.S-S., Cheng, H-C., Dobson, R.C.J., Parker, M.W., Gooley, P.R., Putoczki, T.L. and Griffin, M.D.W. The structure of human interleukin 11 α-receptor reveals the mechanism of cytokine engagement. *Under review* ***#included as Chapter 3***

Xie, S.C., Metcalfe, R.D., Hanssen, E., Yang, T., Gillett, D.L., Leis, A.P., Morton, C.J., Parker, M.W., Spillman, N.J., Wong, W., Tsu, C., Dick, L.R., Griffin, M.D.W., and Tilley, L. (2019). The structure of the PA28–20S proteasome complex from *Plasmodium falciparum* and implications for proteostasis. *Nature Microbiology* 4, 1990-2000 (2019) ***#equal first author, included as Appendix A***

Mobbs, J.I., DiPaolo, A., Metcalfe, R.D., Selig, E., Stapleton, D.I., Griffin, M.D.W., and Gooley, P.R. (2018). Unravelling the Carbohydrate-Binding Preferences of the Carbohydrate-Binding Modules of AMP-Activated Protein Kinase. *ChemBioChem* 19, 229–238 (2018)

Presentations:

Oral presentation, 26th Australian Conference on Microscopy and Microanalysis, '*The structure of the interleukin-11 signalling complex guides therapeutic design*'	Feb. 2020 Canberra
Oral presentation, Lorne Proteins conference, '*The structure of the interleukin-11 signalling complex guides therapeutic design*'	Feb. 2020 Lorne
Poster, Cytokine Society meeting, *'Structural characterisation of an IL-11 signalling antagonist*'	Oct. 2019 Vienna
Poster, American Crystallographic Association conference, '*Structural characterisation of an IL-11 signalling antagonist*'	July 2019 Covington
Poster, American Crystallographic Association, '*The cryo-EM structure of a* Plasmodium *proteasome-activator complex*'	July 2019 Covington
Poster, Protein Society conference, '*Structural characterisation of an IL-11 signalling antagonist*'	June 2019 Seattle
Poster, Protein Society conference, '*The cryo-EM structure of a* Plasmodium *proteasome-activator complex*'	June 2019 Seattle
PhD completion seminar, Bio21 Institute, '*Structural approaches to target the interleukin-11 signalling complex*'	May 2019 Melbourne
Poster, Lorne Proteins conference, '*The cryo-EM structure of a* Plasmodium *proteasome-activator complex*' ***#poster prize awarded***	Feb. 2019 Lorne
Seminar, Inflammation Division, Walter and Eliza Hall Institute (WEHI), '*Structural approaches to target the interleukin-11 signalling complex'*	Dec. 2018 Melbourne
Oral presentation, 19th International Microscopy Conference, *'The structure of the* P. falciparum *20S proteasome in complex with an activator*'	Sep. 2018 Sydney

Poster, Melbourne Proteins Group student symposium, '*What is the structural basis for IL-11 signalling antagonism by IL-11 Mutein?*' ***#poster prize awarded***	July 2018 Melbourne
Oral presentation, 2018 Department of Biochemistry and Molecular Biology student retreat, *'Structural characterisation of a lead IL-11 signalling antagonist'* ***#talk prize awarded***	July 2018 Macedon Ranges
Poster, Lorne Proteins conference, '*What is the structural basis for IL-11 signalling antagonism by IL-11 Mutein?'*	Feb. 2018 Lorne
Oral presentation, 2017 Department of Biochemistry and Molecular Biology student retreat, *'Structural characterisation of a lead IL-11 signalling antagonist'* ***#talk prize awarded***	Oct. 2017 Macedon Ranges
Poster, Melbourne Proteins Group student symposium, '*What is the structural basis of IL-11 signalling antagonism?'* ***#poster prize awarded***	July 2017 Melbourne
Poster, Lorne Proteins conference, '*A SAXS model of the IL-11Rα receptor complex'*	Feb. 2017 Lorne
Poster, 2016 Department of Biochemistry and Molecular Biology student retreat, *'Characterisation of an antagonist of IL-11 signalling, the IL-11 mutein'*	Oct. 2016 Macedon Ranges
Poster, Melbourne Proteins Group student symposium, *'Investigating the receptor interaction of human interleukin-11*'	July 2016 Melbourne
Poster, Lorne Proteins conference, *'Investigating the structural biology and receptor interaction of human interleukin 11'*	Feb. 2016 Lorne

Awards:

Robin Anders Young Investigator Award *Presented at the 2020 Lorne Proteins conference*	2020
Department of Biochemistry and Molecular Biology Travel Award *To attend the 2019 Cytokine Society meeting, Vienna, Austria*	2019
Cytokine Society Milstein Travel Award *To attend the 2019 Cytokine Society meeting, Vienna, Austria*	2019
IUCR/American Crystallographic Association Travel Award *To attend the 2019 ACA meeting, Covington, Kentucky, USA*	2019
Protein Society Finn Wold Travel Award *To attend the 2019 Protein Society meeting, Seattle, Washington, USA*	2019
Bio21 Institute Travel Award *To attend conferences in the USA in June/July 2019*	2019
Poster prize, Lorne Proteins Conference	2019
Poster prize, Melbourne Proteins Group student symposium	2018
Poster prize, Melbourne Proteins Group student symposium	2017
Australian Postgraduate Award	2016-2019

Acknowledgements

"The struggle itself toward the heights is enough to fill a man's heart."

Albert Camus, *The Myth of Sisyphus*[1]

I'd first like to thank my supervisor, Dr. Michael Griffin (now A/Prof. Michael Griffin). I still clearly remember the first conversation I had with Mike – appropriately, after a third-year biochemistry lecture on structural biology. That was the start of an incredibly rewarding and productive working relationship that has lasted for close to five years. I can't thank Mike enough for his support, his willingness to listen to my ideas and in later years, his trust in allowing me to take on several projects unrelated to my main PhD project. Trying to summarise this in a short paragraph is difficult, and requires too many superlatives, so I'll just say that I couldn't have asked for a better supervisor.

During my PhD, I was lucky to have continual input from a great co-supervisor, Prof. Paul Gooley. Paul was always a great source of advice and I always appreciated his input during my PhD. I'd also like to thank my PhD committee members, Prof. Michael Parker, my committee chair, A/Prof. Jeff Babon and Dr. Tracy Putoczki for their thoughtful guidance and input during my degree. I'd particularly like to thank Tracy for forcing me to think about biology occasionally, and for facilitating access to facilities at WEHI during the last year of my PhD.

I'd also like to thank the Australian government for the Australian Postgraduate Award scholarship. The Bio21 Institute, the Department of Biochemistry and Molecular Biology, the Protein Society, the International Cytokine and Interferon Society and the American Crystallographic Association provided financial support to attend conferences in the US and Europe in the last year of my PhD, for which I am grateful.

I would also like to acknowledge that the work described here was conducted on the traditional lands of the Wurundjeri people of the Kulin Nation.

Towards the end of my PhD, I was fortunate to work on several projects related to the *P. falciparum* proteasome and drug design with Dr. Stanley Xie, A/Prof. Eric Hanssen and Prof. Leann Tilley. I'd like to thank them, and all others that were involved in the projects. I enjoyed the distraction, and it was a great opportunity to learn skills that I didn't get a chance to learn in the course of my PhD. Leann in particular was someone I could always turn to advice towards the end of my PhD, and I always appreciated her advice, enthusiasm and knowledge.

Subsequent to this, I was very fortunate to continue to work with Dr. Andrew Leis and A/Prof. Eric Hanssen at the Bio21 Advanced Microscopy Facility. I am deeply grateful for their generosity in providing time on the electron microscopes at Bio21, the time they spent in preparing grids and in image processing and data analysis.

The Griffin lab was a great place in which to do my PhD, and I'm thankful for all members of the lab during my time here – in approximate chronological order, Courtney Zlatic, Zachary Rosenes, Layla Kayla, Emily Selig, Dr. Kahenia Aizel, Cameron Oppy, Pheobe Tou and Clara Christy Kosasih. I would particularly like to acknowledge Courtney's efforts in running the lab, and her help in the lab with insect cell protein expression in the last year in my PhD. Kahenia and I worked closely for three years while she was in the lab. I appreciate her efforts in developing the insect cell protein expression of the IL-11 receptors and the crystallisation of IL-11Rα.

I'd like to also thank all members of the Gooley lab during my time here – particularly Jingyu Zhan, Ashish Sethi, Fei Yan, Shatabdi Chakraborty, Fengjie Wu, Tasneem Vaid and Jesse Mobbs. Through my degree, I shared office and lab space with the Stojanovski and Tilley labs. I'd like to thank all members of the Stojanovski lab - Laura Fielden, Yilin Kang, Tom Jackson, Alex Anderson and Catherine Palmer (and Diana). They were great people to share a room with for most of my PhD, and I always enjoyed our conversations. I'd also like to thank all members of the Tilley lab, particularly Tuo Yang, Olivia Carmo, Oliver Looker, Ben Seager, Jiahong Li, Steven Batinovic, Stanley Xie, Dean Andrew, Boyin Liu, Emma McHugh and David Gillett.

During the last year of my PhD, I enjoyed working at WEHI. I'd like to thank all members of the Putoczki lab, particularly Dr. Paul Nguyen, Suad Abdirahman and Gemma van Duijneveldt for their help with mammalian tissue culture. I'd also like to thank Dr. Emma Petrie and Dr. Cheree Fitzgibbon for their help with insect cell culture. I also enjoyed working with A/Prof. Wai-Hong Tham and Dr. Alvin Lo (and the alpacas), and with Dr. Nadia Kershaw.

I'm very fortunate that I have had access to world-class scientific infrastructure during my PhD. I'd particularly like to thank Dr. Yee-Foong Mok for his efforts in maintaining countless pieces of scientific equipment, and for his skills in analytical ultracentrifugation. I'd also like to thank the staff of the Bio21 NMR and MS facilities. I also made good use of the Australian Synchrotron, and I'd like to thank the beamline scientists at the MX and SAXS beamlines, particularly Dr. Nigel Kirby and Dr. Tim Ryan at the SAXS beamline. I'd like to thank Larissa Doughty for her assistance in performing SPR experiments and Dr. Craig Morton for his help with MD simulations. I'm also grateful for the efforts of Karyn Wilde in producing deuterated IL-11, and Dr. Janet Newman, Dr. Bevan Marshall, and all staff at the CSIRO C3.

During the second and third years of my PhD, I was a member of the biochemistry student association at Bio21, BAMBII. I'd like to thank all members of the 2017 committee – Haiyin Liu, Laura Fielden, Patrick Schriek, Tasneem Vaid and Ilknur Spring. There are too many people to list in the 2018 committee, but I'd particularly like to thank Kayla Wilson for taking over in the middle of 2018.

Broadly, the biochemistry department circa 2015-2020 was a great place to work, and I'd like to thank all members of the department during that time. I'm fortunate that I have many good friends in the department. Thanking everyone risks being perceived as thanking nobody, so I'm particularly grateful for my friendship with Emily Selig, Laura Fielden, Tuo Yang, Xiaojing Sui and Jingyu Zhan.

Before I started in Mike's lab, I was fortunate to work for a little over a year at CSL at Bio21. I'd like to thank my supervisors at the time – Shirley Taylor and Lou Fabri for their patience while I was learning. In addition to them, I'd like to thank all members in the lab at the time, particularly Rebecca Butcher.

Finally, I'd like to thank my family and friends. I'd like to thank some good friends outside of the department, in rough reverse-chronological order – Jon Regan, Elmie Janse van Rensburg, Rosalind Moran, Tanja Cobden, Jasper Dekker and Toby Schneider. I'd also like to thank Laurie and Josie Duncan for their continual hospitality in Melbourne. Finally, I'd like to thank my family, my grandparents, my sister Fionella and my parents, Andrew and Jenny. I'm not sure that I can put into words how much your support has meant to me, so I won't try.

Writing this section and reading over the names this list is a deeply humbling experience. I'm grateful for the support that you have all provided through my PhD, and it is something that I will never forget.

Abbreviations

Ab	Antibody
Au	Absorbance units
au	Arbitrary units
AUC	Analytical ultracentrifugation
CD	Circular dichroism
cIEX	Cation exchange chromatography
CNTF	Ciliary neurotrophic factor
CryoEM	Cryo-electron microscopy
D1-D3	Domain 1 to domain 3
D1-D6	Domain 1 to domain 6
D2-D3	Domain 2 to domain 3
Da	Dalton
DSF	Differential scanning fluorometry
EC	Extracellular
EDTA	Ethylenediaminetetraacetic acid
EM	Electron microscopy
EPO	Erythropoietin
ESI	Electrospray ionization
Fab	Fragment antigen binding
Fc	Fragment crystallisable
FDA	Food and Drug Administration (USA)
Fn3	Fibronectin-type III
G-CSF	Granulocyte colony stimulating factor
GFP	Green fluorescent protein
GH	Growth hormone
GM-CSF	Granulocyte-macrophage colony stimulating factor
Gp130	Glycoprotein 130
GPCR	G-protein coupled receptor
HSQC	Heteronuclear single quantum correlation
ICD	Intracellular domain
IFN	Interferon
Ig	Immunoglobulin
IL	Interleukin
IPTG	Isopropyl-β-D-thiogalactoside
ITC	Isothermal titration calorimetry
JAK	Janus kinase
LA	Lysogeny broth with agar
LB	Lysogeny broth
LIF	Leukemia inhibitory factor
mAb	Monoclonal antibody
MS	Mass spectrum
MS	Mass spectrometry
MST	Microscale thermophoresis
mu	Monomeric ultrastable
Nb	Nanobody
NCS	Non-crystallographic symmetry

NMR	Nuclear magnetic resonance
NOE	Nuclear Overhauser Effect
NUS	Non-uniform sampling
OSM	Oncostatin M
PAGE	Polyacrylamide gel electrophoresis
PBS	Phosphate-buffered saline
PCR	Polymerase chain reaction
pI	Isoelectric point
PPI	Protein-protein interaction
ppm	Parts per million
RMSD	Root mean square deviation of atomic positions
SAXS	Small-angle X-ray scattering
SDS	Sodium dodecyl sulfate
SEC	Size-exclusion chromatography
SHP2	SH2 domain containing tyrosine phosphatase
SNP	Single nucleotide polymorphism
SOB	Super-optimal broth
SOCS	Suppressor of cytokine signalling
SPR	Surface-plasmon resonance
STAT	Signal transducer and activator of transcription
SV	Sedimentation velocity
TB	Terrific broth
TBS	Tris-buffered saline
TEM	Transmission electron microscopy
TEV	Tobacco etch virus
TOF	Time of flight
Tris	Tris(hydroxymethyl)aminomethane
TRX	Thioredoxin
USD	United States dollar
WT	Wild-type

Cytokine receptors are generally denoted with an ‘R’ after the name of the cytokine. For example, the growth hormone receptor is abbreviated GHR.

Amino acid three and one letter codes

Ala	A	Alanine	Leu	L	Leucine
Arg	R	Arginine	Lys	K	Lysine
Asn	N	Asparagine	Met	M	Methionine
Asp	D	Aspartate	Phe	F	Phenylalanine
Cys	C	Cysteine	Pro	P	Proline
Gln	Q	Glutamine	Ser	S	Serine
Glu	E	Glutamate	Thr	T	Threonine
Gly	G	Glycine	Trp	W	Tryptophan
His	H	Histidine	Tyr	Y	Tyrosine
Ile	I	Isoleucine	Val	V	Valine

Table of Contents

Tables of Figures, Supplementary Figures, Supplementary Movies and Supplementary Tables

Figures

Supplementary Figures

Supplementary Movies

Supplementary Tables

Chapter 1 - Introduction

Cytokines are small signalling proteins and have countless roles in physiology, the immune system, and in disease[2]. In the half-century since the discovery of the first cytokines, the interferons in 1957[3], over fifty cytokines have been identified[4]. Interleukin (IL) 11 was first identified in 1990[5], in the decades since, IL-11 has been ascribed a number of physiological roles in haematopoiesis, and pathological roles, including in cardiovascular disease and cancer. This chapter will review the current understanding of cytokine signalling, the mechanisms of cytokine signalling, and the biological significance of IL-11. This chapter will close with a discussion of cytokine pharmacology, and a statement of the aims of this thesis.

1.1 Cytokine signalling, and the structure of cytokines and receptors

1.1.1 Cytokine signalling – a brief history

Interferons were the first cytokines to be identified in 1957 as a secreted protein product induced as a result of virus infection[3] (for historical perspectives, see[6-8]). In the subsequent decades, similar proteins, such as the colony stimulating factors (CSFs)[9-11], IL-2[12,13] and IL-3[14,15] were identified as factors able to support the growth of various hematopoietic cell linages in cell culture. In 1974, the broad term 'cytokine' was introduced, as similar proteins were identified[16] and in 1979 the term 'interleukin' was introduced to standardise the names for the proteins now known as IL-1 and IL-2[17]. Over the next decade, it was recognised through radiolabelling studies that cytokines bound distinct and unique receptors on the cell surface[18], although some cytokines, such as granulocyte-macrophage CSF (GM-CSF), IL-5 and IL-3 were found to compete for a low-affinity receptor[19,20], foreshadowing the identification of a common receptor, the β common receptor, for these cytokines.

Following the discovery of the first cytokines, the mechanisms of intracellular signal transduction by cytokines remained elusive. The first transcriptional activator to be well-characterised was interferon-stimulated gene factor 3 (ISGF3), a multi-component protein complex consisting of what is now known as signal transducer and activator of transcription (STAT)1 and STAT2[21,22]. Subsequently, related STAT proteins were identified as being activated as a consequence of cytokine stimulation[23,24]. It was additionally discovered that these factors were tyrosine

phosphorylated[25,26] on cytokine activation. The kinases responsible for this phosphorylation, the Janus kinases (JAK) were first identified through a PCR screen of a murine hematopoietic cell line[27,28]. Their significance was unclear until they were shown to be activated as a result of cytokine binding in the early 1990s, and to phosphorylate the transcription factors that were already identified as key for interferon signal transduction[29]. Subsequently, different JAK kinases were found to be responsible for signal transduction for several other cytokines[30-32], and negative feedback regulators of the pathway, the suppressors of cytokine signalling (SOCS) proteins were identified in 1997[33-35]. The key components of cytokine signalling using the JAK-STAT pathway were thus understood by the late 1990s, although many of the detailed molecular mechanisms are still unknown and under intense investigation today.

The term 'cytokine' is somewhat poorly defined, as it was introduced before the molecular details of cytokine signalling were understood. This chapter will be limited to discussing cytokines that, like IL-11, signal using the JAK-STAT pathway. These cytokines share a common, four-α helical bundle structure, and share receptors with similar structures[36-38]. Other cytokines, such as the IL-1/IL-18 family and the TNF family are structurally distinct from the four-α helical bundle family[39], and utilise different signalling mechanisms, and are thus beyond the scope of this chapter. Conversely, several protein hormones, such as leptin, growth hormone (GH), prolactin and erythropoietin (EPO) utilise similar signal transduction mechanisms and are structurally related to the four-α helical bundle cytokines and are thus best categorised alongside them[38,40]. Indeed, the discovery of GH and EPO predate that of the interferons by several decades[41,42], but were not recognised as related until they were cloned and sequenced, and significant sequence homology was noted between cytokine receptors, the GHR and the EPOR[43,44].

1.1.2 The structure of cytokines and receptors

By far the most numerous cytokine family is the four-α helical bundle cytokine family, of which IL-11 is a part. These cytokines are further sub-classified based on the structure of the cytokines and their receptors. Both class I cytokines (e.g. GH,

IL-6, IL-11, known collectively as hematopoietic cytokines) and class II cytokines (e.g., IFN-α, IL-10) utilize receptors that are broadly similar in structure and utilize similar intracellular signalling mechanisms[37]. Cytokines from both families possess a four-α helical bundle fold, with the compact α-helical bundle formed by four anti-parallel α-helices, arranged in an up-up-down-down topology[36,37]. This arrangement of helices necessitates long loops joining the helices (Figure 1.1Ai, Aii). Secondary structure in the loops is common, for example, the loop joining the C and D helices in IL-6 (the CD loop) has a short α-helix within the loop[45], and in IL-4[46] and GM-CSF[47], the AB and CD loops form a small anti-parallel β-sheet on the same face of the cytokine (Figure 1.1Aii). The large surfaces created by the four-α helical bundle provides a large, extensive binding surface for the cytokine to bind its receptors.

Cytokine receptors are almost always modular single-pass transmembrane proteins, with a large, extracellular region consisting of multiple all-β immunoglobulin (Ig) domains and fibronectin type III (Fn3) domains[40]. Both domains possess a β-sandwich structure, with two anti-parallel β sheets forming the domains (Figure 1.1Bi, Bii). The exception is the IL-2Rα/IL-15Rα receptors, which consist of two all-β sushi domains, unrelated to the Ig/Fn3 domains utilized by other cytokine receptors[40,48,49]. The two cytokine binding domains consist of two Fn3 domains at approximately a 90° angle, forming the cytokine binding homology region (CHR)[38]. Cytokines bind at the junction of the two domains, which provides a large binding surface. Each of the two domains of the CHR possess conserved features, the first domain of the CHR (D1) has two conserved disulphide bonds, and in class I cytokine receptors, D2 of the CHR has an exceptionally well-conserved Trp-Ser-X-Typ-Ser motif (WSXWS) motif[38]. The WSXWS motif generally forms a short 'ladder' consisting of cation-π interactions between the tryptophan residues in the ladder and arginine residues in the domain. The precise structural role of the WSXWS motif is still unclear. It has a role in stabilising the receptor, mutations in the WSXWS motif result in a non-functional receptor[50,51], and a rare genetic disease results from a mutation in the WSXWS motif in the GHR[52]. In IL-21Rα, the first Trp in the WSXWS motif is C-mannosylated, the modified Trp forms stabilising interactions with other glycans and amino acid residues in the structure[53]. The

extensive glycosylation, both Trp C-mannosylation, and Asn N-linked glycosylation gives IL-21Rα the structure of an 'A-frame', with a glycan chain forming a bridge between the two domains in the receptor. Similar Trp C-mannosylation has been detected in the p40 subunit of IL-12 by mass spectrometry[54], but has not been observed in crystal structures which include p40[55-57], possibly reflecting incomplete incorporation of the modification in recombinant protein. The role of Trp C-mannosylation is unclear. Recent studies[58] have suggested that, in addition to being a stabilising structural element, the WSXWS motif undergoes a conformational change on cytokine binding, suggesting it has a role in receptor activation.

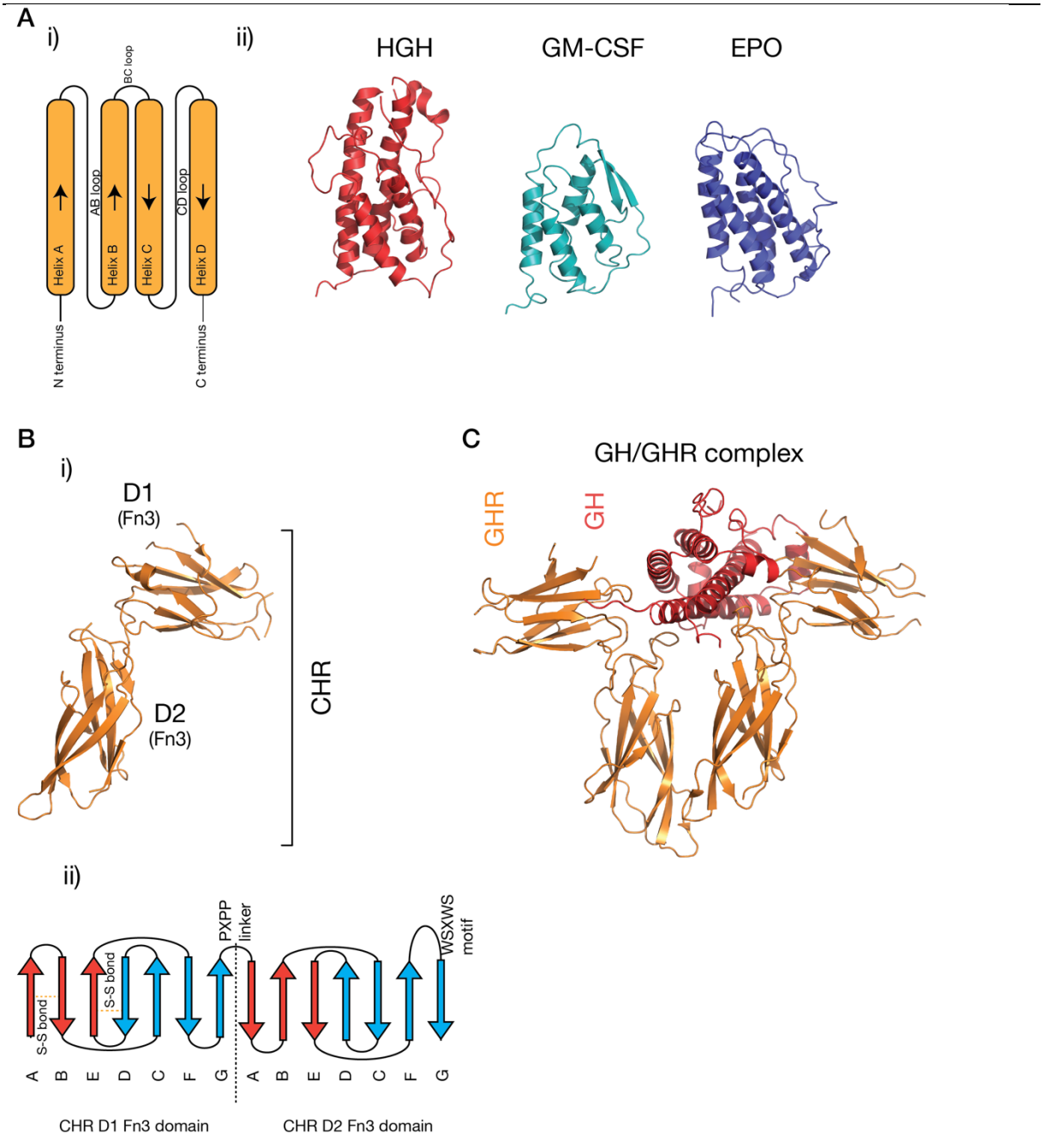

Figure 1.1: The structure of cytokines and receptors.

A) i) The four-α helical bundle topology of hematopoietic cytokines, ii) the structure of several representative cytokines, human growth hormone (PDB ID: 1HGU[59]), GM-CSF (PDB ID: 1CSG[47]) and erythropoietin (PDB ID: 1BUY[60]). B) The structure of the growth hormone receptor (PDB ID: 2AEW[61]). The two Fn3 domains that make up the CHR are indicated, and a typical topology[38] for the two Fn3 domains in the CHR is shown in ii). The conserved disulfide bonds in the N-terminal domain, the linker sequence, and the conserved WSXWS motif are indicated. C) The structure of the growth hormone/growth hormone receptor complex (PDB ID: 3HHR[62]).

In addition to the CHR, cytokine receptors typically consist of additional extracellular domains. These domains have varied roles, for example in correctly orienting the receptor to allow the activation of intracellular kinases[63], cytokine binding[64], or in intracellular trafficking to the membrane[65]. Often, the role of these additional domains remains unclear. Most cytokine receptors are single-pass transmembrane proteins, an exception is the ciliary neurotrophic factor (CNTF) receptor, which is lipid anchored[66]. The structures of cytokine receptor transmembrane domains have also been solved, generally by nuclear magnetic resonance (NMR) spectroscopy[67-70]. Single-pass transmembrane cytokine receptors also possess an intracellular domain. Generally, this domain is poorly characterised and assumed to be disordered[71,72]. This domain, for signal-transducing cytokine receptors is involved in binding signal transducing molecules, such as the JAK, STAT and SOCS proteins.

Understanding the molecular details of cytokine engagement requires detailed structural knowledge of the complexes formed by cytokines and receptors. The first cytokine/receptor complex solved was the GH:GHR complex in 1992 (Figure 1.1C), showing GH binding to a dimer of GHR[62]. The most surprising feature of the structure was the observation that the two chemically distinct binding sites on GH bind nearly identical epitopes on GHR. Following the GH:GHR structure, more complex structures followed, such as the tetrameric viral IL-6[73] complex, the hexameric IL-6[74] complex, and the dodecameric GM-CSF[75] complex, allowing a

thorough understanding of cytokine/receptor engagement from several hematopoietic cytokine families. So far, no high-resolution structures have been solved which include the transmembrane or intracellular regions of cytokine receptors, although low-resolution negative-stain electron microscopy studies have captured dynamics of these complexes[76].

The use of shared signal transducing receptors by cytokines is common. For example, three cytokines utilize the common β chain (β_c), IL-3, IL-5 and granulocyte-macrophage colony stimulating factor (GM-CSF)[77], six cytokines utilize the common γ chain (γ_c), IL-2, IL-7, IL-9, IL-13, IL-15 and IL-21[78], and more than ten cytokines utilize glycoprotein 130 (gp130), such as IL-6, IL-11, IL-30, leukemia inhibitory factor (LIF), CNTF and oncostatin M (OSM)[79]. As structures have now been solved of several representative cytokines from these families, the mechanisms of shared receptor use have begun to be understood. For example, the γ_c receptor has a large binding surface in the CHR, allowing it to bind structurally diverse cytokines[49,78], in contrast, gp130 has a structural rigid, chemically diverse binding surface in the CHR, with different gp130-interacting cytokines interacting with different but overlapping regions of the surface[80]. In shared receptor systems, cytokine-specific receptors, such as the IL-6Rα or IL-15Rα, with restricted expression, serve to restrict the activity of cytokines to specific target cells, in spite of the utilization of identical intracellular signalling pathways.

1.1.3 Intracellular signal transduction by cytokines – the JAK-STAT pathway

In all cases, the formation of the receptor complex serves to allow the activation of downstream signalling pathways to affect a cellular response. The most well-studied pathway activated in response to cytokines is the JAK-STAT pathway (Figure 1.2A). In essence, the JAK-STAT pathway is quite simple, having five key components – ligand, receptor, kinase (JAK), signal transducing molecule (STAT) and negative feedback regulator (SOCS)[39]. Complexity in the JAK-STAT pathway comes from multiple kinases (JAK1, JAK2, JAK3 and TYK2), signal transducing

molecules (STAT1, STAT2, STAT3, STAT4, STAT5a, 5b and STAT6) and negative-feedback proteins (SOCS1-7, CIS)[39].

JAKs are associated with the cytoplasmic domains of signal-transducing cytokine receptors. Structurally, JAKs consist of four domains, a kinase domain, pseudokinase domain, FERM domain and SH2-like (phosphotyrosine-binding) domain. The pseudokinase domain regulates the kinase domain[81], with the term 'Janus kinase' referring to the presence of two kinase domains, real and pseudo, named for the two-faced Roman god[28]. The FERM/SH2-like domains form a single structural unit[82,83], and are responsible for interacting with the cytokine receptor, through defined motifs on the receptor (Box 1 and Box 2)[84]. Cytokine binding results in the activation and auto-phosphorylation of the kinases, which phosphorylate the cytokine receptor at STAT binding sites, serving to recruit STATs. These STATs are themselves phosphorylated, which results in the activation of the STAT dimer, its translocation to the nucleus, and the expression of cytokine responsive genes. These include the SOCS proteins, which are expressed as a consequence of cytokine activation, and serve to negatively regulate the pathway[33]. The SOCS proteins serve to recruit the E3 ligase, Cullin5, resulting in the eventual degradation of the complex in the proteasome[85,86]. Two SOCS proteins (SOCS1[87] and SOCS3[88]) also directly inhibit the kinase activity of the JAKs. Likewise, a class of proteins, the protein inhibitor of activated STAT (PIAS) proteins also serve to inhibit the activity of activated STAT, through mechanisms which include directly blocking the STAT interaction with nuclear DNA[89,90]. Several phosphatases additionally act as negative regulators of signalling, such as the SH2-domain containing phosphatases SHP1/2[91,92] and protein-tyrosine phosphatase (PTP) 1B[93]. The protein Lnk serves as an additional negative regulator of signalling by several cytokines that signal using JAK2[94]. Different kinases are associated with different cytokine receptors – for example, the IFNα/β receptor use TYK2[29] and β_c uses JAK2[95], resulting in the recruitment of different STAT proteins (STAT1/2 for IFNα/βR[29], STAT5 for β_c[95]) and different gene expression programs in response to signalling.

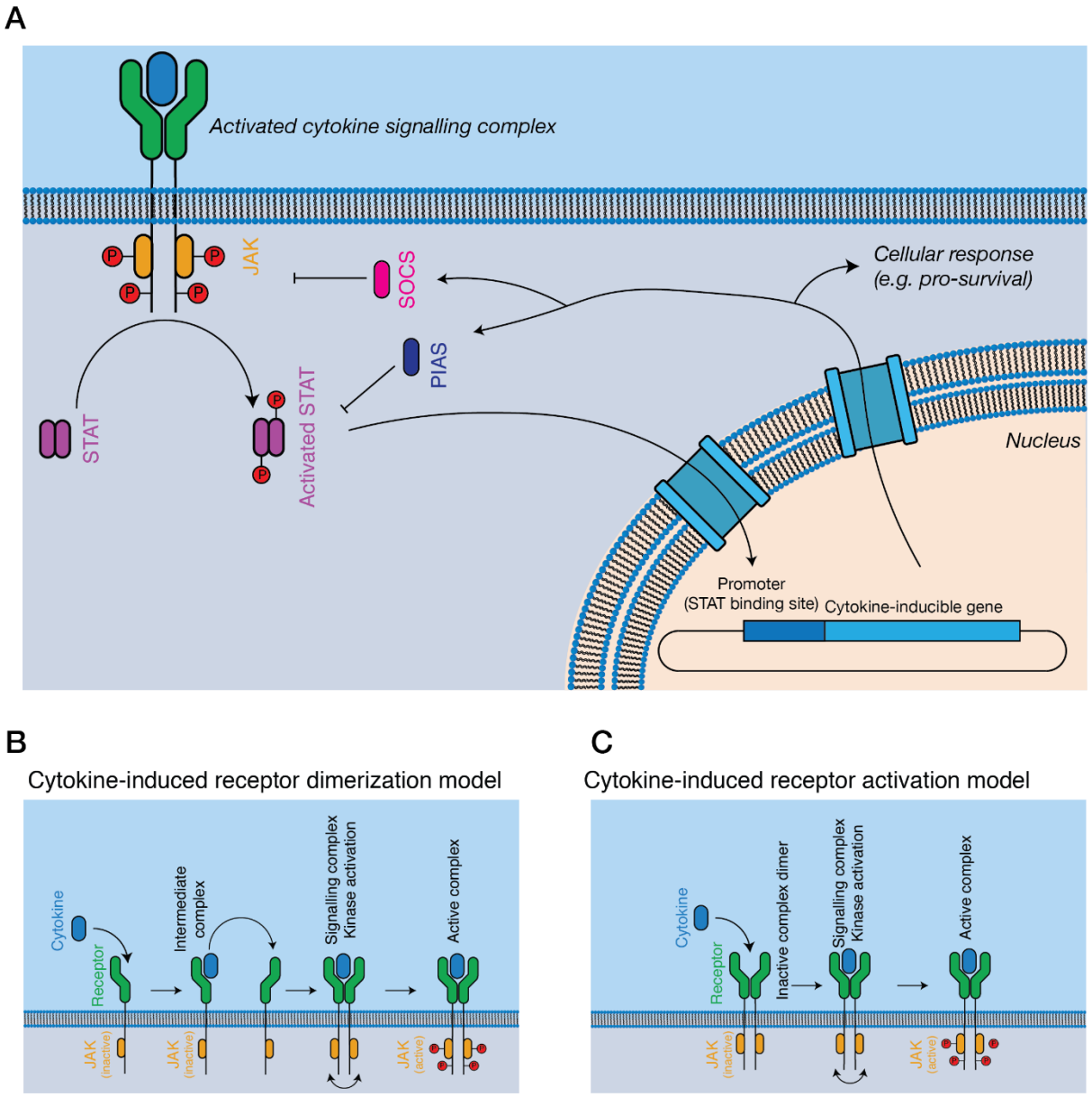

Figure 1.2: Cytokine signal transduction.

A) General schematic of the JAK-STAT pathway. Cytokine binding results in the activation of intracellular kinases (JAKs), which phosphorylate and activate STATs, which subsequently translocate to the nucleus, resulting in altered gene expression, and negative feedback on the pathway through the SOCS proteins. B,C) Models for complex activation. Cytokines are thought to either, B) dimerise receptors on the cell surface, resulting in kinase autophosphorylation and activation or C) bind to pre-dimerised receptors on the cell surface, resulting in receptor activation through a cryptic mechanism.

In addition to the JAK-STAT pathway, cytokines can utilise alternative signalling pathways, such as the mitogen-activated protein kinase (MAPK) pathway, and phosphoinositide 3-kinase (PI(3)K) pathway[95]. Signalling through these pathways is generally less well understood than signalling through the JAK-STAT pathway. The multi-adaptor protein SH2-like domain containing tyrosine phosphatase (SHP2) interacts with several cytokine receptors and provides the link between the receptors and the MAPK pathway[96].

The exact mechanism of cytokine activation of signal transduction, however, remains unclear and a subject of active investigation. A model was proposed by which GH induced dimerization of the GHR, bringing the kinases into close proximity, allowing auto-activation of the kinases by *trans*-phosphorylation[62,97] (Figure 1.2B). Directly contradicting this model was the finding that several cytokine receptors, including GHR[98], EPOR[99] and gp130[100,101] exist as preformed dimers. The consequence of cytokine binding for these receptors is thus not the formation of a signalling complex dimer, but the activation of a pre-formed receptor dimer (Figure 1.2C). The exact mechanism of this process is under active investigation, with the activation mechanisms of GHR and EPOR being the most thoroughly studied[61,98,99,102]. These works suggest a common mechanism of activation by class I cytokine receptors, in which cytokine binding results in a rearrangement of the transmembrane α helices of the receptor, a conformational change that lifts auto-inhibition of the kinase[98]. Determining the universality of such a mechanism will require the study of additional cytokine receptors, particularly those that signal through more complex hetero-dimeric or larger signalling complexes.

1.2 The IL-6 family of cytokines

The IL-6 family of cytokines is the largest family of hematopoietic cytokines (Figure 1.3A). They are unified by the near-universal use of a shared signal transducing receptor, gp130. The distinct biological activity of IL-6 family cytokines is controlled by restricted expression of the cytokine-specific receptors, such as IL-6Rα and IL-11Rα, which are expressed by a limited subset of cells[103]. Several cytokines can bind IL-6Rα in addition to IL-6, CNTF[104], IL-30/p28[105,106] and human herpes virus 8

IL-6 (vIL-6)[107], a viral analogue of IL-6 with approximately 25% sequence identity to mammalian IL-6[108]. Receptor promiscuity is thus a common feature of the IL-6 family.

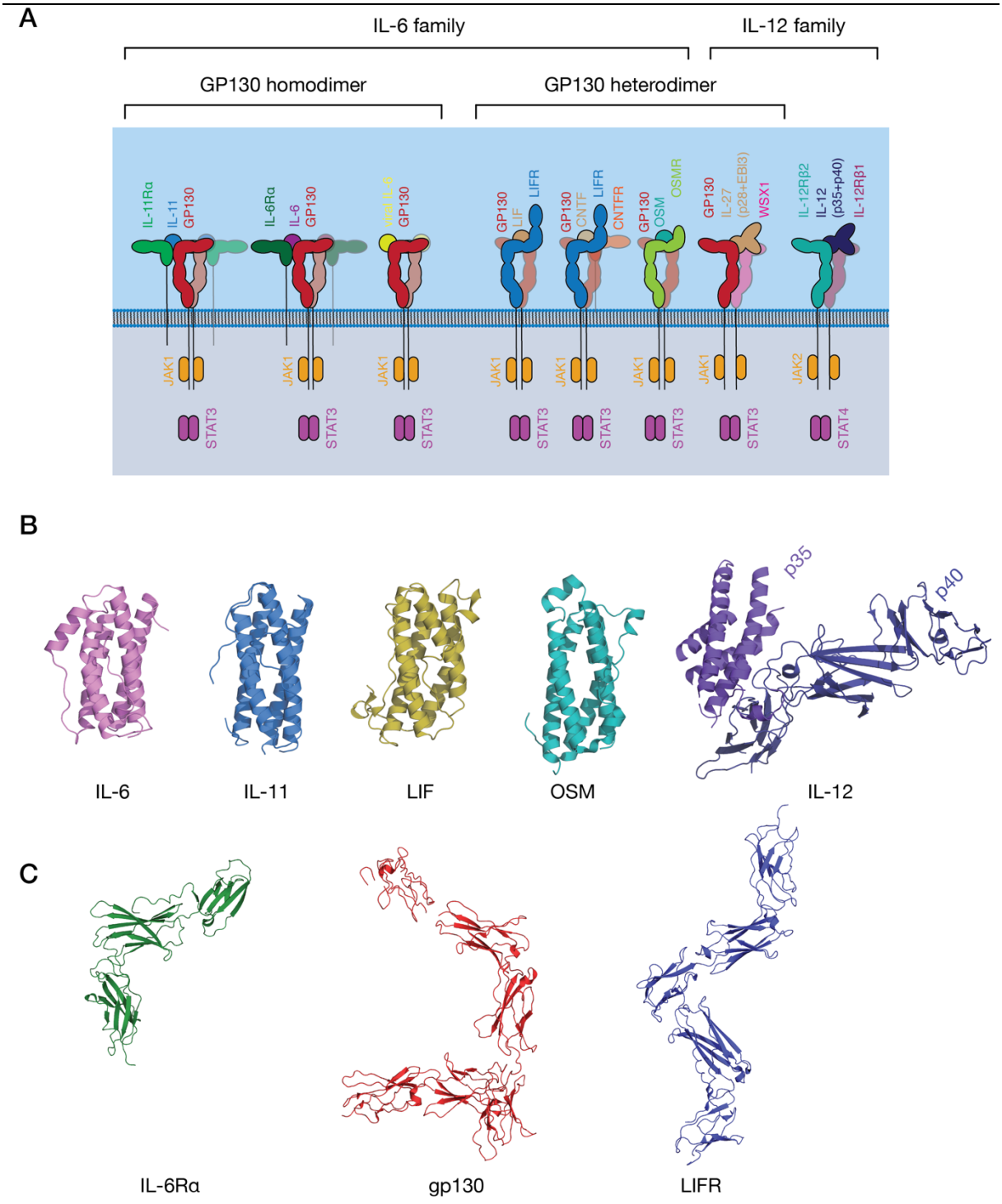

Figure 1.3: The IL-6 family of cytokines.

A) Representative IL-6 family cytokines, showing the diversity in the stoichiometry of signalling complexes employed by the different IL-6 family cytokines. B) The

structure of several IL-6 and IL-12 family cytokines (IL-6, 1ALU[45]; IL-11, 4MHL[109]; LIF, 1LKI[110]; OSM, 1EVS[111]; IL-12, 1F45[55]). C) The structure of two IL-6 family cytokine receptors, IL-6Rα (PDB ID: 1N26), the common signal transducing receptor, gp130 (PDB ID: 3L5H[63]) and the receptor for LIF and several other IL-6 family cytokines, LIFR (PDB ID: 3E0G[71]).

1.2.1 The structure of IL-6 and its receptors

IL-6 is the archetypal IL-6 family cytokine and is the best-characterised IL-6 family cytokine structurally. IL-6 was initially identified under several names in the 1980s[112] as a protein involved in B-cell differentiation[113], a plasmacytoma growth factor[114], and a protein involved in the induction of acute phase proteins in the liver[115]. Subsequent cloning of these proteins showed that they were all identical, thus they were given a common name, IL-6. Structures of IL-6 were solved in 1997[45,116], the structure of IL-6Rα[117] was solved in 2002, and the structure of the IL-6 signalling complex was solved in 2003[74] (Figure 1.3B, C, Figure 1.4Ai). IL-6 is a typical four-α helical bundle cytokine, with the expected up-up-down-down arrangement of α helices, with an additional, short α-helix in the CD loop. The extracellular regions of IL-6Rα consists of three domains[117], an N-terminal Ig-domain, and two membrane-proximal Fn3 domains, which form the IL-6 binding CHR (Figure 1.3C). The N-terminal Ig domain adopts a highly distorted Ig-like fold, and is dispensable for cytokine binding and biological activity[65,74], although there is some evidence that it is required for correct trafficking of the receptor[65]. IL-6 binds the cleft formed by the two Fn3 domains, D2 and D3, which comprise the CHR[74]. C-terminal of the structured extracellular domain, there is a long linker region, predicted to be disordered (52 residues in IL-6), that appears to function as a spacer in the signalling complex between the structured extracellular domains and the membrane[118-120].

Gp130 is the common signal transducing molecule for nearly all IL-6 family cytokines, and some cytokines in the closely related IL-12 family. It was first identified in 1989[121] as the component of the IL-6 signalling complex involved in signal transduction, and subsequently cloned in 1990[122]. Following this, gp130 was

recognised as being a common component of the IL-11[123], OSM[124], LIF and CNTF[125] signalling complexes. Structures of the CHR domains of gp130 became available in 1998[126], and the full-length extracellular region of gp130 in 2010[63] (Figure 1.3C). The extracellular domains of gp130 are those of a typical 'tall' cytokine receptor, consisting of six domains, an N-terminal Ig-like domain, and five Fn3 domains[63]. The first three, membrane-distal domains (D1-D3) are involved in cytokine recognition and complex formation, and are sufficient to bind cytokines and form a complex in solution[74,80]. The membrane-distal domains are also directly involved in gp130 activation, with oncogenic mutations, which result in cytokine-independent activation of gp130 clustering in D2[127]. These mutations are thought to act by disrupting the D2D3 interdomain linker, allowing the receptor to adopt an active conformation in the absence of ligand[128].

The three membrane proximal domains of gp130 (D4-D6) are not directly involved in binding the cytokine, but are required for signal transduction. Deletion of any of the domains results in an inactive receptor[129]. Electron microscopy shows that the membrane-proximal domains are involved in the correct orientation of the intracellular kinases for signal transduction[71,76,130]. In addition to the extracellular domains, gp130 contains a long intracellular domain, which is involved in binding molecules involved in signal transduction. Structurally, little is known about the intracellular domain of gp130, although NMR spectroscopic studies have shown that the intracellular domain is disordered[71]. Kinases bind gp130 at the Box 1 motif in the intracellular domain[84], STAT3[24] and STAT1[131] are the signal transducers used by gp130 cytokines, and cytokine signalling through gp130 is negatively regulated by SOCS3[33,88]. The STAT proteins bind at C-terminal phosphotyrosine residues in the intracellular domain of gp130[132,133], STAT3 binds at Tyr 767, 814, 905 and 915, STAT1 binds at Tyr 905 and 915[134]. SHP2 is also recruited by gp130 in the intracellular domain[135], providing the link between gp130 and the MAPK pathway[136].

1.2.2 The structure of the IL-6 signalling complex

The hexameric structure of the IL-6 signalling complex is shown in Figure 1.4Ai[74]. Prior to the determination of the structure, there was extensive evidence from

analytical ultracentrifugation and electrophoresis that the complex was hexameric, consisting of two copies each of IL-6, IL-6Rα and gp130[67,137,138]. Concurrently, mutagenic studies identified three binding sites on IL-6[67], which were later also seen in the structure of the complex[74]. Site-I is responsible for binding IL-6Rα, site-II is responsible for binding the first molecule of gp130, and site-III is responsible for binding the second molecule of gp130, forming the hexameric signalling complex (Figure 1.4Ai Figure 1.4Aii). Site-I and site-II are positioned on the cytokine in a manner broadly analogous to the receptor-binding sites on growth hormone and form a similar trimeric complex with IL-6, IL-6Rα and gp130, through binding the CHR of IL-6Rα and gp130[40] (Figure 1.4Ai). Site-III is unique to IL-6 family cytokines, and forms a distinct cytokine:Ig domain interaction with D1 of gp130[139]. In the structure, the complex is formed by ten interdependent interfaces between IL-6 and the two receptors, and between the receptors, with the earlier binding events creating composite binding surfaces to enable subsequent receptor recruitment. The structure of the IL-6 signalling complex has aided drug design studies[140], showing its value in the design of novel therapeutics.

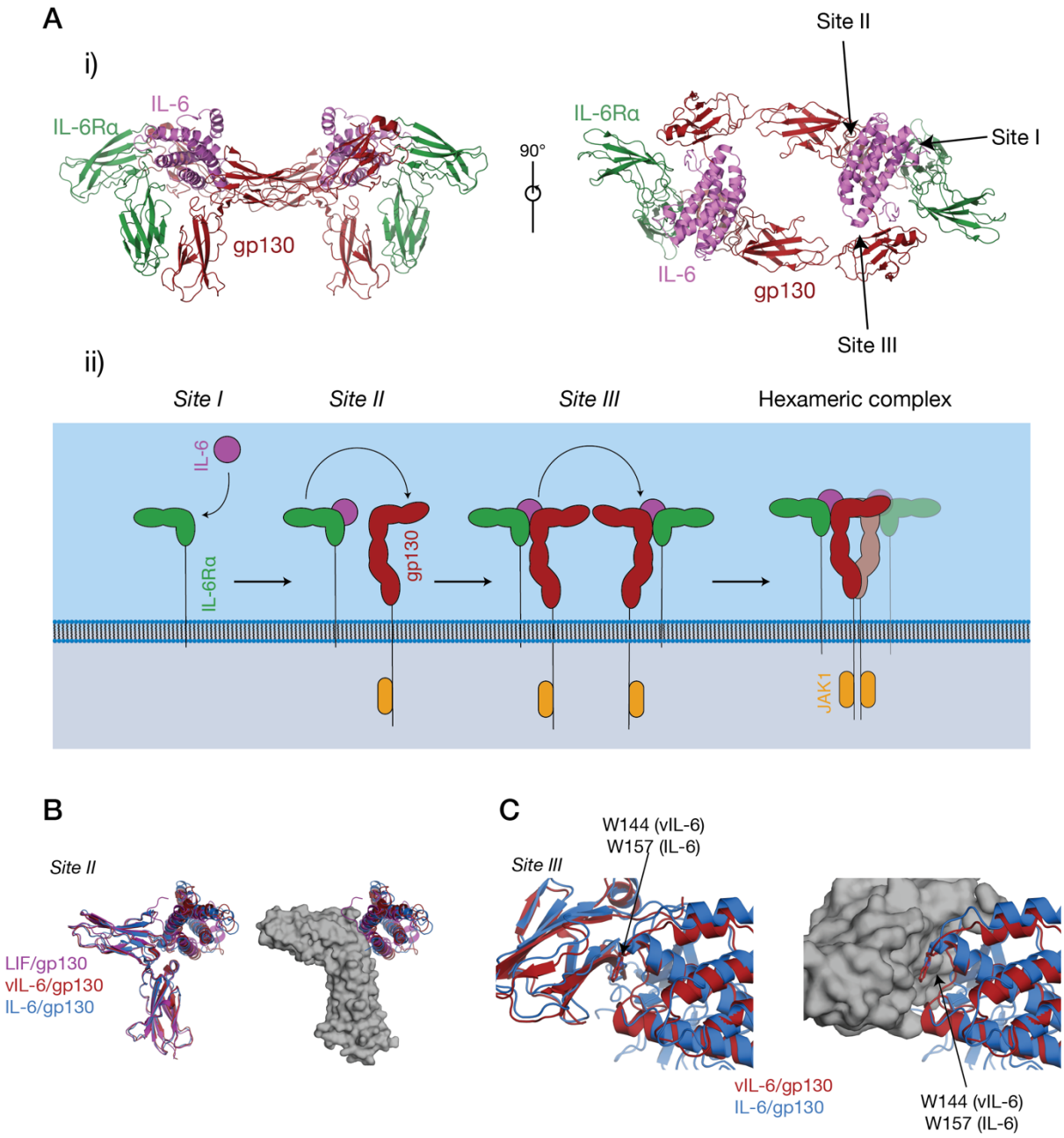

Figure 1.4: The structure of the IL-6 signalling complex.

A) i) Two views of the structure of the complex (PDB ID: 1P9M[74]). The three binding sites on the cytokine (site-I, binding IL-6Rα, site-II, binding gp130, site-III binding gp130), are indicated in the figure. ii) The stepwise assembly of the complex is shown in, with the interactions mediated by each of the binding sites indicated. B) The binding of three IL-6 family cytokines to the CHR of gp130, IL-6, vIL-6 (PDB ID: 1I1R[73]) and LIF (PDB ID: 1PVH[80]). The three cytokines do not induce any rearrangements in the CHR of gp130 but adopt a different pose on the CHR and bind different regions in the interface. C) The binding of IL-6 and vIL-6 to gp130 D1,

the interaction that forms the hexameric complex. The two cytokines engage gp130 D1 in an analogous way. The key tryptophan 'hot-spot' residue in site-III is indicated.

The site-II/CHR region of gp130 is involved in the binding of all gp130-binding cytokines. Alongside the structure of the IL-6 signalling complex, structures were solved of vIL-6 in complex with gp130[73] and LIF in complex with gp130[80]. All three cytokines engage the CHR of gp130 using the site-II region of the cytokine (Figure 1.4B). The structures showed vIL-6, IL-6 and LIF engage distinct binding regions in the CHR of gp130, with the three cytokines adopting a markedly different pose. Surprisingly, the cytokine binding surface of gp130 is extremely rigid, and does not markedly change conformation in response to the binding of different cytokines[80]. The CHR of gp130 presents a large, chemically diverse binding surface, with IL-6, vIL-6 and LIF interacting with different regions on the surface, resulting in each cytokine/gp130 interaction having markedly different thermodynamic properties[80]. The size and 'thermodynamic plasticity'[80] of the CHR of gp130 is thought to result in its promiscuous binding to multiple cytokines[40,80].

IL-6 and vIL-6 interact with the Ig-domain D1 of gp130, and LIF forms a similar, but distinct interaction with Ig-domain D3/Fn3 domain D4 of LIFR through site-III on the cytokine. The interaction between IL-6/gp130 D1 and vIL-6/gp130 D1 is broadly analogous (Figure 1.4C). In both complexes, a key, conserved tryptophan is the major hydrophobic 'hot spot' residue, providing approximately 25% of the buried surface area in the complexes. Likewise, the N-terminus of gp130 forms a short mainchain-mainchain interaction with the AB loop of the cytokine[73,74]. The site-III interface on gp130 D1 is otherwise relatively chemically and structurally featureless[40], providing a low-affinity binding surface that is reliant on prior interactions with other receptors. A similar interaction is formed by LIF, although this interaction is more specific, burying more surface area, and forming more polar interactions[64]. No structural information is available on the gp130 binding epitopes for any other IL-6 family cytokines, including IL-11. Mutagenesis on gp130 shows that IL-11 and IL-6 both require D1 of gp130 for signalling, and bind a similar

epitope in the CHR[141]. Monoclonal antibodies against gp130 have been developed which antagonise signalling through specific cytokines, including IL-11 and IL-6-specific neutralising antibodies, which implies that each cytokine engages gp130 using a structurally different mechanism[142], however the structural basis of this is currently unknown.

No high-resolution structures are available of IL-6 family cytokine/complete extracellular receptor complexes. All complexes described above utilized heavily truncated forms of the receptors to facilitate crystallization. Electron microscopy (both cryogenic and negative stain) has been used to study several complexes, including the IL-6 complex[76,143], the LIF complex[71] and the IL-11 complex[130]. The resolution in these studies is too low to see structural detail of the complex, they reveal a common 'doughnut-shaped' architecture, with the 'legs' of the tall cytokine receptors LIFR and gp130 bent to create a complex with a hole in the middle. The details of the gp130:gp130/LIFR:gp130 contacts in the complex remain to be elucidated and will require the determination of high-resolution structures of complete, extracellular complexes.

Several studies have suggested a tetrameric arrangement for the IL-6 signalling complex, consisting of two copies of gp130, one copy of IL-6 and one copy of IL-6α. This model was based on modelling that pre-dates high-resolution structural information on the IL-6 complex[144,145], and on mutagenesis on gp130[146]. To reconcile this with the existence of a hexameric complex, it was proposed that the a tetrameric complex represented the active signalling form of the IL-6 complex, and the hexameric complex represented an inhibited form of the complex[144]. Subsequent biophysical studies of the IL-6 complex showed that the formation of the hexameric signalling complex is very high affinity[74], and that complex formation is highly cooperative[74,138]. This strongly suggests that IL-6 forms a hexameric complex , with two copies each of IL-6, IL-6Rα and gp130, and that this is the active signalling complex.

1.2.3 Alternative mechanisms of IL-6 signalling

In addition to 'classic' IL-6 signalling through membrane-bound IL-6Rα and gp130, IL-6 can also bind a soluble form of IL-6Rα (sIL-6Rα). The IL-6/sIL-6Rα complex can engage membrane-bound gp130, allowing the stimulation of cells that do not express IL-6Rα, a process known as *trans* signalling[121,147] (Figure 1.5). The soluble IL-6Rα is generated by the membrane-bound metalloproteases, ADAM10 and ADAM17[147]. The physiological antagonist of *trans* signalling is sgp130, which can bind to the IL-6Rα/IL-6 complex extracellularly, neutralising it[148]. IL-6 *trans* signalling is implicated in IL-6 mediated inflammation[147]. In addition to classic and *trans* signalling, recent studies have suggested a signalling mechanism, *trans*-presentation, through which IL-6 binds IL-6Rα on a 'transmitting cell', which then presents the IL-6/IL-6Rα complex to gp130-expressing cells (Figure 1.5)[149,150]. This mechanism has been shown to be critical for the differentiation of T_H17 T helper cells, which is presented IL-6/IL-6Rα in *trans* by dendritic cells[149]. *Trans* presentation has been shown to be possible for IL-11, but does not have a defined biological role[150]. *Trans* presentation has not yet been characterised structurally, indeed; such a signalling mode would require large rearrangements of the IL-6 signalling complex components. Other cytokines such as IL-2[151] and IL-15[152] can utilize similar *trans* presentation mechanisms, where dendritic cells present the cytokine in *trans* to antigen-specific T-cells, although this signalling mode is clearly allowed by the structure of the IL-2/IL-15 signalling complexes[49,153].

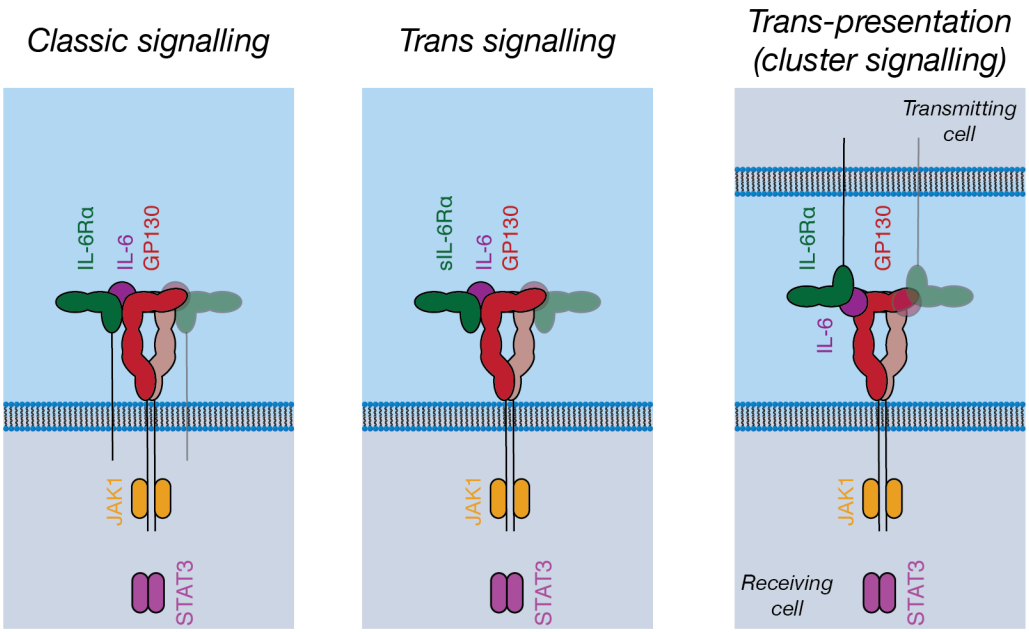

Figure 1.5: Signal transduction by IL-6.

IL-6 can activate intracellular pathways in three ways, 'classic' signalling, in which IL-6 binds to membrane-bound IL-6Rα, which subsequently binds to membrane-bound gp130 on the same cell), 'trans' signalling, in which IL-6 binds to soluble IL-6Rα, subsequently binding membrane-bound gp130, and 'trans-presentation', in which IL-6 binds membrane-bound IL-6Rα on a 'transmitting cell' which subsequently engages gp130 on a neighbouring ('receiving') cell, activating intracellular signalling pathways.

1.2.4 Related receptors – domeless and the IL-12 family

A distant homologue of gp130 has been identified in *Drosophila melanogaster*, the receptor *domeless* (*dome*)[154], which is the likely evolutionary ancestor to all IL-6 family cytokine receptors[155]. *Dome* shares a similar domain structure to gp130 and LIFR, and a putative CHR has been identified in *Dome*, albeit with low sequence identity to the CHR in gp130. A putative ligand for *Dome*, *Unpaired-3* (*Upd3*)[156] has also been identified, alongside JAK kinases (*Hopscotch*) and STAT transcription factors (*Marelle*)[157]. The *Dome-Hopscotch* pathway has been shown to have several roles in *Drosophila* physiology, including in responding to bacterial infection[158], in oogenesis[158], in hemocyte proliferation[159] and in tissue development[160,161], showing that cytokine pleiotropy is a common feature in metazoans. Neither *dome* or *Upd3* have been studied structurally, although recombinant *Upd3* has been produced,

and has been shown by circular dichroism spectroscopy to have a predominately α-helical secondary structure[162]. The JAK-STAT pathway in zebrafish has also been studied, with zebrafish possessing a mammal-like cohort of cytokines, with relatives of all extant mammalian cytokine families present, suggesting that an increase in diversity in cytokines and receptors occurred with the evolution of the adaptive immune system in vertebrates[163,164].

The IL-12 family of cytokines is closely related structurally to the IL-6 family of cytokines, indeed, it has been previously suggested that a clear distinction between the two families is almost impossible[165]. In contrast to the IL-6 family, the IL-12 family cytokines consist of two subunits, a smaller four-α helical subunit, and a larger all-β protein cytokine receptor subunit (Figure 1.3B), which is analogous to the α receptors for IL-6 and IL-11. For example, IL-12 consists of two subunits, p35, analogous to a four-α helical bundle cytokine, and p40, which resembles a class I cytokine receptor[55]. Several IL-12 family cytokines can utilise gp130 as a signal transducer, and one IL-12 family cytokine, p28 (IL-30) can utilize IL-6Rα as the 'cytokine-receptor' subunit[105,106]. Broadly, this suggests an evolutionary relationship between the IL-6 and IL-12 families of cytokines and underscores the promiscuity of cytokine receptors in the IL-12/IL-6 superfamily.

1.2.5 The structure of IL-11

In contrast to IL-6, LIF and other IL-6 family cytokines, little is known about the structure of IL-11. Our laboratory reported the structure of IL-11 in 2014[109] (Figure 1.6A), showing that IL-11 is structurally distinct from IL-6. IL-11 is approximately 5 Å longer than IL-6, suggesting differences in binding mode and geometry. Likewise, the IL-11Rα binding site (site-I) and the first gp130 binding site (site-II) identified through mutagenesis are significantly different in chemical character compared with IL-6, with site-I more hydrophobic. Site-II in IL-11 likely interacts with gp130 through four arginine residues in site-II which are unique to IL-11[109]. No high-resolution structural information on the structure of IL-11Rα or the IL-11 signalling complex is available in the literature, although sequence analysis[123,166] suggests that the IL-6Rα and IL-11Rα receptors are overall broadly structurally similar. Other than

IL-11, no other cytokines are known to interact with IL-11Rα. The IL-11 signalling complex, like the IL-6 signalling complex, is hexameric[167]. Contemporaneous mutagenic studies[168-170] also identified site-I, II and III on IL-11 (Figure 1.6Bi, Bii), suggesting that the two cytokines form an active signalling complex using a broadly similar mechanism. A low-resolution (~30 Å) cryoEM map of the extracellular IL-11 signalling complex is available[130] (Figure 1.6Ci). The map shows that the overall arrangement of the complex is broadly similar to the IL-6 signalling complex (Figure 1.6Cii), although the details of complex formation are not clear at this resolution.

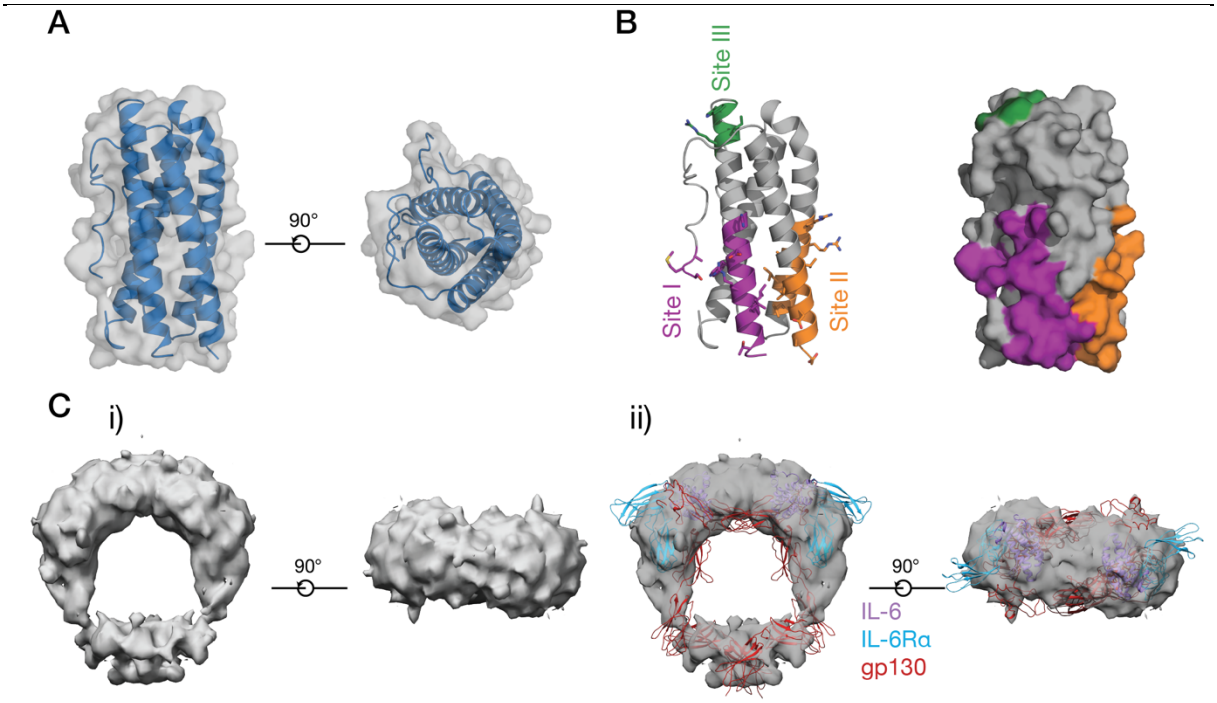

Figure 1.6: The structure of IL-11 and the low-resolution structure of the IL-11 signalling complex.

A) two views of the structure of IL-11 (PDB ID: 4MHL[109]). B) receptor-binding sites on IL-11, which have been identified previously through mutagenic studies on human and mouse IL-11. C) A low-resolution EM map of the extracellular IL-11 signalling complex (EMD-1223[130]) i), additionally shown overlaid with a model of the extracellular IL-6 signalling complex, ii) (generated from PDB IDs: 3L5H[63], 1P9M[74]).

1.3 Biological roles of IL-11

IL-11 is a pleiotropic cytokine with numerous roles in physiology and disease[171]. IL-11 was first identified in 1990, following the discovery of a protein factor that

stimulated a murine plasmacytoma cell line previously thought to be IL-6 dependent[5]. The following year, IL-11 was also identified as a factor secreted from a bone marrow derived cell line culture, which inhibited adipogenesis in preadipocytes[172,173], thus the pleiotropic nature of IL-11 signalling was appreciated early. Roles have subsequently been identified for IL-11 signalling in haematopoiesis, bone homeostasis, cancer and fibrotic diseases[171]. The major biological source of IL-11 currently remains unclear and is a subject of ongoing investigation[109].

1.3.1 IL-11 in haematopoiesis

IL-11 was identified early as a potent hematopoietic factor, acting synergistically in culture with other cytokines, such as IL-3[174,175] and IL-4[176]. In particular, IL-11 was found to have a role *in vitro* in megakaryocytopoiesis, causing the maturation of megakaryocytes, large cells which form platelets[174]. Thus, IL-11, synergistically with other cytokines, was identified as a key factor in the production of platelets. Investigation of the *in vivo* activity of IL-11 followed, finding that IL-11 alone was a potent agent to trigger platelet production. In mice, IL-11 alone is a potent hematopoietic stimulator following radiation therapy and chemotherapy, and markedly increases platelet levels[177]. Recombinant IL-11 is approved in humans to treat thrombocytopenia following radiation treatment[178]. In addition to its well-characterised role in megakaryocytopoiesis , IL-11 has other roles in haematopoiesis[179], for example, in lymphopoiesis[180], in erythropoiesis[181] and in myelopoiesis[182].

1.3.2 IL-11 in bone development

IL-11 has a well-characterised role in bone development and bone homeostasis[183]. IL-11 signalling has a role in promoting osteoblast differentiation, serving to promote bone formation; IL-11Rα knockout mice exhibit impaired bone differentiation[184-186]. Mutations in the genes for IL-11 and IL-11Rα have also been identified which result in abnormalities in the skeletal system. Several genetic studies have found that mutations in the genes for IL-11 and IL-11Rα are associated with a reduction in human height[187,188], showing that IL-11 signalling has

a role in regulating growth. Likewise, similar studies have identified a genetic variant in the gene for IL-11, resulting in a substitution mutation (R112H), which is associated with osteoarthritis and a reduction in height[188,189]. Biochemical characterisation of the mutant has shown that it does not alter the biological activity of IL-11, but compromises the stability of the protein[190].

Over the past decade, a number of studies have identified mutations in the gene for IL-11Rα, *IL11RA*, which cause a genetic disease associated with craniosynostosis[191-193]. Craniosynostosis is a condition in which bone plates in the skull fuse too early, resulting in facial abnormalities and an abnormally shaped skull. The disease is rare, and has been found in families with diverse geographic origins[191]. Generally, the disease occurs as a result of point substitution mutations in the extracellular domains of IL-11Rα, and occur in regions distant from the cytokine or receptor binding sites[191,194]. Several of the mutations have been shown to impair correct folding and secretion of the receptor[194], although in the absence of a high-resolution structure of IL-11Rα, the precise structural consequences of the mutations have remained unclear.

1.3.3 IL-11 in the lung

IL-11 is highly expressed as a consequence of viral induced asthma[195], and overexpression of IL-11 in the airways of mice results in remodelling of the airways, inflammation and asthma-like symptoms[196]. Subsequent studies extended these findings, showing that IL-11 signalling is critical for a T_H2-mediated inflammatory response in the lung[197], and that inhibition of IL-11 signalling in the lung alleviates inflammation, implying that IL-11 signalling is a therapeutic target in asthma[198]. Similarly, IL-11 has been shown to drive lung inflammation in a murine model of *Mycobacterium tuberculosis* infection[199]. These studies show a role for IL-11 signalling in lung inflammation and show that targeting IL-11 signalling is a potential strategy for modulating this inflammation.

1.3.4 IL-11 in reproduction

An additional physiological role for IL-11 is in reproduction[200]. Female knock-out mice lacking the gene for IL-11Rα are infertile, and cannot undergo the uterine transformations required for embryo survival[201]. Likewise, IL-11 and IL-11Rα have been localised to reproductive tissues in early pregnancy in primates, suggesting a role in placentation and decidualization[202]. Related to this, inhibition of IL-11 signalling inhibits decidualization and prevents pregnancy in mice[203] and defects in the production of IL-11 have been associated with anembryonic pregnancy, a cause of miscarriage[204]. Related to its role in placentation, IL-11 signalling inhibits and regulates invasion of extravillous trophoblasts (EVT), cells which are key in placentation for the formation of blood vessels[205-207]. Thus, elevated IL-11 is associated with preeclampsia, a disease where placentation is impaired, resulting in hypertension[205]. Together, these studies show that IL-11 has a key role in driving the tissue transformations that occur as a result of pregnancy.

1.3.5 IL-11 in disease

A number of studies have identified or suggested a role for IL-11 signalling in a number of cancers, including gastrointestinal (GI) cancer[208,209] and breast cancer[210]. STAT3 activation by IL-11 drives several cancer hallmarks[211,212] including cell survival, metastasis and invasion[210].

IL-11 signalling has a well-described role in gastrointestinal cancer. IL-11 levels are significantly higher in a murine model of gastric cancer[209], and IL-11 is the major factor that drives STAT3 activation and corresponding inflammation in murine xenograph models of the cancer[208]. Inhibition of IL-11 signalling results in a reduction of tumour size, validating IL-11 signalling as a therapeutic target. A role for IL-11 signalling in breast cancer has been less well described, but elevated levels of IL-11 are associated with poor patient outcomes[210], and IL-11 and IL-6 is associated with breast cancer metastasis into bone[213]. Consistent with its role in driving tissue transformations in the female reproductive system, elevated IL-11 is associated with endometrial cancer, and is associated with increasing tumour grade[214]. Elevated levels of IL-11 are found in several other types of cancer[215],

including pancreatic cancer[216], skin cancer[217] and bone cancer[218], although a precise role for IL-11 signalling in many of these cancers remains to be defined. Regardless, a broad link between IL-11-driven inflammation and cancer is clear[219], and IL-11 signalling thus presents novel therapeutic targets in cancer.

IL-11 *trans* signalling has recently been identified[220]. The membrane metalloprotease ADAM10 can cleave IL-11Rα to produce sIL-11Rα, which can engage gp130 in an analogous manner to sIL-6Rα[220]. So far, no clear biological role has been ascribed to IL-11 *trans* signalling. Gastrointestinal tumorigenesis is a result of classic IL-11 signalling, not *trans* signalling[221]. Likewise, the inhibition of IL-11 trans signalling in mice does not result in infertility, showing that IL-11 classic signalling is required for fertility in mice[222].

IL-11 signalling is thought to have an anti-inflammatory role in some diseases. IL-11 regulates the production of pro-inflammatory cytokines, such as IL-12, TNF and IL-1, and inflammatory mediators such as nitrous oxide[223,224]. Likewise, IL-11 signalling inhibits the action of the pro-inflammatory transcription factor, NF-κB, and results in the expression of inhibitors of NF-κB[225]. IL-11 signalling has been shown to have a beneficial or regulatory role in some inflammatory diseases. For example, in arthritis[226,227] and in murine models of liver inflammation[228], IL-11 has been shown to decrease the levels of inflammatory cytokines. Similarly, SNPs in the promoter region of the IL-11 gene are also associated with inflammatory bowel disease[229].

IL-11 is also implicated in fibrosis of the heart[230], liver[231] and lung[232,233]. Fibrosis is the generation of excess connective tissue, and is a hallmark of several diseases, including late-stage cardiovascular disease, and liver diseases such as non-alcoholic liver disease. In the heart, IL-11 has recently been identified as a key fibrotic factor, acting downstream of the main fibrotic factor TGFB1, driving fibrotic protein synthesis in an autocrine manner[230]. IL-11 has a similar role in driving inflammation and fibrosis of the liver. Interestingly, in both cases, the effect is driven by non-canonical signalling via the MAPK/ERK pathway, not the canonical JAK-STAT pathway. In models of heart and liver fibrosis, inhibition of IL-11 signalling by

inhibitory antibodies against IL-11Rα has a protective effect, validating IL-11 signalling as a therapeutic target in fibrosis[230,231]. Surprisingly, canonical IL-11 signalling via STAT3 has previously been ascribed to have a cardioprotective role, inhibiting cardiovascular fibrosis and preventing cardiovascular remodelling following myocardial infarction, a contradictory result[234]. This may be a consequence of the source of IL-11 used in either study, as it was shown that human IL-11, previously used to show that IL-11 is cardioprotective, does not activate mouse cardiac fibroblasts, while murine IL-11 strongly activates cardiac fibroblasts[230]. More broadly, this may reflect an inadequate understanding of the species-specific effects of IL-11, or differences in signalling in humans as compared with mice. Alternatively, it may reflect different roles for IL-11 in response to different cardiovascular stresses.

Over the past three decades since its discovery, numerous roles have been identified for IL-11, in diverse aspects of human physiology and disease. This work collectively validates IL-11 as a therapeutic target in several diseases and underscores the need to fully understand the structural basis of IL-11 signalling, to guide the design of novel IL-11 signalling inhibitors.

1.4 Therapeutic targeting of cytokine signalling

Given the role of cytokine signalling in numerous pathological conditions there is broad interest in the development therapeutic agents to modulate cytokine signalling. Generally, inhibition can occur at several points in the cytokine signalling pathway – either in preventing the protein-protein interactions on the cell surface, or by targeting components of the signal transduction machinery within the cell. Likewise, due to the potent biological effects of cytokines, recombinant forms of the cytokines are used as drugs, particularly in immunocompromised individuals.

This section will review several approaches for therapeutic modulation of cytokine signalling. These include small-molecule kinase inhibitors, widely used as drugs, small molecules that inhibit cytokine signalling through gp130, cytokines used as biologic drugs, and monoclonal antibodies targeting cytokine signalling. This

section will close with a discussion of modulators of IL-2 signalling, as IL-2 has been arguably the best explored cytokine from a drug design perspective.

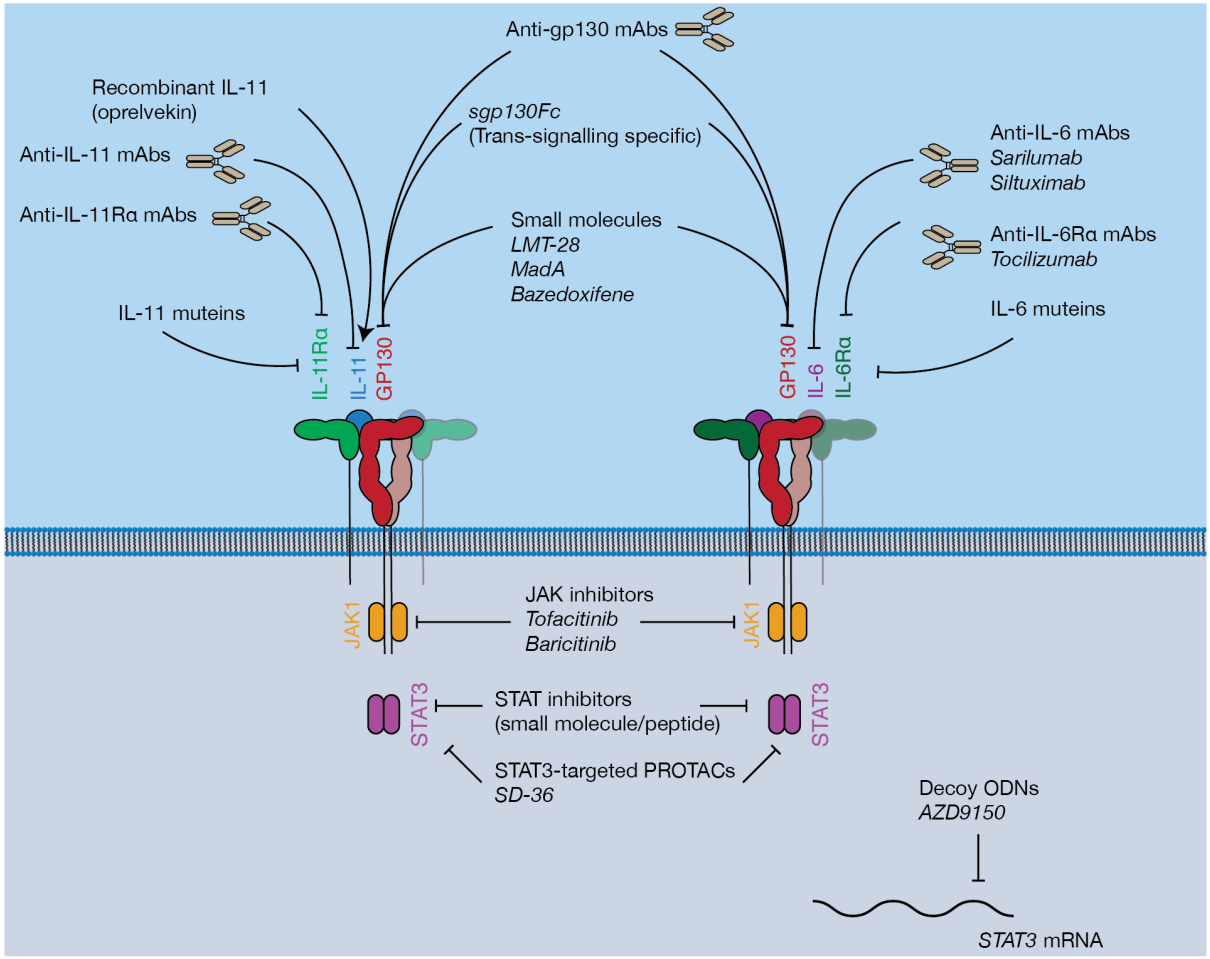

Figure 1.7: Pharmacological approaches to target IL-6 and IL-11 signalling. These include protein antagonists, such as mutants and antibodies, small molecule PPI inhibitors targeting gp130, recombinant IL-11, small molecule inhibitors of proteins in the intracellular JAK-STAT pathway, and decoy oligodeoxynucleotides (ODNs) targeting the *STAT3* mRNA.

1.4.1 Small molecules

1.4.1.1 Inhibitors of intracellular signal transducing proteins

JAK inhibitors are widely used, orally bioavailable, drugs to treat various diseases. These include diseases such as blood cancers and inflammatory diseases, associated with excess cytokine signalling[235] (Figure 1.7). Six JAK inhibitors are used clinically, with several more under clinical development. For example, the

JAK1/2 selective inhibitor ruxolitinib[236] is used to treat a group of rare blood cancers associated with an activating mutation in JAK2. Similarly, tofacitinib (non-selective) and baricitinib (selective for JAK1/2) are JAK inhibitors are used to treat the inflammatory disease rheumatoid arthritis, a consequence of excessive signalling from inflammatory cytokines such as IL-6[237,238]. JAK inhibitors are undergoing clinical trials for a broader array of inflammatory diseases[239]. Challenges with developing JAK inhibitors are largely a consequence of the inherently non-specific nature of the drugs. Indeed, developing inhibitors for a specific kinase has proved challenging. JAK inhibition may be associated with severe side effects, including opportunistic viral infections, likely a consequence of inhibition of interferon-mediated protective antiviral signalling[240]. Similarly, due to the criticality of cytokine driven JAK signalling in haematopoiesis, JAK inhibitors have been noted to cause mild anaemia and neutropenia[241,242]. Regardless, JAK inhibitors are widely used, and efforts to develop novel JAK inhibitors, particularly inhibitors which are selective for a specific kinase, are ongoing.

Inhibitors of STAT activity are in various stages of development[243]. These inhibitors are generally peptides or small molecules designed to inhibit STAT dimerization[244,245], or decoy oligodeoxynucleotides (ODNs) designed to target either the STAT gene directly, or genes that are a target of an activated STAT[246]. Phase I and II trials have been conducted on several drug candidates targeting STAT3[247,248]. Recently, a small-molecule proteolysis targeting chimera (PROTAC), SD-36[249] has also been described for STAT3, which selectively targets STAT3 over other STAT family members for proteolysis in the proteasome. Direct inhibition of activated STATs is at a less advanced stage compared with kinase inhibitors, or drugs targeting the cytokine/receptor interaction directly, current inhibitors are of low potency and have poor pharmacokinetic properties[250]. Generally, direct targeting of STATs does not have clear benefits over existing therapeutic strategies.

1.4.1.2 Inhibitors of signalling through gp130

Several small molecules have been described that are believed to bind to gp130 and inhibit the protein-protein interactions (PPIs) that result in complex formation

(Figure 1.7). Targeting protein-protein interactions using small molecules is inherently difficult, as they present large, flat binding surfaces which are inherently difficult to target with small molecules[251]. Madindoline A (MadA) was a natural product isolated from *Streptomyces nitrosporeus* culture, and shown to inhibit the activity of IL-6 and IL-11 in a culture model[252]. MadA was used in subsequent studies, and it was shown that it inhibits the action of IL-6/IL-11, but not LIF in bone resorption and macrophage differentiation[253], and that MadA binds specifically to gp130, with a low affinity (288 μM)[254]. Chemical synthesis of MadA is difficult[255], and it is produced in low yields by bacterial fermentation, limiting its potential as a drug candidate. An additional IL-6/IL-11 signalling inhibitor binding gp130, LMT-28 was identified by screening a library of approximately 1000 compounds[256]. Computational docking shows that LMT-28 binds to D1 of gp130[257], specifically inhibits IL-6/IL-11 driven cell proliferation, and blocks IL-6-driven inflammation *in vivo*[256]. Likewise, the molecule SC144[258] also inhibits the activity of IL-6 and LIF, likely through binding the CHR of gp130, and suppresses cancer growth in human ovarian cancer xenographs[259].

A final gp130 inhibitor, the drug bazedoxifene, was identified through an *in silico* screen on the IL-6/gp130 site-III interface[260]. Bazedoxifene is an FDA-approved selective estrogen receptor modulator used clinically in combination with other drugs to treat osteoporosis in elderly women[261]. Following the initial identification of bazedoxifene as a gp130 inhibitor, it has been shown to suppress STAT3 activation through IL-6 and inhibit tumour growth in a murine model of rhabdomyosarcoma, a soft-tissue sarcoma[262] and inhibit the proliferation of IL-6 dependent cell lines[263]. Bazedoxifene has also recently been shown to be an effective antagonist of STAT3 activation by IL-11 in human cancer cell lines, and reduce the tumour burden in murine models of gastric cancer[140]. Likewise, bazedoxifene has also been shown to inhibit IL-6 signalling in cell line models of triple negative breast cancer[264]. Despite the challenges, small molecule modulation of these PPIs is potentially invaluable therapeutically. Small molecule inhibitors are more specific for signalling through specific cytokines compared with JAK inhibitors, would likely be cheaper, be orally

bioavailable, and have a shorter half-life compared with biologic therapies, which is beneficial in the event of serious adverse events[265].

1.4.2 Biologics

1.4.2.1 Recombinant cytokines

Recombinant cytokines are used as therapeutics for their effect on the hematopoietic system, either to supplement a deficiency, or to stimulate the hematopoietic system. The first cytokine to be used therapeutically was GH, used to treat GH deficiency in children, which resulted in growth defects[42]. Initially, GH was purified from an endogenous source (pituitary glands from human cadavers) as porcine or bovine GH is poorly active in humans[266,267]. GH derived from this source was used therapeutically from the late 1950s, but was extremely scarce, thus, an early success of recombinant DNA technology was the production of large amounts of biologically active recombinant GH[268], which was FDA-approved in 1985. Likewise, recombinant EPO is used to treat anaemia and increase red blood cell levels, for example, in patients with kidney disease undergoing dialysis[269,270]. In a similar manner, the colony stimulating factor, G-CSF, is widely used to increase neutrophil levels following chemotherapy[271] thus allowing the tolerance of higher doses of chemotherapy[272]. Generally, with some exceptions, recombinant cytokines have not seen wide use therapeutically. Although rare, long-term treatment with recombinant cytokines can result in the generation of endogenous antibodies against the cytokine[273]. For example, long-term treatment with EPO can lead to the production of anti-EPO antibodies, resulting in severe anaemia[274]. More generally, the pleiotropic nature of many cytokines may result in unpredictable and intolerable inflammation-associated side-effects, which limits the use of recombinant cytokines in the clinic[4,275].

As discussed above, IL-11 has well-described hematopoietic activity. As a result, recombinant human IL-11 (oprelvekin) has undergone clinical trials[178,276], and was FDA-approved in 1998[277] for the treatment of thrombocytopenia (low platelet levels) in myelosuppressive chemotherapy, as a substitute for platelet transfusions. Oprelvekin has also undergone a trial for thrombocytopenia in myelodysplastic

syndrome, in which the bone marrow fails to properly mature blood cells[278]. Oprelvekin is, however, not widely used, both for reasons of cost[279] and due to toxicity associated with oprelvekin treatment, which includes mild anaemia, periostitis, edema and in some cases neuropathy[280,281]. This toxicity can be managed by limiting the dose of oprelvekin[282]. IL-11 also has anti-inflammatory properties, thus oprelvekin has also undergone small clinical trials in inflammatory bowel disease[283] and rheumatoid arthritis[284]. Oprelvekin has not been approved or undergone extensive clinical trials for either of these diseases.

1.4.2.2 Monoclonal antibodies

Monoclonal antibodies (mAbs) are a major drug class, with over 80 mAbs on the market for a variety of diseases, and 570 in various stages of clinical development[285]. mAbs are used clinically to target cytokine signalling. These include basiliximab an IL-2Rα mAb used to treat kidney transplant rejection[286], ustekinumab[287]and risankizumab[288] which are mAbs against the p40 subunit of IL-12/IL-23, used to treat psoriasis. mAbs are also used to target IL-5 signalling[289], for example, the anti-IL-6Rα mAb tocilizumab[290] and sarilumab[291]and the anti-IL-6 mAb siltuximab[292] which are used to treat several diseases including rheumatoid arthritis and kidney cancer (Figure 1.7). Antibodies targeting IL-6 signalling inhibitors are also used to treat cytokine release syndrome ('cytokine storms'), a severe and potentially fatal inflammatory immune reaction caused by hyper-activated T-cells and frequently associated with elevated serum IL-6[293,294]. Viral infections can induce cytokine storms, for example influenza[295] and the coronavirus (CoV) severe acute respiratory syndrome (SARS)-CoV[296,297]. IL-6 signalling inhibitors are a promising treatment for severe inflammation caused by SARS-CoV-2, the cause of the 2020 pandemic of coronavirus disease 2019 (COVID-19)[298,299]. Tocilizumab is currently undergoing expedited clinical trials to establish if it is effective in treating severe and critical COVID-19[a].

[a] Clinical trials ChiCTR2000029765, ChiCTR2000030894, NCT04315480.

Antibodies against gp130 have been described[142] which can specifically antagonise signalling through a specific cytokine or cytokines. The structural basis of this specificity is currently unknown, although epitope mapping studies have been conducted on the antibodies[142,300], which show that the IL-11-specific mAb binds the membrane proximal region (D4D6) of gp130, not at the CHR. The OSM/LIF-specific, CNTF-specific and broadly neutralising mAbs bind at the CHR, presumably sterically interfering with cytokine binding. Antibodies against IL-11[233,301] and IL-11Rα[231,302,303] have been described and several antibodies binding IL-11Rα have been patented[b]. The mechanism of action of these antibodies is not described in the literature.

Surprisingly, there is little published information on the structural mechanism of action of approved mAbs targeting cytokine signalling. The exception is a structure of the Fab fragment of basiliximab in complex with IL-2Rα, showing the formation of an extensive, chemically diverse, contact between the Fab and IL-2Rα, allowing the Fab to out-compete the native ligand, IL-2 for IL-2Rα[304]. There are several examples of antibodies developed targeting components of the IL-2/IL-15 signalling complexes[305-307] (discussed below), IL-12/IL-23[56,308], and the IL-3/β_c family of cytokines[309,310]. For example, two antibodies targeting the IL-3 family of cytokines, CSL362[309] (targeting IL-3Rα) and CSL311[310] (targeting β_c) have been structurally characterised, showing that the antibodies sterically occlude binding by IL-3 to IL-3Rα or IL-3/IL-5/GM-CSF to β_c.

1.4.2.3 Soluble gp130

Many of the deleterious, pro-inflammatory effects of IL-6 signalling are believed to be modulated by *trans* IL-6 signalling modulated by cleaved, soluble IL-6Rα[147]. The side effects of existing treatments targeting IL-6 signalling are believed to result from a blockade of classic signalling, resulting in an increased susceptibility to infections, due to the key role for IL-6 signalling in responding to infection[134,311]. Soluble gp130 (sgp130) is the physiological antagonist of IL-6 *trans* signalling[148],

[b] US patents 9,340,618 and 9,796,782, assigned to CSL Limited.

and a fusion protein of sgp130 with an Fc antibody fragment (sgp130Fc) is currently under development as an IL-6 *trans*-signalling specific inhibitor[134]. Sgp130 has been studied in animal models of several inflammatory diseases including in several cancers[312,313], arthritis[314,315], inflammatory bowel disease[316,317] and pancreatitis-associated lung inflammation[318]. In animal models, blockade of IL-6 *trans* signalling does not alter the IL-6 dependent response to infection[311]. Sgp130Fc is currently in a phase II clinical trial for colitis[134]. An anti-*trans* signalling nanobody has also been developed[319] which specifically recognises an epitope formed between IL-6 and IL-6Rα. IL-11 *trans* signalling has not been ascribed the same biological significance as IL-6 *trans* signalling, regardless, sgp130Fc is used as a tool to study IL-11 *trans* signalling[220], and may be a useful therapy in the case that IL-11 *trans* signalling is found to be important pathologically.

1.4.2.4 Designed proteins

Recent years has seen the widespread application of *de novo* protein design in generating novel cytokine signalling antagonists, agonists and modulators. In the past decades, systematic mutagenesis or phage display was used to generate antagonistic variants of IL-6, IL-11 and LIF by altering affinity to IL-6Rα, IL-11Rα or to LIFR, while abolishing affinity to gp130[198,320,321]. There are several examples of non-cytokine-like proteins which have been engineered to activate and modulate signalling through EPOR. Examples include diabodies, which bind to and induce dimerization of EPOR, and result in a cellular response, with precise tuning of the dimer geometry resulting in diabodies which selectively agonise, partially agonise or antagonise EPO signalling[322]. Similarly, agonists, partial agonists and antagonists of EPO signalling have been designed based on a designed ankyrin repeat protein (DARPin) scaffold, allowing fine control of the topology of EPOR signalling dimers[323]. Both studies[322,323] hint at an exciting possibility – that protein design allows the generation of specific or partial agonists of cytokine signalling, allowing fine control of cytokine signalling, and a sophisticated cytokine pharmacology analogous to that currently possible with G-protein coupled receptors (GPCRs).

1.4.3 Case study – IL-2 signalling modulators

IL-2 is a critical cytokine in the immune system[324], and is arguably the cytokine which has best-explored from a drug-design perspective[325], and thus is illustrative of the approaches available to therapeutically target cytokine signalling.

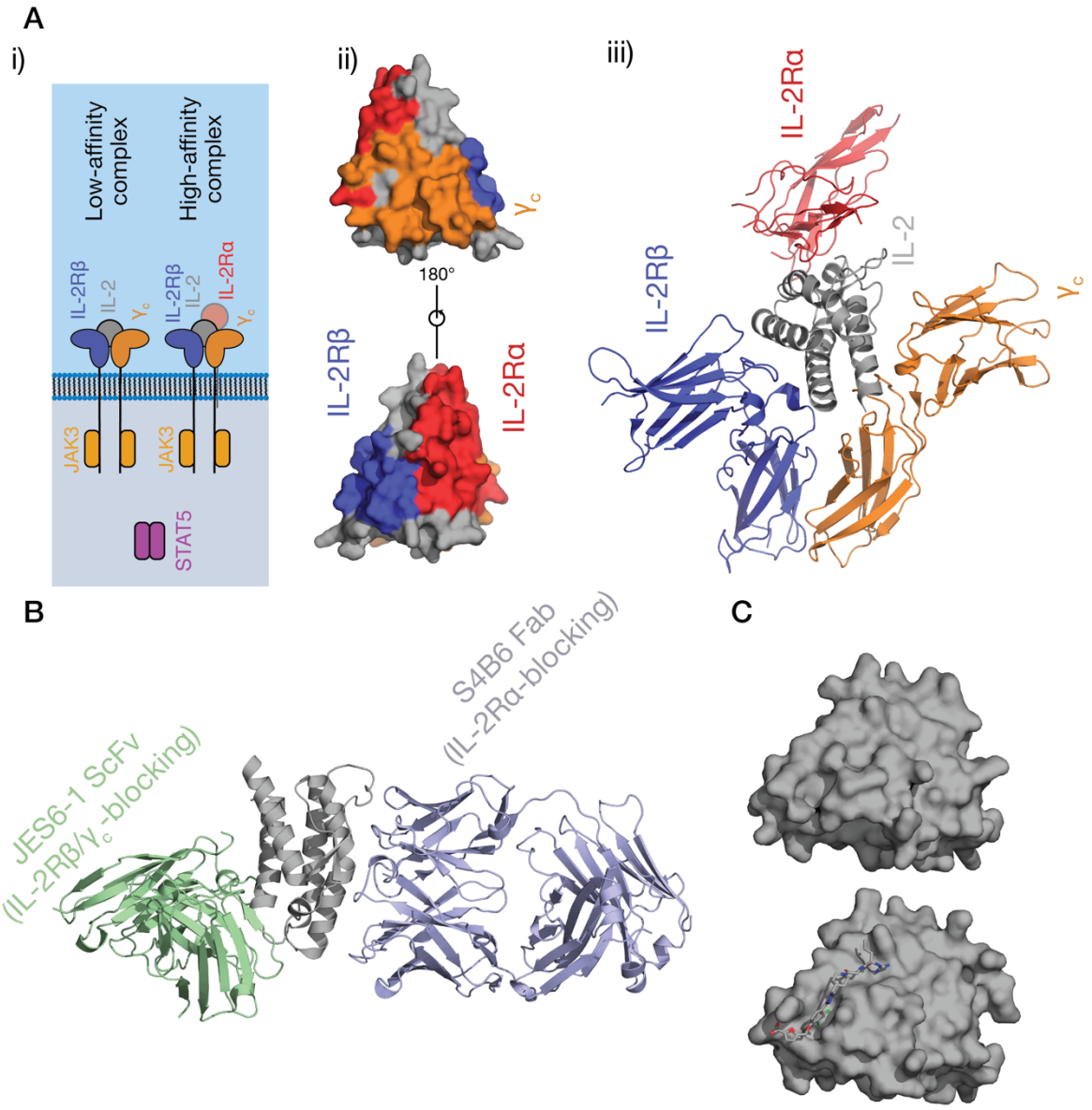

Figure 1.8: The structure and pharmacology of IL-2.

A) The structure of IL-2 and the IL-2 complex. IL-2 can signal through two complexes, i) a high-affinity complex consisting of hetero-trimeric IL-2Rα/β/γ_c, and a lower-affinity complex consisting of dimeric IL-2Rα/β. The binding sites on IL-2 (PDB ID: 1M4C[326]) are shown in ii), identified from the structure of the complex[153]

using the *PISA* server[327]. The structure of the complex (PDB ID: 2B5I[153]) is shown in iii). B) The structure of IL-2 in complex with antibody fragments targeting IL-2[328]. The two antibody fragments, JES6-1 (PDB ID: 4YUE) and S4B6 (PDB ID: 4YQX) bind different surfaces of IL-2, biasing signalling through different receptors. C) The surface of IL-2, shown with and without a small molecule antagonist bound (PDB codes 1M4C, 1PY2[326]). The structures show the major sidechain rearrangement induced by the small molecule on IL-2, creating a hydrophobic binding pocket.

IL-2 binds to three receptors, IL-2Rα (CD25), IL-2Rβ (CD122) and the common γ chain, γ_c (CD132) (Figure 1.8Ai, Aiii). IL-2 can bind either a trimer of the three receptors, forming a high affinity (pM) complex (IL2Rα/β/γ_c) or a dimer of IL2Rβ/γ_c, a lower affinity (nM) complex[153]. The expression of IL-2Rα is highly cell subtype specific – regulatory T cells express IL-2Rα, while cytotoxic T cells/natural killer cells express IL-2Rβ/γ_c but not IL-2Rα[324]. Broadly speaking the response mediated by $CD25^+$ cells is immunosuppressive, while the response mediated by $CD25^-$ cells is immunostimulatory, stimulating an anti-tumour immune response[329]. $CD25^+$ cells are responsive to low levels of IL-2, while $CD25^-/CD122^+$ cells are responsive to high levels of IL-2. As a potent immunostimulant, recombinant IL-2 is used therapeutically in a high dose in late-stage cancer[330]. IL-2 is a very effective treatment in a subset of patients with late stage renal cancer or melanoma[331], with the National Cancer Institute in the United States reporting 9% of late-stage renal cancer patients experiencing complete cancer regression and 12% experiencing partial regression[332]. High-dose IL-2 treatment is, however, associated with severe side effects[333,334]. In high doses, IL-2 is extremely toxic, causing vascular leak syndrome, a potentially fatal condition which can cause hypotension, pulmonary edema, liver damage and kidney failure. This response is largely mediated through $CD25^+$ endothelial cells, and CD25 deficient mice do not display marked IL-2 toxicity[335]. Likewise, long-term treatment with IL-2 may lead to the production of endogenous anti-IL-2 antibodies, which can interfere with the endogenous immune response[336]. IL-2 has been well-characterised structurally, and structures of IL-2[337-339], the IL-2/IL-2Rα complex[48], and the IL-2/IL-2Rα/IL-2Rβ/γ_c complex[153,340] are available, guiding structure-based drug design (Figure 1.8Aii, Aiii).

Antibodies have been developed against IL-2 and the IL-2 receptors (Figure 1.8B). The mAb basiliximab is used therapeutically as an immunosuppressant following kidney transplantation, and a structure of the basiliximab Fab/IL-2Rα complex is available[304]. More recently, antibodies have been developed which either promote or inhibit interactions with IL-2Rα[305-307], which bias IL-2 signalling towards a specific immune cell subset. For example, the antibodies JES6-1[307] and IL-2-F5111[306] promote the activation of $CD25^+$ cells, such as regulatory T cells. JES6-1 functions through occlusion of the IL-2Rβ/γ_c binding sites on IL-2, and through allosterically inhibiting binding to IL-2Rα, resulting in overexpression of $CD25^+$ by $CD25^+$ cells[328]. Similarly, IL-2-F5111 functions through occlusion of the IL-2Rβ binding site, which results in IL-2Rα being made indispensable for IL-2 recruitment[306]. Conversely, antibodies have been developed which inhibit the IL-2/IL-2Rα interaction, such as NARA-1[305] and S4B6[307]. These antibodies bind different epitopes on IL-2, however both function by simple steric occlusion of the IL-2Rα binding site on IL-2[305,328]. Treatment with both antibodies, alone or in combination with recombinant IL-2, serves to robustly stimulate cells expressing high levels of IL-2Rβ (such as $CD8^+$ cytotoxic T cells), while only modestly stimulating $CD25^+$ cells[305,307]. These antibodies thus are promising drug candidates in combination with IL-2, potentially avoiding the deleterious side-effects associated with high-dose IL-2 treatment, associated with activation of endothelial $CD25^+$ cells.

Small molecules have been developed that target IL-2 signalling[265] (Figure 1.8C). The initial IL-2/IL-2Rα inhibitor was an acylphenylalanine derivative, developed to mimic the IL-2 residues involved in IL-2Rα binding[341]. Surprisingly, NMR experiments showed that the inhibitor bound IL-2, and inhibited the IL-2/IL-2Rα interaction[341]. Subsequent hydrogen/deuterium exchange NMR experiments showed that the inhibitor competed with IL-2Rα for IL-2 binding[342], and a crystal structure of IL-2 with the drug showed that drug binding is associated with extensive rearrangement of sidechains in the IL-2Rα binding site, creating a hydrophobic pocket for drug binding[326]. The subsequent determination of the structure of the IL-2/IL-2Rα complex confirmed that the drug bound at a ‘hot spot’

in the IL-2/IL-2Rα interface[343]. More efficacious inhibitors[344-346] were developed targeting the same region on IL-2 through fragment screening and medicinal chemistry approaches, although preclinical development was eventually halted due to concerns about the market for IL-2Rα inhibitors[265].

Protein design has also been used to develop IL-2 'muteins' which serve as potential drugs. Numerous examples have been developed, generally designed through targeted mutagenesis[347,348], yeast display[349] or *de novo* design[350]. Yeast display was used to identify and develop an IL-2 mutant ('super-2') with greatly increased affinity for IL-2Rβ[349]. Surprisingly, the residues identified were in the hydrophobic core, not in the IL-2Rβ contact region, with the mutations stabilising the mutant and priming it for binding with IL-2Rβ[349]. *In vivo*, super-2 is a potent activator of $CD25^-/CD122^+$ cells and has less severe side-effects when compared with high-dose IL-2. Subsequently, the mutations in super-2 were coupled with mutations in the γ_c interface, leading to the generation of potent inhibitors of IL-2 signalling[351]. Although promising, the approach of using cytokine mutants as drugs is not without issues. Mutants often have decreased stability, and due to high sequence identity between the mutant and wild-type cytokine, long-term mutant treatment can lead to the production of antibodies against both the mutant and endogenous cytokine. An approach to overcome this is the use of *de novo* designed proteins. A 'designed IL-2', Neo-2 has recently been developed , with high affinity for IL-2Rβ and γ_c, and no affinity to IL-2Rα[350]. Neo-2, developed using a computational design approach, has low sequence homology to IL-2 (~25%), and is significantly more stable than either wild-type IL-2 or super-2[350]. Neo-2 is a promising therapeutic, activating $CD25^-/CD122^+$ cells and not activating $CD25^+$ cells. Neo-2 is currently under pre-clinical development, and broadly shows the potential of protein design to engineer novel cytokines with beneficial biophysical and therapeutic properties.

The varied approaches used to target IL-2 signalling therapeutically – the use of recombinant IL-2, antibodies, small molecules and protein design illustrate the approaches possible in targeting cytokine signalling therapeutically. So far, only a

subset of these approaches have been explored for IL-11 (Figure 1.7). IL-11 antagonistic[198,352] and agnostic[353] muteins have has been developed, but the structural mechanism of their action is unknown. No antibodies targeting the IL-11 signalling complex components have been well-characterised structurally, and the precise structural mechanism of action of exiting IL-11/IL-11Rα antibodies is unknown. No small molecules targeting IL-11 or the IL-11 signalling complex have been developed, with the exception of the small-molecules which are thought to bind D1 of gp130, described above. This underscores the fact, that in spite of the growing therapeutic potential of IL-11 signalling, there are few drugs targeting IL-11 signalling, and none used clinically. This limits the availability of reagents which may be useful modulators of IL-11 signalling, either experimentally or in the clinic.

1.5 Scope and thesis aims

Briefly, this thesis aims to develop a comprehensive, structural understanding of IL-11 signalling and the interactions which form the IL-11 signalling complex. This thesis also aims to understand the mechanism of action of an existing IL-11 antagonist, IL-11 Mutein.

This thesis includes a chapter outlining in detail the methods developed for the expression and purification of IL-11 and the IL-11 receptors (chapter 2).

The aims of this thesis are:

- To understand the structure of IL-11 and IL-11Rα, the effect of pathogenic mutations in the *IL11RA* gene, and the interaction between IL-11 and IL-11Rα (chapter 3).
- To gain structural knowledge on the formation of the IL-11 signalling complex (chapter 4).
- To understand the mechanism of action of a lead IL-11 signalling antagonist, IL-11 Mutein (chapter 5).

This thesis will close with a general discussion of the results presented in chapters 3-5 (chapter 6).

In addition, this thesis contains a publication[354] on which I was co first-author during my PhD that is outside the direct scope of this thesis (appendix A).

Chapter 2 - Methods for the expression and purification of IL-11 and the IL-11 receptors

2.1 Introduction

Production of adequate amounts of IL-11 and the IL-11 receptors has historically been a major bottleneck in the study of IL-11 signalling. Previously, in our laboratory and others, IL-11 was expressed as a fusion protein with bacterial thioredoxin (TRX), which was subsequently cleaved, leaving full-length IL-11[355]. Previously, IL-11 has also been expressed in *E. coli* using a glutathione-*S*-transferase solubilization tag[352], and in mammalian cells[356]. In our laboratory, we have previously used the TRX solubilization tag, IL-11 was expressed with a very low yield, typically resulting in 200 µg per litre of bacterial culture media (Metcalfe R.D., unpublished observations). To overcome this, we used the solubilising fusion tag maltose binding protein (MBP[357]), which increased yields of IL-11 by approximately tenfold. Truncating the N-terminus of IL-11 also increased the yield, while not perceptibly affecting the biological activity of IL-11 (see Chapter 3). Cytokines are often expressed in *E. coli*, however the disulfide bonds present in many cytokines typically requires laborious oxidative refolding and reverse-phase chromatography purification procedures, such as those employed for IL-2[358], IL-6[359] and IL-24[360].

Likewise, the IL-11 receptors have typically been produced using a mammalian protein expression system (e.g. in Chinese hamster ovary cells), producing highly heterogenous protein that is difficult to study structurally (Griffin M.D.W., unpublished observations). To overcome this, we used the baculovirus/insect cell expression system, which gave reasonable yields of active protein. Insect cell expression is generally the method of choice for the production of cytokine receptors (see for e.g.[63,74,153,360]) for structural characterisation, as it produces homogenous protein with correct disulfide bonding and relatively simple glycosylation, ideal for biophysical and structural characterisation.

This chapter presents detailed methods for the production of IL-11 and the IL-11 receptors. These methods were developed to enable the results presented in subsequent chapters in this thesis. They are presented here in full and in detail for the benefit of future researchers.

2.2 *E. coli* culturing methods

2.2.1 General E. coli *culturing methods*

For suspension bacterial cell culture *E. coli* cells were grown at 37 °C with shaking (200 rpm). Smaller-scale cultures (5 mL) were grown in a 50 mL sterile polypropylene Falcon tube, larger cultures (100 mL – 1 L) were grown in autoclaved glass flasks. Cells were grown in LB supplemented with the appropriate antibiotics. The concentration of antibiotics used were ampicillin 100 µg/mL, kanamycin 50 µg/mL, tetracycline 10 µg/mL and gentamycin 7 µg/mL.

Media for *E. coli* culture was always autoclaved (121 °C) prior to use. Lysogeny broth (LB) was prepared as follows - 10 g/L sodium chloride, 10 g/L tryptone, 5 g/L yeast extract. LB-agar (LA) was prepared by addition of 15% agar. Super optimal broth (SOB) was prepared as follows – 20 g/L tryptone, 5 g/L yeast extract, 10 mM sodium chloride, 2.5 mM potassium chloride, 20 mM magnesium sulphate. Terrific broth (TB) was prepared as follows – 24 g/L yeast extract, 20 g/L tryptone, 4 mL/L glycerol, 17 mM KH_2PO_4, 72 mM K_2HPO_4.

E. coli glycerol stocks were prepared by mixing 300 µL of saturated *E. coli* culture with 200 µL autoclaved 50% glycerol, and stored long-term at -80 °C.

2.2.2 Preparation of chemically competent E. coli

A 5 mL LB culture was inoculated from a glycerol stock of the cell line to be made competent (e.g. DH5α, XL1 Blue, BL21(DE3)) and incubated overnight. The following morning, this culture was used to inoculate 100 mL of LB, which was grown until OD_{600} was 0.5. At this point, flasks were removed from the incubator and incubated at 4 °C for ten minutes, after which the cells were pelleted (4400 *g*, 10 minutes, 4 °C). Cells were then resuspended in 10 mL 100 mM calcium chloride and incubated on ice for one hour, after which they were pelleted (4400 *g*, 10 minutes, 4 °C). Cells were then resuspended in 2 mL 100 mM calcium chloride + 15% glycerol, snap-frozen in liquid nitrogen and stored at -80°C in 100 µL aliquots for later use.

2.2.3 Transformation of chemically competent E. coli

10-100 ng of plasmid DNA was added to a thawed 100 µL aliquot of competent *E. coli* cells. This mixture was incubated on ice for one hour, then incubated at 42 °C for 45 seconds in a water bath, and immediately incubated on ice or five minutes. Following the five-minute incubation, 900 µL SOB was added to the cells, which were then incubated for 45 minutes at 37 °C with shaking (200 rpm). Transformants were selected on LA plates supplemented with the appropriate antibiotic.

2.3 Molecular cloning methods

2.3.1 PCR-based cloning methods

Primers were generally synthesised on a 25 nM scale, purified by cartridge purification (sequencing-grade purity). When required, genes were synthesised by GeneArt (Thermo Fisher Scientific). Genes were either ordered as DNA fragments (marketed as 'GeneArt Strings') which were used as the template for a PCR reaction, with primers against the 5' and 3' end of the fragment or ordered in a transfer vector (pMX) vector, which was digested and sub-cloned into a vector for expression, or ordered cloned in a vector for protein expression.

PCR-based subcloning was used to generate vectors containing full-length and truncated, human and mouse, IL-11, IL-11 Mutein, IL-11Rα_{D3} and some IL-11 mutants in the pET28b MBP vector. Primers were designed against the 5' and 3' end of the IL-11 sequence, containing a 5' SacI restriction enzyme digest site, TEV site and a 3' XhoI restriction enzyme digest site. PCR was performed in a 50 µL reaction volume, with 1 ng template, 200 nM dNTPs, 200 µM forward and reverse primer, 1 × *Pfu* reaction buffer and 1.5 U *Pfu* polymerase. The PCR reaction was conducted for an initial cycle of 95 °C, 2 minutes, thirty cycles of 95 °C, 1 min, 58 °C, 30 seconds, 72 °C, 1.2 minutes and then a final cycle of 72 °C, five minutes. Following PCR, the PCR product was purified using a Qiagen PCR purification kit according to the manufacturer's protocol.

The PCR product, containing the IL-11 sequence was then double-digested along with a vector containing the pET28b MBP sequence. The PCR reaction product

(generally ~2 µg) was double digested along with 5 µg of the pET28b MBP vector. Digests were performed with 200 U each SacI and XhoI, 1 × CutSmart digest buffer (NEB) in 50 µL, and generally performed overnight at 37 °C, to ensure complete digestion of the vector. Following the digest, fragments were resolved on a 1% agarose TAE gel (with 1 × Sybrsafe gel stain), which was run at 100 V for approximately 45 minutes and visualised using blue-light illumination. Bands containing the cut insert or vector were extracted from the gel, and purified using a Qiagen gel extraction kit, according to the manufacturer's protocol. Following gel extraction, the DNA concentration and purity was assessed using UV absorbance at 260 nm, and the ratio of UV absorbance at 260 nm/230 nm and 260 nm/280 nm. Ligations were performed in a 20 µL volume, with 50 ng of vector, 1 × NEB ligation buffer, 4000 U T4 DNA Ligase, 6% PEG 8000 and a 10-fold molar excess of insert (or no insert for a negative control). The ligation mixture was incubated for 15 minutes at room temperature prior to transformation. Alternatively, ligation mixtures were incubated overnight at 16 °C with no PEG 8000. DH5α *E. coli* cells were transformed with 5 µL of the ligation mixture.

Following the overnight incubation, if a significant number of colonies were present on the negative control plates, colonies with the ligation product were screened using colony PCR. Briefly, colonies were resuspended in 100 µL LB with 50 µg/mL kanamycin. A PCR reaction was conducted in 25 µL with 1 × *Taq* master mix (NEB), 1 µL of the resuspended cell mixture and 200 nM each T7 Forward and T7 Reverse primers. The PCR reaction was conducted for an initial cycle of 95 °C, ten minutes, thirty-five cycles 95 °C, 30 seconds, 45 °C, 30 seconds, 68 °C, one minute, then a final cycle of 68 °C, five minutes. The PCR product was analysed on a 1% TAE agarose gel, visualised using blue light. Colonies that contained successful positive ligations were grown overnight in 5 mL LB with 50 µg/mL kanamycin. Following the overnight incubation, the plasmid DNA was purified using a commercial Miniprep kit (Promega) according to the manufacturer's instructions. Purified DNA was Sanger-sequenced at the Australian Genome Research Facility (AGRF), using the T7 Forward and T7 Reverse primers.

To generate the pET28b muGFP-IL-11 and pET28b muGFP-IL-11-Mutein vectors, the muGFP sequence was amplified from the pIQ-muGFP vector (obtained from Dr. Daniel Scott, Florey Institute). Primers were designed against the 5' and 3' end of the muGFP sequence, the 5' primer containing a XbaI restriction site and a ribosome binding site, and the 3' primer containing a SacI site. PCR was conducted essentially as above, the PCR product was double-digested with SacI and XbaI as above, along with the pET28b MBP-IL-11 and pET28b MBP-Mutein vectors. The cut PCR product was ligated into the cut pET28b MBP-IL-11 or pET28b MBP-Mutein vectors as above. The ligation mixture was transformed into *E. coli* DH5α cells, transformants screened, and DNA purified, as above.

To generate the pET11a IL-11Rα$_{D3}$ vector, the IL-11Rα$_{D3}$ sequence was purchased from GeneArt in a pMX transfer vector, with a 5' RBS and XbaI restriction site, and a 3' BamHI restriction site. The pMX IL-11Rα$_{D3}$ vector and the pET11a IL-11 vector were both double-digested with XbaI and BamHI as above. Ligations, screening and DNA purification was conducted as above.

To generate the pET28b muGFP vector, primers were designed against the 5' and 3' end of the muGFP-IL-11 sequence, the 5' primer containing an XbaI restriction site and a ribosome binding site, and the 3' primer containing a stop codon and an XhoI site. PCR, restriction digestion, ligation and screening were conducted essentially as above.

To generate the pFastBac IL-11Rα$_{D1-D3}$, gp130$_{D1-D3}$ and IL-11Rα$_{EC}$ vectors, pBacPac vectors containing the respective sequences were ordered from Genescript. Both the pBacPac vector containing the sequence of interest, and a pFastBac vector were cut with BamHI and XhoI as above, ligated as above, and transformed and screened as above.

2.3.2 Site-directed mutagenesis

Site-directed mutagenesis was used to generate several IL-11 mutants (IL-11$_{\Delta10/W147A}$, IL-11$_{\Delta10/PAIDY}$, IL-11$_{\Delta10/R169A}$, IL-11$_{\Delta10/S53A/W147A}$, IL-11$_{\Delta10/A58P/W147A}$). Primers

were designed incorporating the desired mutation. The site-directed mutagenesis reaction was conducted in a 50 µL volume, with 125 ng of each mutagenesis primer, several concentrations of template (generally 10 ng and 50 ng), 2.5 U *Pfu* Turbo, 1 × *Pfu* Turbo master mix, 2% DMSO and 200 nM dNTPs. The reaction was conducted in a PCR thermal cycler (BioRad T-100), with an initial cycle of 95 °C, 1 minute, 18 cycles of 95 °C, 50 seconds, 60 °C, 50 seconds, 68 °C for 1 minute/kb in vector, followed by a final cycle of 68 °C, 7 minutes. Following the reaction, the product was treated with 20 U *DpnI*, incubated for two hours at 37 °C, then heat-inactivated for 25 minutes at 65 °C. 5 µL of the mutagenesis reaction was transformed into XL1 Blue *E. coli* cells. Following overnight incubation, a single colony was used to inoculate a 5 mL LB culture with the appropriate antibiotic. This culture was incubated at 37 °C overnight with shaking (200 rpm). The DNA was purified and sequenced, as above.

2.4 Bacterial protein expression and purification

Sequences and physical properties of all proteins expressed and purified during this PhD are shown in Supplementary Table 2.1.

2.4.1 Expression of IL-11 variants

A pET28b plasmid, containing His-MBP or His-muGFP, fused to the desired IL-11 variant was transformed into chemically competent ($CaCl_2$) *E. coli* BL21(DE3) cells. Following overnight incubation, a single colony was used to inoculate 100 mL of LB media supplemented with 50 µg/mL kanamycin. This culture was incubated overnight at 37 °C with shaking (200 rpm). This culture was used to inoculate 6-8 L of LB-kanamycin media, with 10 mL of starter culture used per litre of media. These cultures were incubated at 37 °C with shaking (200 rpm) until the optical density of the culture at 600 nm was 0.6-0.7, at which point, 1 mM IPTG was used to induce expression. Cultures were then incubated at 16 °C for 16-18 hours. Following overnight incubation, cultures were harvested by centrifugation (4400*g*, 10 minutes, 4 °C), washed once with nickel-IMAC buffer A (20 mM imidazole, 500 mM NaCl, 50 mM sodium phosphate pH 8), and then resuspended in nickel-IMAC buffer A, in a final volume of 50-100 mL. 6 mM magnesium chloride, a single broad-spectrum

protease inhibitor tablet (Roche) and 5 µL benzonase nuclease (Millipore) was added to the resuspended pellet.

2.4.2 Expression of monoisotopically labelled IL-11 variants

Isotopically labelled IL-11 was prepared using the Marley method[361]. Cells were transformed, and a starter culture prepared, as above. The starter culture was used to inoculate 4-6 L of LB-kanamycin, with 10 mL/L starter culture. Cells were grown at 37 °C with shaking until OD_{600} reached 0.9, at which point cells were pelleted (3260*g*, 8 minutes, 20°C), washed once with 1× M9 salts, pelleted again, then resuspended in 1× M9 salts, supplemented with 0.1% $^{15}NH_4Cl$, 1× trace elements, 0.6% glucose and 10 mM magnesium sulphate (M9 media). After the cells were resuspended in M9 media, they were incubated for a further hour at 37 °C to recover the cells, at which point 1 mM IPTG was added, and the cells were incubated for 16-18 hours at 16 °C. Following overnight incubation, cultures were harvested and washed as above.

2.4.3 Expression of IL-11Rα$_{D3}$

IL-11Rα$_{D3}$ was expressed and purified using a similar method to that described previously[362]. BL21(DE3) cells were transformed with pET11a IL-11Rα$_{D3}$ and a starter culture was prepared in 100 mL LB supplemented with 100 µg/mL ampicillin. This starter culture was used to inoculate a 2 L LB culture (supplemented with 100 µg/mL ampicillin) which was incubated at 37 °C with shaking (200 rpm). When OD_{600} of the culture reached 0.6, protein expression was induced by addition of 1 mM IPTG, and the culture was incubated at 37 °C for a further three hours. Cells were pelleted, washed and resuspended as above, the buffer for resuspension was 50 mM Tris, 100 mM sodium chloride pH 8. The cell pellet was frozen prior to purification.

2.4.4 Expression of tobacco etch virus (TEV) protease

The TEV protease used was a triple mutant L56V, S135G and S219V[363-365] (see Supplementary Table 2.1 for the sequence). L56V and S135G improve the thermal stability of the protease, and S219V removes an internal self-cleavage site. TEV

protease is expressed fused to MBP at the N-terminus, which is cleaved *in vivo* to yield TEV protease N-terminally fused to a His tag. A starter culture was prepared by inoculating 100 mL LB media supplemented with 100 µg/mL ampicillin with a glycerol stock of BL21(DE3) cells transformed with a vector expressing a fusion protein of MBP and TEV protease. This culture was incubated overnight at 37 °C with shaking (200 rpm), then used to inoculate 4-6 L of LB media supplemented with 100 µg/mL ampicillin (10 mL/L starter culture). The culture was grown at 37 °C with shaking (200 rpm) until OD_{600} reached 0.6-0.7, then 1 mM IPTG was added to induce expression. Following induction, the culture was incubated at 16 °C for a further 16-18 hours. Cells were harvested and washed using essentially the same method as IL-11.

2.4.5 Purification of IL-11 variants

The resuspended cell pellet was homogenised using a glass Potter Elvehjem homogeniser, then lysed with three passes through a cell homogeniser (Avestin C3 Homogenizer). The lysate was clarified by centrifugation (30,310*g*, 30 minutes, 4 °C), then filtered through a 0.45 µm syringe filter. The clarified lysate was applied to a HisTrap HP column (2 × 5 mL column, GE Healthcare), pre-equilibrated in nickel-IMAC buffer A (20 mM imidazole, 500 mM sodium chloride, 50 mM sodium phosphate pH 8), at a flow rate of 2 mL/min. Following application of the lysate, the column was washed with five column volumes of nickel-IMAC buffer A, then attached to an Akta liquid chromatography system. The column was eluted with 100% nickel-IMAC buffer B (500 mM imidazole, 500 mM sodium chloride, 50 mM sodium phosphate pH 8), with a gradient over twenty column volumes. Fractions containing MBP-IL-11 (or the variant of interest) were pooled and approximately 15 mg stabilised TEV protease (triple mutant L56V, S135G and S219V, prepared in house, see below) was added[363-365]. The crude IL-11 was dialysed overnight against ion exchange buffer A (20 mM sodium phosphate pH 8), with one buffer change, in a volume of 5 L, at 4 °C.

Following overnight dialysis, the crude IL-11 preparation was centrifuged to remove any visible precipitate (3200 *g*, 10 minutes, 4 °C), then filtered through a 0.22 µm

syringe filter. The clarified dialysate was applied to a HiTrap SP HP mono-S cation exchange column (2 × 5 mL column, GE Healthcare), pre-equilibrated in ion exchange buffer A, at a flow rate of 2 mL/min. Following application of the sample, the column was washed with five column volumes of buffer A, then eluted with a gradient of ion exchange buffer B (20 mM sodium phosphate, 1 M sodium chloride pH 8), over twenty column volumes. Fractions containing IL-11 (or the variant of interest) were pooled, 20 mM imidazole was added, and the salt concentration adjusted to 500 mM. The crude IL-11 was then applied to a second HisTrap HP column, pre-equilibrated in nickel-IMAC buffer A. Following application of the sample, the column was washed with five column volumes of nickel-IMAC buffer A, then three column volumes of nickel-IMAC buffer B. The flow-through and first two wash fractions (containing IL-11) were taken and concentrated to approximately 5 mL using an Amicon centrifugal concentrator with a 10 kDa molecular weight cut-off (MWCO) (Millipore), then applied to a Sephacryl S100 gel filtration column pre-equilibrated in Tris-buffered saline (TBS) (20 mM Tris, 150 mM NaCl) pH 8. Fractions containing IL-11 were identified using SDS-PAGE, pooled and concentrated to 10-20 mg/mL using an Amicon concentrator with a 10 kDa MWCO. The concentration of the purified protein was determined using UV absorbance at 280 nm, with extinction coefficients calculated from the sequence (ProtParam[366]). The purity of the purified protein was assessed using SDS-PAGE, and the correct mass was confirmed using ESI-TOF mass spectrometry. For isotopically labelled samples, the percent of isotope incorporation was determined using mass spectrometry[367]. IL-11 was stored frozen at -80 °C. See Figure 2.1A, B for gels showing typical purity through the purification, and final purity for IL-11$_{\Delta 10}$. See Figure 2.1C for representative cation-exchange chromatography chromatograms, Figure 2.1D for a representative size-exclusion chromatography chromatogram.

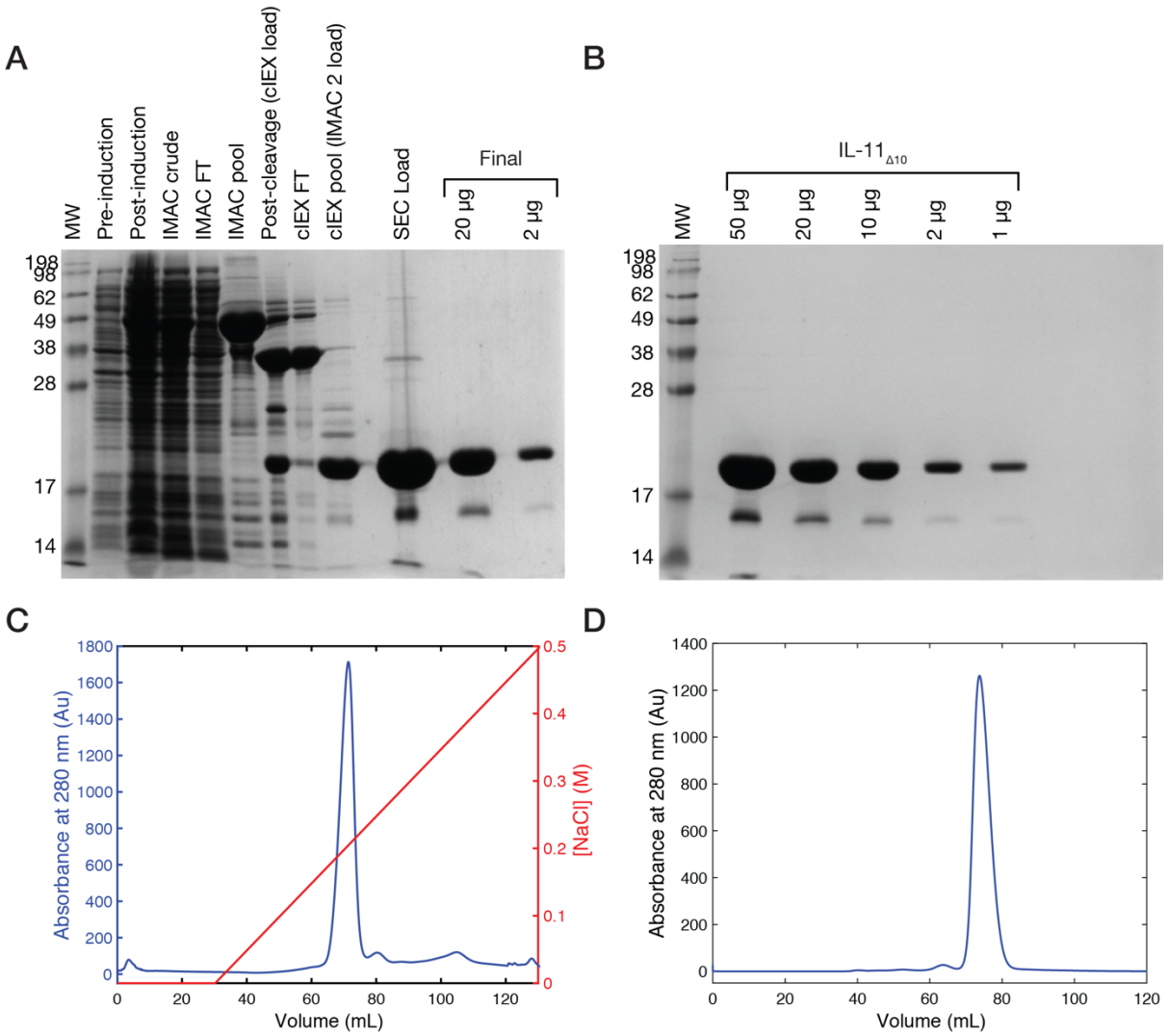

Figure 2.1: Purification of IL-11.

A) Purity through the purification for IL-11$_{\Delta 10}$. B) Expected final purity for IL-11$_{\Delta 10}$. Similar purity was observed for other IL-11 variants. C) A representative cation-exchange chromatogram, D) a representative size-exclusion chromatogram.

2.4.6 Purification of muGFP-IL-11, muGFP-IL-11-Mutein and muGFP

For muGFP fusions, the cells were lysed, the lysate clarified, and the first nickel-affinity chromatography step performed using an essentially identical method as for IL-11. Following the first nickel-affinity chromatography step, the fractions were pooled and dialysed against 20 mM sodium phosphate, pH 8, overnight at 4 °C, in a total volume of 5 L, with one buffer change.

Following overnight dialysis, cation exchange chromatography was performed using an essentially identical method as for IL-11. No subtractive nickel-affinity step was performed, and samples were concentrated to ~5 mL for gel filtration chromatography using a Sephacryl S100 16/60 column, as for IL-11. Fractions were pooled, protein concentration determined using UV absorbance at 280 nm, purity was assessed using SDS-PAGE and the correct mass confirmed using mass spectrometry. The muGFP-IL-11 fusions were stored frozen at -80 °C.

muGFP was purified using a three-step method, cells were lysed, and the first nickel affinity step performed using the same method as muGFP-IL-11. muGFP was dialysed into 20 mM sodium phosphate, pH 6 overnight, at 4 °C, with one buffer change, in a total volume of 5 L. The dialysate was then applied to a single 5 mL Q sepharose-HP anion exchange column, pre-equilibrated in 20 mM sodium phosphate, pH 6, and eluted with 20 mM sodium phosphate, 1 M sodium chloride pH 6. Fractions containing muGFP were pooled and applied to a Sephacryl S100 16/60 gel filtration column, fractions pooled, and protein quality assessed as above. See Figure 2.2A, B for gels showing the expected final purity of muGFP and the muGFP fusions.

Mass spectra of muGFP showed two strong peaks (at 29227.08 Da and 29241.98 Da), around the expected mass of muGFP (29246.80 Da) (Figure 2.2C). GFP chromophore formation involves dehydration and oxidation[368], resulting in a mass change of 20 Da[369] from the sequence molecular mass. The peak at 29227.08 Da (Δmass of 19.7 Da from sequence mass) thus corresponds to muGFP with an intact chromophore. The peak at 29241.98 Da (Δmass of 4.8 Da from the sequence mass) likely corresponds to multiple forms of muGFP with partially reduced chromophores, a result of the acidic and denaturing conditions used for MS. Mass spectra of muGFP-IL-11 (expected mass 48373.17 Da) shows a similar pattern with two peaks around the expected mass (at 48354.61 Da and 48368.65 Da) (Figure 2.2D). The peak at 48354.61 Da (Δmass 18.5 from sequence mass) corresponds to an intact fluorophore, the peak at 48368.65 Da (Δmass 4.5 from sequence mass) corresponds to a partially reduced fluorophore.

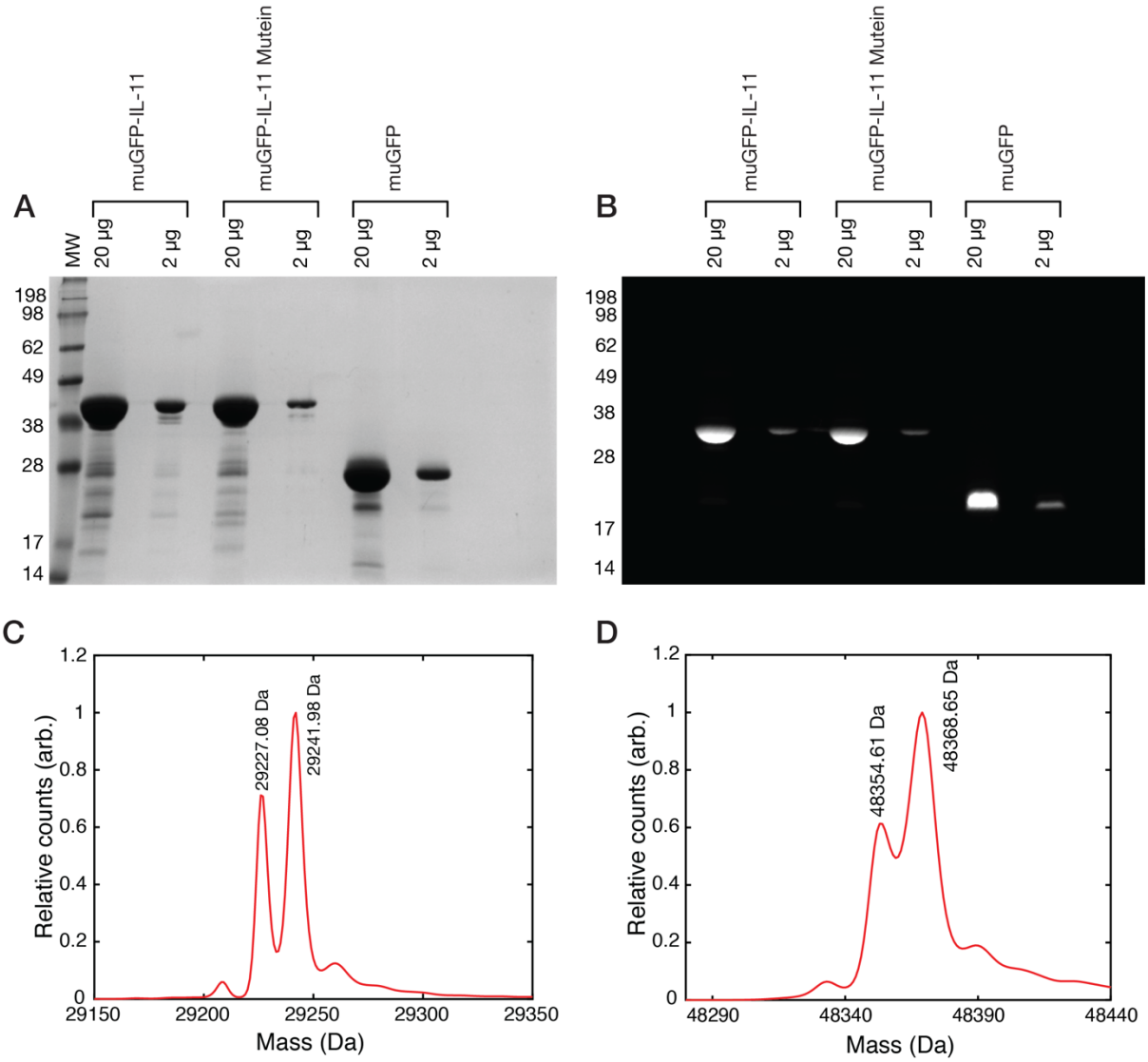

Figure 2.2: Purification of muGFP fusions.

A) Coomassie-stained SDS-PAGE gel, showing the final purity of the muGFP fusion proteins, and of muGFP. Samples in A) were denatured by boiling prior to loading on the gel. B) In-gel fluorescence of muGFP and muGFP fusions[370]. Samples were not denatured prior to loading on the gel, protein was detected by GFP fluorescence following electrophoresis. Note that as muGFP is non-denatured it migrates abnormally[370]. C) Deconvoluted ESI-TOF mass spectrum of muGFP. D) Deconvoluted ESI-TOF mass spectrum of muGFP-IL-11.

2.4.7 Purification of IL-11Rα$_{D3}$

The cell pellet containing IL-11Rα$_{D3}$ inclusion bodies was thawed at room temperature. Once thawed, 80 mg lysozyme (Sigma, provided as a lyophilised powder), 6 mM magnesium chloride and 1 µL benzonase (Millipore) was added to the cells, and the cells were lysed using a sonicator (5 minutes total sonication time, amplitude '40', 15 seconds on/15 seconds off) (Qsonia sonicator, 6.35 mm tip). The lysate was clarified using centrifugation (30,310 *g*, 30 minutes, 4 °C), and the supernatant discarded. The pellet was washed 3-4 times with wash buffer (50 mM Tris, 1 mM EDTA, 1 mM DTT, 100 mM NaCl, 0.2% Triton X-100, pH 8), until the supernatant was clear after washing. Following the final wash, the pellet was washed once with resuspension buffer (50 mM Tris, 100 mM NaCl pH 8) to remove detergent, then resuspended in inclusion body solubilization buffer (6 M GuHCl, 20 mM Tris, 10 mM DTT pH 8), and incubated overnight on a rotary mixer.

Following overnight incubation, the suspension was centrifuged (30,310 *g*, 30 minutes, 4 °C), and the pellet discarded. The supernatant was filtered through a 0.22 µm filter and dialysed against refolding buffer for 24 hours (20 mM Tris, 150 mM NaCl, 1 mM EDTA pH 8), in a total volume of 5 L, with three buffer changes, at 4 °C. After dialysis, the dialysate was filtered through a 0.22 µm filter, concentrated to ~5 mL using an Amicon centrifugal concentrator with a 10 kDa MWCO, and then applied to a Sephacryl S100 gel filtration column, pre-equilibrated in refolding buffer. Fractions containing IL-11Rα$_{D3}$ were pooled and concentrated to approximately 5 mg/mL and stored frozen at -80 °C. A gel showing the final purity is shown in Figure 2.3.

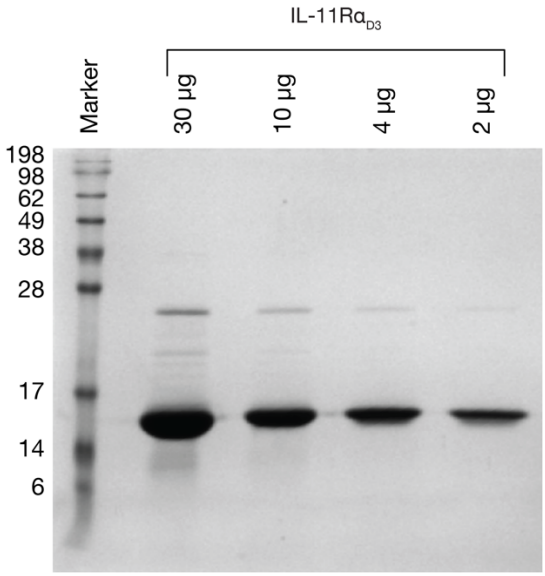

Figure 2.3: SDS-PAGE gel showing the purity of IL-11Rα$_{D3}$.

2.4.8 Purification of TEV protease

Following resuspension of the cell pellet, cells were lysed and clarified using essentially the same method as IL-11. The clarified lysate was applied to a 5 mL HisTrap HP nickel-IMAC column pre-equilibrated in IMAC buffer A (20 mM imidazole, 50 mM sodium phosphate, 500 mM sodium chloride pH 8), at a flow rate of 2 mL/min, following application of the lysate, the column was washed, then eluted with 20 column volumes of nickel-IMAC buffer B (500 mM imidazole, 50 mM sodium phosphate, 500 mM sodium chloride pH 8). Fractions containing TEV protease were pooled, then dialysed overnight against TBS pH 8. After dialysis, the concentration was measured and the TEV protease frozen.

Alternatively, if higher purity TEV protease was required, the TEV protease was subjected to a second cation exchange step. The TEV protease was dialysed overnight against cation exchange buffer A (20 mM sodium phosphate pH 6) following nickel-affinity chromatography. Following overnight incubation, the dialysate was applied to a HiTrap SP HP mono-S cation exchange column (GE Healthcare) pre-equilibrated in cation exchange buffer A, at a flow rate of 2 mL/min. After application of the dialysate, the column was washed with five column volumes of cation exchange buffer A, then eluted with cation exchange buffer B, over a

gradient of 20 column volumes. Peaks containing TEV protease were pooled, dialysed overnight against TBS pH 8, then frozen.

The concentration of the TEV protease was assessed using UV spectroscopy. The purity was assessed using SDS-PAGE and ESI-TOF mass spectrometry. Figure 2.4A shows a gel showing typical purity through the TEV protease purification. Note that two peaks are observed in the cation exchange chromatogram, the first peak is TEV protease with the His tag modified with α-*N*-6-phosphogluconoylation on the His tag (mass 28751.9 Da), and the second peak is unmodified TEV protease (mass 28573.9 Da)[371] (Figure 2.4B, C). Both modified and unmodified TEV protease was active. Figure 2.4D shows the typical final purity for TEV protease prepared using the one-step and two-step methods.

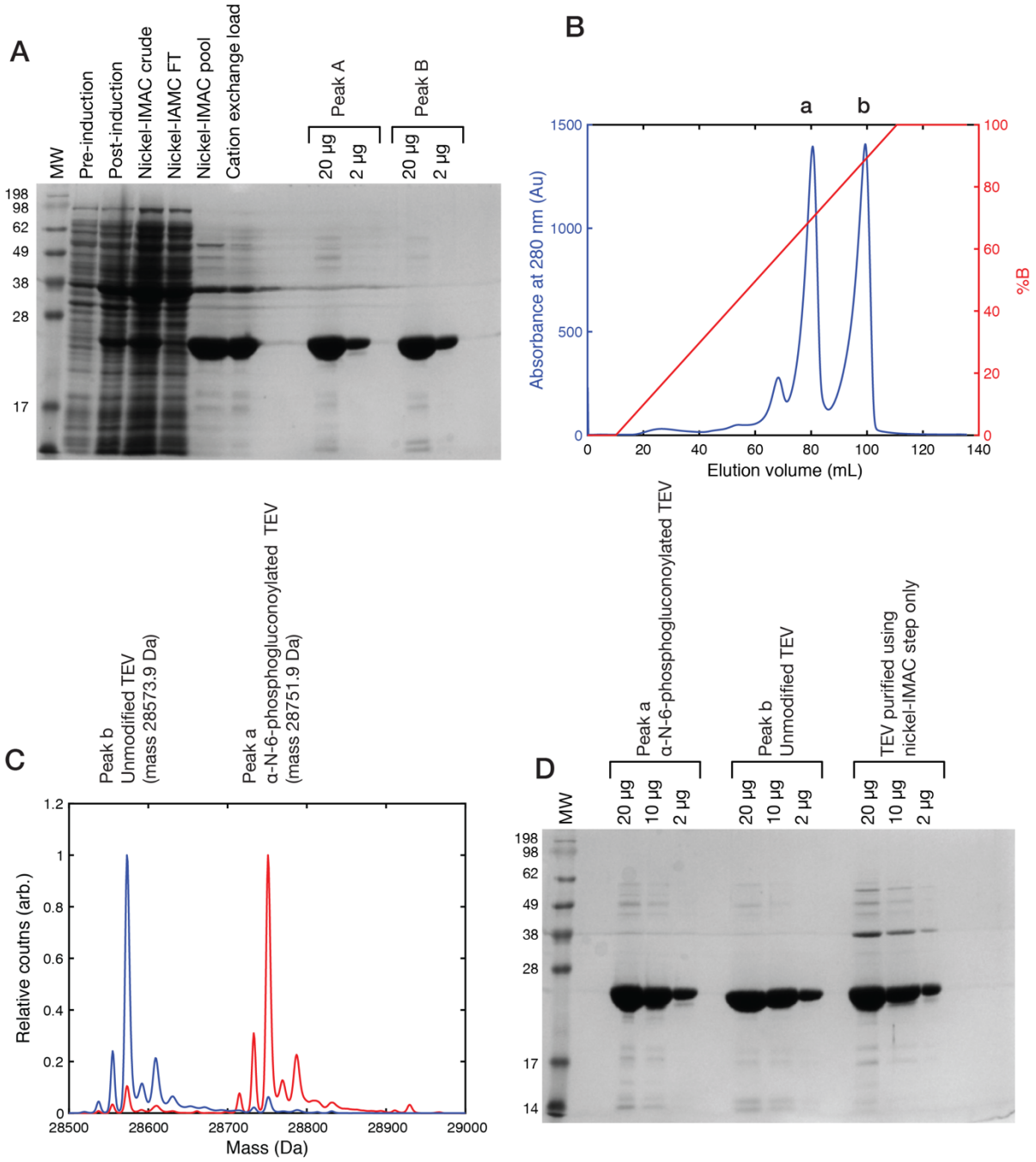

Figure 2.4: Purification of TEV protease.

A) SDS-PAGE gel showing purity through the purification. B) Cation exchange chromatogram, both peaks labelled a and b, contain active TEV. C) Deconvoluted mass spectrum, showing that peak b contains unmodified TEV (expected mass 28573.44 Da, Δmass 0.5 Da), peak a contains TEV with the α-*N*-6-phosphogluconoylation post-translational modification (Δmass 178 Da). D) SDS-PAGE gel, showing the expected final purity for TEV protease purified using the two step (peaks a and b) and one-step method.

2.5 Insect cell culture methods, virus generation, protein expression, and purification

2.5.1 General insect cell culture methods

Sf21 insect cells were maintained in suspension culture, in 1 L Schott bottles, in Lonza Xpress serum-free media, at 27 °C, in the dark, with shaking (130 rpm). For continuous cultures, cell density was generally maintained in log phase, and cells were split to a density of 0.3-0.5 × 10^6 viable cells/mL when in mid-late log phase (5-8 × 10^6 viable cells/mL). Cells were counted manually using a haemocytometer, with viability monitored using tryptan blue staining. Cultures were abandoned after 2-3 months (approximately 30 passages post-thaw), or when a reduction in viability, virus production or protein production was observed.

For freezing, cells were grown to a density of 4-5 × 10^6 viable cells/mL in 200 mL media. Cells were pelleted (500 *g*, 5 minutes), and resuspended in 20 mL freeze media (90% foetal calf serum, 10% DMSO). The resuspended cells were aliquoted, and frozen overnight in a controlled-temperature freezer (1 °C/min) in a -80°C freezer, then stored in the vapor phase of liquid nitrogen (-190 °C).

For thawing, cells were thawed at room temperature, at which point they were added to 20 mL pre-warmed Xpress media. Cells were pelleted (100*g*, 5 minutes), then resuspended in 25 mL Xpress media. Cells were then grown at 27 °C in a 250 mL Schott bottle. Cell density was maintained at ~1-2 × 10^6 viable cells/mL for the week post-thawing.

2.5.2 Generation of recombinant bacmids

Recombinant bacmids for transfection were prepared using the pFastBac system. 10-100 ng of the pFastBac vector containing the gene of interest was added to a 100 µL aliquot of DH10Bac competent cells. Cells were incubated on ice for one hour, then heat-shocked at 42 °C for one minute then incubated on ice for a further five minutes. At this point, 900 µL SOB was added to the cells, the cells were transferred into a 15 mL polypropylene Falcon tube (for aeration) and incubated for four hours at 37 °C with shaking (250 rpm). After the incubation, the transformation

mixture was plated onto LA plates containing 50 µg/mL kanamycin, 10 µg/mL tetracyclin, 7 µg/mL gentamycin, 200 µg/mL X-Gal and 10 µg/mL IPTG, and incubated at 37 °C for 48-72 hours, protected from light. Following this incubation, several large, white colonies were picked, and used to inoculate 5 mL LB, supplemented with 50 µg/mL kanamycin, 7 µg/mL gentamycin and 10 µg/mL tetracyclin.

Following the overnight incubation, the cells were pelleted in a benchtop centrifuge (3200 *g*, 10 minutes, 4 °C) and the pellet resuspended in 300 µL Solution I (15 mM Tris, 10 mM EDTA, 100 µg/mL RNAase A pH 8). 300 µL Solution II (0.2 M sodium hydroxide, 1% SDS) was added to the cells, and incubated for five minutes at room temperature, then 300 µL Solution III (3 M potassium acetate, pH 5.5) was added and incubated on ice for ten minutes. Following this incubation, the mixture was centrifuged at maximum speed (~14,000 *g*) in a minicentrifuge for ten minutes at room temperature. The supernatant was added to 800 µL cold isopropanol, incubated on ice for ten minutes, then centrifuged at maximum speed in a minicentrifuge for 15 minutes at room temperature. The supernatant was removed, and the pellet washed with 500 µL cold 70% ethanol, and then centrifuged at maximum speed in a minicentrifuge for 5 minutes at room temperature. The supernatant was removed, the pellet centrifuged at maximum speed in a minicentrifuge for 5 minutes at room temperature. Any remaining supernatant was removed, and the pellet air-dried for one hour at room temperature. The pellet was resuspended in 100 µL TE buffer (10 mM Tris, 1 mM EDTA pH 8). The concentration of the recombinant bacmid was quantified using UV spectroscopy. Bacmids were stored short-term at 4 °C, and long-term at -20 °C, and were not subject to multiple freeze-thaw cycles.

To verify the presence of the desired insert sequence in the recombinant bacmid, bacmids were screened using PCR. A PCR mix was prepared in 25 µL, with 100 ng bacmid, 1 × OneTaq master mix (NEB), 200 nM each forward and reverse pUC/M13 primers or 200 nM each forward and reverse pFastBac primers and 4% DMSO. The PCR was conducted for an initial cycle of 94 °C, three minutes, thirty-five cycles 94

°C, 45 seconds, 55 °C, 45 seconds, 68 °C, five minutes, then a final cycle of 68 °C, seven minutes. The PCR product was analysed on a 1% TAE agarose gel, visualised using blue light. Recombinant bacmids contained a single band which ran at ~2.3 kbp + the length of the insert (for the pUC/M13 primers) or at the length of the insert (for the pFastBac primers) (Figure 2.5A). Multiple bands or a single band at ~300 bp indicated impure or non-recombinant bacmid, respectively.

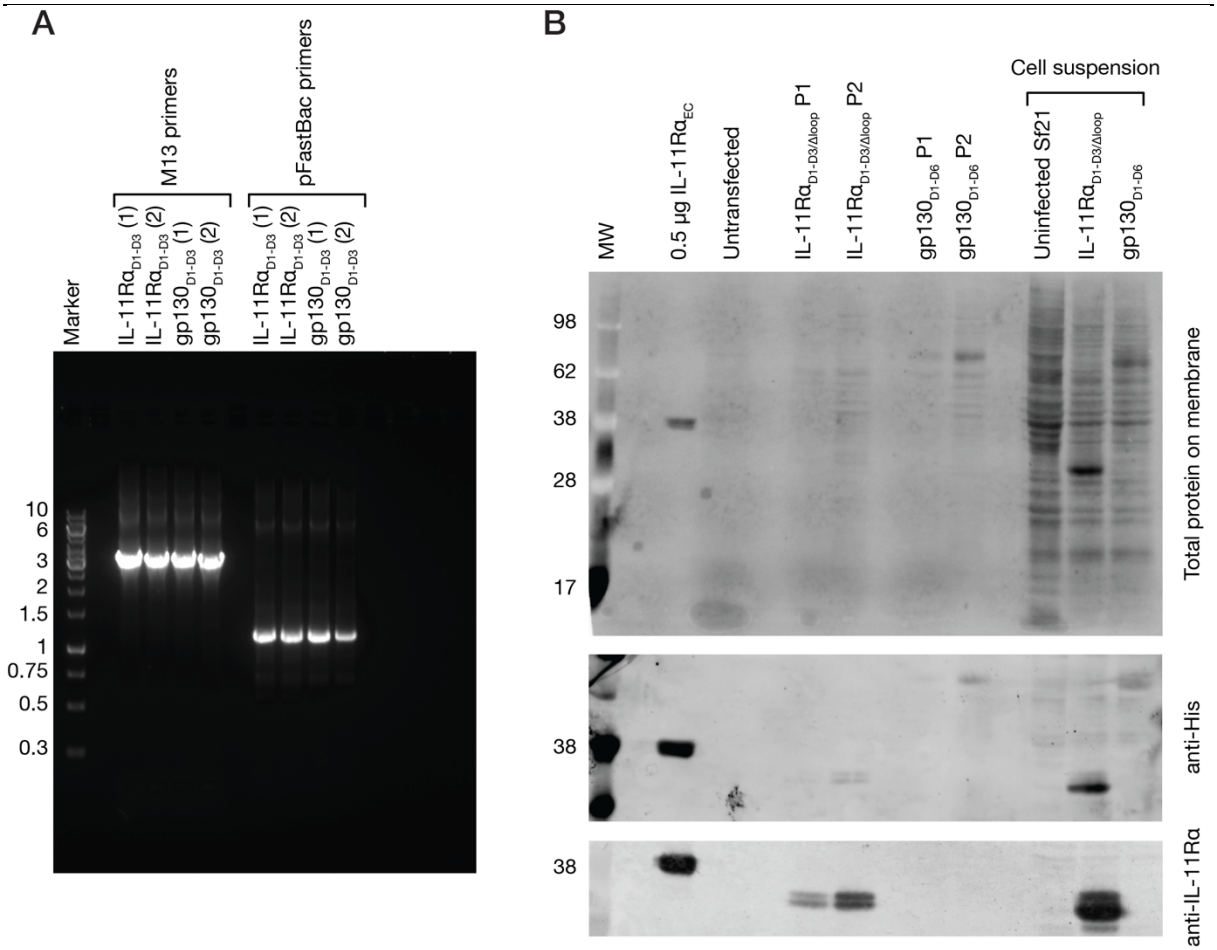

Figure 2.5: Production of recombinant baculovirus.

A) 1% agarose gel showing the PCR product following PCR screening of the bacmid (insert size ~1 kbp). Two primers were used, M17 primers (band size expected ~2.3 kbp + size of insert) and pFastBac primers (band size expected size of insert). B) Western blot showing successful virus production and amplification for the P1 and P2 stocks. A band is present in the blot at the expected size of the IL-11Rα$_{D1-D3/\Delta loop}$ protein (~32 kDa) and the gp130$_{D1-D6}$ protein (~70 kDa), in the supernatant (P1 and P2 viral stocks,) and also in the total cell suspension, showing successful production and amplification of functional virus. Total protein was

detected using ‘stain-free’ membrane imaging (see section 2.6.2), membranes were probed with anti-IL-11Rα antibody SC-993 (Santa Cruz) and anti-His antibody CST 27E8 (Cell Signalling Technologies). Purified IL-11Rα_{EC} is included as a positive control.

2.5.3 Transfection and production of recombinant baculoviruses

Low-passage Sf21 insect cells were transfected at early log phase (2-3 × 10^6 cells/mL). On the day of the transfection, 0.9 × 10^6 cells were plated onto each well of a 6-well tissue culture plate and allowed to adhere in a monolayer for 45 minutes at room temperature. Cells were transfected using Cellfectin-II (Thermo Fischer). Briefly, 1-3 µg of the purified bacmid was added to 100 µL of Xpress media. Separately, 6 µL of Cellfectin-II was added to 100 µL of Xpress media, then the Cellfectin-II mix was added to the diluted bacmid. This mixture was mixed by tapping and incubated at room temperature for 30-45 minutes. Following this incubation, 800 µL Xpress media was added to the Cellfectin-bacmid mix, and the conditioned media was removed from the Sf21 cells. A negative control (untransfected) monolayer was also prepared. The Cellfectin-bacmid complex was slowly added to the monolayer, and then incubated for 5 hours at 27 °C. After the 5 hour incubation, the Cellfectin-bacmid complex was removed, and 2 mL of Xpress media was added to each monolayer after removal of the Cellfectin-bacmid complex. The monolayers were incubated for four days at 27 °C. Following the incubation, the conditioned media, containing a low titre of baculovirus, was removed and centrifuged to remove cell debris (500*g*, 5 minutes, 20 °C). This stock was referred to as the ‘P1 stock’.

To generate higher-titre stocks, 1 mL of the P1 stock was used to infect 100 mL of cells at 1.5 × 10^6 cells/mL. Following infection, the culture was incubated for four days at 27 °C. After the incubation, the cells were centrifuged (500*g*, 5 minutes, 20 °C) and the supernatant was filtered using a 0.22 µm filter. This stock was referred to as the ‘P2 stock’. The P2 stock was used to infect a second culture to generate a high-titre P3 stock, which was used for protein expression. Prior to large-scale

expression, protein expression was verified using western blot (Figure 2.5B, see Supplementary Figure 2.2A for complete membrane images).

2.5.4 Expression of IL-11 receptors

For large-scale secreted protein expression, insect cells were seeded at a density of 1×10^6 cells/mL in 1 L of Xpress media, in a 3 L Fernbach flask. Cells were incubated overnight at 27 °C with shaking (90 rpm). After overnight incubation, cells were infected with 1% v/v P3 viral stock, then incubated at 27 °C for a further 48 hours with shaking (90 rpm). Following this incubation, cells were pelleted (4400*g*, 20 minutes, 4 °C), the pellet discarded, and the supernatant retained and filtered using a 0.22 µm filter. The supernatant was dialysed and concentrated using a Millipore Pellicon tangential flow-filtration device, with two Millipore 10 kDa MWCO filters (P3C010C0), coupled to an Masterflex L/S (Cole-Palmer) peristaltic pump, which was run at a flow rate of 500 mL/min. The supernatant was concentrated to 500 mL, then diluted with 2.5 L of TFF buffer (20 mM Tris, 500 mM sodium chloride pH 8.5), and concentrated again to 500 mL. This concentrated, dialysed sample was filtered (0.22 µm), and imidazole to a final concentration of 20 mM was added.

We note we attempted to express and purify IL-11R$\alpha_{D2\text{-}D3}$ (corresponding to residues 89-297). The protein was expressed but failed to be secreted from the Sf21 cells (Figure 2.6, see Supplementary Figure 2.2B for complete membrane images).

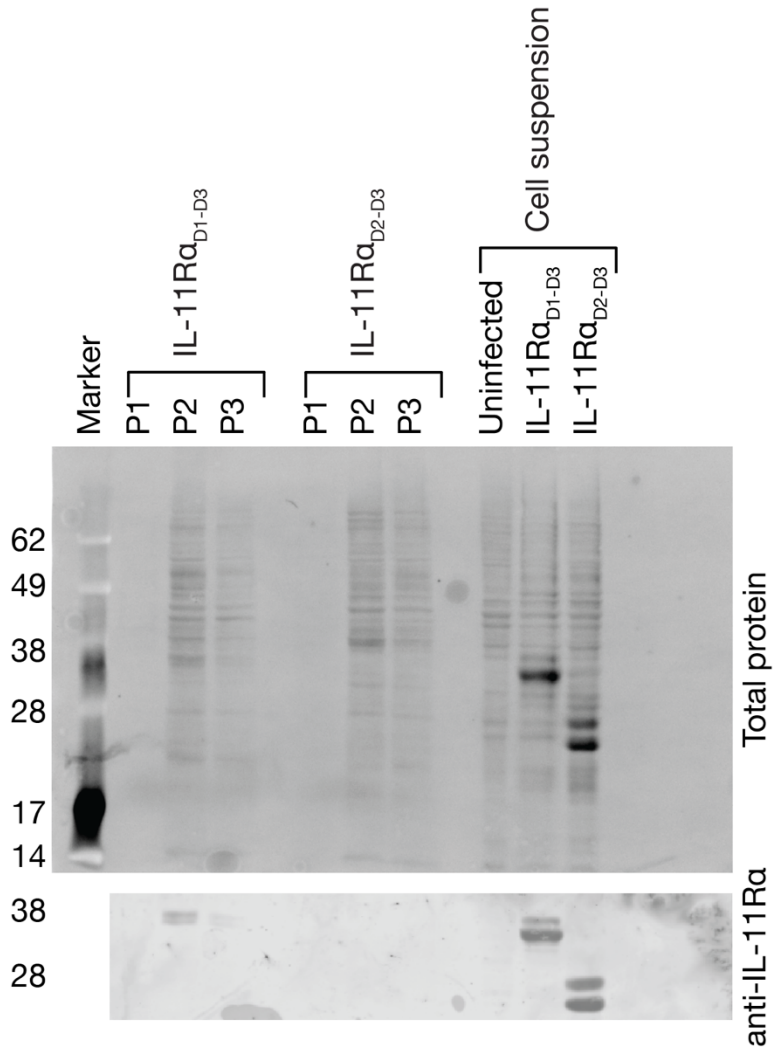

Figure 2.6: Attempted expression of IL-11Rα$_{D2-D3}$.

Western blot, showing viral stock generation for IL-11Rα$_{D2-D3}$. IL-11Rα$_{D2-D3}$ is detected in the cell suspension following P3 generation, but not in the viral stock supernatant, showing that it is expressed and not secreted. A successful IL-11Rα$_{D1-D3}$ transfection is included on the blot as a positive control. Membrane was probed with anti-IL-11Rα antibody SC-130920.

2.5.5 Purification of IL-11 receptors

The conditioned, buffer-exchanged media was applied to a HisTrap HP column (5 mL volume, GE Healthcare), pre-equilibrated in nickel-IMAC buffer A (20 mM Tris, 20 mM imidazole, 500 mM sodium chloride pH 8.5) at flow rate of 5 mL/min. Following application of the sample, the column was washed with five column volumes buffer A, then eluted with a single step of 100% nickel-IMAC buffer B (20 mM Tris, 500 mM imidazole, 500 mM sodium chloride pH 8.5). Fractions containing

purified protein were pooled, and approximately 4 mg purified TEV protease was added. The crude protein was then dialysed overnight against TBS pH 8.5, at 4 °C, with one buffer change. Following overnight incubation, the dialysate was centrifuged (3200*g*, 10 minutes, 4 °C) to remove visible precipitate and applied to a second nickel-IMAC column (5 mL, GE Healthcare). The flow through and wash fractions containing cleaved target protein were taken, then concentrated to ~5 mL using an Amicon centrifugal concentrator with a 10 kDa MWCO. This sample was then applied to a Superdex 2200 16/60 column (GE Healthcare), pre-equilibrated in TBS pH 8.5. Fractions containing pure protein were taken and pooled and concentrated to a final concentration of 2-10 mg/mL. Purified protein was frozen and stored at -80°C.

Due to presence of a non-cleavable C-terminal His tag, a different method was used to purify IL-11Rα$_{EC}$. Nickel-IMAC chromatography was performed as above. The purified protein following nickel-IMAC chromatography was pooled and applied to a Superdex 200 16/60 column pre-equilibrated in TBS pH 8.5. Fractions containing IL-11Rα$_{EC}$ were pooled. IL-11Rα$_{EC}$ was not able to be concentrated using a centrifugal concentrator, so the gel filtration column fractions were frozen without further concentration. Attempts to concentrate IL-11Rα$_{EC}$ using a centrifugal concentrator resulted in protein aggregation and precipitation. An SDS-PAGE gel showing the purity through the purification, and typical purity for the IL-11 receptors is shown in Figure 2.7A, B (see Supplementary Figure 2.2C for complete membrane image). Figure 2.7C shows a typical size-exclusion chromatogram for the purification of gp130$_{D2-D3}$.

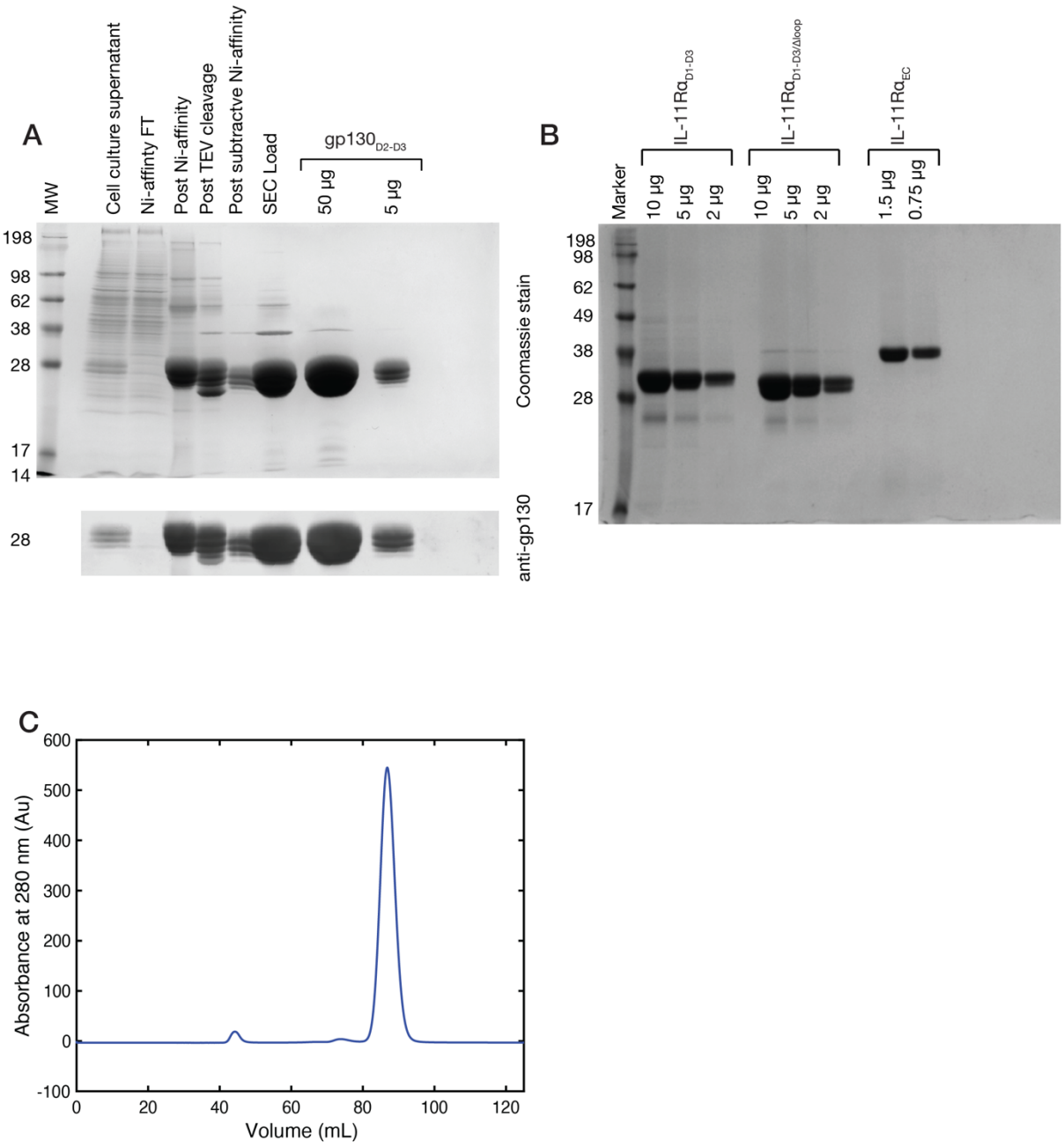

Figure 2.7: Purification of the IL-11 receptors.

A) Gel showing purity through purification, and final purity of $gp130_{D2\text{-}D3}$. A second gel was transferred onto a membrane, which was probed with an anti-gp130 D2 antibody (Abcam, ab128618). B) Gel showing final purity of the IL-11Rα variants $IL\text{-}11R\alpha_{EC}$, $IL\text{-}11R\alpha_{D1\text{-}D3}$ and $IL\text{-}11R\alpha_{D1\text{-}D3/\Delta loop}$. C) Size exclusion chromatogram for the purification of $gp130_{D2\text{-}D3}$.

2.6 Protein electrophoresis and western blotting

2.6.1 SDS-PAGE

SDS-PAGE[372] gels were prepared containing 10%, 12%, 14% or 16% acrylamide (29:1 acrylamide:bis-acrylamide), the acrylamide percentage used depended on the size of the protein being studied. Gels were prepared with a 4% acrylamide stacking gel. The SDS concentration was 0.5%, the stacking gel was buffered with 375 mM Tris pH 6.85 and the resolving gel was buffered with 375 mM Tris pH 8.8. The gels were Bio-Rad mini gels (1.5 mm thickness).

Gels were prepared with 0.05% trichloroethanol for immediate visualization of separation post-electrophoresis[373,374]. Samples were prepared by dilution with 2× reducing SDS-PAGE loading dye (100 mM Tris pH 6.8, 4% SDS, 0.2% bromophenol blue, 20% glycerol, 200 mM β-mercaptoethanol) or 4× reducing SDS-PAGE loading dye (200 mM Tris pH 6.8, 8% SDS, 0.4% bromophenol blue, 40% glycerol, 400 mM β-mercaptoethanol). Samples were boiled (100 °C) for five minutes prior to loading onto the gel. A molecular weight maker (either BioRad Low-Range Protein Marker, cat. 161-0304, discontinued or Invitrogen SeeBlue Plus 2, cat. LC5925) was used to quantify the electrophoretic mobility of the samples. The gels were run at 150-200 V for 1.5-2 hours (until the dye front exited the gel), with 200 mM glycine, 0.1% SDS, 25 mM Tris pH 8.8 used as the running buffer. Gels were then exposed to UV light for 5 minutes (1 minute if the gel was to be transferred onto a membrane for western blot) for visualization using ‘stain-free’ tryptophan fluorescence on a BioRad Chemidock imager. Gels were fixed for at least 15 minutes in fixing solution (30% methanol, 10% acetic acid), washed 3×10 minutes with water, then stained for at least 24 hours in staining solution (0.12% Coomassie G-250, 10% phosphoric acid, 10% ammonium sulphate, 20% methanol,) then destained with multiple water washes[375]. We note that this method is more sensitive then staining by Coomassie R-250, which has previously been employed in our laboratory (Supplementary Figure 2.1).

2.6.2 Western blotting

Post-electrophoresis, gels were wet-transferred onto nitrocellulose membranes with 20% methanol + 1× transfer buffer (48 mM Tris, 39 mM glycine, 0.037% SDS). Transfers were generally conducted at 100 V for 90 minutes, 15 V for 16-18 hours or 30 V for 16-18 hours, depending on the size of the protein. A successful transfer was confirmed by stain-free imaging of the gel and membrane. Membranes were blocked for 2 hours in 1× Odyssey blocking buffer (Li-COR) in TBS pH 7.4+0.05% Tween-20+0.05% sodium azide, then incubated overnight at 4 °C in the primary antibody, diluted in Odyssey blocking buffer in TBS pH 7.4+0.05% Tween-20+0.05% sodium azide. After overnight incubation, membranes were washed 4×5 minutes with TBS pH 7.4+0.05% Tween-20, then incubated for one hour at room temperature, in the dark, with the appropriate secondary antibody in diluted in Odyssey blocking buffer in TBS pH 7.4+0.05% Tween-20+0.05% sodium azide. Membranes were then washed 4×5 minutes with TBS pH 7.4+0.05% Tween-20. Membranes were imaged using a Li-COR Odyssey near-IR fluorescence scanner. Secondary antibodies used were Odyssey cat 926-32211 (goat anti-rabbit)/926-68072 (donkey anti-mouse)/926-32212 (donkey anti-mouse).

2.7 Mass spectrometry

Mass spectra were collected using an Agilent 1200 series HPLC, generally coupled to a C_5 or C_8 reverse-phase column for removal of salt. Alternately, samples were diluted 1:10 with 5 mM ammonium bicarbonate, dialysed against 1 L 5 mM ammonium bicarbonate for 1 hour at room temperature, then directly injected onto the mass spectrometer. Spectra were collected with an Agilent 6220 mass spectrometer, or an Agilent 6520 mass spectrometer. Following collection of the spectra, the spectra were extracted and deconvoluted using Masshunter (Agilent).

For labelled samples, the degree of isotope incorporation was calculated using Equation 2.1[367]:

$$Efficiency\ (\%) = 100\left(\frac{labeled\ MW_{experiment} - unlabeled\ MW_{experiment}}{labeled\ MW_{calculated} - unlabeled\ MW_{calculated}}\right) \quad \text{Eq. 2.1}$$

2.8 Conclusions

A major bottleneck in the study of IL-11 has historically been limited amounts of sample material. The methods presented here have allowed our laboratory to produce large amounts of IL-11 and the IL-11 receptors for subsequent structural analysis. They have also enabled us to generate large amounts of biologically active IL-11 or IL-11 muteins for *in vivo* studies by others.

2.9 Supplementary Material

2.9.1 Supplementary Figures

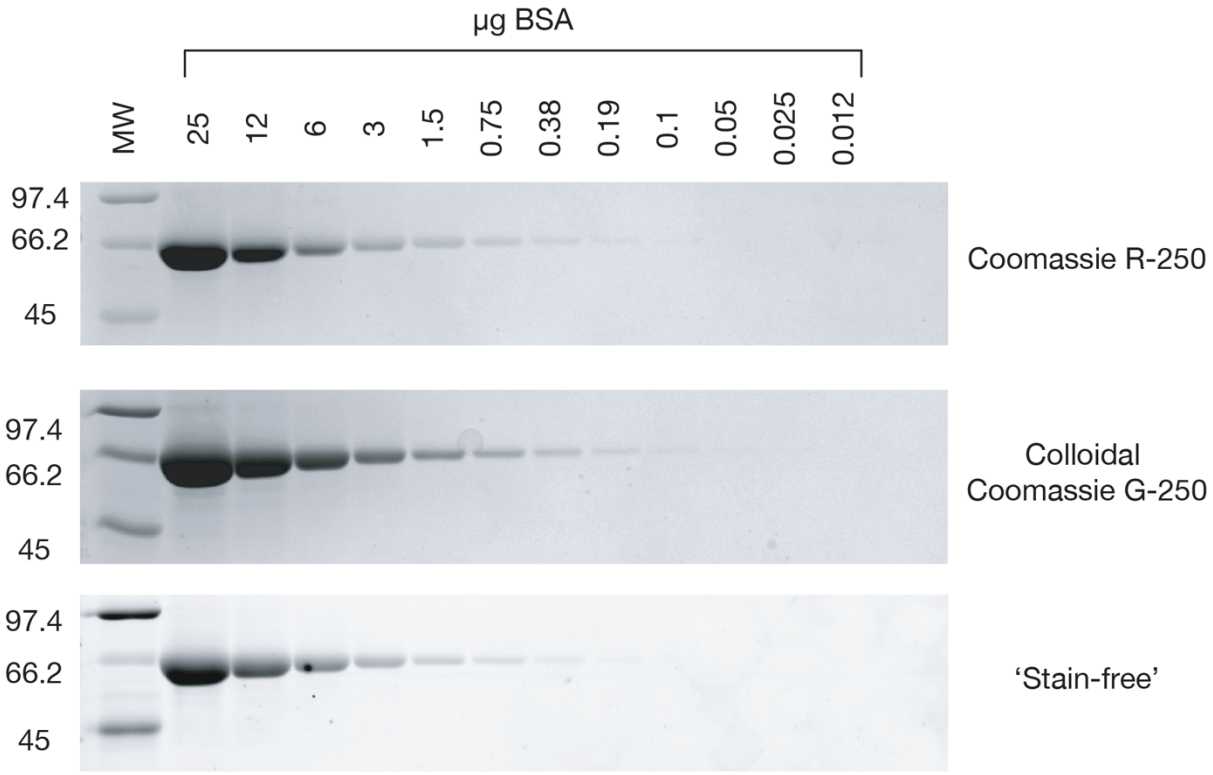

Supplementary Figure 2.1: Comparison of gel staining methods.

A serial dilution of BSA was run on a gel, the gels were then stained using 'conventional' Coomassie R-250 staining (0.1% Coomassie R-250, 10% acetic acid, 50% methanol), 'Blue-silver' Coomassie G-250 staining, or 'stain-free' staining. Coomassie G-250 staining is clearly more sensitive than either of the other two methods and is able to detect ~100 ng BSA.

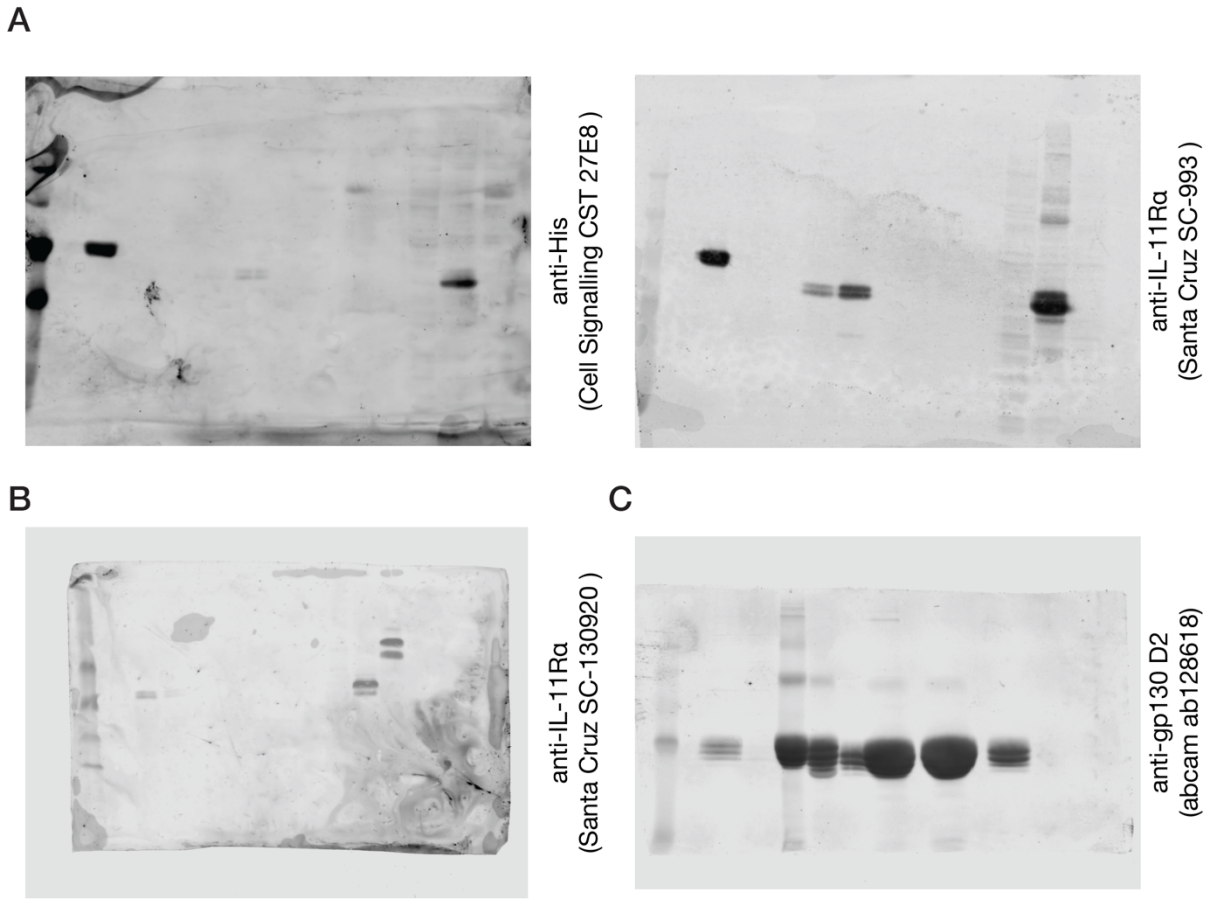

Supplementary Figure 2.2: Complete membrane images.

Complete membrane images for A), the membranes shown in Figure 2.5B, B) the membrane shown in Figure 2.6A and C) the membrane shown in Figure 2.7A

2.9.2 Supplementary Tables

Supplementary Table 2.1: Protein sequences.

Amino acid sequences for the proteins studied during this PhD. Protein sequences are shown following all proteolytic processing (e.g. removal of signal peptide, removal of tags). If applicable, mutations are indicated in red. Sequence molecular weight, isoelectric point and extinction coefficients (at 280 nm) calculated using the *Expasy* server[366].

Name	Sequence	Mass (Da)	pI	ε $(mg/mL)^{-1}$ cm^{-1}
$IL\text{-}11_{FL}$	GPGPPPGPPRVSPDPRAELDSTVLLTRSLLADTRQLAAQLRDKFPADGDHNLDSLPTLAMSAG ALGALQLPGVLTRLRADLLSYLRHVQWLRRAGGSSLKTLEPELGTLQARLDRLLRRLQLLMSRL ALPQPPPDPPAPPLAPPSSAWGGIRAAHAILGGLHLTLDWAVRGLLLLKTRL	19201.44	11.16	0.94
$IL\text{-}11_{\Delta10}$	GSPDPRAELDSTVLLTRSLLADTRQLAAQLRDKFPADGDHNLDSLPTLAMSAGALGALQLPG VLTRLRADLLSYLRHVQWLRRAGGSSLKTLEPELGTLQARLDRLLRRLQLLMSRLALPQPPPD PPAPPLAPPSSAWGGIRAAHAILGGLHLTLDWAVRGLLLLKTRL	18249.32	10.95	0.99
$IL\text{-}11_{FL}$ Mutein	GPGPPPGPPRVSPDPRAELDSTVLLTRSLLADTRQLAAQLRDKFPADGDHNLDSLPTLPAIDY ALGALQLPGVLTRLRADLLSYLRHVQWLRRAGGSSLKTLEPELGTLQARLDRLLRRLQLLMSRL ALPQPPPDPPAPPLAPPSSAAGGIRAAHAILGGLHLTLDWAVRGLLLLKTRL	19228.44	10.69	0.72
$IL\text{-}11_{\Delta10}$ Mutein	GSPDPRAELDSTVLLTRSLLADTRQLAAQLRDKFPADGDHNLDSLPTLPAIDYALGALQLPG VLTRLRADLLSYLRHVQWLRRAGGSSLKTLEPELGTLQARLDRLLRRLQLLMSRLALPQPPPD PPAPPLAPPSSAAGGIRAAHAILGGLHLTLDWAVRGLLLLKTRL	18276.32	10.40	0.77
$IL\text{-}11_{\Delta10/PAIDY}$	GSPDPRAELDSTVLLTRSLLADTRQLAAQLRDKFPADGDHNLDSLPTLPAIDYALGALQLPG	18391.45	10.40	1.06

	VLTRLRADLLSYLRHVQWLRRAGGSSLKTLEPELGTLQARLDRLLRRLQLLMSRLALPQPPPD PPAPPLAPPSSAWGGIRAAHAILGGLHLTLDWAVRGLLLLKTRL			
IL-11$_{\Delta 10/W147A}$	GSPDPRAELDSTVLLTRSLLADTRQLAAQLRDKFPADGDHNLDSLPTLAMSAGALGALQLPG VLTRLRADLLSYLRHVQWLRRAGGSSLKTLEPELGTLQARLDRLLRRLQLLMSRLALPQPPPD PPAPPLAPPSSAAGGIRAAHAILGGLHLTLDWAVRGLLLLKTRL	18134.18	10.95	0.69
IL-11$_{\Delta 10/R169A}$	GSPDPRAELDSTVLLTRSLLADTRQLAAQLRDKFPADGDHNLDSLPTLAMSAGALGALQLPG VLTRLRADLLSYLRHVQWLRRAGGSSLKTLEPELGTLQARLDRLLRRLQLLMSRLALPQPPPD PPAPPLAPPSSAWGGIRAAHAILGGLHLTLDWAVAGLLLLKTRL	18164.21	10.67	0.99
AviTag-IL-11$_{\Delta 10}$	GSPDPRAELDSTVLLTRSLLADTRQLAAQLRDKFPADGDHNLDSLPTLAMSAGALGALQ LPGVLTRLRADLLSYLRHVQWLRRAGGSSLKTLEPELGTLQARLDRLLRRLQLLMSRLA LPQPPPDPPAPPLAPPSSAWGGIRAAHAILGGLHLTLDWAVRGLLLLKTRLGSGSGSLE GLNDIFEAQKIEWHE	20734.96	9.38	1.13
AviTag-IL-11$_{\Delta 10}$ Mutein	GSPDPRAELDSTVLLTRSLLADTRQLAAQLRDKFPADGDHNLDSLPTLPAIDYALGALQ LPGVLTRLRADLLSYLRHVQWLRRAGGSSLKTLEPELGTLQARLDRLLRRLQLLMSRLA LPQPPPDPPAPPLAPPSSAAGGIRAAHAILGGLHLTLDWAVRGLLLLKTRLGSGSGSLE GLNDIFEAQKIEWHE	20761.97	8.37	0.94
IL-11$_{\Delta 10/S53A/W147A}$	GSPDPRAELDSTVLLTRSLLADTRQLAAQLRDKFPADGDHNLDALPTLAMSAGALGALQLPG VLTRLRADLLSYLRHVQWLRRAGGSSLKTLEPELGTLQARLDRLLRRLQLLMSRLALPQPPPD PPAPPLAPPSSAAGGIRAAHAILGGLHLTLDWAVRGLLLLKTRL	18118.18	10.95	0.69
IL-11$_{\Delta 10/A58P/W147A}$	GSPDPRAELDSTVLLTRSLLADTRQLAAQLRDKFPADGDHNLDSLPTLPMSAGALGALQLPG VLTRLRADLLSYLRHVQWLRRAGGSSLKTLEPELGTLQARLDRLLRRLQLLMSRLALPQPPPD PPAPPLAPPSSAAGGIRAAHAILGGLHLTLDWAVRGLLLLKTRL	18160.22	10.95	0.69
IL-11 $_{\Delta 10/S53A/A58P/W147A}$	GSPDPRAELDSTVLLTRSLLADTRQLAAQLRDKFPADGDHNLDALPTLPMSAGALGALQLPG VLTRLRADLLSYLRHVQWLRRAGGSSLKTLEPELGTLQARLDRLLRRLQLLMSRLALPQPPPD	18144.22	10.95	0.69

	PPAPPLAPPSSAAGGIRAAHAILGGLHLTLDWAVRGLLLLKTRL			
Slip-IL-11$_{\Delta 10}$	GSPDPRAELDSTVLLTRSLLADTRQLAAQLRDKFPADGDHNLDSLDSLPTLAMSAGALQL PGVLTRLRADLLSYLRHVQWLRRAGGSSLKTLEPELGTLQARLDRLLRRLQLLMSRLALP QPPPDPPAPPLAPPSSAAGGIRAAHAILGGLHLTLDWAVRGLLLLKTRL	18208.22	10.65	0.69
SlipDY-IL-11$_{\Delta 10}$	GSPDPRAELDSTVLLTRSLLADTRQLAAQLRDKFPADGDHNLDSLDSLPTLAMSDYALQL PGVLTRLRADLLSYLRHVQWLRRAGGSSLKTLEPELGTLQARLDRLLRRLQLLMSRLALP QPPPDPPAPPLAPPSSAAGGIRAAHAILGGLHLTLDWAVRGLLLLKTRL	18358.35	10.10	0.76
muGFP-IL-11	MRGSHHHHHHGSSKGEELFTGVVPILVELDGDVNGHKFSVRGEGEGDATNGKLTLKF ICTTGKLPVPWPTLVTTLTYGVLCFSRYPDHMKRHDFFKSAMPEGYVQERTISFKDDGT YKTRAEVKFEGDTLVNRIELKGIDFKEDGNILGHKLEYNFNSHNVYITADKQKNGIKAYF KIRHNVEDGSVQLADHYQQNTPIGDGPVLLPDNHYLSTQSVLSKDPNEKRDHMVLLE DVTAAGITHGMDELYKLSSGENLYFQGPGPPPGPPRVSPDPRAELDSTVLLTRSLLADT RQLAAQLRDKFPADGDHNLDSLPTLAMSAGALGALQLPGVLTRLRADLLSYLRHVQW LRRAGGSSLKTLEPELGTLQARLDRLLRRLQLLMSRLALPQPPPDPPAPPLAPPSSAWGGI RAAHAILGGLHLTLDWAVRGLLLLKTRL	48373.17	7.37	0.82
muGFP-IL-11 Mutein	MRGSHHHHHHGSSKGEELFTGVVPILVELDGDVNGHKFSVRGEGEGDATNGKLTLKF ICTTGKLPVPWPTLVTTLTYGVLCFSRYPDHMKRHDFFKSAMPEGYVQERTISFKDDGT YKTRAEVKFEGDTLVNRIELKGIDFKEDGNILGHKLEYNFNSHNVYITADKQKNGIKAYF KIRHNVEDGSVQLADHYQQNTPIGDGPVLLPDNHYLSTQSVLSKDPNEKRDHMVLLE DVTAAGITHGMDELYKLSSGENLYFQGPGPPPGPPRVSPDPRAELDSTVLLTRSLLADT RQLAAQLRDKFPADGDHNLDSLPTLPAIDYALGALQLPGVLTRLRADLLSYLRHVQW LRRAGGSSLKTLEPELGTLQARLDRLLRRLQLLMSRLALPQPPPDPPAPPLAPPSSAAGGI RAAHAILGGLHLTLDWAVRGLLLLKTRL	48400.18	7.06	0.74
muGFP	MRGSHHHHHHGSSKGEELFTGVVPILVELDGDVNGHKFSVRGEGEGDATNGKLTLKFI CTTGKLPVPWPTLVTTLTYGVLCFSRYPDHMKRHDFFKSAMPEGYVQERTISFKDDGTY	29246.80	6.13	0.75

	KTRAEVKFEGDTLVNRIELKGIDFKEDGNILGHKLEYNFNSHNVYITADKQKNGIKAYFK IRHNVEDGSVQLADHYQQNTPIGDGPVLLPDNHYLSTQSVLSKDPNEKRDHMVLLED VTAAGITHGMDELYKLSSGENLYFQG			
TEV protease	GHHHHHHHGESLFKGPRDYNPISSTICHLTNESDGHTTSLYGIGFGPFIITNKHLFRRN NGTLVVQSLHGVFKVKNTTTLQQHLIDGRDMIIIRMPKDFPPFPQKLKFREPQREERIC LVTTNFQTKSMSSMVSDTSCTFPSGDGIFWKHWIQTKDGQCGSPLVSTRDGFIVGIH SASNFTNTNNYFTSVPKNFMELLTNQEAQQWVSGWRLNADSVLWGGHKVFMVK PEEPFQPVKEATQLMNRRRRR	28573.44	9.59	1.20
IL-11Ra$_{D3}$	MSILRPDPPQGLRVESVPGYPRRLRASWTYPASWPSQPHFLLKFRLQY RPAQHPAWSTVEPAGLEEVITDAVAGLPHAVRVSARDFLDAGTWSTWSP EAWGTPSTGTIPKEIPAWGQLHTQPEVE	13974.79	6.40	3.08
IL-11Ra$_{EC}$	SSPCPQAWGPPGVQYGQPGRSVKLCCPGVTAGDPVSWFRDGEPKLLQGPDSGLG HELVLAQADSTDEGTYICQTLDGALGGTVTLQLGYPPARPVVSCQAADYENFSCTW SPSQISGLPTRYLTSYRKKTVLGADSQRRSPSTGPWPCPQDPLGAARCVVHGAEFWS QYRINVTEVNPLGASTRLLDVSLQSILRPDPPQGLRVESVPGYPRRLRASWTYPASWP SQPHFLLKFRLQYRPAQHPAWSTVEPAGLEEVITDAVAGLPHAVRVSARDFLDAGTW STWSPEAWGTPSTGTIPKEIPAWGQLHTQPEVEPQVDSPAPPRPSLQ PHPRLLDHRDSVHHHHHHHH	38167.77	6.58	2.13
IL-11Ra$_{D1-D3}$	GSSPCPQAWGPPGVQYGQPGRSVKLCCPGVTAGDPVSWFRDGEPKLLQGPDSGLGHEL VLAQADSTDEGTYICQTLDGALGGTVTLQLGYPPARPVVSCQAADYENFSCTWSPSQISGL PTRYLTSYRKKTVLGADSQRRSPSTGPWPCPQDPLGAARCVVHGAEFWSQYRINVTEVN PLGASTRLLDVSLQSILRPDPPQGLRVESVPGYPRRLRASWTYPASWPSQPHFLLKFRLQY RPAQHPAWSTVEPAGLEEVITDAVAGLPHAVRVSARDFLDAGTWSTWSPEAWGTPSTGT	32179.12	6.57	2.35

IL-11Rα$_{D1-D3/\Delta loop}$	GSSPCPQAWGPPGVQYGQPGRSVKLCCPGVTAGDPVSWFRDGEPKLLQGPDSGLGH ELVLAQADSTDEGTYICQTLDGALGGTVTLQLGYPPARPVVSCQAADYENFSCTWSPS QISGLPTRYLTSYRKKTVGGSPSTGPWPCPQDPLGAARCVVHGAEFWSQYRINVTEVNP LGASTRLLDVSLQSILRPDPPQGLRVESVPGYPRRLRASWTYPASWPSQPHFLLKFRLQY RPAQHPAWSTVEPAGLEEVITDAVAGLPHAVRVSARDFLDAGTWSTWSPEAWGTPSTGT	31409.26	6.23	2.40
Gp130$_{D1-D3}$	GELLDPCGYISPESPVVQLHSNFTAVCVLKEKCMDYFHVNANYIVWKTNHFTIPKEQY TIINRTASSVTFTDIASLNIQLTCNILTFGQLEQNVYGITIISGLPPEKPKNLSCIVNEGKKMRC EWDGGRETHLETNFTLKSEWATHKFADCKAKRDTPTSCTVDYSTVYFVNIEVWVEAENAL GKVTSDHINFDPVYKVKPNPPHNLSVINSEELSSILKLTWTNPSIKSVIILKYNIQYRTKDASTWSQI PPEDTASTRSSFTVQDLKPFTEYVFRIRCMKEDGKGYWSDWSEEASGITYED	34527.05	5.57	1.85
Gp130$_{D2-D3}$	GLPPEKPKNLSCIVNEGKKMRCEWDGGRETHLETNFTLKSEWATHKFADCKAKRDTPTSCTVDYST VYFVNIEVWVEAENALGKVTSDHINFDPVYKVKPNPPHNLSVINSEELSSILKLTWTNPSIKSVIILKYN IQYRTKDASTWSQIPPEDTASTRSSFTVQDLKPFTEYVFRIRCMKEDGKGYWSDWSEEASGITYED	23156.02	5.65	2.18
Gp130$_{EC}$	GELLDPCGYISPESPVVQLHSNFTAVCVLKEKCMDYFHVNANYIVWKTNHFTIPKEQY TIINRTASSVTFTDIASLNIQLTCNILTFGQLEQNVYGITIISGLPPEKPKNLSCIVNEGKK MRCEWDGGRETHLETNFTLKSEWATHKFADCKAKRDTPTSCTVDYSTVYFVNIEVWV EAENALGKVTSDHINFDPVYKVKPNPPHNLSVINSEELSSILKLTWTNPSIKSVIILKYNIQYR TKDASTWSQIPPEDTASTRSSFTVQDLKPFTEYVFRIRCMKEDGKGYWSDWSEEASGITYE DRPSKAPSFWYKIDPSHTQGYRTVQLVWKTLPPFEANGKILDYEVTLTRWKSHLQNYTVN ATKLTVNLTNDRYLATLTVRNLVGKSDAAVLTIPACDFQATHPVMDLKAFPKDNMLWVE WTTPRESVKKYILEWCVLSDKAPCITDWQQEDGTVHRTYLRGNLAESKCYLITVTPVYADGPG SPESIKAYLKQAPPSKGPTVRTKKVGKNEAVLEWDQLPVDVQNGFIRNYTIFYRTIIGNETAVNV DSSHTEYTLSSLTSDTLYMVRMAAYTDEGGKDGPEFTFTTPK	67125.11	6.23	1.94

Chapter 3 The structure of human interleukin 11 α-receptor reveals the mechanism of cytokine engagement

Riley D. Metcalfe[1], Kaheina Aizel[1,2,4], Courtney O. Zlatic[1], Paul M. Nguyen[2,3], Craig J. Morton[1], Daisy Sio-Seng Lio[1], Heung-Chin Cheng[1], Renwick C.J. Dobson[1,5], Michael W. Parker[1,6], Paul R. Gooley[1], Tracy L. Putoczki[2,3,4*], Michael D.W. Griffin[1*].

[*]For correspondence, putoczki.t@wehi.edu.au, mgriffin@unimelb.edu.au.

[1] Department of Biochemistry and Molecular Biology, Bio21 Molecular Science and Biotechnology Institute, The University of Melbourne, Parkville, Victoria, Australia,
[2] Inflammation Division, The Walter and Eliza Hall Institute of Medical Research, Parkville, Victoria, Australia
[3] Personalised Oncology Division, The Walter and Eliza Hall Institute of Medical Research, Parkville, Victoria, Australia
[4] Department of Medical Biology and Department of Surgery, University of Melbourne, Parkville, Victoria, Australia
[5] Biomolecular Interaction Centre and School of Biological Sciences, University of Canterbury, Christchurch, New Zealand
[6] ACRF Rational Drug Discovery Centre, St. Vincent's Institute of Medical Research, Fitzroy, Victoria, Australia

3.1 Abstract

Interleukin (IL)-11 activates multiple intracellular signalling pathways through formation of a complex with its cell surface α-receptor, IL-11Rα, and the β-subunit receptor, gp130. Dysregulated IL-11 signalling is implicated in several diseases, and mutations in IL-11Rα that reduce signalling are associated with hereditary cranial malformations. We present the first crystal structure of human IL-11Rα, and a structure of human IL-11 that reveals new detail. Disease-associated mutations in IL-11Rα are generally distal to putative ligand binding sites. Molecular dynamics simulations show that these mutations destabilise IL-11Rα and may have indirect effects on the cytokine binding region. We show that IL-11 and IL-11Rα form a 1:1 complex with nanomolar affinity and present a model of the complex. Our data show that the mechanisms of IL-11/IL-11Rα binding differ substantially from similar cytokines. This work reveals key determinants of IL-11 engagement by IL-11Rα that may be exploited in development of strategies to modulate complex formation.

3.2 Introduction

Interleukin (IL)-11 is a member of the IL-6 family of cytokines, which includes IL-6, leukemia inhibitory factor (LIF), oncostatin M, ciliary neutrophilic factor, IL-27, IL-31, cardiotrophin-1, cardiotrophin-like cytokine, and neuropoietin [40]. Activation of downstream signalling pathways by these cytokines is generally initiated via the formation of oligomeric receptor complexes that include the β-subunit signalling receptor, gp130, and one or more cytokine-specific co-receptors [122,376]. The majority of our structural and mechanistic understanding of this cytokine family is based on structural information available for IL-6 and LIF and their receptors [71,74,80].

Characterisation of the *in vivo* source of IL-11 has only recently begun, as a result of emerging links to multiple pathologies. IL-11 has classically been associated with haematopoiesis [5]; however, it has more recently been identified as the major cytokine involved in gastrointestinal tumorigenesis, and is a promising therapeutic target [208]. IL-11 also has emerging roles in cardiovascular and liver fibrosis [230,231]. Mutations in the IL-11 specific alpha-receptor, IL-11Rα, have gained increased interest as a result of their causative role in hereditary diseases that are typified by

craniosynostosis and delayed tooth eruption [191-194]. Several of these mutations have been shown to impair IL-11 signalling *in vitro* [194].

Following secretion, IL-11 is believed to interact with IL-11Rα, which is expressed on tissue specific cell populations [103]. This binary complex is thought to subsequently engage gp130 [74,167]. Previous mutagenesis and structural studies indicate that IL-11 interacts with its receptors through three independent sites on its surface [109]. Site-I is responsible for IL-11Rα binding; Site-II binds a gp130 molecule and contributes to the formation of a trimeric complex; and Site-III engages with a second gp130 molecule, resulting in the cooperative formation of a hexameric signalling complex containing two copies of each component [167].

Upon formation of the signalling complex, Janus kinases (JAK) associated with the cytoplasmic regions of gp130 are activated, although the exact mechanisms of activation remain unclear [39]. As IL-11Rα does not bind JAKs at its cytoplasmic domain, signalling is thought to result from trans-activation of JAK molecules bound to the cytoplasmic domains of the two gp130 molecules of the hexameric signalling complex. JAK activation then leads primarily to phosphorylation and activation of signal transducer and activator of transcription (STAT) 3. Activation of other signalling pathways, including the ERK/MAPK pathway and the PI(3)K pathway, is less well understood.

The structural basis of IL-6 signalling has been well studied and the structure of the hexameric IL-6 signalling complex has been solved [74]. Low-resolution electron microscopy studies of the IL-11 signalling complex suggest that the overall arrangement is likely similar to that of IL-6 [130]. We previously reported the first crystal structure of human IL-11 [109] and showed that while the topology is similar to IL-6, IL-11 is significantly elongated, suggesting different geometry of the signalling complex. Despite the growing biological importance of IL-11 signalling, molecular understanding of the structure and assembly of the IL-11 signalling complex remains in its infancy.

Here, we present the first crystal structure of human IL-11Rα and a new, more complete structure of IL-11 that reveals structural details of functionally important regions. Disease-associated mutations in IL-11Rα are generally located distal to putative binding surfaces of the receptor. Molecular dynamics simulations reveal the mechanisms by which several of these mutations disrupt the structure of IL-11Rα and thereby prevent signalling. We present a model of the IL-11/IL-11Rα complex, and in combination with biophysical and mutagenic characterisation of the cytokine/receptor interaction show that IL-11Rα and IL-6Rα engage their cognate cytokines with similar affinities, but use surprisingly different structural and thermodynamic mechanisms. Our work provides structural and mechanistic detail of the first step of formation of the IL-11 signalling complex that may be exploited in the development of molecules that can modulate complex formation.

3.3 Results and Discussion

3.3.1 The structure of the extracellular domains of the interleukin 11 receptor

The complete extracellular region of IL-11Rα (IL-11Rα$_{EC}$; residues 1-341 of the mature protein after signal peptide cleavage) was expressed in the insect cell line, Sf21, and purified from the cell culture supernatant. To reduce formation of disulfide-linked dimers, the C226S mutation [362] was present in all IL-11Rα constructs described in this work. Crystals of IL-11Rα$_{EC}$ were in space group $P6_522$ and the structure was refined at a resolution of 3.43 Å. Data and refinement statistics are presented in Supplementary Table 3.1 and representative electron density is shown in Supplementary Figure 3.1A, B.

The structure of IL-11Rα$_{EC}$ consists of an N-terminal Ig-like domain (D1) and two fibronectin-type III (FnIII) domains (D2, D3) that form the cytokine-binding homology region (CHR) (Figure 3.1A). The receptor is ‘L-shaped’, with D2 and D3 forming the CHR at and angle of approximately 80° with respect to each other. D1 is oriented at an angle of approximately 70° relative to D2. The overall arrangement of the three domains forming the extracellular region is similar to other IL-6 family α–chain cytokine receptors. Two protein molecules are present in the asymmetric unit, forming a crystallographic dimer in a ‘head-to-head’ configuration through an

interaction between D2 of each receptor molecule (Figure 3.1B). The structures of the two protein molecules in the asymmetric unit are very similar, with the same overall domain arrangement and an overall α-carbon RMSD of 2.0 Å. The C-terminus of the receptor is more complete in chain A, forming a crystal contact with a protein molecule in a neighbouring asymmetric unit. The absence of density for the complete C-terminus may be a result of disorder, or due to the presence of an endoproteinase (Glu-C) during the crystallization experiment. N-linked glycans are observed at N105 and N172, consistent with sites predicted from the sequence.

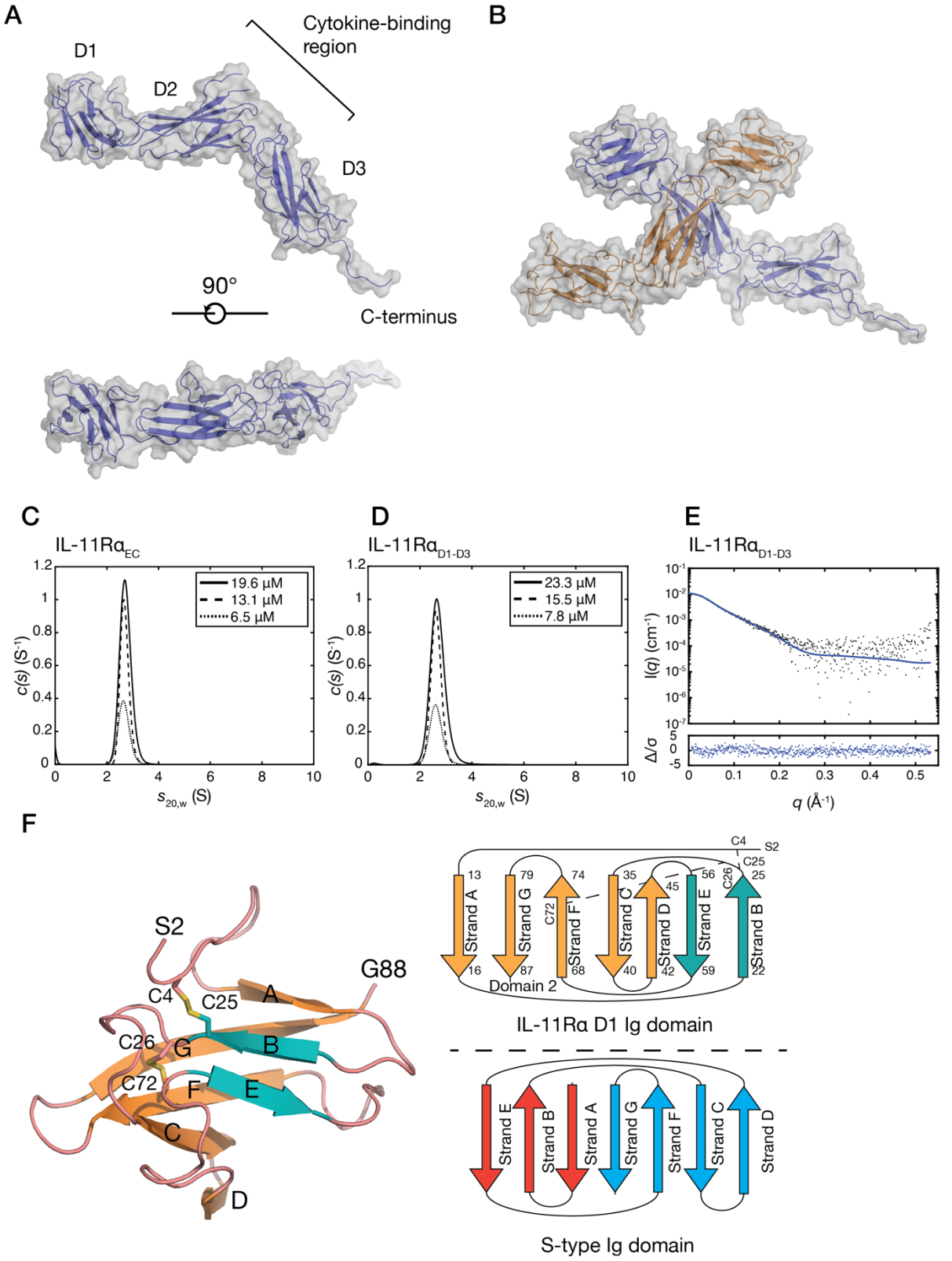

Figure 3.1: The crystal structure of IL-11Rα$_{EC}$.

A) Two views of the structure of IL-11Rα$_{EC}$. Each of the domains and the section of the C-terminus that is defined in the electron density are indicated. B) The asymmetric unit of the IL-11Rα crystal structure, formed by two IL-11Rα molecules,

with an extensive contact between D2 of the two molecules. C) Continuous sedimentation coefficient (c(s)) distributions for IL-11Rα$_{EC}$ at three concentrations, showing that IL-11Rα$_{EC}$ is primarily monomeric in solution under the conditions tested. Slight concentration dependence in the sedimentation coefficient suggests the formation of a transient oligomer. D) c(s) distributions for IL-11Rα$_{D1-D3}$ at several concentrations. E) Small-angle X-ray scattering data for IL-11Rα$_{D1-D3}$, overlaid with the theoretical scattering profile calculated from molecule A of the crystal structure of IL-11Rα$_{EC}$ (χ^2 =1.05). F) The structure (left) and topology (top right) of D1 from chain B of IL-11Rα$_{EC}$ with disulfide bonds indicated. Loops are coloured pink, the two strands contributing to the smaller, anti-parallel β-sheet blue, and the five strands contributing to the larger, mixed parallel/anti-parallel β-sheet orange. A topology diagram of the typical s-type Ig domain is also shown (bottom right).

The interface formed between the two IL-11Rα monomers in the asymmetric unit of the crystal structure is extensive, with a buried surface area of 1088 Å^2, as determined by *PISA* analysis (Figure 3.1B) [327]. To establish whether IL-11Rα$_{EC}$ self-associates in solution, we used sedimentation velocity-analytical ultracentrifugation (SV-AUC) at protein concentrations of 6.5 μM-19.5 μM, (0.25 - 0.75 mg/mL) (Figure 3.1C; Supplementary Figure 3.1Ci). These experiments show that IL-11Rα$_{EC}$ is predominantly monomeric in solution with a standardised sedimentation coefficient ($S_{20,w}$) of 2.70 S at 13.0 μM. This represents a molecular mass of 41.3 kDa, assuming a frictional ratio of 1.57 calculated from the fit to the SV data (Supplementary Figure 3.1Ci), in good agreement with the expected molecular mass from the sequence (38.2 kDa). The theoretical sedimentation coefficient, calculated from the crystal structure coordinates of chain A using *HYDROPRO* [377] was 2.92, consistent with the experimental value. A small, concentration-dependent increase in weight-average sedimentation coefficient was observed, from 2.67 S at 6.5 μM to 2.72 S at 19.5 μM, suggesting the formation of a weak-affinity dimer. Such dimerisation is likely extremely subtle, although is possible that this dimerisation is increased at the cell membrane, where the receptor may be concentrated in lipid rafts, analogous to other cytokine receptors [61,100], and can diffuse in only two dimensions, increasing its effective concentration.

To study the solution properties of IL-11Rα without the C-terminal extension, we generated a construct comprising only domains D1-D3 (IL-11Rα$_{D1-D3}$; residues 1-297 of the mature protein). The standardised sedimentation coef1ficient of IL-11Rα$_{D1-D3}$ measured at a protein concentration of 15.5 μM (0.5 mg/mL) was 2.62 S (Figure 3.1D; Supplementary Figure 3.1Cii; Supplementary Table 3.2), corresponding to a molecular weight of 34.9 kDa, given a frictional ratio of 1.47, in good agreement with the sequence molecular weight (32.1 kDa). Similar to the IL-11Rα$_{EC}$, a small concentration-dependent increase in weight average 1. We also analysed IL-11Rα$_{D1-D3}$ using small-angle X-ray scattering (SAXS). The SAXS profile of IL-11Rα$_{D1-D3}$ agrees well with the monomer of the crystal structure coordinates (χ^2 = 1.05) (Figure 3.1E; Supplementary Table 3.3; Supplementary Figure 3.1D), confirming that the crystal structure accurately represents the solution conformation of the structured, extracellular domains of IL-11Rα.

D1 of IL-11Rα forms an Ig-like domain with an unusual s-type topology [378] (Figure 3.1F). The Ig-like β sandwich of D1 consists of seven β strands arranged as two β sheets, the first consisting of a mixed parallel/anti-parallel sheet of five β strands (A, C, D, F and G) and the second consisting of two β strands (B and E). The A strand, which typically forms a three-strand anti-parallel β-sheet with strands B and E instead forms a parallel β-sheet with strand G. A short β-strand corresponding to strand D is present in chain B of the asymmetric unit, forming an anti-parallel β-sheet with strand C. However, strand D is not present in chain A, suggesting some flexibility of this region of D1. The overall topology is similar to D1 of IL-6Rα [117]. Two disulfide bonds are present in D1, one between C26 in the B/C linker and C72 in strand F. A disulfide bond in a similar position is present in the D1 of IL-6Rα [117]. A second disulfide bond is present between C4 and C25 in strand B, which was not predicted from sequence analysis or homology. The disulfide bond is well-supported in the electron density and confirmed in a simulated-annealing omit map (Supplementary Figure 3.1A). The unusual fold of D1 may be a consequence of these disulfides, with the C4-C25 disulfide serving to sterically constrain strand A, preventing the formation of a typical anti-parallel β-sheet with strands B and E.

Cytokines generally bind to the CHR surface at the junction between FnIII-type domains D2 and D3, with D3 also involved in interacting with other receptors comprising the complete signalling complex [40]. D2 of IL-11Rα contains the two disulfide bonds expected for the first domain in the CHR (between C98 and C108, and between C148 and C158). D3 of IL-11Rα contains the conserved tryptophan-arginine ladder (comprising tryptophan residues 282, 285, 246 and arginine residues 239, 270 and 274), which includes the strongly conserved WSXWS sequence motif. Like IL-6Rα and other cytokine receptors, the sequence containing the WSXWS motif forms a short polyproline type-II helix that is stabilised by sidechain-mainchain interactions and the tryptophan-arginine ladder.

Overall, the IL-11 binding region is made up of four loops, formed by residues 98-106 (between strands A and B), 129-145 (between strands C and D) and 160-169 (between strands D and E) in D2, and residues 220-232 (between strands B and C) in D3. Part of the loop between strands C and D of D2 (residues 132-139 of chain A and 132-141 of chain B) is not defined in the electron density. To our knowledge, a similar large and disordered loop in the CHR has not yet been described for any other cytokine receptor. The membrane-proximal region of D3 serves to engage gp130, to complement the Site-II interaction on the cytokine. This region is similar in topology and surface charge in both IL-6Rα and IL-11Rα, suggesting that the mechanism of α-receptor engagement with gp130 is similar between the two receptors.

The configuration of the CHR is different between IL-11Rα and IL-6Rα (Supplementary Figure 3.1Ei). In IL-11Rα, the relative positioning of D2 and D3, which is more similar to that of gp130 (Supplementary Figure 3.1Eii), creates a smaller cytokine binding surface than IL-6Rα. The electrostatic surface potential in the cytokine binding sites also differ between the two proteins (Supplementary Figure 3.1Fi). The IL-6 binding site in IL-6Rα is noticeably more charged than that of IL-11Rα, with a negatively charged patch formed by several acidic residues in the loop formed between strands F and G in D3, which mediate a number of

electrostatic contacts to IL-6 in the IL-6 signalling complex (Supplementary Figure 3.1Fii) [74,117]. These structural differences imply that IL-11Rα employs different structural mechanisms from IL-6Rα to engage its cognate cytokine at Site-I.

3.3.2 Pathogenetic mutations disrupt the structure of IL-11Rα

A number of pathogenic mutations have been identified in the gene for IL-11Rα, *IL11RA*, resulting in point-substitution mutations in IL-11Rα that cause a genetic disease featuring craniosynostosis and delayed tooth eruption [191-194]. Mapping the disease-associated mutations onto our structure of IL-11Rα indicates that very few of the mutations are in the putative IL-11 or gp130 binding sites (Figure 3.2A).

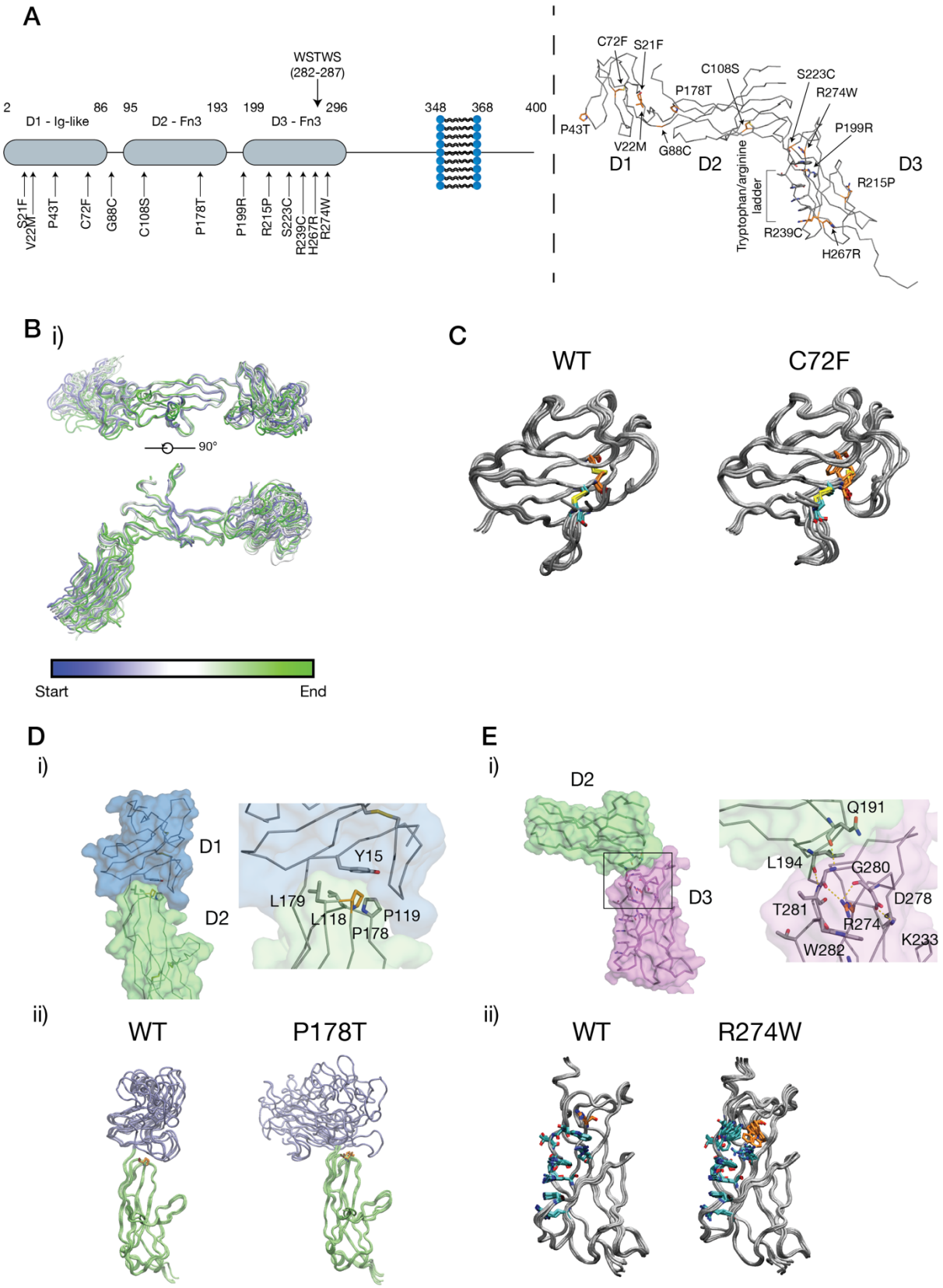

Figure 3.2: MD simulations of craniofacial disease associated mutations in IL-11Rα.

A) Disease associated mutations that have been identified in IL-11Rα. These mutations are shown mapped onto the structure and primary occur in D1, inter-domain turns and D3. B) Structural dynamics from a 50 ns MD simulation of IL-11Rα. i) Superposition of frames from the simulation. Ten frames are shown, coloured by simulation time. C) Frames from a 50 ns MD simulation of the C72F mutant. Frames are shown overlaid through the simulation. D) The structural impact of the P178T mutation, i) showing the location of P178 at the D1/D2 interface, and ii) showing frames from the MD simulation, showing that the P178T mutation destabilizes the native position of the D1. E) The structural impact of the R274W mutation, i) showing the position of R274, at the extreme end of the tryptophan-arginine ladder in D3. R274 also forms a hydrogen-bond network, stabilising the D2/D3 interface, ii) shows frames from an MD simulation, showing that the R274W mutation disrupts the tryptophan-arginine ladder and the D2/D3 interface.

To investigate the effects of the mutations on the structure of IL-11Rα, we ran a series of short (50 ns) all-atom molecular dynamics (MD) simulations on IL-11Rα (Figure 3.2B) and several of the disease mutants (Supplementary Movie 3.1, Supplementary Movie 3.2, Supplementary Movie 3.3). In IL-11Rα, the Cα RMSD and backbone amide bond order parameters (S^2) calculated from the MD trajectory indicate a low level of local disorder, and overall local rigidity within each of the three domains (Figure 3.2B; Supplementary Figure 3.2A). However, the three domains are dynamic with respect to each other throughout the simulation (Figure 3.2B; Supplementary Figure 3.2B). The loops comprising the IL-11 binding site are relatively rigid and do not undergo large motions on the timescale of the simulation.

MD simulations of IL-11Rα with the disease-associated mutations suggest that several of these destabilise key structural elements in the receptor or destabilise inter-domain interfaces. One mutation, C72F, removes a disulfide bond in D1, which likely has a role in stabilizing the unusual Ig-fold of D1. Introducing this mutation to D1 destabilises the domain, and results in the loop joining strands F and G adopting a markedly different conformation (Figure 3.2C, Supplementary Movie 3.1). A second mutation, P176T, is located in a loop in D2 that faces D1. This mutation

alters the D1/D2 interdomain interface during the simulation, causing a large change in the D1/D2 interdomain distance and a large shift in the relative pose of D1 and D2. This is likely due to removal of the interaction of P176 with a pocket on D1 that stabilises the D1/D2 interface (Figure 3.2D, Supplementary Movie 3.2).

Two mutations, R239C and R274W are situated within the tryptophan-arginine ladder in D3 of the receptor. The R274W mutation destabilises the tryptophan-arginine ladder, and results in the destabilization of the membrane-distal region of D3. R274 also contributes to a hydrogen-bonding network at the D2/D3 interdomain interface in the wild type receptor (Figure 3.2E, Supplementary Movie 3.3). The mutation thus destabilizes the D2/D3 linker, and results in an increase in flexibility at the D2/D3 interface, potentially disrupting the IL-11 binding interface and reducing cytokine affinity.

Several mutations have no appreciable impact on the structural dynamics within the timescale of the simulation. For example, P43T does not greatly alter the flexibility of the affected loop in D1, C108S does not appear to alter D2 through the simulation, nor does R239C destabilize D3 or the tryptophan-arginine ladder. The apparently minor effects of these mutations on the structure and their positioning distal to the putative cytokine and gp130 binding regions of the receptor suggest cryptic mechanisms that impair IL-11 signalling. Conversely, two mutations (R215P, H276R) are close to the putative gp130 binding region of D3, and thus may act by directly altering signalling complex formation at this interface.

Together our simulations show that the effect of a subset of the craniosynostosis mutations in IL-11Rα is to destabilise the structure of IL-11Rα. Both the R274W and P176T mutations have previously been shown to result in impaired expression of IL-11Rα at the cell surface contributing to reduced IL-11 mediated STAT3 activation [194]. Our results suggest that destabilisation of the structure and/or reduced capacity of the receptor to fold correctly due to these mutations is sufficient to stall correct trafficking of the receptor. D1 of IL-6Rα has previously been shown to be involved in intracellular trafficking of the receptor [65]. Thus, destabilisation of D1 or the D1/D2

interface of IL-11Rα may also result in a lack of correct processing of the receptor. In the case of the R274W mutation, indirect destabilisation of the cytokine binding surface of the receptor may also reduce IL-11 binding capacity by mutant IL-11Rα that is correctly expressed at the cell surface, further reducing the potential for formation of the active signaling complex.

3.3.3 The high-resolution structure of interleukin 11

In our previous structure of human IL-11 parts of the long loops between helices A and B and between helices C and D were poorly defined [109]. Thus, we aimed to solve a more complete structure of IL-11 to gain further insight into these loops.

To facilitate growth of crystals that diffracted to high resolution we truncated IL-11 by ten residues at the N-terminus, removing a proline-rich sequence that was not defined in our previous structure of IL-11, indicating that it is dynamic. We named this new construct IL-$11_{\Delta 10}$ (residues 11-178 of the mature protein) and the 'full-length' construct containing the N-terminal proline-rich sequence, IL-11_{FL}. Both IL-11_{FL} and IL-$11_{\Delta 10}$ have similar high thermal stability, as measured by differential scanning fluorimetry [379]. The temperatures of hydrophobic exposure (T_h; a measure of thermal stability) were 83.8 °C and 87.0 °C for IL-$11_{\Delta 10}$ and IL-11_{FL} respectively (Supplementary Figure 3.3A), indicating that the truncation has a small destabilising effect. Stimulation of human colon cancer cell line, DLD1 with either $11_{\Delta 10}$ or IL-11_{FL} results in similar levels of activation of STAT1 and STAT3 (Figure 3.3A) indicating that they have similar biological activity. We note that N-terminally truncated IL-11 constructs have been used previously with no reported alteration in biological activity [380,381].

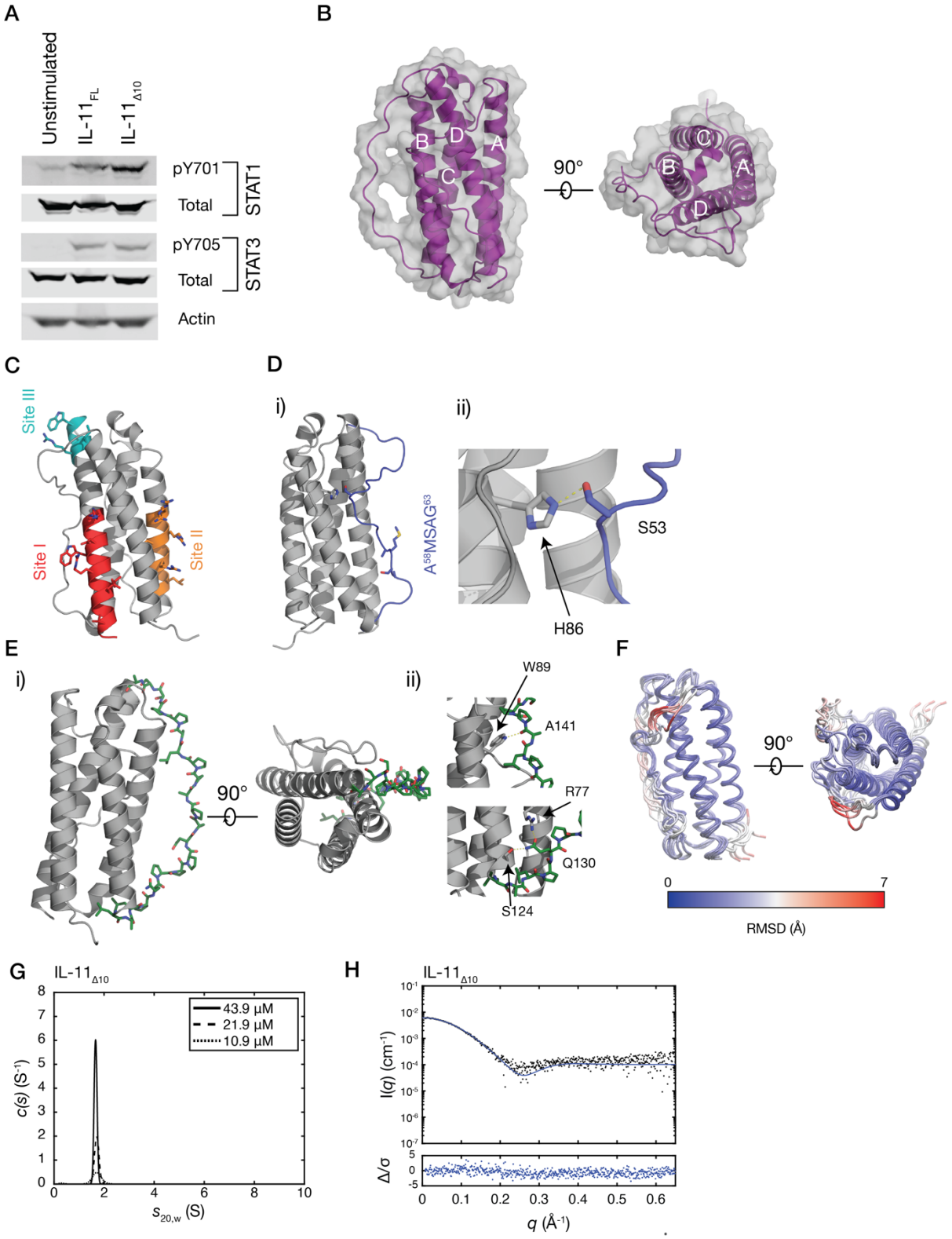

Figure 3.3: Biological activity and crystal structure of IL-11$_{\Delta 10}$.

A) Western blot, showing activation of STAT1 and STAT3 by IL-11$_{FL}$ and IL-11$_{\Delta 10}$ in the colon cancer cell line, DLD1. Complete membrane images are shown in Supplementary Figure 3.9A. B) Two views of the structure of IL-11$_{\Delta 10}$. The four

helices in the structure are labelled. C) Regions previously implicated in binding the IL-11 receptors. Site I is involved in binding IL-11Rα, site II and III subsequently interact with the shared receptor gp130. D) i) The loop between the A and B helices (AB loop; blue). The residues mutated in the IL-11 antagonist are indicated. The interaction between the loop and core 4-helix bundle structure is shown in ii), with H105 and S75 forming a hydrogen bond. E) The CD loop (green), part of which forms a polyproline helix. Two views of the helix are shown in i). The interactions stabilising the N and C-terminal parts of the polyproline helix are shown in ii). F) 100 ns MD simulation of IL-11 $_{\Delta 10}$. Frames are overlaid at 20 ns intervals, coloured by alpha carbon (Cα) RMSD. The α-helical core is stable through the simulation, while the loops undergo dynamic motions. G) c(s) distributions for IL-11$_{\Delta 10}$, at three concentrations, showing that it is monomeric in solution. H) Small-angle X-ray scattering data for IL-11$_{\Delta 10}$, overlaid with the theoretical scattering profile calculated from the crystal structure coordinates (χ^2 = 1.43).

Crystals of IL-11$_{\Delta 10}$ were rod-like plates in space group $P2_12_12$, and the structure was refined at a resolution of 1.62 Å. Data and refinement statistics are presented in Supplementary Table 3.1 and representative electron density is shown in Supplementary Figure 3.3B. Overall, the structure of IL-11$_{\Delta 10}$ is similar to our previously-solved structure of IL-11, forming a typical cytokine four-α-helical bundle in an up-up-down-down configuration (Figure 3.3B). The positions of helix A and helix D are subtly shifted between the two structures, with the four-α-helical bundle formed by IL-11$_{FL}$ slightly more compact compared with IL-11$_{\Delta 10}$ (Supplementary Figure 3.3C). This is likely a consequence of crystal contacts formed by helix A and D. A *cis* proline (P103) is also observed at the C-terminal end of the 3_{10} helical section of helix C. The equivalent proline in our previous structure of IL-11 is in the *trans* configuration (Supplementary Figure 3.3D). Both proline cis/trans isomers are strongly supported by electron density in their respective structures, suggesting that P103 can adopt either the *cis* or *trans* isomer and that the 3_{10} helix is dynamic in solution. The three receptor binding sites of the cytokine are not significantly altered in the structure (Figure 3.3C) [109].

Importantly, our higher resolution structure of IL-$11_{\Delta 10}$ allows the extended loops joining helices A and B and helices C and D to be included in the model. The AB loop is formed by 26 residues between F43 and L69, (Figure 3.3D). The position of the AB loop in IL-11 is stabilised by hydrophobic interactions between residues L54 and P55 of the loop and the α-helical core, and a hydrogen bond between S53 of the loop and H86 in helix B. This central region of the loop is well defined in the electron density. The N and C terminal regions of the loop do not appear to closely contact the core structure or form any crystal contacts and are thus less well defined in the electron density. The disordered nature of this loop, adjacent to Site I, may thus have consequences for IL-11 binding to IL-11Rα and the formation of the IL-11 signalling complex. The AB loop has been targeted for mutagenesis in an IL-11 antagonist, with several residues in the C-terminal region of the loop (comprising A59 to G64) mutated in an effort to increase the affinity for IL-11Rα [198], thus the AB loop appears to have an important role in receptor binding and complex formation. Similarly, the N-terminal region of the corresponding loop of IL-6 forms part of Site-III, and is involved in interacting with gp130 to form the complete signalling complex [74].

The CD loop of IL-11 forms an unusually long polyproline type II (PP2) helix (Figure 3.3E), comprising 14 residues and the majority of the sequence in the CD loop. The loop contacts the B helix, with polar contacts between W89 and the backbone carbonyl of A141, and between R85 and P138, serving to stabilise the C-terminal end of the PP2 helix. The N-terminal end of the PP2 helix is stabilised by contacts between Q130, S124 and R77. The central portion of the PP2 helix does not contact the core structure. To our knowledge, an equivalently long polyproline helix has not been observed in the structure of any other cytokine. It is unlikely that the PP2 helix has any role in signalling complex formation, as it is distant from the receptor binding sites. Instead, the likely function of the helix is structural – to efficiently join the C-terminal end of helix C and the N-terminal end of helix D, which are 44 Å apart, with a relatively short sequence of 21 residues. The relative rigidity of the PP2 helix may also serve to limit dynamic motions of this loop and may aid stability of the structure.

To further study the dynamic nature of the loops of IL-11, we ran a series of short (100 ns) molecular dynamics simulations on IL-11 (Figure 3.3F). In the timescale of the simulation, the four-α-helical bundle is stable and does not undergo large movements (Figure 3.3F; Supplementary Figure 3.3E). In common with other IL-6 family cytokines that have been studied by NMR, the α-helices show 'helical fraying,' and are more dynamic at the ends of the helices, compared with the core (Figure 3.3F) [382,383]. While the PP2 helix structure of the CD loop is preserved throughout the simulation, the loop undergoes lateral movements. The AB loop is generally highly dynamic on the timescale of the simulation, although the central portion of the loop is stabilised by interactions with α-helical core. Both the N- and C-terminal ends of the AB loop, implicated in gp130 and IL-11Rα binding respectively, are highly dynamic on the timescale of the simulation.

We used SV-AUC to determine the oligomeric state of IL-$11_{\Delta 10}$ at concentrations of 10 μM-40 μM (0.2-0.8 mg/mL). c($s_{20,w}$) distributions show single, symmetrical peaks around 1.7 S (Figure 3.3G; Supplementary Table 3.2). This value represents a molecular mass of 17.2 kDa, given a frictional ratio of 1.28 calculated from data acquired at 40 μM (Supplementary Figure 3.3F), in good agreement with the monomer molecular mass (18.2 kDa). The theoretical sedimentation coefficient, calculated from our crystal structure coordinates using *HYDROPRO* [377] was 1.76, providing further evidence that IL-$11_{\Delta 10}$ is monomeric in solution. SAXS data for IL-$11_{\Delta 10}$ agrees well with the theoretical scattering profile calculated for the crysta11l structure coordinates (χ^2 = 1.43), showing that the structure is representative of the solution conformation (Figure 3.3H; Supplementary Table 3.2; Supplementary Table 3.3; Supplementary Figure 3.3G). SV-AUC also shows that IL-11_{FL} is monomeric in solution, and the theoretical scattering profile of IL-$11_{\Delta 10}$ agrees with the solution scattering profile of IL-11_{FL} (χ^2 = 3.21) (Supplementary Figure 3.4A-D; Supplementary Table 3.2; Supplementary Table 3.3).

3.3.4 IL-11 and IL-11Rα interact with nanomolar affinity

We used SV-AUC to investigate the interaction between IL-11 and IL-11Rα. For these experiments, the complex was formed by mixing 5 μM IL-$11_{\Delta10}$ and 5 μM IL-$11R\alpha_{EC}$ immediately prior to the experiment, with no further purification. The appearance of a peak in the c($s_{20,w}$) distribution with a sedimentation coefficient of 3.2 S, larger than either IL-$11_{\Delta10}$ and IL-$11R\alpha_{EC}$ alone, indicated formation of a complex between IL-$11R\alpha_{EC}$ and IL-$11_{\Delta10}$ (Figure 3.4Ai). The estimated molecular weight of this species was 60.8 kDa, given a frictional ratio of 1.71, consistent with a complex forming with 1:1 stoichiometry (Supplementary Figure 3.5A; Supplementary Table 3.2). A similar complex is formed between IL-$11_{\Delta10}$ and IL-$11R\alpha_{D1\text{-}D3}$ (Figure 3.4Aii; Supplementary Table 3.2: sedimentation coefficient 3.3, molecular weight 55.8 kDa, frictional ratio 1.61), IL-11_{FL} and IL-$11R\alpha_{EC}$ (sedimentation coefficient 3.2, molecular weight 60.5 kDa, frictional ratio 1.71) and between IL-11_{FL} and IL-$11R\alpha_{D1\text{-}D3}$ (Supplementary Figure 3.6A; Supplementary Figure 3.7D; Supplementary Table 3.2; sedimentation coefficient 3.3, molecular weight 55.9 kDa, frictional ratio 1.61).

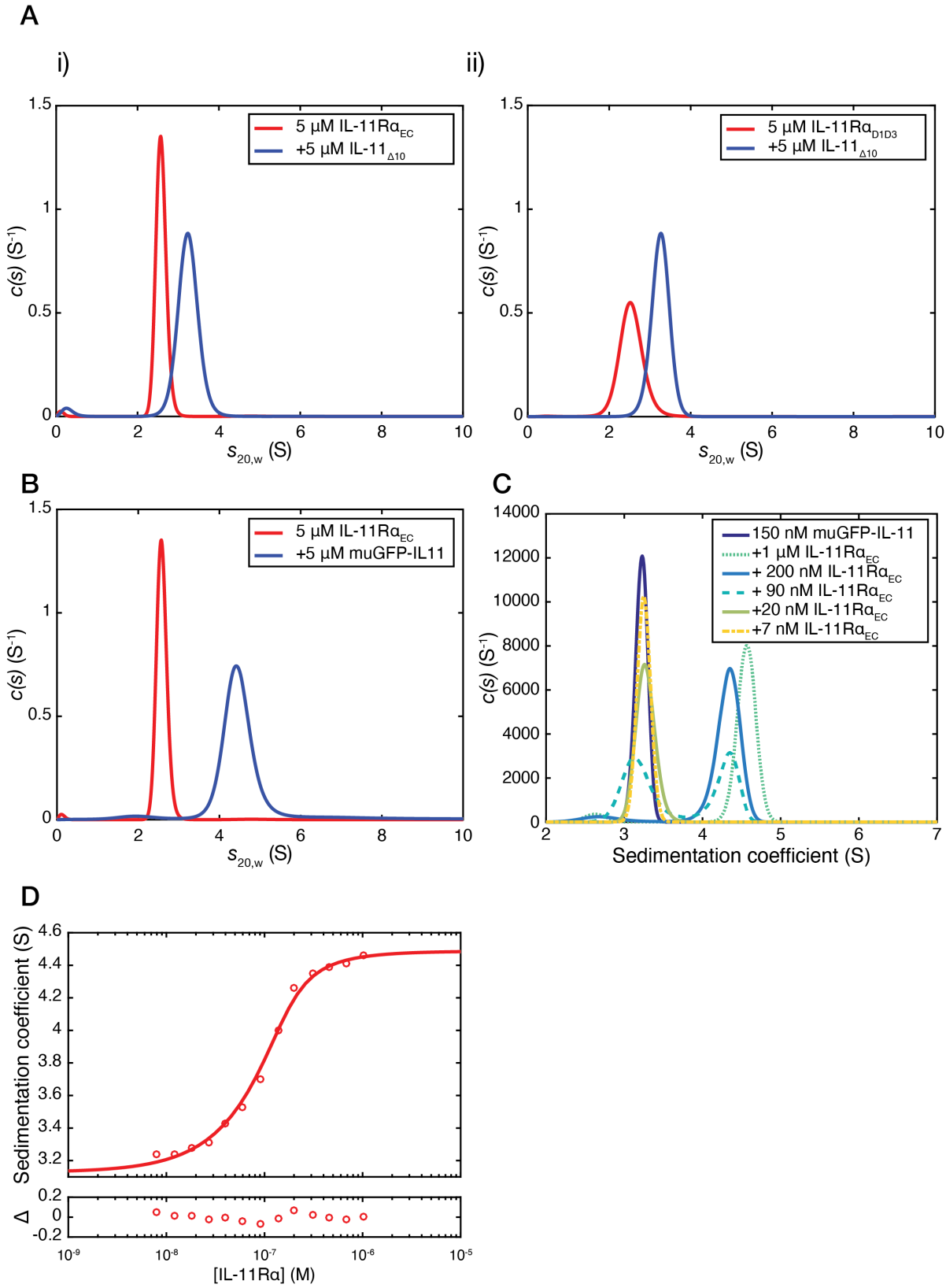

Figure 3.4: SV-AUC analysis of the IL-11/IL-11Rα complex.

A) Continuous sedimentation coefficient (c(s)) distributions for the complex between i) IL-11Rα$_{EC}$ and IL-11$_{Δ10}$, ii) and IL-11Rα$_{D1-D3}$ and IL-11$_{Δ10}$. The complex was formed

by mixing 5 μM IL-11 and 5 μM IL-11Rα prior to the experiment, with no further purification. The c(s) distribution for 5 μM IL-11Rα$_{EC}$ or IL-11Rα$_{D1-D3}$ is shown in all panels. B) The c(s) distribution for muGFP-IL-11, and muGFP-IL-11 in complex with IL-11Rα. The complex was formed by mixing 5 μM muGFP-IL-11 and IL-11Rα prior to the experiment, with no further purification. The c(s) distribution for 5 μM IL-11Rα$_{EC}$ is also shown. C) Fluorescent-detected c(s) distributions for the muGFP-IL-11/IL-11Rα complex at concentrations close to the K_D of the interaction. IL-11Rα concentrations are indicated in the figure, muGFP-IL-11 was at a constant concentration of 150 nM. D) Sedimentation coefficient isotherm for muGFP-IL-11 binding to IL-11Rα. The concentration of muGFP-IL-11 was 150 nM, titrated with increasing concentrations of IL-11Rα. The best-fit to the data yielded a K_D of 22 nM [68% CI 14-35 nM].

To determine the dissociation constant for the IL-11/IL-11Rα interaction, we used fluorescence-detected SV-AUC (FD-AUC), which can accurately measure proteins present at nanomolar and picomolar concentrations[384]. We expressed IL-11$_{FL}$ N-terminally fused to a monomeric, ultrastable (mu) green fluorescent protein (GFP) [385]. SV-AUC showed that muGFP-IL-11 is monomeric across a wide concentration range (Supplementary Figure 3.6B, Supplementary Figure 3.7E) and forms a complex with IL-11Rα$_{EC}$ in a 1:1 stoichiometry at concentrations of 5 μM of each component (Figure 3.4B; Supplementary Figure 3.5B; Supplementary Table 3.2). Complex formation was apparent at concentrations of IL-11Rα$_{EC}$ in the nanomolar range, with two peaks observed in c($s_{20,w}$) distributions corresponding to free muGFP-IL-11 and muGFP-IL-11 in complex with IL-11Rα$_{EC}$ (Figure 3.4C; Supplementary Figure 3.5C; Supplementary Table 3.2). We generated a sedimentation coefficient isotherm for the titration of IL-11Rα$_{EC}$ against muGFP-IL-11, which, when fit to a 1:1 binding model, gave a K_D of 22 nM [68% confidence interval 14-35 nM] (Figure 3.4D; Supplementary Figure 3.5C). This is consistent with the dissociation constant for similar site I cytokine/α-receptor interactions. For example, IL-6 and IL-6Rα interact with a K_D of 9 nM [74], IL-2 and IL-2Rβ interact with a K_D of 144 nM [386] and IL-7 interacts with IL-7Rα with a K_D of approximately 50 nM [387]. In each of these cases, the complete signalling complex is formed by further

high-affinity interactions between the cytokine/α-receptor complex and other receptors. These experiments show that the IL-11/IL-11Rα$_{EC}$ interaction also fits into this paradigm; an initial low-nanomolar affinity step to form the complex between IL-11 and IL-11Rα occurs first, allowing subsequent engagement by gp130.

The tendency of GFP to form weakly-associating dimers with a K_D of approximately 100 μM has previously limited the use of GFP in quantitative biophysical experiments [388]. The monomeric, ultrastable GFP used here does not detectably dimerise [385], allowing it to be used as a genetically-encoded fluorescent tag for biophysical experiments. Previous efforts to use FD-AUC to measure high-affinity protein-protein interactions have generally relied on covalent modification of one of the interacting partners with a fluorescent dye, with previous studies noting that the use of covalent dyes as fluorescent labels alters the binding properties of the proteins under investigation [389]. The use of a genetically encoded, monomeric fluorescent fusion tag overcomes this limitation, as the addition of a fusion protein does not alter regions of the target protein directly involved in protein-protein interactions. This allows the accurate measurement of nanomolar-affinity dissociation constants in the analytical ultracentrifuge, without requiring the covalent modification of one of the proteins involved in the interaction.

3.3.5 The IL-11Rα/IL-11 interaction is entropically driven

We used isothermal titration calorimetry (ITC) to complement our FD-AUC binding experiments above, and to examine the thermodynamic basis of cytokine-receptor engagement (Supplementary Table 3.4). ITC shows that IL-11$_{\Delta 10}$ interacts with IL-11Rα$_{EC}$ and IL-11Rα$_{D1\text{-}D3}$ with similar affinities, with K_D values of 40 ± 20 nM and 23 ± 3 nM respectively (n=3, standard error; Figure 3.5Ai and 5Aii). These values are consistent with our AUC experiments and show that the C-terminal extension of IL-11Rα does not significantly affect IL-11 binding. We also measured the affinity for the interaction between IL-11$_{FL}$ and IL-11Rα$_{EC}$, K_D of 55 ± 14 nM (n=3, standard error; Supplementary Figure 3.6C), showing that deletion of the N-terminus of IL-11 does not significantly alter affinity for IL-11Rα ($p = 0.58$). The thermodynamics of the

IL-$11_{\Delta10}$/IL-$11R\alpha_{D1-D3}$ interaction are strongly driven by entropy (ΔH = -25 ± 2 kJ/mol, ΔS = 66 ± 7 J/molK). mechanisms to engage their cognate cytokines. We also measured the IL-$11_{\Delta10}$/IL-$11R\alpha_{D1-D3}$ interaction using ITC at two additional temperatures (283 and 298 K) to determine the heat capacity of the reaction, ΔC_p (Supplementary Figure 3.6D, Supplementary Table 3.4). The heat capacity was measured as -3.3 ± 0.07 kJ/molK (mean ± standard error). An empirical relationship exists between heat capacity and total buried surface area, a large negative ΔC_p being consistent with a large buried surface area [390-392], suggesting that the IL-11/IL-11Rα is hydrophobic in nature, and results in the burying of a large amount of hydrophobic surface.

Overall, our ITC results are consistent with our structure of IL-$11R\alpha_{EC}$, with the cytokine binding site lacking large charged or hydrophilic regions, suggesting a hydrophobic interaction that is primarily driven by a positive change in entropy. This contrasts strongly with the IL-6/IL-6Rα interaction, which is strongly exothermic, with a corresponding unfavourable entropy change (ΔH -100 kJ/mol, ΔS -192 J/molK at 283 K), a consequence of the structural differences between the two cytokines and receptors [74]. Thus, in spite of apparent structural similarity, IL-6Rα and IL-11Rα employ different thermodynamic mechanisms to engage their cognate cytokine.

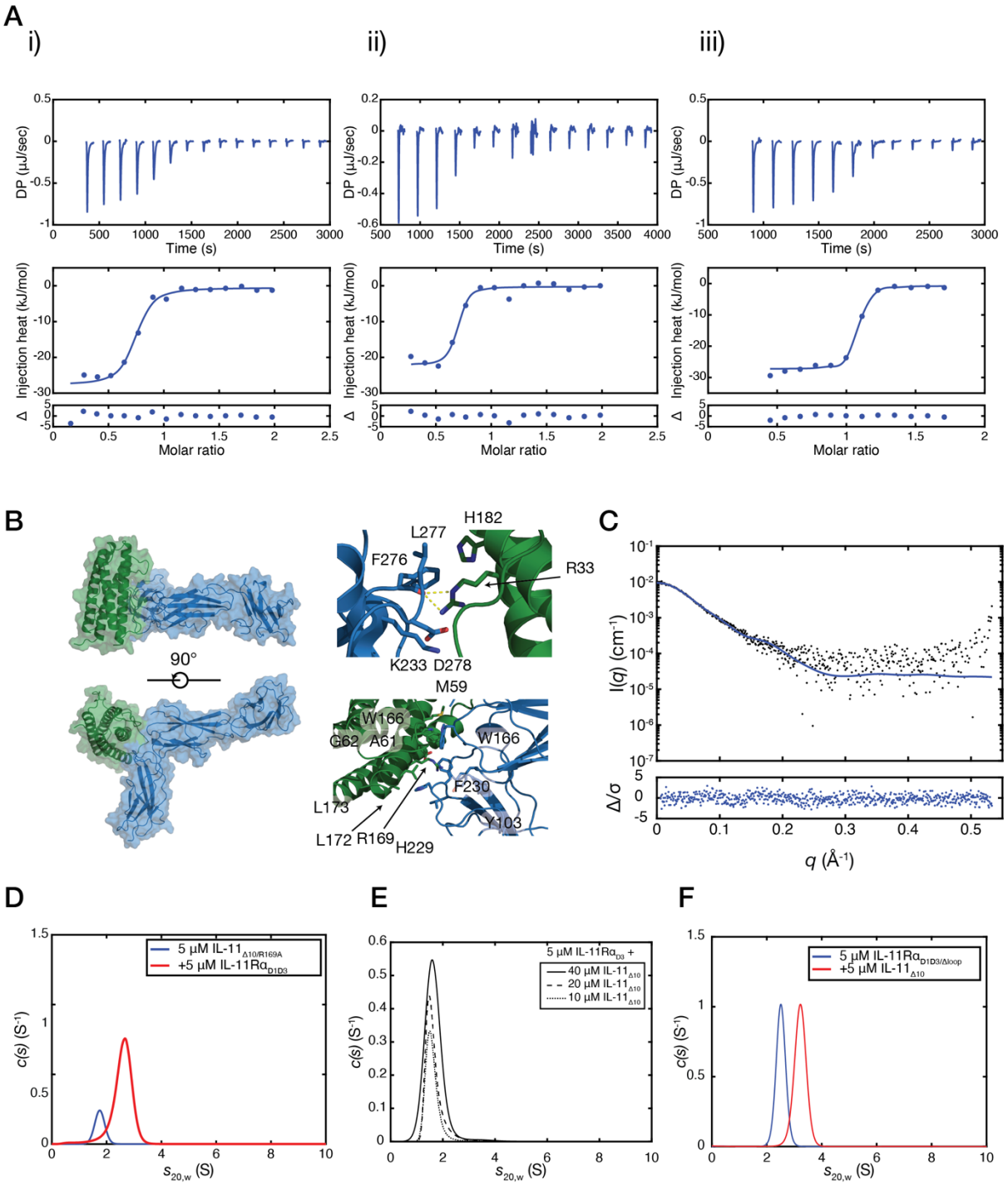

Figure 3.5: Thermodynamics and molecular model of the interaction between IL-11 and IL-11Rα.

Thermodynamics and molecular model of the interaction between IL-11 and IL-11Rα. A) Isothermal titration calorimetry isotherms for the interaction between i) IL-$11_{\Delta10}$ and IL-$11R\alpha_{EC}$ (K_D = 40 ± 20 nM), ii) IL-$11_{\Delta10}$ and IL-$11R\alpha_{D1\text{-}D3}$ (K_D = 23 ± 3 nM), and iii) IL-$11_{\Delta10}$ and IL-$11R\alpha_{D1\text{-}D3/\Delta loop}$ (K_D = 8 ± 4 nM). A representative titration of three replicates is shown for each. All experiments were conducted at 30 °C (303 K)

with approximately 10 μM IL-11Rα in the cell, and a 10-fold molar excess of IL-$11_{\Delta10}$ in the syringe. B) Model of the IL-$11R\alpha_{EC}$/IL-$11_{\Delta10}$ complex. i) Two views of the complex. ii) Details of the interface with residues previously implicated in receptor binding highlighted. C) The experimental SAXS profile for the IL-11Rα/IL-$11_{\Delta10}$ complex overlaid with the theoretical scattering profile calculated from the model coordinates (χ^2 = 1.03). An *ab initio* model is presented in Supplementary Figure 3.8. D) Continuous sedimentation coefficient (c(s)) distributions for the complex between IL-$11R\alpha_{D1\text{-}D3}$ and IL-$11_{\Delta10/R169A}$. The broad peak in the c(s) distribution suggests that the complex formed is lower-affinity compared to IL-$11_{\Delta10}$. E) Continuous sedimentation coefficient (c(s)) distributions showing that IL-$11R\alpha_{D3}$ does not interact with IL-$11_{\Delta10}$ at high affinity. No significant complex formation was observed with increasing concentrations of IL-$11_{\Delta10}$ in the presence of 5 μM IL-$11R\alpha_{D3}$. F) Continuous sedimentation coefficient (c(s)) distributions for the complex between IL-$11R\alpha_{D1\text{-}D3/\Delta loop}$ and IL-$11_{\Delta10}$. The complex was formed by mixing 5 μM IL-$11R\alpha_{D1\text{-}D3/\Delta loop}$ with 5 μM IL-$11_{\Delta10}$ and centrifuged without further purification.

3.3.6 A model of the IL 11/IL-11Rα binary complex provides detail of the structural mechanism of engagement.

To investigate the structural mechanism of IL-11 binding by IL-11Rα, we constructed a model of the IL-11/IL-11Rα complex. Using the structure of the IL-6 signalling complex (PDB ID: 1P9M [74]), we aligned IL-11 and IL-11Rα to their homologous chains in the IL-6 complex, and refined this model using *RosettaDock* of the *Rosie* server [393,394]. The top-scoring model, with a buried surface area of 567 Å^2, was taken as the representative model (Figure 3.5B). The IL-6/IL-6Rα interface in the IL-6 signalling complex has a surface area of 706 Å^2. This is consistent with the initial cytokine-receptor interaction forming a transiently stable complex. The model shows that the missing CD loop in D2 of IL-11Rα, which we did not include in the model, is in close proximity to the binding site.

To validate our docked model, we performed SAXS on the IL-11/IL-11Rα complex. The complex was formed by mixing IL-$11R\alpha_{D1\text{-}D3}$ and IL-$11_{\Delta10}$ at an equimolar ratio, prior to SAXS measurement. The molecular mass was measured as 50.1 kDa,

consistent with a 1:1 complex (Supplementary Table 3.3). Theoretical scattering for the docked model fits the experimental SAXS data well ($\chi 2 = 1.04$) (Figure 3.5C; Supplementary Table 3.3; Supplementary Figure 3.6E), showing that the model accurately represents the overall shape of the binary IL-11Rα/IL-11 complex. Similarly, the model agrees well with an *ab initio* model of the complex, generated using *DAMMIN* (Supplementary Figure 3.8A, B). The theoretical sedimentation coefficient of the *ab initio* model is 3.3. in agreement with the experimental value.

We used the *PISA* server[327] to analyse the interactions formed between the two proteins in the docked model. The major interacting residues of IL-11 are R33, M59, A61, G62, and several residues in the C-terminus of the cytokine, particularly R169 (Figure 3.5B). R33, in the N-terminal helix of the cytokine, and H182 helix D, both form hydrophobic interactions with F276, L277 and D278 in the FG loop in D3 of the receptor. Similar contacts are formed in the five top scoring models. An extensive contact is formed between the C-terminal region of the cytokine and the receptor in the model. IL-11 residues D165, W166, R169, L172 and L173 form an extensive hydrophobic interaction with H229 and F230 in the BC loop of D3 of the receptor, with a small contribution from Y103 in the AB loop of D2. A contact is also formed by M59, A61 and G62 in the AB loop of IL-11 with Y166 in the EF loop of D2 of the receptor.

As R169 of IL-11 makes a key intermolecular contact in our model, we constructed and purified the IL-$11_{\Delta 10/R169A}$ mutant. SV-AUC analysis of 5 μM IL-$11R\alpha_{D1\text{-}D3}$ in the presence of 5 μM IL-$11_{\Delta 10/R169A}$ results in a peak in the sedimentation coefficient distribution of approximately 2.7 S (Figure 3.5D; Supplementary Figure 3.7A; Supplementary Table 3.2), less than that for the IL-$11_{\Delta 10}$/IL-$11R\alpha_{D1\text{-}D3}$ complex (3.3 S), showing that the R169A mutation substantially decreases affinity for IL-11Rα. Stimulation of DLD1 cells with IL-$11_{\Delta 10/R169A}$ shows greatly reduced potency in activation of STAT3 than the wild type cytokine (Supplementary Figure 3.6F), consistent with the reduction in IL-11Rα binding leading to impaired formation of the active signalling complex. Residues important for biological activity of IL-11 have previously been identified by site-directed mutagenesis of human and mouse

IL-11 [168-170], and these mutagenesis experiments further support our model. Substitution of R33, D165, W166, R169, L172 and L173 all reduce the biological activity of IL-11[168-170]. The N-terminal region of the AB loop of IL-11, containing the interacting residues M59, A61 and G62 has previously been targeted by phage-display and mutagenesis to alter the binding of IL-11 to IL-11Rα, thus, this region has also been shown to be key for the interaction.

Our model predicts that IL-11 forms interfaces of 225 Å^2 and 369 Å^2 with D2 and D3 respectively. Previously, the isolated D3 of IL-11Rα was reported to bind IL-11 with an affinity of 48 nM [362]. We expressed, purified and refolded D3 of IL-11Rα (IL-11Rα$_{D3}$; residues 192-315 of the mature protein) from *E. coli* inclusion bodies. Circular dichroism spectroscopy indicated that the protein was folded (Supplementary Figure 3.6G), and SV-AUC analysis showed a single, narrow peak in the c($s_{20,w}$) distribution with sedimentation coefficient of 1.5 S (calculated from the fit to the data at 28 μM) and no concentration dependent change (Supplementary Figure 3.6H; Supplementary Figure 3.7F; Supplementary Table 3.2), indicating a homogenous product that did not self-associate in the concentration range measured. SV-AUC analysis of IL-11Rα$_{D3}$ (5 μM) with increasing concentrations of IL-11$_{Δ10}$ showed no concentration dependent increase in sedimentation coefficient, with weight average $s_{20,w}$ of 1.67 S at 10 μM IL-11$_{Δ10}$, 1.66 S at 20 μM, and 1.62 S at 40 μM (Figure 3.5E; Supplementary Figure 3.7B; Supplementary Table 3.2). As the theoretical sedimentation coefficient of the IL-11/IL-11Rα$_{D3}$ complex is 2.62 S, these data indicate that IL-11Rα$_{D3}$ does not bind IL-11 with the high affinity previously reported.

An apparently unique feature of the IL-11 binding site in IL-11Rα is a loop between strands C and D in D2 of the receptor. Our model of the binary complex suggests that this loop may contact bound cytokine and, therefore, could have a role in binding IL-11, through the formation of beneficial polar contacts between the loop and cytokine or by providing additional buried surface area. To investigate this, we generated a construct, IL-11Rα$_{D1\text{-}D3/Δloop}$, in which residues 132 to 140 in the loop were removed and replaced by two glycine residues. SV-AUC showed that IL-

11Rα$_{D1\text{-}D3/\Delta loop}$ is monomeric in solution and formed a complex with IL-11$_{\Delta 10}$ with the expected 1:1 stoichiometry (Figure 3.5F; Supplementary Figure 3.7C). ITC shows that the K_D of the interaction between IL-11$_{\Delta 10}$ and IL-11Rα$_{D1\text{-}D3/\Delta loop}$ is 8 ± 4 nM (n=3; Figure 3.5Aiii), not significantly different from that of IL-11$_{\Delta 10}$ and IL-11Rα$_{D1\text{-}D3}$ (p = 0.21). Thus, removal of the loop does not significantly alter the affinity for the interaction between IL-11Rα and IL-11$_{\Delta 10}$, suggesting that the loop does not participate directly in cytokine binding. This is consistent with the observation that the IL-11/IL-11Rα interaction is driven by an increase in entropy; a disordered loop adopting an ordered conformation is an inherently entropically unfavourable process and is unlikely to occur during complex formation without a corresponding enthalpically favourable process. It is possible that the dynamic loop functions to partially shield the hydrophobic regions of the cytokine binding surface in the absence of cytokine, thereby reducing the potential of this region to participate in deleterious, non-specific interactions. This function would be consistent with our observation that other cytokine receptors that have more hydrophilic character at their cytokine binding regions, such as IL-6Rα, do not possess this dynamic loop structure.

3.4 Conclusion

The increasing identification of roles for IL-11 in a broad range of diseases underscores the need to thoroughly understand the structure of IL-11, its receptors, and the overall molecular mechanism of IL-11 signalling complex formation. Here, we have solved the crystal structure of human IL-11Rα and a new structure of human IL-11 that reveals detail of functionally important loop regions. We show that several mutations in IL-11Rα that are associated with disease act to disrupt key structural elements in IL-11Rα, for example through disrupting interdomain interfaces, or conserved structural motifs within the receptor. We present a model of the complex and validate this model through biophysical and mutagenic analysis. We propose that a dynamic loop proximal to the cytokine binding region of IL-11Rα functions to protect this region from nonspecific interactions. Our data elucidate the structural and thermodynamic mechanisms of IL-11 binding by IL-11Rα and show that this engagement is mediated by both D2 and D3 of the receptor. Together, this

work reveals key structural determinants of cytokine engagement by IL-11Rα on the pathway to formation of the active signalling complex. This molecular detail can be exploited in future development of agents that can modulate this process.

3.5 Materials and Methods

3.5.1 Protein expression and purification

Human IL-11Rα$_{EC}$ with N-terminal honeybee-melittin signal peptide and C-terminal 8x His tag, was expressed in Sf21 insect cells. Recombinant protein was purified using nickel-affinity chromatography and gel filtration chromatography. IL-11Rα$_{D1-D3}$ and IL-11Rα$_{D1-D3/\Delta loop}$ with N-terminal honeybee-melittin signal peptide, 8x His tag, and TEV cleavage site were expressed in Sf21 cells. Recombinant protein was purified from conditioned media using nickel-affinity chromatography and gel filtration chromatography. Cleavable tags were removed using TEV protease. IL-11Rα$_{D3}$ was refolded and purified from bacterial inclusion bodies as previously described [362]. All IL-11Rα constructs contained the C226S mutation to reduce formation of disulfide crosslinked dimers [362].

IL-11$_{FL}$, IL-11$_{\Delta 10}$, and IL-11$_{\Delta 10/R169A}$ with N-terminal 6x His tag, maltose binding protein, and a TEV protease cleavage site (MBP-IL-11$_{FL}$ or MBP-IL-11$_{\Delta 10}$) were expressed in BL21(DE3) *E. coli* cells. All constructs were purified by nickel-affinity chromatography, followed by cation exchange chromatography, and gel-filtration chromatography. Tag removal was achieved using TEV protease. muGFP-IL-11 was expressed and purified as above with no TEV cleavage.

3.5.2 Crystallization and X-ray data collection

IL-11Rα$_{EC}$ was crystallized using the sitting-drop vapor diffusion method. Initial crystals were obtained at 293 K in the precipitant 28% PEG 400, 0.2 M calcium chloride and 0.1 M sodium HEPES pH 7.5. Crystallization drops were produced by mixing 1.1 mg/mL IL-11Rα$_{EC}$ in a ratio of 1:0.9:0.1 with the precipitant and the endoproteinase Glu-C. Spherulites appeared after 24 hours, these were used to prepare a micro-seed stock [395]. Subsequent seeding gave needle clusters in the condition 20% PEG 3350, 0.2 M lithium citrate. Seeding using these needle crystals

produced single crystals in the condition 0.1 M HEPES pH 8, 20 mM sodium chloride, 1.6 M ammonium sulfate, 67 mM NDSB-195. Crystallization drops were produced by mixing 1.5 µL IL-11Rα$_{EC}$ (1 mg/mL), 0.65 µL precipitant, 0.4 µL NDSB-195, 0.15 µL Glu-C and 0.3 µL seed. Spindle-like crystals appeared after 48 hours and grew to approximate dimensions 20 µm × 7 µm × 7 µm.

IL-11$_{\Delta10}$ was crystallised using the sitting-drop vapor diffusion method. Crystals were obtained at 293 K in the precipitant 30% PEG 3350, 0.2 M ammonium sulfate, 0.1 M Tris pH 8.5. Crystals appeared after 24 hours as thick bundles of two-dimensional plates. These crystals were used for micro-seeding, providing single crystals in the precipitant 18% PEG 3350, 0.1 M bis-tris propane pH 9, 0.2 M ammonium sulfate, 5 mM praseodymium chloride. Crystallisation drops were produced by mixing 1.5 µL IL-11$_{\Delta10}$ (5 mg/mL), 1.5 µL precipitant and 0.5 µL seed. Plates appeared overnight and grew to approximate dimension 500 × 20 × 5 µm after equilibration against precipitant for one week.

Crystals were flash-cooled in liquid nitrogen directly from crystallization drops, and X-ray diffraction data were collected at 100 K at the Australian Synchrotron MX2 beamline [396].

3.5.3 X-ray data processing and structure refinement

Diffraction data were indexed, integrated and scaled using *XDS* [397], analysed using *POINTLESS* [398] and merged using *AIMLESS* [399] from the *CCP4* suite. Initial phase estimates for IL-11Rα were obtained by molecular replacement with Phaser [400], using individual domains of IL-11Rα from unpublished Fab-bound structures as the search models. Refinement was performed using *phenix.refine* with non-crystallographic symmetry torsion restraints [401], followed iteratively by manual building using *Coot* [402]. Several cycles of simulated annealing were performed early in the refinement to reduce potential model bias. Translation/libration/screw (TLS) refinement was performed in the final rounds, with each domain defined as a separate TLS group. Simulated annealing composite omit maps were calculated using *Phenix*.

Initial phase estimates for IL-$11_{\Delta 10}$ were obtained using molecular replacement with *Phaser* [400], using our previous structure of IL-11 (PDB ID:4MHL)[109] as the search model. Auto-building with simulated annealing was performed in *phenix.autobuild* to reduce phase bias from the search model. Refinement was performed in *phenix.refine* [401] with iterative manual building using *Coot* [402]. TLS refinement was performed using a single TLS group containing all protein atoms. Explicit riding hydrogens were used throughout refinement and included in the final model, the atomic position and B factors for hydrogens were not refined.

Residues of both structures are numbered according to the mature protein sequence after cleavage of signal peptides.

3.5.4 Absorbance-detected sedimentation velocity analytical ultracentrifugation

Absorbance-detected SV-AUC experiments were conducted using a Beckman Coulter XL-I analytical ultracentrifuge, equipped with UV-visible scanning optics. Reference and sample solutions were loaded into double-sector 12 mm cells with quartz windows and centrifuged using an An-60 Ti or An-50 Ti rotor at 50,000 rpm and 20 °C. Radial absorbance data were collected at 280 nm, in continuous mode. All experiments were conducted in TBS (20 mM Tris, 150 mM sodium chloride) pH 8 or 8.5. IL-$11_{\Delta 10}$ and muGFP-IL-11 was centrifuged at concentrations of 0.8, 0.4 and 0.2 mg/mL. IL-11Rα was centrifuged at concentrations of 0.75, 0.5 and 0.25 mg/mL. Complexes of IL-11 and IL-11Rα were prepared by mixing 5 μM each of IL-11 and IL-11Rα and centrifuged without further purification. Sedimentation data were fitted to a continuous sedimentation coefficient (c(s)) model, with floating frictional ratios using *SEDFIT* [403]. Buffer density, viscosity and the partial specific volume of the protein samples were calculated using *SEDNTERP* [404]. For the complexes between IL-11 and IL-11Rα, and muGFP-IL-11 and IL-11Rα, the partial specific volume used was 0.73 mL/g. The theoretical sedimentation coefficients of IL-$11_{\Delta 10}$ and IL-11Rα were calculated using *HYDROPRO*, using standard conditions (water, 20 °C) [377].

3.5.5 Fluorescence-detected sedimentation velocity analytical ultracentrifugation

Fluorescence-detected SV experiments were conducted using a Beckman XL-A analytical ultracentrifuge, equipped with an Aviv Biomedical fluorescence detection system. Sample solutions were loaded into double-sector 12 mm cells with quartz windows and centrifuged using an An-50 Ti rotor. Experiments were conducted at 50,000 rpm and 20 °C. muGFP-IL-11 was centrifuged at a concentration of 150 nM (0.007 mg/mL).

To generate the sedimentation coefficient isotherm, the concentration of muGFP-IL-11 was 150 nM, and 1.5-fold serial dilution series of IL-11Rα was prepared starting from a concentration of 1 μM in TBS pH 8.0. To prevent non-specific absorption of muGFP-IL-11 to cell components, 0.2 mg/mL κ-casein (Sigma-Aldrich) was added to the samples [384]. Sedimentation velocity data were processed in *SEDFIT* as above. c(s) distributions were integrated between 1.0 S and 6.0 S. The isotherm was fitted to a 1:1 hetero-association model in *SEDPHAT*, with K_A and the sedimentation coefficients of muGFP-IL-11 and the complex floated in the analysis [405]. The 68% confidence interval was estimated using *SEDPHAT*.

3.5.6 Small-angle X-ray scattering

SAXS experiments were conducted at the Australian Synchrotron SAXS/WAXS beamline, using co-flow to limit radiation damage and allow higher X-ray flux onto the sample, and an optimised chromatography system to limit sample dilution [406-408]. The X-ray beam energy was 11,500 eV (λ = 1.078 Å). For IL-$11_{\Delta 10}$ and IL-11_{FL}, the sample-to-detector distance used was 2038 mm, providing a total q range of 0.007-0.664 $Å^{-1}$, $q=(4\pi\sin\theta)/\lambda$. For IL-11R$\alpha_{D1\text{-}D3}$ and the IL-11R$\alpha_{D1\text{-}D3}$/IL-$11_{\Delta 10}$ complex, the sample-to-detector distance used was 2539 mm, providing a total q range of 0.006-0.534 $Å^{-1}$. Data were collected following fractionation with an in-line size-exclusion chromatography column (Superdex 200 5/150 Increase, GE Healthcare,) pre-equilibrated in TBS pH 8.5, 0.2 % sodium azide. The IL-11R$\alpha_{D1\text{-}D3}$/IL-$11_{\Delta 10}$ complex was prepared by mixing IL-11R$\alpha_{D1\text{-}D3}$ and IL-$11_{\Delta 10}$ in a 1:1.5 molar ratio. Data were collected from a 1.5 mm capillary under continuous flow, with frames collected every second. Data reduction and was performed using the Scatterbrain software,

SEC-SAXS analysis using CHROMIXS [409] and the ATSAS suite [409,410]. Frames averaged were taken from a region of the peak with a minimal change in the R_g. Theoretical scattering profiles from the crystal structure coordinates were calculated and fit to the experimental scattering data using CRYSOL 13[411]. *Ab initio* models were calculated using *DAMMIF* [412] and *DAMMIN* [413,414]. Ten models were calculated using *DAMMIF*, the models averaged using *DAMAVER*, the averaged model was used as a starting model for *DAMMIN*. A summary of the SAXS data acquisition and processing is given in Supplementary Table 3.3.

3.5.7 Molecular-dynamics simulations

All MD simulations were performed using NAMD 2.1.3b1 [415] and the CHARMM22 forcefield [415,416] at 310 K in a water box with periodic boundary conditions. Simulations were analysed in VMD 1.9.3 [417]. A model of IL-11Rα was created based on chain B of the crystal structure. The missing loop (residues 132 to 141) was rebuilt using the PHYRE2 server [418]. The missing loop was excluded from all representations of the trajectories and the analysis. The disordered C-terminus was not simulated in the model. The structures were solvated (box size 88.8 × 126.6 × 53.9 Å), and ions were added to an approximate final concentration of 0.15 M NaCl. Simulations of IL-11Rα was carried out with 10 ps minimisation, followed by 50 ns MD. Mutations were introduced to this equilibrated model, and a further simulation was carried out with 10 ps minimization, then 50 ns MD. An additional 50 ns MD was also performed for the un-mutated IL-11Rα. The interdomain distance distributions were calculated using a script in VMD, which defined a centroid for each of the three domains and measured the change in distance through the MD simulation. A model of the complete IL-$11_{\Delta 10}$ structure was created based on the crystal structure. For residues with multiple orientations, only one orientation was selected. The structure was solvated (box size 53.6 × 53.1 × 74.9 Å), and ions added to approximate final concertation of 0.15 M NaCl. A MD simulation was performed using a 10 ps minimisation time, followed by 100 ns MD.

3.5.8 Differential scanning fluorimetry

Protein samples were analysed by DSF at a concentration of 0.1 mg/mL in TBS pH 8.5, with 2.5 × SYPRO Orange dye (Sigma Aldrich). 20 µL of the sample was loaded into 96-well qPCR plate (Applied Biosystems), and four technical replicates of each sample were analysed. The plates were sealed, and samples heated in an Applied Biosystems StepOne Plus qPCR instrument, from 4 °C to 95 °C, with a 1% gradient. Unfolding data were analysed using a custom script in MATLAB r2016a. The temperature of hydrophobic exposure (T_h), was defined as the minimum point of the first derivative curve, and used to compare the thermal stability of different proteins [379].

3.5.9 Isothermal titration calorimetry

Protein samples were buffer exchanged into TBS pH 8.5 using gel filtration before analysis by ITC. ITC data were collected at 303 K using a MicroCal iTC200 (GE Healthcare). Titrations were performed using 15 2.5 µL injections of IL-11, after an initial injection of 0.8 µL. IL-11Rα was present at a concentration of 10 µM and the concentration of IL-11 was 10-fold greater than the concentration of IL-11Rα. Titration data were integrated using *NITPIC* [419,420], and analysed in *SEDPHAT* using a 1:1 interaction model [405]. Each titration was conducted in triplicate, values stated are the mean ± standard error of the mean.

3.5.10 In vitro cell culture

DLD1 cells were grown in RPMI+10% foetal calf serum, in a 10% CO_2 atmosphere. Cells were grown to confluency in 6-well plates, the media was removed and cells were treated with IL-$11_{\Delta 10}$ or IL-11FL at a concentration of 50 ng/mL in RPMI, or RPMI as a vehicle control, and incubated for one hour. Cells were then washed with cold PBS and lysed in RIPA buffer. Protein concentration was determined by the bicinchoninic acid (BCA) assay. Lysates were diluted with SDS-PAGE loading buffer, resolved on a 10% polyacrylamide gel and wet transferred to a nitrocellulose membrane. The membranes were blocked, incubated with the indicated primary antibodies (for phospho-STAT3 CST cat 9145; for phospho-STAT1 CST cat 9167, for total STAT3 CST cat 4904 for total STAT1 CST cat 9172, for actin Sigma cat

A1978), then detected using conjugated fluorescent secondary antibodies (Odyssey cat 926-32211/926-68072), and visualised using the Odyssey Infrared Imaging System (LI-COR Biosciences).

3.5.11 Docking

In silico docking was performed using the Docking2.0 algorithm, part of the *ROSIE* server [393,394,421]. An initial approximation of the complex orientation was generated by overlaying the IL-11Rα and IL-11 structures with IL-6Rα and IL-6 in the IL-6 signalling complex structure [74]. This model was used as input to the 'docking_local_refine' protocol of *RosettaDock*, which limits rotations/transitions of the complex components. The top ten scoring models were analysed using the *PISA* server[327] to determine the buried surface area [327]. The top-scoring model, with the highest buried surface area, was taken as the representative model.

3.5.12 Circular dichroism spectroscopy

Circular dichroism (CD) experiments were conducted using an Aviv CD spectrometer (410-SF). Spectra were collected for 12 μM IL-11Rα$_{D3}$ at 20 °C, in 50 mM sodium phosphate pH 8.0 over a wavelength range of 260-190 nm in 1 nm steps with an averaging time of 4 s, using a 1 mm path length quartz cuvette. Each measurement (sample and blank) was collected in triplicate. Buffer signal was subtracted, and data were converted to mean residue ellipticity.

3.5.13 Statistical analysis

Statistical significance was determined using a 2-tailed, paired t test in Microsoft Excel v. 16.27 for Mac OSX.

3.5.14 Code availability

The computational codes and mathematical algorithms used in this study are available from the corresponding authors upon request.

3.5.15 Data availability

Coordinates and structure factors for IL-11Rα and IL-$11_{\Delta 10}$ were deposited in the Protein Data Bank with accession codes 6O4P and 6O4O respectively. SAXS data and models were deposited in the SASBDB with accession codes SASDGH2, SASDGJ2, SASDGG2 and SASDGK2 for IL-$11_{\Delta 10}$, IL-11_{FL}, IL-$11R\alpha_{D1D3}$ and the IL-$11_{\Delta 10}$/IL-$11R\alpha_{D1D3}$ complex, respectively.

3.5.16 Acknowledgements

This work was supported by the National Health & Medical Research Council of Australia (APP1147621, APP1080498). M.D.W.G is the recipient of an Australian Research Council Future Fellowship (project number FT140100544). T.L.P is the recipient of a Victorian Cancer Agency Fellowship (MCRF16009). M.W.P. is National Health & Medical Research Council of Australia Research Fellow (APP1117183). Funding from the Victorian Government Operational Infrastructure Support Scheme to St Vincent's Institute and the New Zealand Royal Society Marsden Fund to R.C.J.D. (contract UOC1506) is acknowledged. Parts of this research were conducted at the SAXS/WAXS and MX2 beamlines of the Australian Synchrotron, part of the Australian Nuclear Science and Technology Organisation, and made use of the ACRF Detector at the MX2 beamline. Initial crystallisation screens were conducted at the CSIRO Collaborative Crystallisation Centre (www.csiro.au/C3), Melbourne, Australia.

Author Contributions: R.D.M., K.A., C.O.Z., P.M.N., C.J.M., D.S.S.L, H.C.C., R.C.J.D, T.L.P. and M.D.W.G performed the experimental work and analysed the data. M.D.W.G. and T.L.P. conceived the study. M.D.W.G., T.L.P., P.R.G., and M.W.P. supervised the project. All authors contributed to the writing of the manuscript.

Competing interests: The authors declare no competing interests.

Additional information: Supplementary Information accompanies this paper.

3.6 Supplementary Materials

3.6.1 Supplementary Figures

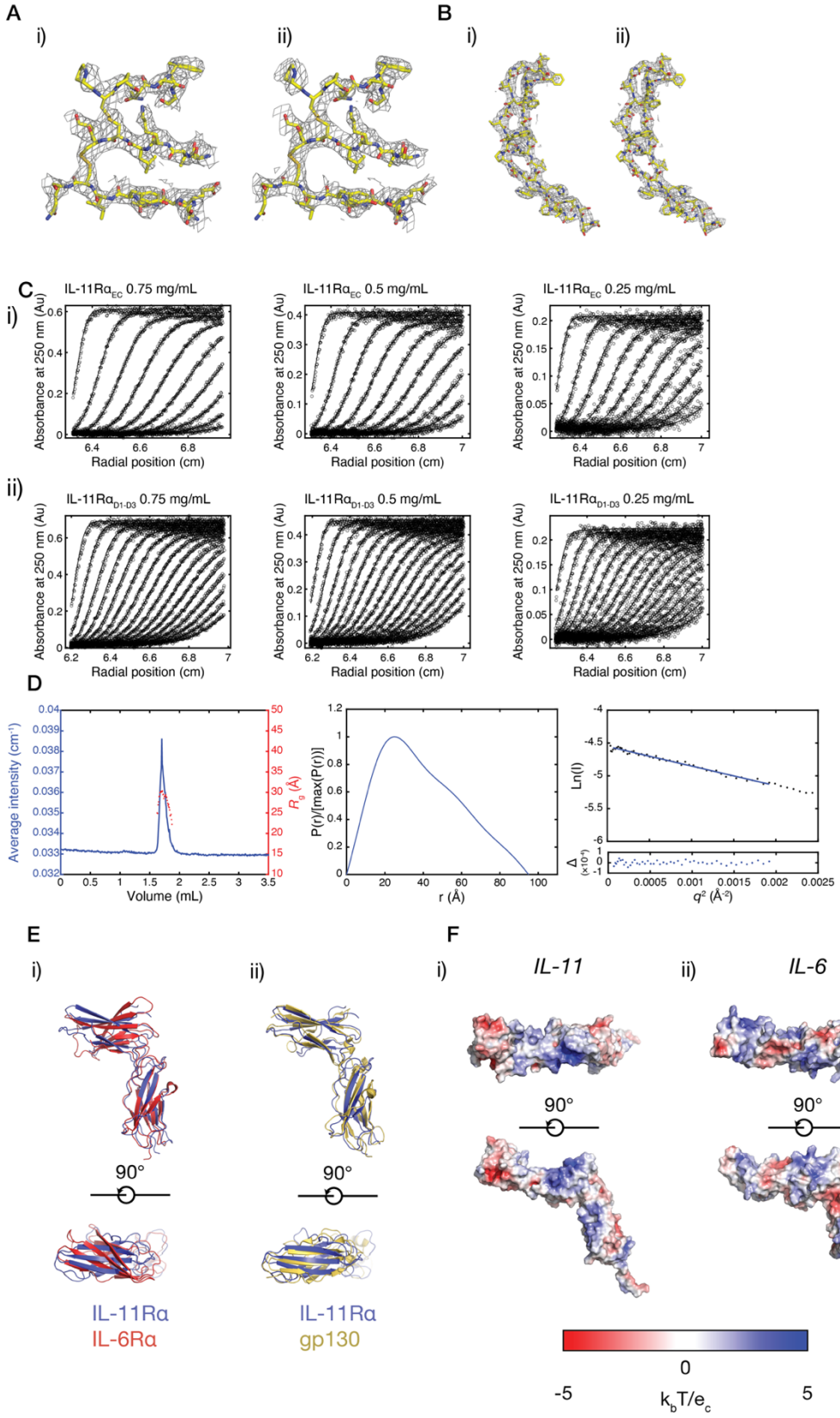

Supplementary Figure 3.1: Overlay of cytokine receptor structures, and representative density for IL-11Rα$_{EC}$.

A) Electron density for the two disulfide bonds in D1 of IL-11Rα (contoured at 1 σ), i) 2Fo-Fc map, ii) simulated annealing composite-omit map. B) Electron density for the WSXWS motif and surrounding residues for D3 of IL-11Rα (contoured at 1 σ), i) 2Fo-Fc map, ii) simulated annealing composite-omit map. C) Raw AUC data (circles) overlaid with the best fit to a continuous size distribution [c(s)] model for the distributions shown in Figure 1C and 1D. D) Supplementary SAXS data for IL-11Rα$_{D1-D3}$, showing the SEC-SAXS chromatograms, a pairwise distance distribution (P(r)) plot and a Guinier plot, for the data shown in Figure 1E. E) The cytokine-binding domains of IL-11Rα overlaid with the cytokine-binding domains of gp130 (PDB ID: 1I1R, gp130 chain shown), and IL-6Rα (PDB ID: 1N26). F) Surface electrostatics for IL-11Rα, i) and IL-6Rα, ii) (PDB ID: 1N26) calculated using APBS.

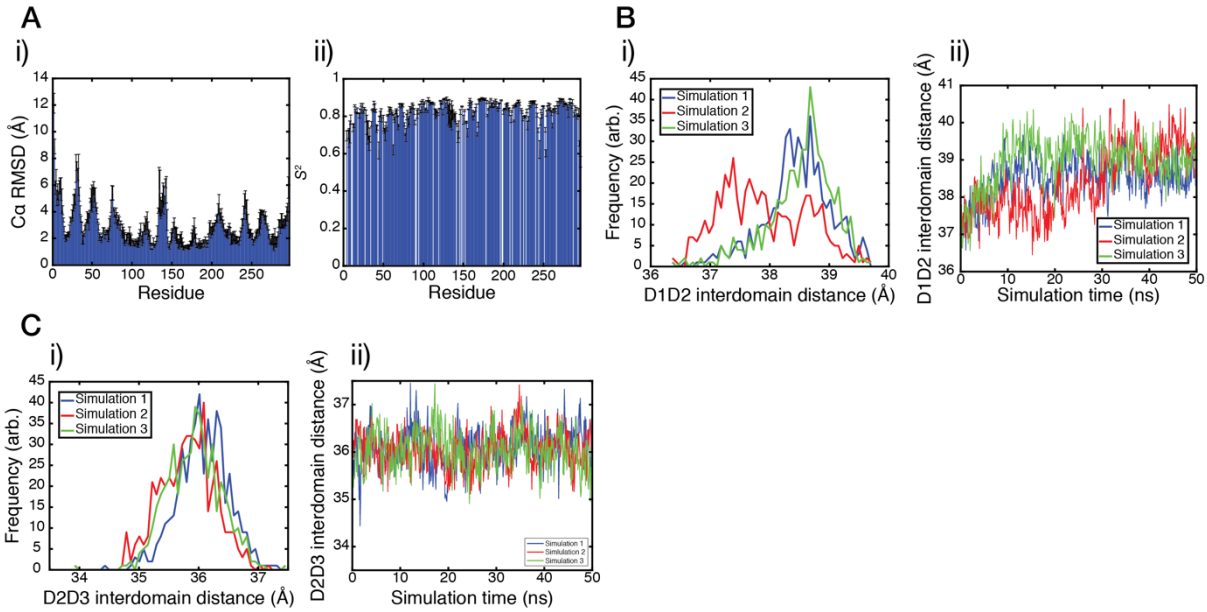

Supplementary Figure 3.2: Supplementary MD data.

A) Cα RMSD and order parameter values for all residues in IL-11Rα (n=3 50 ns simulations). Error bars are standard deviations, calculated from 3 50 ns simulations. B) i) Interdomain distance distributions for the D1-D2 interdomain distance, and ii) interdomain distance through each of the 50 ns simulations. C) i) Interdomain distance distributions for the D2D3 interdomain distance, and ii) interdomain distance through each of the 50 ns simulations.

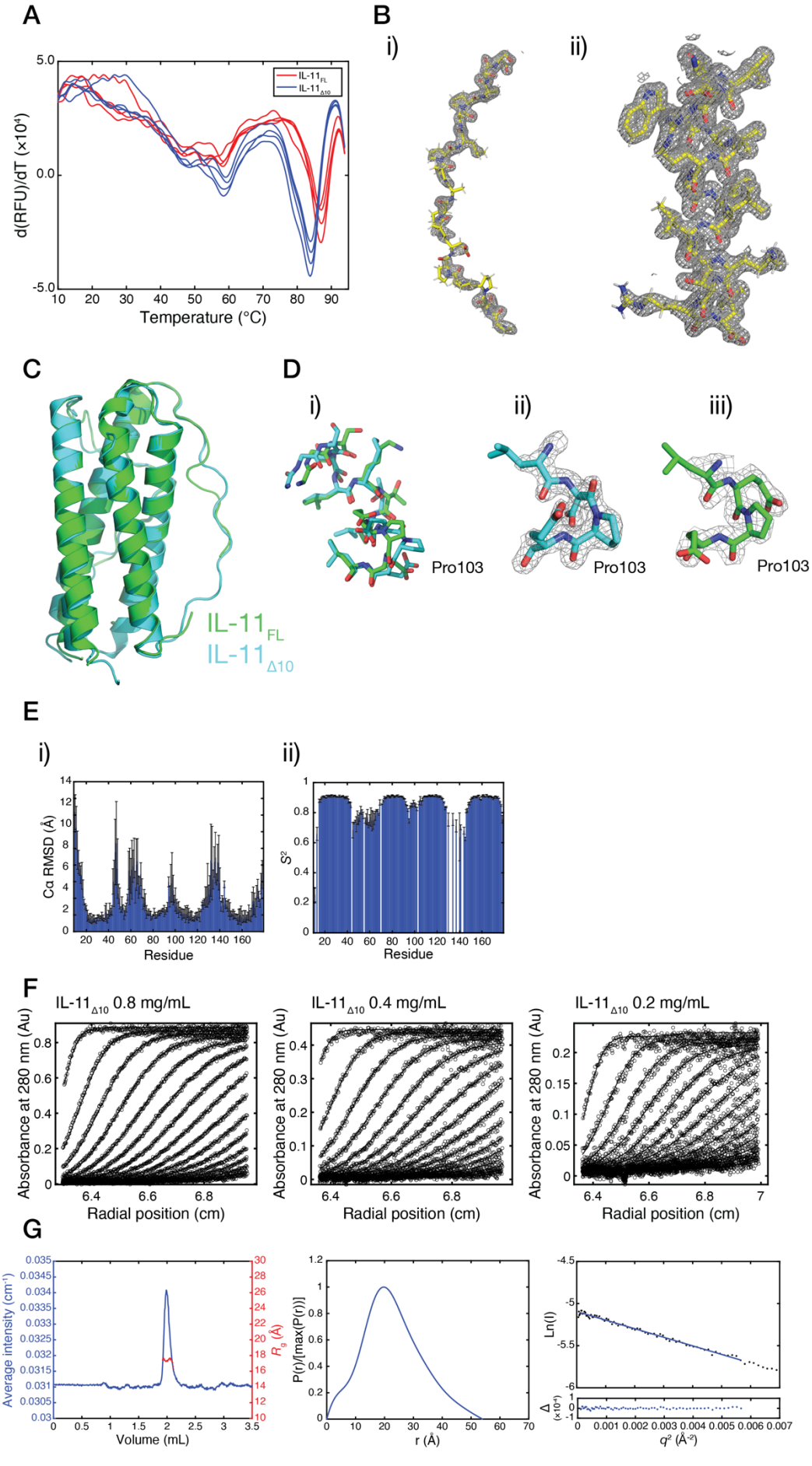
A
B
i)
ii)
C
D
i)
ii)
iii)
Pro103
Pro103
Pro103
E
i)
ii)
Cα RMSD (Å)
Residue
Residue
F
Absorbance at 280 nm (Au)
Radial position (cm)
Radial position (cm)
Radial position (cm)
G
Average intensity (cm⁻¹)
Volume (mL)
P(r)/[max(P(r))]
r (Å)
Ln(I)
q² (Å⁻²)

Supplementary Figure 3.3: Characterisation of IL-11$_{\Delta 10}$ and comparison of previous and current IL-11 structures.

A) Differential scanning fluorimetry data, showing that both proteins have very similar thermal stability, and that both are exceptionally stable B) Representative density for the structure of IL-11$_{\Delta 10}$. i) a portion of the polyproline helix, and ii) a C-terminal portion of helix D. Maps contoured at 1 σ. C) Structural alignment of previous (PDB ID: 4MHL) and current IL-11 structures, showing that they have a similar structure (rmsd 0.5 Å), with a slight difference in position of the A and D helices. D) Comparison of P103 in 4MHL and the structure of IL-11$_{\Delta 10}$. i) shows an overlay of the 3_{10} helix in both structures, showing the *cis-trans* isomerism exhibited by Pro103, ii-iii) shows the density supporting the position of Pro 103 in, ii) IL-11$_{\Delta 10}$ and iii), 4MHL (maps contoured at 1.5 σ). E) Cα RMSD and order parameter values for all residues in IL-11 (n=3 100 ns simulations), calculated from the MD simulation. Error bars are standard deviations. F) Raw AUC data (circles) overlaid with the best fit to a continuous size distribution [c(s)] model for the distributions shown in Figure 3.3G. G) SEC-SAXS chromatogram, a pairwise distance distribution (P(r)) plot, and a Guinier plot for the SAXS data shown in Figure 3.3H.

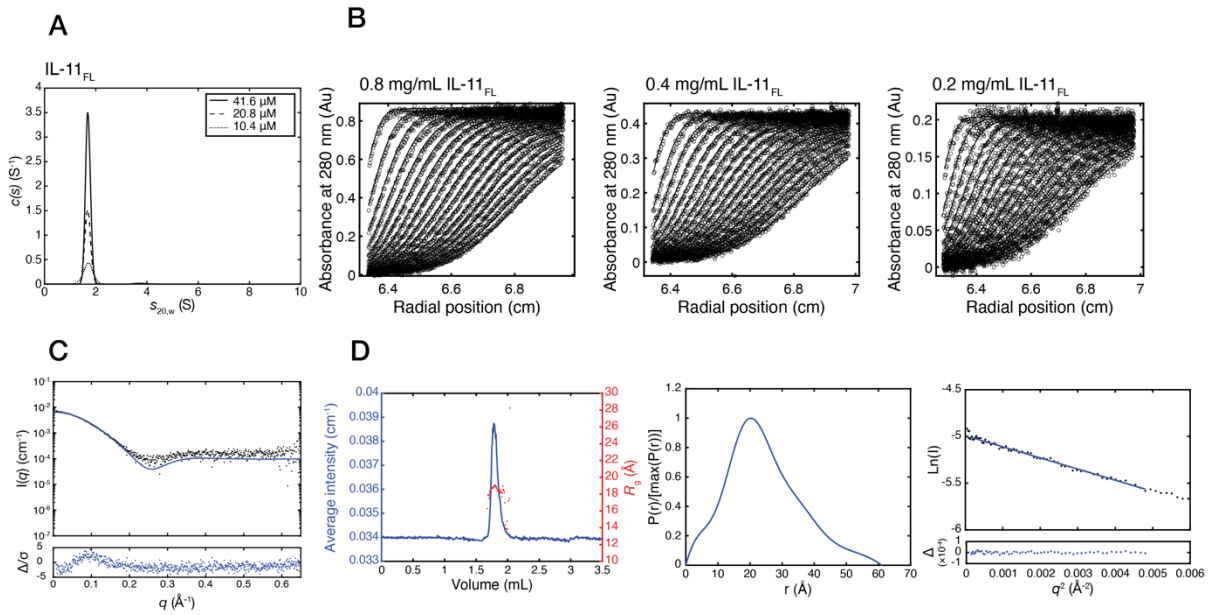

Supplementary Figure 3.4: Biophysical characterisation of IL-11$_{FL}$.

A) c(s) distributions for IL-11$_{FL}$, at three concentrations, showing that it is monomeric in solution. B) Raw AUC data (circles) overlaid with the best fit to a continuous size distribution [c(s)] model for the distribution shown in (A). C) SAXS data for IL-11$_{FL}$, with the fit to the structure of IL-11$_{\Delta 10}$ overlaid (χ^2 = 3.21). D) SEC-SAXS chromatogram, pairwise distance distribution (P(r)) plot, and Guinier plot for IL-11$_{FL}$.

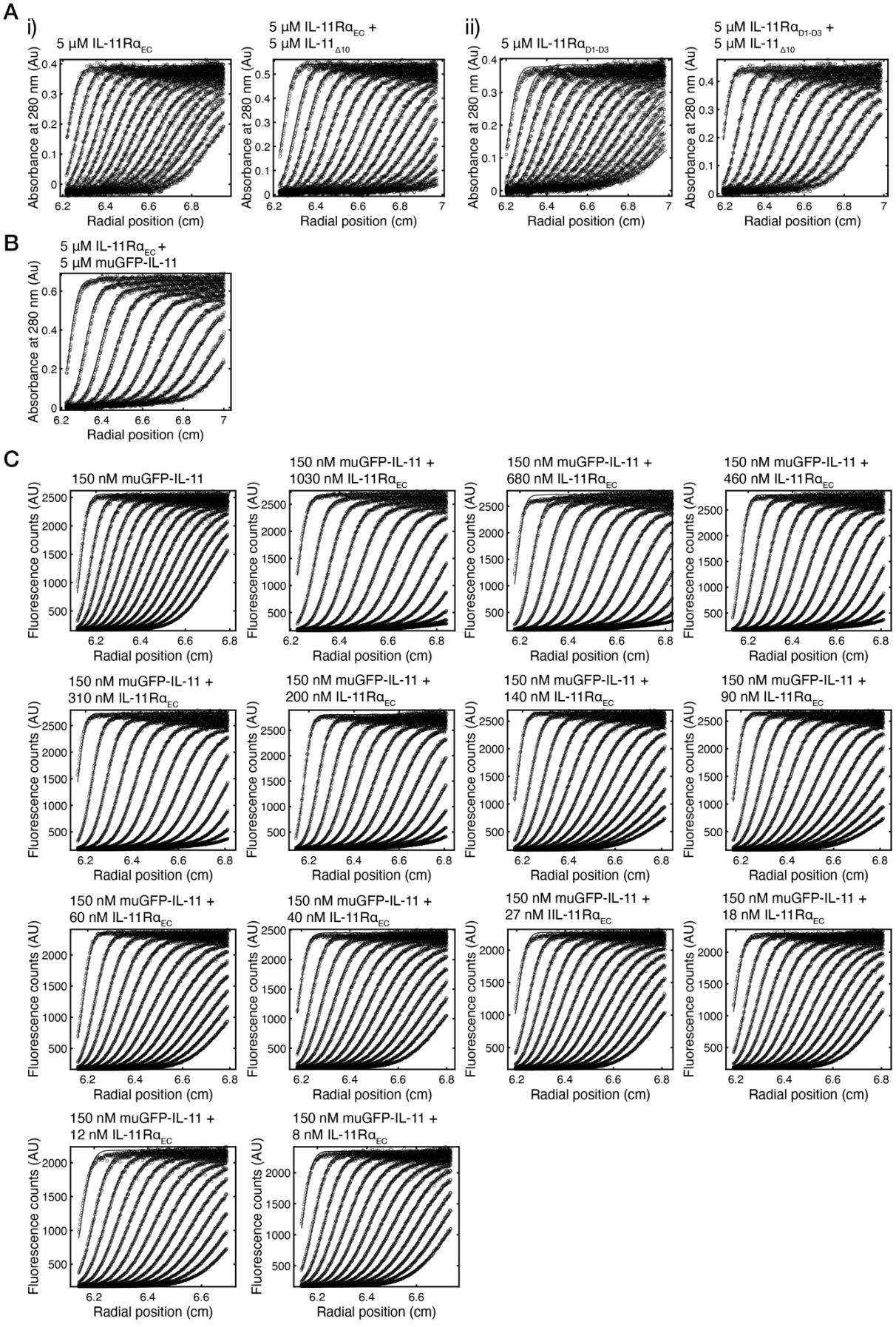
A
i)
5 μM IL-11Rα$_{EC}$
5 μM IL-11Rα$_{EC}$ +
5 μM IL-11$_{Δ10}$
ii)
5 μM IL-11Rα$_{D1-D3}$
5 μM IL-11Rα$_{D1-D3}$ +
5 μM IL-11$_{Δ10}$
Absorbance at 280 nm (Au)
Radial position (cm)
B
5 μM IL-11Rα$_{EC}$ +
5 μM muGFP-IL-11
C
150 nM muGFP-IL-11
150 nM muGFP-IL-11 +
1030 nM IL-11Rα$_{EC}$
150 nM muGFP-IL-11 +
680 nM IL-11Rα$_{EC}$
150 nM muGFP-IL-11 +
460 nM IL-11Rα$_{EC}$
150 nM muGFP-IL-11 +
310 nM IL-11Rα$_{EC}$
150 nM muGFP-IL-11 +
200 nM IL-11Rα$_{EC}$
150 nM muGFP-IL-11 +
140 nM IL-11Rα$_{EC}$
150 nM muGFP-IL-11 +
90 nM IL-11Rα$_{EC}$
150 nM muGFP-IL-11 +
60 nM IL-11Rα$_{EC}$
150 nM muGFP-IL-11 +
40 nM IL-11Rα$_{EC}$
150 nM muGFP-IL-11 +
27 nM IIL-11Rα$_{EC}$
150 nM muGFP-IL-11 +
18 nM IL-11Rα$_{EC}$
150 nM muGFP-IL-11 +
12 nM IL-11Rα$_{EC}$
150 nM muGFP-IL-11 +
8 nM IL-11Rα$_{EC}$
Fluorescence counts (AU)
Radial position (cm)

Supplementary Figure 3.5: Raw AUC data for Figure 3.4.

Raw AUC data (circles) overlaid with the best fit to a continuous size distribution [c(s)] model for the distributions shown in, A) i) Figure 3.4Ai, ii) Figure 3.4Aii, B) Figure 3.4B, C) the titration shown in Figure 3.4D.

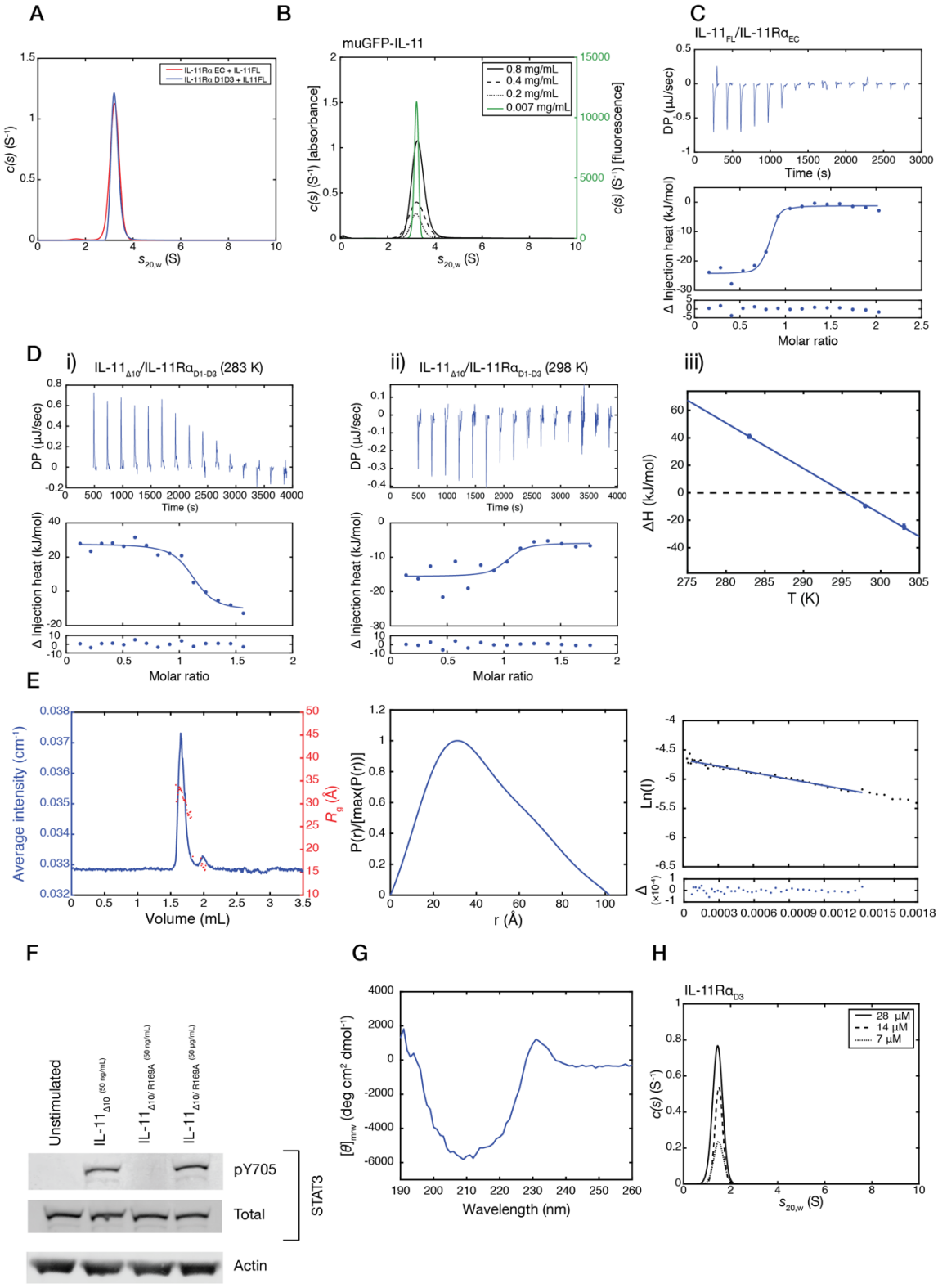

Supplementary Figure 3.6: Biophysical characterization of muGFP-IL-11, IL-11Rα D3 and the IL-11$_{FL}$/IL-11Rα complex.

A) c(s) distribution for the complexes formed between IL-11$_{FL}$ and IL-11Rα$_{ECD}$, and IL-11$_{FL}$ and IL-11Rα$_{D1-D3}$. The complexes were formed by mixing 5 μM IL-11 and IL-

11Rα prior to the experiment, with no further purification. B) c(s) distributions for muGFP-IL-11 at four concentrations measured using both absorbance (black) and fluorescence (green) detection, showing that it is monomeric in solution. C) Isothermal titration calorimetry isotherm for the interaction between IL-11_{FL} and IL-$11R\alpha_{EC}$. The K_D was 55 ± 8 nM (n=3 titrations, representative titration shown). D) Measurement of ΔC_p for the IL-$11_{\Delta 10}$/IL-$11R\alpha_{D1\text{-}D3}$ interaction. Titrations at two additional temperatures are shown in i), 283 K and ii) 298 K. The heat capacity plot is shown in iii). E) SEC-SAXS chromatogram, pairwise distance distribution (P(r)) plot, and Guinier plot for the IL-$11_{\Delta 10}$/IL-$11R\alpha_{D1\text{-}D3}$ complex data shown in Figure 3.5C. F) Western blot, showing activation of STAT3 by both IL-$11_{\Delta 10}$ and IL-$11_{\Delta 10/R169A}$ in the colon cancer cell line DLD1 (complete membrane images are shown in Supplementary Figure 3.9B). G) CD spectrum for IL-$11R\alpha_{D3}$, showing a characteristic all-β spectrum, showing the protein is well folded. H) c(s) distributions for IL-$11R\alpha_{D3}$ at three concentrations, showing that it is monomeric in solution.

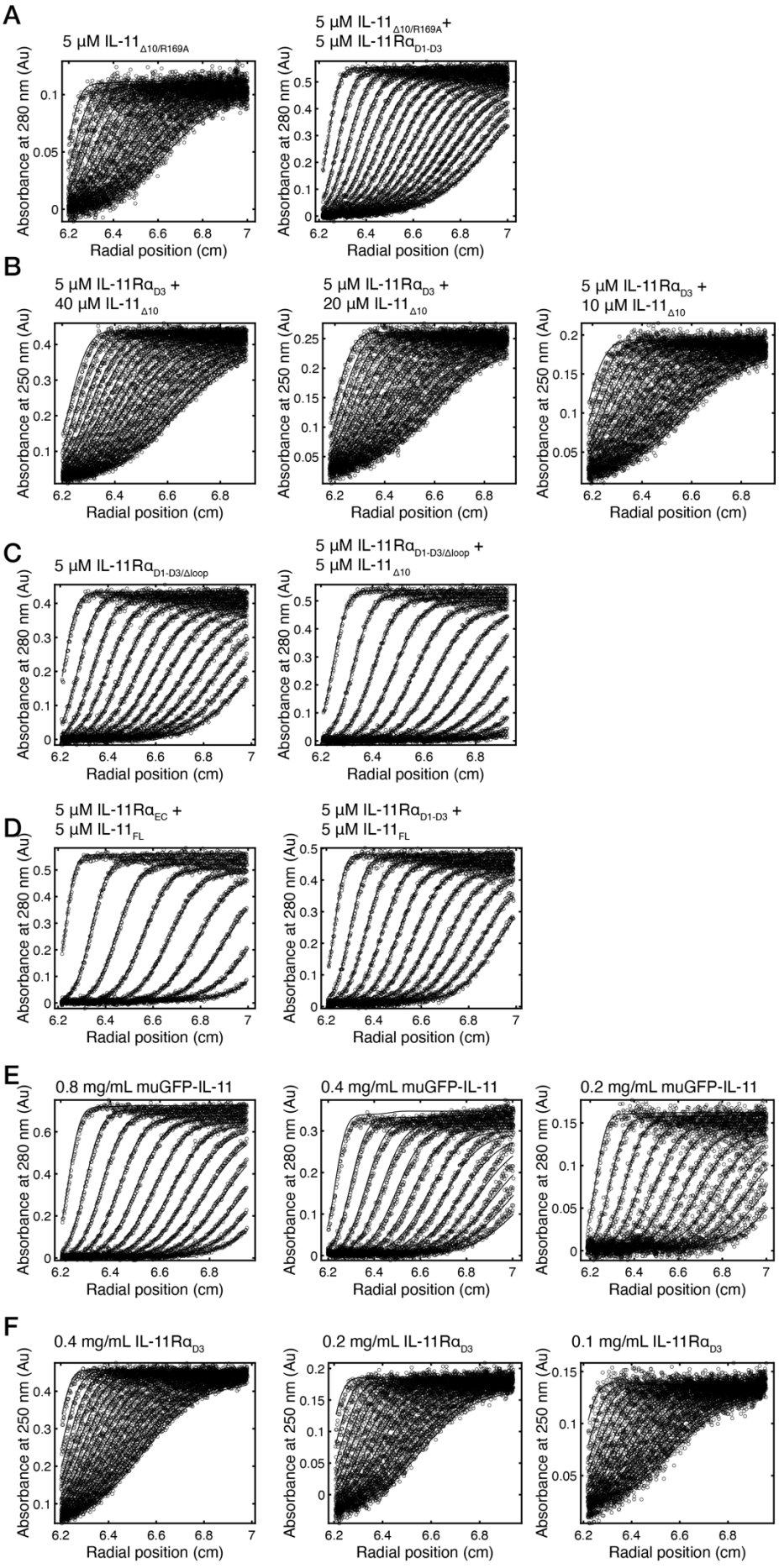
A
5 µM IL-11Δ10/R169A
5 µM IL-11Δ10/R169A+
5 µM IL-11Rα D1-D3
B
5 µM IL-11Rα D3 +
40 µM IL-11Δ10
5 µM IL-11Rα D3 +
20 µM IL-11Δ10
5 µM IL-11Rα D3 +
10 µM IL-11Δ10
C
5 µM IL-11Rα D1-D3/Δloop
5 µM IL-11Rα D1-D3/Δloop +
5 µM IL-11Δ10
D
5 µM IL-11Rα EC +
5 µM IL-11FL
5 µM IL-11Rα D1-D3 +
5 µM IL-11FL
E
0.8 mg/mL muGFP-IL-11
0.4 mg/mL muGFP-IL-11
0.2 mg/mL muGFP-IL-11
F
0.4 mg/mL IL-11Rα D3
0.2 mg/mL IL-11Rα D3
0.1 mg/mL IL-11Rα D3
Absorbance at 280 nm (Au)
Absorbance at 250 nm (Au)
Radial position (cm)

Supplementary Figure 3.7: Raw AUC data for Figure 3.5 and Supplementary Figure 3.6.

Raw AUC data (circles) overlaid with the best fit to a continuous size distribution [c(s)] model for the distributions shown in, A) Figure 3.5D ,B) Figure 3.5E, C) Figure 3.5F, D) Supplementary Figure 3.6A, E) Supplementary Figure 3.6B, F) Supplementary Figure 3.6G.

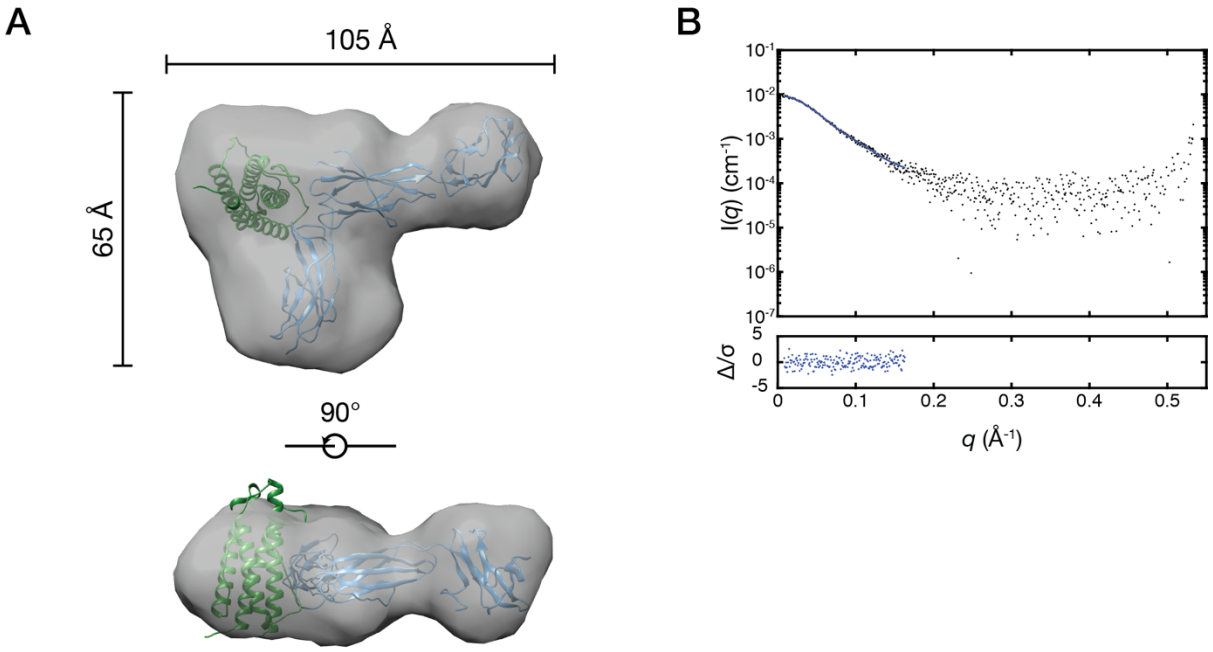

Supplementary Figure 3.8: *Ab initio* model of the IL-11Rα$_{D1-D3}$/IL-11$_{\Delta10}$ complex. A) *Ab initio* model (calculated using *DAMMIN*, see Methods), overlaid with the docked model. B) Fit of the *DAMMIN* model to the data (χ^2 = 1.04).

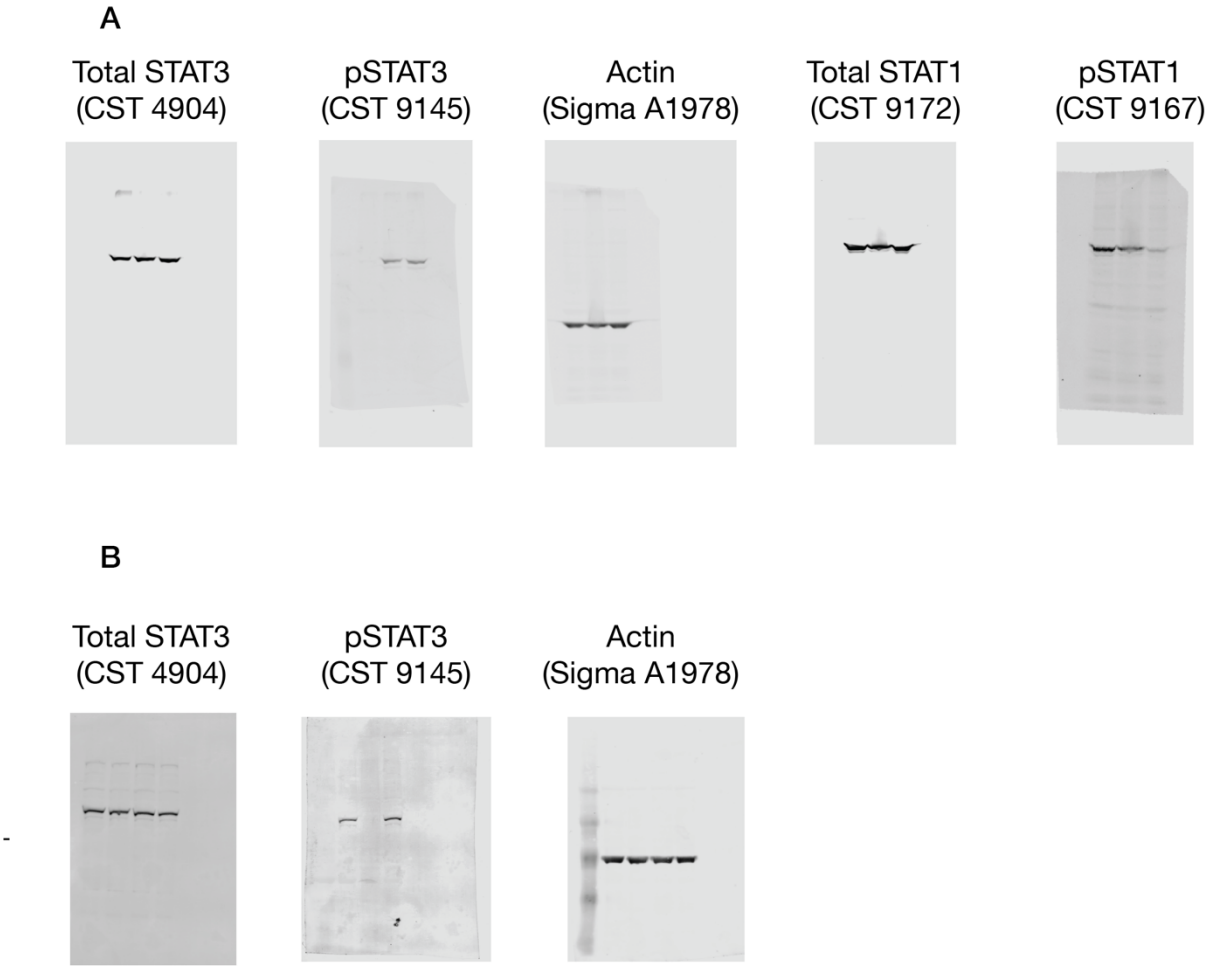

Supplementary Figure 3.9: Complete membrane images.

Complete membrane images for, A) the blots shown in Figure 3.3 A and B) the blots shown in Supplementary Figure 3.6E.

3.6.2 Captions for supplementary movies

Supplementary movies are available for viewing online at https://melbourne.figshare.com/s/4c40699f8e42bcd0c9fa.

Supplementary Movie 3.1: Animation of MD simulation of WT IL-11Rα and the IL-11Rα C72F mutant.

Supplementary Movie 3.2: Animation of MD simulation of WT IL-11Rα and the IL-11Rα P176T mutant.

Supplementary Movie 3.3: Animation of MD simulation of WT IL-11Rα and the IL-11Rα R274W mutant.

3.6.3 Supplementary Tables

Supplementary Table 3.1: X-ray data collection and structure refinement statistics for IL-11Rα and IL-11$_{\Delta 10}$.

Values for the highest resolution shell are given in parentheses.

	IL-11Ra	*IL-11$_{\Delta 10}$*
Data collection		
Space group	*P*6$_5$22	*P*2$_1$2$_1$2
Wavelength (Å)	0.9537	0.9537
Number of images	60	3600
Oscillation range per image (°)	1.0	0.1
Detector	ADSC Quantum 315r	Eiger 16M
Cell dimensions		
a, *b*, *c* (Å)	171.46, 171.46, 107.94	39.02, 133.76, 27.18
α, β, γ (°)	90, 90, 120	90, 90, 90
Resolution (Å)	45.67-3.43 (3.70-3.43)	37.46-1.62 (1.68-1.62)
R_{sym}[†]	0.575 (1.770)	0.0774 (1.031)
R_{meas}[§]	0.611 (1.901)	0.0808 (1.071)
R_{pim}[‡]	0.307 (0.952)	0.0227 (0.286)
$CC_{1/2}$	0.904 (0.436)	0.999 (0.764)
I/σ(*I*)	3.9 (1.1)	17.79 (2.08)
Total observations	92918	244140
Unique reflections	12990	18927
Completeness (%)	99.5 (98.5)	99.95 (99.89)
Multiplicity	7.2 (7.3)	12.9 (13.6)
Wilson *B*-factor (Å^2)	65.0	24.0
Refinement		
Resolution (Å)	45.67-3.43 (3.55-3.43)	37.5-1.62 (1.72-1.62)
Reflections used in refinement	12962 (1243)	18925 (1845)

R_{free} reflections	612 (57)	908 (84)
R_{work}	0.244 (0.318)	0.1739 (0.2515)
R_{free}	0.298 (0.342)	0.1926 (0.2742)
Protein molecules in asymmetric unit	2	1
Total non-hydrogen atoms	4580	1470
Protein	4433	1319
Ligand/ion	147	6
Solvent	0	145
Mean *B*-factor (Å^2)	65.9	36.02
Protein	64.9	35.33
Ligand/ion	97.4	47.58
RMSD		
Bond lengths (Å)	0.002	0.010
Bond angles (°)	0.58	1.36
Ramachandran Plot		
Favoured (%)	95.10	98.80
Allowed (%)	4.55	1.20
Outliers (%)	0.35	0.00

† $R_{sym} = \sum_{hkl}\sum_i |I_i(hkl) - \langle I(hkl)\rangle| / \sum_{hkl}\sum_i I_i(hkl)$

§ $R_{meas} = \sum_{hkl}[N/(N-1)]^{1/2}\sum_i |I_i(hkl) - \langle I(hkl)\rangle| / \sum_{hkl}\sum_i I_i(hkl)$

‡ $R_{pim} = \sum_{hkl}[1/(N-1)]^{1/2}\sum_i |I_i(hkl) - \langle I(hkl)\rangle| / \sum_{hkl}\sum_i I_i(hkl)$

$CC_{1/2}$ = Pearson correlation coefficient between independently merged half data sets.

Supplementary Table 3.2: SV-AUC data and analysis.

Protein/complex	Expected mass (kDa)	Calculated mass (kDa)	Frictional ratio	Sedimentation coefficient (S)	Predicted sedimentation coefficient (S)	Concentration
IL-11Rα$_{EC}$	38.2	41.3	1.57	2.7	2.9	13.0 μM
IL-11Rα$_{D1-D3}$	32.2	34.9	1.47	2.6	2.9	15.5 μM
IL-11$_{Δ10}$	18.2	17.2	1.28	1.7	1.8	43.9 μM
IL-11$_{FL}$	19.2	19.2	1.38	1.7	1.8	41.2 μM
IL-11$_{Δ10}$/IL-11Rα$_{D1-D3}$ complex	50.4	55.8	1.61	3.3	3.3	5 μM each component
IL-11$_{Δ10}$/IL-11Rα$_{EC}$ complex	56.4	60.8	1.71	3.2	3.3	5 μM each component
IL-11$_{FL}$/IL-11Rα$_{EC}$ complex	57.4	55.9	1.61	3.3	3.3	5 μM each component
muGFP-IL-11	48.3	52.2	1.45	3.3		16.5 μM
muGFP-IL-11/IL-11Rα$_{EC}$ complex	86.5	86.7	1.58	4.5		5 μM each component
IL-11$_{Δ10/R169A}$	18.2	18.1	1.27	1.7		5 μM

IL-11$_{\Delta 10/R169A}$/IL-11Rα$_{D1-D3}$ complex	50.4	34.8	1.47	2.5	5 μM each component
IL-11Rα$_{D3}$	14.0	12.8	1.32	1.5	28.5 μM
IL-11Rα$_{D3}$/IL-11$_{\Delta 10}$ complex	32.2	17.9	1.46	1.6	5 μM IL-11Rα$_{D3}$, 40 μM IL-11$_{\Delta 10}$
IL-11Rα$_{D1-D3/\Delta loop}$	31.4	36.3	1.58	2.5	5 μM
IL-11Rα$_{D1-D3/\Delta loop}$/IL-11$_{\Delta 10}$ complex	49.6	49.6	1.51	3.2	5 μM each component

Supplementary Table 3.3: SAXS data and analysis.

	IL-11$_{\Delta10}$	IL-11$_{FL}$	IL-11Rα$_{D1-D3}$	IL-11Rα$_{D1-D3}$/ IL-11$_{\Delta10}$ complex
SAXS data collection				
Instrument/source	Australian Synchrotron SAXS/WAXS beamline equipped with Pilatus 2M detector and sheath-flow cell for SEC-SAXS.			
Wavelength (Å)	1.078			
Beam energy (keV)	11.5			
Beam size (μm)	250 × 130			
Sample-to-detector distance (mm)	2038		2539	
q measurement range (Å^{-1}) [a]	0.007-0.664		0.006-0.534	
Absolute scaling method	Comparison with scattering from 1 mm pure water			
Normalization	To transmitted intensity from beamstop counter			
Exposure time	1 s measurements from SEC-SAXS elution			
Sample temperature (K)	293			
SEC-SAXS parameters				
Column	Superdex 200 5/150 Increase			
Flow rate (mL/min)	0.45			
Loading concentration (mg/mL)	5	5	2.2	2.65
Injection volume (μL)	50			
Solvent	20 mM Tris-HCl pH 8.5, 150 mM NaCl, 0.2% sodium azide			
Software employed				
SAXS data reduction	*I*(*q*) vs *q* using Scatterbrain 2.8.2, SEC-SAXS solvent subtraction using *CHROMIXS* from *ATSAS* 2.8.3			
Basic analysis (Guinier, *P(r)*, molecular mass)	*PRIMUS* from *ATSAS* 2.8.3 *GNOM* from *ATSAS* 2.8.3			
Shape modelling	*DAMMIF* from *ATSAS* 2.8.3 *DAMAVER* from *ATSAS* 2.8.3 *DAMMIN* from *ATSAS* 2.8.3			

Calculation of theoretical intensities	*CRYSOL* from *ATSAS* 2.8.3			
Structural parameters				
Mass from V_c (kDa) (expected mass, ratio to expected, in brackets) [b]	16.3 (18.2, 0.90)	17.2 (19.2,0.90)	33.5 (32.2, 1.04)	50.1 (50.4, 0.99)
Guinier analysis [c]				
R_g (Å)	17.43 ± 0.11	18.89 ± 0.11	30.16 ± 0.32	33.07 ± 0.37
I(0) (cm^{-1})	0.0061 ± 2.4 ×10^{-5}	0.0068 ± 2.4 ×10^{-5}	0.011 ± 6.7 ×10^{-5}	0.0094 ± 6.4 ×10^{-5}
qR_g min,max	0.18, 1.31	0.21,1.31	0.25, 1.30	0.27, 1.29
P(r) analysis [c]				
R_g (Å)	17.59 ± 0.74	19.00 ± 0.90	31.20 ± 0.14	33.41 ± 0.21
I(0) (cm^{-1})	0.0061 ± 2.1 ×10^{-3}	0.0068 ± 2.3 ×10^{-3}	0.0094 ± 5.7 ×10^{-3}	0.0093 ± 5.1 ×10^{-3}
D_{max} (Å)	54	61	95	102
Porod volume ($Å^3$)	21700	27600	41200	85500
Shape modelling				
DAMMIF (10 calculations, default parameters)				
q range for fitting (Å)				0.008-0.16
Symmetry, anisotropy assumptions				*P*1, none
NSD (standard deviations)				0.797 (0.100)
χ^2 range				1.035-1.036
Constant adjustment to intensities				8.31 ×10^{-5}
Resolution (from *SASRES*) [d] (Å)				36
DAMMIN (default parameters)				
q range for fitting (Å)				0.008-0.16

Symmetry, anisotropy assumptions	*P*1, none
χ^2	1.035
Constant adjustment to intensities	8.36×10^{-5}

Atomic modelling

CRYSOL (no constant subtraction)

Structure	PDB ID: 6O4O	PDB ID: 6O4O	PDB ID: 6O4P, chain A, residues 2-297 [e]	Docked model
χ^2	1.43	3.21	1.05	1.03
Calculated R_g (Å)	17.41	17.69	32.17	33.97
SASBDB IDs for data and models:	SASDGH2	SASDGJ2	SASDGG2	SASDGK2

[a] $q=(4\pi\sin\theta)/\lambda$

[b] 422

[c] Errors from *AUTORG* or *GNOM*, ± standard deviation

[d] 423

[e] Corresponding to the residues present in the IL-11Rα_{D1-D3} construct.

Supplementary Table 3.4: Isothermal titration calorimetry (ITC) data for the interaction between IL-11 and IL-11Rα.

Values shown are mean ± standard error of the mean, n = 3 for all.

		K_D (nM)	ΔH (kJ/mol)	ΔS (J/molK)	ΔG (kJ/mol)	Incompetent receptor fraction [d]	T (K)
$IL\text{-}11_{\Delta 10}$	$IL\text{-}11R\alpha_{EC}$	40 ± 20	-24 ± 0.6	65 ± 7	-44 ± 2	0.30 ± 0.03	303
	$IL\text{-}11R\alpha_{D1\text{-}D3}$	23 ± 3	-25 ± 2	66 ± 7	-45 ± 0.3	0.28 ± 0.06	303
	$IL\text{-}11R\alpha_{D1\text{-}D3}$	25 ± 2	-10 ± 0.4	120 ± 10	-46 ± 2.6	0.09 ± 0.04	298
	$IL\text{-}11R\alpha_{D1\text{-}D3}$	130 ± 20	41 ± 1	280 ± 5	-38 ± 0.4	0.05 ± 0.02	283
	$IL\text{-}11R\alpha_{D1\text{-}D3/\Delta loop}$	8 ± 4	-26 ± 0.9	70 ± 6	-47 ± 1	0.06 ± 0.05	303
IL-11 FL	$IL\text{-}11R\alpha_{EC}$	55 ± 14	-25 ± 1	59 ± 6	-44 ± 0.7	0.27 ± 0.03	303

[d] Similar to 'n' See [405].

Chapter 4 - The structure of the interleukin-11 signalling complex

Riley D. Metcalfe[1], Eric Hanssen[1,2], Kaheina Aizel[1,3,4], Andrew P. Leis[2], Courtney O. Zlatic[1], Paul R. Gooley[1], Tracy L. Putoczki[2,4,5*], Michael D.W. Griffin[1*].

[*]For correspondence, mgriffin@unimelb.edu.au.

[1] Department of Biochemistry and Molecular Biology, Bio21 Molecular Science and Biotechnology Institute, The University of Melbourne, Parkville, Victoria, Australia,
[2] Advanced Microscopy Facility, Bio21 Molecular Science and Biotechnology Institute, The University of Melbourne, Melbourne, Victoria, Australia
[3] Inflammation Division, The Walter and Eliza Hall Institute of Medical Research, Parkville, Victoria, Australia
[4] Department of Medical Biology and Department of Surgery, University of Melbourne, Parkville, Victoria, Australia
[5] Personalised Oncology Division, The Walter and Eliza Hall Institute of Medical Research, Parkville, Victoria, Australia

4.1 Abstract:

Interleukin (IL)-11 is an IL-6 family cytokine which signals by forming a complex with its cell surface receptors, the IL-11 specific receptor IL-11Rα and the shared receptor glycoprotein (gp) 130. This complex results in downstream signalling through signal transducer and activator of transcription (STAT) 3, which drives classical cancer hallmarks including cell survival and proliferation. Inhibition of IL-11 signalling is a validated target in several cancers. Despite this, few IL-11 signalling inhibitors are available. Development of inhibitors is hindered by a lack of knowledge on the structure and assembly of the IL-11 signalling complex. Here, we present the medium-resolution cryo-electron microscopy and crystal structures of the IL-11 signalling complex. These structures allow detailed mapping of the binding interfaces that form the complex. Our insights are supported by extensive solution biophysical measurements, which allow us to understand the thermodynamic basis of complex assembly. Overall, the structures we present here will enable the development of novel IL-11 signalling inhibitors, which will be potential therapeutics.

4.2 Introduction:

Interleukin (IL) 11 is a cytokine with several well-described physiological roles, and an emerging role in disease[171]. IL-11 is classically associated with haematopoiesis[5] and megakaryocytopoiesis[174]. Recently, a role for IL-11 signalling has been identified in gastrointestinal tumorigenesis[208] and in fibrosis of the heart[230], lung[233] and liver[231]. Therapeutic inhibition of IL-11 signalling is a validated therapeutic target in these diseases, but informed design of IL-11 signalling inhibitors is hindered by a lack of structural information on the molecular mechanisms underpinning IL-11 signalling.

IL-11 is a member of the IL-6 family of cytokines, which also includes IL-6, leukemia inhibitory factor (LIF), oncostatin M, IL-27 and IL-31[40]. IL-11 activates downstream signalling pathways by engaging with its two receptors, the IL-11 specific receptor IL-11Rα, and the shared receptor gp130, forming a signalling complex which is likely hexameric[167]. Mutagenesis on human and mouse IL-11[168-170] has identified

three binding sites on IL-11. Site-I is responsible for binding IL-11Rα, site-II is responsible for binding a gp130 molecule, forming a putative trimeric complex, and site-III engages a second gp130 molecule, to form the complete, hexameric signalling complex. Our structural knowledge of the formation of the IL-11 signalling complex is limited, and our mechanistic understanding is largely based on homology to the IL-6 family cytokines that have been best characterised structurally, leukemia inhibitory factor (LIF) and IL-6[71,74,80].

IL-11, IL-6 and human herpes virus IL-6 (vIL-6[107], a viral analogue of IL-6 with ~25% sequence identity to mammalian IL-6) are the only known IL-6 family cytokines that solely signal through a complex which incorporates a gp130 homodimer[40,138], which is responsible for intracellular signal transduction. Signal transduction molecules, such as the Janus kinases (JAK) and signal transducer and activator of transcription (STAT) proteins associate with the intracellular regions of gp130[39]. Structures have been solved of the extracellular, cytokine-binding regions of the vIL-6 and IL-6 signalling complexes[73,74]. In the IL-6 signalling complex, the complex is formed by ten interlocking interfaces between IL-6 and IL-6Rα, IL-6 and gp130, and IL-6Rα and gp130. Complex formation is thus highly cooperative. Biophysical analysis of complex formation shows that the complex is hexameric in solution[138], and the complex forms in three nanomolar-affinity steps[74]. We have previously solved the structure of IL-11[109] and IL-11Rα (chapter 3). Combined with biophysical measurements, these structures suggest that IL-11 and IL-6 use distinct mechanisms to engage their cognate receptor (chapter 3).

Here, we present both the cryo-electron microscopy (cryoEM) structure and the crystal structure of the IL-11 signalling complex. Our structures allow mapping in detail the interacting regions on the proteins which form the complex. We have also extensively biophysically characterised the interaction between IL-11, IL-11Rα and gp130. Overall, our structure provides a basis for the future rational design of agents targeting the extracellular IL-11 signalling complex.

4.3 Results and Discussion

4.3.1 The IL-11 signalling complex is hexameric in solution

We expressed and purified IL-11 from *Escherichia coli* BL21(DE3) cells, and IL-11Rα and gp130 from *Spodoptera frugiperda* Sf21 cells. Following purification of the complex components, the complex was reconstituted *in vitro* and purified by gel filtration, giving highly pure complex for subsequent structural study (Supplementary Figure 4.2A, see Supplementary Figure 4.4 for complete membrane and gel images). We used an N-terminal truncation of human IL-11 (IL-$11_{\Delta 10}$), and receptor constructs containing the D1-D3 domains of the receptors (IL-$11R\alpha_{D1\text{-}D3}$ and $gp130_{D1\text{-}D3}$), which is the minimum gp130 size for hexameric complex formation in IL-6[138].

We used analytical ultracentrifugation (AUC) and small-angle X-ray scattering (SAXS) to establish the solution stoichiometry of the IL-11 signalling complex. The IL-$11R\alpha_{D1\text{-}D3}$/$gp130_{D1\text{-}D3}$/IL-$11_{\Delta 10}$ complex has weight-averaged sedimentation coefficient 7.08 S and predicted mass 178.7 kDa, given a frictional ratio of 1.6 (Figure 4.1Ai, Supplementary Figure 4.1Ai, Supplementary Table 4.1), consistent with the formation of a hexameric complex (expected molecular mass of complex from sequence 169.8 kDa). Mouse IL-$11_{\Delta 10}$ forms a similar complex with the human IL-11 receptors (Figure 4.1Aii, Supplementary Figure 4.1Aii, Supplementary Table 4.1, weight-averaged sedimentation coefficient 7.07 S, mass 171.7 kDa, frictional ratio 1.6), implying that murine IL-11 can bind and activate IL-11 signalling in humans. We calculated the theoretical sedimentation coefficient of the IL-11 signalling complex (using the crystal structure as the model, including D1 of the receptor) using *HYDROPRO*[377]. The theoretical sedimentation coefficient of the complex is 6.76, consistent with the experimental sedimentation coefficient. We also generated $gp130_{EC}$, a gp130 construct containing all extracellular domains (residues 1-591), including the three fibronectin type III (Fn3) domains which are dispensable for complex formation[63,74]. IL-$11_{\Delta 10}$/$gp130_{EC}$/IL-$11R\alpha_{D1\text{-}D3}$ likewise form a hexameric complex (Figure 4.1Aiii, Supplementary Figure 4.1Aiii, Supplementary Table 4.1 weight-averaged sedimentation coefficient 8.50 S, mass 236.2 kDa and frictional ratio 1.6, expected mass 235.0 kDa). Likewise, muGFP-IL-11 forms a

hexameric complex with gp130$_{D1-D3}$ and IL-11Rα$_{EC}$ (Figure 4.1B, Supplementary Figure 4.1B, Supplementary Table 4.1, weight-averaged sedimentation coefficient 8.67 S, mass 242.7 kDa, frictional ratio 1.62, expected mass 230.2 kDa). These results show that IL-11 forms a hexameric complex with its two receptors.

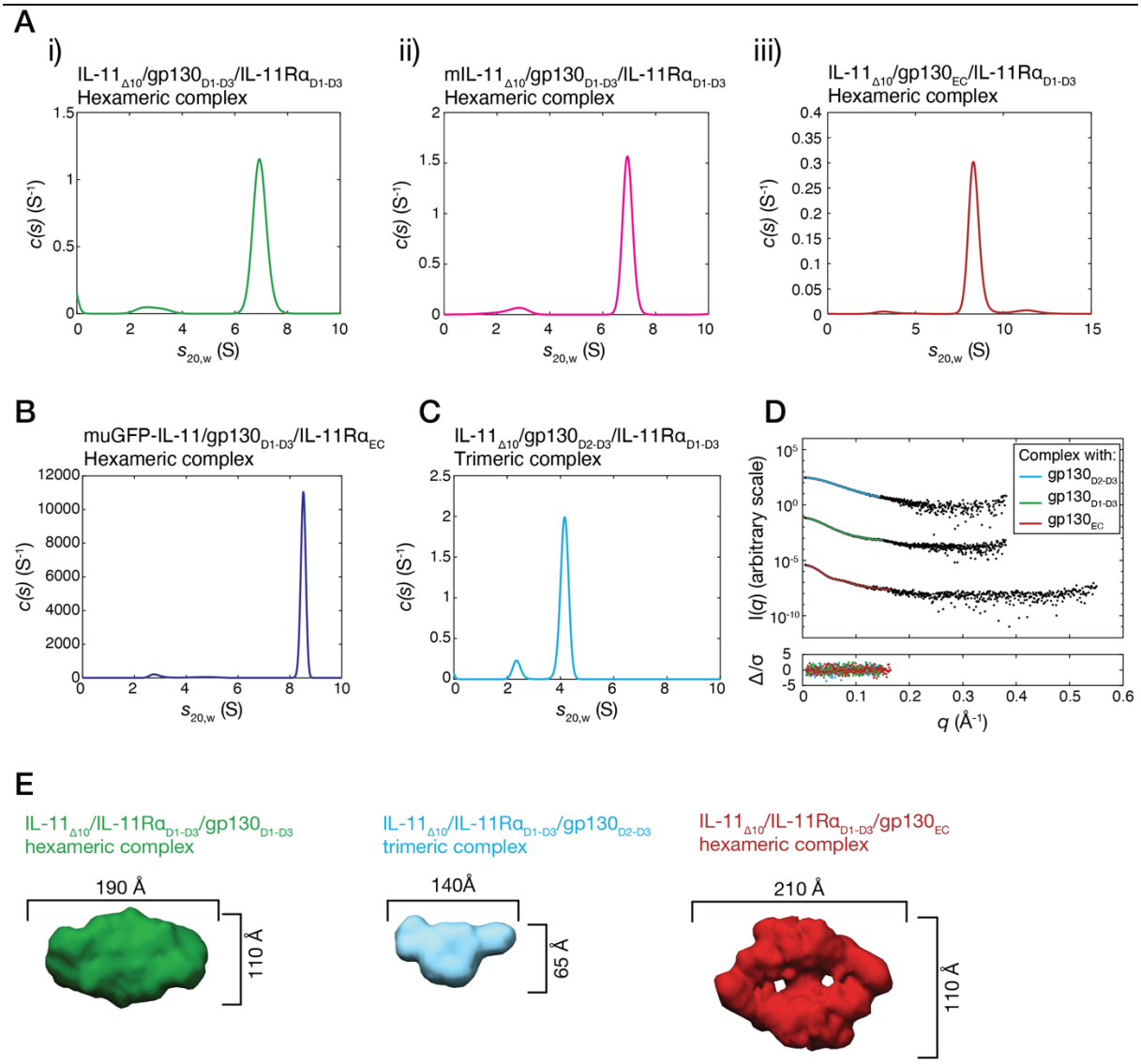

Figure 4.1: The IL-11 complex is hexameric in solution.

A) Continuous sedimentation coefficient (c(s)) distributions for the complexes formed by, i) human IL-11$_{Δ10}$ and the human IL-11 receptors, ii) mouse IL-11$_{Δ10}$ and the human IL-11 receptors, iii) human IL-11$_{Δ10}$, IL-11Rα$_{D1-D3}$ and full-length extracellular gp130 (gp130$_{EC}$). B) Fluorescence-detected c(s) distribution for the hexameric complex formed by muGFP-IL-11 and the IL-11 receptors. C) c(s) distribution for the trimeric complex formed by gp130$_{D2-D3}$. D) SAXS profiles for the hexameric IL-11 complex (formed by gp130$_{D1-D3}$ and gp130$_{EC}$), and the trimeric

complex formed by $gp130_{D2-D3}$. Fits shown are to the *ab initio* models in E). E) *Ab initio* models, calculated from the scattering data in E), for the hexameric and intermediate trimeric complexes.

We also generated $gp130_{D2-D3}$[138], a gp130 construct consisting of residues 102 to 304, lacking D1 of gp130, which is responsible for formation of the hexameric complex in the IL-6 signalling complex (Figure 4.1C, Supplementary Figure 4.1C). $IL\text{-}11_{\Delta10}/gp130_{D2-D3}/IL\text{-}11R\alpha_{D1-D3}$ form a complex with weight-averaged sedimentation coefficient 4.23 S, mass 71.3 kDa, given frictional ratio 1.47, consistent with the formation of an intermediate, trimeric complex (expected mass of trimer 73.6 kDa, Supplementary Table 4.1).

We collected SAXS scattering profiles for the trimeric complex formed by $IL\text{-}11R\alpha_{D1-D3}/gp130_{D2-D3}/IL\text{-}11_{\Delta10}$ and the hexameric complexes formed by $IL\text{-}11R\alpha_{D1-D3}/gp130_{D1-D3}/IL\text{-}11_{\Delta10}$ and $L\text{-}11R\alpha_{D1-D3}/gp130_{EC}/IL\text{-}11_{\Delta10}$ (Figure 4.1D, E, Supplementary Table 4.2, Supplementary Figure 4.1D-F). The structural parameters calculated from the scattering data are consistent with a trimeric and hexameric complex respectively (Supplementary Table 4.2), with the determined molecular masses consistent with the sequence, and those measured by SV-AUC. *Ab intio* models calculated from the scattering data are likewise consistent with the $IL\text{-}11R\alpha_{D1-D3}/gp130_{D2-D3}/IL\text{-}11_{\Delta10}$ complex being trimeric, and the $IL\text{-}11R\alpha_{D1-D3}/gp130_{D1-D3}/IL\text{-}11_{\Delta10}$ complex being hexameric (Figure 4.1E). We have previously shown by SAXS and AUC that IL-11 and IL-11Rα form an initial binary complex with 1:1 stoichiometry (chapter 3). Combined with these results, this shows that the IL-11 signalling complex forms in three steps. IL-11 first engages IL-11Rα, then engages a first molecule of gp130, forming an intermediate trimeric complex, which then dimerises to form the hexameric complex.

4.3.2 The IL-11 signalling complex forms in three moderate affinity steps

We used isothermal titration calorimetry (ITC) to measure the affinity and thermodynamics of complex assembly (Figure 4.2A, B). We have previously (chapter 3) measured the interaction between IL-11 and IL-11Rα by ITC, showing that it is a

high affinity interaction which is entropically dominated. We also studied the interaction between the IL-11/IL-11Rα complex and gp130 to establish the thermodynamics of higher-order complex assembly.

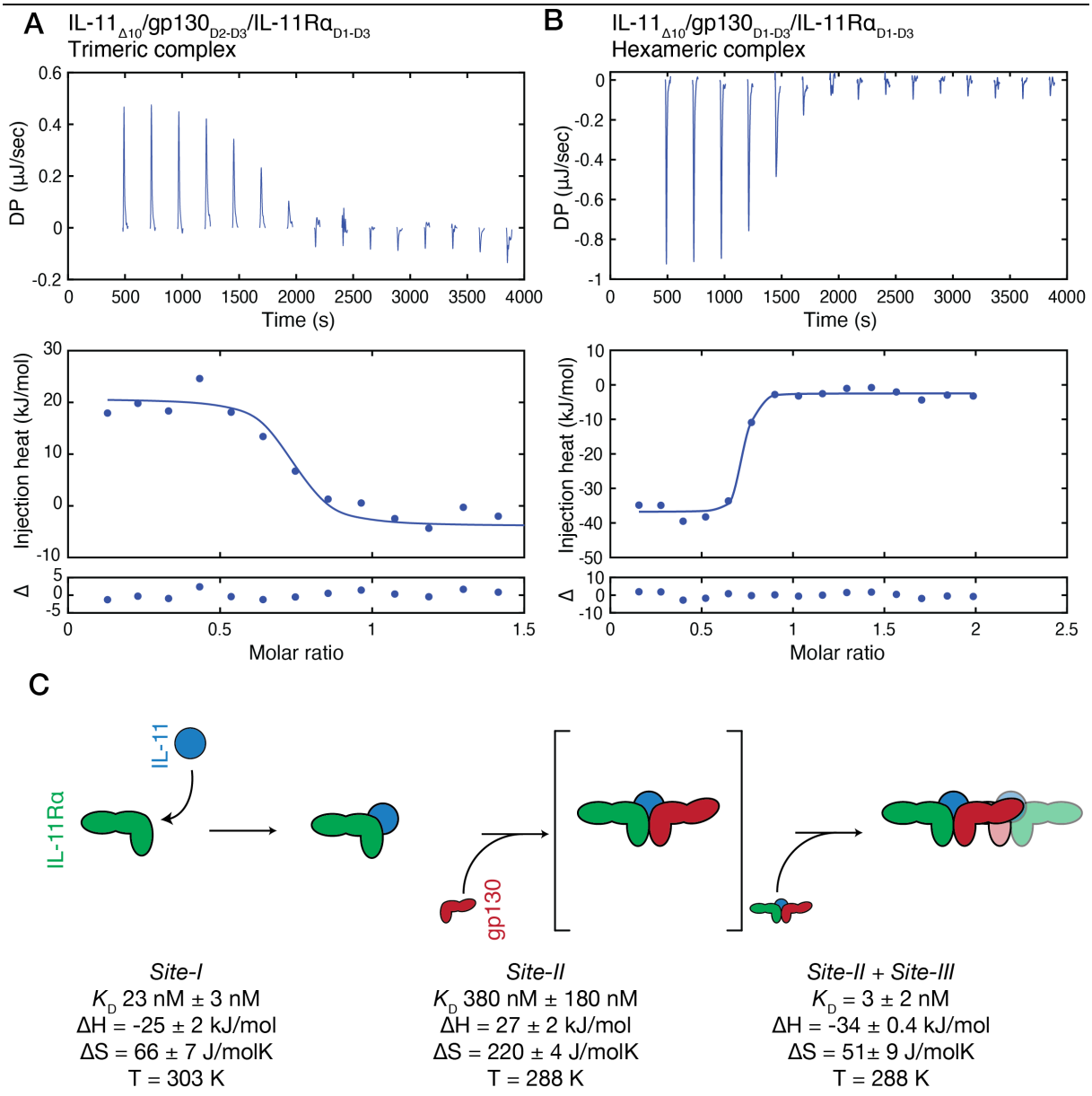

Figure 4.2: Thermodynamics of signalling complex assembly.

Thermodynamics of signalling complex assembly. A) ITC thermograms for, A) the interaction between IL-11$_{\Delta10}$/IL-11Rα$_{D1\text{-}D3}$ and gp130$_{D2\text{-}D3}$, and B) the interaction between IL-11$_{\Delta10}$/IL-11Rα$_{D1\text{-}D3}$ and gp130$_{D1\text{-}D3}$. C) Summary of complex assembly thermodynamics.

The interaction between IL-11$_{\Delta10}$/IL-11Rα$_{D1\text{-}D3}$ and gp130$_{D2\text{-}D3}$, corresponding to the formation of the intermediate trimeric complex, is moderate affinity (K_D 380 ± 180

nM, ΔG -40 ± 2 kJ/mol, n = 3 titrations, values give as mean ± SE) and strongly driven by entropy (Figure 4.2B, see Supplementary Table 4.3 for full thermodynamic parameters).

The final interaction to form the hexameric complex involves D1 of gp130. The interaction between IL-11$_{\Delta 10}$/IL-11Rα$_{D1\text{-}D3}$ and gp130$_{D1\text{-}D3}$ is relatively high affinity (K_D 3 ± 2 nM, ΔG -49 ± 3 kJ/mol, n = 3 titrations, value given as mean ± SE) (Figure 4.2B, Supplementary Table 4.3). The interaction between the three proteins involves two thermodynamically coupled interactions involving site-II and site-III on the cytokine, thus the affinity measured reflects both a contribution from the site-II and site-III interaction. The interaction involving site-III alone is extremely low affinity (ΔG -9 kJ/mol, K_D ~ mM), showing that the site-III interface on the cytokine is relatively low affinity. The high-affinity formation of the complete hexameric signalling complex requires the formation of a large, composite binding surface involving IL-11 and each of the IL-11 receptors.

4.3.3 The cryoEM structure of the IL-11 signalling complex

We solved the structure of the IL-11 signalling complex to understand in detail the molecular mechanisms underpinning signalling complex formation. Complexes were purified by gel filtration, then vitrified for subsequent imaging by cryoEM. Initial 2D classification revealed class averages in which secondary structure was clearly visible (Supplementary Figure 4.2A B). We obtained a three-dimensional reconstruction of the signalling complex at 3.47 Å resolution (judged by the gold standard half-map FSC = 0.143 criterion) (Figure 4.3A, Supplementary Figure 4.2C). We used this reconstruction to build and refine the structure of the IL-11 signalling complex (Figure 4.3B, see Supplementary Table 4.4 for image processing and refinement statistics, see Supplementary Figure 4.2D, E for representative density and local resolution maps).

The overall structure of the complex resembles a table. IL-11, D1-D3 of gp130 and D2-D3 of IL-11Rα are clearly visible in the cryoEM density. D1 of IL-11Rα is not visible in the density, suggesting that it is flexible in solution. N-linked glycans are

visible on IL-11Rα in the same position as in the crystal structure (at asparagine 105 and 172), additional N-linked glycans are also visible on gp130 (at asparagine 21, 61 and 135, Supplementary Figure 4.2Eii). Secondary structure is visible in the density, the α-helical bundle of the cytokine is clearly defined, sidechains are visible, disulphide bonds are generally visible, and β-strands are generally separated, consistent with a map reconstructed at this resolution (Supplementary Figure 4.2E).

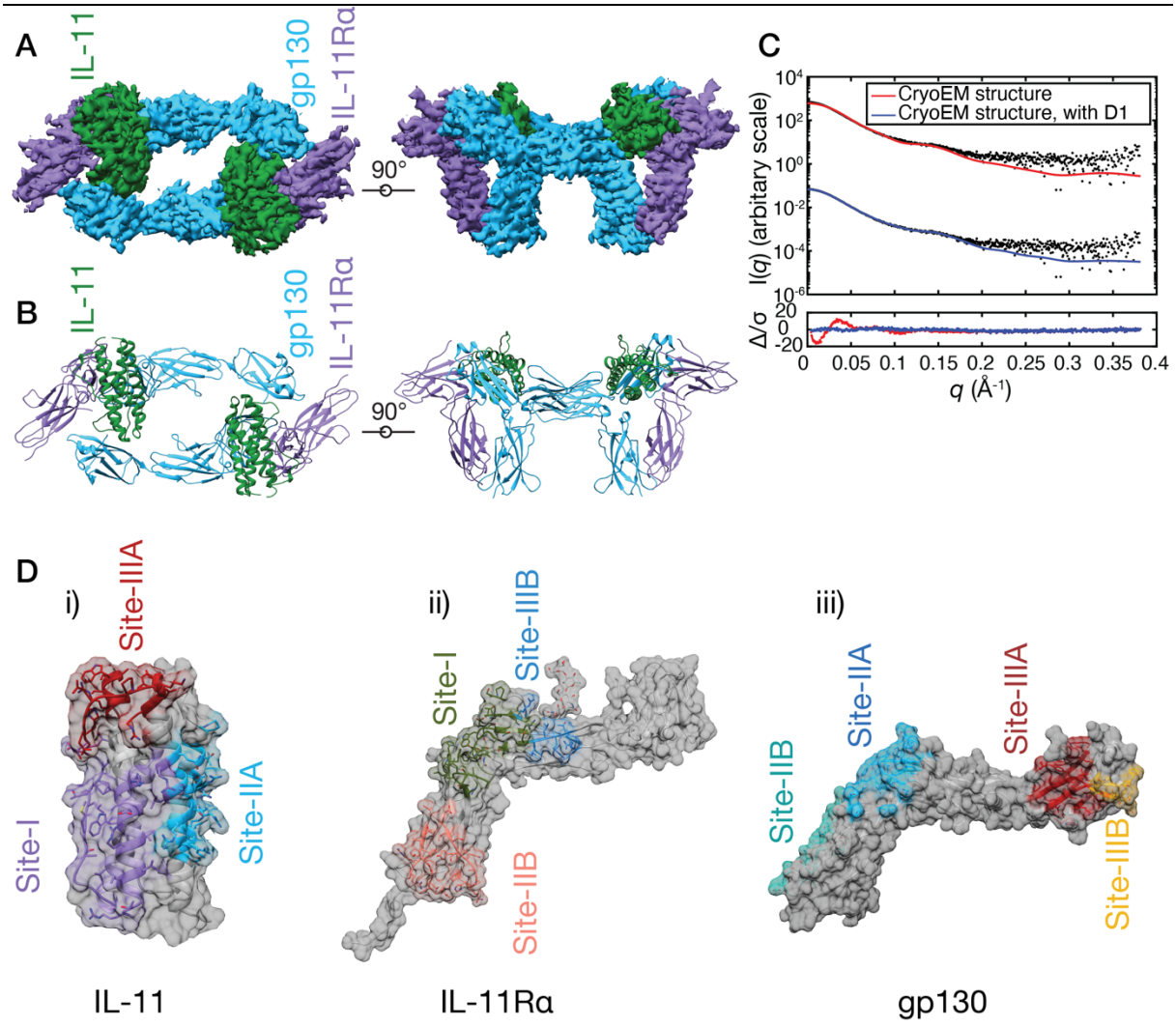

Figure 4.3: The cryoEM structure of the IL-11 signalling complex.

A) CryoEM density map, with the density for each of the three protein chains highlighted. B) Structural model of the IL-11 signalling complex derived from the cryoEM map. C) *CRYSOL* fit of the cryoEM structure of the hexameric IL-11 signalling complex structure, with D1 of IL-11Rα both included and not included to the signalling complex scattering data. D) Binding interfaces on IL-11, i) IL-11Rα, ii)

and gp130, iii) identified from the cryoEM structure. Interfaces are shown mapped onto the crystal structure of IL-11 (chapter 3), IL-11Rα (chapter 3), and gp130[73].

We used SAXS to show that the cryoEM structure of the IL-11 signalling complex matches the solution structure (Figure 4.3C). The fit of the structure coordinates to the scattering data is poor (χ^2 = 14.7), likely reflecting a contribution to the solution scattering from the missing D1 domain of IL-11Rα. To account for this, we generated a model of the complex, with D1 present, by superposition of our crystal structure of IL-11Rα with the IL-11Rα chain in the signalling complex structure. These coordinates fit the scattering data more accurately (χ^2 = 2.1), showing that when the absent domain is accounted for, the cryoEM structure accurately reflects the solution structure of IL-11Rα.

4.3.4 Ten interlocking interfaces form the IL-11 signalling complex

Our model of the IL-11 signalling complex allows interrogation of the interactions and binding surfaces that form the complex. Overall, the formation of the complex results in the burying of 6450 Å^2 of surface area (as determined using the *PISA* server[327]). The binding sites on IL-11 identified from the complex structure are similar to those previously identified by mutagenesis on human and mouse IL-11[168,169,198] (Figure 4.3Di). The structure reveals additional contacts between the AB loop and the receptors which were previously not identified by mutagenesis (Figure 4.3Di), and also allows mapping of the binding interfaces on IL-11Rα which have not previously been extensively studied by mutagenesis (Figure 4.3Dii), and comparison of the binding interface on gp130 with other cytokines (Figure 4.3Diii).

4.3.5 The site-I interface

The first interaction in the formation of the complex is the interaction between IL-11 and IL-11Rα, mediated through site-I on the cytokine (Figure 4.4A). Site-I has previously been identified on the cytokine through mutagenetic studies as being located on the C-terminal end of the D helix and in the AB loop[168,169,198]. In the complex, the AB loop of IL-11 undergoes a rearrangement from the crystal structure of IL-11 on binding to IL-11Rα (Figure 4.4Bi). The rearrangement of the loop results

in the formation of a small helix on the C-terminal end of the loop. Several sidechains (M59, S60, W166, R169) in the AB loop and in the D helix also undergo a rearrangement, and an internal hydrogen bond is formed between S60 and W166, presumably stabilising this conformation of the loop (Figure 4.4Bii). The cation-π interaction formed by R169 and W166, and the hydrophobic interaction between M59 and W166 are broken on complex formation (Figure 4.4Bii). The AB loop makes extensive hydrophobic and electrostatic contacts with IL-11Rα. D48 in the N-terminal end of the loop forms a salt bridge with K129 in IL-11Rα (Figure 4.4Ci). The C-terminal end of the AB loop likewise forms several hydrogen bonds, between M59 in IL-11 and S167/K128 in IL-11Rα, between S60 in IL-11 and F165 in IL-11Rα, and between G62 in IL-11 and A163 in IL-11Rα (Figure 4.4Cii). Although not directly involved in the interaction with IL-11Rα, W166 and R75 on IL-11 contribute to the hydrogen bond network, and likely stabilise the interaction with IL-11Rα (Figure 4.4Cii).

Further contacts are made by the N-terminal end of the D-helix of IL-11, which has been previously shown by mutagenesis to be critical for IL-11Rα binding[168,169,198], and is a common binding site in other cytokines (e.g. IL-6[74], GH[62]). The main contact formed by helix D is between R169, which protrudes into a hydrophobic pocket formed by F165, H229, F230, D275 and A279 on IL-11Rα (Figure 4.4Ciii). The guanidinium group of R169 additionally forms a salt bridge with the carboxylate group of D275. This is consistent with previous mutagenesis showing that R169 is critical for high-affinity IL-11Rα binding by IL-11 (chapter 3). Overall, site-I buries 1070 Å^2 of surface area in the complex and is predominately hydrophobic in character, consistent with the high affinity, entropically driven interaction that we have previously observed by ITC (chapter 3).

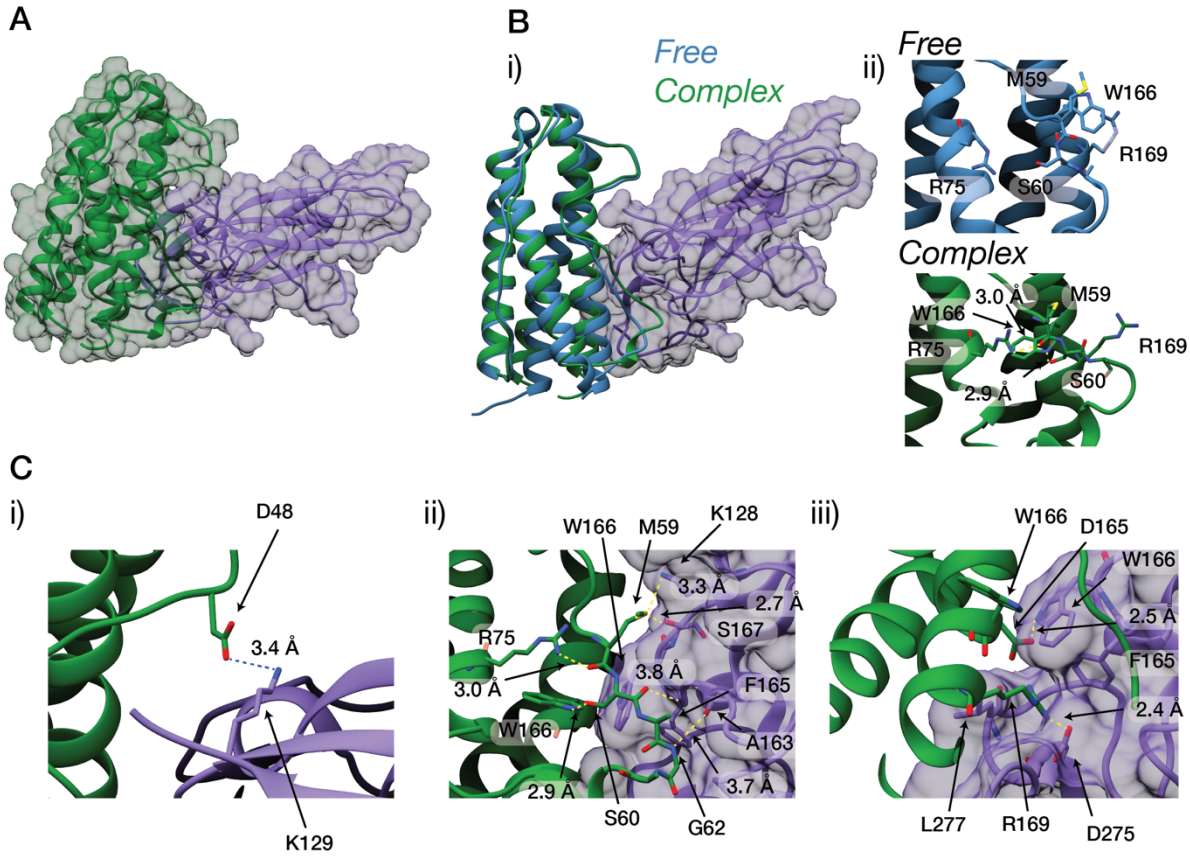

Figure 4.4: The site-I interface.

A) The interface between IL-11 and IL-11Rα. B) The conformational change in the AB loop of IL-11 that occurs on IL-11Rα binding. An overlay of the unbound IL-11 crystal structure (chapter 3) and IL-11 bound to IL-11Rα from the cryoEM structure is shown in i). The sidechain rearrangements that occur are shown in ii). C) Detail of the interactions that form the complex, with i) showing the hydrogen bond formed between IL-11 D48 and IL-11Rα K129, ii) showing the interactions between the C-terminal end of the AB loop of IL-11 and IL-11Rα, and iii) showing the interactions between the D-helix of IL-11 and IL-11Rα, including the hydrophobic pocket bound by R169.

4.3.6 The site-II interface

The formation of the trimeric intermediate complex between IL-11Rα, IL-11 and gp130 requires the formation of a composite binding site between IL-11 and IL-11Rα, which together engage gp130 (Figure 4.5A). This interaction requires two coupled interfaces – site-IIA between IL-11 and gp130, and site-IIB between D3 of IL-11Rα and D3 of gp130 (Figure 4.5A). Overall, the interaction buries 1320 Å^2 of

surface area, each interface contributes approximately the same amount of buried surface area, 700 Å^2 from the site-IIA interface, and 620 Å^2 from the site-IIB interface. The site-IIB interface is electrostatic in nature, resulting in the formation a complex hydrogen bond network between the two receptors, many of which require the participation of backbone atoms on either receptor (Figure 4.5B). In total, 13 hydrogen bonds are formed. The key residues forming the hydrogen bond network are R212, R213 and D260 on IL-11Rα and D254 and R259 on gp130 (Figure 4.5B).

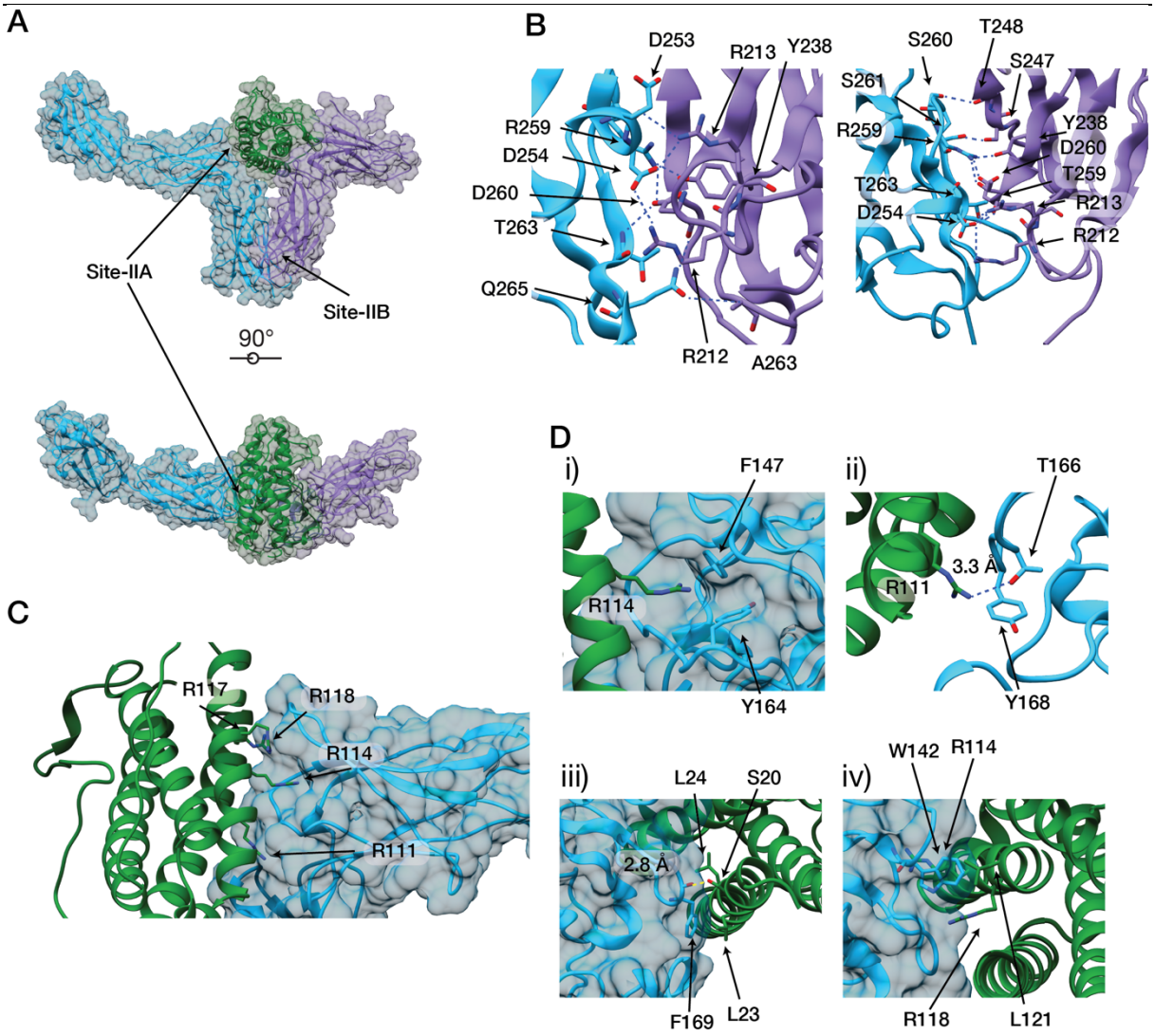

Figure 4.5: The site-II interface.

A) An overall view of the site-II interface in the IL-11 signalling complex. B) Two views of the site-IIB interface in the complex, with key residues and hydrogen bonds indicated (as dashed lines). C) The site-IIA interface, with the four key arginine residues indicated. D), i) details of the cation-π interaction formed by IL-11 R114, ii) the interactions formed by IL-11 R111, iii) the hydrophobic and hydrogen

bonding interactions formed by gp130 F169, iv), the interactions formed by gp130 W142.

The site-IIA interface is hydrophobic in character. Consistent with previous mutagenic studies[168,169], the main contact by the cytokine is formed by the N-terminal end of the A helix, and the C-terminal end of the B helix on the cytokine (Figure 4.5C). R114 on the cytokine forms the major contact, protruding into a pocket formed by the rearrangement of hydrophobic sidechains on gp130 on complex formation (Figure 4.5C, Di), additionally forming a cation-π interaction with F147. Three other arginine residues on the cytokine (111, 117, 118) which are on the same face on the cytokine[109], form interactions with gp130 (Figure 4.5C). The guanidinium group of R111 forms a hydrogen bond with T166, and R111 additionally forms a cation-π contact with Y166 (Figure 4.5Dii). R117 and 118 form predominately hydrophobic contacts with gp130. On gp130, the majority of contacts are formed by residues 142-147 and residues 164-172, two loops which together form a binding pocket for interactions with the cytokine. On gp130, F169 and W142 are the key contacting residues (Figure 4.5Diii, iv). F169 has previously been identified as being critical for cytokine engagement by gp130, and forms a key hydrophobic contact in previously solved structures of cytokine:gp130 complexes (e.g. the IL-6 hexameric complex[74], the LIF/gp130 complex[80] and the vIL-6 trimeric complex[73]). In the IL-11 complex, F169 forms a hydrophobic contact with L23 in the N-terminus of IL-11 (Figure 4.5Diii). The backbone amide group of F169 additionally forms a hydrogen bond with the hydroxyl oxygen of S20 of IL-11. W142 on gp130 forms predominately hydrophobic interactions with the B-helix of IL-11 (Figure 4.5Div).

Overall, the nature of the interfacing residues is consistent with the ITC measurement for the IL-$11_{\Delta 10}$+IL-$11R\alpha_{D1\text{-}D3}$/$gp130_{D2\text{-}D3}$ interaction. The interaction measured by ITC is moderate affinity, and strongly driven by entropy (Figure 4.2A, Supplementary Table 4.3), consistent with the relatively hydrophobic interface that we observed in the structure.

Structures have previously been solved of vIL-6[73], IL-6[74] and LIF[80] in complex with the CHR of gp130, allowing analysis of the mode of interaction between different cytokines and the shared binding surface on gp130[80,107]. IL-11 binding does not induce major rearrangements of the backbone of the CHR of gp130, with the gp130 chains from the four structures not differing greatly in conformation (Figure 4.6A). A common binding site in the CHR[80,107] has previously been identified from the structures of the vIL-6/gp130 and LIF/g130 complexes. IL-11 adopts a similar overall orientation to IL-6 and LIF and binds a similar surface on the CHR of gp130, although the pose adopted by the three cytokines is distinct (Figure 4.6A, B). In spite of the similar binding surfaces utilised by IL-11 and IL-6 on gp130, the chemical nature of the interactions differ. As discussed above, the IL-11/gp130 site-II interaction is formed predominately by hydrophobic and cation-π interactions between conserved arginine residues on IL-11, and the conserved hydrophobic binding pocket on gp130. For IL-6, the overall pose of the cytokine on gp130 is similar, and a similar binding interface is utilised (Figure 4.6A, B), but the chemical nature of the interactions differ. For example, the N-terminus of IL-6 forms several hydrogen bonds with the CHR of gp130, for which there is no equivalent in IL-11, likewise, there are no equivalent cation-π interactions in the IL-6/gp130 CHR interaction[74]. This is consistent with previous reports suggesting that the gp130 CHR interface is thermodynamically promiscuous, and able to form distinct interactions with several distinct cytokines[80].

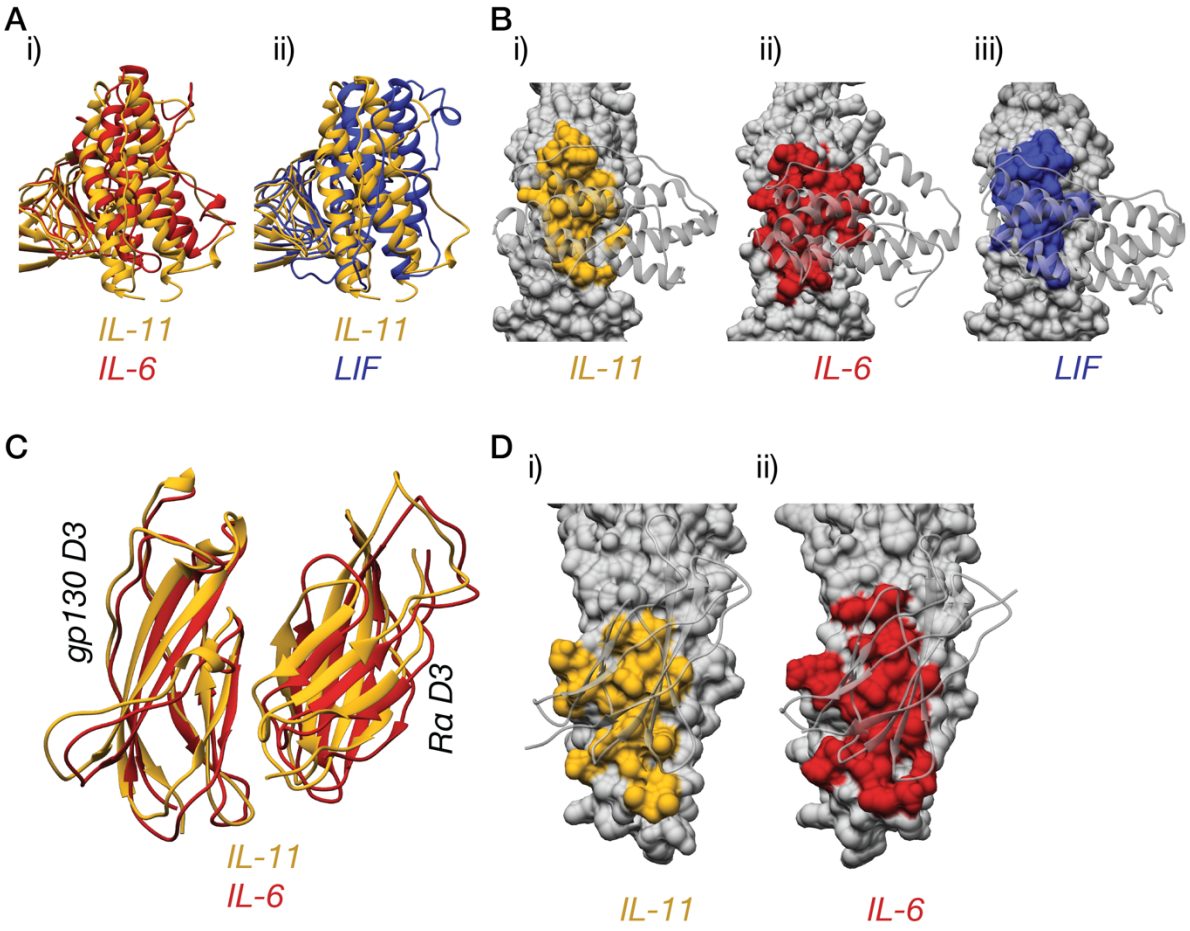

Figure 4.6: The site-II interfaces of IL-6 family cytokines.

A) Overlay of the IL-11/gp130 site-II interface and the IL-6/gp130 site-II interface i), and the LIF site-II interface, ii). B) The surface bound on gp130 by IL-11, i), IL-6, ii) and LIF, iii). C) Overlay of the IL-11Rα/gp130 site-IIB interface and the IL-6/gp130 site-IIB interface. D) The surface bound on gp130 by IL-11Rα D3, i), and IL-6Rα D3, ii).

Both IL-6Rα and IL-11Rα form an interaction between D3 of the receptors and D3 of gp130 (site-IIB). The main contact between gp130 and the α-receptor in both contacts is formed by residues 253 to 266 in D3 of gp130 (Figure 4.6C, D). Both interfaces bury similar amounts of surface area (670 Å^2 for IL-6Rα/gp130, 610 Å^2 for IL-11Rα/gp130). Likewise, in both complexes, D254 and R259 in D3 of gp130 both form salt bridges to the α-receptor, and a hydrogen bond is formed between T263 and the α-receptor. The main difference in site-IIB between the two complexes are three additional hydrogen bonds formed in the IL-11 complex between IL-11Rα and

gp130, making the interface overall more electrostatic in nature. This suggests that the same surface on D3 of gp130 has an ability to promiscuously form interactions with different cytokine α-receptors, analogous to the same ability that is possessed by the CHR of gp130.

Different cytokines also interact with gp130 using distinct thermodynamic mechanisms. IL-6, IL-11 and CNTF each interact with the CHR of gp130 in a moderate affinity, manner, strongly driven by entropy[80] (Figure 4.2A, Supplementary Table 4.3), while LIF interacts with the same surface with a high affinity, strongly driven by enthalpy[80]. This could be related to the requirement for a co-receptor for the interaction between IL-11, IL-6 and the CHR of gp130. LIF, which can engage the CHR of gp130 without a co-receptor, may require the formation of several entropically favourable, specific hydrogen bonds, to form a high-affinity, specific complex.

4.3.7 The site-III interface

The final interaction to form the hexameric complex is a second coupled interaction, between IL-11 and gp130 D1 (site-IIIA) and between D2 of IL-11Rα and D1 of gp130 (site-IIIB). Overall, the interaction buries 810 Å^2 of surface area, 590 Å^2 from the site-IIIA interface, and 220 Å^2 from the site-IIIB interface (Figure 4.7A, B). In agreement with previous mutagenic studies[352] and with homology to IL-6 and other IL-6 family cytokines[74], the key contact residue is W147 in the cytokine, which is responsible for burying 15% of the total surface area. W147 binds flat against D1 of gp130 and forms a hydrogen bond with N92 in gp130 (Figure 4.7Aii). Other contacts are formed by residues adjacent to W147 and the N-terminal end of the AB loop, which forms predominately hydrophobic contacts to the N-terminus and D1 of gp130, along with two hydrogen bonds involving R40 and D46 in the AB loop (Figure 4.7A). The second, smaller interface between D2 of IL-11Rα and D1 of gp130 (site-IIIB) is less extensive, and likely accessory in complex formation (Figure 4.7B), largely formed by a small loop in gp130 D1 (residues 86-89) packing against a sheet in IL-11Rα D2. The interface results in the burying of a small amount of surface area (220 Å^2) and no electrostatic interactions. When combined with the

site-II interface, the site-II+site-III interaction is high affinity (Figure 4.2A, Supplementary Table 4.3), as measured by ITC, consistent with the large amount of combined surface area buried by the two interfaces, as well as the formation of several electrostatic interactions. Our ITC measurements show that the site-III interface alone is low affinity (~mM), consistent with the relatively small amount of surface area buried by that interface.

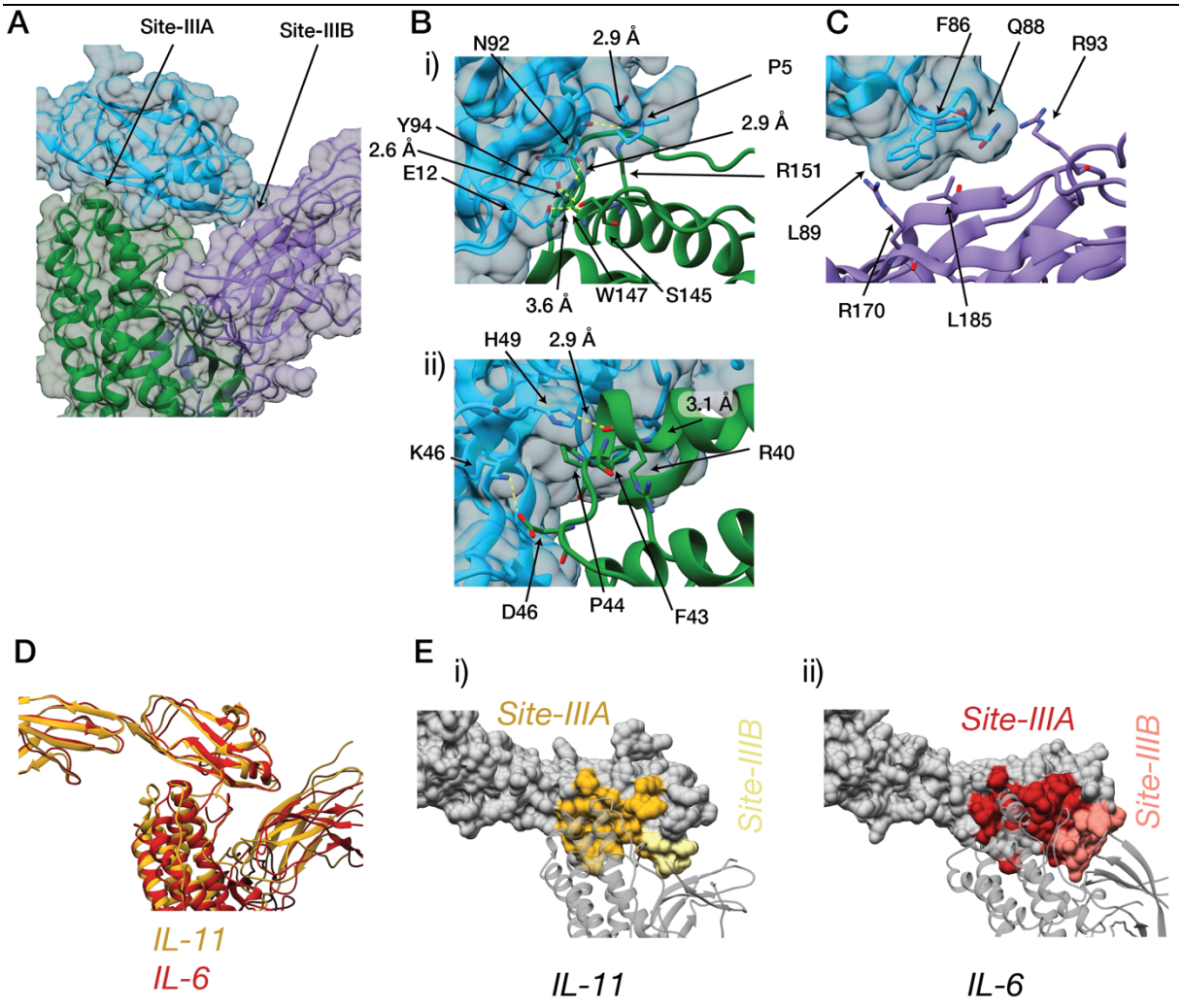

Figure 4.7: The site-III interface.

A) The site-III interface between IL-11, IL-11Rα and gp130. The site-IIIA interface is formed by IL-11 and gp130, the site-IIIB interface is formed by IL-11Rα and gp130. B) Key interactions forming the site-IIIA interface between IL-11 and gp130, i) showing contacts formed by W147 and adjacent residues on IL-11, and ii) showing contacts formed by the AB loop on IL-11. C) The site-IIIB interface formed by IL-

11Rα and gp130. D) Overlay of the site-III interfaces of IL-11 and IL-6. E) Surfaces bound by IL-11/IL-11Rα, i) and IL-6/IL-6Rα, ii) on D1 of gp130.

The site-IIIA interface between the cytokine and D1 of gp130 is unique to IL-11, IL-6 and vIL-6. Other IL-6 family cytokines, such as LIF, form a similar cytokine/Ig domain interaction, but with alternative receptors, such as the LIFR, and not with gp130[80]. In the IL-11, IL-6 and vIL-6 complexes, the site-IIIA interface is broadly similar, the main difference is the relative contribution of the N-terminus of gp130. In the IL-6 and vIL-6 complexes, it interacts closely with the AB loop of the cytokine[73,74], forming multiple hydrogen bonds to the cytokine, and is responsible for burying ~50% of the total surface area. In the IL-11 complex the N-terminus of gp130 does not form any hydrogen bonds with the cytokine and is responsible for burying ~30% of the total surface area in the complex (Figure 4.7D, E). A second interface unique to the IL-6 and IL-11 signalling complexes is the site-IIIB interface. In both complexes, the interface is not extensive, burying a small amount of the total surface area on complex formation (220 Å^2 for IL-11Rα/gp130 D1, 310 Å^2 for IL-6Rα/gp130 D1), and resulting in the formation of few electrostatic contacts (Figure 4.7E). In both complexes, the same loop on gp130 D1, comprising residues 85-89 makes the primary contact with the α-receptor. Site-IIIB is slightly more extensive in the IL-6 complex, unlike in the IL-11 complex, a second contact is formed by the loop comprising residues 35-37 in gp130 (Figure 4.7E). The additional contact formed by IL-6Rα may be a consequence of the differing D2-D3 interdomain orientations adopted by the two receptors. Both site-III interfaces are similar in overall affinity and thermodynamics[74] (Figure 4.2C).

4.3.8 The crystal structure of the IL-11 signalling complex

We also obtained diffracting crystals of the IL-11 signalling complex. The complex used for crystallisation experiments differed from that used for cryoEM experiments, consisting of IL-11Rα$_{EC}$, IL-11$_{FL}$ and gp130$_{D1-D3}$. Small three-dimensional crystals grew in space group *P* 3$_1$ 1 2. Due to low resolution and high anisotropy (Supplementary Table 4.5 see Supplementary Figure 4.3A-C for representative density), we used the cryoEM structure of the IL-11 signalling hexamer for phasing

by molecular replacement (Figure 4.8A). Due to the high anisotropy present in the data, we used the *STARANISO* server[424] to process the data with an anisotropic resolution cut-off. Three hexamers are present in the asymmetric unit (Figure 4.8B), each hexamer forming one side of a triangle. We used non-crystallographic symmetry (NCS) constraints (strict NCS) to aid refinement and built against NCS-averaged maps, taking advantage of the six-fold NCS present in the structure. D1 of IL-11Rα is visible in the density and included in the model (Figure 4.8A, Supplementary Figure 4.3A). The crystal structure shows that D1 of IL-11Rα is not involved in any interactions required to form the complex. A single hexamer from the crystal structure agrees well with the SAXS solution scattering of the IL-11 signalling hexamer (χ^2 = 2.3) (Figure 4.8C, Supplementary Table 4.2).

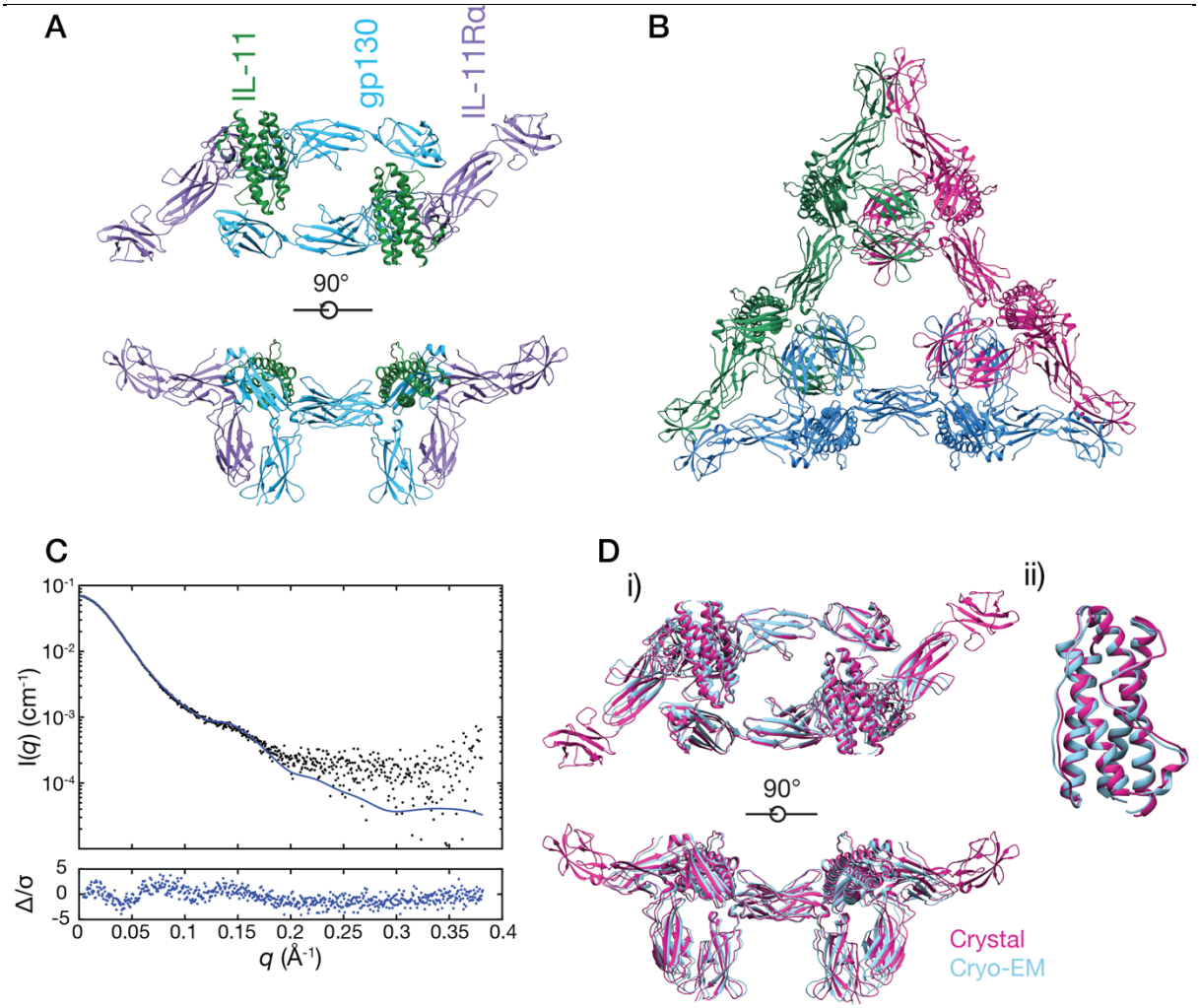

Figure 4.8: The crystal structure of the IL-11 signalling complex.

The crystal structure of the IL-11 signalling complex. A) The crystal structure of the complex. B) The asymmetric unit, with three hexamers present, each coloured

individually. C) Fit of one hexamer from the crystal structure coordinates to the SAXS scattering profile of the IL-11 signalling complex (χ^2 = 2.3). D) compares the crystal and cryoEM structures. An overlay of the crystal and cryoEM structures is shown in i). An overlay of the cytokine from both structures is shown in ii).

Overall, the two models of the IL-11 signalling complex do not greatly differ (RMSD 2 Å, Figure 4.8Di) and the conclusions described above regarding the interactions forming the complex are also valid for the crystal structure of the complex. The cytokine structures from both complex structures agree well (Figure 4.8Dii). The main difference is a slight repositioning of the AB loop close to site-I, by approximately 2 Å, a minor change given the low resolution of both structures. The AB loop does not form any crystal contacts in the crystal structure of the complex, however the repositioning of the loop may be an indirect consequence of crystal contacts formed by other parts of the signalling complex. Similarly, the position of D3 of both IL-11Rα and gp130 differ slightly between the two structures (Figure 4.8Di). These domains make extensive crystal contacts between adjacent hexamers in the crystal structure of the complex. D3 of gp130 and D3 of IL-11Rα is also poorly defined in the cryoEM density, which may also account for the differences, as the position of the domain will be less restrained by the density through refinement.

4.4 Conclusion

IL-11 is a promising therapeutic target in a number of diseases, however, therapeutic targeting of IL-11 is hindered by a lack of detailed structural knowledge of the mechanisms underpinning IL-11 signalling. The structure, combined with our biophysical and thermodynamic analysis, allows us to map in detail the ten interfaces that drive complex formation, and understand mechanistic similarities and differences in IL-11 signalling compared with other cytokines. Broadly, this work allows the development of novel agents to inhibit IL-11 signalling by disrupting signalling complex formation, which may be useful therapeutically.

4.5 Materials and Methods

4.5.1 Expression and purification of IL-11 and the IL-11 receptors

IL-11, IL-11Rα and gp130 were expressed and purified according to previously described protocols (Chapter 2, 3 this thesis).

4.5.2 Purification of the IL-11 signalling complex

The IL-11 signalling complex was prepared by mixing equimolar amounts of IL-$11_{\Delta 10}$, IL-$11R\alpha_{D1\text{-}D3}$ and $gp130_{D1\text{-}D3}$. The complex was incubated on ice for one hour, then concentrated to approximately 500 µL using an Amicon centrifugal concentrator (10 kDa MWCO). It was then applied to a Superdex 200 10/30 gel filtration column, pre-equilibrated in TBS pH 8. Fractions containing the intact signalling complex were pooled and concentrated 1-5 mg/mL. The purity of the complex was assessed using native-PAGE and sedimentation-velocity analytical ultracentrifugation.

4.5.3 Analytical ultracentrifugation

AUC experiments were conducted largely as previously described for the IL-11Rα/IL-11 complex (chapter 3). SV-AUC experiments were conducted using a Beckman Coulter XL-I analytical ultracentrifuge, equipped with UV-visible scanning optics. Samples were centrifuged using an An-60 Ti or An-50 Ti rotor at 50,000 rpm and at 20 °C. Sedimentation data were fitted to a continuous sedimentation coefficient c(*s*) model, with floating frictional ratios using *SEDFIT*[403]. Buffer density, viscosity and the partial specific volume of the protein samples were calculated using *SEDNTERP*[404]. For complexes, the partial specific volume used was 0.73 mL/g.

Fluorescence SV-AUC experiments were conducted using a Beckman XL-A analytical ultracentrifuge, equipped with an Aviv Biomedical fluorescence detection system. Experiments were conducted at 50,000 rpm and 20 °C. Data were processed using *SEDFIT*, as above.

4.5.4 Small-angle X-ray scattering

SAXS experiments were conducted at the Australian Synchrotron SAXS/WAXS beamline [406-408]. Complexes for SAXS were prepared by mixing equimolar amounts of the IL-11 complex components prior to X-ray scattering experiments. The X-ray beam energy was 11,500 eV (λ = 1.078 Å), the sample-to-detector distance is noted in Supplementary Table 4.2. Data were collected following fractionation with an in-line size-exclusion chromatography column (Superdex 200 5/150 Increase, GE Healthcare,) pre-equilibrated in TBS pH 8.5, 0.2 % sodium azide. Data were reduced and analysed using Scatterbrain, CHROMIXS[409] and ATSAS[409,410], data were analysed using CRYSOL and DAMMIF/DAMAVER/DAMMIN[412-414]. A summary is given in Supplementary Table 4.2.

4.5.5 Isothermal titration calorimetry

Protein samples were buffer exchanged into TBS pH 8.5 using gel filtration prior to analysis by ITC. ITC data was collected using a MicroCal iTC 200 (GE Healthcare). Titrations were performed using 15 2.5 µL injections of the cytokine ligand, after an initial injection of 0.8 µL. IL-11Rα$_{D1-D3}$ was present at a concentration of 10 µM and the concentration of the cytokine in the syringe was 10-fold greater than the concentration of IL-11Rα. Following the formation of the cytokine/receptor complex, gp130$_{D1-D3}$ or gp130$_{D2-D3}$ was loaded in the syringe at a concentration approximately 10-fold greater than the concentration of IL-11Rα in the cell, a subsequent titration of gp130 against the cytokine/IL-11Rα$_{D1-D3}$ complex was then performed at 288 K. Titration data were integrated using *NITPIC*[419,420], and analysed in *SEDPHAT* using a 1:1 interaction model[405]. Each titration was conducted in triplicate, values stated are the mean ± standard error of the mean.

4.5.6 Native-PAGE

Native-PAGE gels were prepared as 1.5 mm thickness, 6% acrylamide gels with a 3% stacking gel (29:1 acrylamide:bis-acrylamide ratio). Tris pH 8.8 was used to buffer both the stacking and resolving gel, with 0.5% TCE used for visualisation, as above. Samples were diluted with 2× loading dye (100 mM Tris pH 6.8, 0.2% bromophenol blue, 20% glycerol) prior to electrophoresis. The marker used was the

Invitrogen NativeMark standard (Invitrogen, cat. LC0725). Gels were run at 100 V for 4 hours at 4 °C with 200 mM glycine, 25 mM Tris pH 8.8 used as the running buffer. Gels were visualised by staining with Coomassie Blue G-250[375].

Gels were wet transferred to nitrocellulose membranes, blocked, and probed with the primary antibodies, abcam ab128618 (anti-gp130), Santa Cruz SC-993 (anti-IL-11Rα) or Santa Cruz SC-7924 (anti-IL-11). The secondary antibody used was Odyssey cat 926-32211, and the fluorescent western blot was visualised using an Odyssey scanner (Li-COR).

4.5.7 Cryo-electron microscopy – data collection and 3D reconstruction

Cryo-EM was performed at the Bio21 Institute Advanced Microscopy Facility, The University of Melbourne. The complex (at 0.5 mg/mL) was blotted onto UltrAuFoil grids (R2/2, Quantifoil Micro Tools GmbH) that had been subjected to glow discharge (25mA for 30 s). Grids were imaged using a Gatan K2 direct detector mounted on a Talos Arctica (FEI, Hillsborough, Oregon) with a 70-μm objective aperture. The detector was operated in counting mode. The complex was imaged at a 1.31 Å/ pixel (100,000 × microscope magnification) with a defocus range of -0.8 to -2.0 μm. The dose rate was 3.2 electrons $Å^{-2}$ s^{-1} with 10 s exposures captured in 40 frames for a total dose of 52 electrons $Å^{-2}$. Movies were acquired both untitled and with tilts of up to 35 °.

Analyses were carried out using RELION-3.0[425,426]. Movie motion was corrected using MotionCor2.1. Cryosparc 2.1[427] was used for CTF estimation using the patch CTF estimation routine. A total of 3,082,536 particles were extracted from 2,010 motion-corrected movies. After 2D class averaging in Cryosparc 2.1 625,866 particles were retained and were re-extracted in RELION-3.0 with the original defocus from Cryosparc 2.1. After 3D classification 204,455 particles were used for the final 3D refinement. Final refinement with symmetry gave a map with a resolution of 3.47 Å. Resolution was estimated using gold standard FSC = 0.143 calculated using a relaxed solvent map. Maps were sharpened using *phenix.auto_sharpen*[428].

4.5.8 Cryo-electron microscopy – Model building and refinement

Previously published models of IL-11 (chapter 3, PDB ID: 6O4O) and gp130 (chain A from PDB ID: 1I1R[73]), and the IL-11Rα chain from an unpublished antibody-bound structure of IL-11Rα were docked into the electron density map using *UCSF Chimera* to generate an initial model of the IL-11 signalling complex. This model was refined using *phenix.real_space_refine*[429-431], followed by manual model-building in *Coot*[429] and automated refinement in *phenix.real_space_refine*. Strict NCS was enforced in refinement. Reference model restraints were used throughout refinement, using the initial models as the reference models. Geometry validation was performed using the *phenix.validation_cryoem* tool (incorporating *MOLProbity*) and *EMRinger*[432,433]. Structures were visualised using either *PyMOL* 2.2 or *UCSF Chimera*. Structures were aligned using the *Matchmaker* algorithm in *UCSF Chimera* or the *CE* algorithm[434] in *PyMOL* 2.2. Map-model FSC curves were calculated in *Phenix*. Figures were prepared using *UCSF Chimera*.

4.5.9 Protein crystallisation and X-ray data collection

Crystals of the IL-11 signalling complex were grown in the condition 180 mM magnesium chloride, 15.3% PEG 3350, 100 mM potassium sodium tartrate, 90 mM sodium HEPES pH 7.25 and 1.8% tert-butanol. Crystallisation drops were prepared by mixing equal volumes of the precipitant and IL-11 signalling complex (at 3 mg/mL), and 10 µL of a seed stock (prepared according to the method of Luft and DeTitta[395]). The IL-11 signalling complex used for crystallisation experiments used the constructs IL-11Rα$_{EC}$, IL-11$_{FL}$ and gp130$_{D1-D3}$. Crystals were flash-cooled in liquid nitrogen directly from crystallization drops, and X-ray diffraction data were collected at 100 K at the Australian Synchrotron MX2 beamline[396]. X-ray data collection statistics are tabulated in Supplementary Table 4.5.

4.5.10 X-ray data processing and structure refinement

Diffraction data were indexed, integrated and scaled using *XDS*[397], analysed using *POINTLESS*[398] and merged using *AIMLESS*[399] from the *CCP4* suite. Due to the highly anisotropic nature of the data, an ellipsoidal resolution cutoff was applied

using the *STARANISO*[424] server. Initial phase estimates were obtained using molecular replacement with *Phaser*[400] using the cryoEM structure of the IL-11 signalling complex as the search model (with glycans removed). Refinement was performed in *phenix.refine*[401] with rigid-body refinement and simulated annealing. Strict NCS restraints (NCS constraints) were used in refinement. Reference model restraints were used, using the high-resolution structures of the complex components. Iterative model-building was performing using *Coot*[402] using NCS-averaged maps. NCS map averaging was performed in *Coot*. Figures were prepared using *PyMOL 2.2* or *UCSF Chimera*. Refinement statistics are tabulated in Supplementary Table 4.5.

4.6 Supplementary Material

4.6.1 Supplementary Figures

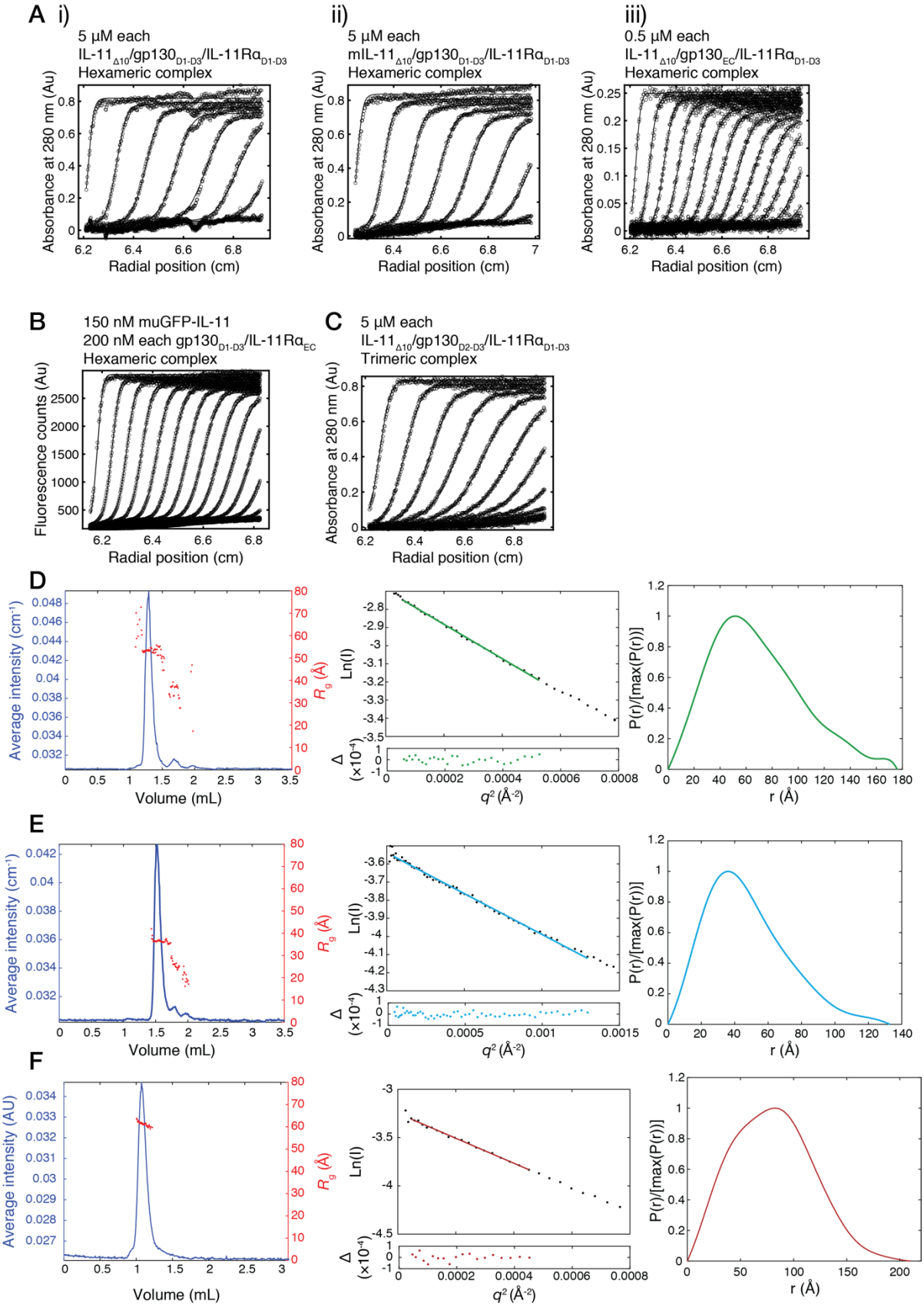

Supplementary Figure 4.1: Supplementary AUC and SAXS data for Figure 4.1. A) Raw sedimentation velocity scans for the data shown in Figure 4.1Ai-iii. B) Raw sedimentation velocity scans for the data shown in Figure 4.1Bi-ii. C) Raw sedimentation velocity scans for the data shown in Figure 4.1C. D) The SEC-SAXS chromatogram, Guinier plot and pairwise distance distribution (P(r)) plot for the hexameric complex formed by IL-11$_{\Delta10}$/gp130$_{D1\text{-}D3}$/IL-11Rα$_{D1\text{-}D3}$. E) The SEC-SAXS chromatogram, Guinier plot and pairwise distance distribution (P(r)) plot for the hexameric complex formed by IL-11$_{\Delta10}$/gp130$_{D2\text{-}D3}$/IL-11Rα$_{D1\text{-}D3}$. F) The SEC-SAXS chromatogram, Guinier plot and pairwise distance distribution (P(r)) plot for the hexameric complex formed by IL-11$_{\Delta10}$/gp130$_{EC}$/IL-11Rα$_{D1\text{-}D3}$.

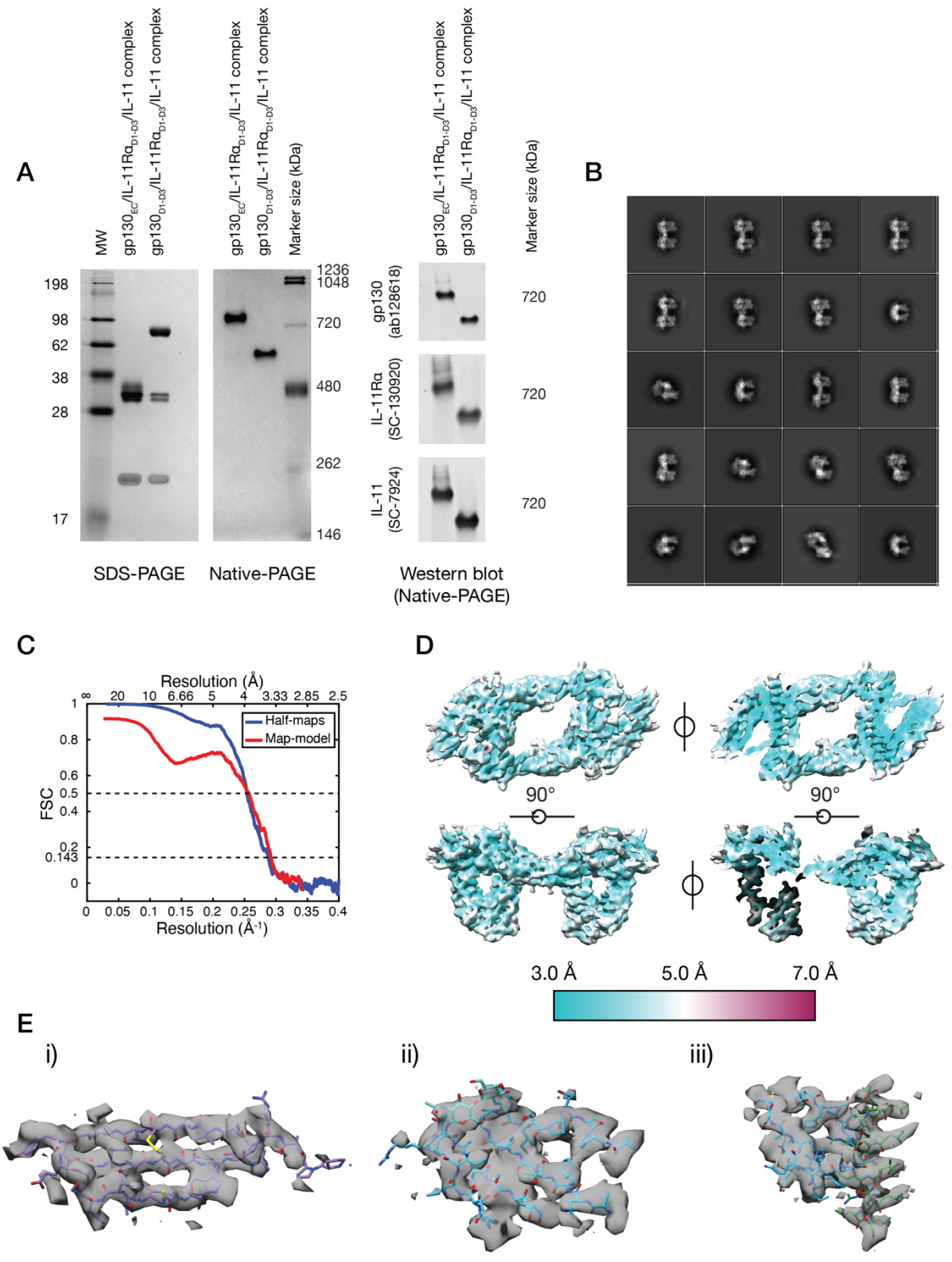

Supplementary Figure 4.2: Supplementary cryoEM data for the IL-11 signalling complex.

A) SDS-PAGE and Native-PAGE gels for the purified complexes, with a western blot to show that all components are incorporated into the purified complex. Complete

membrane/gel images are shown in Supplementary Figure 4.4. Primary antibodies used were SC-130920 (IL-11Rα), SC-7925 (IL-11), ab128618 (gp130). B) A selection of 2D class averages generated from the cryoEM data. C) Half-map and map model FSC curves. D) Local resolution maps. E) Representative cryoEM density, i) showing part of the β sheet in D2 of IL-11Rα, ii) showing part of D1 of gp130, with a glycan visible, iii) showing the site-II interface between IL-11 and gp130.

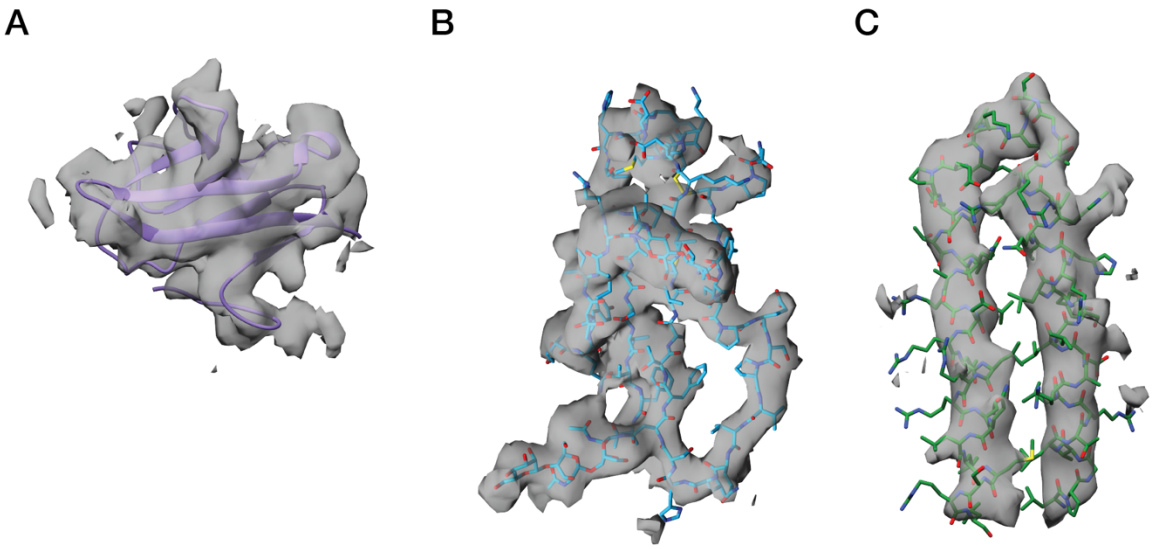

Supplementary Figure 4.3: Representative electron density for the crystal structure of the IL-11 signalling complex.

A) Electron density for D1 of IL-11Rα (from chain C). B) Part of D1 of gp130, with two glycans visible. C) The B and C helices of IL-11. Maps are $2F_o$-F_c maps, with missing F_{obs} not filled, contoured at 1 σ.

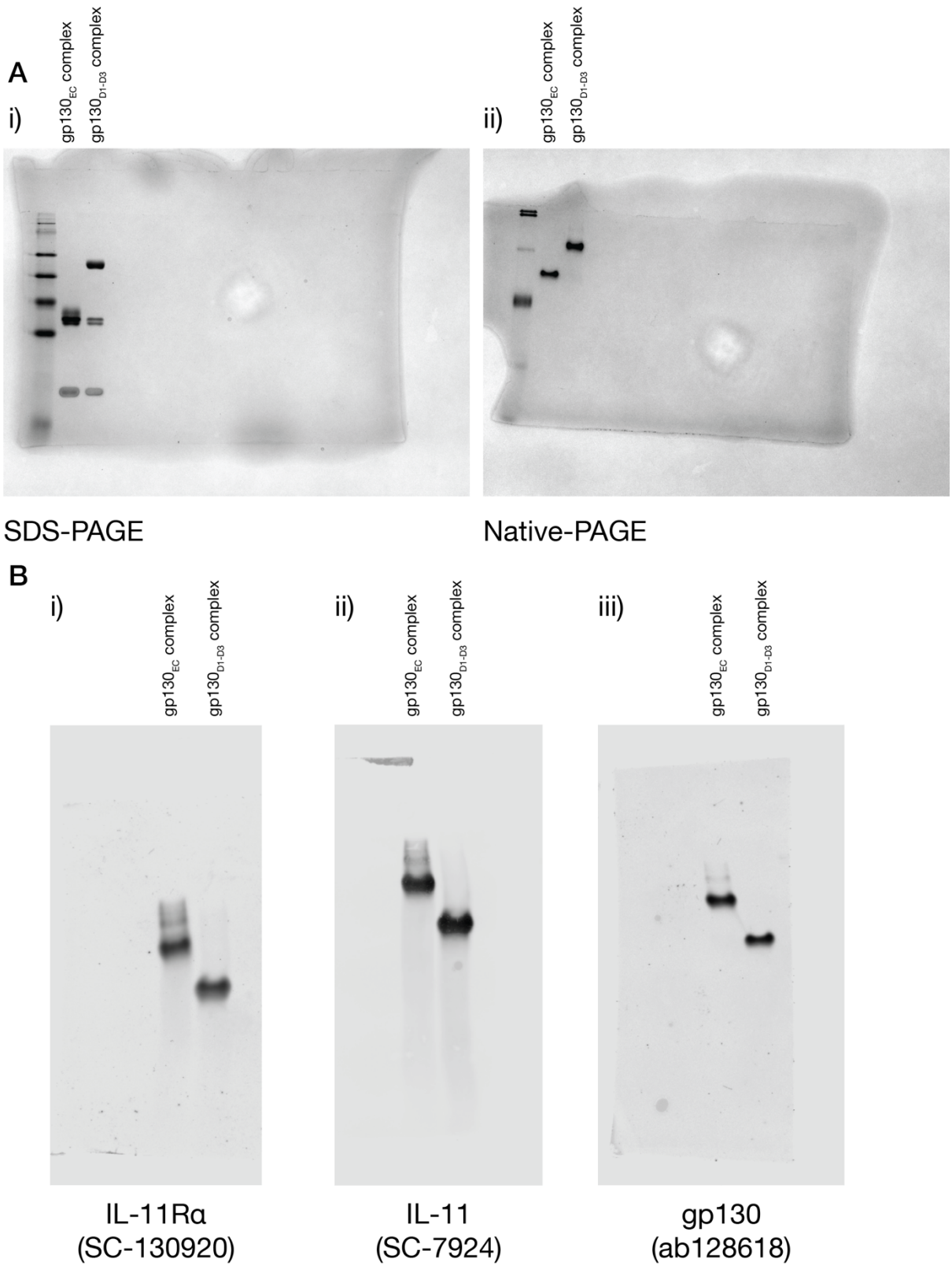

Supplementary Figure 4.4: Complete gel and membrane images for Supplementary Figure 4.2.

A) Complete gel images, i) for the SDS-PAGE gel, ii) for the native-PAGE gel. B) Complete membrane images for, i) the membrane probed for IL-11Rα, ii) the

membrane probed for IL-11, iii) the membrane probed for gp130. Antibodies are indicated in the figure.

4.6.2 Supplementary Tables

Supplementary Table 4.1: SV-AUC data and analysis.

Protein/complex	Expected mass (kDa)	Calculated mass (kDa)	Frictional ratio	Sedimentation coefficient (S)	Predicted sedimentation coefficient (S)	Concentration
IL-11Rα$_{D1-D3}$/gp130$_{D1-D3}$/IL-11$_{\Delta10}$ complex	169.8	178.7	1.6	7.08	6.76	5 μM each component
IL-11Rα$_{D1-D3}$/gp130$_{D1-D3}$/mIL-11$_{\Delta10}$ complex	169.9	171.7	1.6	7.07		5 μM each component
IL-11Rα$_{D1-D3}$/gp130$_{EC}$/IL-11$_{\Delta10}$ complex	235.0	236.2	1.6	8.50		500 nM each component
IL-11Rα$_{D1-D3}$/gp130$_{D1-D3}$/muGFP-IL-11 complex	230.2	242.7	1.6	8.67		150 nM mGFP-IL-11, 200 nM each IL-11Rα$_{EC}$/gp130$_{D1-D3}$

IL-11$_{\Delta 10}$/gp130$_{D2-D3}$/IL-11Rα$_{D1-D3}$ complex	73.6	71.3	1.5	4.23	5 μM each component

Supplementary Table 4.2: SAXS data collection and analysis statistics.

	IL-11$_{\Delta 10}$/gp130$_{D2-D3}$/IL-11Ra$_{D1-D3}$ trimeric complex	*IL-11$_{\Delta 10}$/gp130$_{D1-D3}$/IL-11Ra$_{D1-D3}$ hexameric complex*	*IL11$_{\Delta 10}$/gp130$_{EC}$/IL-11Ra$_{D1-D3}$ hexameric complex*
SAXS data collection			
Instrument/source	Australian Synchrotron SAXS/WAXS beamline equipped with Pilatus 2M detector and sheath flow cell for SEC-SAXS.		
Wavelength (Å)	1.078		
Beam energy (keV)	11.5		
Beam size (µm)	250 × 130		
Sample-to-detector distance (mm)	3538		2210
q measurement range (Å^{1}) [a]	0.004-0.38		0.005-0.55
Absolute scaling method	Comparison with scattering from 1 mm pure water		
Normalization	To transmitted intensity from beamstop counter		
Exposure time	1 s measurements from SEC-SAXS elution		
Sample temperature (K)	293		
SEC-SAXS parameters			
Column	Superdex 200 5/150 Increase		
Flow rate (mL/min)	0.45		0.4
Loading concentration (mg/mL)	2	2	2
Injection volume (µL)	50		50
Solvent	20 mM Tris-HCl pH 8.5, 150 mM NaCl, 0.2% sodium azide		
Software employed			
SAXS data reduction	*I*(*q*) vs *q* using Scatterbrain 2.8.2, SEC-SAXS solvent subtraction using *CHROMIXS* from *ATSAS* 2.8.3		
Basic analysis (Guinier, *P(r)*, molecular mass)	*PRIMUS* from *ATSAS* 2.8.3, *GNOM* from *ATSAS* 2.8.3		
Shape modelling	*DAMMIF* from *ATSAS* 2.8.3, *DAMAVER* from *ATSAS* 2.8.3, *DAMMIN* from *ATSAS* 2.8.3		

Calculation of theoretical intensities	*CRYSOL* from *ATSAS* 2.8.3		
Structural parameters			
Mass from V_c (kDa) (expected mass, ratio to expected, in brackets) [b]	81.6 (73.6, 0.90)	182.2 (169.8, 0.93)	290.0 (234.8, 0.81)
Guinier analysis [c]			
R_g (Å)	36.49 ± 0.14	53.10 ± 0.19	61.99 ± 0.46
I(0) (cm^1)	0.029 ± 7×10^{-5}	0.068 ± 1.4×10^{-4}	0.039 ± 2.2×10^{-4}
qR_g min,max	0.24, 1.31	0.41, 1.22	0.42, 1.32
P(r) analysis [c]			
R_g (Å)	37.52 ± 0.15	54.08 ± 0.13	62.66 ± 0.37
I(0) (cm^1)	0.02908 ± 6.8×10^{-5}	0.0677 ± 1.2×10^{-4}	0.03891 ± 1.9×10^{-4}
D_{max} (Å)	133	176	210
Porod volume ($Å^3$)	127000	404000	709000
Shape modelling			
DAMMIF (10 calculations, default parameters)			
q range for fitting (Å)	0.007-0.15	0.007-0.15	0.007-0.16
Symmetry, anisotropy assumptions	*P*1, none	*P*2, none	*P2*, none
Constant adjustment to intensities	1.49×10^{-4}	5.11×10^{-4}	None
NSD (standard deviations)	0.912 (0.083)	1.281 (0.176)	1.064 (0.026)
χ^2 range	0.997-0.971	1.114-1.129	1.018-1.092
Resolution (from *SASRES*) [d] (Å)	44 ± 3	50 ± 4	62 ± 5
DAMMIN (default parameters)			
q range for fitting (Å)	0.007-0.15	0.007-0.15	0.007-0.16
Symmetry, anisotropy assumptions	*P*1, none	*P2*, none	*P2*, none
χ^2	0.955	1.009	0.962
Constant adjustment to intensities	1.485×10^{-4}	5.03×10^{-4}	1.75×10^{-4}
Atomic modelling			

CRYSOL (no constant subtraction)	
Structure	IL11 signalling complex cryoEM structure, D1 not included (this work)
χ^2	14.7
Calculated R_g (Å)	47.39
Structure	IL11 signalling complex cryoEM structure, D1 included (this work)
χ^2	2.1
Calculated R_g (Å)	53.82
Structure	IL11 signalling complex cryoEM structure, D1 included (this work)
χ^2	2.3
Calculated R_g (Å)	54.50

[a] $q=(4\pi\sin\theta)/\lambda$

b 422

[c] Errors from *AUTORG* or *GNOM*, ± standard deviation

d 423

Supplementary Table 4.3: ITC data for complex formation.

Values are mean ± standard error of the mean, n = 3 for all.

		K_D (nM)	ΔH (kJ/mol)	ΔS (J/molK)	ΔG (kJ/mol)	Incompetent receptor fraction [d]
IL-$11_{\Delta10}$/IL-$11R\alpha_{D1-D}$	$gp130_{D2-D3}$	380 ± 180	27 ± 2	220 ± 4	-40 ± 2	0.25 ± 0.03
	$gp130_{D1-D3}$	3 ± 2	-34 ± 0.4	51 ± 9	-49 ± 3	0.32 ± 0.008

[d] Similar to 'n' See [405].

Supplementary Table 4.4: CryoEM data collection and model building statistics.

	IL-11 signalling complex
Data collection and image processing	
Magnification	100,000
Electron energy (kV)	200
Electron exposure ($e^-/Å^2$)	52
Defocus range (μm)	0.8-2.0
Pixel size (Å)	1.31
Starting model	*De novo*
Symmetry imposed	C2
Total number of micrographs	2010
Initial particle images	3,082,563
Final particle images	204,455
Map resolution (Å)	3.47
FSC threshold	0.143
Model building and refinement	
Initial models used	PDB 6O4O (chapter 3), PDB 1I1R (chain A), unpublished structure of IL-11Rα
Model resolution (Å)	3.93
FSC threshold	0.5
Sharpening *B* factor ($Å^2$)	151.24
Model composition	
Nonhydrogen atoms	10610
Amino acid residues	1326
Protein molecules	10
Real-space correlation	
CCvolume	0.67
CCmask	0.67
Mean Protein B factor ($Å^2$)	41.53
RMS deviations	

Bond lengths (Å)	0.008 (0)
(outliers > 4σ)	
Bond angles (°)	1.605 (40)
(outliers > 4σ)	
Validation	
EMRinger score [e]	1.20
MolProbity score [f]	1.74
Clashscore	4.95
Rotamer outliers (%)	1.23
CaBLAM outliers (%) [f]	2.01
Cβ outliers	0.48
Ramachandran plot	
Favoured (%)	93.74
Allowed (%)	6.11
Outliers (%)	0.15

e 432

f 433

Supplementary Table 4.5: X-ray data collection and model building statistics.

Values in parenthesises are for the highest resolution shell.

	IL-11 signalling complex [a]
Data collection	
Space group	*P* 3_1 1 2
Cell dimensions	
a, *b*, *c* (Å)	163.41, 163.41, 506.62
α, β, γ (°)	90, 90, 120
Resolution (Å)	49.275-3.779 (4.197-3.779)
R_{sym} [b]	0.286 (2.522)
R_{meas} [c]	0.294 (2.584)
R_{pim} [d]	0.064 (0.558)
$I/\sigma(I)$	10.6 (1.5)
Total number observations	947761 (48027)
Total number unique	45270 (2262)
Completeness (spherical)	58.1 (10.8)
Completeness (ellipsoidal)	92.8 (72.0)
Multiplicity	20.9 (21.2)
$CC_{1/2}$	0.998 (0.548)
Model building and refinement	
Resolution (Å)	40.8656-3.7794 (3.9144-3.7794)
Reflections used in refinement	43,181 (296)
R_{free} reflections	2054 (21)
R_{work}	0.2774 (0.4017)
R_{free}	0.2933 (0.4009)
Protein molecules in asymmetric unit	18
Number atoms:	35886
Protein	34914
Ligand	972
Average B *factor*	165.46

Protein	163.89
Ligand	221.85
R.m.s. deviations	
Bond lengths (Å)	0.01
Bond angles (°)	1.56
Ramachandran plot	
Favoured (%)	93.76
Allowed (%)	7.33
Outliers (%)	1.09
Validation	
MolProbity score [f]	2.13
Clashscore	16.18
Rotamer outliers (%)	0.03
Cβ outliers	0

---

[a] Values given are calculated by *STARANISO*[424] after removing poorly measured reflections due to anisotropy.

[b] $R_{sym} = \sum_{hkl}\sum_i |I_i(hkl) \quad \langle I(hkl)\rangle| / \sum_{hkl}\sum_i I_i(hkl)$

[c] $R_{meas} = \sum_{hkl} [N/(N\ 1)]^{½} \sum_i |I_i(hkl) \quad \langle I(hkl)\rangle| / \sum_{hkl}\sum_i I_i(hkl)$

[d] $R_{pim} = \sum_{hkl} [1/(N\ 1)]^{½} \sum_i |I_i(hkl) \quad \langle I(hkl)\rangle| / \sum_{hkl}\sum_i I_i(hkl)$

$CC_{1/2}$ = Pearson correlation coefficient between independently merged half data sets.

Chapter 5 - Basis for IL-11 signalling antagonism by the lead IL-11 signalling inhibitor, IL-11 Mutein

Riley D. Metcalfe[1], Kaheina Aizel[1,2,4], Courtney O. Zlatic[1], Karyn L. Wilde[3], Paul M. Nguyen[3,5], Larissa Doughty[1], Craig J. Morton[1], Michael W. Parker[1,6], Paul R. Gooley[1], Tracy L. Putoczki[2,4,6], Michael D.W. Griffin[1*].

[*]For correspondence, mgriffin@unimelb.edu.au.

[1] Department of Biochemistry and Molecular Biology, Bio21 Molecular Science and Biotechnology Institute, The University of Melbourne, Parkville, Victoria, Australia,
[2] Inflammation Division, The Walter and Eliza Hall Institute of Medical Research, Parkville, Victoria, Australia
[3] Department of Medical Biology and Department of Surgery, University of Melbourne, Parkville, Victoria, Australia
[3] National Deuteration Facility, Bragg Institute, ANSTO, Lucas Heights, New South Wales, Australia
[5] Personalised Oncology Division, The Walter and Eliza Hall Institute of Medical Research, Parkville, Victoria, Australia
[6] ACRF Rational Drug Discovery Centre, St. Vincent's Institute of Medical Research, Fitzroy, Victoria, Australia

5.1 Abstract

Inhibition of interleukin (IL)-11 signalling is a validated therapeutic target in a number of diseases, including in heart disease and cancer. Despite this, few IL-11 signalling antagonists are available, and none have been thoroughly mechanistically characterised. Here, we characterise the lead IL-11 signalling inhibitor, IL-11 Mutein, an antagonistic IL-11 mutant. We have characterised the interaction between IL-11 Mutein and the IL-11 receptors, IL-11Rα and gp130, showing that IL-11 Mutein functions by completely abolishing the formation of the hexameric IL-11 signalling complex. The structure of IL-11 Mutein shows that the mutations induce large structural changes in the cytokine. Integrating our biochemical, biological and structural data, we propose a mechanism of action for IL-11 Mutein by which it binds the IL-11 binding site on IL-11Rα in a different pose, sterically occluding the subsequent formation of the hexameric complex.

5.2 Introduction

Interleukin (IL)-11 is a pleiotropic cytokine with numerous roles in human physiology, and disease[171]. IL-11 has numerous roles in normal human physiology and in haematopoiesis[5], but has recently been identified as a cytokine with roles in gastrointestinal (GI) cancer[208] and in fibrosis of the heart, lung and liver[230,231,233]. In both these conditions, therapeutic inhibition of IL-11 signalling, either using cytokine mutants or antibodies has been shown to be therapeutically beneficial in murine and murine xenograph models of these diseases, highlighting IL-11 signalling as a rich therapeutic target. In spite of this, the structural basis of IL-11 signalling inhibition by current IL-11 signalling inhibitors is poorly understood.

IL-11 is a member of the IL-6 family of cytokines[40], and like nearly all members of the IL-6 family, signals using a common signal transducing receptor, glycoprotein (gp) 130. IL-11 first engages with an IL-11 specific receptor, IL-11Rα, and subsequently engages with gp130 in two steps, forming a hexameric signalling complex consisting of two copies each of IL-11, IL-11Rα and gp130. Three receptor binding sites on the cytokine are responsible for the interaction (Figure 5.1A), site-I is responsible for binding IL-11Rα, site-II is responsible for binding the first

molecule of gp130, and site-III is responsible for forming the hexameric signalling complex (Figure 5.1A,B). These binding sites have been identified through mutagenesis on human and mouse IL-11[168-170], and in the structure of the IL-6[74] and IL-11 (chapter 4) signalling complexes (Figure 5.1A). Formation of the IL-11 signalling complex results in intracellular signalling through the JAK-STAT and MAPK/ERK pathways[39].

Previously, antagonistic mutants of IL-11 have been designed through site-directed mutagenesis. Removal of a key tryptophan residue in site-III of IL-6 family cytokines (Trp157[67] in IL-6, 147[352] in IL-11), virtually abolishes binding to gp130 at site-III, thus preventing the formation of the hexameric signalling complex, and preventing activation of downstream signal transduction. The IL-11_{W147A} mutant antagonises IL-11 signalling in several cell culture models of IL-11 signalling[352]. A more potent antagonistic mutant was designed from the IL-11_{W147A} mutant using phage display, IL-11 Mutein[198]. To design IL-11 Mutein, potential residues adjacent to site-I were identified using a homology model of mouse IL-11, then sequences that increased affinity to IL-11Rα were identified using phage display. Phage display identified the sequence ^{58}PAID^{62}Y, which replaced ^{58}AMSA^{62}G in the AB loop of IL-11, a sequence in proximity to site-I (Figure 5.1Aii). The sequence is shared by both human and mouse IL-11. ELISA assays suggested that the ^{58}PAID^{62}Y substitution increased affinity to IL-11Rα by approximately twentyfold[198]. The two mutations were thus thought to act synergistically (Figure 5.1C), with the W147A mutation abolishing binding to gp130, and the PAIDY mutation increasing affinity for IL-11Rα, allowing IL-11 Mutein to outcompete IL-11 for IL-11Rα. IL-11 Mutein has been used as a reagent in several studies to inhibit IL-11 signalling, for example, it has been used to inhibit IL-11-associated lung inflammation in mice[198], to inhibit IL-11-driven inflammation in murine xenograph models of GI cancer[208], and to prevent IL-11-associated tissue transformations associated with pregnancy[203].

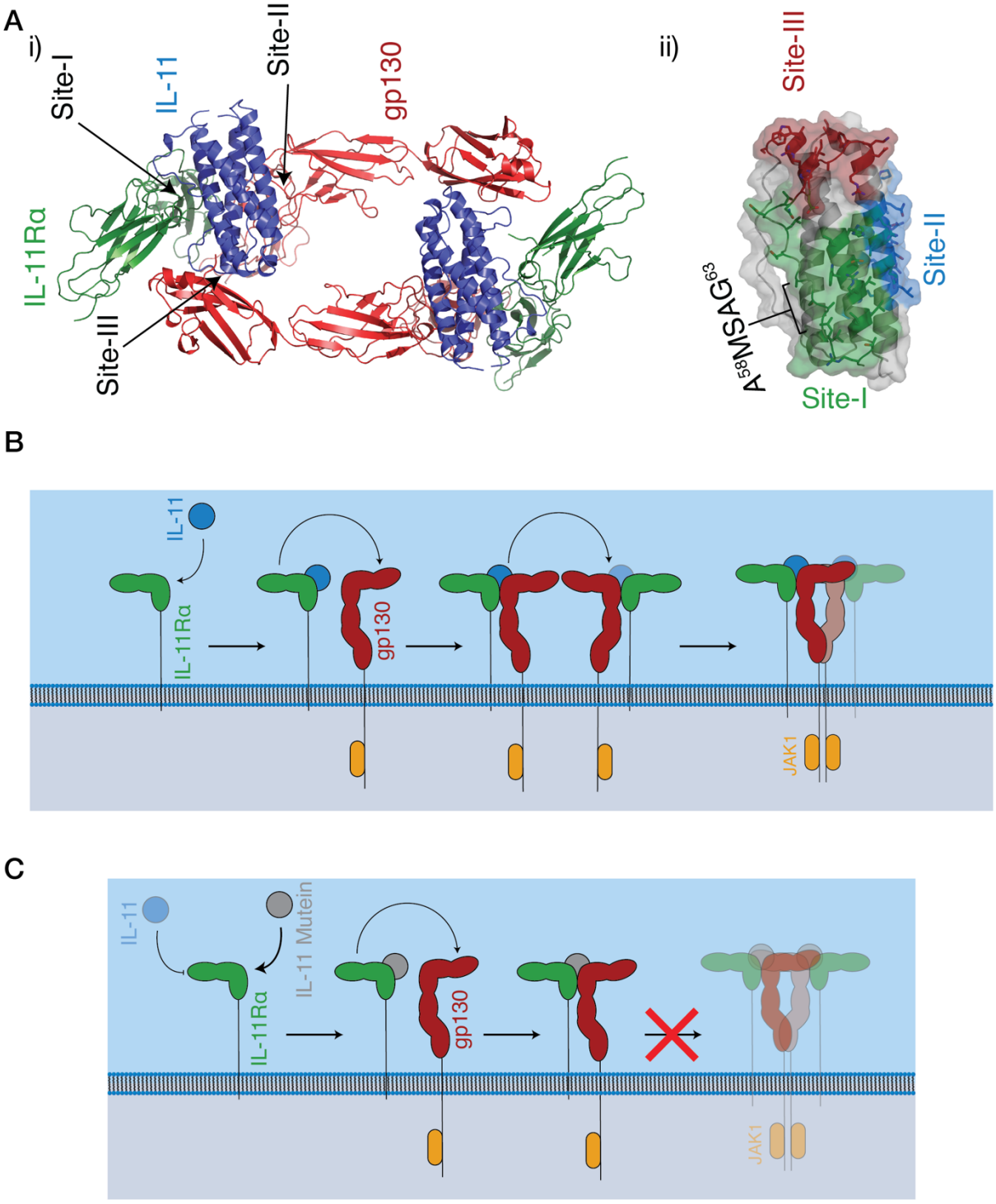

Figure 5.1: The structure and formation of the IL-11 signalling complex.

The cryo-electron microscopy (cryoEM) structure of the IL-11 signalling complex, A). The cryoEM structure is shown in i), with the three binding sites on IL-11 indicated in the complex (see Chapter 4). The binding sites on IL-11 are shown in ii), with the position of the $A^{58}MSAG^{62}$ residues indicated. A model for the stepwise formation of the complex is shown in B). The previously proposed model of the antagonistic action of IL-11 Mutein is shown in C), with IL-11 Mutein outcompeting

IL-11 for IL-11Rα binding, subsequently not forming a hexameric complex with gp130 to activate signalling through STAT3.

Antagonistic mutants have been developed for other cytokines. A leukemia inhibitory factor (LIF) mutein was designed using phage display, to identify residues which greatly increased affinity for the LIF receptor (LIFR)[320]. A similar mutant has been designed for IL-2. Yeast display and *in vitro* evolution was used to design an IL-2 signalling agonist which can bind the signalling IL-2 receptors, IL-2Rβ and γ_c, signal in the absence of IL-2Rα[349]. The mutations identified were in the hydrophobic core of the protein, and act to stabilise the IL-2Rβ binding conformation, thus favour binding to IL-2Rβ. More recently, an IL-2 mutein was designed using *de novo* protein design, which allowed the generation of a protein with low sequence identity to IL-2 that interacted with the IL-2 receptors with high affinity[350]. The designed protein is thermally stable, and has beneficial immunogenic properties, so represents a novel approach for designing cytokine signalling antagonists.

Here, we structurally, biophysically and biochemically characterise IL-11 Mutein, a lead IL-11 signalling inhibitor. We also present a comprehensive NMR study of IL-11 and IL-11 Mutein, assigning the majority of the backbone amides in both proteins and undertaking a study of the fast (ps-ns) dynamics of both proteins. We complemented this with molecular dynamics simulations of IL-11 Mutein. The crystal structure of IL-11 Mutein shows that the mutations in IL-11 Mutein in the AB loop cause a large shift in the position of the AB loop, which alters the loop close to site-I on the cytokine. To investigate the effect of the change in AB loop conformation on biological activity, we designed a series of mutants which recapitulated the change without the complete set of mutations present in IL-11 Mutein. Integrating these experiments, we propose a model for the antagonistic action of IL-11 Mutein, which will guide the design of future IL-11 signalling inhibitors.

5.3 Results and Discussion

5.3.1 IL-11 Mutein is a potent inhibitor of IL-11 signalling

Human IL-11 Mutein was expressed in the *Escherichia coli* cell line BL21(DE3) using an essentially identical method to IL-11. We also expressed and purified a ten-residue N-terminal truncation of IL-11 Mutein (IL-$11_{\Delta 10}$ Mutein), analogous to the ten-residue truncation of IL-11 described previously (chapter 3). These methods produced highly pure protein (Supplementary Figure 5.1A-C) in a high yield, approximately 3 mg/L bacterial culture for full-length IL-11 Mutein, and 6 mg/L for IL-$11_{\Delta 10}$ Mutein. We also produced the W147A mutant (IL-$11_{\Delta 10/W147A}$), the tryptophan mutant in site-III from which IL-11 Mutein is derived, which expressed to similar levels as IL-$11_{\Delta 10}$. We additionally produced murine IL-$11_{\Delta 10}$ (mIL-$11_{\Delta 10}$) and mIL-$11_{\Delta 10}$ Mutein, which expressed to similar levels compared to human IL-11 (approximately 1 mg/L for mIL-$11_{\Delta 10}$, 10 mg/L for mIL-$11_{\Delta 10}$ Mutein).

IL-11 Mutein has been used previously as a tool to inhibit IL-11 signalling in experimental models of disease[198,208]. To test the biological activity of IL-11 Mutein, and to confirm that the N-terminal truncation did not affect the inhibitory activity of IL-11 Mutein, we stimulated the human colon cancer cell line DLD1 with IL-$11_{\Delta 10}$ alone and in combination with IL-$11_{\Delta 10}$ Mutein or IL-$11_{\Delta 10/W147A}$. Both mutants inhibited IL-11 induced STAT3 phosphorylation, showing that they were effective antagonists of IL-11 signalling (Figure 5.2A, see Supplementary Figure 5.15A for complete membrane images). Similar results were observed for mIL-$11_{\Delta 10}$/mIL-$11_{\Delta 10}$ Mutein (Figure 5.2A). Surprisingly, IL-$11_{\Delta 10/W147A}$ activates STAT3, both alone and in combination with IL-$11_{\Delta 10}$, albeit to a lower level compared to IL-$11_{\Delta 10}$, showing that the W147A mutation alone is not sufficient to completely block IL-11 signalling (Figure 5.2A).

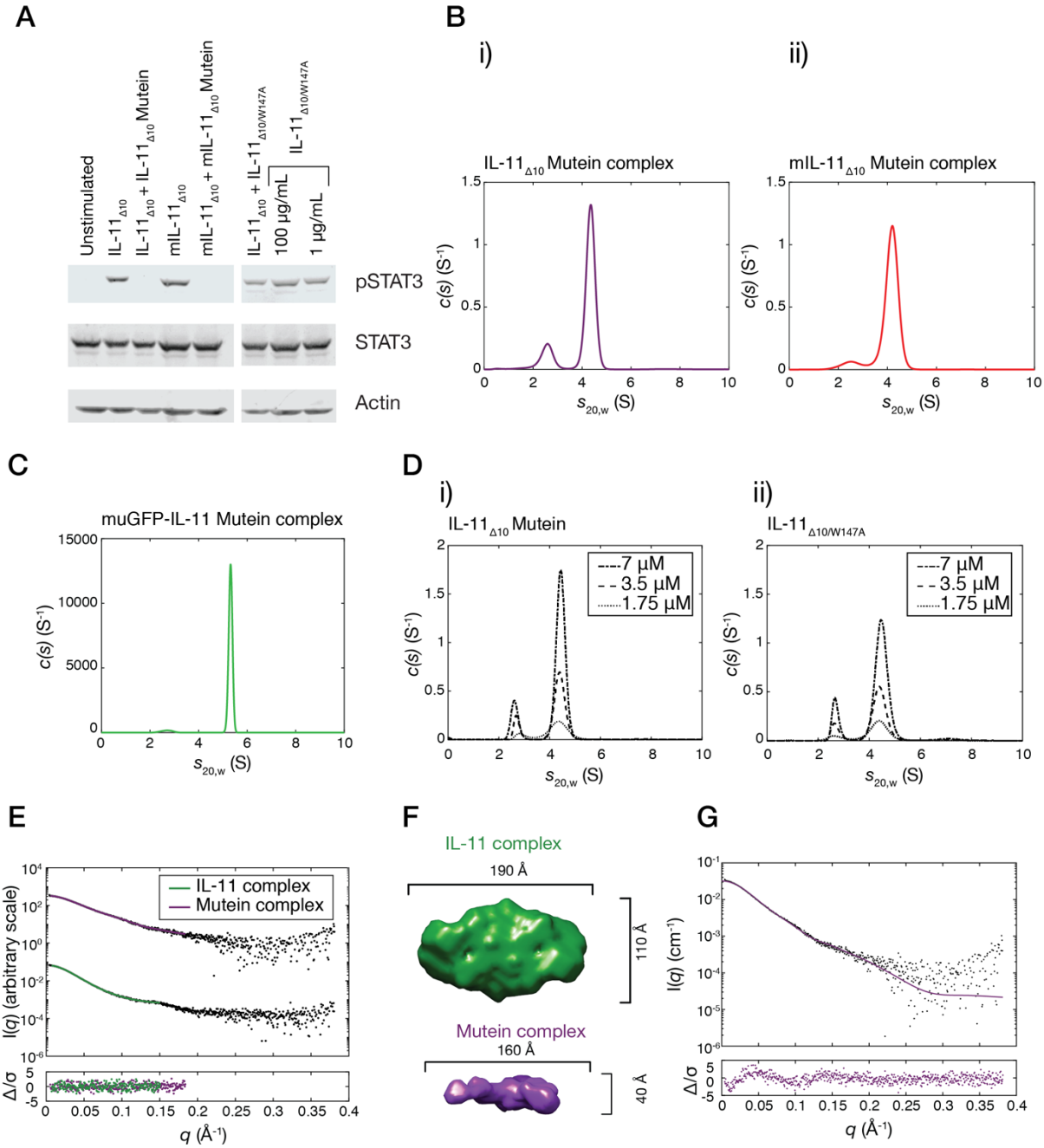

Figure 5.2: IL-11 Mutein does not activate intracellular signalling pathways, and forms a trimeric complex with gp130.

A) Western blot, showing the activation of STAT3 in the colon cancer cell line DLD1. Human and mouse IL-11 activate STAT3, while human and mouse IL-11 Mutein inhibit IL-11 induced STAT3 activation. IL-11$_{\Delta10/W147A}$ activates STAT3, alone and in combination with IL-11$_{\Delta10}$. B) Continuous sedimentation coefficient (c(s)) distributions, showing the complexes formed by i) human IL-11$_{\Delta10}$ Mutein and ii) mouse IL-11$_{\Delta10}$ Mutein with IL-11Rα$_{D1\text{-}D3}$ and gp130$_{D1\text{-}D3}$. Each complex was formed by mixing 5 µM of each protein, which was then immediately centrifuged. C)

Continuous sedimentation coefficient (c(s)) distribution showing the complex formed by 150 nM muGFP-IL-11 Mutein, 500 nM IL-11Rα$_{EC}$ and 1 μM gp130. The formation of the complex was monitored using fluorescence-detected SV-AUC. D) IL-11$_{Δ10}$ Mutein does not form a hexameric complex at high concentrations, ii), while IL-11$_{Δ10/W147A}$ forms a transient hexameric complex at high concentrations of IL-11$_{Δ10/W147A}$, gp130$_{D1-D3}$ and IL-11Rα$_{EC}$. E) SAXS data for the IL-11$_{Δ10}$ Mutein/IL-11Rα$_{D1-D3}$/gp130$_{D1-D3}$ trimeric complex and the IL-11$_{Δ10}$/IL-11Rα$_{D1-D3}$/gp130$_{D1-D3}$ hexameric complex. Fits are shown to the *ab intio* models in F). The models in F) were calculated using *DAMMIN*/*DAMMIF* and show that the trimeric complex formed by IL-11$_{Δ10}$ Mutein is approximately half the size and shape of the hexameric complex formed by IL-11$_{Δ10}$. G) *CRYSOL* fit of one half of the hexameric IL-11 signalling complex crystal structure to the IL-11$_{Δ10}$ Mutein complex scattering data (χ^2 = 1.56).

We used sedimentation velocity (SV) analytical ultracentrifugation (AUC) experiments to study the stoichiometry of the complexes formed by IL-11$_{Δ10}$ Mutein and IL-11$_{Δ10/W147A}$. In contrast to IL-11, which forms a hexameric signalling complex with its receptors, consisting of two copies each of IL-11, IL-11Rα and gp130, IL-11$_{Δ10}$ Mutein forms a trimeric complex, with the weight-averaged sedimentation coefficient ($s_{20,w}$) measured as 4.33 S and mass measured as 87.0 kDa, given a frictional ratio of 1.6, consistent with a 1:1:1 complex of IL-11$_{Δ10}$ Mutein, IL-11Rα$_{D1-D3}$ and gp130$_{D1-D3}$ (expected mass of complex 84.7 kDa) (Figure 5.2Bi, Supplementary Figure 5.2Ai, Supplementary Table 5.1). mIL-11$_{Δ10}$ Mutein also forms a similar complex with the human IL-11 receptors (weight-averaged sedimentation coefficient 4.26, mass 80.5 kDa, frictional ratio of 1.6) (Figure 5.2Bii, Supplementary Figure 5.2Aii, Supplementary Table 5.1). Likewise, we also expressed and purified IL-11 Mutein N-terminally fused with monomeric ultrastable (mu) GFP[385], allowing us to monitor complex formation using fluorescence-detected SV-AUC (see Chapter 3) (Figure 5.2C). muGFP-IL-11 Mutein formed a similar trimeric complex with IL-11Rα$_{EC}$ and gp130$_{D1-D3}$, with weight-averaged sedimentation coefficient 5.42 S and mass 116.7 kDa given a frictional ratio of 1.6 (expected mass of complex 121.1 kDa). (Figure 5.2C, Supplementary Figure 5.2B, Supplementary Table 5.1).

We also undertook SV-AUC experiments to study the stoichiometry of the complex formed by the IL-11$_{\Delta10/W147A}$ mutant, undertaking SV-AUC experiments at three concentrations of the IL-11$_{\Delta10/W147A}$ and IL-11$_{\Delta10}$ Mutein complexes (Figure 5.2Di, ii, Supplementary Figure 5.2Ci, ii, Supplementary Table 5.1). The predominant species is a similar trimeric complex, with weight-averaged sedimentation coefficient 4.48 S and mass 91.1 kDa (given a frictional ratio of 1.63). A peak consistent with a small proportion of hexameric complex was observed (at approximately 7 S, approximately 2% of the total signal), showing that the W147A mutation alone is not sufficient to prevent the formation of the hexameric IL-11 signalling complex. IL-11 Mutein did not form a hexameric complex, even at high concentrations of cytokine and receptors (Figure 5.2Di). This is consistent with our experiments showing the W147A mutation does not completely abolish STAT3 activation in DLD1 cells. Taken together, both the SV-AUC experiments and STAT3 activation assays showed that IL-11$_{\Delta10/W147A}$ can form a signalling complex, albeit with much lower affinity compared to wild-type IL-11. It additionally suggests that the IL-11 PAIDY mutations serve to further disrupt the binding to gp130 at site-III, compared to the W147A mutation alone. Further evidence for the formation of a hexameric signalling complex by IL-11 $_{\Delta10/W147A}$ could involve using live-cell microscopy to detect the formation of the complex on the cell membrane[322,435,436].

To gain additional insight into the stoichiometry and solution structure of the complex formed by IL-11 Mutein, we used small angle X-ray scattering (SAXS). Consistent with our AUC data, our SAXS parameters are consistent with the formation of a trimeric complex with 1:1:1 stoichiometry (Figure 5.2E, Supplementary Figure 5.2D, Supplementary Table 5.2). We also generated *ab initio* models from the SAXS data for both the trimeric IL-11 Mutein complex. The dimensions of the models are consistent with the Mutein complex being half the size in one dimension of the hexameric complex (Figure 5.2E, F). Likewise, the scattering profile from one half of the IL-11 complex crystal structure (*i.e.* one IL-11:IL-11Rα:gp130 trimer) agrees well with the scattering data for the Mutein complex (χ^2 = 1.56) (Figure 5.2G). The theoretical sedimentation coefficient (4.4 S, calculated using *HYDROPRO*[377]) of this complex is likewise consistent with the

experimental sedimentation coefficient (4.33 S). Our SAXS and AUC data thus show that IL-11$_{\Delta10}$ Mutein functions by preventing the dimerization of two cytokine/α-receptor/gp130 trimers to form a complete signalling hexamer. In addition, IL-11$_{\Delta10}$ Mutein is a more potent antagonist compared to IL-11$_{\Delta10/W147A}$ alone, implying that the potent antagonistic effect of IL-11 Mutein is a result of synergy between the W147A and PAIDY mutations.

5.3.2 IL-11 and IL-11 Mutein bind IL-11Rα with comparable affinity

Sandwich-ELISA experiments measured the affinity of IL-11 Mutein to IL-11Rα as being 1 nM, twenty times stronger compared to wild-type IL-11[198]. We measured the affinity of IL-11$_{\Delta10}$ Mutein and IL-11$_{\Delta10/W147A}$ for IL-11Rα$_{D1-D3}$ using ITC. Contradicting previous results, IL-11$_{\Delta10}$ Mutein binds IL-11Rα$_{D1-D3}$ with very similar affinity compared to IL-11$_{\Delta10/W147A}$ (K_D 38 ± 9 nM, compared to 10 ± 8 nM for IL-11$_{\Delta10/W147A}$, p = 0.22) (Figure 5.3Ai, Bi, Supplementary Table 5.3). Likewise, the thermodynamics of the interaction are very similar. We also studied the same interaction using microscale thermophoresis, giving comparable results (K_D 50 nM [lower value unbounded, 168 nM, 68% confidence interval], compared to 9 nM [lower value unbounded, 28 nM, 68% confidence interval] for IL-11) (Figure 5.3Ci, ii, Supplementary Table 5.3). These experiments show that, in contrast to previous results[198], IL-11 Mutein and IL-11 bind IL-11Rα with very similar affinity.

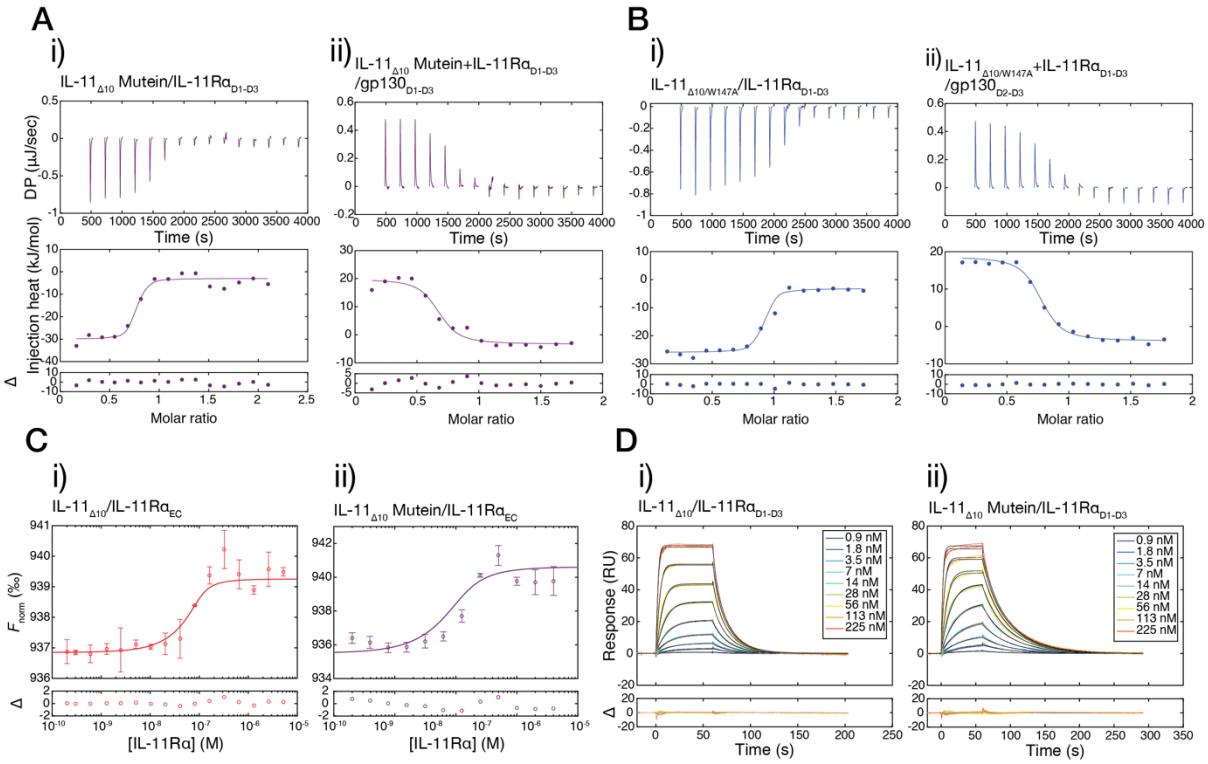

Figure 5.3: IL-11$_{\Delta10}$ and IL-11$_{\Delta10}$ Mutein interact with IL-11Rα with comparable affinity, but different kinetics.

A) ITC data and isotherms for the interaction between IL-11Rα$_{D1-D3}$ and IL-11$_{\Delta10}$ Mutein (K_D = 38 ± 9 nM, n = 3 titrations, mean ± SE), i) and IL-11$_{\Delta10}$ Mutein/IL-11Rα$_{D1-D3}$ and gp130$_{D1-D3}$ (K_D = 55 ± 4 nM, n = 3 titrations), ii). Representative titrations shown. B) MST isotherms for the interaction between labelled IL-11$_{\Delta10}$ and IL-11Rα$_{EC}$, (K_D = 9 nM [unbounded, 0.028 nM], 68% CI), i) and labelled IL-11$_{\Delta10}$ Mutein and IL-11Rα$_{EC}$ (K_D = 50 nM [unbounded, 0.168 nM]), ii). In both figures, circles represent the average of F_{norm}, error bars indicate the standard deviation. C) SPR sensograms for the interaction between immobilised IL-11$_{\Delta10}$ and IL-11Rα$_{D1-D3}$ (K_D = 78 ± 0.7, n = 2, mean ± SE), i) and immobilised IL-11$_{\Delta10}$ Mutein and IL-11Rα$_{D1-D3}$, (K_D = 33 ± 3, n = 2) ii). Full thermodynamic and kinetic parameters are given in Supplementary Table 5.3.

To form the trimeric complex, the IL-11 Mutein/IL-11Rα complex interacts with gp130 through site-II. We used ITC to measure the affinity of this interaction (Figure 5.3Aii), and the equivalent interaction between IL-11$_{\Delta10/W147A}$ and gp130 (Figure 5.3Bii). IL-11$_{\Delta10}$ Mutein binds gp130 (site-II) with higher affinity compared to IL-

$11_{\Delta10/W147A}$ (K_D = 55 ± 4 nM for IL-$11_{\Delta10}$ Mutein, K_D = 130 ± 10 nM for IL-$11_{\Delta10/W147A}$, p = 0.027) (Supplementary Table 5.3).

We used surface plasmon resonance (SPR) to measure the kinetics and affinity of IL-$11_{\Delta10}$ and IL-$11_{\Delta10}$ Mutein binding to IL-11Rα$_{D1-D3}$ (Figure 5.3Ci, ii). To immobilise IL-11 and IL-11 Mutein to the surface we produced constructs with a C-terminal biotinylation sequence (AviTag), to permit *in vivo* biotinylation in *E. coli*. This method gave material that was approximately 95% pure (by SDS-PAGE) and 25% biotinylated (by mass spectrometry) (Supplementary Figure 5.1D, E). The affinity measured by SPR was 78 ± 0.7 nM for the IL-$11_{\Delta10}$/IL-11Rα$_{D1-D3}$ interaction and 33 ± 3 nM for the IL-$11_{\Delta10}$ Mutein/IL-11Rα$_{D1-D3}$ interaction. In spite of the similar affinity, the kinetics differ between the two interactions, with IL-11 Mutein undergoing a slower dissociation after interacting with IL-11Rα (k_d 1.1 ± 0.02 × 10^{-1} s^{-1} for IL-11, 0.34 ± 0.007 × 10^{-1} s^{-1} for IL-11 Mutein). The affinity measured by SPR, ITC and MST are comparable (Supplementary Table 5.3), in all cases, showing a moderate-affinity interaction in the 10-100 nM range.

The different kinetic parameters measured in the SPR experiments suggest that, in spite of similar affinity, IL-11 and IL-11 Mutein engage IL-11Rα using a different mechanism. This suggests that the effect of the PAIDY mutations does not simply act through increasing the affinity to IL-11Rα. Instead, as shown by our AUC and biological data, the mutations likely act synergistically with the W147A mutation to disrupt binding to gp130 in site-III. There are two mechanisms that may cause this. First, the PAIDY mutations may themselves directly lower affinity to gp130, resulting in a synergistic effect in combination with the W147A mutation, which already substantially antagonise the binding to gp130 site-III. Alternatively, the PAIDY mutations may result in IL-11 Mutein binding IL-11Rα or the gp130 CHR with a different pose, sterically occluding subsequent interactions with D1 of gp130 to form the complete hexameric complex.

5.3.3 The structure of IL-11 Mutein

To understand the structural basis of IL-11 Mutein antagonism, we solved the structure of IL-$11_{\Delta10}$ Mutein and IL-$11_{\Delta10/W147A}$ (Figure 5.4A). Crystals of IL-11 Mutein were large plates (Supplementary Figure 5.3A) and diffracted to a resolution of 1.8 Å, crystals of IL-$11_{\Delta10/W147A}$ were rods, diffracting to a resolution of 1.48 Å (Supplementary Figure 5.3A). We note that efforts to solve the structure of full-length IL-11 Mutein were not successful, eight months of screening resulting in thin needles which were not diffraction-quality (Supplementary Figure 5.3A). Representative density for each map is shown in Supplementary Figure 5.3B, C. X-ray data collection and refinement statistics are presented in Supplementary Table 5.4.

We used SAXS to show that the solution structures of IL-$11_{\Delta10}$ Mutein and IL-$11_{\Delta10/W147A}$ accurately match the crystal structure coordinates (χ^2 = 1.37 for IL-$11_{\Delta10}$ Mutein, 0.91 for IL-$11_{\Delta10/W147A}$) (Figure 5.4B, Supplementary Figure 5.4Ai, ii, Supplementary Table 5.2). We also used SV-AUC to show that both proteins are monomeric in solution (Figure 5.4Ci,ii, Supplementary Figure 5.4Bi ii). The weight-averaged sedimentation coefficient ($s_{20,w}$) of IL-$11_{\Delta10}$ Mutein is 1.68, the measured molecular weight is 19.4 kDa, assuming a frictional ratio of 1.39, in good agreement with the molecular weight predicted from the sequence (18.2 kDa). Similar values were obtained for IL-$11_{\Delta10/W147A}$ (weight-averaged sedimentation coefficient 1.71, mass 19.4 kDa, frictional ratio 1.39) (Figure 5.4Cii, Supplementary Figure 5.4Cii).

Overall, the structure of IL-$11_{\Delta10}$ Mutein and IL-$11_{\Delta10}$ are not greatly different (rmsd 1.3 Å, Figure 5.4D), as the four-α helical bundle is not greatly perturbed by the PAIDY mutations in the AB loop. Likewise, comparison of the IL-$11_{\Delta10}$ and IL-$11_{\Delta10/W147A}$ structures shows that the W147A mutation does not disrupt the core α-helical bundle, the two structures are essentially identical (rmsd 0.3 Å, Figure 5.4E). Pro103, which we have previously observed in both *cis* and *trans* isomers in crystal structures of IL-11 (chapter 3), is in the *trans* isomer in the crystal structure of IL-$11_{\Delta10}$ Mutein, and in the *cis* isomer in the structure of IL-$11_{\Delta10/W147A}$.

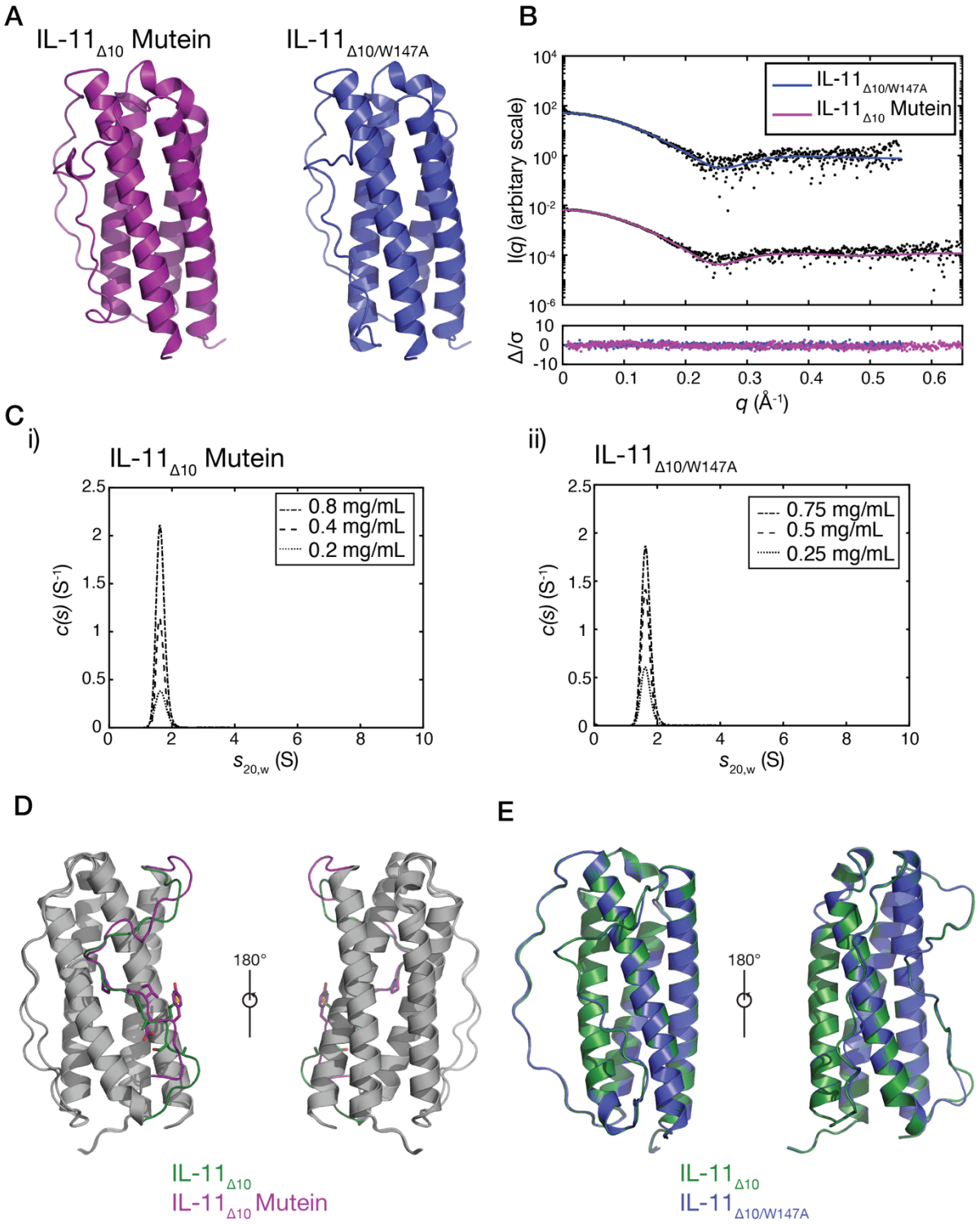

Figure 5.4: The structure of IL-11$_{\Delta 10}$ Mutein and IL-11$_{\Delta 10/W147A}$.

A) Thee crystal structure of the two proteins. B) SAXS scattering profile for IL-11$_{\Delta 10}$ Mutein, the fit shown is to the crystal structure coordinates (χ^2 = 1.37). C) Continuous sedimentation coefficient distributions (c(s)) for IL-11$_{\Delta 10}$ Mutein, i) and IL-11$_{\Delta 10/W147A}$, ii), each at three concentrations, which confirm the monomeric nature of each protein. D) Overlay of the structures of IL-11$_{\Delta 10}$ and IL-11$_{\Delta 10}$ Mutein (RMSD

1.3 Å), with the AMSAG/PAIDY residues indicated as sticks. E) An overlay of the structure of IL-11$_{\Delta 10}$ and IL-11$_{\Delta 10/W147A}$, showing that they are essentially identical (rmsd 0.3 Å).

Clear density is observed for the five mutated residues in both structures (Supplementary Figure 5.3B, C). In both IL-11 and IL-11 Mutein, the AB loop makes similar contacts with the α-helical core of the protein, mediated by different residues in the loop. The major interaction anchoring the loop to the core of the protein in IL-11 is a hydrogen bond between the Oγ of Ser53 and the Nε of His86 in the B helix (Figure 5.5A). In IL-11 Mutein, the equivalent interaction is made between the Oγ of Thr56 and the Nε of His86, which results in a conformational change in the loop (Figure 5.4D). In addition, both proteins form a common set of hydrophobic interactions between hydrophobic sidechains in the loop and the α helical core. These interactions are formed by Leu52, Leu55 and Pro56 in IL-11, and Leu54, Leu57 and Pro58 in IL-11 Mutein. Pro58 is the first residue in the PAIDY set of mutations (Figure 5.5Bi, ii). A consequence of the PAIDY mutations in IL-11 is thus the duplication of a 'LX(S/T)LP' motif, which is responsible for stabilising the position of the AB loop by making extensive electrostatic and hydrophobic contacts to the core of the protein (Figure 5.5Bi, ii). The position of the mutated residues in both structures is different, with the loop in IL-11 being shifted by approximately two residues towards the apical end of the cytokine compared to IL-11 Mutein (Figure 5.4D). The Cα to Cα distance between Ala58 in IL-11 and Pro58 in IL-11 Mutein is 8.9 Å when overlaid, illustrating the major shift in loop position between the two proteins. A consequence of the shift in the AB loop is B helix is slightly shorter in IL-11 Mutein, by approximately one helical turn (Figure 5.5A).

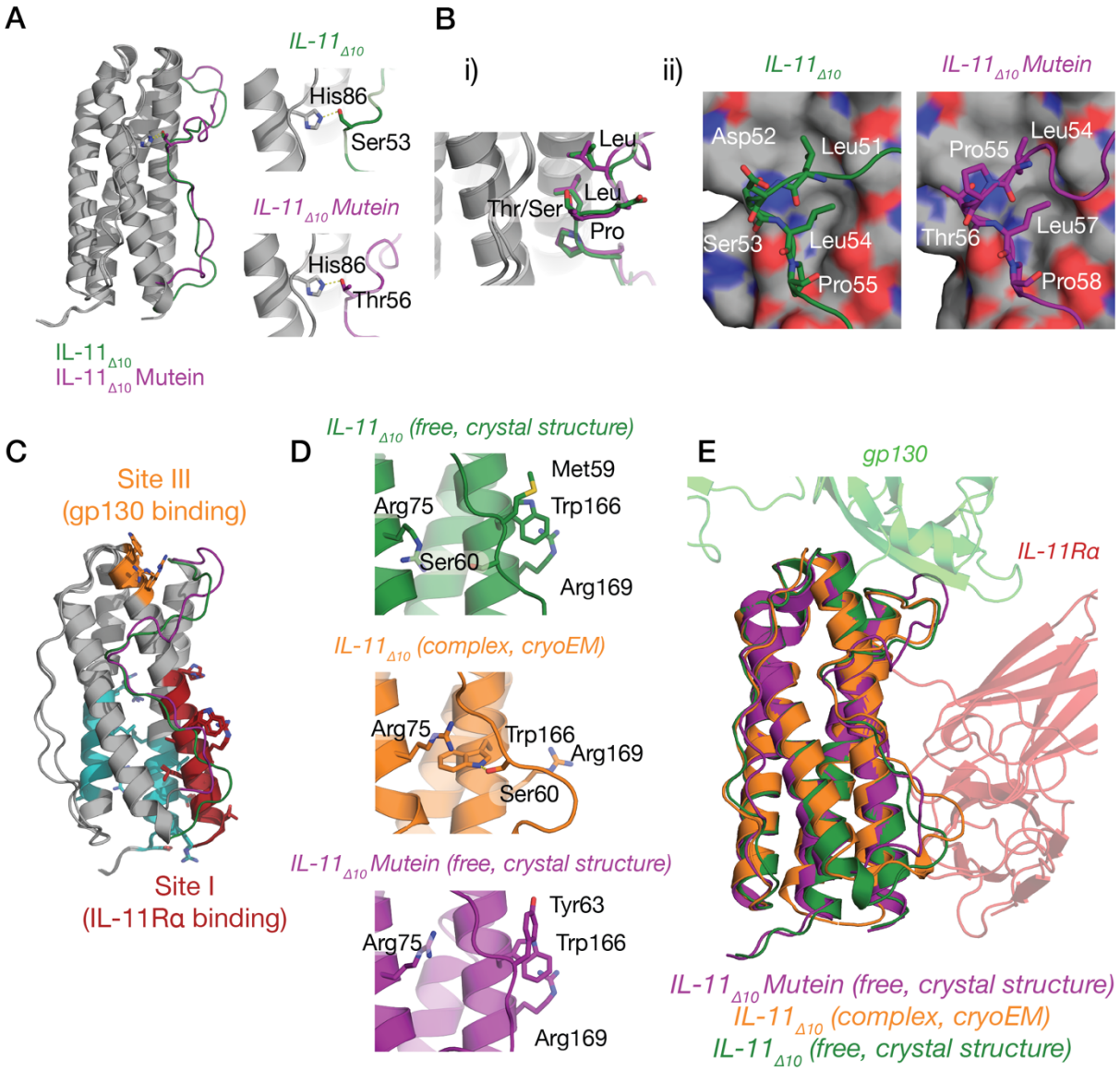

Figure 5.5: Loop-core contacts in IL-11$_{\Delta 10}$ and IL-11 $_{\Delta 10}$ Mutein.

A) The hydrogen bond formed between the AB loop in both proteins and His86 in the core structure. In IL-11$_{\Delta 10}$, the bond is formed by Ser53 in the AB loop, in IL-11Δ10 Mutein, the bond is formed by Thr56. B) Hydrophobic contacts made between the loop and the core in both proteins. Both proteins make nearly identical contacts, i), although the residues making these contacts differ, ii). C) The mutated loop is in close proximity to two receptor binding sites, site-I and site-III. D) Met59/Trp166/Arg169 form a hydrophobic interaction, which is disrupted on complex formation. This interaction is altered in IL-11$_{\Delta 10}$ Mutein. E) Overlay of the crystal structures of IL-11$_{\Delta 10}$ Mutein, IL-11$_{\Delta 10}$ and the cryoEM structure of the IL-11 signalling complex. The mutations in IL-11$_{\Delta 10}$ Mutein likely alter contacts to both gp130 and IL-11Rα.

As shown by our structure of the IL-11 signalling complex (chapter 4), the mutated residues in the AB loop are in close proximity to site-I. In both structures, there are extensive intramolecular contacts between the C-terminal end of the AB loop and residues in site-I. For example, in the structure of IL-11 Mutein there is a hydrophobic stacking interaction between Tyr62 and Trp166 in site-I. In IL-11, the equivalent interaction is made between Met59 and Trp166 (Figure 5.5D). In IL-11 Met59, Ser60 and Trp166 undergo a rearrangement on complex formation (chapter 4), the structural changes that we observe in IL-11 Mutein may disrupt this, thus altering binding to IL-11Rα (Figure 5.5D). The shift in the AB loop in IL-11 Mutein also affects residues close to site-III (Figure 5.5C, E), including a portion of the loop which forms contacts with gp130 in the cryoEM structure of the complex (chapter 4). The displacement of the AB loop close to site-III may serve to further destabilise the site-III/gp130 D1 interface, for example, by making the N-terminal end of the AB loop, which forms part of site-III, more dynamic, resulting in an additional entropic penalty to binding gp130. This effect, in combination with the loss of binding surface from the W147A mutation, may result in a lack of ability for IL-11 Mutein to bind gp130 at site-III, results in a large decrease in STAT3 phosphorylation through gp130. The PAIDY mutations also directly affect residues that are involved in IL-11Rα binding, and alter intramolecular interactions between the AB loop and the core the of the protein, potentially the mechanism for the difference in receptor binding kinetics that we observed using SPR.

Both IL-$11_{\Delta 10}$ Mutein and IL-$11_{\Delta 10}$ crystallised in different space groups ($P\,2_1$ for IL-$11_{\Delta 10}$ Mutein, $P\,2_1\,2_1\,2$ for IL-$11_{\Delta 10}$,) consequently, the crystal contacts formed by each protein differ. In both cases, the majority of contacts are formed by the four-α-helical bundle, which is very well-defined in the density, and consequently has lower *B* factors (Supplementary Figure 5.5A). Notably, the central portion of the AB loop, which is anchored by a hydrogen bond to His86 in the β helix, is well-defined in the density in both structures, and does not make crystal contacts. In both structures, the N-terminal end of the AB loop makes few crystal contacts, likely accounting for the poor definition of the loop in the density. In the IL-$11_{\Delta 10}$ structure, the C-terminal

end of the loop contacts several arginine residues in the B helix (Arg77 and Arg85). In the IL-$11_{\Delta 10}$ Mutein structure, this region of the loop contacts the CD loop from a neighbouring molecule in the crystal lattice, stabilising these otherwise dynamic regions of the protein. Overall, the differences in the crystal lattice and crystal contacts between the two proteins (Supplementary Figure 5.5B) mean that caution must be taken in interpreting differences in density and in the relative *B* factors between the two structures, indeed, proper study of the structural dynamics requires a computational or solution-based technique.

5.3.4 NMR spectroscopy and backbone amide resonance assignment of IL-11 and IL-11 Mutein

To study the structural dynamics of IL-11 and IL-11 Mutein, we used nuclear magnetic resonance (NMR) spectroscopy. NMR has been used to study the solution structure and structural dynamics of several cytokines, including the IL-6 family cytokines IL-6[116,382] and LIF[383,437]. In IL-6, the loops have previously been noted to be very dynamic[382], in contrast to LIF, where the loops are less dynamic[383]. In both cytokines, loop dynamics are thought to have a role in receptor binding and complex formation.

Initial NMR experiments on uniformly ^{15}N labelled IL-$11_{\Delta 10}$ and IL-$11_{\Delta 10}$ Mutein gave NMR spectra with poor spectral resolution and poor signal dispersion in the ^{1}H-^{15}N HSQC spectrum (Supplementary Figure 5.6A, B). We note that in both spectra more peaks are observed in the spectrum than are predicted from the sequence, likely a consequence of *cis*/*trans* proline isomerism from either Pro103 in helix C, which we have observed in both the *cis* and *trans* isomer in crystal structures or *cis*/*trans* isomerism in the polyproline helix. The relative population of related peaks vary as a function of temperature (Supplementary Figure 5.6A-C), it has previously been noted that for extensive *cis*/*trans* interconversion to occur, elevated temperature is required[438]. This temperature dependence likely reflects extensive *cis*/*trans* proline interconversion or very long timescale structural dynamics (tens of minutes to hours). Poor spectral resolution has been noted previously when studying cytokines by NMR, as the large, α-helical nature of cytokines inherently results in lower

spectral resolution (for e.g. IL-6[439], prolactin[440], oncostatin M[441]). Indeed, extensive *cis/trans* proline isomerism was observed in IL-3[442], which resulted in split peaks and complex spectra.

To attempt to overcome the poor spectral quality, we produced perdeuterated IL-$11_{\Delta 10}$ and IL-$11_{\Delta 10}$ Mutein. Deuteration is a common strategy for improving the spectral resolution of proteins, particularly larger proteins with low NMR spectral resolution. Mass spectrometry confirms that both proteins are perdeuterated (Supplementary Figure 5.6D). Replacement of ^{1}H with ^{2}H suppresses spin diffusion and increases the relaxation rates of ^{13}C, improving spectral resolution[443], thus aiding in resonance assignment. Deuteration improved the spectral quality of both proteins, with decreased linewidth and peak intensity (Figure 5.6A, B).

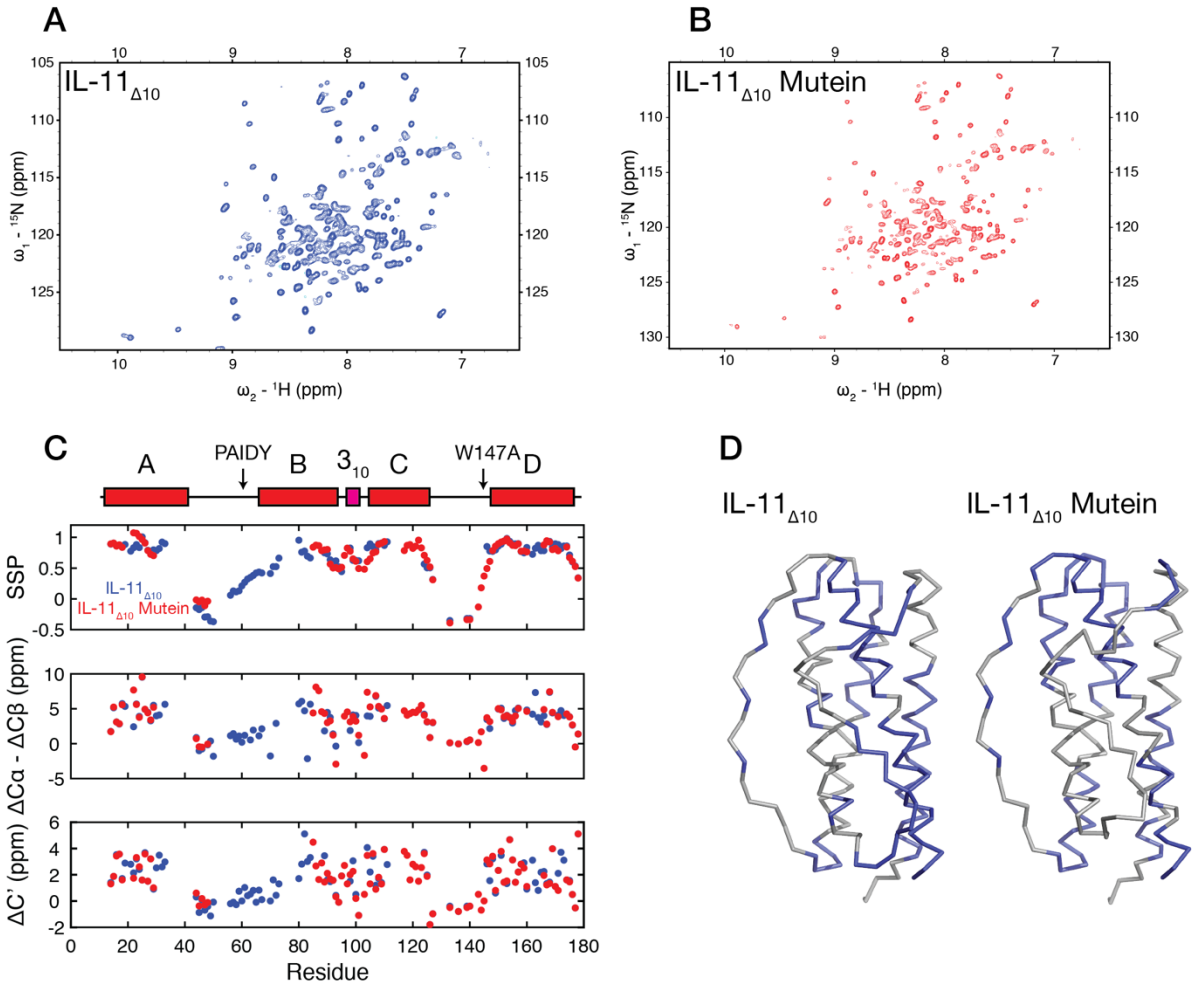

Figure 5.6: Spectral assignment of IL-11$_{\Delta 10}$ and IL-11 $_{\Delta 10}$ Mutein.

A) and B) show ^{1}H-^{15}N TROSY-HSQC spectra for IL-11$_{\Delta 10}$, A) and IL-11$_{\Delta 10}$ Mutein B). Each spectrum was collected with 200 µM protein at 20 °C in 50 mM sodium phosphate pH 6 at 18.8 T. C) Secondary structure prediction from SSP and secondary chemical shifts for both proteins. This shows the extent of the assignment, and that the predicted solution secondary structure matches the crystal structure. D) Assigned residues mapped onto the crystal structure of both proteins.

Using a standard triple-resonance assignment strategy (see section 5.5.10), we were able to attain partial assignments for both IL-11 and IL-11 Mutein (Supplementary Figure 5.7, Supplementary Figure 5.8, Supplementary Table 5.5, Supplementary Table 5.6, for strip plots, see Supplementary Figure 5.9 and Supplementary Figure 5.10). In IL-11$_{\Delta 10}$, we assigned 96 backbone amide resonances (62% of the non-proline residues), in IL-11$_{\Delta 10}$ Mutein we assigned 80

backbone amide resonances (53% of the non-proline residues). In both proteins, we obtained comprehensive sequence coverage in the α-helical bundle core and were able to assign several residues in the AB and CD loops in both proteins. Predicted secondary structure for both IL-11 and IL-11 Mutein, determined from both secondary structure propensity[444] and secondary chemical shifts matches the crystal structures (Figure 5.6C). The assigned residues are shown mapped onto the crystal structure in Figure 5.6D. A complete list of peak assignments for both proteins is given in Supplementary Table 5.5 and Supplementary Table 5.6.

We have limited assignments for prolines in the CD loop polyproline helix in both IL-$11_{\Delta 10}$ and IL-$11_{\Delta 10}$ Mutein, and we have assigned the proline at the N-terminal end of the 3_{10} helix (Pro103) in IL-$11_{\Delta 10}$ Mutein. *Cis* and *trans* prolines have characteristic Cα and Cβ chemical shifts, with the chemical shift of a *cis* proline being shifted slightly upfield relative to a *trans* proline. The average Cβ chemical shift is 31.75 ± 0.98 ppm (mean ± SD) for *trans* proline and 34.16 ± 1.15 ppm for a *cis* proline[445]. In IL-$11_{\Delta 10}$ Mutein, we assigned four prolines in the CD loop (Pro133, Pro136, Pro139 and Pro143), all with a Cβ chemical shift of ~30.5 ppm, suggesting that they are *trans* prolines, consistent with the crystal structure. We assigned Pro133, Pro136 and Pro139 in IL-$11_{\Delta 10}$, the Cβ chemical shift of these prolines is likewise consistent with these prolines being in the *trans* isomer. We have previously observed Pro103 in both the *cis* and *trans* isomer in structures of IL-11. We assigned the Cβ of Pro103 in IL-$11_{\Delta 10}$ Mutein, which has a chemical shift of 33.14 ppm, indicating that in solution Pro103 is likely in the *cis* conformation.

5.3.5 Solution structural dynamics of IL-11 and IL-11 Mutein

We used NMR spectroscopy to study the structural dynamics of both IL-$11_{\Delta 10}$ and IL-$11_{\Delta 10}$ Mutein. We collected a full set of spin-relaxation experiments, both ^{15}N transverse (^{15}N-R_2) and longitudinal (^{15}N-R_1) relaxation rates, and the ^{15}N-{^{1}H} heteronuclear NOE (^{15}N-{^{1}H} NOE) on both proteins at 18.8 T (Figure 5.7Ai,ii). These parameters report on fast (ps-ns) dynamics in proteins (such as amide bond rigidity) and molecular tumbling (on the ns timescale)[446]. Briefly, a more positive ^{15}N-{^{1}H} NOE and ^{15}N-R_2 value implies amide bond rigidity, and more negative ^{15}N-R_1 value

indicates amide bond rigidity. An important caveat is that the measured ^{15}N-R_2 can also be increased by slow chemical exchange between two distinct conformational states on the µs-ms timescale, and by protein self-association, both factors which result in a ^{15}N-R_2 value greater than average. To investigate the oligomerization propensity of both proteins, we collected a series of ^{15}N-R_2 experiments at several different concentrations of IL-11 Mutein (Figure 5.7Bi,ii). These experiments showed a clear concentration dependence in ^{15}N-R_2, showing that IL-11 Mutein undergoes self-association in solution. Exchange between a small and larger species will complicate analysis of relaxation parameters by model-free approaches[446], particularly due to the increased ^{15}N-R_1 and ^{15}N-R_2 rates. A similar phenomenon has been noted for other cytokines, such as growth hormone (GH) [447] and prolactin[440].

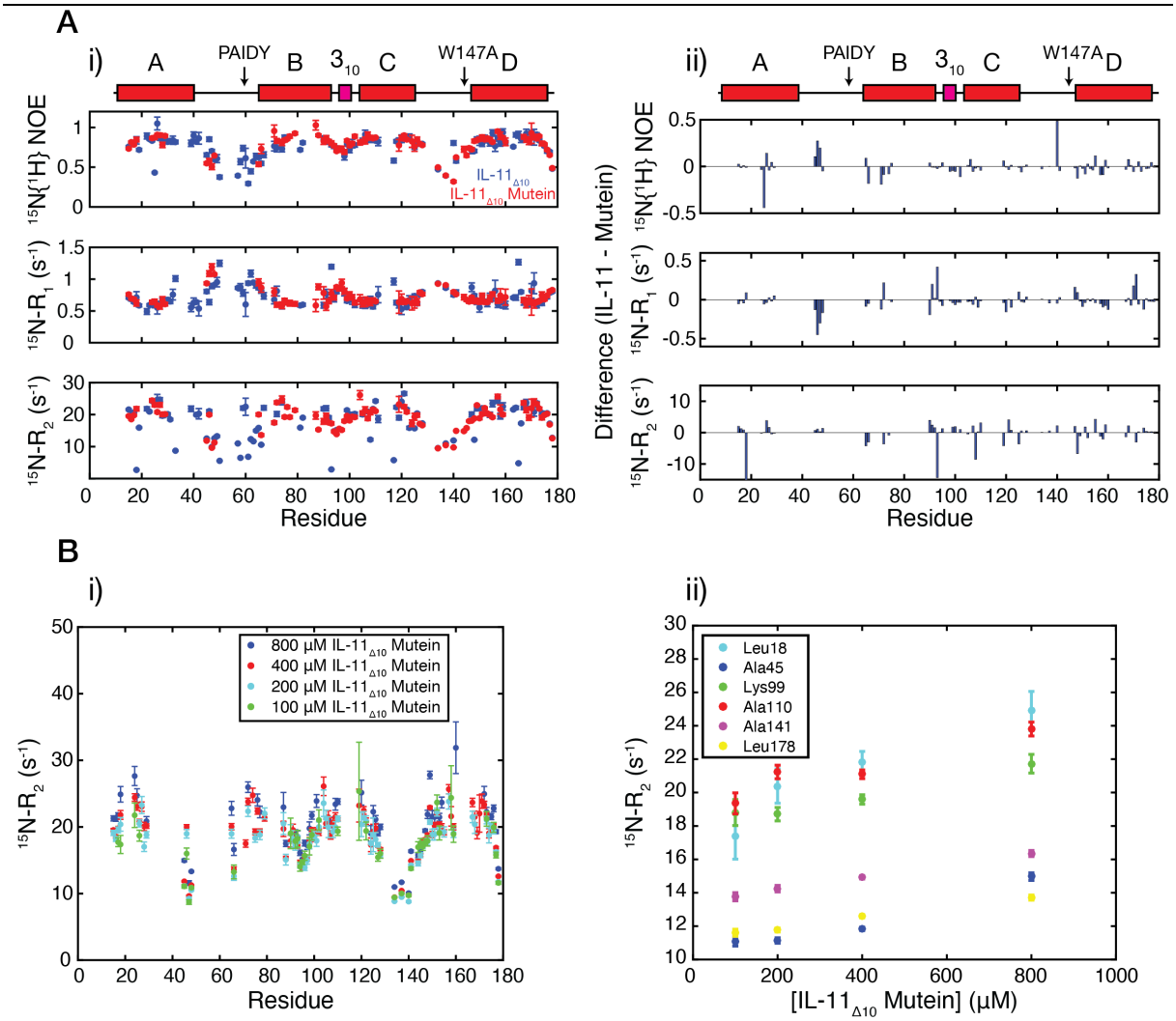

Figure 5.7: Backbone amide relaxation parameters for IL-11$_{\Delta10}$ and IL-11$_{\Delta10}$ Mutein.

A) i) ^{15}N-{^{1}H} NOE, ^{15}N-R_1 and ^{15}N-R_2 rates for both IL-$11_{\Delta10}$ and IL-$11_{\Delta10}$ Mutein. ii) The difference between each parameter for each protein. Values acquired at 20 °C and on an 18.8 T spectrometer, using 400 µM protein in 50 mM sodium phosphate pH 6. B) i) ^{15}N-R_2 relaxation rate at several concentrations for IL-$11_{\Delta10}$ Mutein, showing clear concentration dependence in ^{15}N-R_2. ii) Concertation dependence in ^{15}N-R_2 for selected residues in IL-$11_{\Delta10}$ Mutein.

The ^{15}N-{^{1}H} NOE reflects fast-timescale (ps-ns) protein dynamics, with a more negative ^{15}N-{^{1}H} NOE suggesting that a particular residue is more dynamic. The ^{15}N-{^{1}H} NOE is also the least sensitive of the three parameters to a contribution from protein self-association[446]. Overall, for both IL-11 and IL-11 Mutein, the helical regions of the protein are quite stable on a fast timescale (Figure 5.7Ai,ii). A similar trend is apparent for both the ^{15}N-R_1 and ^{15}N-R_2, with the caveat that these parameters are likely influenced and increased by self-association, as we measured a concentration dependent increase in the ^{15}N-R_2 rate for IL-11 Mutein (Figure 5.7Ai,ii). The ends of the helices are generally more dynamic then the centre of the helices, a phenomenon known as helical fraying[382,383], which we observed in our MD studies of IL-11 and has been observed in MD and NMR studies of other cytokines[382,383]. Overall, there are no large differences in the internal structural dynamics of the helices in IL-11 Mutein, compared to IL-11.

As discussed above, the majority of assignments in both proteins were obtained in the α-helical core. We were able to assign several residues in both the AB and CD loop in both IL-11 and IL-11 Mutein, giving probes into the structural dynamics in these loops (Figure 5.7Ai). In both proteins, the AB loop is quite dynamic. The residues in the N-terminal end of the AB loop, which we assigned in both proteins have a more negative ^{15}N-{^{1}H} NOE in IL-11 Mutein, reflecting differences in fast dynamics between the two proteins. Interestingly, the same region is displaced in the crystal structure of IL-11 Mutein, showing that the PAIDY mutations in IL-11 Mutein likely also alter loop dynamics in IL-11.

Like other cytokines, IL-11 is clearly challenging to study using NMR, due to complex spectra likely resulting from extensive slow exchange in the protein. Additionally, IL-11 undergoes self-association in solution, significantly complicating any solution dynamics study. Future approaches to simplify the spectra could involve utilising selective isotope labelling, as was done for IL-6[382]. Regardless, due to self-association complicating any NMR study into IL-11, future efforts are likely better directed to other approaches, for example, through molecular dynamics simulations.

5.3.6 Molecular dynamics simulations

We undertook a molecular dynamics study into IL-11 Mutein as an alternative approach to the NMR experiments described above. We ran a series of short (100 ns) MD simulations on both IL-11 (described in Chapter 3) and IL-11 Mutein (Figure 5.8Ai, B). The overall results from the simulation of IL-11 Mutein are broadly in agreement with the NMR results described above. Comparison of the simulations run for IL-$11_{\Delta10}$ and IL-$11_{\Delta10}$ Mutein show that the overall dynamic profile of the two proteins is quite similar, the main difference being a shift in the least dynamic point in the AB loop (Figure 5.8Ai, B). In IL-$11_{\Delta10}$, the loop is stabilised around the Ser53-His86 hydrogen bond, in IL-$11_{\Delta10}$ Mutein it is stabilised around the Thr56-His86 hydrogen bond. This does alter the overall dynamics of the loop in the simulation, with the C-terminal AB loop sequence, which is mutated in IL-$11_{\Delta10}$ Mutein being more constrained compared to the same sequence in IL-$11_{\Delta10}$. In both proteins, the hydrogen bond between the AB loop and His86 is relatively stable, with the γ oxygen of Ser53/Thr56 and the ε nitrogen of His86 remaining within 4 Å through the simulation for two of the three IL-11 simulations and IL-11 Mutein simulations (Figure 5.8C). Both the ^{15}N-{^{1}H} NOE values and electron density suggest that the N-terminal end of the AB loop is more dynamic in IL-$11_{\Delta10}$ Mutein. This is supported by the MD simulations. A second difference in the structure is the presence of a *trans* proline residue (Pro103) in IL-$11_{\Delta10}$ Mutein. The region around this residue is more dynamic in IL-$11_{\Delta10}$ Mutein, when compared to IL-$11_{\Delta10}$ (Figure 5.8Aii) suggesting that the *cis* conformation of the proline residue is more favoured in both

proteins, and the timescale of the simulation is too short to observe *cis/trans* proline isomer conversion.

To further probe the structural dynamics of both proteins, we ran a longer (1 μs) simulation of both IL-$11_{\Delta 10}$ and IL-$11_{\Delta 10}$ Mutein (Figure 5.8D, Supplementary Figure 5.11, Supplementary Movie 5.1, Supplementary Movie 5.3). On this timescale, in both proteins, the AB loop is not greatly dynamic, and does not greatly change conformation, with the exception of the N-terminal end of the AB loop, which adopts an altered, more stable conformation approximately 200 ns into the simulation (Figure 5.8Dii, Supplementary Figure 5.11B, Supplementary Movie 5.3). In IL-$11_{\Delta 10}$ Mutein, the Thr56 Oγ/His86 Nε hydrogen bond is stable through the 1 μs simulation, with both atoms remaining within hydrogen bonding distance through the majority of the simulation (Figure 5.8E). The Ser53 Oγ/His86 Nε hydrogen bond is notably less stable through the 1 μs simulation, with the hydrogen bond being broken for most of the simulation (Figure 5.8E). Overall, the MD simulations show that the four-α helical bundle of IL-$11_{\Delta 10}$ Mutein is stable. They also show that the Thr56 Oγ/His86 Nε hydrogen bond is stable in IL-$11_{\Delta 10}$ Mutein, and stabilised relative to the Ser53 Oγ/His86 Nε hydrogen bond in IL-$11_{\Delta 10}$. Thus, a consequence of the mutations in IL-$11_{\Delta 10}$ Mutein is that the AB loop is stabilised around the Thr56 Oγ/His86 Nε hydrogen bond.

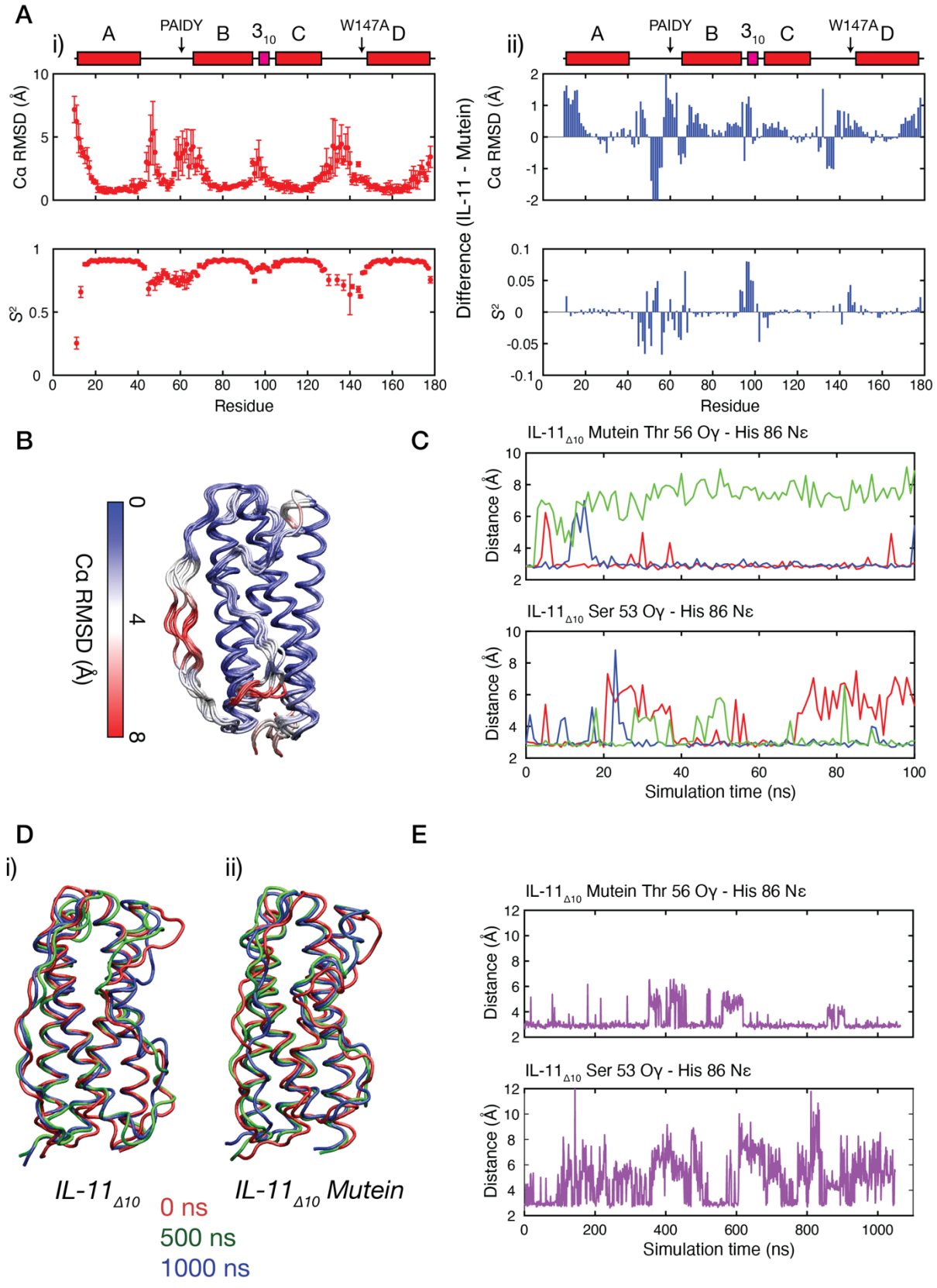

Figure 5.8: Molecular dynamics simulation for IL-11$_{\Delta 10}$ Mutein.

A) i) The Cα RMSD and amide bond order parameter (S^2), calculated from three 100 ns MD simulations (error bars are standard deviations). ii) The difference between

RMSD and the amide bond order parameter, S^2 between IL-11$_{\Delta10}$ and IL-11$_{\Delta10}$ Mutein (values for IL-11$_{\Delta10}$ are presented in Chapter 3). B) Overlay of frames through one 100 ns MD simulation for IL-11$_{\Delta10}$ Mutein. Frames are overlaid every 20ns. Frames are coloured according to Cα RMSD, with the scale indicated. C) Distance between the γ oxygen of Thr56/Ser53 in IL-11$_{\Delta10}$ Mutein or IL-11 $_{\Delta10}$, and the ε nitrogen in His86 through the three simulations in IL-11$_{\Delta10}$/IL-11$_{\Delta10}$ Mutein. Each of the three simulations is coloured differently in the plot. D) Overlay of frames from the 1 μs simulations of IL-11$_{\Delta10}$ and IL-11$_{\Delta10}$ Mutein. E) Distance between the γ oxygen of Thr56/Ser53 in IL-11$_{\Delta10}$ Mutein or IL-11$_{\Delta10}$ and the ε nitrogen in His86 through the 1 μs simulation.

5.3.7 IL-11 Mutein is more thermally stable than IL-11

Given that the mutations in the AB loop in IL-11 Mutein alter the position of the AB loop and change the nature of loop-core interactions in IL-11 Mutein, we hypothesised that this may have an impact on the thermal stability of the proteins. Using differential scanning fluorometry (DSF), we measured the thermal stability of IL-11$_{\Delta10}$, IL-11$_{\Delta10/W147A}$ and IL-11$_{\Delta10}$ Mutein. IL-11$_{\Delta10}$ Mutein (T_h = 89.73 ± 0.17 °C, mean ± SE, n = 3 independent experiments) is significantly more stable than IL-11$_{\Delta10/W147A}$ (T_h = 87.29 ± 0.29 °C), ΔT_h = 1.43 °C, p = 0.035, showing that the PAIDY mutations increase the stability of IL-11$_{\Delta10}$. IL-11$_{\Delta10/W147A}$ is also increased in thermal stability compared with IL-11$_{\Delta10}$ (T_h = 84.34 ± 0.39 °C) ΔT_h = 2.46 °C, p = 0.031, the overall change in stability between IL-11$_{\Delta10}$ and IL-11$_{\Delta10}$ Mutein is 3.89 °C (Figure 5.9A). Similarly, mIL-11$_{\Delta10}$ Mutein (T_h = 85.18 ± 0.03 °C) is significantly stabilised relative to mIL-11$_{\Delta10}$ (T_h = 78.34 ± 0.34 °C), ΔT_h = 6.84 °C, p = 0.0028 (Figure 5.9B).

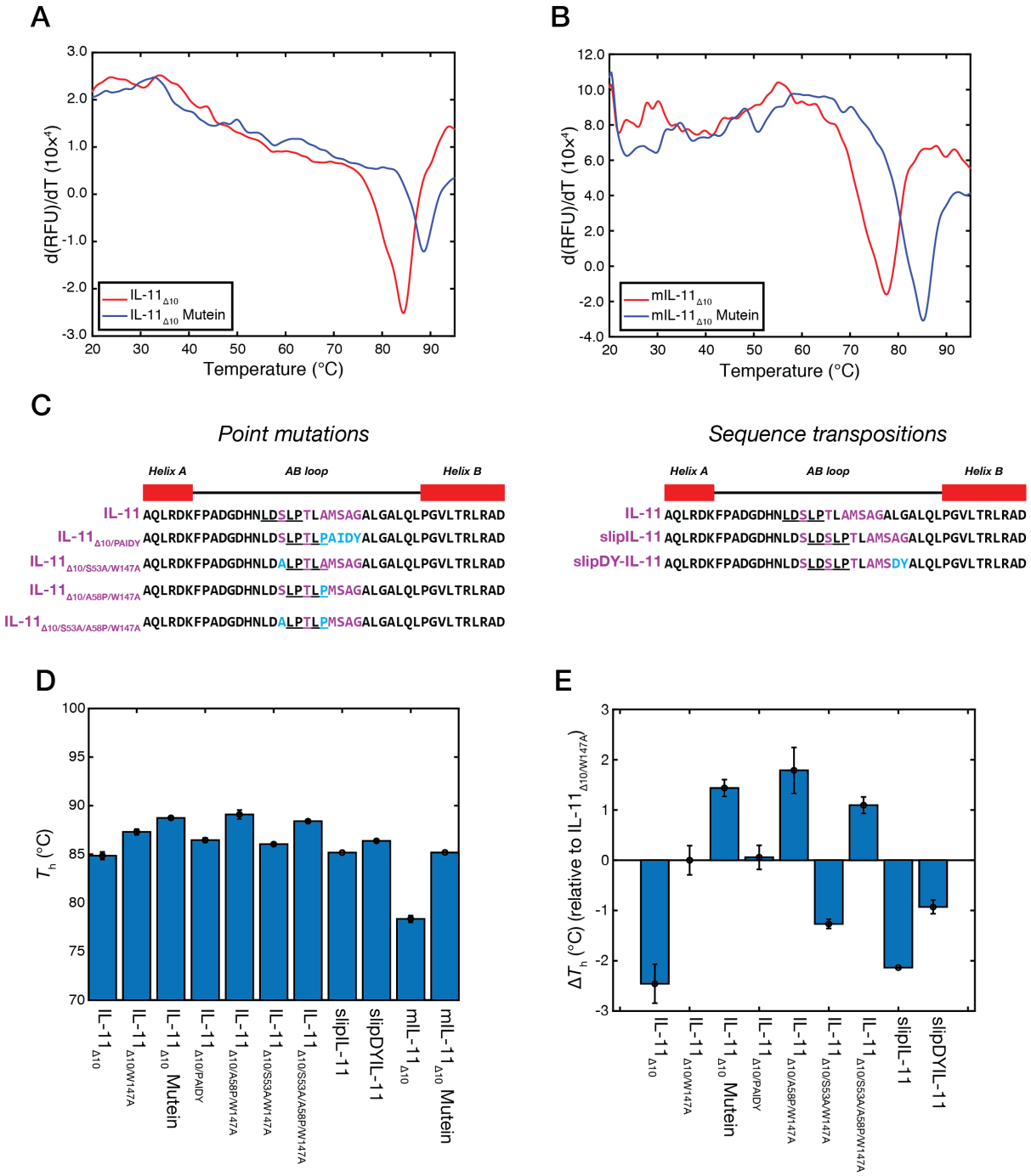

Figure 5.9: IL-11$_{\Delta 10}$ Mutein is thermally stabilised relative to IL-11$_{\Delta 10}$.

A) First-derivative DSF melt curve for IL-11$_{\Delta 10}$ and IL-11$_{\Delta 10}$ Mutein, showing that IL-11$_{\Delta 10}$ Mutein is stabilised relative to IL-11$_{\Delta 10}$. Curve shown is an average of four technical replicates. B) First-derivative DSF for mIL-11$_{\Delta 10}$ and mIL-11$_{\Delta 10}$ Mutein, showing that mIL-11$_{\Delta 10}$ Mutein is stabilised relative to mIL-11$_{\Delta 10}$. Curve shown is an average of four technical replicates. C) Sequences of mutants designed to mimic IL-11 Mutein. The 'LX(S/T)LP' motif is underlined for all mutants, and key residues involved in loop-core interactions are coloured purple. Residues which are mutated

are coloured blue. D) Thermal stability of the IL-11$_{\Delta10}$ mutants measured using DSF. Values are given as mean ± SE, n = 3 independent experiments. Note that the y-axis does not start at 0 °C. E) Stability of the IL-11$_{\Delta10}$ mutants, given relative to IL-11$_{\Delta10/W147A}$.

We reasoned that this change in thermal stability could be used to screen novel mutants of IL-11 Mutein in which the AB loop may be shifted in position without the PAIDY mutations. These mutants would allow us to 'decouple' the shift in the AB loop without the full set of PAIDY mutations, allowing us to determine if the antagonistic effect of IL-11 Mutein is solely a consequence of the shift in position of the AB loop that we observe in the crystal structure of IL-11 Mutein. We designed a set of five mutants. Three were point mutations in the AB loop, one removing the serine that forms the hydrogen bond to the core in IL-11 (IL-11$_{\Delta10/S53A/W147A}$), one replacing Ala58 with a proline, (IL-11$_{\Delta10/A58P/W147A}$), and one combining both mutations (IL-11$_{\Delta10/S53A/A58P/W147A}$) (Figure 5.9C). Two mutations were transpositions of the sequence in IL-11, in which part of the IL-11 sequence was shifted, designed to mimic the structural changes we see in IL-11 Mutein, slipIL-11 and slipDY-IL-11 (Figure 5.9C). We also generated IL-11$_{\Delta10/PAIDY}$, an IL-11 construct with the PAIDY mutations in the AB loop but lacking the W147A mutation.

We measured the thermal stability of the six mutants using DSF. The two transposition mutants (slipIL-11 and slipDYIL-11) and IL-11$_{\Delta10/S53A/W147A}$ both destabilise the protein relative to IL-11$_{\Delta10/W147A}$ (Figure 5.9D, E). Two of the point mutants, IL-11$_{\Delta10/A58P/W147A}$ and IL-11$_{\Delta10/S53A/A58P/W147A}$ stabilise the protein relative to IL-11$_{\Delta10/W147A}$ (Figure 5.9D, E), suggesting that they mimic the change in loop position in IL-11 Mutein. IL-11$_{\Delta10/PAIDY}$ is also stabilised relative to IL-11$_{\Delta10}$.

5.3.8 Point mutations in the AB loop mimic the structural changes in IL-11 Mutein

To assess the nature of the loop changes in each mutant, we undertook crystallization trials for all mutants. We solved the crystal structures of IL-11$_{\Delta10/PAIDY}$, IL-11$_{\Delta10/A58P/W147A}$ and IL-11$_{\Delta10/S53A/A58P/W147A}$ all of which gave crystals which diffracted to below 2 Å (Figure 5.10A, Supplementary Table 5.4).

Unsurprisingly, the AB loop in IL-$11_{\Delta10/PAIDY}$ mimics the position of the AB loop in IL-$11_{\Delta10}$ Mutein (Figure 5.10A, B). There is very poor density supporting the position of the N-terminal end of the AB loop in IL-$11_{\Delta10/PAIDY}$, so these residues were not included in the model. The lack of definition of the AB loop suggests that the loop is further destabilised in IL-$11_{\Delta10/PAIDY}$ compared with IL-$11_{\Delta10}$ Mutein. The IL-$11_{\Delta10/S53A/A58P/W147A}$ mutant broadly mimics the position of the AB loop in IL-$11_{\Delta10}$ Mutein (Figure 5.10C). The hydrogen bond between Thr56 and His86 is present, and the central portion of the AB loop makes similar contacts in both structures (Figure 5.10C). The precise contacts made between the C-terminal end of the loop (PMSAG in the mutant), differ compared with IL-$11_{\Delta10}$ Mutein. Tyr62, which interacts with Trp166 in IL-$11_{\Delta10}$ Mutein is not present in IL-$11_{\Delta10/S53A/A58P/W147A}$, instead, a similar interaction is formed by the backbone atoms of Ala61/Gly62 and Trp166, causing the position of this region of the loop to slightly differ between the two proteins (Figure 5.10C).

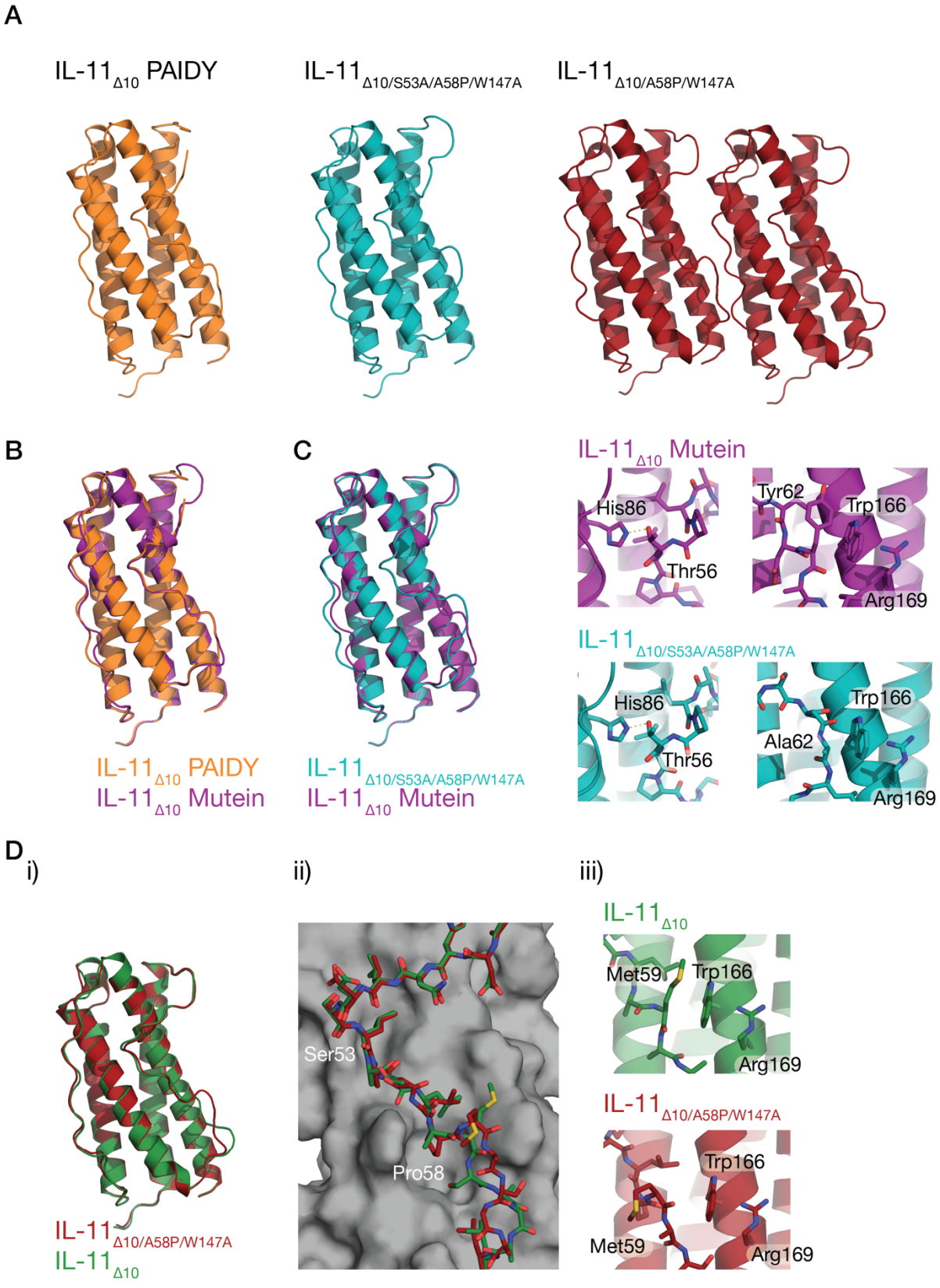

Figure 5.10: The structure of novel IL-11 mutants designed to mimic IL-11 Mutein.

A) The structure of IL-$11_{\Delta10/PAIDY}$, IL-$11_{\Delta10/S53A/A58P/W147A}$ and IL-$11_{\Delta10/A58P/W147A}$. Note that IL-$11_{\Delta10/A58P/W147A}$ crystallised with two molecules in the asymmetric unit. B) Overlay of the structures of IL-$11_{\Delta10}$ Mutein and IL-$11_{\Delta10/PAIDY}$, showing that they are identical. C) Overlay of the structure of IL-$11_{\Delta10}$ Mutein and IL-$11_{\Delta10/S53A/A58P/W147A}$, showing that both form similar loop-core interactions, both forming a hydrogen bond between Thr56 and His86. The interactions between the C-terminal end of the AB loop and site-I differ. D) i) Comparison of the structures of IL-$11_{\Delta10}$ and IL-$11_{\Delta10/A58P/W147A}$. ii) The AB loop in both structures adopts a similar position, with Pro58 creating a kink in the loop in IL-$11_{\Delta10/A58P/W147A}$. iii) The interaction between Trp166 and the AB loop differ as a result of this kink, with IL-$11_{\Delta10/A58P/W147A}$ not forming an interaction between Met59 and Trp166.

Surprisingly, given the significant thermal stabilisation associated with the IL-$11_{\Delta10/A58P/W147A}$ mutant, the AB loop in IL-$11_{\Delta10/A58P/W147A}$ adopts a nearly identical position compared to IL-11 (Figure 5.10Di, ii), including a hydrogen bond between Ser53 and His86 (Figure 5.10Dii). Pro56 of the mutant sits in a small pocket formed between the B and D helices. The contacts formed between Trp166 and the AB loop also differ between IL-$11_{\Delta10/A58P/W147A}$ and IL-$11_{\Delta10}$, leading to a slight difference in the position of the AB loop (Figure 5.10Diii). This is likely a consequence of a restriction in conformational flexibility as a result of the substitution of Ala for Pro. The IL-$11_{\Delta10/A58P/W147A}$ mutant crystallised with two protein molecules in the asymmetric unit (Figure 5.10A), related by a translation (approximately 30 Å along y). The translational non-crystallographic symmetry (NCS) is confirmed through a strong peak in the Patterson function (72.998% relative to origin, 27.16 Å from the origin), strongly suggestive of translational NCS. In practise, the translational NCS did not hinder refinement, and the model converged to acceptable *R* factors (R_{work} 0.1864, R_{free} 0.2122). Both protein chains in the asymmetric unit are structurally very similar (rmsd 0.89 Å), although they are not identical, for example Trp166 adopts a different rotamer in each protein chain. IL-$11_{\Delta10}$ crystallised in space group $P\,2_1\,2_1\,2$, and IL-$11_{\Delta10/A58P/W147A}$ crystallised in $P\,2_1\,2_1\,2_1$, the crystal contacts in both structures are broadly similar.

We ran molecular dynamics simulations on IL-$11_{\Delta10/S53A/A58P/W147A}$ and IL-$11_{\Delta10/A58P/W147A}$ (Figure 5.11). The MD simulations show that the AB loop in IL-$11_{\Delta10/S53A/A58P/W147A}$ is stabilised around the Thr56 Oγ/His86 Nε hydrogen bond, analogous to the stabilisation that we observe in IL-$11_{\Delta10}$ Mutein (Figure 5.8Ai). In one of the simulations, the hydrogen bond is broken, but does not move far from the starting position. In the other two simulations, the hydrogen bond is stable through the simulation and anchors the AB loop around Thr56 (Figure 5.11A-C). The AB loop in the simulations of IL-$11_{\Delta10/A58P/W147A}$ undergoes large movements through two of the three 100 ns simulations. In two of the simulations, the hydrogen bond between Ser53 and His86 is broken early in the simulation. No hydrogen bonds are re-formed between His86 and the AB loop, the loop stabilised by several hydrophobic loop-core contacts between the C-terminal end of the loop and helices B and D, particularly Trp166 in site-I (Figure 5.11C, D, E , Supplementary Figure 5.12B, C, Supplementary Movie 5.2).

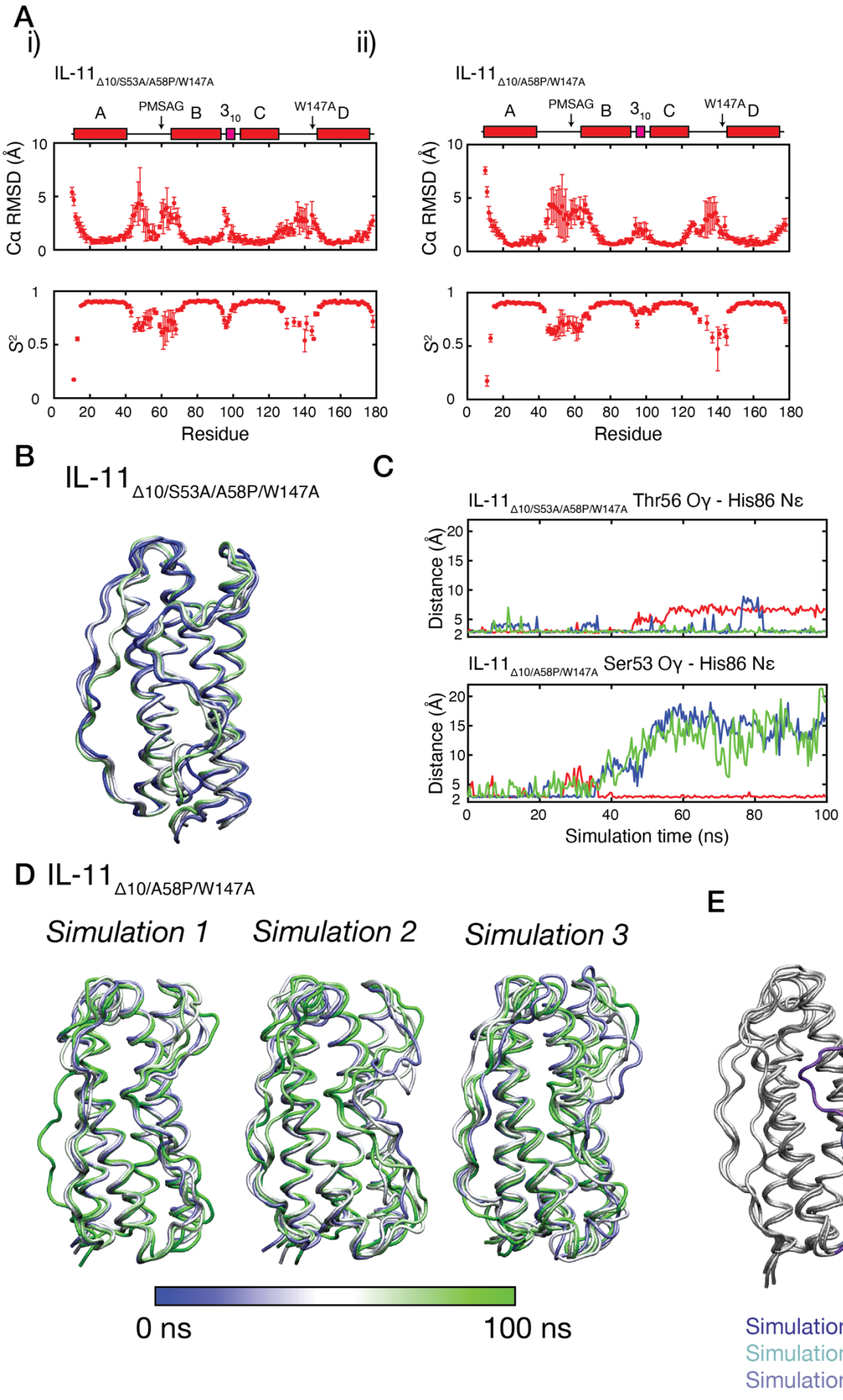
A
i)
IL-11 Δ10/S53A/A58P/W147A
A
PMSAG
B
3 10
C
W147A
D
Cα RMSD (Å)
10
5
0
S2
1
0.5
0
0 20 40 60 80 100 120 140 160 180
Residue
ii)
IL-11 Δ10/A58P/W147A
A
PMSAG
B
3 10
C
W147A
D
Cα RMSD (Å)
10
5
0
S2
1
0.5
0
0 20 40 60 80 100 120 140 160 180
Residue
B
IL-11 Δ10/S53A/A58P/W147A
C
IL-11 Δ10/S53A/A58P/W147A Thr56 Oγ - His86 Nε
Distance (Å)
20
15
10
5
2
IL-11 Δ10/A58P/W147A Ser53 Oγ - His86 Nε
Distance (Å)
20
15
10
5
2
0 20 40 60 80 100
Simulation time (ns)
D IL-11 Δ10/A58P/W147A
Simulation 1
Simulation 2
Simulation 3
E
0 ns
100 ns
Simulation 1
Simulation 2
Simulation 3

Figure 5.11: MD simulations of the novel IL-11 mutants.

A) RMSD through the MD simulation and amide bond order parameter (S^2) for, i) IL-$11_{\Delta10/S53A/A58P/W147A}$ and ii) IL-$11_{\Delta10/A58P/W147A}$. B) Overlay of frames through one 100 ns MD simulation for IL-$11_{\Delta10/S53A/A58P/W147A}$. Frames are overlaid every 20ns, coloured by simulation time, as indicated by the scale in the figure. C) Overlay of frames through three 100 ns MD simulation for IL-$11_{\Delta10/A58P/W147A}$. Frames are overlaid every 20ns, coloured by simulation time, as indicated by the scale in the figure. D) Final position of the AB loop through each of the three 100 ns MD simulations for IL-$11_{\Delta10/A58P/W147A}$.

In each of the three simulations, the IL-$11_{\Delta10/A58P/W147A}$ mutant does not appear to reach an equilibrium position (Figure 5.11D, E). We ran a 1 μs simulation to investigate this (Figure 5.12). Approximately 300 ns into the simulation, the C-terminal end of the AB loop reaches a stable minimum (Figure 5.12, Supplementary Figure 5.13, Supplementary Movie 5.3). Here, hydrophobic contacts between Met59 and a hydrophobic pocket formed by Leu73, Leu119, Leu122, Leu171 and Leu174 stabilize the C-terminal end of the loop (Figure 5.12Bi, ii). As we observed in our 100 μs simulations (Figure 5.11B, D), the hydrogen bond between Ser53 and His86 is broken early in the simulation, and does not reform (Figure 5.12Bi), thus, the central and C-terminal end of the loop remains relatively flexible through the simulation.

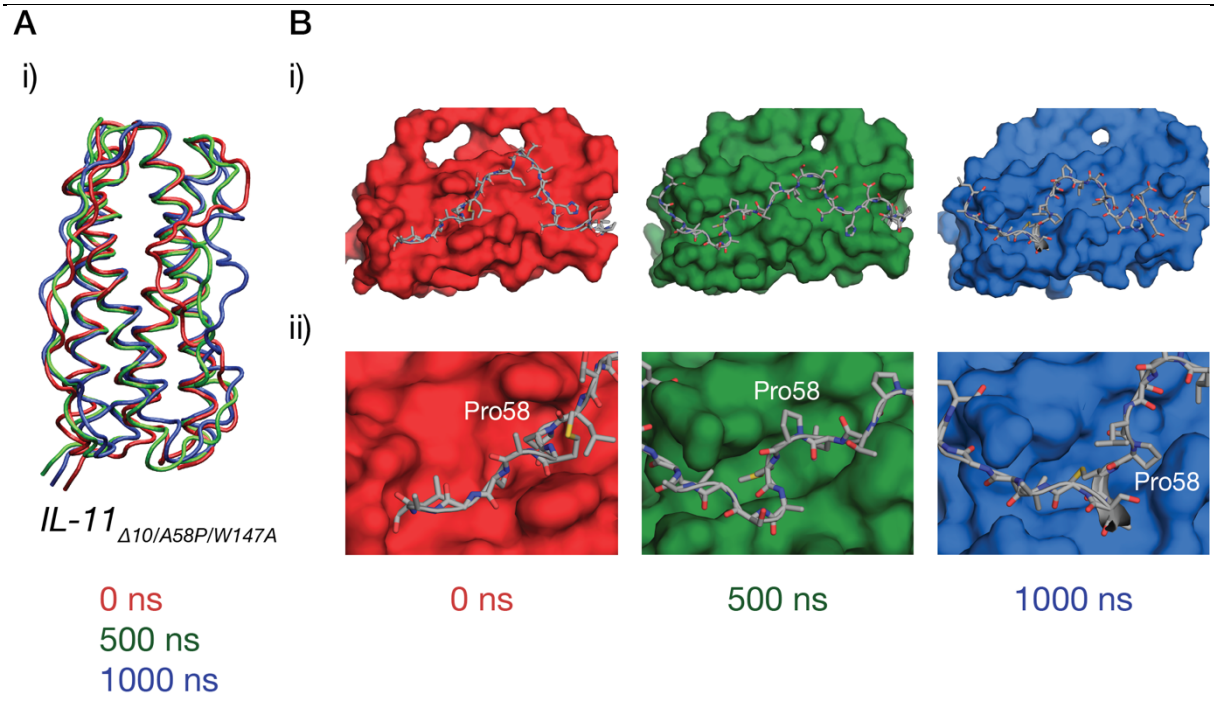

Figure 5.12: 1 μs simulation of the IL-$11_{\Delta10/A58P/W147A}$ mutant.

A) Overlay of frames from the 1 μs simulations of IL-11$_{\Delta10/A58P/W147A}$. B) Interactions between the AB loop and the core of the protein through the simulation, i). During the simulation, Met59 contacts a hydrophobic pocket formed by the helical core of IL-11, ii).

We studied the complexes formed by the new IL-11 mutants using SV-AUC (Figure 5.13A, Supplementary Table 5.1). These experiments showed that IL-11$_{\Delta10/PAIDY}$ forms a hexameric complex with IL-11Rα and gp130, analogous to the complex formed by IL-11 (Figure 5.13Ai). The ability of IL-11$_{\Delta10/PAIDY}$ to form a hexameric complex shows that IL-11 Mutein requires both the PAIDY and W147A mutations to act as a full IL-11 signalling antagonist. Both IL-11$_{\Delta10/A58P/W147A}$ and IL-11$_{\Delta10/S53A/A58P/W147A}$ form trimeric complexes with IL-11Rα and gp130 (Figure 5.13Aii, iii, Supplementary Table 5.1), similar to the complexes formed by IL-11$_{\Delta10}$ Mutein and IL-11$_{\Delta10/W147A}$ (Figure 5.2B,D).

We also undertook experiments to measure the stimulatory potential of the new mutants. We stimulated DLD1 cells with IL-11 in the presence of the inhibitory mutants. Qualitatively, none of the new mutants match the inhibitory potential of IL-11 Mutein (Figure 5.13B, see Supplementary Figure 5.15B for complete membrane images), all permitting limited STAT3 activation, compared with the complete abolition of STAT3 activation by IL-11 Mutein. We do observe the formation of a small proportion of hexameric complex in the c(s) distributions for the IL-11$_{\Delta10/A58P/W147A}$ and IL-11$_{\Delta10/S53A/A58P/W147A}$ complexes (Figure 5.13Aii, iii), consistent with our observation that they activate STAT3 *in vitro*. The mutants do activate STAT3 to varying levels, with IL-11$_{\Delta10/S53A/W147A}$ and slipDYIL-11 being the most potent antagonistic mutants. Both mutations resulted in the destabilisation of IL-11$_{\Delta10}$ (Figure 5.9D, E), their antagonistic effect may be a consequence of this destabilisation, either of the AB loop specifically, or of the entire protein.

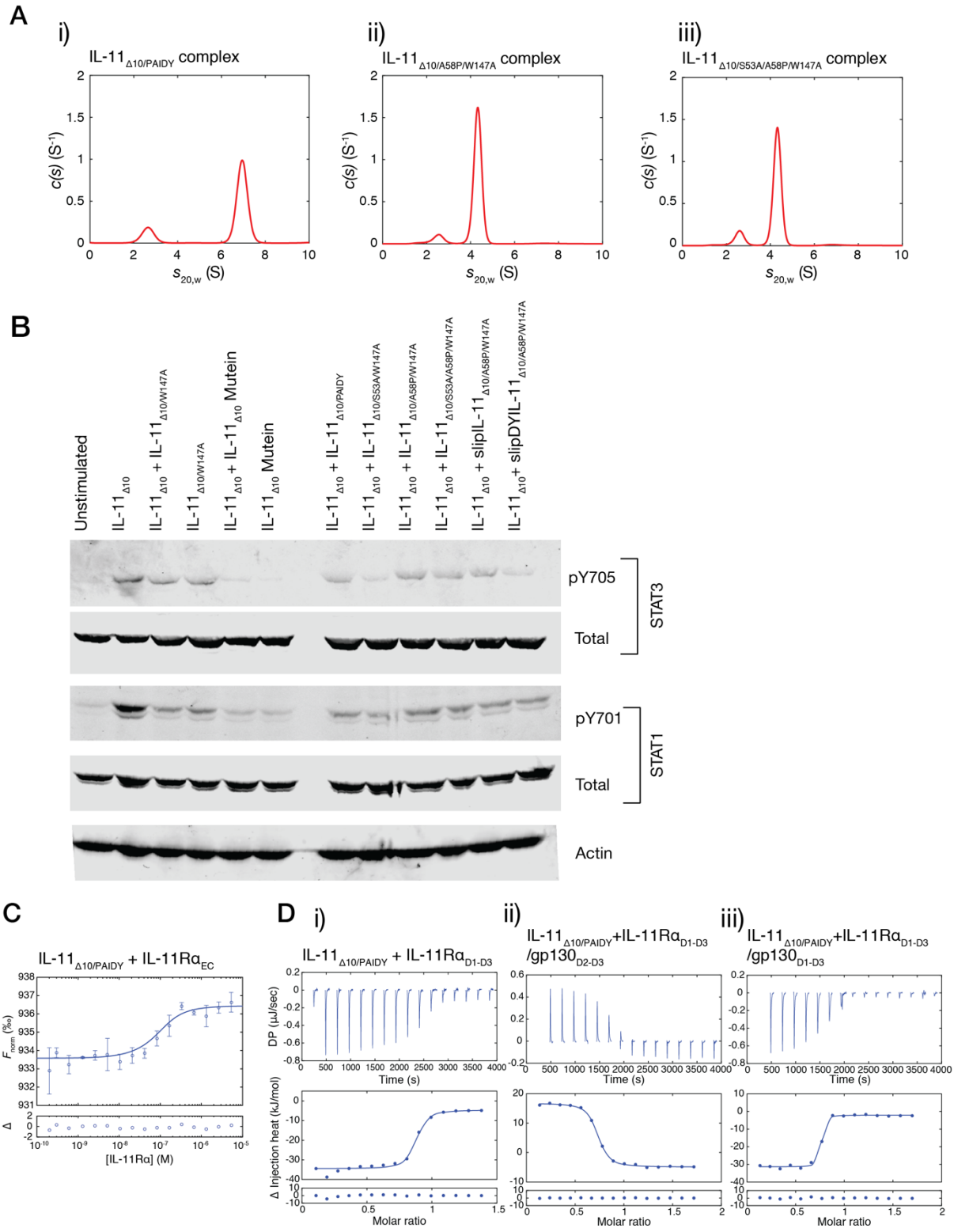

Figure 5.13: Biochemical characterisation of novel IL-11 mutants.

A) Continuous sedimentation coefficient (c(s)) distributions for the complexes formed between, i) IL-11$_{\Delta10/PAIDY}$, IL-11Rα $_{D1-D3}$ and gp130$_{D1-D3}$, ii) IL-11$_{\Delta10/A58P/W147A}$, IL-11Rα$_{D1-D3}$ and gp130$_{D1-D3}$ and iii) IL-11$_{\Delta10/S53A/A58P/W147A}$, IL-11Rα$_{D1-D3}$ and gp130$_{D1-D3}$. Each complex was formed by mixing 5 µM of each protein, which was then

immediately centrifuged. B) STAT1 and STAT3 stimulatory potential of each mutant, measured using western blot. C) MST isotherm for the interaction between IL-11Rα$_{EC}$ and $_{IL\text{-}11\Delta10/PAIDY}$ K_D 51 nM [17 nm, 121 nM, 68% CI], circles represent the average of F_{norm}, error bars indicate the standard deviation, n = 3. D) ITC data and isotherm for the interaction between IL-11Rα$_{D1\text{-}D3}$ and IL-11$_{\Delta10/PAIDY}$, K_D 81 ± 45 nM, i), IL-11Rα$_{D1\text{-}D3}$/IL-11$_{\Delta10/PAIDY}$ and gp130$_{D2\text{-}D3}$, K_D 59 ± 16 nM, ii) and IL-11Rα$_{D1\text{-}D3}$/IL-11$_{\Delta10/PAIDY}$ and gp130$_{D1\text{-}D3}$ K_D 21 ± 17nM, iii). Values given as mean ± standard error, n = 3. For complete thermodynamic parameters, see Supplementary Table 5.3,

---

These mutants and experiments effectively 'decouple' the shift in the position of the AB loop that we observe in the crystal structures from the antagonistic activity of IL-11 Mutein. The mutant IL-11$_{\Delta10/S53A/A58P/W147A}$, which had the same Thr56 Oγ/His86 Nε hydrogen bond that we observed in IL-11 Mutein, does not have the same antagonistic ability as IL-11 Mutein. This shows that the shift in loop position is not alone sufficient for Mutein antagonism – mutants designed to alter the position of the loop without the additional mutations present in IL-11 Mutein are poorer antagonists then IL-11 Mutein, showing that the full set of mutations in IL-11 Mutein are required for potent antagonism, not simply the shift in the AB loop. More detailed interrogation of the mechanistic basis of this will require the precise quantitation of STAT3 activation by the mutants and IL-11, for example, using flow cytometry methods that have been used previously[208].

5.3.9 Mechanism for antagonism by IL-11 Mutein

As discussed above, there are two potential mechanisms for antagonism by IL-11 Mutein. The PAIDY mutations in the AB loop can reduce affinity for gp130 at site-III, acting synergistically with the W147A mutation to completely abolish affinity to gp130. Alternatively, IL-11 Mutein may bind IL-11Rα with a distinct orientation, preventing the formation of the downstream signalling complex. The formation of a stable complex by IL-11$_{\Delta10/PAIDY}$, detectable by AUC at reasonably low concentrations suggests that PAIDY mutations do not greatly decrease affinity for gp130. To directly test this, we measured the affinity for signalling complex formation by IL-11$_{\Delta10/PAIDY}$. MST and ITC show that the affinity for the IL-11$_{\Delta10/PAIDY}$

/IL-11Rα$_{D1-D3}$ interaction is comparable to the IL-11$_{\Delta10}$ Mutein/IL-11Rα$_{D1-D3}$ interaction (K_D = 51 nM [17 nm, 121 nM, 68% CI] by MST, 81 ± 45 nM by ITC, n = 3 titrations) (Figure 5.13Ci, Di, Supplementary Table 5.3). We also measured the affinities for the interaction with gp130$_{D2-D3}$ and gp130$_{D1-D3}$. IL-11$_{\Delta10/PAIDY}$/IL-11Rα$_{D1-D3}$ interacts with gp130$_{D2-D3}$ with an affinity of 59 ± 16 nM, and gp130$_{D1-D3}$ with an affinity of 21 ± 17 nM (Figure 5.13Dii, iii, Supplementary Table 5.3). Overall, these affinities are comparable for the equivalent site-II interaction by IL-11 Mutein, and the equivalent site-III interaction by IL-11. Thus, a model by which IL-11 Mutein functions through a simple 'reverse-avidity' effect is not plausible.

Clearly, the W147A mutation is responsible for the majority of the loss in affinity for gp130 D1, which is not unexpected, as Trp147 buries 118 Å^2 of surface area when binding gp130 D1, 15% of the total surface area buried by site-III. We do not have a method to accurately measure the affinity for the formation of the IL-11 signalling hexamer by IL-11$_{\Delta10/W147A}$, but our AUC experiments suggest that the affinity is in the micromolar-millimolar range, an affinity which would be difficult to measure using ITC. The IL-11$_{\Delta10/W147A}$ mutation clearly does not totally abolish gp130 hexamer formation and given that the effective concentration of gp130 at the cell membrane is likely to be very high, this permits the activation of STAT3 by IL-11$_{\Delta10/W147A}$. IL-11 Mutein abolishes this activation, likely by binding to a different surface on IL-11Rα and the CHR of gp130. The trimeric complex formed by IL-11 Mutein is unable to dimerise to form a signalling hexamer, explaining the potency of IL-11 Mutein (see Figure 5.14 for a schematic description of this proposed mechanism). IL-11$_{\Delta10/PAIDY}$, which lacks the W147A mutation, can form the hexameric signalling complex, as site-III on the cytokine is not sufficiently sterically disrupted to prevent downstream complex formation.

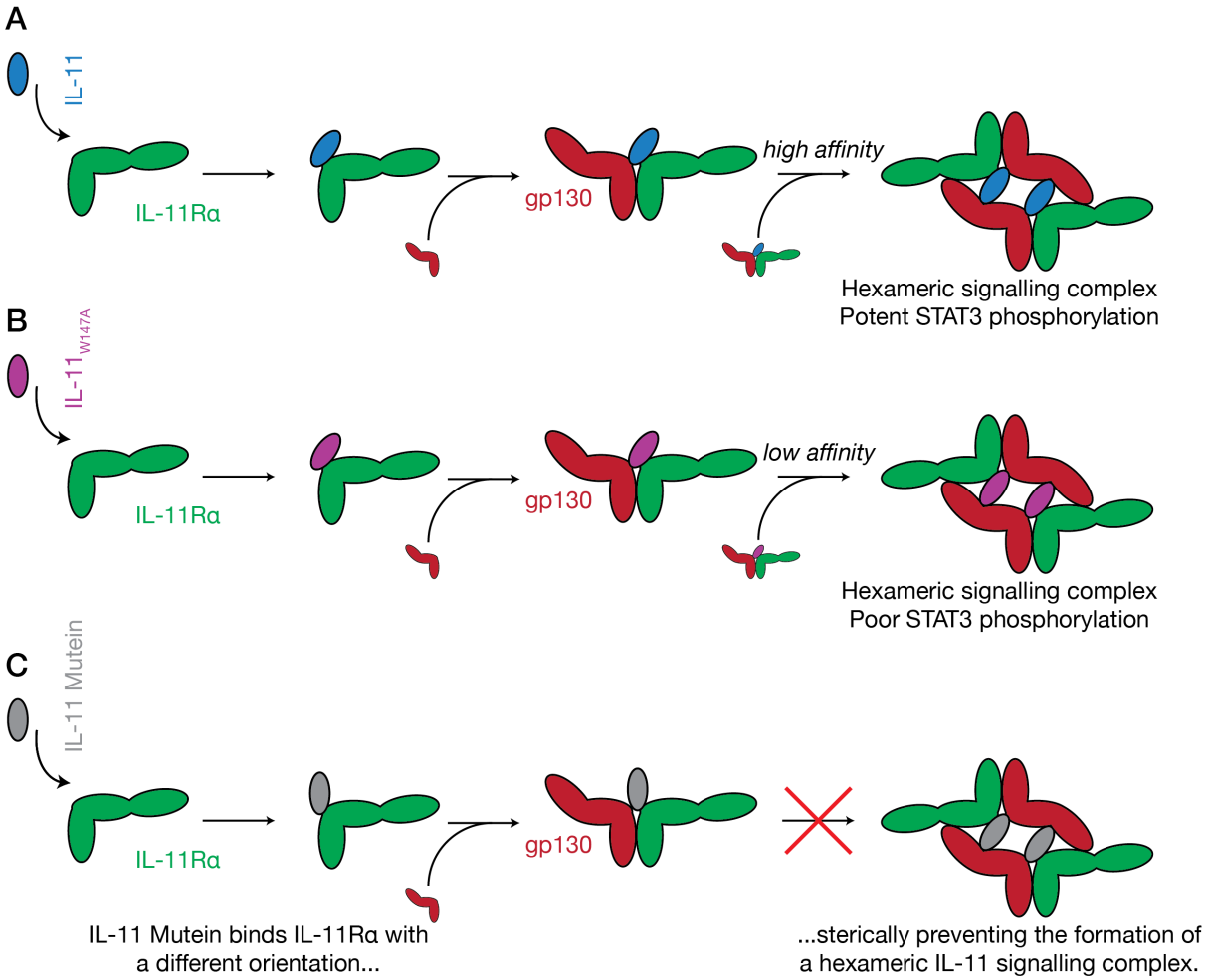

Figure 5.14: Proposed mechanism of action of IL-11 Mutein.

IL-11, A) binds to IL-11Rα with an orientation that allows the subsequent dimerization of two gp130-containing trimers, to form a hexameric signalling complex. IL-11_{W147A}, B) binds to IL-11Rα with the same orientation, as no residues involved in IL-11Rα binding are mutated. However, the W147A mutation reduces affinity for gp130 at site-III, resulting in decreased STAT3 activation. We propose that IL-11 Mutein, C) binds IL-11Rα with a different orientation compared with IL-11 (likely exaggerated here). This orientation prevents the subsequent dimerization of two gp130-contaning trimers, preventing STAT3 activation.

The differences in kinetics may also be involved in IL-11 Mutein antagonism. A slower off rate when binding IL-11Rα may make the formation of an IL-11 Mutein/IL-11Rα/gp130 complex more favourable compared to an IL-11/IL-11Rα/gp130 complex. More generally, differences in receptor kinetic engagement have been shown in other systems, such as the EPO/EPOR system[436], to result in

biased signalling through preferential activation of alternative signalling pathways. IL-11 Mutein abolishes both STAT3 and STAT1 activation (Figure 5.13B), but we did not investigate other signalling pathways such as the MAPK/ERK pathway. These may be investigated in the future.

Further investigation and validation of the model proposed above (Figure 5.14) clearly requires high-resolution structural information on the binding mode between IL-11 Mutein and its receptors. This structural information will provide a detailed understanding of the molecular mechanisms underpinning IL-11 Mutein antagonism, in particular the role of the mutations in the AB loop.

5.4 Conclusion

IL-11 signalling has recently been implicated in a number of different pathologies, including cardiovascular fibrosis and GI cancer. Inhibition of IL-11 signalling is validated as a therapeutic strategy in these diseases, using either IL-11 Mutein, or monoclonal antibodies. Despite this, there is little published structural information on the mechanism of action of any IL-11 signalling inhibitor. This study represents the first structural characterisation of an IL-11 signalling inhibitor. We suggest that IL-11 and IL-11 Mutein bind IL-11Rα and gp130 with a different orientation, which prevents the formation of the downstream signalling complex. Combined with information on the structure of the IL-11 and IL-11 Mutein ternary complexes, this will guide the future design of novel cytokine-like antagonists of IL-11 signalling.

5.5 Materials and methods

5.5.1 Protein expression and purification

The sequence containing human IL-11 Mutein, mouse IL-11 or IL-11 Mutein was purchased from GeneArt and subsequently sub-cloned into the pET28b vector, with N-terminal hexahistidine tag, maltose binding protein and TEV protease cleavage site. Mutant sequences were either purchased from GeneArt or the mutations were introduced using site-directed mutagenesis (Agilent QuickChange kit). IL-11 Mutein and the other IL-11 mutants were expressed and purified using essentially an identical method to that used for the purification of IL-11 (see Chapter 2 and

Chapter 3). All DNA constructs were sequenced at the Australian Genome Research Facility (Parkville, Victoria). The identity of each purified protein was confirmed using electrospray ionisation-time of flight (ESI-TOF) mass spectrometry, using an Agilent 6220 mass spectrometer. Protein purity was assessed using SDS-PAGE.

The IL-$11_{\Delta 10}$ or IL-$11_{\Delta 10}$ Mutein sequence, C-terminally fused to an Avitag biotinylation sequence (GLNDIFEAQKIEWHE) was purchased from GeneArt, and subcloned into the pET28b vector as above, and purified using an identical method to IL-11 (see Chapter 2). The degree of biotinylation was assessed using ESI-TOF mass spectrometry using an Agilent 6220 mass spectrometer.

^{15}N Isotopically labelled IL-$11_{\Delta 10}$ and IL-$11_{\Delta 10}$ Mutein were expressed using the Marley method[361]. Briefly, *E. coli* BL21(DE3) cells were transformed with plasmids expressing MBP-IL-$11_{\Delta 10}$ or MBP-IL-$11_{\Delta 10}$ Mutein, successful transformants were grown overnight in selective lysogeny broth (10 g/L tryptone, 10 g/L NaCl, 5 g/L yeast extract), which was then used to inoculate large-scale LB cultures. These cultures were grown until OD_{600} was greater than 0.7, then cells were pelleted (4,300 rpm, 7 minutes, 20 °C), washed once with M9 salts (5 g/L KH_2PO_4, 6.8 g/L Na_2HPO_4, 0.5 g/L NaCl pH 7.4), then resuspended in one quarter volume M9 minimal media (M9 salts supplemented with 0.1% $^{15}NH_4Cl$, 0.6% glucose, trace element mix and 10 mM $MgSO_4$). The resuspended cells were incubated at 37 °C for one hour, induced with 1 mM IPTG, then incubated overnight at 16 °C. Deuterated ($^{15}N/^{2}H$ and $^{15}N/^{13}C/^{2}H$) IL-$11_{\Delta 10}$ and IL-$11_{\Delta 10}$ Mutein was expressed and purified at the National Deuteration Facility, part of the Australian Nuclear Science and Technology Organisation using established protocols for the high-yield production of deuterated protein[448]. Isotopically labelled IL-$11_{\Delta 10}$ and IL-$11_{\Delta 10}$ Mutein was purified using an identical method to unlabelled protein. The degree of labelling[367] was assessed using ESI-TOF mass spectrometry (Agilent 6220 mass spectrometer).

The IL-11 receptors were expressed, secreted from Sf21 insect cells and purified from the culture media, using an identical method to that described in Chapter 2.

5.5.2 Analytical ultracentrifugation

SV-AUC experiments were conducted effectively as described in Chapter 2 using a Beckman XL-I analytical ultracentrifuge. The sedimenting boundaries were monitored by UV absorbance at 230 nm or 280 nm, in continuous mode, depending on the absorbance of the sample in the cell. All experiments were conducted in TBS (20 mM Tris, 150 mM sodium chloride) pH 8 or 8.5. Buffer density, viscosity and partial specific volume of the protein samples were calculated using *SEDNTERP*, for complexes between IL-11 and the IL-11 receptors, the partial specific volume used was 0.73 mL/g. Data were fitted to a continuous sedimentation coefficient (c(s)) model using *SEDFIT*[403], as described in Chapter 2. The theoretical sedimentation coefficients of IL-$11_{\Delta10}$ and IL-11Rα were calculated using *HYDROPRO*, using standard conditions (water, 20 °C)[377].

The IL-$11_{\Delta10}$ Mutein/IL-$11_{\Delta10/W147A}$ complex concentration series (Figure 5.2D) was prepared by mixing equimolar amounts (7 μM) of IL-$11_{\Delta10}$ Mutein or IL-$11_{\Delta10/W147A}$ with $gp130_{D1\text{-}D3}$ and $IL\text{-}11R\alpha_{EC}$, which was then diluted 1:2 twice.

Fluorescence SV-AUC experiments were conducted using a Beckman XL-A analytical ultracentrifuge, equipped with an Aviv Biomedical fluorescence detection system. Experiments were conducted at 50,000 rpm and 20 °C. Data were processed using *SEDFIT*, as above.

5.5.3 Cell culture

DLD1 cells were grown in RPMI+10% foetal calf serum (FCS), in a 10% CO_2 atmosphere. Cells were grown to confluency in 6-well plates, the media was removed and cells were treated with IL-$11_{\Delta10}$ at a concentration of 50 ng/mL in RPMI, or IL-$11_{\Delta10}$ with an antagonistic mutant at a concentration of 50-100 μg/mL, or RPMI as a vehicle control, and incubated for one hour. Cells were then washed with cold PBS and lysed in RIPA buffer. Protein concentration was determined by the bicinchoninic acid (BCA) assay. Lysates were diluted with SDS-PAGE loading buffer, resolved on a 10% polyacrylamide gel and wet transferred to a nitrocellulose membrane. The membranes were blocked, incubated with the indicated primary

antibodies (for phospho-STAT3 CST cat 9145; for phospho-STAT1 CST cat 9167, for total STAT3 CST cat 4904 for total STAT1 CST cat 9172, for actin Sigma cat A1978), then detected using conjugated fluorescent secondary antibodies (Odyssey cat 926-32211/926-68072), and visualised using the Odyssey Infrared Imaging System (LI-COR Biosciences).

5.5.4 Small-angle X-ray scattering

SAXS experiments were performed largely as described in Chapters 3 and 4. SAXS experiments were conducted at the Australian Synchrotron SAXS/WAXS beamline [406-408]. The X-ray beam energy was 11,500 eV (λ = 1.078 Å), the sample-to-detector distance is noted in Supplementary Table 5.2. Data were collected following fractionation with an in-line size-exclusion chromatography column (Superdex 200 5/150 Increase, GE Healthcare,) pre-equilibrated in TBS pH 8.5, 0.2 % sodium azide. Data were reduced and analysed using Scatterbrain, CHROMIXS[409] and ATSAS[409,410], data were analysed using CRYSOL and DAMMIF/DAMAVER/DAMMIN[412-414]. A summary is given in Supplementary Table 5.2.

5.5.5 Isothermal titration calorimetry

ITC experiments were performed largely as described in Chapter 3 and 4. Protein samples were buffer exchanged into TBS pH 8.5 using gel filtration prior to analysis by ITC. ITC data was collected using a MicroCal iTC 200 (GE Healthcare). Titrations were performed using 15 2.5 µL injections of the cytokine ligand, after an initial injection of 0.8 µL. IL-11Rα$_{D1-D3}$ was present at a concentration of 10 µM and the concentration of the cytokine was 10-fold greater than the concentration of IL-11Rα. The formation of the cytokine/IL-11Rα$_{D1-D3}$ complex was performed at 303 K. Following the formation of the cytokine/receptor complex, gp130$_{D1-D3}$ was loaded in the syringe at a concentration approximately 10-fold greater than the concentration of IL-11Rα in the cell, a subsequent titration of gp130$_{D1-D3}$ against the cytokine/IL-11Rα$_{D1-D3}$ complex was then performed at 288 K. Titration data were integrated using *NITPIC*[419,420], and analysed in *SEDPHAT* using a 1:1 interaction model[405]. Each titration was conducted in triplicate, values stated are the mean ± standard error of

the mean. Significance of differences were calculated using a two-tailed paired t-test in Microsoft Excel.

5.5.6 Microscale thermophoresis

MST experiments were performed using a Nanotemper NT.115 MST. IL-$11_{\Delta 10}$, IL-$11_{\Delta 10}$ Mutein and IL-$11_{\Delta 10/PAIDY}$ were dialysed against PBS (50 mM sodium phosphate, 150 mM sodium chloride pH 7.5) overnight, and labelled with DyeLight 650 NHS-ester (Thermo Fisher) according to the manufacturer's protocol. IL-11Rα_{EC} was buffer-matched with the fluorescently labelled cytokine by dialysis immediately prior to the experiment. A sixteen-point twofold dilution series of IL-11Rα_{EC} was prepared, starting at a concentration of approximately 10 µM, this receptor was subsequently diluted 1:2 with 200 nM labelled cytokine in PBS + 0.2% Tween 20. This mixture was incubated in the dark for at least one hour, then loaded into Nanotemper premium-coated capillaries, then analysed on a Nanotemper NT.115 MST. An MST laser power of 40 was used. Each dilution series was prepared and measured in triplicate. The triplicate data were analysed in *PALMIST*[449], errors are given as a 68% confidence interval. F_{norm} was determined using the temperature jump mode in *PALMIST*.

5.5.7 Surface plasmon resonance

SPR experiments were conducted using a Biacore T200, at 25 °C, in TBS pH 8.5 + 0.05% Tween, running at 30 µL/min. Biotinylated IL-$11_{\Delta 10}$ and IL-$11_{\Delta 10}$ Mutein were loaded onto separate channels on a SAHC 1500M streptavidin chip (Xantec). Both proteins were immobilised until R_{max} was approximately 70. High levels of non-specific binding were noted with both constructs, the chip was washed extensively with 1 M NaCl, until the baseline was stable, to remove non-specifically bound protein. A nine-point, two-fold dilution series of both IL-11Rα_{D1-D3} was prepared, starting at a concentration of approximately 500 nM. Each IL-11Rα dilution was injected over both flow cells in triplicate, reference-subtracted data was generated by subtracting the response from channels in which no protein was loaded, to channels containing protein. Data were fitted to a 1:1 kinetic model, the Biacore analysis software was used to determine association (k_a) and dissociation (k_d) rates,

and the dissociation constant, K_D. Each dilution series was prepared and analysed in duplicate; values are given as mean ± standard error.

5.5.8 Protein crystallisation and X-ray data collection

Initial crystals of IL-$11_{\Delta10}$ Mutein were obtained using a similar screening approach to IL-$11_{\Delta10}$, in the precipitant 30% PEG 3350, 0.2 M ammonium sulfate, 0.1 M Tris pH 8.5, 20 °C. These initial crystals were used to prepare a microseed stock[395]. Large, single plates of IL-11 Mutein grew in the condition 27% PEG 3350, 0.1 M bis-tris propane pH 9, 0.2 M ammonium sulfate, 5 mM praseodymium chloride, 20 °C. Crystallisation drops were produced by mixing 1.5 µL precipitant, 1.5 µL IL-$11_{\Delta10}$ Mutein (5 mg/mL) and 0.5 µL seed. Crystals of IL-$11_{\Delta10}$ Mutein were large plates, with approximate dimensions 200 × 200 × 5 µm. A similar approach was used to crystallise the IL-11 mutants IL-$11_{\Delta10/W147A}$, IL-$11_{\Delta10/PAIDY}$, IL-$11_{\Delta10/S53A/A58P/W147A}$ and IL-$11_{\Delta10/A58P/W147A}$. These mutants were cross seeded with seed generated from IL-$11_{\Delta10}$ or IL-$11_{\Delta10}$ Mutein crystals and grew in very similar conditions to IL-$11_{\Delta10}$ Mutein. Crystals of IL-11 Mutein full-length grew in 1.3 M ammonium sulphate, 200 mM Tris pH 8, 10 mM phenol, 20 °C, with seeding. Crystals of IL-11 Mutein full-length were very thin needles.

Crystals were flash-cooled in liquid nitrogen directly from crystallization drops, and X-ray diffraction data were collected at 100 K at the Australian Synchrotron MX2 beamline[396]. X-ray data collection statistics are tabulated in Supplementary Table 5.4.

5.5.9 X-ray data processing and structure refinement

Diffraction data were indexed, integrated and scaled using *XDS*[397], analysed using *POINTLESS*[398] and merged using *AIMLESS*[399] from the *CCP4* suite. Initial phase estimates were obtained using molecular replacement with *Phaser*[400], using our either our original structure of IL-11 (PDB ID: 4MHL)[109], our high-resolution structure of IL-$11_{\Delta10}$ (PDB ID: 6O4O, chapter 3) or our structure of IL-$11_{\Delta10}$ Mutein as the search model. Auto-building with simulated annealing was performed in *phenix.autobuild* to reduce phase bias from the search model. Refinement was

performed in *phenix.refine*[401] with iterative manual building using *Coot*[402]. TLS refinement was performed using a single TLS group containing all protein atoms. Explicit riding hydrogens were used throughout refinement and included in the final model, the atomic position and *B* factors for hydrogens were not refined. Residues of all structures are numbered in an identical manner to our structure of IL-$11_{\Delta10}$ (chapter 3, PDB ID: 6O4O), according to the mature protein sequence after cleavage of signal peptides. Structures were aligned using the CE[434] algorithm in *PyMOL* 2.2. Figures were prepared using *PyMOL* 2.2. Refinement statistics are tabulated in Supplementary Table 5.4.

5.5.10 Nuclear magnetic resonance spectroscopy

NMR experiments were performed using either an 18.8 T (800 MHz ^{1}H resonance) Bruker Avance II spectrometer, or a 16.4 T (700 MHz ^{1}H resonance) Bruker Avance IIIHD spectrometer. NMR spectra were processed with NMRPipe[450], for spectra acquired with non-uniform sampling (NUS), spectra were reconstructed with qMDD[451]. Spectra were visualised and analysed using NMRFAM-Sparky[452]. All NMR samples were prepared in 50 mM sodium phosphate pH 6, 0.02% NaN_3, 5% $^{2}H_2O$, experiments were conducted at 20 °C. Due to the relatively large size of IL-11, and as we used perdeuteration to improve spectral quality, all NMR experiments with deuterated protein were acquired as TROSY experiments[453].

NMR assignment was conducted with 800 µM ^{15}N/^{13}C/^{2}H IL-$11_{\Delta10}$ Mutein or 200 µM ^{15}N/^{13}C/^{2}H IL-$11_{\Delta10}$ and were collected at 18.8 T, 20 °C. ^{1}H-^{15}N TROSY-HSQC spectra were acquired before and during the acquisition of the triple-resonance spectra to monitor integrity of the sample. HSQC spectra were assigned using a standard triple-resonance assignment strategy (see strip plots in Supplementary Figure 5.9, Supplementary Figure 5.10). Six TROSY[453] triple resonance experiments were acquired, HNCO/HN(CA)CO, HN(CO)CA/HNCA and HNCACB/HN(CO)CACB, all with 10% NUS and ^{2}H decoupling. Each pair of spectra can be used to establish sequential residue connectivity. For example, the HN(CO)CA spectrum, there is one peak in the ^{13}C dimension of the spectrum for each backbone amide peak in the HSQC. The carbon chemical shift of this peak corresponds to the ^{13}Cα chemical

shift of the residue preceding the residue that gives rise to the NH peak in the HSQC ($^{13}C\alpha_{(i-1)}$). In the HNCA spectrum, the same backbone amide peak gives rise to two peaks in the ^{13}C dimension of the spectrum, which correspond to the $^{13}C\alpha$ chemical shift of the residue that give rise to the NH peak in the HSQC ($^{13}C\alpha_{i}$), the second peak corresponds to the carbon chemical shift of the residue preceding the residue that gives rise to the NH peak in the HSQC ($^{13}C\alpha_{(i-1)}$). Sequential residue connectivity can be established using this pair of spectra (see strip plots in Supplementary Figure 5.9, Supplementary Figure 5.10).The chemical identity of the residue can also be determined by comparison with tabulated values, as different residues have characteristic Cα and Cβ chemical shifts. In this manner, the connectivity and identity of amide peaks in the HSQC can be established.

For assignment, peaks were picked in the ^{1}H-^{15}N HSQC spectrum, this was used to pick the 3D spectra. Peaklists were uploaded to the PINE server[454] for automated assignment, these automated assignments were curated and extended manually. Solution secondary structure was assessed using the SSP program[444], with chemical shifts referenced from RefDB[455].

Backbone relaxation parameters (^{15}N-R_1, ^{15}N-R_2 and ^{15}N-{^{1}H} NOE) were measured at 18.8 T (^{15}N frequency 81 MHz, ^{1}H frequency 800 MHz) with 400 µM IL-$11_{\Delta10}$ or IL-$11_{\Delta10}$ Mutein. ^{15}N-R_1 and ^{15}N-R_2 parameters were recorded as TROSY-type[456] single-scan interleaved pseudo-3D datasets[457]. For the ^{15}N-R_1 experiment the following relaxation delay times were used, 0.01 s, 0.05 s, 0.1 s, 0.3 s, 0.5 s, 0.7 s, 0.9 s and 1.5 s, the 0.01 s, 0.3 s and 0.9s delay times were each repeated once. For the ^{15}N-R_2 experiment, the following relaxation delay times were used, 1x, 2x, 4x, 6x, 8x, 10x, 12x, 14x, where x = 0.01696 s, the 1x, 6x and 10x delay times were each repeated once. The experiments were analysed in relax-gui[458-460], where they were fitted to an exponential decay model $I(t) = I_0 e^{-Rt}$, where I is the peak height and t the delay time. Errors were estimated using 500 Monte Carlo simulations in relax-gui. ^{15}N-{^{1}H} NOE values were measured as two ^{1}H-^{15}N HSQC spectra, collected in an interleaved manner with and without a proton saturation pulse of 4 s, then an additional delay of 5 s [457,461]. Values were determined in relax-gui[458-460] as the ratio of

peak heights in the saturated and unsaturated spectra respectively, errors were estimated as the noise in the spectra.

Self-association for IL-$11_{\Delta10}$ Mutein was assessed by determining the ^{15}N-R_2 rate at four concentrations of IL-$11_{\Delta10}$ Mutein (800 μM, 400 μM, 200 μM, 100 μM). Spectra were acquired and processed as above.

5.5.11 Molecular dynamics simulations

All MD simulations were performed using NAMD 2.1.3b1[415] and the CHARMM22 forcefield[415,416] at 310 K in a water box with periodic boundary conditions. Simulations were analysed in VMD 1.9.3[417]. A model of each IL-$11_{\Delta10}$ mutant was built based on the crystal structure, for residues with multiple orientations, only one was selected. The two missing residues in the structure of IL-$11_{\Delta10/PAIDY}$ were built using the Phyre2[418] server. For IL-$11_{\Delta10/A58P/W147A}$, chain B of the crystal structure was used. The structures were solvated (box size 53.6 × 53.1 × 74.9 Å), and ions added to approximate final concertation of 0.15 M NaCl. The MD simulations was performed using a 10 ps minimisation time, followed by 100 ns MD. Each MD simulation was performed in triplicate, values are given as mean ± standard deviation. Simulations were analysed as in Chapter 2.

5.5.12 Differential scanning fluorometry

Protein samples were analysed by DSF at a concentration of 0.1 mg/mL in TBS pH 8 + 0.02% sodium azide, with 2.5 × SYPRO Orange dye (Sigma Aldrich). 20 μL of the sample was loaded into 96-well qPCR plate (Applied Biosystems), and four technical replicates of each sample were analysed. The plates were sealed, and samples heated in an Applied Biosystems StepOne Plus qPCR instrument, from 20 °C to 95 °C, with a 1% gradient. Unfolding data were analysed using a custom script in MATLAB r2019a. The temperature of hydrophobic exposure (T_h), was defined as the minimum point of the first derivative curve, and used to compare the thermal stability of different proteins[379]. All experiments were repeated three times, values are given as mean ± standard error. Significance of differences were calculated using a two-tailed paired t-test in Microsoft Excel.

5.6 Supplementary Material

5.6.1 Supplementary Figures

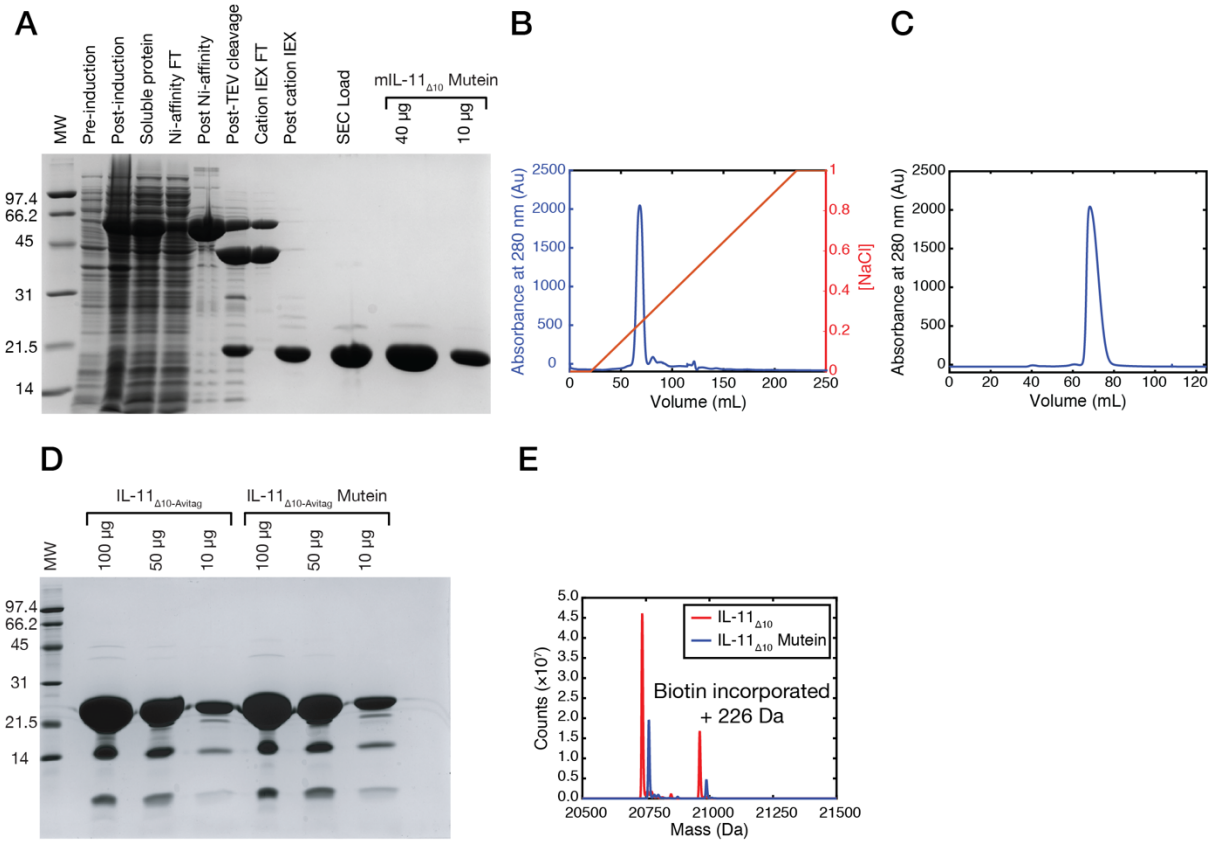

Supplementary Figure 5.1: Purification of IL-11$_{\Delta 10}$ Mutein.

A) Gel showing the purity of mIL-11$_{\Delta 10}$ Mutein through various stages in the purification, and the final purity. B) cation-exchange chromatogram, and C) gel-filtration chromatogram. D) Gel showing the purity of Avitagged IL-11$_{\Delta 10}$ and IL-11$_{\Delta 10}$ Mutein, E) a deconvoluted mass spectrum, showing the successful incorporation of biotin in both proteins.

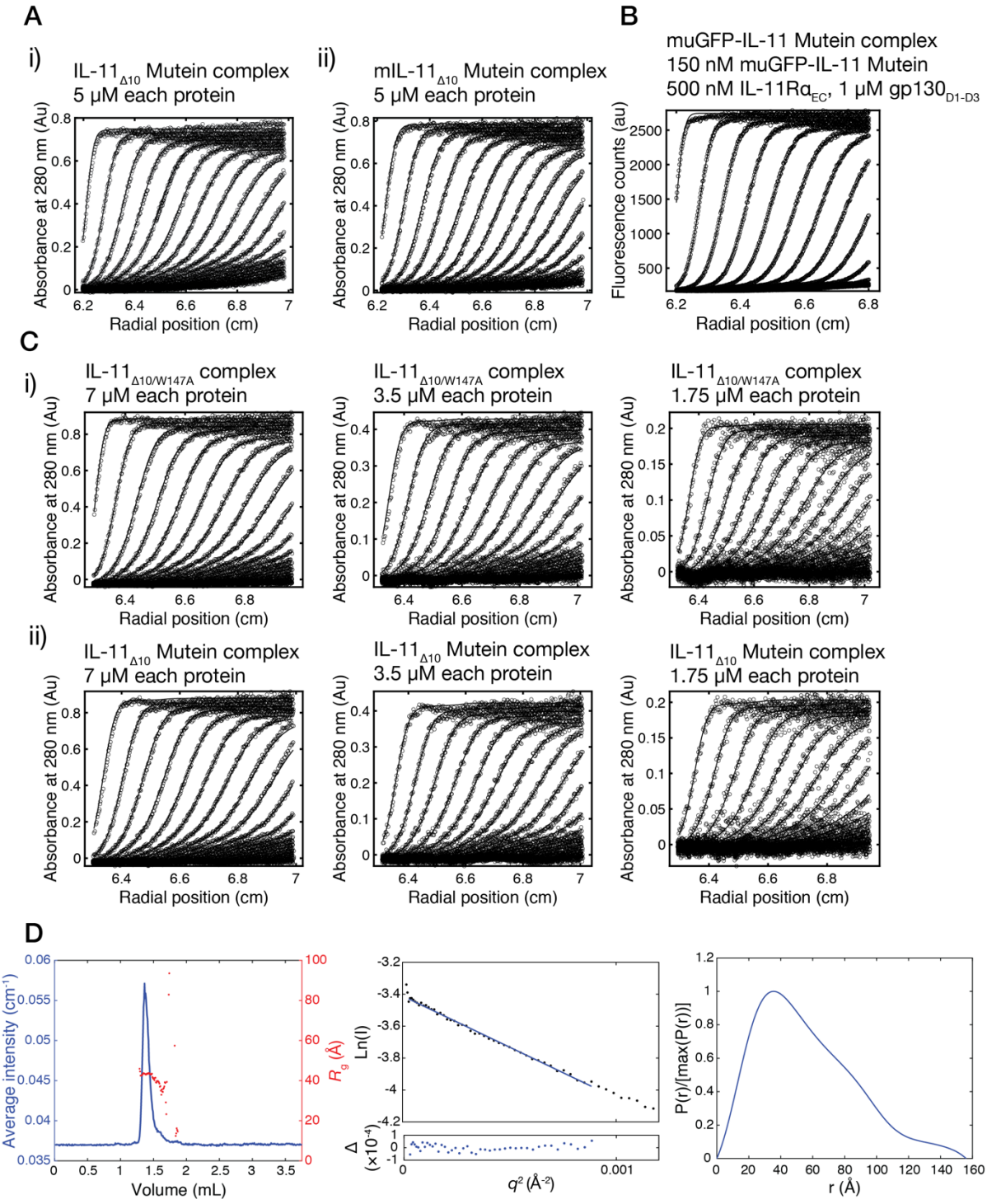

Supplementary Figure 5.2: Raw AUC data and supplementary SAXS data for Figure 5.2.

A) The raw AUC scans for Figure 5.2Bi (i) and Figure 5.2Bii (ii). B) The raw fluorescence AUC scans for Figure 5.2C. C) Raw AUC scans for Figure 5.2Ci (i) and Figure 5.2Cii (ii). D) SEC-SAXS chromatogram, Guinier plot and P(r) plot for the IL-$11_{\Delta 10}$ Mutein trimeric complex.

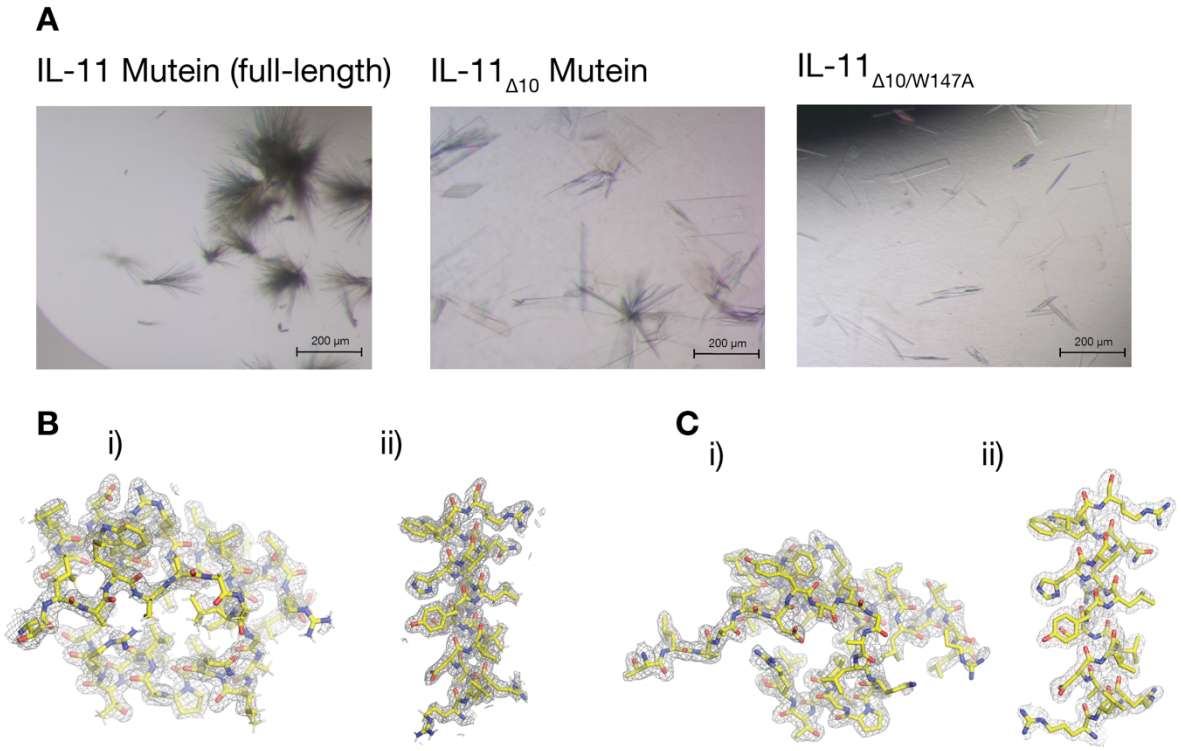

Supplementary Figure 5.3: Crystals and representative density.

A) Crystals of IL-11 Mutein full length, IL-$11_{\Delta10}$ Mutein and IL-$11_{\Delta10/W147A}$. B) Representative density for IL-$11_{\Delta10/W147A}$, i) density for the AMSAG sequence, and ii) density for the B helix. C) Representative density for IL-$11_{\Delta10}$ Mutein, density for the PAIDY sequence, and ii) density for the B helix.

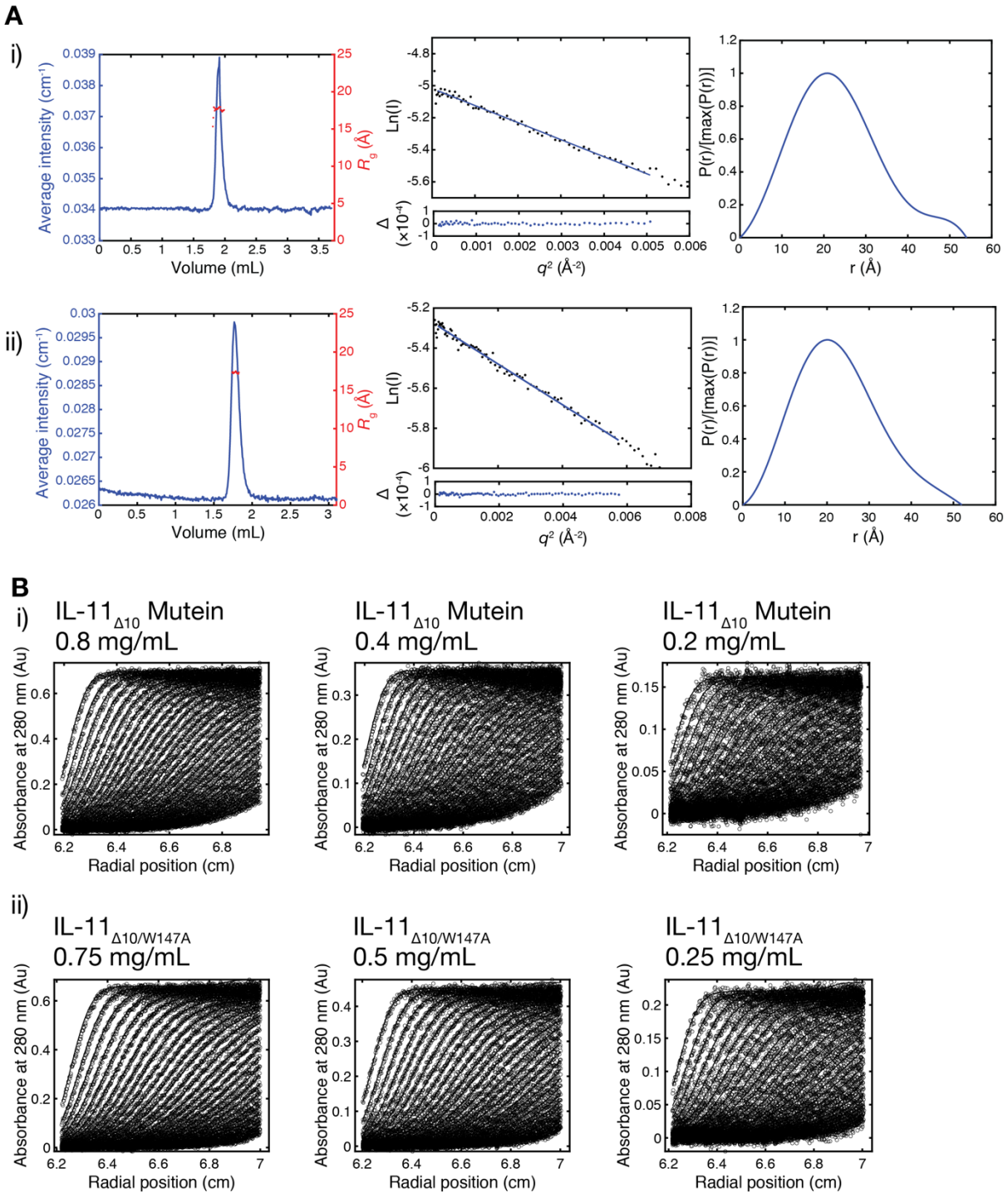

Supplementary Figure 5.4: Supplementary SAXS and AUC data for Figure 5.4. A) Supplementary SAXS data for IL-11$_{\Delta 10}$ Mutein, i) and IL-11$_{\Delta 10/W147A}$, ii) showing the SEC-SAXS chromatogram, a pairwise distance distribution (P(r)) plot and a Guinier plot, for the data shown in Figure 5.4B. B) Raw AUC data (circles) overlaid with the best fit to a continuous size distribution [c(s)] model for the distributions shown in Figure 5.4C.

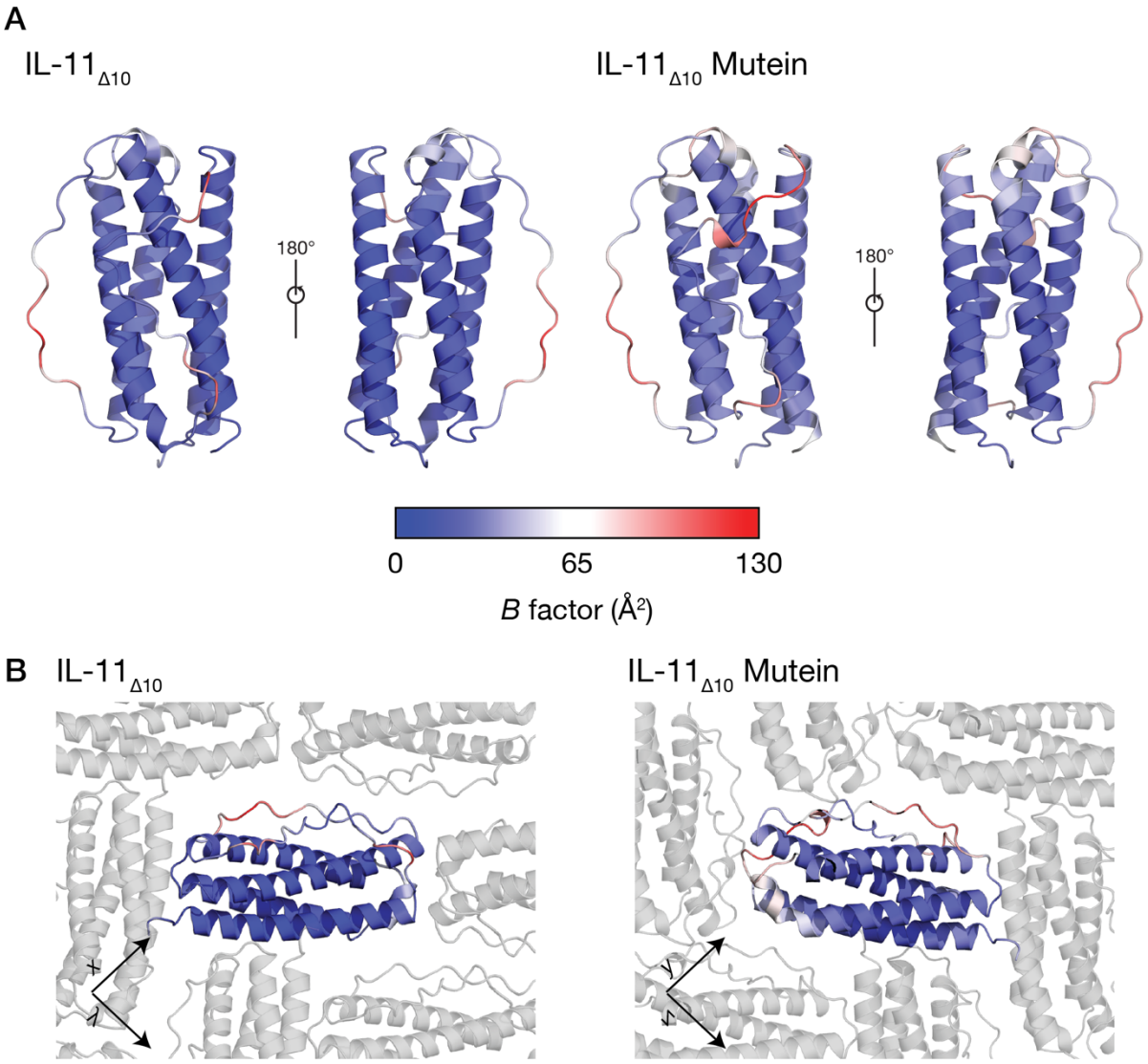

Supplementary Figure 5.5: *B* factors for IL-11$_{\Delta 10}$ and IL-11 $_{\Delta 10}$ Mutein.

A) The structure of each protein, coloured by the Cα *B* factor. B) Crystal lattice of both IL-11$_{\Delta 10}$ and IL-11$_{\Delta 10}$ Mutein, showing how the *B* factors are influenced by crystal contacts.

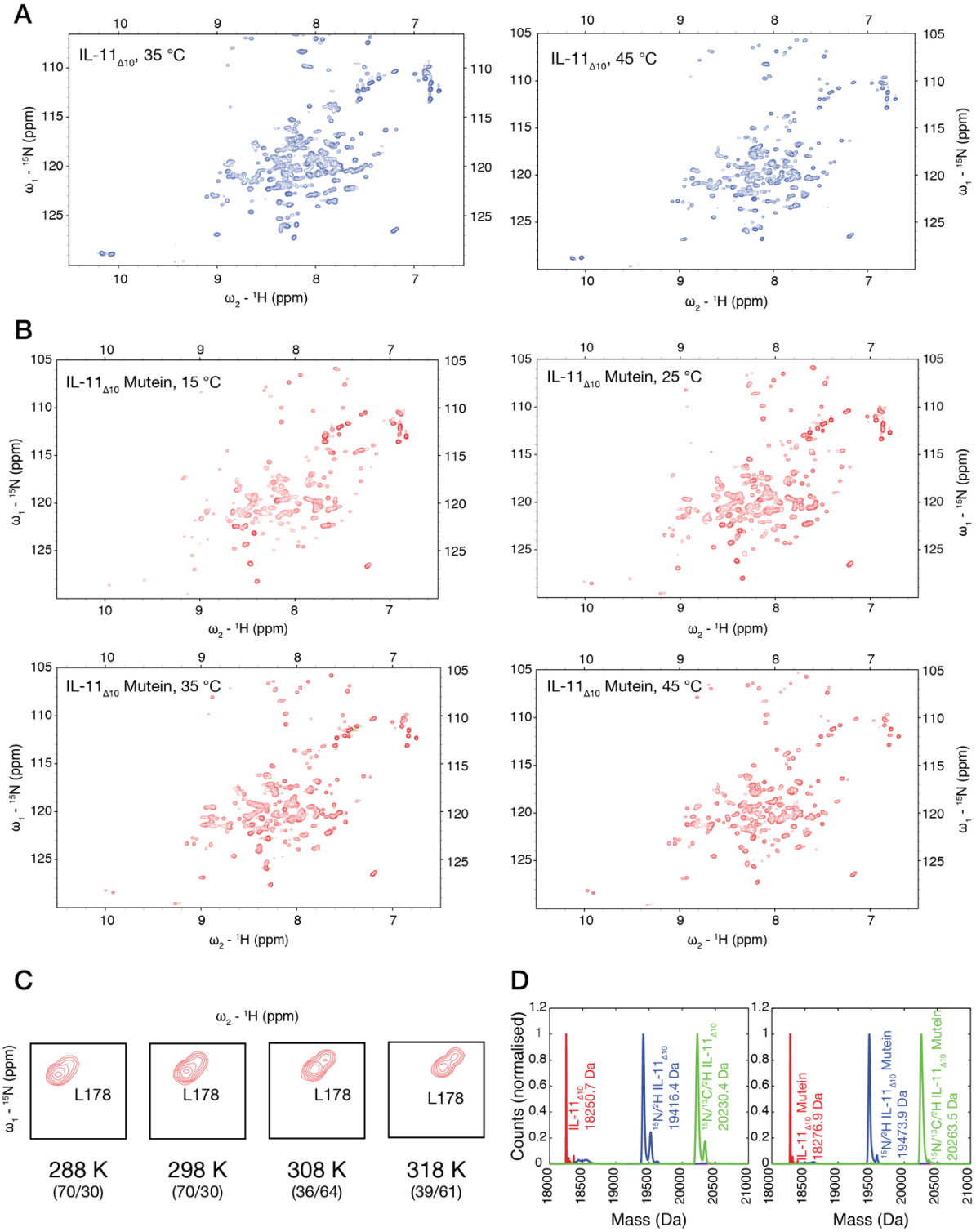

Supplementary Figure 5.6: HSQC spectra of IL-11$_{\Delta10}$ and IL-11 $_{\Delta10}$ Mutein.

A) Two ^{1}H-^{15}N HSQC spectra collected on 450 µM ^{15}N-IL-11$_{\Delta10}$ at both 35 °C and 45 °C. B) Four ^{1}H-^{15}N HSQC spectrum collected on 1.2 mM ^{15}N-IL-11$_{\Delta10}$ Mutein at four temperatures, as indicated in the figure. C) Temperature dependence in peak intensity for Leu178 in the ^{1}H-^{15}N HSQC spectrum of ^{15}N-IL-11$_{\Delta10}$ Mutein. The

relative proportion of the main peak and shoulder for Leu178 was calculated from the peak height. D) Deconvoluted mass spectrum, showing successful deuterium incorporation in $^{15}N/^{13}C/^{2}H$ IL-$11_{\Delta 10}$ (expected MW of $^{15}N/^{13}C$ IL-$11_{\Delta 10}$ 19299.49 Da), and in $^{15}N/^{13}C/^{2}H$ IL-$11_{\Delta 10}$ Mutein (expected MW of $^{15}N/^{13}C$ IL-$11_{\Delta 10}$ Mutein 19328.48 Da).

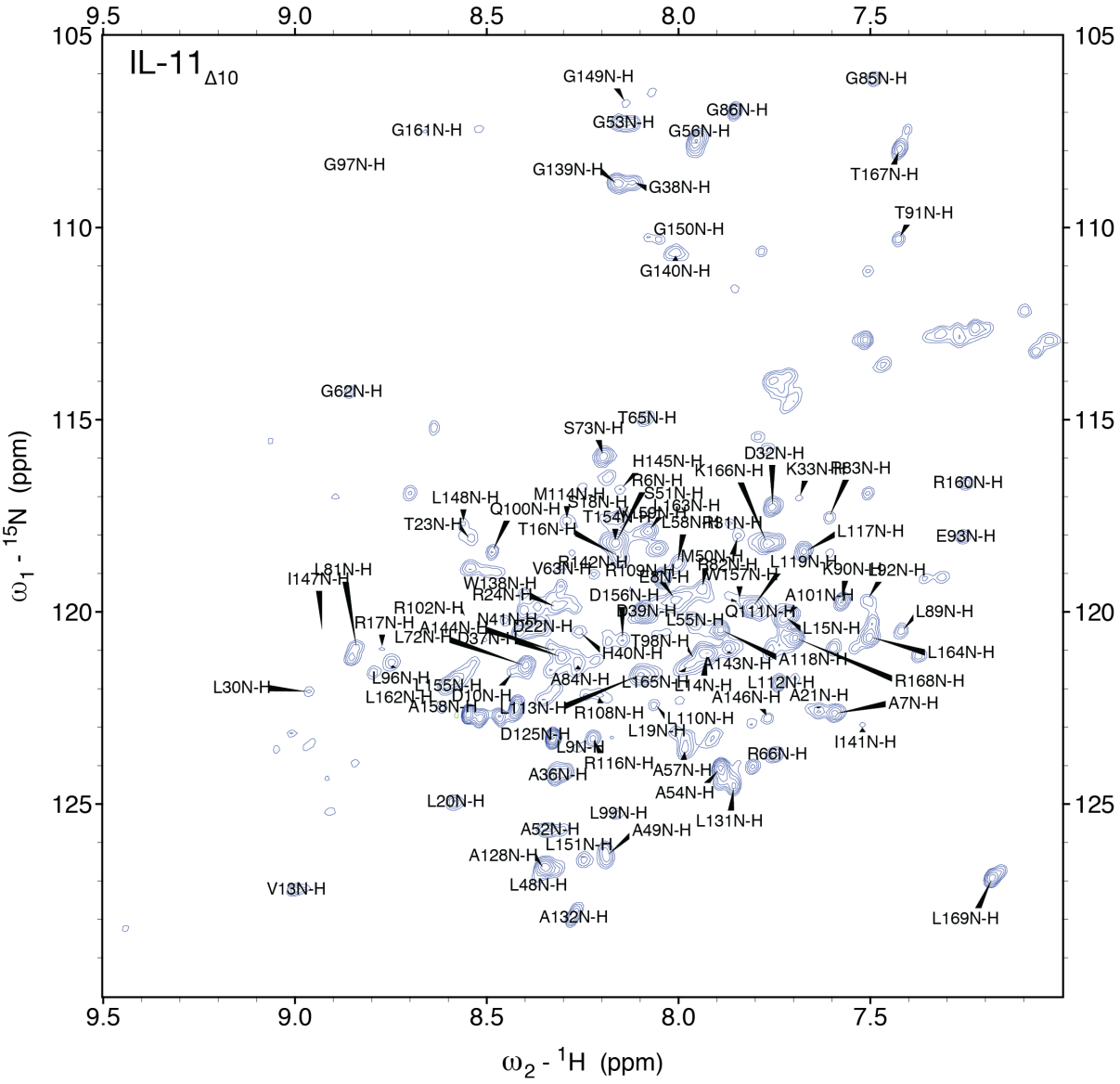

Supplementary Figure 5.7: Assigned ^{1}H-^{15}N TROSY-HSQC spectrum for IL-11$_{\Delta 10}$.

Spectrum collected on 200 µM ^{15}N/^{13}C/^{2}H-IL-11$_{\Delta 10}$ at 20 °C, on an 18.8 T spectrometer.

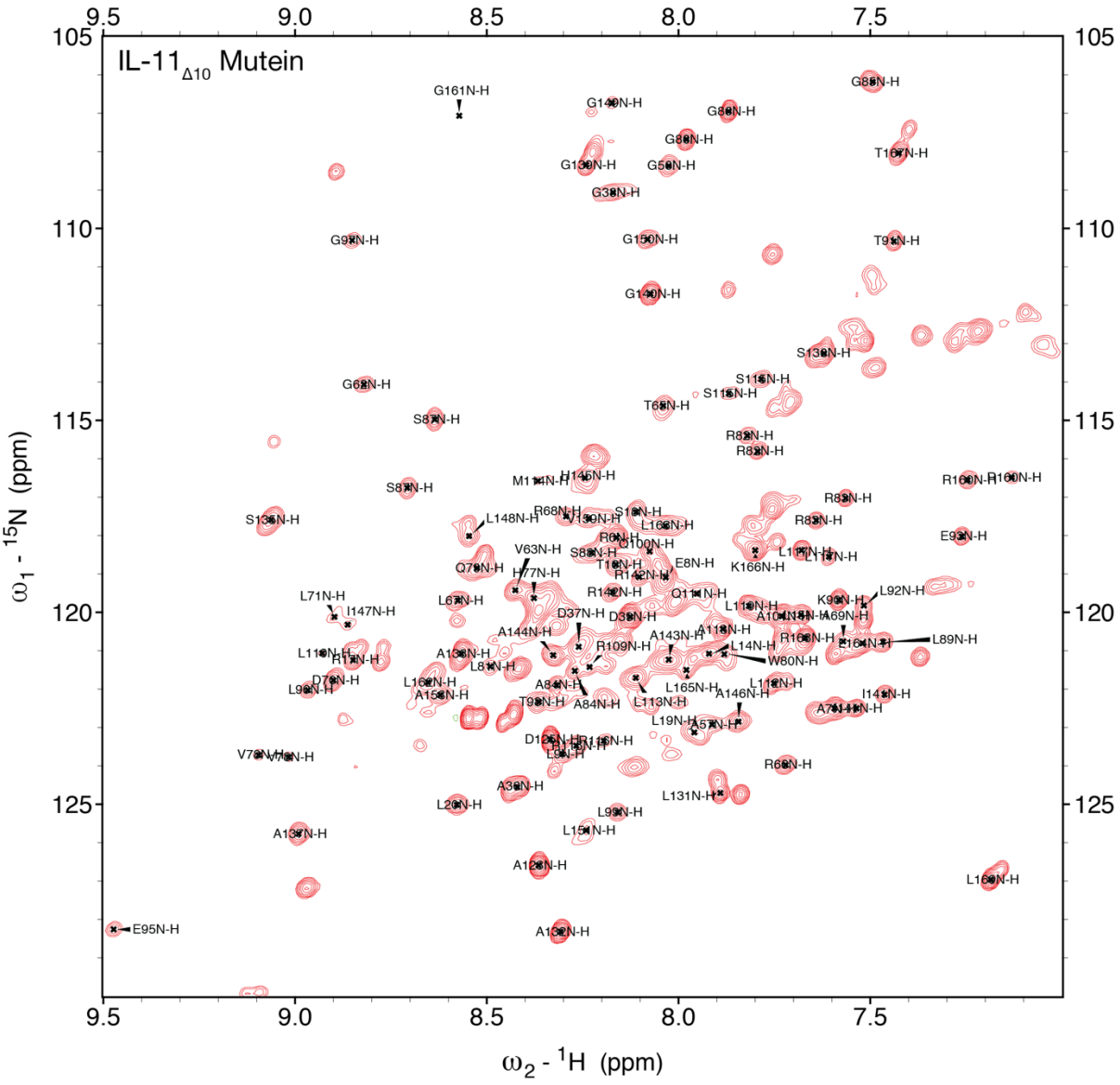

Supplementary Figure 5.8: Assigned ^{1}H-^{15}N TROSY-HSQC spectrum for IL-11$_{\Delta 10}$ Mutein.

Spectrum collected on 800 µM ^{15}N/^{13}C/^{2}H-IL-11$_{\Delta 10}$ Mutein at 20 °C, on an 18.8 T spectrometer.


HNCA/HN(CO)CA
45
50
55
60
65
ω2 (13C) (ppm)
R177 Cα
R178 Cα
K176 Cα
K175 Cα
L174 Cα
L173 Cα
HN(CA)CO/HNCO
172
174
176
178
180
182
R177 C'
T176 C'
K175 C'
L174 C'
L178 C'
L173 C'
L178
ω1 (15N) 127.0 ppm
ω3 (1H) 7.818 ppm
R177
ω1 (15N) 120.7 ppm
ω3 (1H) 7.696 ppm
T176
ω1 (15N) 108.0 ppm
ω3 (1H) 7.424 ppm
K175
ω1 (15N) 118.2 ppm
ω3 (1H) 7.769 ppm
L174
ω1 (15N) 121.4 ppm
ω3 (1H) 7.502 ppm

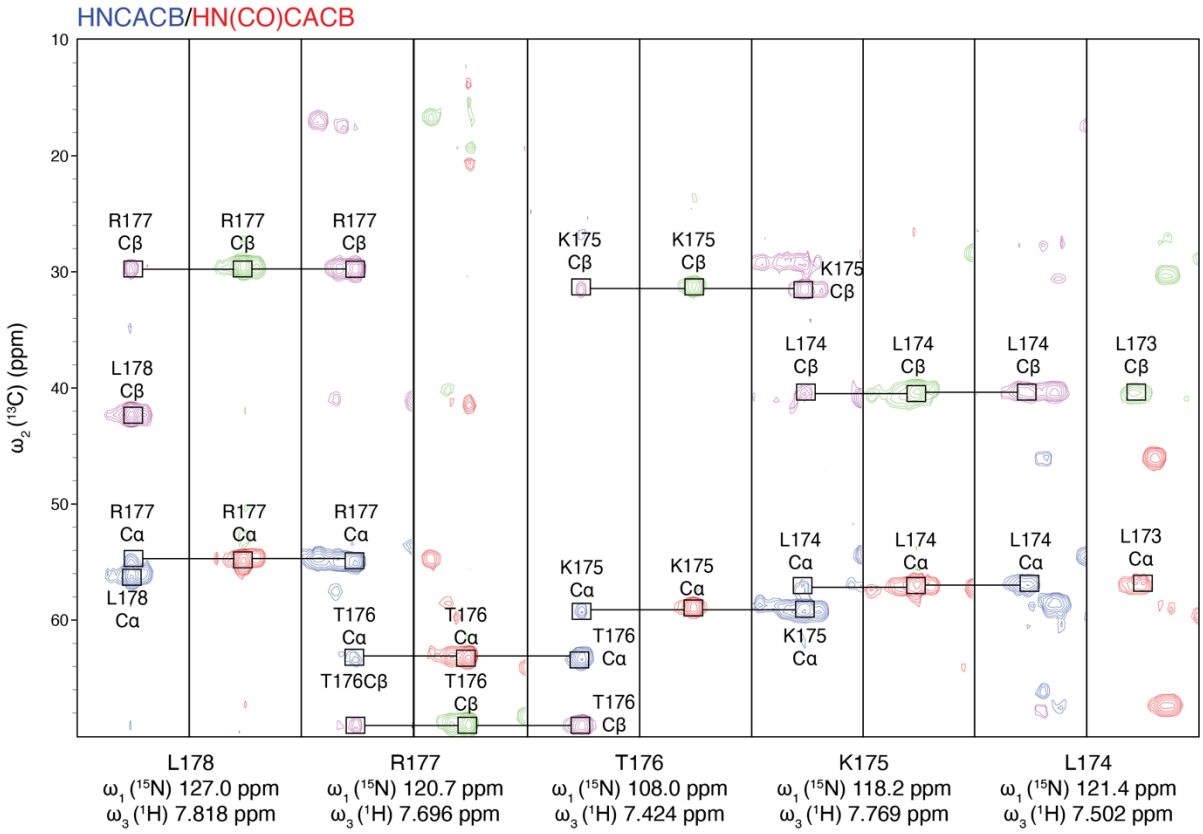

Supplementary Figure 5.9: Strip plots for the C-terminal residues of IL-11$_{\Delta 10}$. Peak strips are shown for the HNCO/HN(CA)CO, HNCA/HN(CO)CA and HNCACB/HN(CO)CACB pairs. Spectra collected on 200 μM ^{15}N/^{13}C/^{2}H-IL-11$_{\Delta 10}$ at 20 °C, on an 18.8 T spectrometer. All spectra collected as TROSY-type spectra. Note Supplementary Figure 5.9 covers two pages.

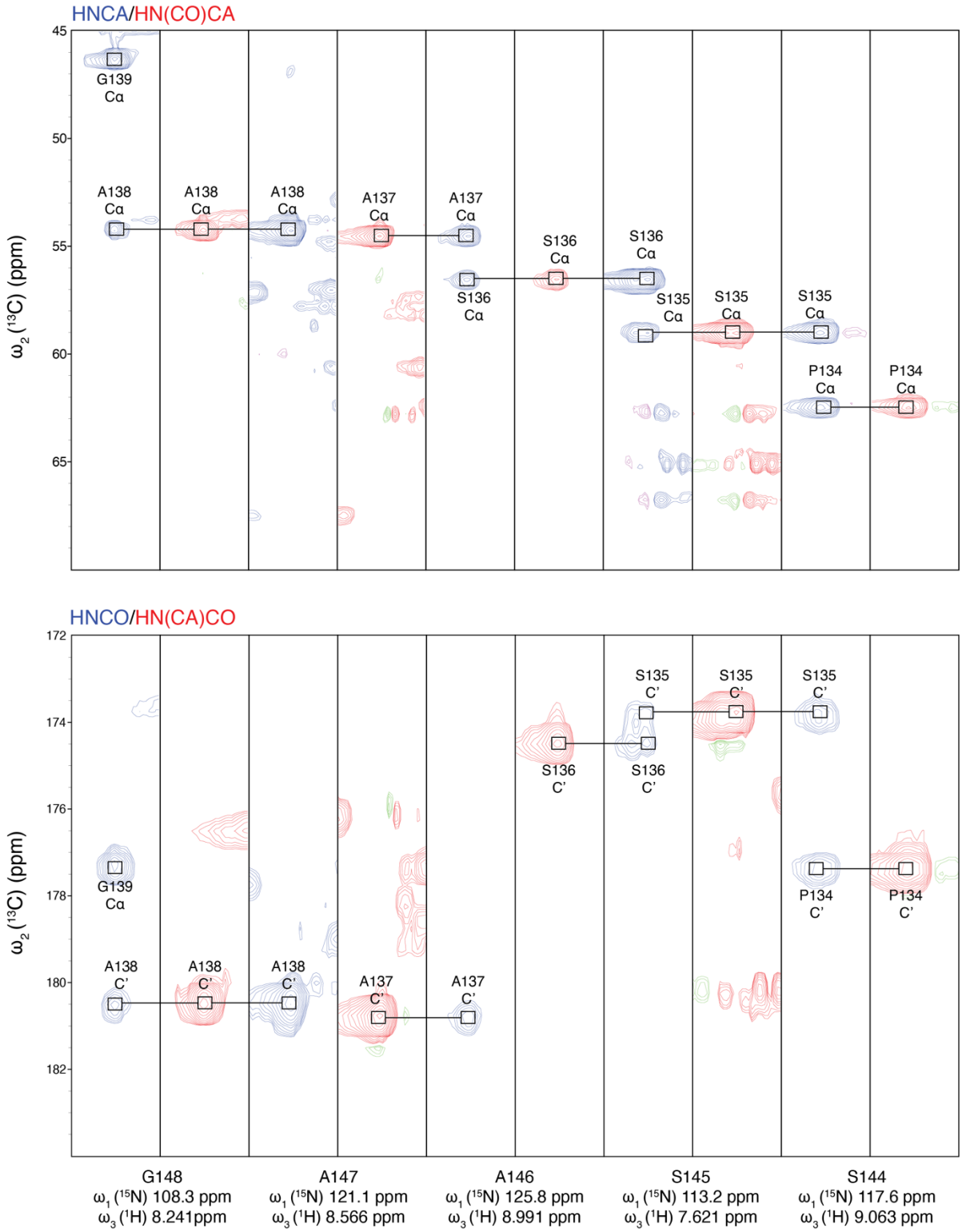
HNCA/HN(CO)CA
HNCO/HN(CA)CO
ω2 (13C) (ppm)
45
50
55
60
65
172
174
176
178
180
182
G139 Cα
A138 Cα
A137 Cα
S136 Cα
S135 Cα
P134 Cα
G139 C'
A138 C'
A137 C'
S136 C'
S135 C'
P134 C'
G148
ω1 (15N) 108.3 ppm
ω3 (1H) 8.241ppm
A147
ω1 (15N) 121.1 ppm
ω3 (1H) 8.566 ppm
A146
ω1 (15N) 125.8 ppm
ω3 (1H) 8.991 ppm
S145
ω1 (15N) 113.2 ppm
ω3 (1H) 7.621 ppm
S144
ω1 (15N) 117.6 ppm
ω3 (1H) 9.063 ppm

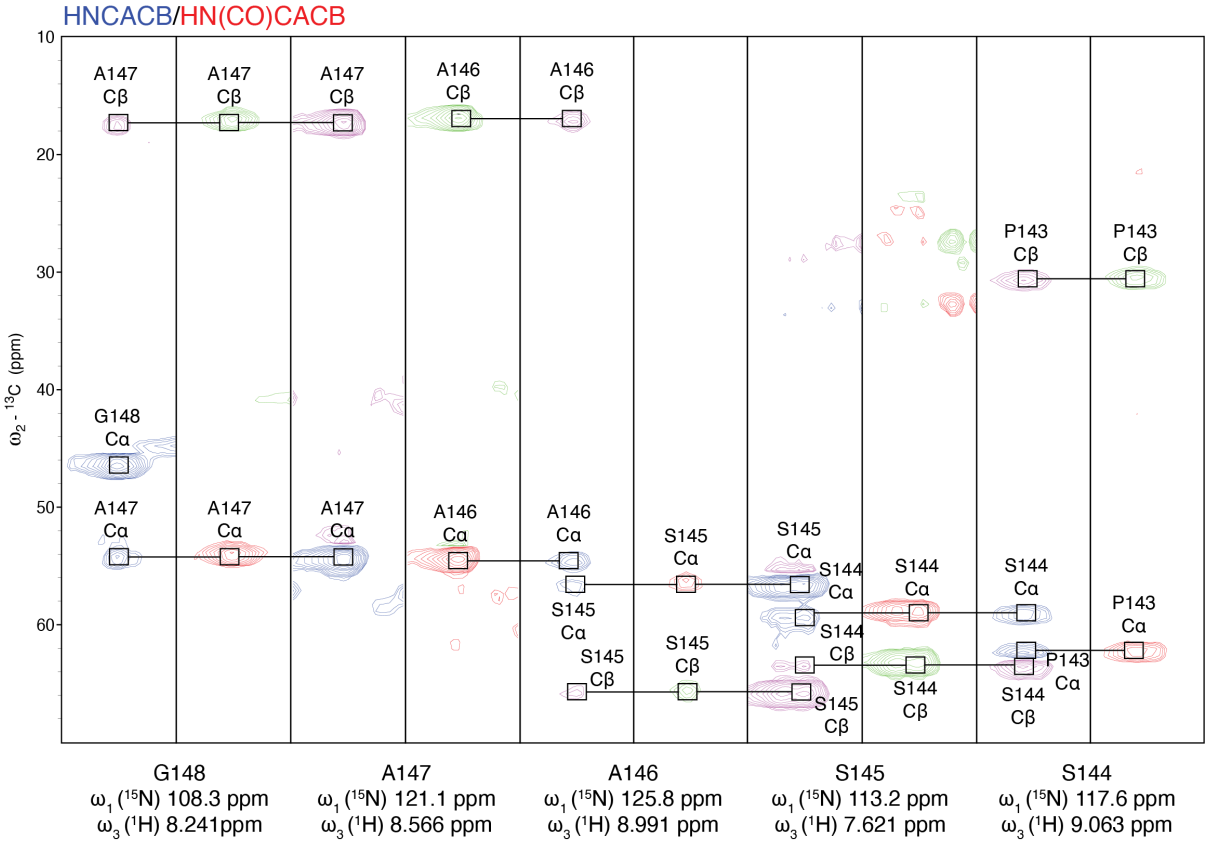

Supplementary Figure 5.10: Strip plots for part of the D helix and CD loop of IL-11$_{\Delta 10}$ Mutein.

Peak strips are shown for the HNCO/HN(CA)CO, HNCA/HN(CO)CA and HNCACB/HN(CO)CACB pairs. Spectra collected on 800 μM ^{15}N/^{13}C/^{2}H-IL-11$_{\Delta 10}$ Mutein at 20 °C, on an 18.8 T spectrometer. All spectra collected as TROSY-type spectra. Note Supplementary Figure 5.10 covers two pages.

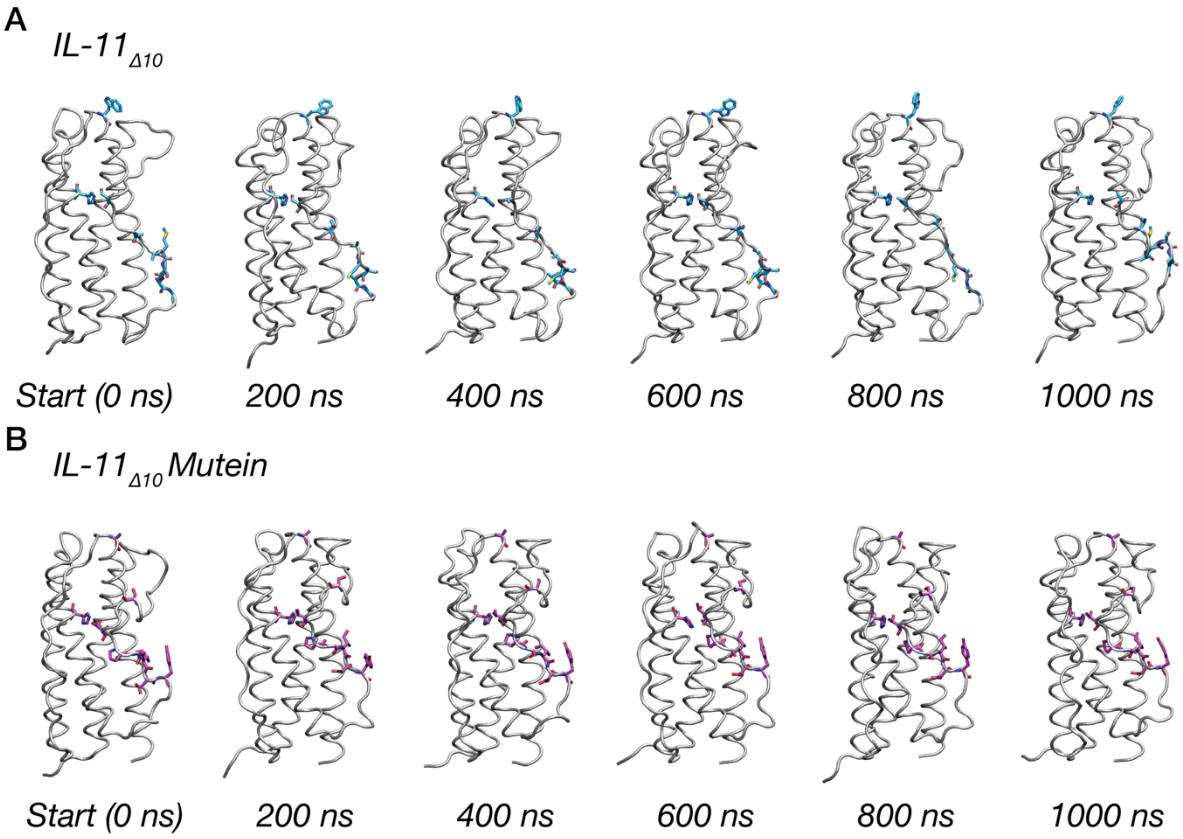

Supplementary Figure 5.11: Frames shown at 200 ns intervals from 1 µs MD simulations of IL-11$_{\Delta 10}$ and IL-11$_{\Delta 10}$ Mutein.

Residues involved in loop core interactions, the AMSAG/PAIDY sequence, and W147/A147 are highlighted in the frames. The α-helical core is coloured grey. A) Frames from the IL-11$_{\Delta 10}$ simulation, B) frames from the IL-11$_{\Delta 10}$ Mutein simulation.

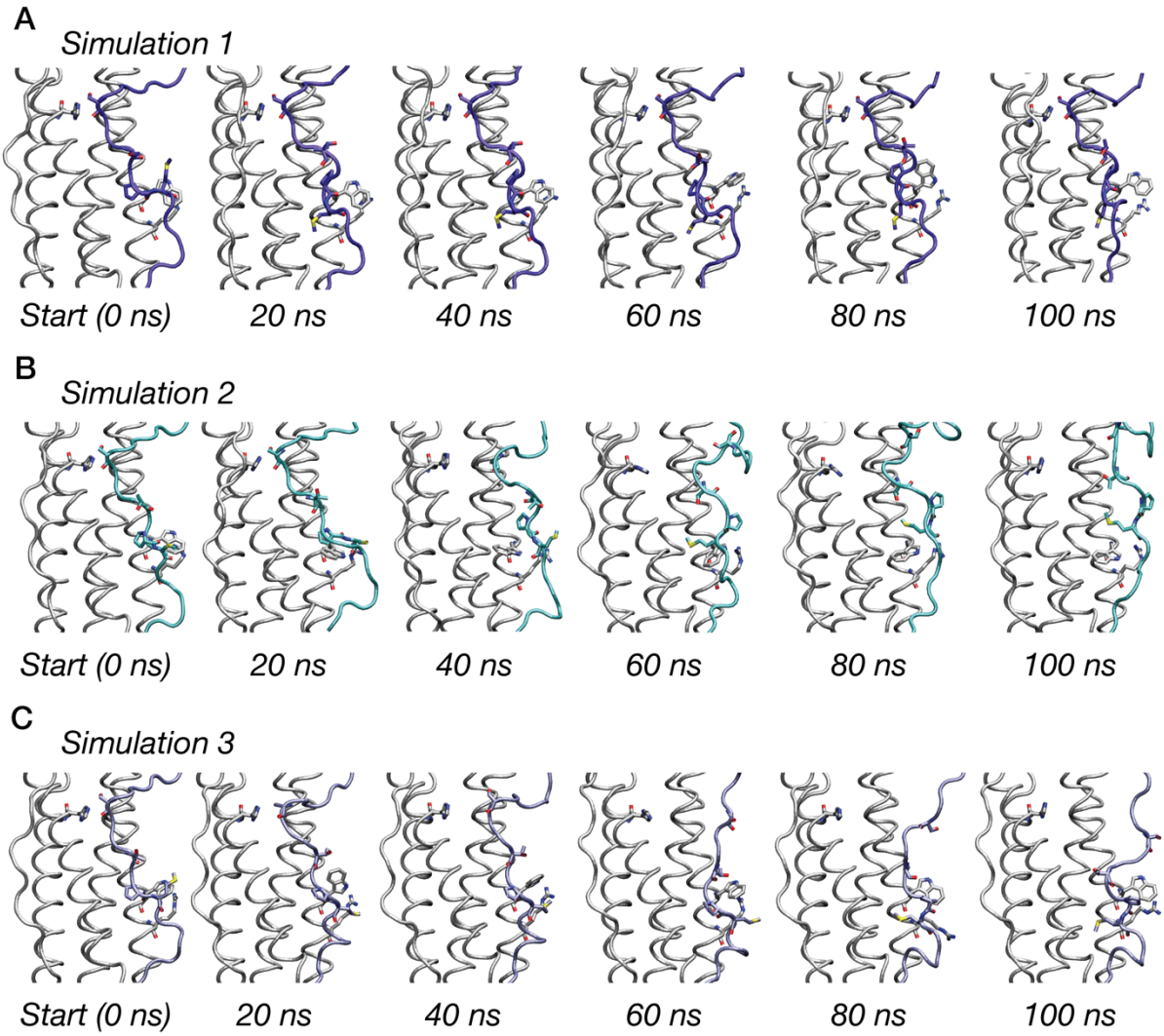

Supplementary Figure 5.12: Frames shown at 20 ns intervals from the three 100 ns MD simulations of IL-11$_{\Delta 10A58P/W147A}$.

The AB loop is highlighted in the frames, the α-helical core is coloured grey. A) Frames from simulation 1, B) frames from simulation 2 and C) frames from simulation 3.

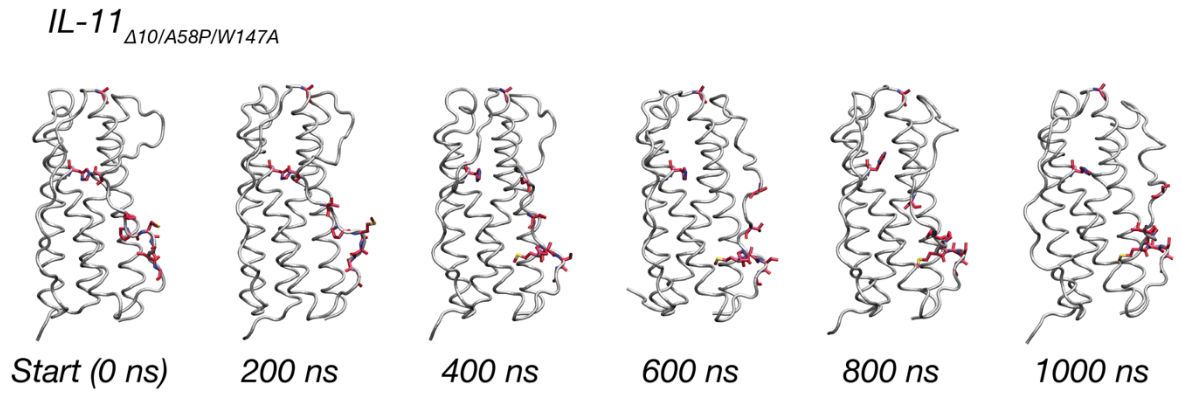

Supplementary Figure 5.13: Frames shown at 200 ns intervals from 1 µs MD simulations of IL-11$_{\Delta 10/A58P/W147A}$.

Residues involved in loop core interactions, the PMSAG sequence, and A147 are highlighted in the frames, the α-helical core is coloured grey.

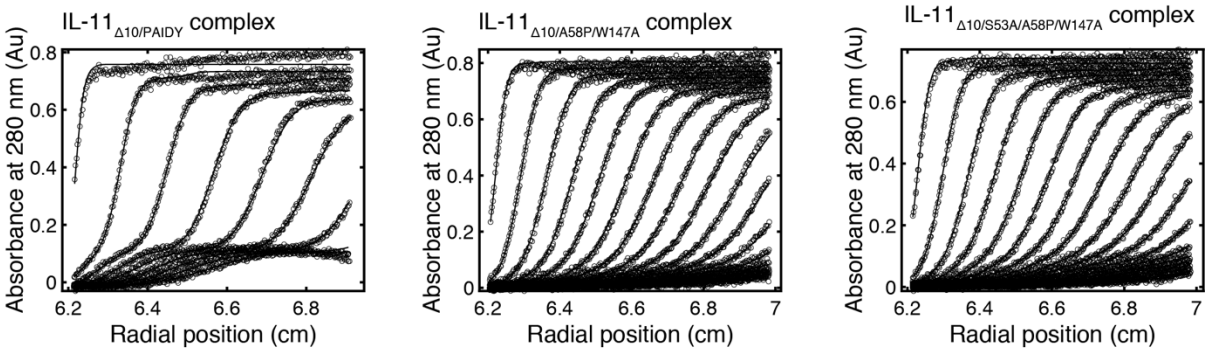

Supplementary Figure 5.14: Raw AUC data for the distributions shown in Figure 5.13.

Raw AUC data are shown as circles, overlaid with the best fit to a continuous size distribution [c(s)] model.

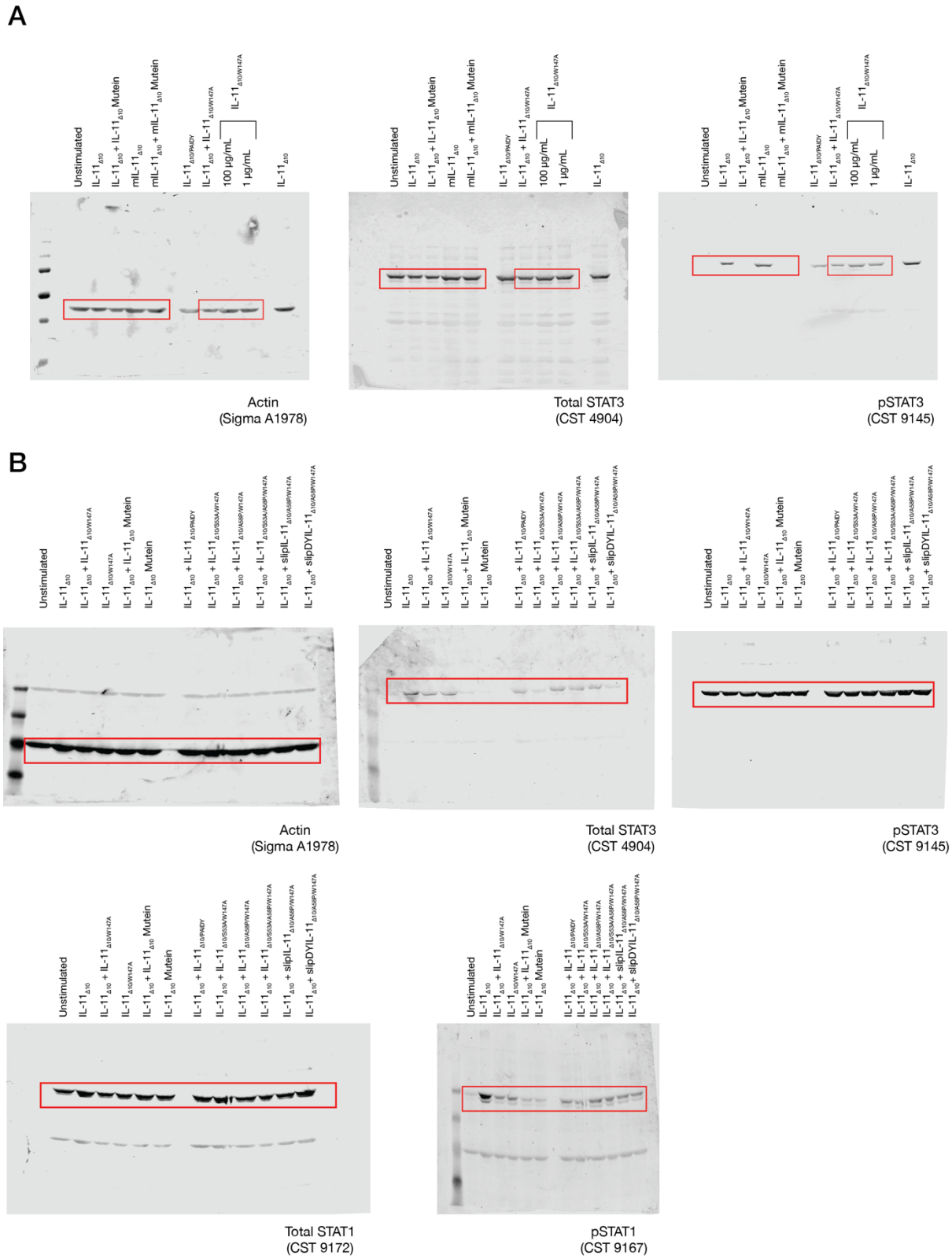

Supplementary Figure 5.15: Complete membrane images.

A) Complete images for Figure 5.2A, B) complete images for Figure 5.13B. The red box in the figure indicates the regions cropped to generate the figure. Antibodies used to probe the membrane are indicated in the figure.

5.6.2 Captions for supplementary movies

Supplementary movies are available for viewing online at https://melbourne.figshare.com/s/98b745061f7bb4c1d845.

Supplementary Movie 5.1: 1 μs molecular dynamics simulations for IL-11$_{\Delta 10}$ and IL-11$_{\Delta 10}$ Mutein.
The 1 μs simulation is shown in the movie. Residues involved in key loop-core interactions, the AMSAG sequence, and W147 are indicated in the movie. The trajectory frames are smoothed (window of 5 frames).

Supplementary Movie 5.2: 100 ns molecular dynamics simulations for IL-11$_{\Delta 10/A58P/W147A}$.
Three simulations are shown sequentially in the movie. Residues involved in key loop-core interactions are shown in the movie. The trajectory frames were smoothed (window of 5 frames).

Supplementary Movie 5.3: 1 μs molecular dynamics simulations for IL-11$_{\Delta 10}$ Mutein.
The 1 μs simulation is shown in the movie. Residues involved in key loop-core interactions, the PAIDY sequence, and A147 are indicated in the movie. The trajectory frames are smoothed (window of 5 frames).

5.6.3 Supplementary Tables

Supplementary Table 5.1: SV-AUC data and analysis.

Protein/complex	Expected mass (kDa)	Calculated mass (kDa)	Frictional ratio	Sedimentation coefficient (S)	Concentration
IL-11Rα$_{D1-D3}$/gp130$_{D1-D3}$/IL-11$_{\Delta10}$ Mutein complex	84.7	87.0	1.6	4.33	5 µM each component
IL-11Rα$_{D1-D3}$/gp130$_{D1-D3}$/mIL-11$_{\Delta10}$ Mutein complex	84.8	80.5	1.6	4.26	5 µM each component
IL-11Rα$_{D1-D3}$/gp130$_{D1-D3}$/muGFP-IL-11 Mutein complex	121.1	116.7	1.6	5.42	150 nM muGFP-IL-11 Mutein, 500 nM IL-11Rα$_{EC}$, 1 µM gp130$_{D1-D3}$
IL-11Rα$_{D1-D3}$/gp130$_{D1-D3}$/IL-11$_{\Delta10/W147A}$ complex	84.7	91.1	1.6	4.48	7 µM each component
IL-11$_{\Delta10}$ Mutein	18.2	19.4	1.4	1.7	43.9 µM

IL-11$_{\Delta 10/W147A}$	18.2	19.4	1.4	1.7	41.1 μM
IL-11Rα$_{D1-D3}$/gp130$_{D1-D3}$/IL-11$_{\Delta 10/A58P/W147A}$ complex	84.7 (trimer)	84.3	1.6	4.32	5 μM each component
IL-11Rα$_{D1-D3}$/gp130$_{D1-D3}$/IL-11$_{\Delta 10/S53A/A58P/W147A}$ complex	84.7 (trimer)	88.5	1.6	4.40	5 μM each component
IL-11Rα$_{D1-D3}$/gp130$_{D1-D3}$/IL-11$_{\Delta 10/PAIDY}$ complex	169.8 (hexamer)	170.6	1.6	7.07	5 μM each component

Supplementary Table 5.2: SAXS data acquisition and data processing statistics.

For the $IL11_{\Delta10}$ hexamer (Figure 5.2), these statistics are presented in Chapter 4.

	$IL11_{\Delta10}$ Mutein trimeric complex	*$IL11_{\Delta10}$ Mutein*	*$IL11_{\Delta10/W147A}$*
SAXS data collection			
Instrument/source	Australian Synchrotron SAXS/WAXS beamline equipped with Pilatus 2M detector and sheathflow cell for SEC-SAXS.		
Wavelength (Å)	1.078		
Beam energy (keV)	11.5		
Beam size (µm)	250 × 130		
Sample-to-detector distance (mm)	3538	2038	2210
q measurement range ($Å^{1}$) [a]	0.004-0.38	0.007-0.664	0.005-0.55
Absolute scaling method	Comparison with scattering from 1 mm pure water		
Normalization	To transmitted intensity from beamstop counter		
Exposure time	1 s measurements from SEC-SAXS elution		
Sample temperature (K)	293		
SEC-SAXS parameters			
Column	Superdex 200 5/150 Increase		
Flow rate (mL/min)	0.45		0.4
Loading concentration (mg/mL)	2	5	5
Injection volume (µL)	50		
Solvent	20 mM Tris-HCl pH 8.5, 150 mM NaCl, 0.2% sodium azide		
Software employed			
SAXS data reduction	*I*(*q*) vs *q* using Scatterbrain 2.8.2, SEC-SAXS solvent subtraction using *CHROMIXS* from *ATSAS* 2.8.3		

Basic analysis (Guinier, *P(r)*, molecular mass)	*PRIMUS* from *ATSAS* 2.8.3, *GNOM* from *ATSAS* 2.8.3		
Shape modelling	*DAMMIF* from *ATSAS* 2.8.3, *DAMAVER* from *ATSAS* 2.8.3, *DAMMIN* from *ATSAS* 2.8.3		
Calculation of theoretical intensities	*CRYSOL* from *ATSAS* 2.8.3		
Structural parameters			
Mass from V_c (kDa) (expected mass, ratio to expected, in brackets) [b]	87.9 (84.9, 0.96)	16.7 (18.2, 0.91)	16.7 (18.2, 0.91)
Guinier analysis [c]			
R_g (Å)	43.41 ± 0.18	17.82 ± 0.13	17.36 ± 0.12
I(0) (cm^1)	$0.033 \pm 8.4\times10^{-5}$	$0.0066 \pm 2.6\times10^{-5}$	$0.0051 \pm 2.1\times10^{-5}$
qR_g min,max	0.23, 1.29	0.20, 1.27	0.2, 1.32
P(r) analysis [c]			
R_g (Å)	45.24 ± 0.19	17.80 ± 0.88	17.33 ± 0.69
I(0) (cm^1)	$0.033 \pm 9.7\times10^{-5}$	$0.0066 \pm 2.2 \times 10^{-5}$	$0.0051 \pm 1.6 \times 10^{-5}$
D_{max} (Å)	156	54	52
Porod volume ($Å^3$)	159000	20000	22200
Shape modelling			
DAMMIF (10 calculations, default parameters)			
q range for fitting (Å)	0.00054 – 0.18		
Symmetry, anisotropy assumptions	*P*1, none		
Constant adjustment to intensities	1.67×10^{-4}		
NSD (standard deviations)	1.028 (0.081)		

χ^2 range	0.9981.018		
Resolution (from *SASRES*) [d] (Å)	47 ± 4		
DAMMIN (default parameters)			
q range for fitting (Å)	0.00054 – 0.18		
Symmetry, anisotropy assumptions	*P*1, none		
χ^2	0.975		
Constant adjustment to intensities	1.58×10^{-4}		
Atomic modelling			
CRYSOL (no constant subtraction)			
Structure	IL-11 hexamer crystal structure, one trimer (chapter 3, this thesis)	IL-$11_{\Delta 10}$ Mutein crystal structure (this work)	IL-$11_{\Delta 10/W147A}$ crystal structure (this work)
χ^2	1.56	1.37	0.91
Calculated R_g (Å)	43.58	17.61	17.39

[a] $q=(4\pi\sin\theta)/\lambda$

b 422

[c] Errors from *AUTORG* or *GNOM*, ± standard deviation

d 423

Supplementary Table 5.3: Binding affinities measured during this study.

For all ITC experiments, n = 3, for SPR experiments n = 2, errors given as standard errors. For MST experiments, n = 3, errors given as a 68% confidence interval calculated in *PALMIST*.

		Method	T (K)	K_D (nM)	ΔH (kJ/mol)	ΔS (J/molK)	ΔG (kJ/mol)	k_d ($\times 10^1$ s^1)	k_a ($\times 10^6$ M^1 s^1)
$IL11_{\Delta10}$ Mutein	$IL11Ra_{D1-D3}$	ITC	303	38 ± 9	25 ± 1.3	64 ± 4	44 ± 0.08		
$IL11_{\Delta10}$ Mutein/IL-$11Ra_{D1-D3}$	$gp130_{D1-D3}$	ITC	288	55 ± 4	23 ± 0.8	218 ± 3	40 ± 0.07		
$IL11_{\Delta10/W147A}$	IL-$11Ra_{D1-D3}$	ITC	303	10 ± 8	-22 ± 0.6	87 ± 11	-49 ± 2.7		
$IL11_{\Delta10/W147A}$/ IL-$11Ra_{D1-D3}$	$gp130_{D2-D3}$	ITC	288	130 ± 10	24 ± 0.8	220 ± 5	-38 ± 0.2		
$IL11_{\Delta10/PAIDY}$	IL-$11Ra_{D1-D3}$	ITC	303	81 ± 45	30 ± 2.2	39 ± 3.6	42 ± 1.4		
$IL11_{\Delta10/PAIDY}$/$IL11Ra_{D1-D3}$	$gp130_{D2-D3}$	ITC	288	60 ± 16	25 ± 0.9	220 ± 3	-39 ± 0.7		
$IL11_{\Delta10/PAIDY}$/$IL11Ra_{D1-D3}$	$gp130_{D1-D3}$	ITC	288	21 ± 17	31 ± 2.9	52 ± 6.4	46 ± 2.3		
$IL11_{\Delta10}$	IL-$11Ra_{D1-D3}$	SPR	298	78 ± 0.7				1.1 ± 0.02	1.4 ± 0.21
$IL11_{\Delta10}$ Mutein	IL-$11Ra_{D1-D3}$	SPR	298	33 ± 3				0.34 ± 0.007	1 ± 0.10
$IL11_{\Delta10}$	IL-$11Ra_{EC}$	MST	298	9 nM [unbounded, 0.028 nM]					

$IL11_{\Delta 10}$ Mutein	$IL\text{-}11R\alpha_{EC}$	MST	298	50 nM [unbounded, 0.168 nM]					
$IL11_{\Delta 10/PAIDY}$	$IL\text{-}11R\alpha_{EC}$	MST	298	51 nM [17 nm, 121 nM]					

Supplementary Table 5.4: X-ray data collection and refinement statistics.

Values in parentheses are for the highest resolution shell.

	IL11$_{\Delta 10}$ *Mutein*	*IL11*$_{\Delta 10/W147A}$	*IL11*$_{\Delta 10/PAIDY}$	*IL11*$_{\Delta 10/A58P/W147A}$	*IL11*$_{\Delta 10/S53A/A58P/W147A}$
Data collection					
Space group	*P* 2_1	*P* 2_1 2_1 2	*P* 2_1	*P* 2_1 2_1 2_1	*P* 2_1
Wavelength (Å)	0.9537	0.9537	0.9537	0.9537	0.9537
Number of images	3600	3600	3600	3600	3600
Oscillation range per image (°)	0.1	0.1	0.1	0.1	0.1
Detector	Eiger 16M	Eiger 16M	Eiger 16M	Eiger 16M	Eiger 16M
Cell dimensions					
a, *b*, *c* (Å)	27.23, 37.097, 68.532	38.505, 133.996, 27.087	27.249, 37.551, 70.482	38.871, 54.311, 134.558	27.063, 37.306, 68.582
α, β, γ (°)	90, 101.306, 90	90, 90, 90	90, 100.614, 90	90, 90, 90	90, 100.67, 90
Resolution (Å)	37.101.80 (1.841.80)	44.671.48 (1.511.48)	37.551.47 (1.491.47)	44.851.60 (1.631.60)	37.311.70 (1.731.70)
R_{sym}[†]	0.07 (1.167)	0.082 (1.859)	0.049 (0.639)	0.120 (1.957)	0.060 (1.200)
R_{meas}[§]	0.083 (1.374)	0.089 (2.003)	0.059 (0.758)	0.130 (2.114)	0.071 (1.438)
R_{pim}[‡]	0.043 (0.719)	0.034 (0.743)	0.031 (0.403)	0.049 (0.794)	0.037 (0.784)
$CC_{1/2}$	0.999 (0.603)	0.999 (0.590)	0.999 (0.811)	0.999 (0.566)	0.999 (0.599)
$I/\sigma(I)$	11.8 (1.4)	12.9 (1.3)	14.7 (2.1)	12.3 (1.3)	13.3 (1.3)
Total observations	85885 (5234)	313134 (16025)	161933 (7264)	506292 (25175)	1001634724
Unique reflections	12637 (761)	24354 (1182)	24094 (1120)	38570 (1889)	14775744
Completeness (%)	100.0 (100.0)	100.0 (100.0)	99.6 (94.3)	100.0 (99.8)	98.897.4
Multiplicity	6.8 (6.9)	12.9 (13.6)	6.7 (6.5)	13.1 (13.3)	6.86.3
Wilson *B* factor (Å^2)	25.604	23.185	24.030	15.938	24.8
Refinement					
Resolution (Å)	33.611.80 (1.861.80)	37.021.48 (1.531.48)	34.651.47 (1.521.47)	34.591.60 (1.661.60)	33.701.70 (1.761.70)

Reflections used in refinement	12627 (1241)	24296 (2361)	24073 (2337)	38478 (3754)	14736 (1377)
R_{free} reflections	1144 (133)	2361 (245)	2225 (213)	3571 (404)	747 (55)
R_{work}	0.1976 (0.3180)	0.1857 (0.2953)	0.1983 (0.2663)	0.1864 (0.3036)	0.1983 (0.2837)
R_{free}	0.2227 (0.3069)	0.2039 (0.2926)	0.2145 (0.3163)	0.2122 (0.3341)	0.2184 (0.3848)
Protein molecules in asymmetric unit	1	1	1	2	1
Total nonhydrogen atoms	1390	1429	1376	2928	1364
Protein	1304	1308	1281	2560	1279
Ligand/ion	5	6	5	12	6
Solvent	81	115	90	356	79
Mean B *factor (Å²)*	45.76	39.3	53.1	30.3	47.4
Protein	45.75	39.0	53.7	29.6	47.6
Ligand/ion	70.61	56.8	53.9	37.1	51.5
RMSD					
Bond lengths (Å)	0.01	0.01	0.01	0.01	0.01
Bond angles (°)	1.33	1.14	1.17	1.00	1.03
Ramachandran Plot					
Favoured (%)	98.20	98.80	98.77	98.80	97.60
Allowed (%)	1.80	1.20	0.62	1.20	2.40
Outliers (%)	0.0	0.0	0.59	0.00	0.00

† $R_{sym} = \sum_{hkl}\sum_i |I_i(hkl) \langle I(hkl)\rangle| / \sum_{hkl}\sum_i I_i(hkl)$

§ $R_{meas} = \sum_{hkl} [N/(N\ 1)]^{½} \sum_i |I_i(hkl) \langle I(hkl)\rangle| / \sum_{hkl}\sum_i I_i(hkl)$

‡ $R_{pim} = \sum_{hkl} [1/(N\ 1)]^{½} \sum_i |I_i(hkl) \langle I(hkl)\rangle| / \sum_{hkl}\sum_i I_i(hkl)$

$CC_{1/2}$ = Pearson correlation coefficient between independently merged half data sets

Supplementary Table 5.5: IL-11$_{\Delta 10}$ peak assignments.

Residue	Chemical shift (ppm)				
	^{1}H	^{15}N	^{13}C'	^{13}Cα	^{13}Cβ
Pro14			178.3	64.47	31.19
Arg15	8.169	118.2	177.9	59.36	28.46
Ala16	7.597	122.6	181.2	54.21	17.32
Glu17	8.048	119.1	180	58.11	28.63
Leu18	8.268	123.6	178.6	58.17	39.89
Asp19	17.86	121.5	179.2	57.76	39.09
Thr21			177.5	67.11	
Val22	9.009	127.2	177.8	62.22	30.45
Leu23	7.928	113.5	180.1	58.53	40.3
Leu24	7.732	120.2	179.3	57.39	40.94
Thr25	8.157	118.6	176.3	67.91	66.86
Arg26	8.779	120.9	179.7	60	29.33
Ser27	8.155	117.5	176	60.95	62.1
Leu28	8.004	123.2	180.1	56.91	41.1
Leu29	8.592	125	177.8	58.63	40.59
Ala30	7.637	122.6	180.2	54.75	16.98
Asp31	8.362	120.4	179.8	57.25	39.81
Thr32	8.543	118.1	177.3	67.38	
Arg33	8.337	119.6	179	59.14	27.74
Pro44			177.2	63.35	30.95
Ala45	8.323	124.3	176.8	51.63	18.87
Asp46	8.321	121.4	176.4	53.43	40.87
Glu47	8.121	108.9	173.2	44.59	
Asp48	8.096	120	175.9	53.73	40.57
His49	8.261	120.6	173.7	54.86	28.6
Asn50	8.457	120.3	175	52.68	39.81
Thr56			174.5	61.53	68.87
Leu57	8.376	126.9	176.8	54.76	40.79
Ala58	8.193	126.3	177.4	52.16	17.74
Met59	7.94	119.4	176.1	55.03	31.63
Ser60	8.021	116.9	174.5	57.91	63.36
Ala61	8.357	125.6	178.7	52.95	17.98
Glu62	8.161	107.3	174.3	44.83	
Ala63	7.894	124.1	178.2	52.47	18.16
Leu64	7.963	120.3	177.7	55.29	40.81
Glu65	7.959	107.9	173.8	44.67	
Ala66	7.986	123.5	178.5	52.64	17.74
Leu67	8.006	118.7	177	55.83	41.16
Pro70			176.9	63.57	33.81
Glu71	8.862	114.3	175.5	47.26	
Val72	8.315	118.9	176.1	64.09	31.83
Leu73	7.691	118.5	178.2	56.98	
Leu80			178.6	58.04	39.79

Leu81	8.403	121.4	179.7	57.71	39.1
Ser82	8.2	116	179.6	61.26	62.2
Tyr83	8.098	121.6	178.4	57.63	40.77
Leu84	8.51	120.7	180.2	58.67	40.48
Trp89			179.6	57.88	27.95
Leu90	8.792	120.8	178.5	57.56	40.54
Arg91	7.849	118.1	177.5	58.75	29.23
Arg92	7.611	117.5	177.6	57.03	29.88
Ala93	8.271	121.6	178.1	51.74	18.32
Gly94	7.494	106.2	173.8	45.81	
Gly95	7.856	106.9	175.8	44.16	
Leu98			178.4	54.53	40.11
Lys99	7.501	120.4	179.4	58.85	30.94
Thr100	7.788	110.6	175.2	64.05	68.48
Leu101	7.599	120.9	175.8	53.74	41.06
Glu102	7.379	121.2	174.9	60.66	26.04
Glu104			180.5	59.13	28.49
Leu105	8.75	121.3	179.1	57.34	40.88
Gly106	8.857	108.4	177.3	46.13	
Thr107	7.95	121	175.9	66.01	67.7
Leu108	8.166	125.2	178.6	58.3	40.66
Gln109	8.491	118.5	177.3	59.75	27.78
Ala110	7.715	120.2	181.6	54.58	17.23
Arg111	8.553	120.2	178.8	59.38	28.16
Ser124			178.2	60.93	62.36
Arg125	8.227	123.3	178	57.26	28.4
Leu126	7.675	118.5	175.1	54.31	40.9
Ala127	7.893	120.5	176.7	52.24	15.46
Leu128	7.809	119.9	175	52.43	39.9
Pro133			176.5	62.29	30.66
Asp134	8.331	123.3	174	52.66	39.61
Pro136			176.1	62.24	30.75
Ala137	8.352	126.6	175	49.6	17.18
Pro139			176.5	62.07	30.26
Leu140	7.863	124.5	176.5	53.79	40.73
Ala141	8.278	127.9	175.5	50.11	16.72
Ala146			180.5	54.38	17.13
Trp147	8.477	119	177.7	58.7	28.42
Gly148	8.157	108.9	177.1	46.47	
Gly149	8.009	110.7	174.5	46.44	
Ile150	7.524	123	177.9	63.4	36.06
Arg151	8.226	119.1	179.5	59.74	28.9
Ala152	7.87	120.9	179.1	54.56	17.16
Ala153	8.319	121.1	179	55.39	17.55
His154	8.156	116.8	179.5	60.04	30.38
Ala155	7.771	122.7	180.8	54.72	17.98
Ile156	8.935	120.6	177	64.91	37.79

Leu157	8.566	117.8	179.1	57.15	39.51
Gly158	8.14	106.7	176.7	46.52	
Gly159	8.054	110.4	176.8	46.66	
Leu160	8.252	126.5	177.8	57.16	39.8
Leu162			180	57.65	40.88
Thr163	8.161	118.2	176.1	66.98	68.13
Leu164	8.566	121.6	177.7	57.08	40.8
Asp165	8.147	120.6	178.5	57.43	40.99
Trp166	7.839	119.8	178.4	60.46	28.35
Ala167	8.625	122.6	179	54.8	18.27
Val168	8.075	117.4	177.1	67.4	30.69
Arg169	7.253	116.7	180	59.2	29.04
Gly170	8.668	107.5	175	46.59	
Leu171	8.695	122	179	57.5	40.89
Leu172	8.082	117.9	180.6	57.33	40.05
Leu173	7.523	120.8	180	57.01	40.43
Leu174	7.984	121.3	178.5	57.07	40.37
Lys175	7.773	118.2	177.9	59.11	31.45
Thr176	7.424	107.9	175.2	63.23	69.06
Arg177	7.7	120.7	175.5	55	29.71
Leu178	7.185	126.9	182	56.19	42.28

Supplementary Table 5.6: IL-11$_{\Delta 10}$ Mutein peak assignments.

Residue	Chemical shift (ppm)				
	^{1}H	^{15}N	^{13}C'	^{13}Cα	^{13}Cβ
Pro14			178.2	64.52	31.27
Arg15	8.162	118.1	177.9	59.47	28.47
Ala16	7.596	122.5	181.1	54.18	17.3
Glu17	8.034	119.1	180	58.1	28.57
Leu18	8.308	123.8	178.5	58.21	40.09
Val22			177.4	67.51	30.47
Leu23	7.927	121.1	180.2	58.5	40.34
Leu24	7.68	120	179.5	57.41	41.1
Thr25	8.166	118.8	176.3	68	66.9
Arg26	8.852	121.2	179.6	59.98	29.29
Ser27	8.113	117.3	176	61	62.23
Leu28	7.962	123.1	180.1	56.91	40.97
Leu29	8.581	125	177.9	58.64	40.89
Pro44			177.5	63.32	31.07
Ala45	8.428	124.6	177.3	51.8	18.47
Asp46	8.255	120.8	176.5	53.79	40.97
Glu47	8.175	109	173.6	44.73	
Asp48	8.129	120.1	176.2	53.92	40.66
Arg85			180.5	58.82	28.66
His86	8.395	119.6	177.5	61.63	27.63
Val87	9.055	123.8	177.3	67.51	30.57
Gln88	8.538	118.9	178.8	58.97	27.41
Trp89	7.99	120.4	177.6	60.15	27.71
Leu90	8.496	121.3	179	57.01	41.46
Arg91	7.81	115.6	177.7	58.66	29.63
Arg92	7.603	117.3	177.6	56.95	29.97
Ala93	8.298	121.7	178	51.76	20.92
Gly94	7.497	106.2	173.8	45.78	
Gly95	7.926	107.3	175.8	44.16	
Ser96	8.639	115	177.2	60.99	62.7
Ser97	8.229	118.5	175.8	61.02	62.12
Leu98	7.468	120.8	178.9	55.11	39.43
Lys99	7.548	117.3	178.6	58.3	30.62
Thr100	7.438	110.3	174.9	63.5	68.76
Leu101	7.482	119.6	175.8	54.07	40.33
Glu102	7.262	118	176.1	53.7	27.96
Pro103			177.4	62.98	33.14
Glu104	9.476	128.2	179.9	61.73	27.69
Leu105	8.968	122	178.2	57.72	39.91
Gly106	8.854	110.3	177.5	46.03	
Thr107	8.369	122.4	175.6	66.01	67.6
Leu108	8.162	125.2	178.7	58.35	40.47
Gln109	8.078	118.4	177.2	59.84	27.9

Ala110	7.731	120.2	181.6	54.69	17.29
Arg117			179.8	58.99	28.52
Arg118	8.236	121.4	179.5	57.96	28.13
Leu119	8.928	121.2	178.5	57.43	40.59
Gln120	7.954	119.5	178.7	58.87	27.38
Leu121	7.758	121.9	179.5	57.49	40.49
Leu122	8.118	121.7	178.4	57.67	40.29
Met123	8.362	116.5	177.9	59.78	31.98
Ser124	7.785	113.9	178.1	60.97	62.54
Arg125	8.238	123.4	177.9	57.3	28.4
Leu126	7.645	118.5	175.1	54.28	40.88
Ala127	7.887	120.4	176.7	52.27	15.44
Leu128	7.821	119.8	175	52.51	39.83
Pro133			176.4	62.35	30.69
Asp134	8.336	123.3	174	52.75	39.8
Pro136			176.1	62.26	30.77
Ala137	8.366	126.6	175	49.68	17.21
Pro139			176.4	62.15	30.29
Leu140	7.892	124.7	176.5	53.82	40.75
Ala141	8.309	128.3	175.7	50.17	16.72
Pro143			177.4	62.28	30.6
Ser144	9.074	117.3	173.8	59.06	63.01
Ser145	7.625	113.3	174.5	56.58	65.77
Ala146	8.994	125.8	180.8	54.55	17.05
Ala147	8.57	121.1	180.5	54.25	17.31
Gly148	8.238	108.2	177.3	46.35	
Gly149	8.075	111.7	174.7	46.59	
Ile150	7.501	122.3	177.9	63.37	35.97
Arg151	8.141	119.3	179.8	59.81	29.2
Ala152	8.067	121.2	179.1	54.8	17.16
Ala153	8.284	121.3	179.2	55.37	17.57
His154	8.251	116.6	179.5	59.94	30.3
Ala155	7.847	122.9	180.8	54.73	17.74
Ile156	8.87	120.3	177	65.09	38.74
Leu157	8.547	117.8	179.1	57.3	39.72
Gly158	8.176	106.7	176.7	46.53	
Gly159	8.084	110.3	176.4	46.79	
Leu160	8.252	125.8	178	57.25	40.08
Trp166			178.1	60.86	27.86
Ala167	8.629	122.1	178.9	54.67	18.09
Val168	8.24	117.6	177	67.46	30.66
Arg169	7.188	116.5	180	59.22	28.97
Gly170	8.586	107.2	175	46.54	
Leu171	8.656	121.8	177.7	57.22	40.81
Leu174			178.5	57.12	40.32
Lys175	7.801	118.4	177.8	59.06	31.43
Thr176	7.426	108	175.2	63.37	69.16

Arg177	7.67	120.7	175.5	54.98	29.7
Leu178	7.186	126.9	182	56.28	42.36

Chapter 6 – Discussion and conclusion

6.1 General discussion

Cytokines are a loosely defined class of proteins with numerous roles in physiology and disease[2]. The largest class of cytokines is the four-α helical bundle 'superfamily'[38,40]. Due to the role of cytokine signalling in normal physiology, particularly in the immune system, and the role of dysregulated cytokine signalling in diseases including cancer, understanding the molecular mechanisms underpinning cytokine signalling is critically important. This is both for general scientific interest and therapeutic interest, as a comprehensive understanding of cytokine signalling allows the informed design of novel therapeutics.

Interleukin-11 (IL-11) has classically been associated with haematopoiesis[5] and megakaryocytopoiesis[174]. In recent years, IL-11 signalling has been assigned roles in several diseases, including in fibrotic diseases[230,233], and in cancer[208]. For this reason, IL-11 signalling inhibitors are under active preclinical development by our group and others. Rational design of these inhibitors is hindered by a lack of knowledge on the structure of the IL-11 receptor, and the IL-11 signalling complex. A low resolution cryoEM map of the IL-11 signalling complex was reported in 2007[130], and our laboratory solved the structure of IL-11 in 2014[109], other than this, there is no published structural knowledge on the structure of IL-11, IL-11Rα or the complex that IL-11 forms with IL-11Rα and gp130. The overarching aim of this thesis was to address this gap in our knowledge.

A prerequisite for the results discussed here was the development of robust and reliable methods for the production of IL-11 and the IL-11 receptors. We reported new methods for the expression and purification of IL-11 and IL-11Rα and designed several functional IL-11 fusions. Specifically, the methods presented for the high-level production of IL-11 have enabled the production of large amounts of biologically active IL-11 Mutein for functional *in vivo* studies by others. We also presented methods for the expression of IL-11Rα. Broadly, these methods allowed the subsequent structural studies presented in this thesis. They have also allowed the production of large amounts of recombinant protein for immunisation (of both mice and alpacas) to develop antibodies that will be useful agents for the

modulation of IL-11 signalling. In the future, the ability to rapidly and easily produce large amounts of biologically active IL-11 and IL-11Rα will enable and significantly simplify structural and biological studies of IL-11 signalling.

The specific receptor for IL-11 is IL-11Rα. In chapter 3, we presented the crystal structure of IL-11Rα. Our crystal structure showed differences to related cytokine receptors. In particular, the cytokine binding site had a more hydrophobic character, which was corroborated experimentally by ITC experiments. We also observed structural differences in IL-11Rα when compared with IL-6Rα, particularly in the relative positioning of D2 and D3. Mutations in IL-11Rα have previously been implicated in a genetic disease associated with craniosynostosis. Using our structure, we showed that several of the mutations disrupted structural elements or interdomain interactions. The structure will allow rationalisation of the effect of new disease mutations as they are discovered and will also enable existing disease and cancer associated mutations to be mapped to the structure (e.g. those on the *COSMIC* database[462]).

We also designed, developed and characterised a fusion of IL-11 with a monomeric, ultrastable GFP[385]. The use of GFP in quantitative biophysical experiments has previously been hindered by transient self-association of GFP[388] (with a K_D of approximately 100 μM). Our experiments to measure the muGFP-IL-11/IL-11Rα interaction using AUC are a proof-in-principle study that muGFP fusions can be used in quantitative biophysical experiments. The K_D that was measured by fluorescence AUC was in close agreement with the K_D obtained using other techniques (including ITC, MST and SPR), providing validation of the fluorescence AUC/muGFP approach. The muGFP-IL-11 fusion could also be a useful reagent more generally, for example, in microscopy or to detect IL-11Rα expressing cells in fluorescence activated cell sorting (FACS) experiments.

A full understanding of the interactions that form the IL-11 signalling complex necessitated the determination of the structure of the IL-11 signalling complex. In parallel, we solved the structure of the complex by X-ray crystallography and

cryoEM. We were able to map in detail the interfaces that form the complex, giving us a detailed, atomic-level understanding of the complex and the interactions that form it. The structures did not reveal any unexpected interfaces, with the ten interfaces forming the complex analogous to the ten present in the hexameric IL-6 complex[74]. We complemented our structures with extensive biophysical analysis of the complex, showing that it is hexameric in solution and forms in three steps.

Our cryoEM structure of the IL-11 signalling complex is the first four α-helical bundle cytokine signalling complex to be solved to high resolution by cryoEM. The term 'resolution revolution,' from a now-classic perspective in *Science*[463] has become cliché to describe the advances in cryoEM technology and methodology over the past half-decade. The structures of biologically important proteins and protein complexes, both large and small, are now routinely solved by cryoEM[354,464-474]. It is used to solve the structure of targets, which, for reasons of inherent conformational heterogeneity[354,464,468] or limited availability of sample material[354,469,471,472], would be intractable by traditional high-resolution structural biology techniques. It is somewhat surprising that no other cryoEM structures of cytokine signalling complexes have been reported. Our efforts to solve the complex by cryoEM were hindered by preferential complex orientation, leading to severe orientation bias, which we could not overcome with extensive screening of blotting conditions, addition of detergents or crosslinkers, or by altering buffer conditions. In other respects, the IL-11 signalling complex was well suited for studies by cryoEM, being easily reconstituted *in vitro* and purified, stable, not prone to dissociation on vitrification and homogenous. Our efforts to solve the complex structure by cryoEM were more rapid then efforts to solve the complex structure by X-ray crystallography, and the phasing and refinement of the crystal structure was greatly simplified by the cryoEM structure. It is also worth noting that the quality of the cryoEM density maps was generally higher than the X-ray electron density maps, despite the nominally similar resolution, as the phase information obtained from the cryoEM data was more accurate than that obtainable by crystallography. Six years into the resolution revolution, X-ray crystallography remains the method of choice to study cytokine signalling complexes[323,350,360,475]. CryoEM will likely find utility in the

study of entire extracellular complexes and full-length cytokine signalling complexes, including the transmembrane and intracellular regions, which have so far been intractable to study by crystallographic methods.

The structures of the IL-11 signalling complex presented here are the fourth high-resolution IL-6 family cytokine structures to be reported. Previously, high-resolution structures have been reported of the viral IL-6[73] and IL-6[74] signalling complexes and LIF[80] in complex with gp130. Our structures allow comparison of the binding surfaces accessed on gp130 by the cytokines. The cytokines bind a common binding surface in the CHR of gp130[80,107]. IL-11 and IL-6 bind similar surfaces on the CHR of gp130. Sidechain rearrangements on cytokine binding to gp130 result in a different surface presented to the different cytokines, with four arginine residues on IL-11 protruding into pockets formed by this rearrangement. IL-6Rα and IL-11Rα also form interactions with gp130, the chemical nature of these interactions differing between the two cytokines. The final interaction that forms the signalling complex is between site-III on the cytokine and D1 of gp130. This interaction is unique to IL-6, IL-11 and vIL-6, LIF forms a similar, yet distinct, interaction with Ig domain D3 and D4 of LIFR[64]. A similar region on the four cytokines is involved in forming the interaction, with a conserved tryptophan residue in site-III being the critical residue for the interaction. The site-III interface in the IL-6/IL-11 complexes includes a second, coupled, interface between the α-receptor and gp130 (site-IIIB). In both complexes the interface is relatively small, burying approximately 200 $Å^2$ in surface area, and is accessory to complex formation. Overall, the site-III interface in the IL-6 complex is more extensive compared with the equivalent interface in the IL-11 complex. The IL-11 site-III interface is more electrostatic in character, which likely explains the overall similar affinity between the two interactions. More generally, the similar complexes formed by the IL-6 family cytokines, and broadly chemically similar interfaces, likely imply a common ancient evolutionary origin of the cytokines and receptors in the family.

An overarching question in cytokine signalling is how complex formation on the extracellular side transmits a signal to the JAK kinases associated with the

intracellular side of the receptor, to activate the kinases and trigger the intracellular signal transduction cascade. This question is one shared with other signalling systems, for example, in recent years much effort has been expended in gaining a molecular-level understanding of receptor activation and signal transduction in G-protein coupled receptors[468,476,477] and in the insulin receptor[478-480]. The cytokine system for which the mechanism of signal transduction has been best explored is the growth hormone/growth hormone receptor system. GHR exists as a preformed dimer in the cell membrane[98]. Growth hormone binding results in the activation of the pre-formed receptor dimer, due to a rearrangement of the transmembrane α-helices, which results in the lifting of the auto-inhibition of the intracellular kinases[98]. The universality of this mechanism, however, remains to be established. This is particularly the case for more complex cytokine signalling systems. There is evidence that gp130 is pre-dimerised in the cell membrane[100,101] and activating mutations in D2 of gp130 have been described[127,128], showing that gp130 can be active in the absence of cytokine. For IL-6 and IL-11, this does lend support to a mechanism analogous to that of growth hormone, where cytokine binding activates a preformed cytokine-receptor dimer. Other IL-6 family cytokines, such as LIF and OSM signal through a heterodimer of gp130 and a second receptor, which is likely not pre-dimerised[100], so the mechanism for signalling induction is likely different. Broadly, the mechanism for JAK activation by gp130 remains to be established.

A second question raised by the structures of the IL-11 signalling complex is the role of the membrane-proximal domains of gp130 (D4-D6), the disordered linker in IL-11Rα and the transmembrane domains in both receptors. Low resolution cryoEM maps have been published of the complete extracellular IL-6 complex[143], the IL-11 complex[130], and the LIF complex[71], and a negative-stain EM study has been reported of the complete IL-6 complex, including the intracellular domains[76]. Combined with the full-length extracellular structure of gp130[63], these maps allow models to be developed of the full-length extracellular complexes. The resolution in these structures was not high enough to identity or describe interactions between the D4-D6 ‘legs’ of the two gp130 molecules in the complex, or between the disordered membrane-proximal linker of the α-receptor and gp130. An open

question is the role of the disordered linker in the α-receptor – does it merely function as a spacer between the structured domains and the transmembrane domain, or does it contribute additional binding affinity to the complex? This has been explored previously, with the IL-6Rα/IL-11Rα linker shown to be a requirement for classic signalling, but not a requirement for cell-surface expression[118,119], with a minimum length of 22 residues in IL-6Rα [119] or 23 residues in IL-11Rα [118] required for classic signalling. The linkers are interchangeable between the two proteins, suggesting that they do not form complex-specific interactions[120]. The transmembrane domains are also interchangeable between IL-6Rα and IL-11Rα [120] The existence of low-affinity interactions between the linker regions and other components of the signalling complexes, which may contribute energy to complex formation, has not been investigated. Likewise, interactions between the transmembrane domains of gp130 and the α-receptors have not been investigated. Overall, the answers to these questions necessitate the acquisition of high-resolution information on the complete extracellular signalling complexes formed by IL-11 and IL-6.

The mechanistic role of the non-signalling IL-6 and IL-11 α-receptors is also unclear. The IL-6 family α-receptors clearly have a role in restricting cytokine signalling to specific cell types[481], which lead to distinct biological effects from IL-6 and IL-11. The use of cytokine α-receptors is common to other signalling systems. For example, in the IL-2/IL-15 system, the IL-2Rα/IL-15Rα receptor presents the cytokine to a dimer of the signalling receptors, IL-2Rβ/γ_c, either on the same cell or in *trans*[151,152]. Here, the α-receptor does not form extensive contacts with the remainder of the complex[49,153] and IL-2/IL-15 can bind IL-Rβ/γ_c in the absence of the α-receptor[482]. The distinct biological effects from IL-2Rα/IL-15Rα dependent signalling are most likely a consequence of limited expression of the α-receptors, and differential effects from activation of cells with and without the α-receptor[329]. The interaction between IL-6/IL-11Rα and gp130 is fundamentally different in character, with interactions between the α-receptor and gp130 critical for complex formation, and the cytokine not engaging gp130 in the absence of the composite binding interface formed with the α-receptor. The role of the α-receptors in

downstream signal transduction, if any, remains to be characterised. For example, the distinct interactions formed between the extracellular domains of gp130 and the cytokine/α-receptor complex may affect downstream intracellular signalling. There may be additional, uncharacterised interactions between the unresolved extracellular regions, the transmembrane domains, and the intracellular region of the α-receptor. A potentially informative cytokine signalling here is viral IL-6, which can form a gp130-containing signalling complex both with and without IL-6Rα[107]. The presence of IL-6Rα increases the potency of vIL-6[107], but distinct responses from IL-6Rα-dependent and independent vIL-6 signalling have not been studied. An equivalent to vIL-6 has not been identified for IL-11, but the influence of the α-receptors could be studied using a protein design approach. For example, IL-11 mimics could be designed which can bind gp130 in the absence of IL-11Rα or retain the gp130 binding sites from IL-11, and gain IL-6Rα binding. Investigating the biological effects of such designer cytokines could lead to insights into the roles, of the α-receptors in signal transduction. A similar approach has been used recently to design a novel IL-6/CNTF mimic with unique biological effects[483], and has been used previously to design cytokine mimics that activate non-natural receptor dimers[484]. Establishing if the α-receptors merely act as a structural scaffold in complex formation or serve to affect or bias downstream signal transduction pathways remains to be investigated.

Our ultimate goal in structurally characterising the IL-11 signalling complex was to provide a structural scaffold for the design of future inhibitors. As discussed extensively in Chapter 1, several approaches are used to modulate the interactions involved in cytokine signalling, such as targeting with antibodies, mutant cytokines, designed proteins and small molecules. So far, existing IL-11 antagonists have been designed based on homology models of IL-11, or by homology to other IL-6 family cytokines, as no high resolution structural information was available for IL-11 or the IL-11 signalling complex[198,352].

Efforts to develop antibodies and nanobodies targeting the IL-11 signalling complex are ongoing in our laboratory, and we have already used the structural knowledge

presented in this thesis to understand the mechanism of action of a Fab fragment from an antibody against IL-11Rα (Griffin M.D.W., unpublished), which is a preclinically validated IL-11 inhibitor. We are also undertaking a mouse and alpaca immunisation program to develop novel antibodies and nanobodies. Our structures will allow the rationalisation of the mechanism of action of the antibodies or nanobodies, especially when combined with high-resolution structures of the antibody/antigen or nanobody/antigen complexes. The antibodies that we will develop will be useful experimental tools, particularly as we are currently lacking robust and validated experimental tools. They may find use experimentally as IL-11 signalling inhibitors or to detect IL-11 or the IL-11 receptors, for example, to detect IL-11Rα by western blotting or to detect IL-11Rα or IL-11Rα-expressing cells in FACS experiments or using microscopy. Non-neutralising nanobodies in particular will be useful reagents for microscopy, as the relatively small size of a nanobody when compared with a full-length antibody is ideal for super-resolution microscopy, as the fluorophore is located closer to the epitope it targets[485-487]. Antibodies that specifically neutralise IL-11 signalling may eventually become drug candidates to treat diseases resulting from aberrant IL-11 signalling.

Small molecule targeting of protein-protein interactions is inherently difficult, as the binding interfaces are large and typically difficult to target using small molecules[251]. Several small molecules targeting gp130 have been previously described[252,256,260]. One small molecule, the drug bazedoxifene, which was identified by an *in silico* screen of the IL-6/gp130 D1 interface[260]. Bazedoxifene is effective in inhibiting IL-11 signalling[140]. In our structure of the IL-11 signalling complex, the binding surface on gp130 presented to IL-11 is similar, rationalising the fact that bazedoxifene inhibits signalling by both IL-6 and IL-11. More generally, our structures of IL-11 and the IL-11 signalling complex also allow future studies to screen and develop small molecules targeting signalling. A fragment-based approach has been used previously to design an IL-2/IL-2Rα inhibitor[488], *in silico* screening is also a common approach[260].

No small molecules have been designed which target the IL-11/IL-11Rα interaction. Given the importance of loop-core interactions in controlling the stability of the AB loop, and in engaging with IL-11Rα, it is tempting to speculate that a small molecule could be designed or identified that binds to the C-terminal end of the AB loop and the D helix of the cytokine, at the site-I binding interface. Such a small molecule could induce sidechain rearrangements which would stabilise the four-helix bundle, disrupt the native loop-core interactions and disrupt binding to IL-11Rα. Small molecules with a similar mechanism of action have been described for the IL-2/IL-2Rα binding interface[265,326]. The development of small molecules targeting the IL-11/IL-11Rα interaction is greatly aided by the structures presented here of IL-11, IL-11Rα and the IL-11 signalling complex. Such an effort would undoubtedly be challenging but would lead to useful therapeutic candidates.

Specific inhibition of IL-6 family cytokine signalling is likely best achieved by targeting of the α-receptor for the cytokine of interest. In light of the structures now available of the IL-6, IL-11, LIF and vIL-6[73,74,80] complexes with gp130, it is interesting to speculate on the possibility of antibodies, nanobodies or small molecules targeting gp130 that could specifically antagonise signalling through one cytokine. The site-III interface shared by IL-6, vIL-6 and IL-11 on D1 of gp130 is unique to those cytokines, so antibodies targeting D1 should, in principle, block signalling via IL-6/IL-11/vIL-6, but not other IL-6 family cytokines. Antibodies have been described previously that specifically antagonise signalling by IL-6 family cytokines, including IL-11, CNTF and LIF/OSM specific antibodies[142]. The structures of the IL-6 family cytokine complexes show that IL-6, IL-11 and LIF bind a common surface on the CHR[80], thus, these antibodies likely do not function by binding the CHR of gp130. The antibodies likely act by disrupting interactions between the cytokine receptors and gp130, for example, by targeting the LIFR/gp130 or CNTFR/gp130 interfaces, which so far remain uncharacterised. Another possibility is the presence of interactions involving the D4-D6 domains of gp130 are involved in cytokine-specific interactions, and that these interactions could be targeted to inhibit signalling. The IL-11 specific antibody was shown to bind an epitope in D4 of gp130[300], these potential interactions may thus be a tractable target.

We also investigated the lead IL-11 signalling inhibitor, IL-11 Mutein[198]. We showed that mutations introduced in IL-11 Mutein alter the position of the AB loop, which forms several contacts to IL-11Rα in the IL-11 signalling complex. We showed biochemically that these mutations alter the kinetics of binding to IL-11Rα and combined with a mutation in Site-III of the cytokine (W147A), completely abolish binding to gp130. Properly understanding the mechanism of IL-11 signalling inhibition ultimately requires a structure of the ternary complex formed by IL-11 Mutein and the IL-11 receptors. Generally, and as discussed above, our studies into the mechanism of IL-11 Mutein illustrate the value of structures of the IL-11 signalling complex in understanding IL-11 signalling inhibitors.

Mutagenesis and protein design have been used for decades to design inhibitors of cytokine signalling, for example, in addition to IL-11, inhibitors have been designed for IL-6[321], LIF[320] and IL-2[347-349] by mutation, yeast display or phage display. Limited mutation of the endogenous cytokine can lead to issues with immunogenicity when used therapeutically, as antibodies are raised against the endogenous protein[273]. An approach to overcome this is *de novo* protein design. An IL-2 variant was recently designed *de novo*[350], with low sequence identity to wild-type IL-2 (~25%), but functionally able to bind IL-2Rβ and γ_c. Treatment with the designed protein is not likely to result in the generation of antibodies that would inhibit endogenous IL-2, and was also engineered for stability, a useful characteristic for a protein therapeutic. Continued structural characterisation of the IL-11 Mutein/IL-11Rα/gp130 complex will hopefully identify the distinct region on IL-11Rα and the CHR of gp130 that is bound by IL-11 Mutein on IL-11Rα. Eventually, this may permit the *de novo* design of an IL-11 signalling inhibitor, based on the interfaces formed by IL-11 Mutein with its receptors.

6.2 Concluding statement

Cancer is known as the ‘emperor of maladies’, and the effort to develop better approaches to treat cancer has a history arguably as long as medicine itself[489]. The most important advance in cancer treatment in the past half-century was the

realisation that direct targeting of the molecular abnormality causing the cancer can lead to effective and specific treatments[490-492]. Dysregulated intracellular or intercellular signalling is frequently a molecular cause underpinning cancer, as well as diseases more generally[212]. Signalling by the cytokine IL-11 has recently been implicated in gastrointestinal cancer[208], along with other diseases including fibrotic diseases of the heart and lung[230,233]. In the coming years, we hope that the structural knowledge we have presented here will allow and aid in the development of novel drugs and antibodies targeting the IL-11 signalling complex, which we hope will find value as novel therapeutic candidates, and eventually as drugs to treat cancers associated with excess IL-11 signalling. More generally, the structural and mechanistic knowledge presented here will allow the development of a mechanistic, molecular understanding of IL-11 signalling, and place the mechanisms used by IL-11 to signal in the context of cytokine signalling more broadly.

Appendix A- The structure of the PA28/20S proteasome complex from *Plasmodium falciparum* and implications for proteostasis

Stanley C. Xie[1^], Riley D. Metcalfe[1^], Eric Hanssen[1,2^], Tuo Yang[1], David L. Gillett[1], Andrew P. Leis[2], Craig J. Morton[1], Michael J. Kuiper[3], Michael W. Parker[1,4], Natalie J. Spillman[1], Wilson Wong[5], Christopher Tsu[6], Lawrence R. Dick[6], Michael D.W. Griffin[1†] and Leann Tilley[1†*]

^These authors contributed equally

[†]Dual senior corresponding authors: ltilley@unimelb.edu.au and mgriffin@unimelb.edu.au.

[1]Department of Biochemistry and Molecular Biology and [2]Advanced Microscopy Facility, Bio21 Molecular Science and Biotechnology Institute, The University of Melbourne, Melbourne, VIC 3010, Australia

[3]Data61 CSIRO, Docklands VIC 8012, Australia

[4]Australian Cancer Research Foundation Rational Drug Discovery Centre, St Vincent's Institute of Medical Research, Fitzroy, Victoria 3065, Australia

[5]Infection and Immunity Division, The Walter and Eliza Hall Institute, Parkville, VIC 3052, Australia

[6]Oncology Clinical R&D, Takeda Pharmaceuticals International Co., Cambridge, Massachusetts 02139, USA

A.1 Preface

This appendix is the author-approved version of a publication[354] that I co-first authored during my PhD. The text in this appendix has been lightly edited from the author approved version of the manuscript, for consistent formatting with the remainder of the thesis. The figures and text are unchanged. References are numbered to be consistent with the remainder of the thesis.

My main contribution to the project was building and refining the structures of the *P. falciparum* proteasome in complex with the PA28 activator. I also contributed to the refinement of the crystal structure of PA28, contributed the SAXS and AUC analysis of PA28 and prepared the structural figures in the paper below.

As I did not contribute greater that 50% of the work required for this publication, and as the topic differs greatly from the remainder of the thesis, it is not appropriate to include it as a chapter. Readers interested in the structural biology of the proteasome, the mechanism of action of 11S activators, or the proteasome as a drug target, are directed to relevant reviews[493-496], the previously published structure of the *P. falciparum* proteasome[469] and to high-resolution cryo-EM structures of the 26S proteasome that were published alongside this manuscript in 2018[464,470,497,498].

A.2 Abstract

The activity of the proteasome 20S catalytic core is regulated by protein complexes that bind to one or both ends. The PA28 regulator stimulates 20S proteasome peptidase activity *in vitro*, but its role *in vivo* remains unclear. Here we show that genetic deletion of the PA28 regulator from *Plasmodium falciparum* (*Pf*PA28) renders malaria parasites more sensitive to the antimalarial drug, dihydroartemisinin, pointing to a role for PA28 in protection against proteotoxic stress. The crystal structure of *Pf*PA28 reveals a bell-shaped molecule with an inner pore showing strong segregation of charges. Small-angle X-ray scattering (SAXS) shows that disordered loops, not resolved in the crystal structure, extend from the *Pf*PA28 heptamer and surround the pore. Using single particle cryo-electron microscopy (cryo-EM), we solved the structure of *Pf*20S in complex with one and two regulatory *Pf*PA28 caps at resolutions of 3.9 and 3.8 Å, respectively. *Pf*PA28 binds *Pf*20S asymmetrically, strongly engaging subunits only on one side of the core. *Pf*PA28 undergoes rigid body motions relative to *Pf*20S. Molecular dynamics simulations support conformational flexibility and a leaky interface. We propose lateral transfer of short peptides through the dynamic interface as a mechanism facilitating release of proteasome degradation products.

A.3 Introduction

The proteasome is a multi-subunit enzyme complex that is needed for cellular homeostasis in eukaryotes. As an organism that undergoes rapid growth and cell division in an oxidatively stressed environment, the malaria parasite, *Plasmodium falciparum*, is heavily reliant on its protein turnover machinery. Accordingly, proteasome inhibitors exhibit parasiticidal activity against all life stages[499,500]. Importantly, inhibitors of the proteasome strongly synergise artemisinin-induced killing of *P. falciparum* in culture and *P. berghei in vivo*[469,501]. This synergism is thought to result from proteasome inhibitor-induced exacerbation of the consequences of artemisinin-induced protein damage[502].

Structures of the 20S proteasome from several organisms are available, including the archaeon, *Thermoplasma acidophilum*, the pathogenic bacterium,

Mycobacterium tuberculosis, *Saccharomyces cerevisiae*, *P. falciparum,* mouse and human[469,503-507]. These share a common, basic architecture. The 20S catalytic core comprises two heptameric β rings sandwiched between heptameric α rings. The N-termini of the α2, α3 and α4 subunits serve to block the proteasome pore, forming a closed gate that prevents uncontrolled substrate access[507-509].
The proteasome is activated by the binding of protein regulators that open the α subunit gate. The most well-studied activator is the 19S regulatory particle[510]. The less well-studied heptameric PA28 activator (also known as 11S or REG)[511] stimulates the 20S peptidase activity in a manner that is independent of ubiquitin and ATP[511].

Ablation of PA28α/β in mammalian cell lines is associated with increased levels of oxidised and poly-ubiquitylated proteins[512]. Similarly, a double knock-out of PA28γ and another nuclear proteasome activator, p200, leads to increased oxidative stress in sperm[513]. This has led to the suggestion that PA28 facilitates the degradation of oxidised or unfolded proteins[514-516]. Hybrid complexes of 20S with 19S and PA28 are observed[517] and it has been suggested that PA28 also facilitates or modifies protein degradation by the 19S/20S complex, for example by altering the length or composition of peptide products or enhancing egress of products[518,519].
In this work, we show that recombinant *P. falciparum* PA28 enhances *Pf*20S-mediated degradation of fluorogenic peptides and an intrinsically unstructured protein. Genetic deletion of *Pf*PA28 increases sensitivity to dihydroartemisinin (DHA), indicating a role in proteostasis. Single particle cryo-electron microscopy (cryo-EM) reveals an asymmetric interface between *Pf*PA28 and *Pf*20S and provides insight into the activation mechanism. *Pf*PA28 is dynamic with respect to *Pf*20S, which may facilitate product egress from the proteasome under conditions of proteotoxic stress, and underpin the protection provided by *Pf*PA28 against DHA-induced protein damage.

A.4 Results and Discussion

A.4.1 Pf*PA28 facilitates degradation of unstructured proteins in vitro and damaged proteins in vivo*

*Pf*20S, purified from saponin-permeabilised, schizont-infected red blood cells (RBCs), migrates on Blue-Native PAGE with an apparent molecular mass of ~700 kDa (Supplementary Figure A.1A). Recombinant *Pf*PA28 enhances the cleavage of fluorogenic substrate by purified *Pf*20S (Figure A.1A). Carfilzomib strongly inhibits the β2 and β5 activities, but only weakly inhibits β1 activity (Figure A.1A), as previously reported[520].

In mammalian cells, p16 (a lysine-less cell cycle kinase inhibitor with intrinsically low structural stability[521,522]) is targeted for degradation by ubiquitin-independent components of the proteasome, particularly PA28γ[523,524]. P16 is gradually degraded by *Pf*20S even in the absence of an activator (Figure A.1B), but degradation is significantly enhanced upon addition of *Pf*PA28 (Figure A.1B). Carfilzomib partially inhibits the degradation of p16.

Using CRISPR/Cas9 gene editing, we successfully generated PA28 knock-out lines of *P. falciparum* (ΔPA28_1 and ΔPA28_2; Supplementary Figure A.1B-E). No difference in growth rates is observed (Supplementary Figure A.1F), demonstrating that *Pf*PA28 is not required under unstressed conditions. Ring stage PA28 knock-out parasites exhibit a 2-fold increased sensitivity to DHA (Figure A.1C; Supplementary Figure A.1G), which has been shown to damage parasite proteins and to compromise proteasome function[502], indicating a role for *Pf*PA28 (either directly or indirectly) in the parasite's response to proteotoxic stress.

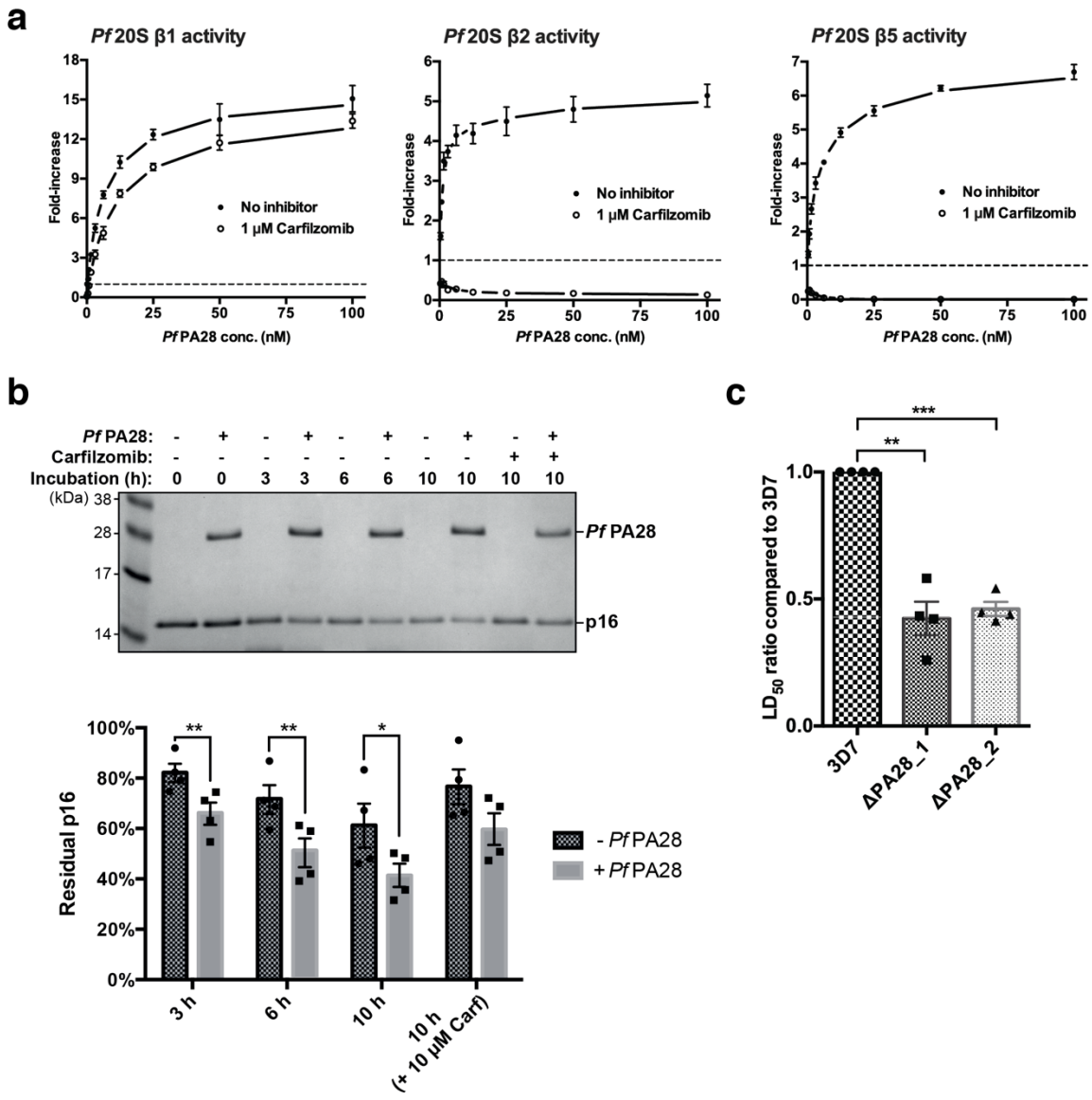

Figure A.1: Functional characterisation of *Pf*PA28.

(a) *Pf*PA28 enhances the rate of cleavage of AMC-tripeptide substrates by *Pf*20S. Each AMC substrate was incubated with 1 nM *Pf*20S proteasome, activated by increasing concentrations of *Pf*PA28. Dashed lines illustrate the level of *Pf*20S activity without *Pf*PA28. Data represent mean ± S.E.M from 3 independent experiments. (b) *Pf*PA28 enhances the ability of *Pf*20S to degrade p16. Human p16 recombinant protein was incubated with *Pf*20S in the absence or presence of *Pf*PA28 for the indicated periods. 10 μM carfilzomib was added to one set of the samples with 10 h incubation. A representative gel from 4 independent experiments is shown. Quantification of the gels (n=4) is shown in the bar chart with error bars representing S.E.M. *P<0.05 and **P<0.01 for paired two-tailed t-test. For 3 h test,

P=0.0031, t=8.8 and df=3. For 6 h test, P=0.0077, t=6.4 and df=3. For 10 h test, P=0.0257, t=4.1 and df=3. (c) Cultures of wildtype 3D7 or ΔPA28_1 or ΔPA28_2 clones at the ring stage (7-8 h post invasion) were exposed to increasing concentrations of DHA for 3 h, before removal of the drug and analysis of viability in the next cycle. Ratio of LD_{50} values for each parasite line relative to the parental 3D7 line is shown. Data represent mean ± S.E.M from 4 independent experiments. $^{**}P<0.01$ and $^{***}P<0.001$ for unpaired two-tailed t-test with Welch's correction. For the 3D7 and ΔPA28_1 comparison, P=0.0031, t=8.7 and df=3. For the 3D7 and ΔPA28_2 comparison, P=0.0003, t=19.4 and df=3.

A.4.2 P. falciparum *PA28 forms a heptameric structure with a charge-segregated pore*

We solved the crystal structure of self-assembled *Pf*PA28 at a resolution of 3.1 Å. (See statistics and representative density in Supplementary Table A.1 and Supplementary Figure A.2a). The asymmetric unit comprises two bell-shaped heptamers, each with 7-fold rotational symmetry (Supplementary Figure A.2b). Each heptamer has an opening of approximately 20 Å at the apical (narrow) end and 35 Å at the basal end, connected by a central channel with a diameter (20 Å minimum) sufficient to pass peptide and unfolded polypeptide substrates/ products (Figure A.2a,b). Each monomer comprises four long α-helices (Figure A.2c). In naming the chains of the crystal structure, we have assumed that the N-terminal section and the helical bundle that forms the largest interacting surface between the helices belong to the same molecule, which is the configuration of *Trypanosoma brucei* (*Tb*) PA26[525].

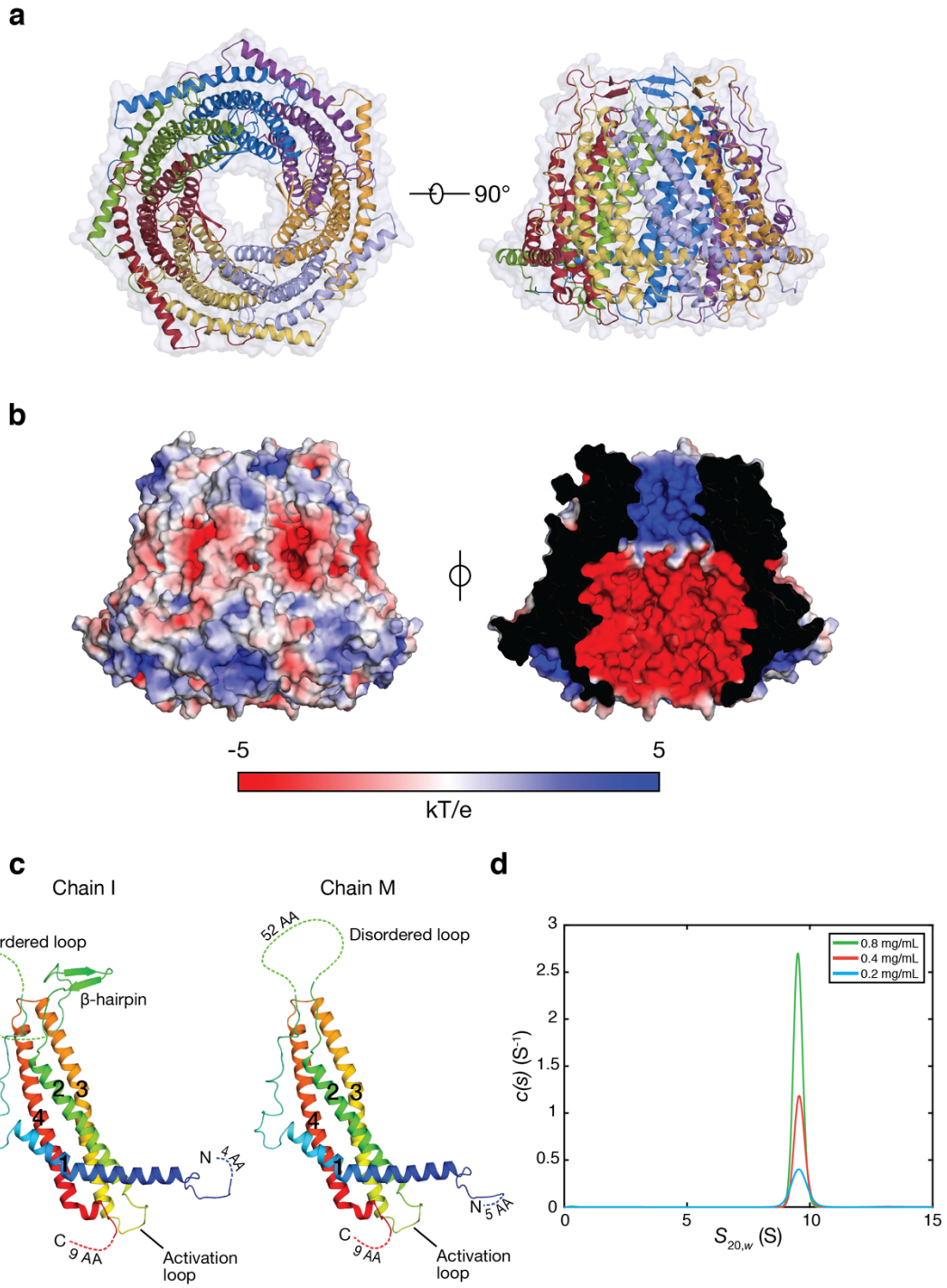

Figure A.2: Crystal structure and sedimentation velocity analysis of *Pf*PA28. (a) Top and side views of ribbon and surface representations. Each monomer within the heptamer comprises four long α-helices. (b) Electrostatic potential of the surface of *Pf*PA28 and the channel through the heptamer (cross section, right). Basic residues line the 20 Å apical pore entrance and acidic residues line the 35 Å basal pore entrance. (c) Ribbon structures of representative *Pf*PA28 monomers with and without the apical β-hairpin. Disordered regions are shown as dotted lines and their

amino acid lengths are provided. (d) Continuous sedimentation coefficient (c(s)) distributions for *Pf*PA28 at three concentrations (each assessed in singlicate), showing that *Pf*PA28 is a heptamer. Raw sedimentation velocity data is shown in Supplementary Figure A.2D-F.

Calculation of the electrostatic charge on the surface of the channel through the heptamer reveals a highly basic region at the apical end, while acidic residues line the base of the pore (Figure A.2b). While other 11S activators exhibit charged residues lining the pore (see helix 3, Supplementary Figure A.2c), the sharp separation of positive and negative charges appears to be a feature of *Pf*PA28.

The sequence between helices 1 and 2 comprises a large loop. The N-terminal part of this loop (residues Asn50 – Lys75; Figure A.2c) makes specific contacts with the helical bundle structure and is well defined in the electron density in all molecules. Conversely, residues ~Asn77 to ~Leu127 are generally poorly defined. Weak density in three molecules of each heptamer resolved part of this loop (from ~Gly107) revealing a short β-hairpin (see Figure A.2c) bordering the edge of the apical pore, with ~Asn77 to ~Asp106 remaining disordered. The nature of the density around this structure suggests that the occupancy of residues in the hairpin is low.

Both the N- and C-termini, situated at the base of the heptamer, are poorly resolved in the electron density, suggesting disorder of these regions. In all but one molecule, the N-terminal 4 to 6 residues of the protein were not resolved. In one chain (K), residues 1 to 7 form a well resolved α-helix and the entire N-terminus was built. Several residues of this helix provide crystal contacts with the neighbouring heptamer in the lattice, possibly stabilising this structural element. The sequence C-terminal to residue Lys269 or Asn270 was not resolved in the electron density, indicating a flexible C-terminus.

Mutagenesis of human PA28α implicates residues in the loop between helices 2 and 3 (RIEDGNNFG, the ‘activation loop’) as being responsible for binding to or

activation of the proteasome[526]. The sequence of this activation loop is exceptionally well conserved, and identical in human PA28α and *Pf*PA28 (Supplementary Figure A.2c). These loops are visible at the basal (proteasome interface) side of the *Pf*PA28 structure (Figure A.2c).

The apical loop of *Pf*PA28 is longer than the corresponding human PA28α loop (39 residues)[527] (Supplementary Figure A.2c). By contrast, the flexible loop is much shorter in *Tb*PA26; and *Tb*PA26 has an internal loop in helix 3, which forms a diaphragm-like structure that blocks the pore[525].

Continuous sedimentation coefficient [c($s_{20,w}$)] distributions for *Pf*PA28 exhibit a single symmetrical peak (Figure A.2d; Supplementary Figure A.2d-f) with a weight-averaged standardised sedimentation coefficient of 9.5 S. This value corresponds to a molecular mass of 216 kDa (assuming a frictional ratio (f/f0) of 1.3 estimated from the fit to the data for 0.8 mg/mL) consistent with the predicted molecular mass of the *Pf*PA28 heptamer (231,875 Da), confirming that the dimer of heptamers present in the asymmetric unit is due to crystal contacts.

A.4.3 P. falciparum *PA28 has flexible polypeptide features at the apical and basal surfaces*

Small-angle X-ray scattering (SAXS) and molecular dynamics (MD) simulations were applied to gain insight into the disordered N- and C-termini regions (see Supplementary Table A.2; Supplementary Figure A.3). Models generated from SAXS data using *CORAL*[528] (Figure A.3; Supplementary Figure A.4a,b) show that the apical loops extend away from the *Pf*PA28 structured core. Theoretical sedimentation coefficients calculated for the *CORAL* model with asymmetric loops and the *Pf*PA28 crystal structure coordinates alone were 9.2 S and 11.0 S, respectively. The agreement of the former with the experimental sedimentation coefficient provides further evidence for the extended conformation of the loops. *Ab initio* models (*GASBOR*; [529]; Figure A.3c,d; Supplementary Figure A.4c) support our crystal structure and hybrid models.

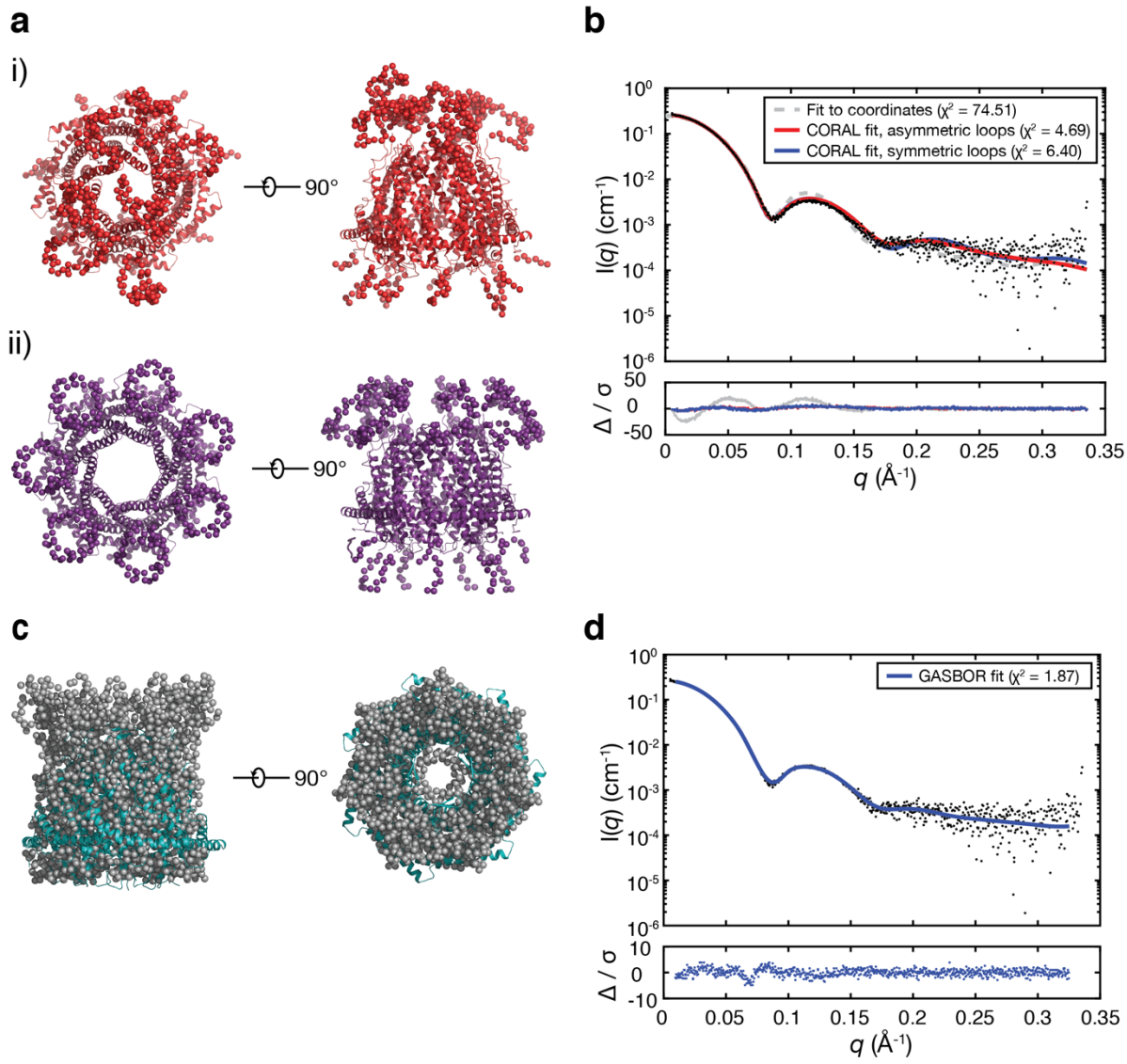

Figure A.3: Small angle X-ray scattering analysis of *Pf*PA28.

(a) Representative *CORAL* models generated assuming (i) no symmetry (P1) for the apical loops, ii) P7 symmetry for the apical loops. The loops extend outwards from the apical end of *Pf*PA28. The flexible N and C termini were also modelled. (b) Scattering data (representing one of 3 experiments) with the fits shown to the crystal structure coordinates alone and both *CORAL* models. (c) *Ab initio* model generated using *GASBOR*, with the *Pf*PA28 structure coordinates overlaid. (d) Scattering data (representing one of 3 experiments) with fit to the model in (c). All additional *CORAL* models generated are shown in Supplementary Figure A.4.

Two short (30 ns) MD simulations support the dynamic nature of the apical loops (Supplementary Figure A.5). During the simulation, the *Pf*PA28 core relaxed from the

starting structures (which are constrained by crystal packing; initial root-mean-square deviation (RMSD) values after minimisation = 0.15 Å, 0.18 Å; final RMSD = 2.69 Å, 2.63 Å; Supplementary Figure A.5; Supplementary Movie A.1). The relaxation indicates flexibility of the individual monomers within the heptameric structure.

It is interesting to consider the function of the flexible apical loops, which are highly charged locally, but neutral overall. One possibility is that the loops act as entropic bristles[530,531], enhancing the solubility of the complex. Entropic fluctuations of these loops may provide a selectivity filter that prevents non-specific interactions and excludes large proteins. Another possibility is that dynamic motions of the loops and of the individual *Pf*PA28 monomers fine-tunes the stability of *Pf*20S/ *Pf*PA28 interface.

A.4.4 Pf*PA28 activates* Pf*20S using a mechanism distinct from the 19S complex*

Blue Native-PAGE reveals the efficient formation of singly and doubly capped *Pf*20S/*Pf*PA28 complexes (Supplementary Figure A.1a). Dissociation of the complex during vitrification was overcome by chemical stabilisation (with 0.1% glutaraldehyde, as validated in other studies[532-535]). 3D class averages of samples prepared for single particle cryo-EM reveal the uncapped (n = 36,211), single-capped (n = 57,337) and double-capped (n = 27,688) complexes (Supplementary Figure A.6a-c). We observe dynamic features at the end of the *Pf*PA28 cap (Supplementary Figure A.6c, arrows), likely corresponding to the dynamic apical loops and consistent with our SAXS models. After 3D classification and refinement, we generated density maps for the single-capped, double-capped and uncapped 20S proteasome at resolutions of 3.92 Å, 3.82 Å and 3.54 Å, respectively, as judged by the gold standard half-map FSC = 0.143 criterion (Supplementary Figure A.7a). We used these maps to build and refine the structures (Figure A.4a,b, Supplementary Figure A.6d). The local resolution for *Pf*PA28 is significantly lower than that for *Pf*20S (Supplementary Figure A.7b).

The structures reveal a continuous channel (Figure A.4c) through which unfolded substrates/products can enter and exit. Prediction of the electrostatic surface reveals highly charged regions on the outside of the barrel and in the interior channel (Figure A.4d, Supplementary Figure A.6e). The pore formed by the α subunit ring is highly basic, contrasting the highly acidic nature of the base of the *Pf*PA28 pore.

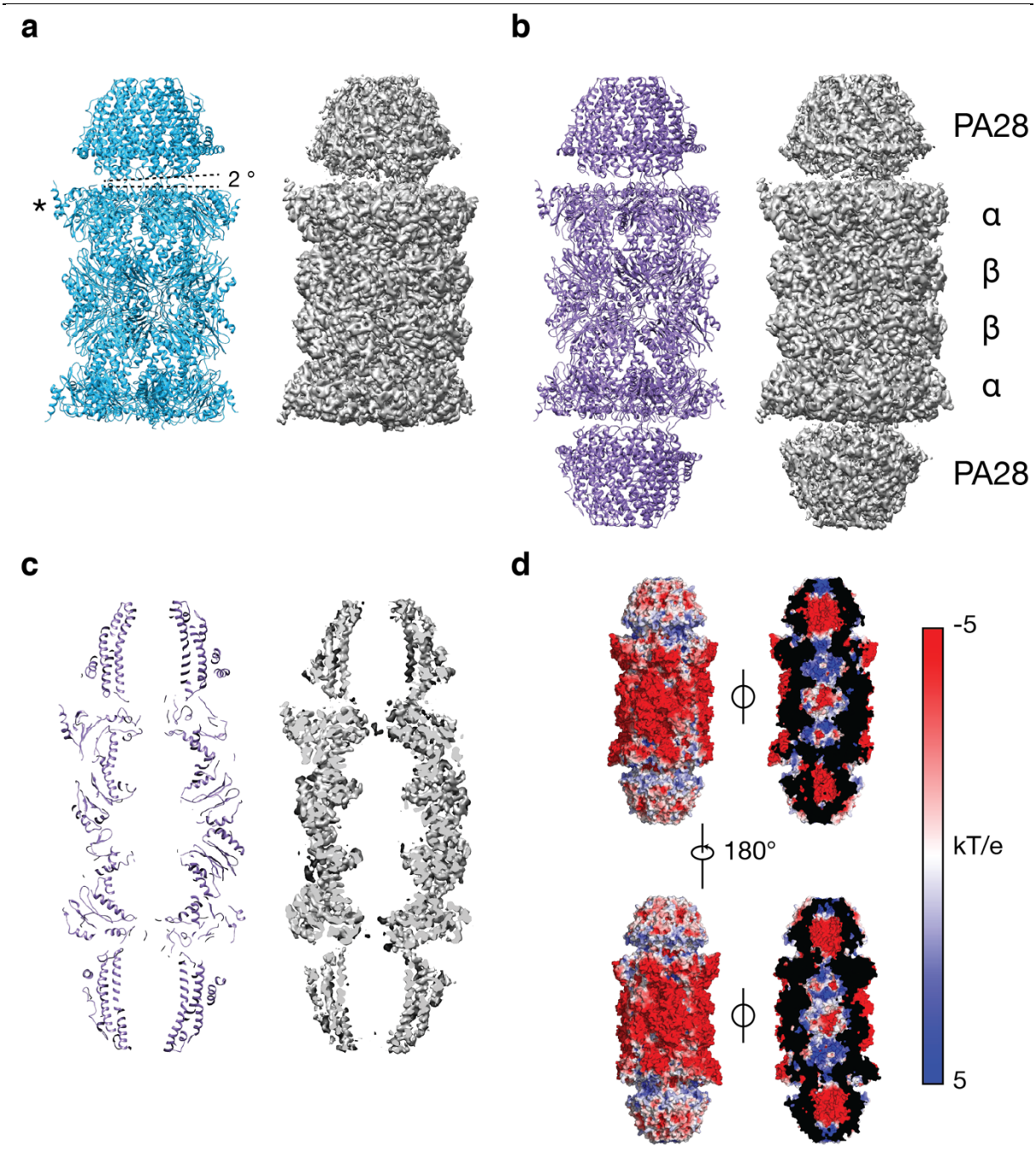

Figure A.4: The structure of the *Pf*PA28/*Pf*20S complex.

Cryo-EM density maps of single-capped *Pf*20S (a) and double-capped *Pf*20S (b), alongside the structures. The position of the α4 subunit is marked with an asterisk and the direction of tilt is indicated for the single-capped complex (dashed lines). (c) Cross-section of the double-capped complex showing the continuous channel formed by *Pf*20S and *Pf*PA28. (d) Electrostatic surface potential of the double-capped complex, showing a number of charged regions on the surface of *Pf*20S, and the highly basic nature of the α subunit pore.

The single-capped *Pf*20S map permits direct comparison of the α-subunit rings with and without bound *Pf*PA28. The uncapped ring shows density consistent with the N-termini of the α2, α3 and α4 subunits adopting extended 'closed' conformations that block the pore (Figure A.5a). A series of contacts stabilises this configuration, with key interactions between α2-Glu5, α3-Ala2, α6-Ser123 and α7-Trp129, between α3-Tyr5 and α1-His10, and between α3-Asp6 and α4-Arg5 (Figure A.5bi). In contrast, the α5, α6, α7 and α1 subunits of the uncapped ring adopt an 'open-like' conformation, with the N-termini pointing away from the pore and approximately aligned with the central axis of the core particle. Thus, these N-termini do not appear to participate in blocking the pore in the closed state. A similar arrangement of α-subunit N-termini is observed in our un-complexed *Pf*20S structure (Supplementary Figure A.6d).

In the *Pf*PA28/*Pf*20S complex (capped ring) the α2, α3 and α4 N-terminal extensions appear to adopt a disordered conformation, with no density supporting the positions of residues beyond α2-Leu10, α3-Ser7 and α4-Thr8 (Figure A.5c). This suggests that *Pf*PA28 destabilises the extended, closed conformations of the α2, α3 and α4 N-termini and that these termini become dynamic, thereby allowing access to *Pf*20S (Figure A.5c). This contrasts with the 19S/20S proteasome, where the α2, α3 and α4 N-termini adopt a defined open conformation when all Regulatory Particle Triple-A (Rpt) ATPase subunits are engaged with the α subunit ring[464].

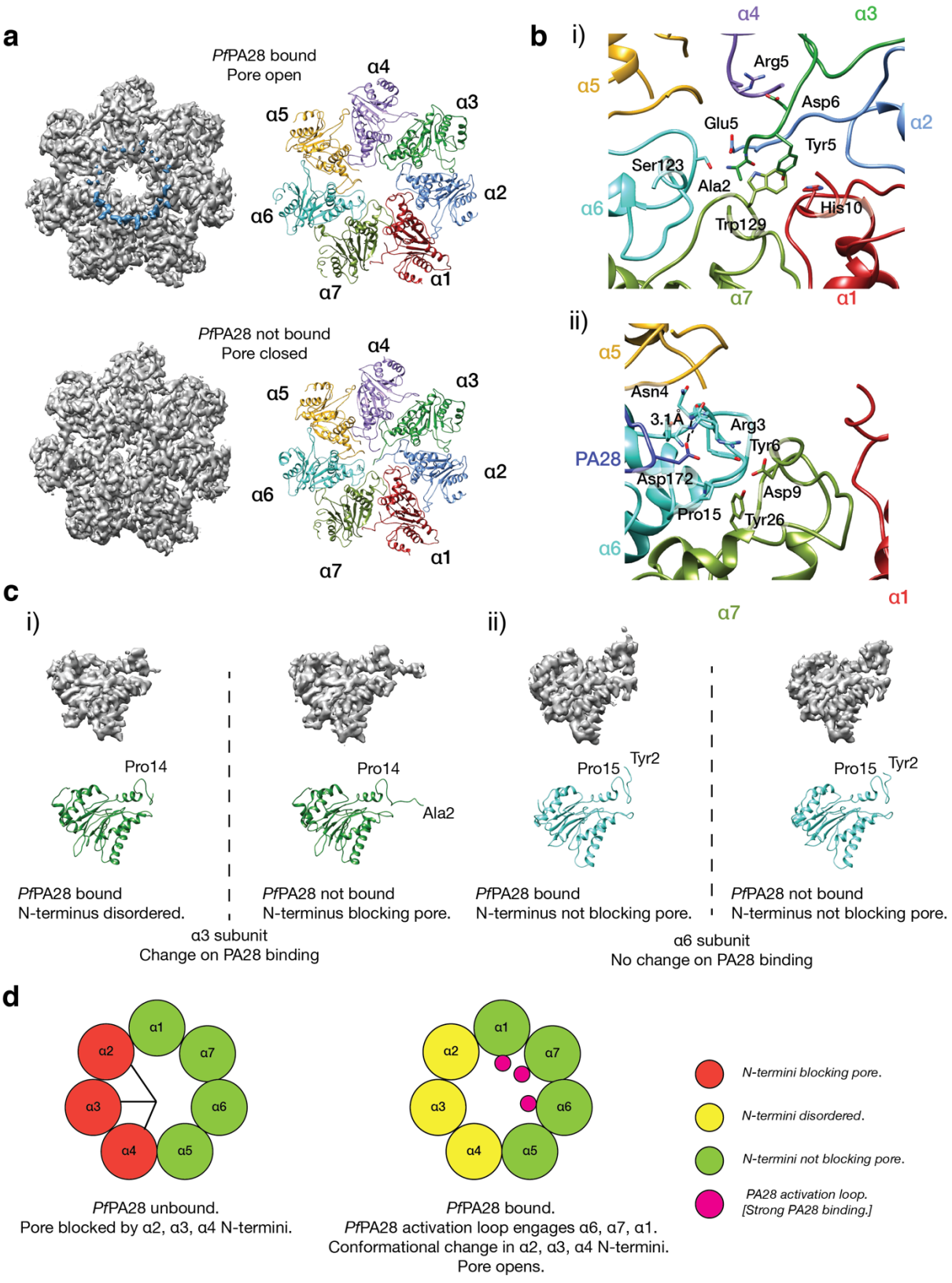

Figure A.5: Proteasome gate control in *Pf*20S.

(a) Structures and cryo-EM density of the bound (top) and unbound (bottom) *Pf*20S α subunit ring from the single-capped complex, showing that the pore opens as a consequence of *Pf*PA28 binding. Density for the activation loops is shown in blue in

the bound α subunit ring, revealing that the activation loop is only strongly defined for *Pf*AP28 monomers binding one half of the ring. (b) Interactions stabilising the i) closed and ii) open states of the pore. i) The interactions between the α2, α3 and α4 N-termini stabilise the closed state of the pore. ii) The interaction between *Pf*PA28 and the α6 subunit, illustrating the hydrogen bonds formed between *Pf*PA28 Asp172 and α6-Arg3 and α6-Asn4, and the conserved activation cluster formed between the α7 and α6 subunits, which stabilise the 'open state' of the α6 N-terminus. (c) Structure and cryo-EM density for the α3 (i) and α6 (ii) subunits when unbound, and when bound to *Pf*PA28. The N-terminus of the α3 subunit is destabilised by *Pf*PA28 binding, while the α6 subunit does not undergo a significant structural change. (d) Schematic depicting the configuration of the α-subunit N-termini in the unbound and *Pf*PA28 bound states and the positions of the well-defined *Pf*PA28 activation loops at the α-subunit ring.

Upon formation of the complex, the N-termini of the α5, α6, α7 and α1 subunits interact with the activation loops of *Pf*PA28. These α subunit N-termini do not undergo large conformational shifts (Figure A.5c), but become noticeably better defined in the density, suggesting stabilisation of this structural element. The activation loops of *Pf*PA28 appear to bind directly to the N-termini of the adjacent α-subunits. For example, Asp172 of *Pf*PA28 appears to form interactions with the backbone amides of α6-Arg3 and α6-Asn4 (Figure A.5bii), suggesting that *Pf*PA28 directly stabilises the α subunit N-termini. Stabilisation of the N-termini also involves a strongly conserved 'activation cluster', consisting of an N-terminal tyrosine and proline from one α-subunit interacting with an N-terminal aspartate and tyrosine from the adjacent α-subunit. For example, α6-Pro15 and α6-Tyr6 form an interaction network with α7-Tyr26 and α7-Asp9, as described for the *T. acidophilum* (*Ta*) 20S/ PA26 complex[525] and the yeast 20S/ PA26 complex[536].

The activation loop is only strongly defined in the density for a subset of the *Pf*PA28 monomers in the *Pf*PA28/*Pf*20S complex, namely the monomers interacting with the α5, α6, α7 and α1 subunits - with the activation loops interacting with the α6 and α7 subunits being the most well defined (Supplementary Figure A.8a).

Furthermore, atomic displacement factors (ADP) for *Pf*PA28 are lower for subunits bound to α6, α7 and α1 than those bound to α2, α3 and α4, with these differences most apparent at and around the activation loops (Supplementary Figure A.8b). These observations suggest *Pf*PA28 binds most strongly those α subunits whose N-termini are already primed for interaction. The axis of *Pf*PA28 is tilted toward the α3/α4 subunits with respect to that of the *Pf*20S core by approximately 2° in both the single- and double-capped structures, resulting in a visible lean of *Pf*PA28 (Figure A.4a). The direction of this tilt - towards from the α subunits that bind less strongly to the *Pf*PA28 activation loops - suggests that it is the geometry of the α-ring, rather than the asymmetrical binding interactions, that imposes this angular displacement.

In the complex of *Tb*PA26 with *S. cerevisiae* (*Sc*) 20S, Glu102 in the *Tb*PA26 activation loop (the equivalent of Asp172 in *Pf*PA28) binds to the proline reverse turn in the N-terminal region of the interacting α subunits, causing a radial displacement of the α subunits relative to the unbound *Sc*20S, and destabilising the closed state[525,537]. In contrast, *Pf*PA28 binding does not induce any large structural rearrangements in the α subunits of *Pf*20S, with the exception of a small displacement of approximately 1.5 Å of the N-terminal helix (helix 0) of the α6 subunit, which has the effect of slightly increasing the diameter of the pore (Supplementary Figure A.8c). We note that the position of the activation loops in the complexes differs between *Tb*PA26 and *Pf*PA28, caused by a small rotation of the cap around its axis relative to the α subunit ring (Supplementary Figure A.8e).

The C-termini of 11S activators have previously been reported to be critical for activator binding but not, alone, sufficient to induce gate opening[537,538]. In our structure, we observe weak density for part of the C-terminus for only one *Pf*PA28 subunit, and only in the double-capped complex (Supplementary Figure A.8d), suggesting that the *Pf*PA28 C-termini are generally dynamic in the complexes. The resolved *Pf*PA28 C-terminus extends toward the interface between the α1 and α7 subunits and makes contacts with residues of the α1 subunit, mediated primarily by the sidechain of *Pf*PA28 His274. The C-terminal four residues are not defined in the

density, implying flexibility. In the complex of *Tb*PA26 with *Ta*20S, the C-terminal carboxylate forms a specific interaction with a conserved α subunit lysine[525]. Thus, the nature of the *Pf*PA28 interactions at this position is different to that described for *Tb*PA26 and *Ta*20S[525]. Taken together, these data indicate that PA28 and PA26 interact with the core particle and trigger gate opening using related but distinct mechanisms.

The activation mechanism used by 11S activators differs substantially from that employed by 19S activators, where the C-terminal HbYX (hydrophobic, tyrosine, any residue) motif of the hexameric Rpt ATPase inserts into pockets formed between the α subunits, resulting in a rotation of the α subunits in the pore and rearrangement of the gating N-termini, with no direct interaction between the Rpt ATPase and the N-terminal region of the α subunits[497,538]. Thus, proteasome activators can employ diverse mechanisms of binding and activation. This may reflect the different physiological roles of the activators, with the 19S activator requiring a mechanism to tightly control pore access, as it transitions between a series of open and closed states in an ATP-driven manner[464,497]. In contrast, 11S activators may not require tight regulation of pore opening, particularly if their role is to open the pore to facilitate rapid egress of degraded products in hybrid 19S/20S/11S complexes.

A.4.5 Pf*PA28 undergoes substantial motions on* Pf*20S*

Consensus maps of the *Pf*PA28/*Pf*20S complexes show well-defined density for the proteasome core particle, but relatively poorly defined density for *Pf*PA28, resulting in lower local resolution for *Pf*PA28 (Supplementary Figure A.7b). These data suggest that *Pf*PA28 and *Pf*20S are dynamic with respect to each other. Multi-body refinement in *Relion 3*[539] improved the resolution and map quality in the core particle, although the resolution in *Pf*PA28 remains poor (Supplementary Figure A.7). Analysis of the principal components of the movement using the *relion.flex.analyse* program reveals that approximately 30% of the movement of the complex is described by the first three eigenvectors for both the single- and double-capped complexes (Figure A.6a, Supplementary Figure A.9a). For the single-capped

complex, eigenvector 1 corresponds approximately to a movement of *Pf*PA28 from the α4/α5 to α1 subunits and a small clockwise rotation, eigenvector 2 describes movement of *Pf*PA28 from the α6/α7 to α3 subunits, and eigenvector 3 describes movement of *Pf*PA28 from the a5 to α1/α2 subunits (Figure A.6b, Supplementary Movie A.2). Histograms of the amplitudes along the three eigenvectors for the single-capped *Pf*20S are unimodal, indicative of continuous motions. For double-capped *Pf*20S the movements of the two *Pf*PA28 heptamers vary for each eigenvector. Eigenvector 1 describes movement from the α1 subunit to the α4/α5 subunits for the first *Pf*PA28 cap, and from α4 to α1/α7 subunits for the second *Pf*PA28 heptamer. Eigenvector 2 corresponds to movements from the α5/α6 to α2 subunits for both *Pf*PA28 heptamers, and eigenvector 3 describes movement from the α2/α3 to α6 subunits for the first *Pf*PA28, and from α1 to α4/α5 subunits for the second *Pf*PA28 (Supplementary Figure A.9b). Movies of the reconstructed densities for these three eigenvectors illustrate the movements of *Pf*PA28 relative to *Pf*20S in the single-capped structure (Supplementary Movie A.2 and Supplementary Movie A.3). As the dynamic motions in the complex are formed by linear combinations of all eigenvectors[540], these data suggest that *Pf*PA28 precesses on top of the core particle in a non-correlated manner.

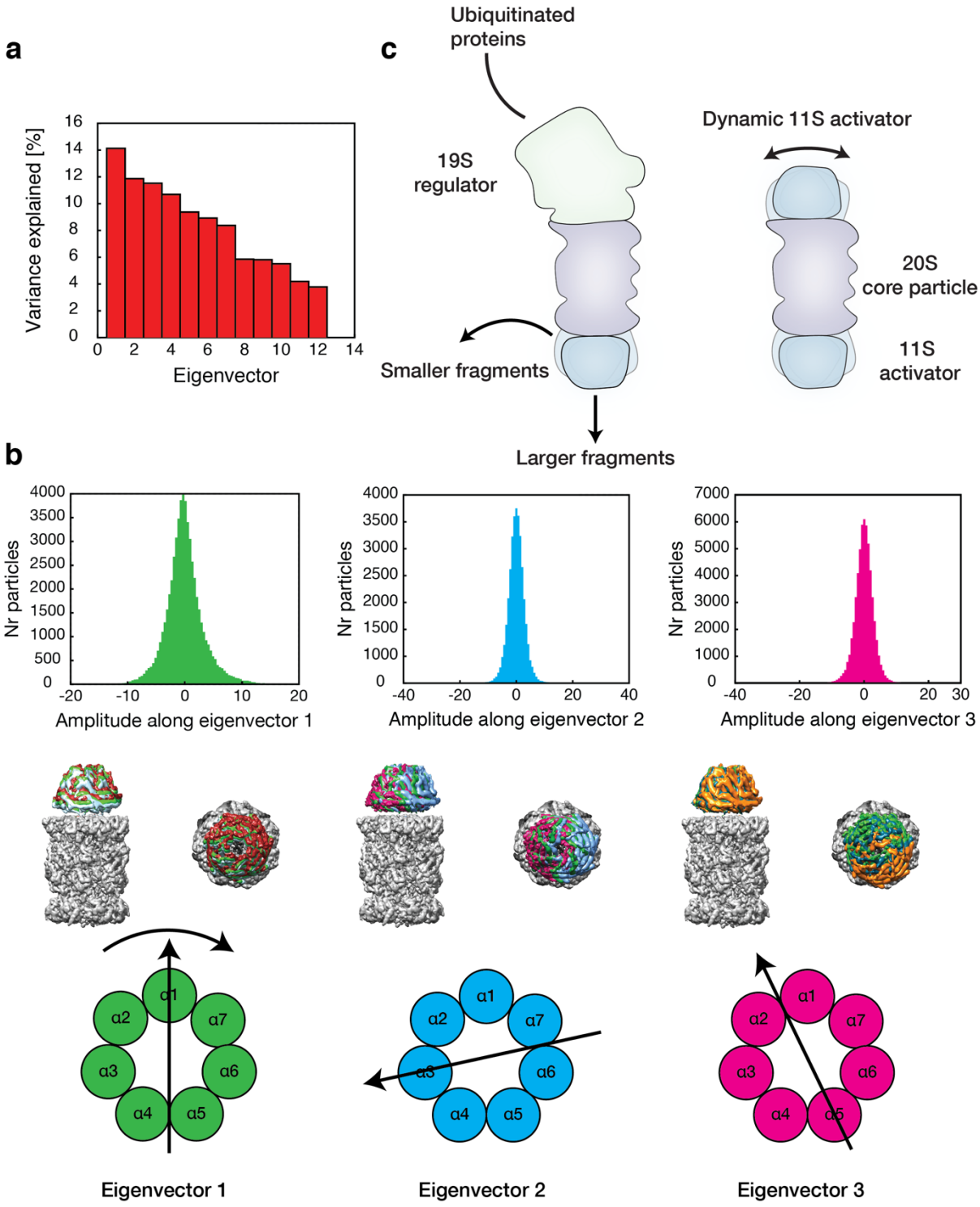

Figure A.6: Pivoting motion of the single-capped *Pf*20S/*Pf*PA28 complex.

(a) Contributions of all eigenvectors to the motion in the single-capped complex. (b) Top. Histograms of the amplitudes along the first three eigenvectors in the single-capped complex. Middle. Density maps visualizing the motions along the eigenvectors. Bottom. Schematics showing the approximate movement corresponding to the eigenvectors. (c) Model of the dynamic interface in the

*Pf*PA28/20S/19S complex, and proposal for egress of products through both the *Pf*PA28 pore and windows at the interface.

It is established that the 19S regulatory particle varies in position with respect to the 20S core particle, a movement that is critical for substrate processing and pore opening[497,498,541]. The dynamics of *Pf*PA28 are not involved in gate opening, as the pore appears to remain open in all reconstructed maps, and the movement of *Pf*PA28 is not correlated with or driven by ATP hydrolysis. We considered the possibility that the stabilisation protocol employed (treatment with 0.1% glutaraldehyde) might affect the conformational flexibility of the complex. To address this, we collected additional data from samples that were not chemically stabilised. Partial dissociation of particles during vitrification resulted in a lower number of complexes in the data, thus limiting the refinement. 9482 single-capped complex particles were obtained from 622 movies, resulting in a resolution of 4.69 Å. Despite the lower resolution, the main features are similar, including the reconstructed motions of *Pf*PA28 on the *Pf*20S core (Supplementary Figure A.10).

The presence of small 'side windows' between the 20S subunits has been noted previously in structures of the proteasome core particle; and proposed as an alternative route for the exit of processed peptides[507,542]. Similar side windows are visible in the structure of *Pf*20S (Supplementary Figure A.9c). By analogy, we propose that the openings formed by the movement of *Pf*PA28 may present an alternative exit route for processed peptides, avoiding the need for products to traverse the highly charged *Pf*PA28 pore. To interrogate potential exit routes, we built models representing the most displaced positions of *Pf*PA28 on the *Pf*20S core and examined the motions of the water molecules over a period of 2 ns (Supplementary Figure A.11). Waters exit both through the pore and at the *Pf*PA28/*Pf*20S interface in the model representing one of the tilt extremes.

We propose that the dynamics of *Pf*PA28 allows egress of peptide products in hybrid 11S/20S/19S complexes (see Figure A.6c for our proposed model). It is important to note that *Tb*PA26 has internal loops that block the pore, preventing the

entry or exit of even small peptide substrates[525]. The possibility of substrate exit through the 11S/20S interface may explain how *Tb*PA26 (with a blocked pore) can act as an activator.

Our work provides insight into how *Pf*PA28 could protect malaria parasites against the proteotoxic stress induced by treatment with DHA. *Pf*PA28 may play a role as an activator of ubiquitin-independent degradation of proteins by *Pf*20S and/or may form hybrid complexes with *Pf*19S/*Pf*20S and enhance processivity. The structural flexibility of *Pf*PA28 and of the *Pf*PA28/*Pf*20S interface may facilitate release of products and potentially help regenerate proteasomes that become clogged with difficult-to-degrade proteins.

In conclusion, our structural analysis of a cognate 11S/20S complex provides detailed insights into the interactions that stabilise the interface and facilitate passage of substrates into and products out of the catalytic core. We have modelled the highly dynamic apical loops of *Pf*PA28, which may prevent non-specific interactions of substrates, but may also fine-tune the stability of the *Pf*PA28/*Pf*20S interface. Indeed, we observed multiple conformations of *Pf*PA28 on the *Pf*20S core that may facilitate product egress. We show that *Pf*PA28 enhances the ability of *Pf*20S to degrade small peptide substrates and a larger unstructured polypeptide. In addition, we provide evidence for a role of *Pf*PA28 in protecting *P. falciparum* from proteotoxicity. Taken together with data from previous studies, our work provides increasingly strong evidence that PA28 plays an important role under conditions of proteotoxic stress.

A.5 Methods

A.5.1 Culturing and cell lines

P. falciparum parasites used in this study were propagated in O+ human erythrocytes (Australian Red Cross Blood Service) in RPMI-1640, supplemented with GlutaMAX™, 25 mM HEPES (ThermoFisher), 5% (v/v) human serum (Australian Red Cross Blood Service), 0.25% (w/v) AlbuMAX II (Life Technologies), 10 μM $_{D}$-glucose, 22 μg/mL gentamycin, and 0.5 mM hypoxanthine, and incubated at 37°C

in an atmosphere of 1% O_2, 5% CO_2 and 94% N_2. Cultures were monitored by Giemsa staining of methanol-fixed blood smears. Culture media was replaced at least every 48 h and parasitemia was maintained below 10% to ensure health of cultures. *P. falciparum* strains used in this study: 3D7 laboratory strain, ΔPA28_1 and ΔPA28_2 clones.

A.5.2 Assessment of fitness and DHA sensitivity

Relative fitness was determined by following synchronised ring cultures (initiated at 0.8% haematocrit, 0.8% parasitemia) for 11 days with equivalent dilutions applied regularly to wildtype and knock-out infected RBCs. Raw parasitemia counts were corrected for dilutions and normalised to the wildtype at day 11. For drug sensitivity assays, tightly synchronised ring stage parasites (7-8 h post invasion (h.p.i.)) at 0.2% hematocrit and 1-2% parasitemia were subjected to 3-h drug pulse with DHA (Sigma-Aldrich) at 37°C and returned to culture until parasites reached trophozoite stage of the following cycle. Parasitemia was determined by staining with 2 μM Syto-61 (Invitrogen) and measuring fluorescence by flow cytometry (FACSCanto™ II cytometer; Becton Dickinson) with analysed using FlowJo (version 10). Survival (%) represents the parasitemia normalised to untreated (100% survival) and "kill treated" (0% survival) controls, where "kill treated" refers to samples treated with 2 μM DHA for 48-72 h.

A.5.3 Genetic disruption of PfPA28 and characterisation of the knock-out

The single guide RNA (sgRNA) targeting sequence was designed using the CHOPCHOP tool with guide rank #6 (185 bp from 5' exon region) chosen for use in this study based on location within the *Pf*PA28 sequence (accessed April, 2017)[543]. This sgRNA sequence and its reverse complement (1+2; Supplementary Table A.4) were annealed and InFusion cloned into a modified, BtgZI digested, pAll-In-One (pAIO) plasmid[544]. The modified pAIO (pAIO-DHFR) contains the hDHFR selection cassette (amplified from pHHT-TK (Duraisingh, Triglia, & Cowman, 2002)) in place of the yDHODH selection cassette. The final vector was named pAIO-DHFR-PA28.

*Pf*PA28 5' and 3' homology donor templates were PCR amplified from *P. falciparum* 3D7 genomic DNA using primers listed in Supplementary Table A.4 (3+4 for 5' donor template; 5+6 for 3' donor template) and inserted between AvrII/NcoI (for 5' donor template) and SpeI/SacII (for 3' donor template) in the vector pUF-TK (derived from the pUF-1 vector[545], with TK negative selection cassette replacing the yFCU selection cassette[546] resulting in the vector pUF-TK-PA28. For transfection, pUF-TK-PA28 vector (150 µg) was linearised at the NotI site and co-transfected with pAIO-DHFR-PA28 (50 µg) into *P. falciparum* (3D7 strain). Positive selection (2 µM DSM-1; Malaria Research and Reference Reagent Resource Center (MR4)) was applied 24 h post-transfection. Transfectants were cloned by limiting dilution resulting in four independent clones. Verification of the desired integration event was achieved by PCR using primers indicated in Supplementary Table A.4 (7+8+9). Two clones (ΔPA28_1 and ΔPA28_2) were chosen for DHA sensitivity assays.

A.5.4 Preparation of P. falciparum PA28

The *Pf*PA28 construct comprised a 6 x histidine tag at the N-terminus followed by a TEV protease cleavage sequence and the *Pf*PA28 gene (ID: PF3D7_0907700) from *P. falciparum*. The sequence was codon optimised for *E. coli*, synthesised and cloned into the pET-11a expression vector (GenScript). The vector was transformed into *E. coli* BL21(DE3) cells and expressed in 2 L of LB media. Cell pellets were resuspended in 40 mL lysis buffer containing 20 mM Tris-HCl, pH 7.4, 150 mM NaCl, 20 mM imidazole, 25 mM KCl, 1 mM $MgCl_2$, 1 mM DTT and 1x protease inhibitor cocktail (Roche). Cells were lysed by sonication (Microtip, QSonica) and the lysate was clarified by centrifugation at 30,000 g for 25 min. The supernatant was applied to a 5 mL HisTrap HP column (GE Healthcare) and washed with 50 mL binding buffer containing 20 mM Tris-HCl, pH 7.4, 150 mM NaCl, 20 mM imidazole, 25 mM KCl, 1 mM $MgCl_2$ and 1 mM DTT. His-*Pf*PA28 was eluted using a 0-500 mM imidazole gradient in the above buffer over 50 mL. The eluted His-*Pf*PA28 was dialysed overnight at 4°C against 20 mM Tris-HCl, pH 7.4, 150 mM NaCl, 25 mM KCl, 1 mM $MgCl_2$, 1 mM DTT with the addition of His-tagged TEV protease (L56V/S135G/S219V triple-mutant[364]). Cleaved His tags from His-*Pf*PA28 and TEV protease were removed by running the dialysed protein through a HisTrap HP

column and collecting the flow-through. *Pf*PA28 was further purified by gel filtration using a Superdex 200 column (GE Healthcare). The molecular mass of purified *Pf*PA28 was verified using mass spectroscopy. Mass spectra were collected using an Agilent 1200 HPLC, coupled to an Agilent 6220 Accurate-Mass ESI-TOF mass spectrometer.

A.5.5 Preparation of P. falciparum proteasome

P. falciparum 20S proteasome was purified from infected RBCs using a modification of a published procedure[520]. Frozen pellets of sorbitol-synchronised mature stage-parasite, prepared from 4 L from of *P. falciparum* culture (4% hematocrit and 10% parasitemia), were thawed on ice and resuspended in 30 ml lysis buffer containing 20 mM Tris-HCl, pH 7.4, 5 mM $MgCl_2$ and 1 mM DTT. The lysate was incubated on ice for 1 h with vigorous vortexing every 5-10 min. The lysate was clarified by centrifugation at 30,000 g for 20 min and filtered through a 0.22 µm syringe filter. The supernatant was applied to a 5 mL HiTrap Heparin HP column (GE Healthcare) and washed with 20 mM Tris-HCl, pH 7.4. Protein was eluted using a 0-2 M NaCl gradient in 20 mM Tris-HCl, pH 7.4 over 50 mL. The eluted protein containing *Pf*20S proteasome was dialysed overnight at 4°C against 20 mM Tris-HCl, pH 7.4. The dialysed protein was applied to a 5 mL HiTrap DEAE FF column (GE Healthcare) and washed with 20 mM Tris-HCl, pH 7.4. Protein was eluted using a 0-1 M NaCl gradient in 20 mM Tris-HCl, pH 7.4 over 50 mL. Fractions containing *Pf*20S proteasome were pooled and further purified by gel filtration using a Superose 6 Increase column (GE Healthcare). The purity of each fraction was analysed by Native-PAGE and the fractions of highly pure *Pf*20S proteasome were concentrated and stored at -80°C.

Mass spectrometry was used to determine the level of human proteasome contamination in the purified samples. 7 µg of the purified *Pf*20S proteasome was reduced with DTT and alkylated with iodoacetamide. The sample was then subjected to SDS-PAGE and the gel fraction containing 14-38 kDa bands was excised. In-gel digestion with trypsin was performed and peptide content was analysed by LC-MS/MS[547] and the data were processed using Proteome Discoverer

1.4 employing a user-defined protein database containing human and *Pf*20S proteasome subunits. Peptide pairs of human and *Pf*20S subunits with similar amino acid sequences were selected and used to estimate the amount of *Pf*20S relative to human proteasome. Signal intensity (peak area) from multiple peptide pairs was determined.

A.5.6 Sedimentation velocity analysis of PfPA28

*Pf*PA28 samples were diluted to 0.2 mg/mL, 0.4 mg/mL and 0.8 mg/mL in 20 mM Tris-HCl, pH 7.4, 150 mM NaCl and 0.5 mM tris(2-carboxyethyl)phosphine (TCEP). 380 µL aliquots at each concentration were loaded into double-channel quartz window cells (Beckman Coulter), with the above buffer in the reference compartment. Cells were placed in a Ti-60 rotor (Beckman Coulter) and centrifuged at 50,000 rpm (201,600 *g*) at 20°C using an XL-I analytical ultracentrifuge (Beckman Coulter). Radial absorbance data were acquired at a wavelength of 280 nm, with radial increments of 0.003 cm, in continuous scanning mode. The sedimenting boundaries were fitted to a model that describes the sedimentation of a distribution of sedimentation coefficients with no assumption of heterogeneity (c(s)) using the program SEDFIT[548]. Data were fitted using a regularisation parameter of p = 0.95, floating frictional ratios, and 250 sedimentation coefficient increments. *HYDROPRO* was used to calculate the theoretical sedimentation coefficients for the crystal structure and hybrid SAXS models[377]. Standard conditions were used (water, 20°C).

A.5.7 Crystallisation and X-ray diffraction data collection

*Pf*PA28 was crystallised using the sitting drop vapour diffusion technique at 20°C. Drops contained 1.5 µL of protein (7 mg/mL in Tris-HCl (20 mM, pH 7.4)), 100 mM NaCl, 25 mM KCl, 1 mM $MgCl_2$, 1 mM DTT) and 1.5 µL of crystallant solution (20 mM HEPES, pH 6.5 and 2 M ammonium sulfate). Crystals of approximate dimension 20 µm x 100 µm appeared after equilibrium against crystallant for a week and continued to grow for a further 4 weeks. Crystals were flash-cooled in liquid nitrogen directly from the crystallisation drop, and data were collected at 100 K and a wavelength of 0.9537 Å using the Eiger 16M detector at the MX2 beamline of the Australian Synchrotron.

Diffraction data were indexed and integrated using XDS[397] and analysed using *POINTLESS*[398], prior to merging by *AIMLESS*[399] from the *CCP4* software suite[549]. R_{free} reflections were chosen in thin shells. Initial phase estimates were obtained by molecular replacement in *PHASER*[400] using the crystal structure coordinates of the human PA28α (REGα) heptamer (PDB ID: 1AVO)[527] as the search model. Phases were improved using *PARROT* and the structure was rebuilt using *BUCCANEER*[550,551]. The most complete monomer was then used to reconstruct the asymmetric unit using non-crystallographic symmetry operators. Automated structure refinement using *phenix.refine*[552] was followed iteratively by manual model building in *COOT*[402]. Structure refinement was performed using non-crystallographic symmetry (NCS) torsion restraints and translation/libration screw (TLS) refinement with each chain comprising a single TLS group. Ramachandran plot analysis showed 94.98% of residues in favoured regions, 4.95% in allowed regions, and 0.07% outliers. Surface electrostatics were evaluated using the Adaptive Poisson-Boltzmann Solver (APBS) software [553] in PyMol.

A.5.8 Small Angle X-Ray Scattering (SAXS) analysis

Small angle X-ray scattering (SAXS) analyses were conducted at the Australian Synchrotron SAXS/WAXS beamline, using co-flow to reduce radiation damage and allow higher X-ray flux onto the sample, and an optimised chromatography system to limit sample dilution[406-408]. The sample-to-detector distance was 2682 mm, and the X-ray beam energy was 12,000 eV (λ = 1.0332 Å), providing a total q range of 0.005 – 0.334 $Å^{-1}$, $q=(4\pi\sin\theta)/\lambda$. Data were collected following fractionation using an in-line size-exclusion chromatography column (Superdex 200 5/150 Increase; GE Healthcare) pre-equilibrated in buffer containing 20 mM Tris-HCl, pH 7.4, 150 mM NaCl and 0.5 mM TCEP. *Pf*PA28 was loaded at three concentrations, 1 mg/mL, 5 mg/mL and 10 mg/mL. We used the data collected at 10 mg/mL loading for analysis. Data were collected from a 1.5 mm capillary under continuous flow, with frames collected every second. Data reduction and buffer averaging was performed using the Scatterbrain software, and data was further analysed using the ATSAS suite[410]. The theoretical scattering profile from the *Pf*PA28 structure was calculated

and fitted to the experimental scattering data using *CRYSOL*[411]. Rigid body models were calculated using *CORAL*[528]. *Ab initio* models were calculated using *GASBOR*, fitting to reciprocal space[529]. A summary of the SAXS data acquisition and processing is given in Supplementary Table A.2.

A.5.9 Formation of Pf20S and PfPA28 complex

Frozen aliquots of *Pf*20S proteasome and *Pf*PA28 were thawed. *Pf*20S and *Pf*PA28 were mixed with a molar ratio of 1 : 1 or 1 : 2 (*Pf*20S : *Pf*PA28) in 25 mM Tris-HCl, pH 7.4, 100 mM NaCl, 5 mM $MgCl_2$ and 1 mM DTT. The mixture was incubated for 15 min at room temperature. Formation of the complex was assessed by Native-PAGE and the double PA28 capped proteasome was the predominant species in the mixture.

A.5.10 Cleavage of small peptide substrates by Pf20S and PfPA28

Enhancement of proteasome activity mediated by *Pf*PA28 was determined using Ac-nLPnLD-AMC (Bachem) for caspase-like (β1) activity, Ac-WLR-AMC (custom, Anaspec, Freemont, CA) for trypsin-like (β2) activity and Ac-WLA-AMC (custom, Anaspec, Freemont, CA) for chymotrypsin-like (β5) activity. Optimal activity of all three *Pf*20S catalytic subunits was achieved using the reaction buffer consisting of 50 mM Tris, 5 mM $MgCl_2$, 1 mM DTT, 0.01% BSA, pH 7.4. The reaction was initiated by adding 1nM *Pf*20S to the AMC substrates with increasing concentrations of *Pf*PA28. The incubation was performed at 37°C for 2 h. Release of AMC fluorophore (Ex: 360 nm, Em: 450 nm) was measured using a fluorescence microplate reader (FLUOstar, BMG Labtech). Slopes of AMC formation from 30 min to 120 min were determined to assess the cleavage rate.

A.5.11 Degradation of p16 by Pf20S and PfPA28

Human p16 recombinant protein was purchased form Novus Biologicals. 1.4 μM human p16 protein was incubated with 50 nM *Pf*20S in the absence or presence of 300 nM *Pf*PA28 at 37°C for 3, 6 and 10 h. Reaction buffer consists of 50 mM Tris, 5 mM $MgCl_2$ and 1 mM DTT. Reactions were stopped by the additional of SDS

loading buffer and boiled briefly. Samples were run on a 4-12% Bis-Tris acrylamide gel and quantification was performed using ImageJ.

A.5.12 Cryo-EM sample preparation and data acquisition

Cryo-EM was performed at the Bio21 Institute Advanced Microscopy Facility, The University of Melbourne (www.microscopy.unimelb.edu.au). Initial studies revealed extensive dissociation of the complex during vitrification. To overcome this problem, samples of *Pf*20S and *Pf*PA28 (at a 1:1 ratio; 500 μg/mL) were treated with 0.1% glutaraldehyde (5 min, 4°C), then prepared on UltrAuFoil grids (R2/2, Quantifoil Micro Tools GmbH) that had been subjected to glow discharge (25mA for 30 s). The samples were applied to the grid at 100% humidity, 4°C, in a Vitrobot MarkIV (FEI, Hillsboro, OR) and blotted for 3 s with a blot force of -1, before the grid was frozen by plunging in liquid ethane. Grids were imaged using a Gatan K2 direct detector and GIF bio Quantum energy filter mounted on a Talos Arctica (FEI, Hillsborough, Oregon) with a 70-μm objective aperture. The detector was operated in counting mode and the energy filter in zero-loss mode with a slit of 20 eV. The complex was imaged at a 1.31 Å/ pixel (100,000 × microscope magnification) with a defocus range of -1.5 to -2.5 μm. The dose rate was 3.2 electrons $Å^{-2}$ s^{-1} with 10 s exposures captured in 40 frames for a total dose of 32 electrons $Å^{-2}$.

A.5.13 Image processing and reconstruction

All analyses were carried out using the RELION3.0 pipeline[425,426]. Movie motion was corrected using MotionCor2.1 and Gctf1.06 was used for CTF estimation. A total of 212,749 particles were extracted from 5,200 motion-corrected movies. After reference-free 2D class averaging, 160,563 particles were retained, from which 3,600 were used to create a *de novo* model. The particles were then subjected to 3D class averages with 6 classes and 36,211 particles were retained for uncapped 20S, 57,337 for single-capped and 27,688 for double-capped. Multibody refinement was carried out for *Pf*PA28/*Pf*20S complexes. Masks were generated from initial consensus maps using 15 Å low pass filtered density corresponding to the *Pf*PA28 and *Pf*20S components, a binarisation threshold of 0.006 was used, which was extended by 3 pixels and a soft edge of 7 pixels was added. Analysis of *Pf*PA28

motions was achieved by alignment of the 20S core for each resulting map. Final refinement with symmetry gave resolutions of 3.54 Å for the uncapped (C2 symmetry), 3.92 Å for the single-capped (C1 symmetry) and 3.82 Å (C2 symmetry) for the double-capped 20S proteasome. For the unstabilised single-capped structure, 9482 particles (including only 958 particles from tilts less than 45°) were used to generate the maps, resulting in a resolution of 4.69 Å. Resolution was estimated using gold standard FSC = 0.143 calculated using a relaxed solvent map.

A.5.14 Model building and refinement for cryo-EM structures

For model building, the initial refined maps were sharpened using *phenix.auto_sharpen*[428]. Initial rigid body fitting was carried out in *Chimera*, followed by automated refinement in *phenix.real_space_refine*, then cycles of manual refinement in *COOT*[402] and automated refinement in *phenix.real_space_refine*[402,431]. Modified coordinates from the previously published structure of *Pf*20S[469] and our *Pf*PA28 crystal structure coordinates were used as initial models. The *Pf*PA28 cap was built from chain M of the crystal structure of *Pf*PA28 using NCS operators. The refined double-*Pf*PA28 capped structure was used as the starting model for the uncomplexed *Pf*20S and single-*Pf*PA28 capped structures. Due to the low resolution of the maps, and to ensure plausible model geometry, Ramachandran restraints were used throughout refinement[554]. Reference model restraints were used for *Pf*PA28, and NCS constraints were used for *Pf*20S and double-capped *Pf*20S. Peptide planarity constraints were additionally used. Protein regions that were not well-recovered in the map were not modelled. All sidechains were included in the model and all *Pf*PA28 activation loops were retained. Geometry validation was performed using the *phenix.validation_cryoem* tool (incorporating *MOLProbity*) and *EMRinger*[432,433]. Structures were visualised using either *PyMOL* 2.2 or *Chimera*. Map-model FSC curves were calculated in *Phenix*. Surface electrostatics were evaluated using the Adaptive Poisson-Boltzmann Solver (APBS) software[553] in PyMol. Axes of *Pf*PA28 heptamer and *Pf*20S were calculated in *Chimera* using residues 175-219 (helix 3) of *Pf*PA28 and all residues of *Pf*20S. A summary of the cryo-EM data processing and model building is provided in Supplementary Table A.3.

A.5.15 MD simulations

Two models of the complete *Pf*PA28 structure were created on the basis of the two copies of the protein in the asymmetric unit of the crystal structure (PDB ID: 6DFK). For each model the missing loops were built using MODELLER 9.20[555] and the structures were solvated and ionised to be electrically neutral with 0.15 M NaCl. Simulations were carried out for each model at 310 K with a 5 ns equilibration phase followed by 30 ns MD using NAMD 2.13[415] and analysed with VMD[417]. RMSD calculations were made by comparison of the α carbon (CA) atoms of the crystallographic *Pf*PA28 monomers with structures at various time-points during the corresponding simulations.

For simulations of the *Pf*20S/*Pf*PA28 single-capped structure the missing residues in the cryo-EM structure of the single-capped proteasome (PDB ID: 6MUX) were initially built using MODELLER 9.20 then refined by minimisation incorporating secondary structure restraints derived from PSIPRED[556] analysis of the subunit sequences. For simulations of the escape of water from the *Pf*20S/*Pf*PA28 single-capped structure, the missing residues in the cryo-EM structure of the single capped proteasome (PDB ID: 6MUX) were built using MODELLER 9.20 then refined by minimisation, incorporating secondary structure constraints derived from PSIPRED86 analysis of the subunit sequences. The position of *Pf*PA28 on this single cap model was adjusted to give structures matching the two extreme cap positions observed in the cryo-EM data, resulting in three final models. The three single cap models were solvated and ions added as described for *Pf*PA28 above. Simulation was carried out for each model at 310 K for several nanoseconds using NAMD, and the ability of water molecules to transit from within the *Pf*PA28 cavity in each model examined using VMD.

A.5.16 Statistical analysis

The significance of differences was determined by two-tailed paired and unpaired Student's t-test for Figures 1b and 1c, respectively. For Supplementary Figure A.1f, the significance was examined using two-tailed ratio paired Student's t-test. P

values are represented as $P < 0.05$, *; $P < 0.01$, **; $P < 0.001$, ***. All statistical analyses were performed with GraphPad Prism v6.0 for Mac OS X.

A.5.17 Code availability

The computational codes or mathematical algorithms used in this study are available from the corresponding authors upon request.

A.5.18 Data availability

The coordinates and structure factors for *Pf*PA28 were deposited in the Protein Data Bank with accession code 6DFK. SAXS data and models were deposited into the SASBDB with accession code SASDES6. The coordinates for the uncapped, single *Pf*PA28-capped, and double *Pf*PA28-capped *Pf*20S, were deposited in the Protein Data Bank with accession codes 6MUW, 6MUX and 6MUV, and the density maps were deposited in the Electron Microscopy Data Bank with accession codes EMD-9258, EMD-9259 and EMD-9257, respectively. The density map for the unstabilised *Pf*PA28 single-capped complex was deposited in the Electron Microscopy Data Bank with accession code EMD-20073. The data that support the findings of this study are available from the corresponding authors upon request.

A.6 Supplementary Information

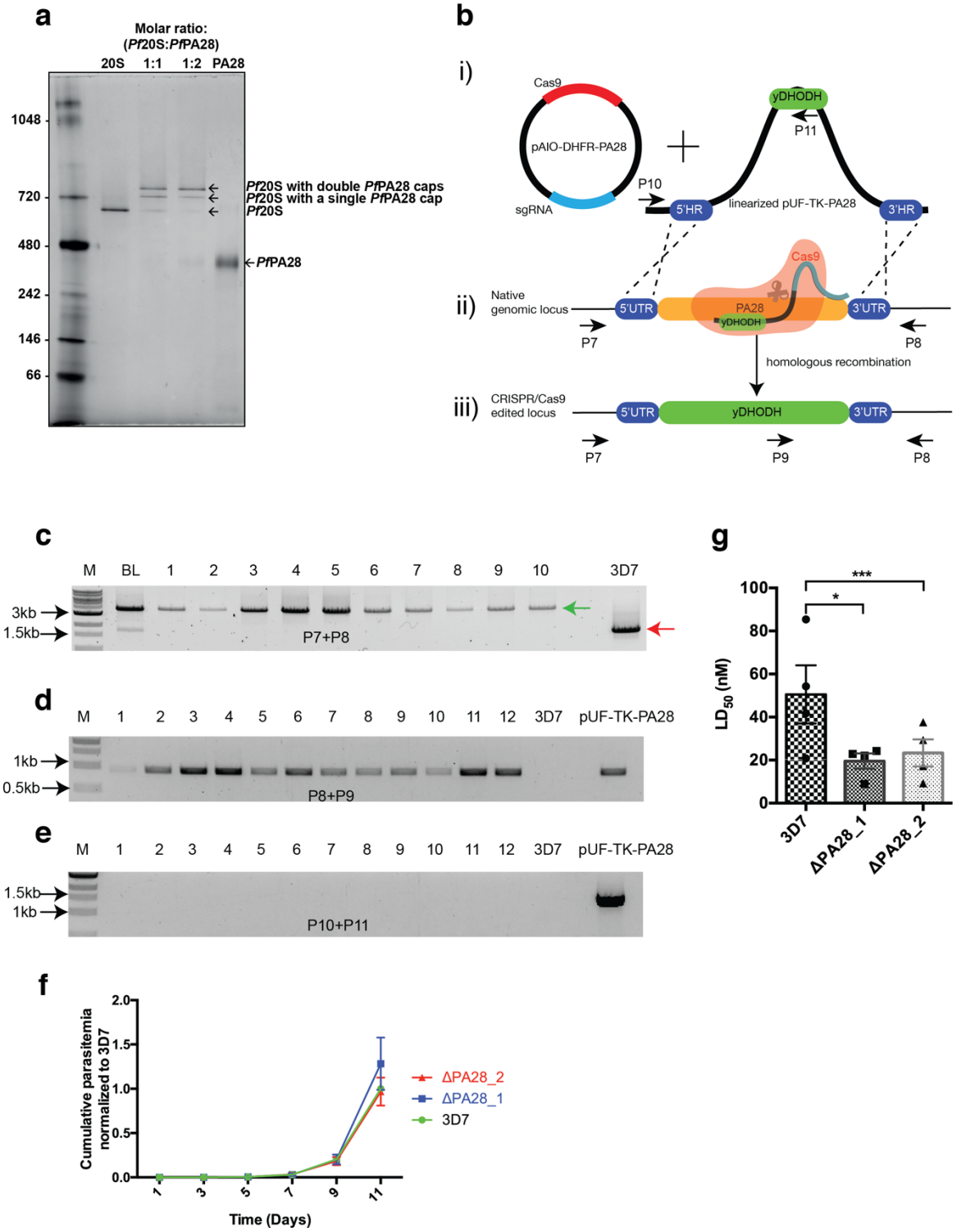

Supplementary Figure A.1: Generation of the PfPA28/Pf20S complex and molecular analysis of the PfPA28 knock-out.

(a) *P. falciparum* 20S proteasome was purified from infected RBCs using a three-step chromatographic procedure. *Pf*20S and *Pf*PA28 were mixed at a molar ratio of 1:1 or 1:2. Formation of the complex was assessed by Native-PAGE. This is a

representative gel from 3 independent experiments with similar results. (b) Schematic of strategy used for generating Δ*Pf*PA28 strains. The desired integration event was achieved using CRISPR/Cas9 editing. i) pAIO-DHFR-PA28 vector expressing both the sgRNA and Cas9 endonuclease. Linearised pUF-TK-PA28 vector, containing 5' and 3' homology regions (HR) of *Pf*PA28 gene and yeast DHODH (yDHODH). ii) *Pf*PA28 is targeted by sgRNA and cleaved by Cas9. iii) *Pf*PA28 is replaced with yDHODH gene by homologous recombination. Primers for PCR validation are shown in Supplementary Table A.4. (c) PCR screening using primers flanking the 5' and 3' UTR regions (P7+P8). The 3D7 parent has a band at 1.8 kb representing endogenous *Pf*PA28 (red arrow). Before limiting dilution (BL) the ΔPA28 culture has two bands, 3.9 kb for the yDHODH integration and 1.8 kb for the native *Pf*PA28. Ten clones (1-10) were analysed following limiting dilution. Only the band at 3.9 kb (green arrow) is present. (d) Twelve clones (1-12) were further validated using PCR (P8+P9). Bands at 0.9 kb are present in each of the twelve clones and pUF-TK-PK28 vector but not in 3D7. (e) Validation of absence of residual pUF-TK-PK28 vector in clones 1-12 using PCR (P10+P11). The band at 1.5 kb is present only in the pUF-TK-PA28 vector. (f) Analysis of growth rates. *Pf*PA28 wildtype and two knock-out clones were synchronised (initiated at 0.8% haematocrit, 0.8% parasitemia ring stage) and followed for 11 days. Equivalent dilutions were applied as required to wildtype and knock-out infected RBCs. Nucleic acids were stained with SYTO 61 and parasitemia assessed by flow cytometry. Raw values were corrected for dilutions and normalised to the wildtype at day 11. Data represent mean $\pm$ S.E.M from 3 independent experiments. (g) Cultures of wildtype 3D7 or ΔPA28_1 or ΔPA28_2 clones at the ring stage (7-8 h post invasion) were exposed to increasing concentrations of dihydroartemisinin (DHA) for 3 h, before removal of the drug and analysis of viability in the next cycle. Mean LD_{50} values $\pm$ S.E.M from 4 independent experiments. $^{*}P<0.05$ and $^{***}P<0.001$ for ratio paired two-tailed t-test. For the 3D7 and ΔPA28_1 comparison, P=0.0127, t=5.4 and df=3. For the 3D7 and ΔPA28_2 comparison, P=0.0009, t=13.5 and df=3.

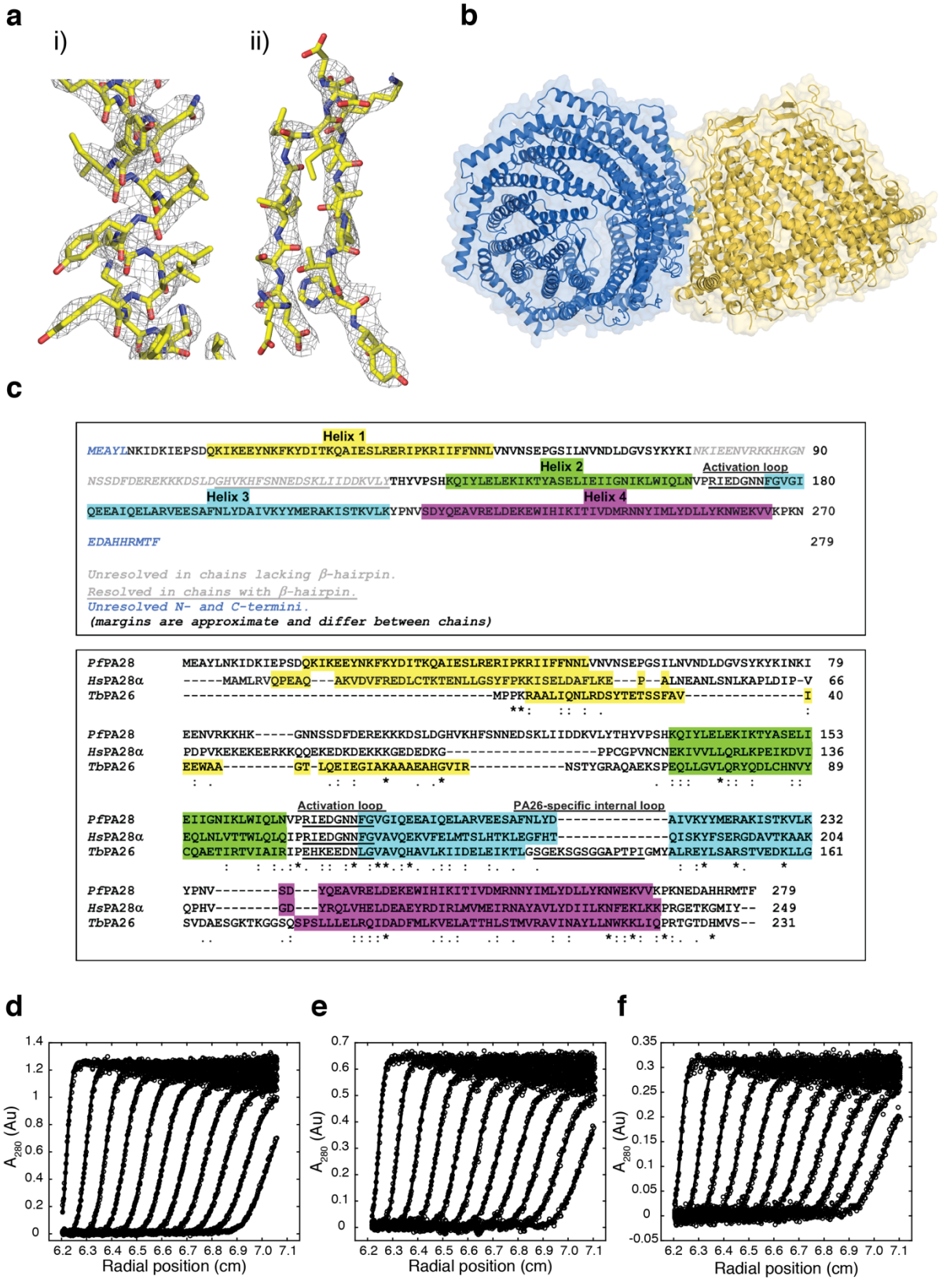

Supplementary Figure A.2: *Pf*PA28 structure, sequence and sedimentation analyses.

(a) Representative 2*Fo-Fc* map of *Pf*PA28, showing i) part of helix 4 (contoured at 1.5 σ), ii) the apical β-turn (contoured at 1 σ). (b) Representation of the asymmetric unit. As in Figure A.2c, helices 2 to 4 form a helical bundle and provide the majority of the interactions within the monomers. Helix 4 is capped by a short helical segment oriented approximately orthogonally to the long axis of the helical bundle. The N-terminal helix (helix 1) lies on the outer surface of the heptamer and contains a kink induced by Pro42. This helix wraps around the base of the bell, providing a belt that runs across the surface of the helical bundle, and interacts with helix 1 of the adjacent monomer. (c) Top. *Pf*PA28 sequence with relevant features indicated. Bottom. Sequence alignment of *Tb*PA26, human PA28α and *Pf*PA28 generated using Clustal W2 (www.ebi.ac.uk/Tools/msa/clustalw2/). Helices were assigned based on the crystal structures for PA26: PBD 1Z7Q, HuPA28: PDB 1AVO and *Pf*PA28: our structure. (d-f) Raw analytical ultracentrifugation-sedimentation velocity data for *Pf*PA28 (collected at three concentrations, each measured in singlicate), overlaid with fits to a continuous sedimentation coefficient (c(s)) model, at (d) 0.8, (e) 0.4 and (f) 0.2 mg/mL.

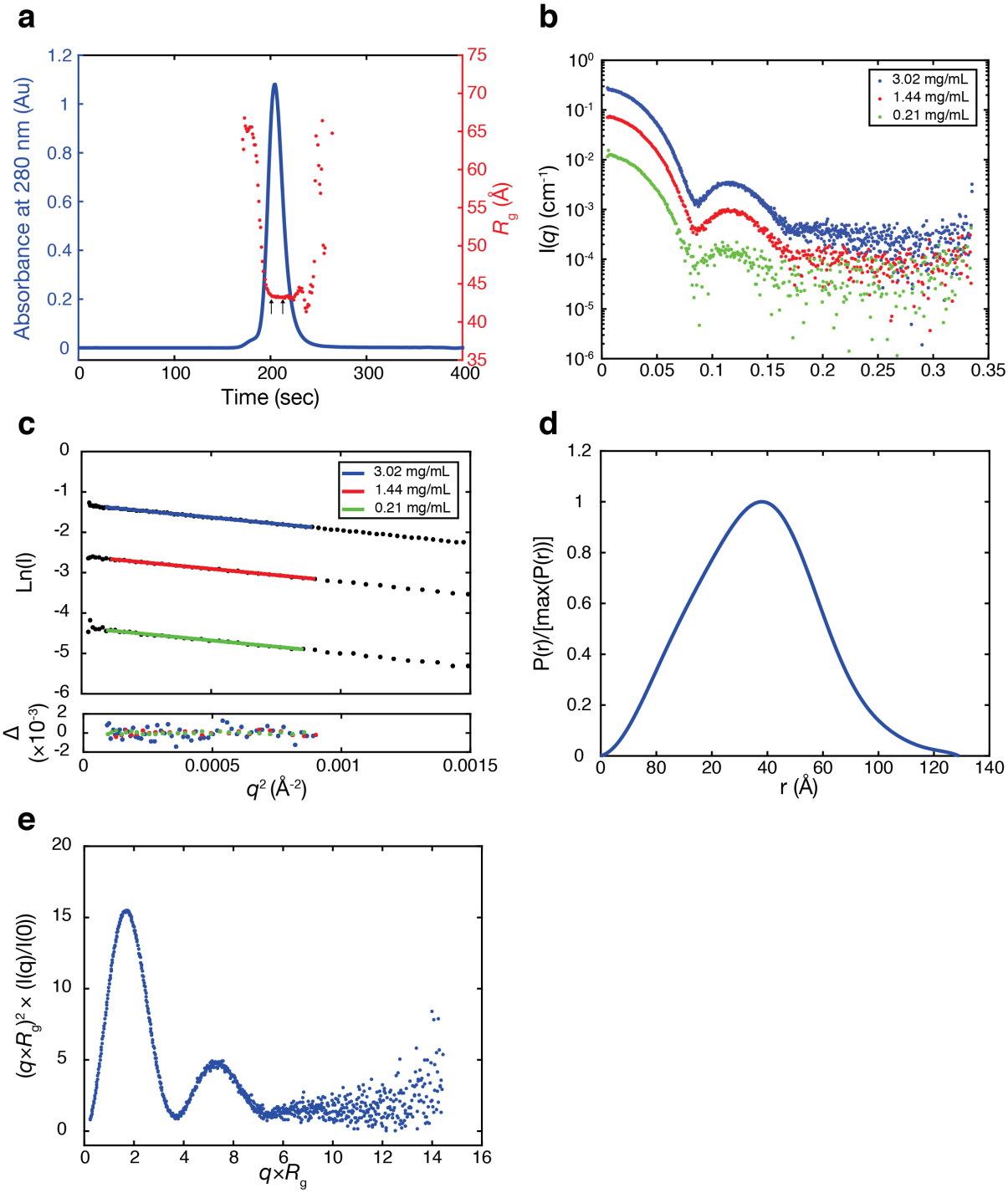

Supplementary Figure A.3: Quality analysis of SAXS data for *Pf*PA28.

(a) SEC-SAXS chromatogram (representative of data collected at three concentrations, each in singlicate). The frames used for analysis are indicated. (b) SAXS data collected at loading concentrations of 10 mg/mL (used for all modelling), 5 mg/mL and 1 mg/mL. No concentration-dependence was observed for the scattering profiles in (b), nor was any concentration dependence observed in the Guinier plot in (c). The concentrations indicated in the panels (b) and (c) are the

effective concentrations following SEC chromatography that were used for SAXS analysis. The plot of the pairwise distance distribution function (P(r) plot) is shown in (d), and (e) shows a dimensionless Kratky plot, both calculated from the data acquired at a loading concentration of 10 mg/mL.

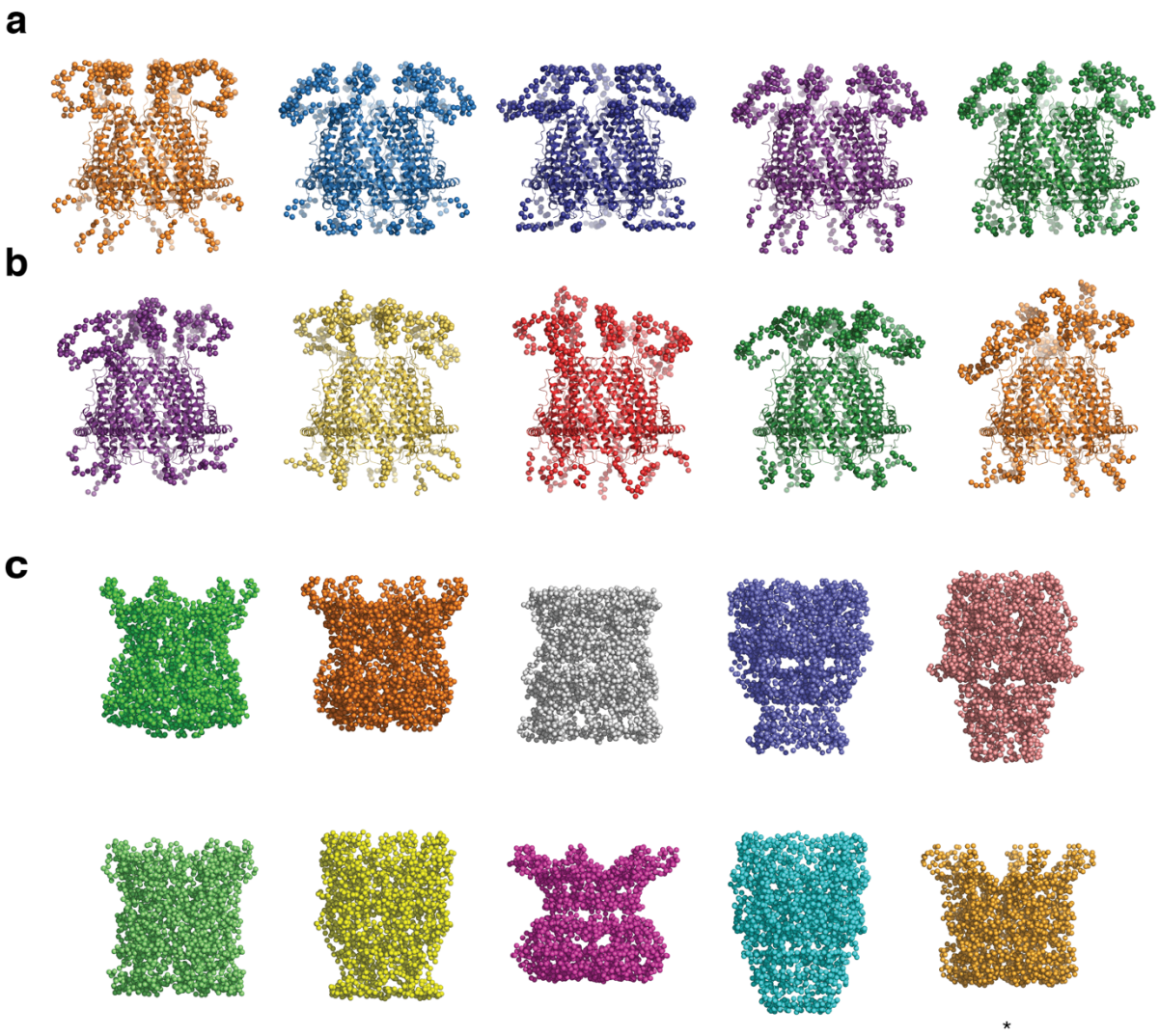

Supplementary Figure A.4: Modelling of PfPA28 structure based on SAXS analysis.

(a) Five *CORAL* models generated assuming loop symmetry. (b) Five *CORAL* models generated assuming loop asymmetry. The five models generated did not differ substantively. These models show that the apical loops extend away from the *Pf*PA28 structured core. (c) Ten *GASBOR* models calculated from the scattering profile. The outlier (as judged by *DAMAVER*) is indicated with an asterisk. These models support our crystal structure and hybrid models. Additionally, we used *HYDROPRO* to calculate the theoretical coefficient for molecules corresponding to the crystal structure and the hybrid models[377]. The theoretical sedimentation coefficient for *Pf*PA28, without considering the apical loops, is 11 S, and 9.2 S with asymmetric loops (9.1 S for the model with symmetric loops), in good agreement

with the experimental sedimentation coefficient, and providing further evidence for the extended conformation of the loops.

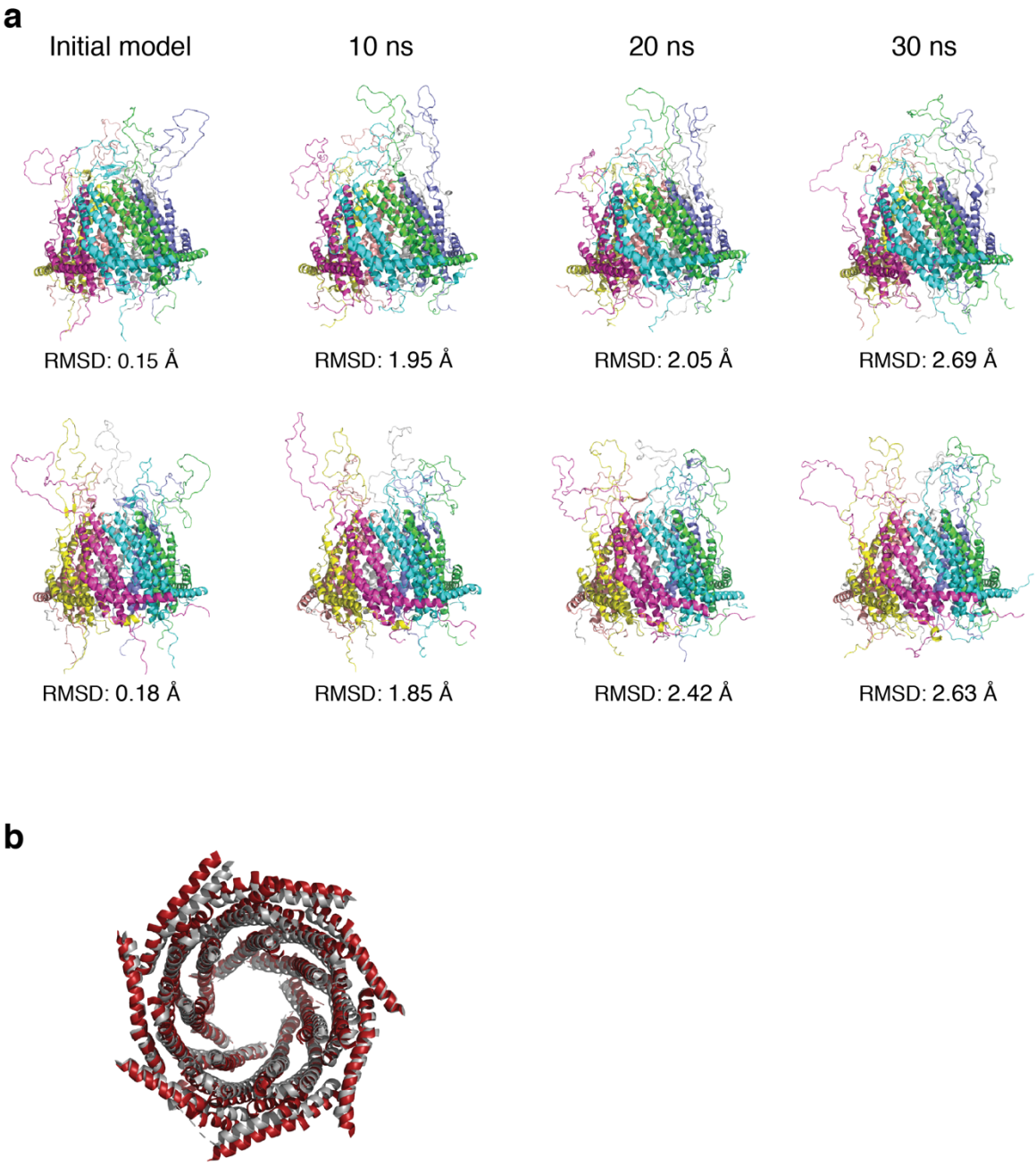

Supplementary Figure A.5: Variation in the loop structure and core of PfPA28 during MD simulation.

(a) Each row of structures shows cartoon representations of MD results for two separate *Pf*PA28 models, built using the structures present in the asymmetric unit of the *Pf*PA28 crystal structure 6DFK. The initial models after minimisation are shown on the left, with subsequent structures being taken at 10 ns time points from the MD simulation. Clearly there is extensive variation in the position of the apical loops, while the heptameric ring undergoes a subtle asymmetric expansion. RMSD values reported are for the α carbon atoms of the helical core residues at each time

point compared to the original crystallographic structures. (b) Overlay of the helices of the initial (grey) and final (red) MD structures from the same heptamer model. See Supplementary Movie 1 for animation of the MD simulation images.

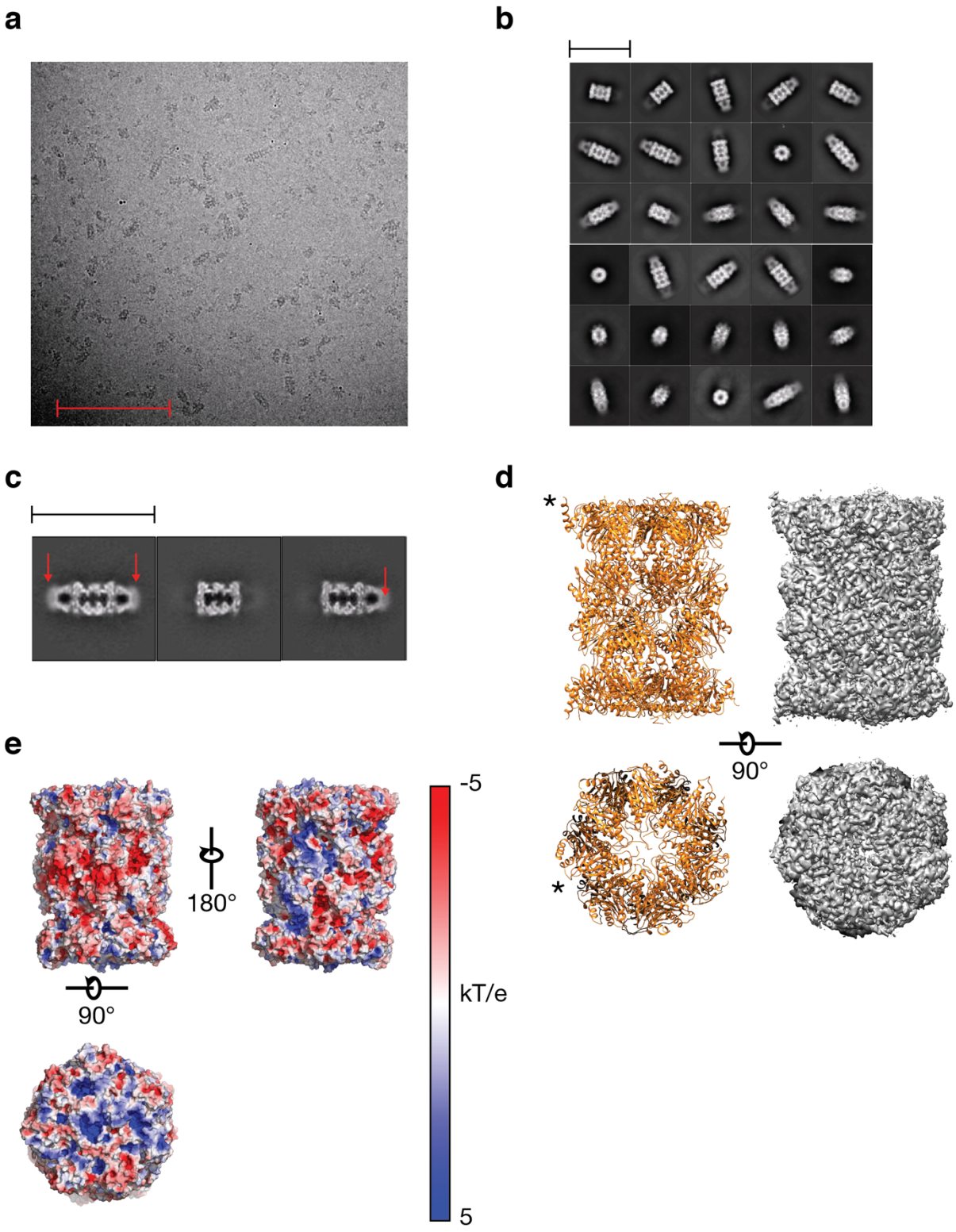

Supplementary Figure A.6: *Pf*20S/*Pf*PA28 raw data, class averages and 20S maps.

(a) Representative micrograph (from 5200 collected). (b) 2D class averages. (See Supplementary Table A.3 for particle numbers). (c) 3D classifications of uncapped, single-capped and double-capped *Pf*20S. (See Supplementary Table A.3 for

particle numbers), with arrows indicating the apparent flexible features at the apical end of *Pf*PA28. (d) Cryo-EM density for the uncapped *Pf*20S proteasome, alongside the structure. (e) Surface electrostatics for *Pf*20S. Scale bar: (a) 200 nm. Box size (b,c) 45 nm.

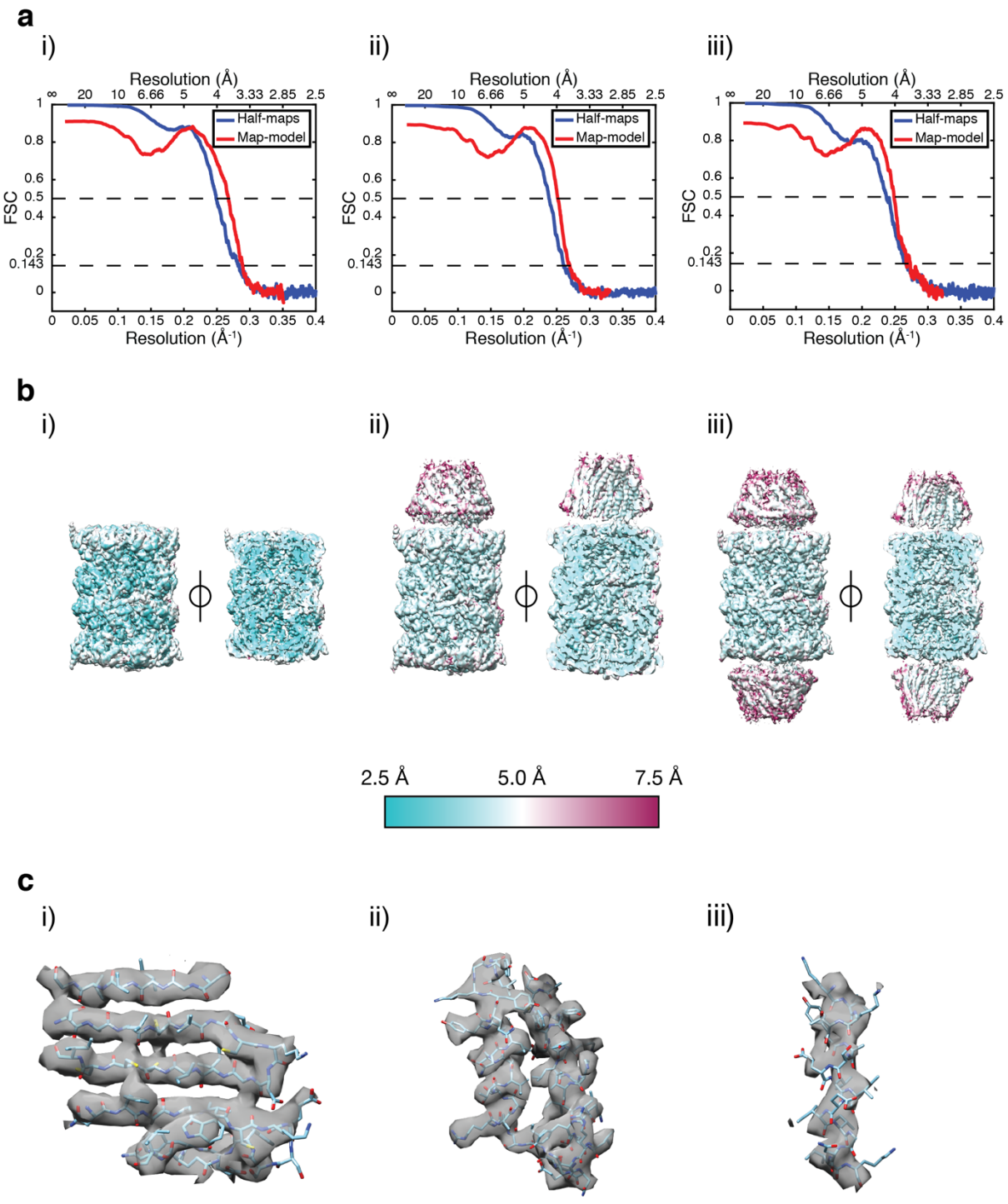

Supplementary Figure A.7: Resolution estimation.

(a) Gold standard half-map and map-model FSC curves for the i) uncapped, ii) single-capped and iii) double-capped complexes. (See Supplementary Table A.3 for particle numbers used for the calculation). (b) Local resolution maps for the i) uncapped, ii) single-capped and iii) double-capped complexes. (c) Representative cryo-EM density (contoured at 5 σ) for the single-capped structure, showing i)

density for a β-sheet in the α7 subunit, ii) density for two α-helices in the β5 subunit and iii) density for helix 2 in *Pf*PA28.

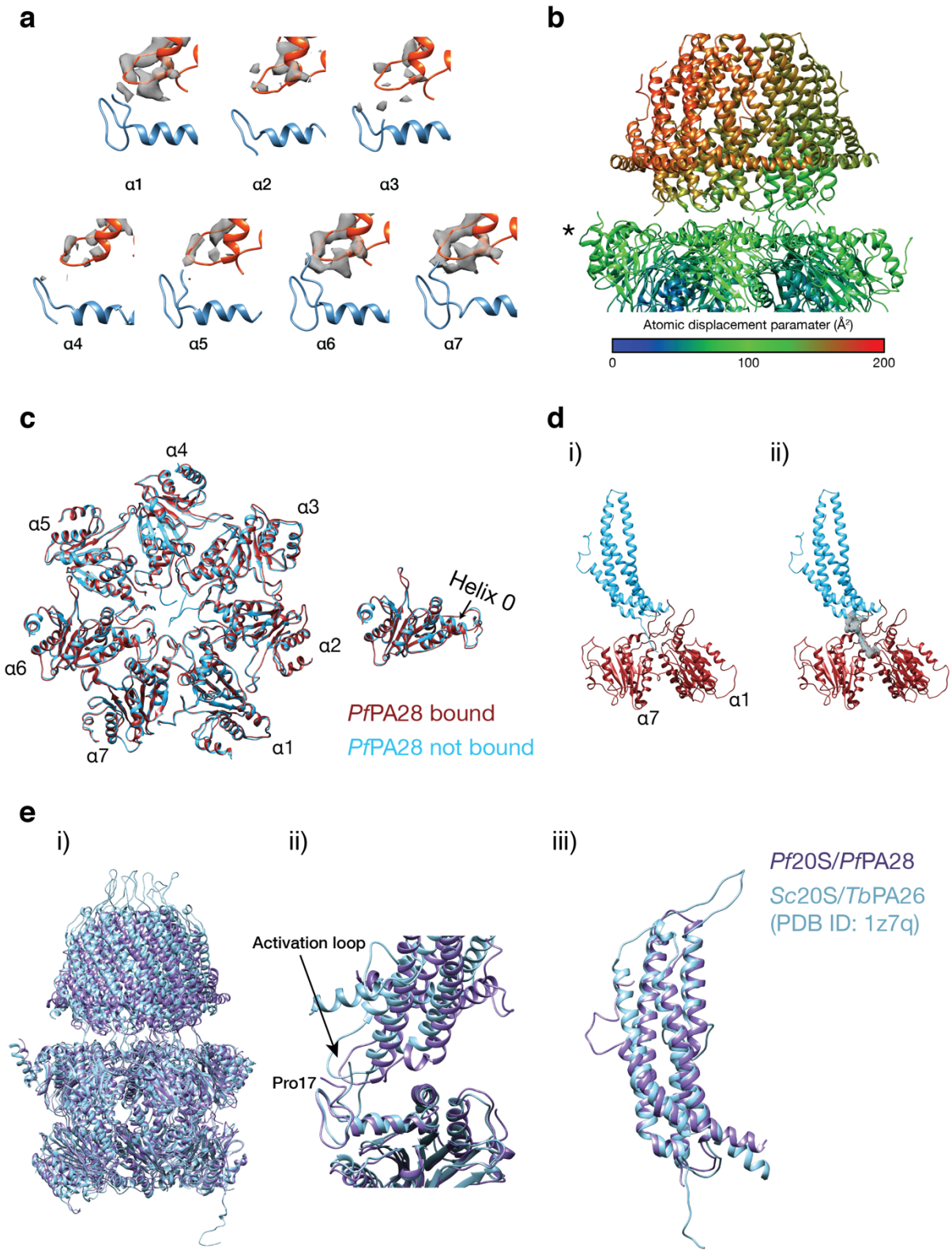

Supplementary Figure A.8: Asymmetric binding of PfPA28 to Pf20S.

(a) Density for the activation loop of all *Pf*PA28 monomers binding *Pf*20S from the single-capped complex, contoured at 5 σ. All activation loops were included in the final model. (b) The single-capped complex coloured by atomic displacement

parameter (ADP). The position of the α4 subunit is marked with an asterisk. (c) Structural overlay of the bound and unbound α subunit rings in the single-capped *Pf*20S structure, showing the small displacement of helix 0 in the α6 subunit. (d) Weak density supporting the position of the C-terminus of the *Pf*PA28 monomer binding the α1 and α7 subunits in the double-capped complex, contoured at 3 σ. (e) Alignment of the structure of the *Pf*PA28/*Pf*20S complex with the structure of the *Sc*20S/*Tb*PA26 complex[525]. i) Superposition of the activator, α, and β rings, showing the rotation of *Tb*PA26 with respect to *Pf*PA28. ii) The position of the activation loop of the two structures in the alignment shown in (i). iii) An independent alignment of one *Pf*PA28 subunit with a *Tb*PA26 subunit showing overall subunit structural similarity.

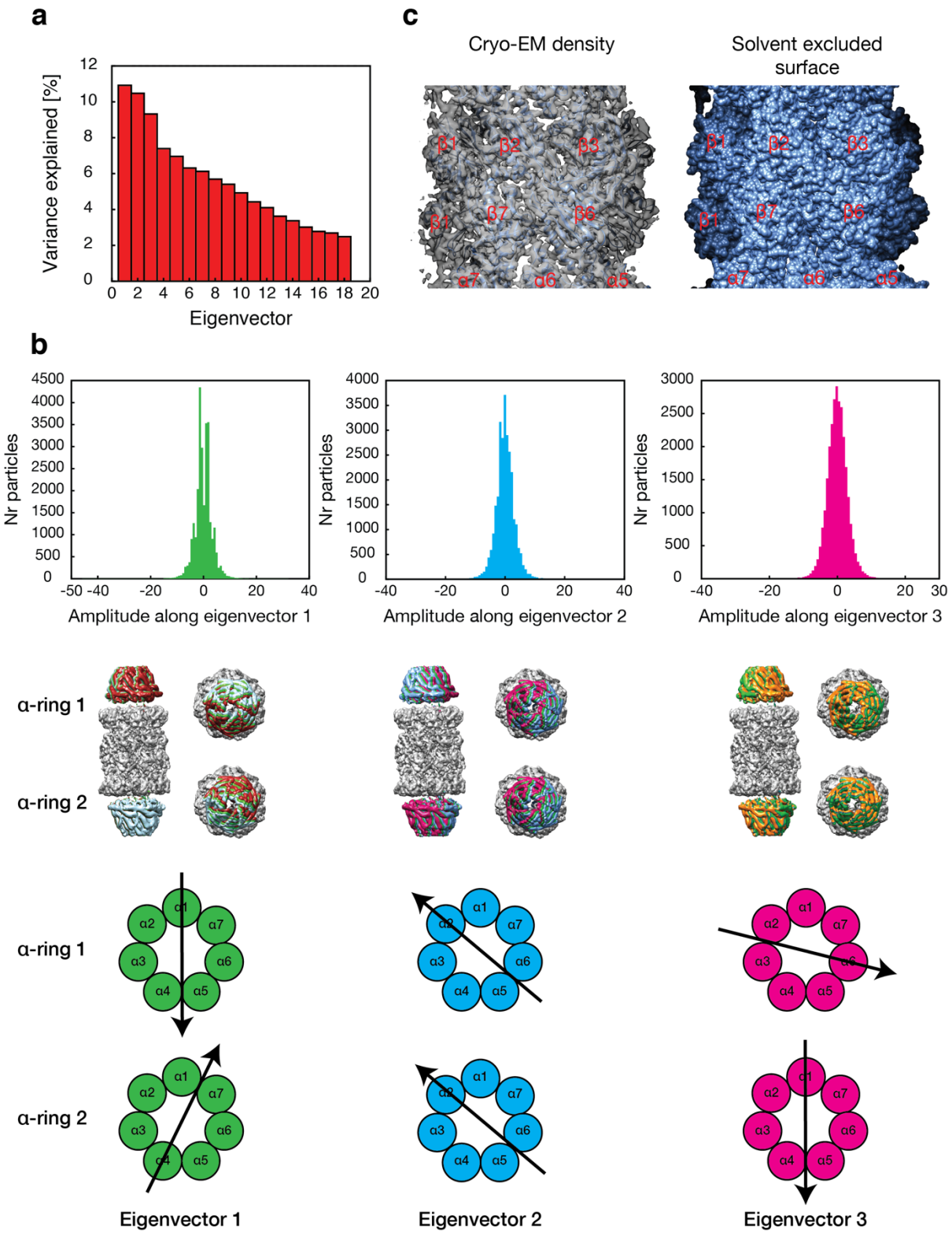

Supplementary Figure A.9: Interface and pivoting motion of the double-capped Pf20S/PfPA28 complex.

(a) Contributions of all eigenvectors to the motion in the double-capped complex. (b) Top. Histograms of the amplitudes along the first three eigenvectors in the double-capped complex. The histogram for the first eigenvector is bimodal in

character, appearing to consist of two unimodal distributions, likely a combination of two unimodal distributions for each *Pf*PA28/*Pf*20S interface, as it is unlikely that the motion is correlated across the core *Pf*20S particle. Middle. Density maps visualizing the motion along the eigenvectors. Bottom. Schematic showing the approximate movement corresponding to the eigenvectors. (c) Cryo-EM density and solvent accessible surface for the double-capped *Pf*PA28/*Pf*20S complex showing side-windows visible in the core particle. The example shown is formed at the interface between the β1/β2/α1 subunits and represents a possible route of substrate egress.

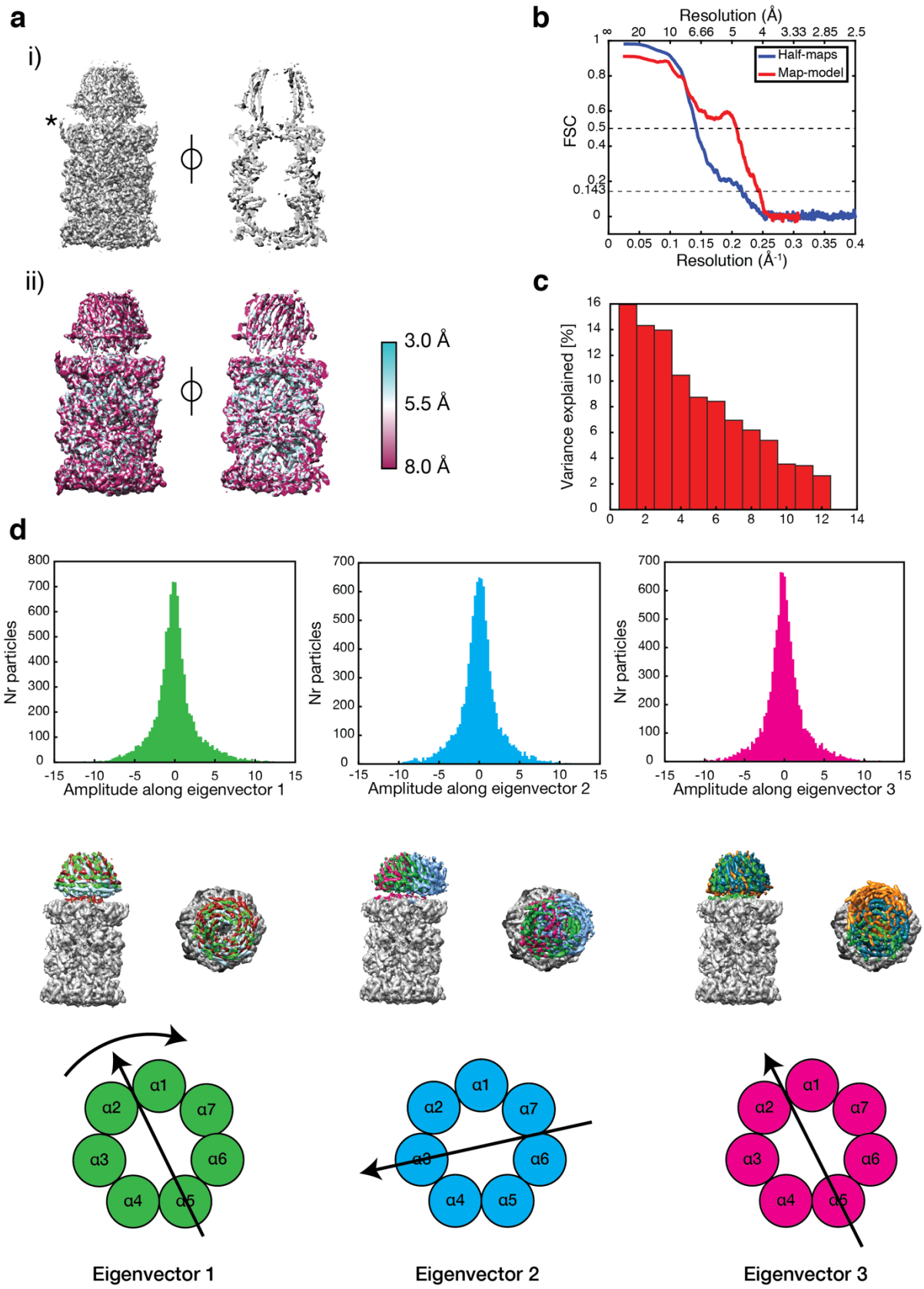

Supplementary Figure A.10: Structure and dynamics of the unstabilised PfPA28/Pf20S complex.

(a) Cryo-EM density map of the unstablised single-capped *Pf*20S and cross-section showing the continuous channel formed by *Pf*20S and *Pf*PA28. The asterisk indicates the position of the α4 subunit. (b) Gold standard half-map and map-model FSC curves for the unstablised single-capped complex. (c) Contributions of all eigenvectors to the motion in the unstablised single-capped complex. (d) Top. Histograms of the amplitudes along the first three eigenvectors in the unstablised complex. Middle. Density maps visualizing the motions along the eigenvectors. Bottom. Schematic showing the approximate movement corresponding to the eigenvectors.

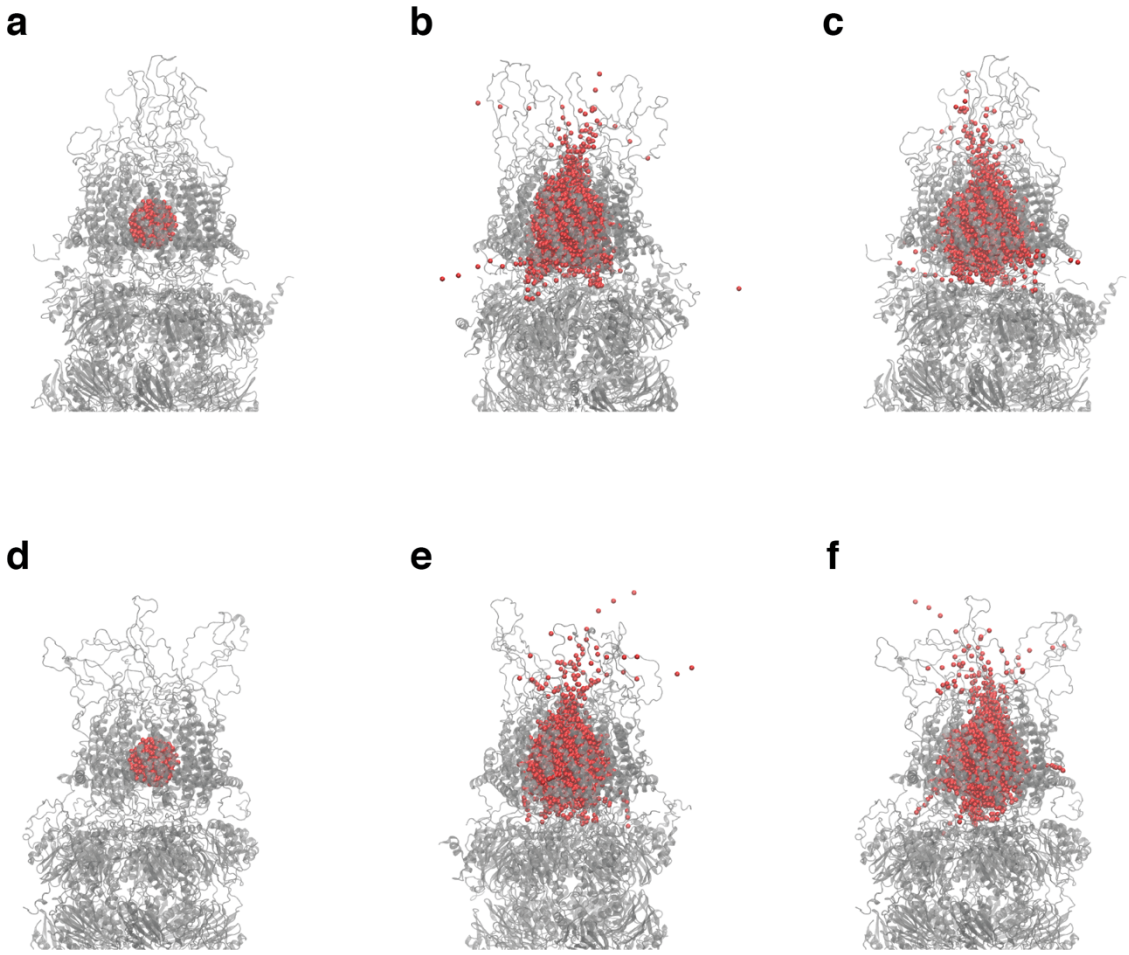

Supplementary Figure A.11: Molecular dynamics simulation of water molecules at the PfPA28/Pf20S interface.

Diagrammatic representation of the mobility of water molecules in the interface between *Pf*PA28 and *Pf*20S in MD simulations of two extremes of the observed distribution of *Pf*PA28 positions. Structures of two different *Pf*PA28 orientations are shown, with panels (a-c) representing an extreme tilted orientation and panels (d-f) representing a more central position of the cap. The proteins are shown as a transparent grey cartoon and the water molecules as red spheres. Panels (a) and (d) show the initial set of water molecules chosen, a sphere of 13Å radius centered within the PA28 vestibule containing ~310 waters. Panels (b) and (e) show the evolution of the position of these water molecules over 10 frames (2 ns) of MD simulation with panels (c) and (f) showing orthogonal views of the same data. Waters are observed to escape the *Pf*PA28 vestibule through the *Pf*PA28/20S interface as well as through the pore. Sideways escape is dependent on the cap

position, with more solvent taking this route in the off-centered *Pf*PA28 position in panels (a-c).

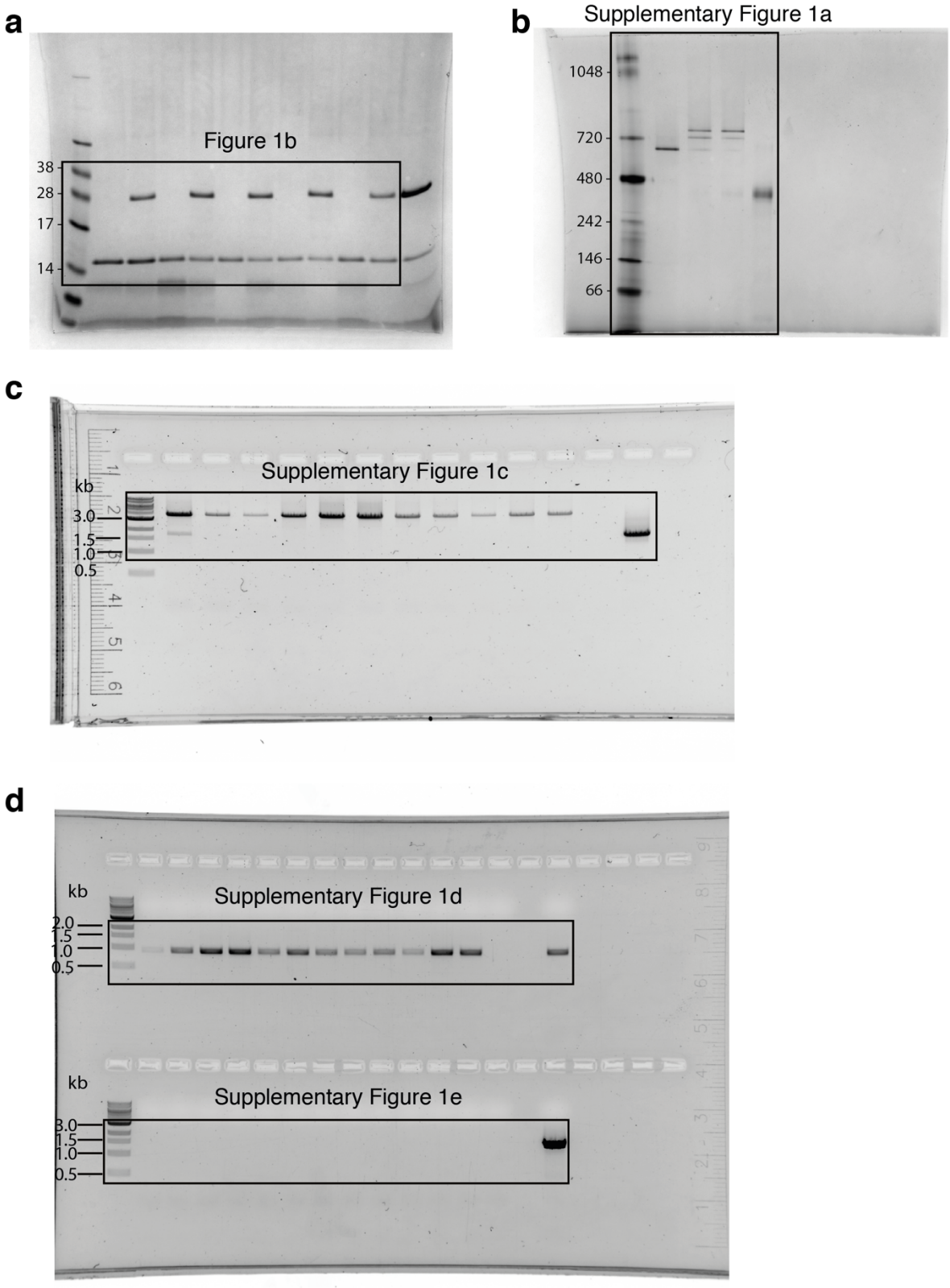

Supplementary Figure A.12: Full-length raw gel images.

Sections of the full gels that were used to generate figures are indicated in the boxes. (a) Figure A.1. (b) Supplementary Figure A.1A. (c) Supplementary Figure A.1C. (d) Supplementary Figure A.1D, E.

A.7 Supplementary Tables

Supplementary Table A.1: X-ray diffraction data collection and refinement statistics for *Pf*PA28.

	*Pf*PA28
Data collection	
Space group	$P3_121$
Cell dimensions	
a, *b*, *c* (Å)	166.49, 166.49, 399.16
α, β, γ (°)	90, 90, 120
Resolution (Å)	48.89-3.10 (3.15-3.10)
R_{sym}	0.275 (2.236)
$CC_{1/2}$	0.996 (0.513)
$I / \sigma I$	7.5 (1.2)
Completeness (%)	100.0 (100.0)
Redundancy	10.4 (10.7)
Refinement	
Resolution (Å)	48.89-3.10 (3.21-3.10)
No. reflections	116839 (11348)
R_{work} / R_{free}	0.182 (0.299) / 0.225 (0.317)
No. atoms	26498
Protein	26198
Ligand/ion	300
B-factors	77.9
Protein	77.0
Ligand/ion	148.6
R.m.s. deviations	
Bond lengths (Å)	0.004
Bond angles (°)	0.93

Values in parentheses are for highest-resolution shell. A single crystal was used.

Supplementary Table A.2: SAXS data and analysis.

SAXS data collection	
Instrument/source	Australian Synchrotron SAXS/WAXS beamline equipped with Pilatus 1M detector and sheath-flow cell for SEC-SAXS.
Wavelength (Å)	1.0332
Beam energy (keV)	12
Beam size (μm)	250 × 130
Sample-to-detector distance (mm)	2682
q measurement range ($Å^{-1}$) [a]	0.005 – 0.334
Absolute scaling method	Comparison with scattering from 1 mm pure water
Normalisation	To transmitted intensity from beamstop counter
Exposure time	1 s measurements from SEC-SAXS elution
Sample temperature (K)	295
SEC-SAXS parameters	
Column	Superdex 200 5×150 Increase
Flow rate (mL/min)	0.45
Loading concentration (mg/mL)	10
Injection volume (μL)	50
Average concentration in combined data frames (mg/mL)	3.02
Solvent	20 mM Tris-HCl, pH 7.4, 150 mM NaCl, 0.5 mM TCEP, 0.1% sodium azide
Software employed	

SAXS data reduction	*I*(*q*) vs *q* using Scatterbrain 2.8.2, SEC-SAXS solvent subtraction using *CHROMIXS* from *ATSAS* 2.8.3
Basic analysis (Guinier, *P(r)*, molecular mass)	*PRIMUS* from *ATSAS* 2.8.3
Ab initio modelling	*GASBOR*, fitting to reciprocal space, models aligned and compared using *DAMAVER* and *DAMCLUST* from *ATSAS* 2.8.3
Calculation of theoretical intensities	*CRYSOL* from *ATSAS* 2.8.3
Atomic structure (hybrid) modelling	*CORAL* from *ATSAS* 2.8.3

Structural parameters [b]	3.02 mg/mL	1.44 mg/mL	0.21 mg/mL
Mass from V_c (kDa) (ratio to expected, 232.2 kDa in brackets) [2]	263.0 (1.13)	257.8 (1.11)	259.0 (1.12)
Guinier analysis [c]			
R_g (Å)	43.26 ± 0.05	43.19 ± 0.29	42.98 ± 2.04
I(0) (cm^{-1})	0.27 ± 1.9×10^{-4}	0.075 ± 1.2×10^{-4}	0.013 ± 5.5×10^{-5}
qR_g min,max	0.41, 1.29	0.45, 1.30	0.42, 1.29
P(r) analysis			
R_g (Å)	42.54 ± 0.02	42.69 ± 0.04	43.14 ± 0.17
I(0) (cm^{-1})	0.2657 ± 1.3×10^{-4}	0.07454 ± 7.7×10^{-5}	0.01273 ± 5.7×10^{-5}
D_{max} (Å)	129	129	129
Porod volume ($Å^3$)	484000	454000	488000

Ab initio modelling [d]	
GASBOR (fitting to reciprocal space, 10 calculations, constant subtraction allowed)	
q range	0.00955-0.32511
Constant subtracted	1.127×10^{-4} - 9.718×10^{-5}
Symmetry, anisotropy assumptions	P7, unknown anisotropy
Number of Shannon channels	13.37
Number of dummy residues	280
χ^2 range	1.68-2.16
NSD (standard deviations)	1.230 (0.135), 1 model rejected
Atomic modelling [d]	
CRYSOL (no constant subtraction)	
Crystal structure	PDB ID: 6DFK (this work), chains H-N
χ^2	74.51
Calculated R_g (Å)	39.92
CORAL (symmetric loops, 5 calculations, no constant subtraction)	
Starting structure	PDB ID: 6DFK (this work), chain M
Symmetry assumptions	P7 (core and flexible residues)
Flexible residues modelled	6 residues at N terminus, 52 residues in internal loop, 9 residues at C terminus
χ^2 range	6.40 – 5.56
CORAL (asymmetric loops, 5 calculations, no constant subtraction)	
Starting structure	PDB ID: 6DFK (this work), chain M
Symmetry assumptions	P1, core with P7 symmetry

Flexible residues modelled	6 residues at N terminus, 52 residues in internal loop, 9 residues at C terminus
χ^2 range	4.69-5.51

SASBDB IDs for data and models: *SASDES6*

---

[a] $q=(4\pi\sin\theta)/\lambda$

[b] Structural parameters given at three concentrations (corresponding to loading concentrations of 10 mg/mL, 5 mg/mL and 1 mg/mL). The data acquired at a loading concentration of 10 mg/mL was deposited in the SASBDB.

[c] Errors from *AUTORG* or *GNOM*, mean $\pm$ standard deviation

[d] All *ab initio* and atomic modelling used the data acquired at a loading concentration of 10 mg/mL.

Supplementary Table A.3: CryoEM data collection and model building statistics.

	*Pf*20S	*Pf*20S + single *Pf*PA28 cap	*Pf*20S + double *Pf*PA28 caps	*Pf*20S + single *Pf*PA28 cap (unfixed)
Data collection and image processing				
Magnification	100,000	100,000	100,000	100,000
Electron energy (kV)	200	200	200	200
Electron exposure (e^- /Å^2)	28	28	28	28
Defocus range (μm)	1.5-3	1.5-3	1.5-3	1.5-3
Pixel size (Å)	1.31	1.31	1.31	1.31
Starting model	*De novo*	*De novo*	*De novo*	*De novo*
Symmetry imposed	C2	C1	C2	C1
Total number of micrographs	5200	5200	5200	622
Initial particle images	212,749	212,749	212,749	18,893
Final particle images	36,211	57,337	27,688	9482
Map resolution (Å)	3.54	3.92	3.82	4.6
FSC threshold	0.143	0.143	0.143	0.143
Model building and refinement				
Initial models used	PDB 5FMG	PDB 6MUV	PDB 6MUW, 6DFK (chain M)	
Model resolution (Å)	3.74	3.97	4.02	
FSC threshold	0.5	0.5	0.5	
Sharpening *B* factor (Å^2)	108.12	125.48	111.50	

Model composition			
Nonhydrogen atoms	49798	60284	71112
Amino acid residues	6252	7501	8796
Protein molecules	28	35	42
Real-space correlation			
CCvolume	0.80	0.80	0.80
CCmask	0.82	0.82	0.81
Mean Protein B factors (Å^2)			
*Pf*20S	77.80	67.46	65.17
*Pf*PA28	n/a	152.88	172.60
Overall	77.80	83.23	98.51
RMS deviations			
Bond lengths (Å) (outliers > 4σ)	0.007 (0)	0.009 (2)	0.008 (0)
Bond angles (°) (outliers > 4σ)	1.034 (42)	1.216 (100)	1.219 (98)
Validation			
EMRinger score [e]	1.51	1.35	1.15
MolProbity score [f]	1.93	1.99	1.96
Clashscore	7.03	7.40	7.34
Rotamer outliers (%)	0.95	0.80	1.10
CaBLAM outliers (%) [i]	4.67	4.58	3.52
Cβ outliers	0	0	0.07
Ramachandran plot			
Favoured (%)	90.19	88.87	90.73
Allowed (%)	9.64	10.96	9.13

Outliers (%)	0.16	0.18	0.14

e 432

f 433

Supplementary Table A.4: Primers used for the generation and characterisation of the PfPA28 knock-out transfectant.

P1)TAAGTATATAATATTTTAACATTTAATATACTCCCGTTTTAGAGCTAGAA

P2) TTCTAGCTCTAAAACGGGAGTATATTAAATGTTAAAATATTATATACTTA

P3) CAGGCGCCAGCCTAGG CACATGGAATTGTATTATAAATATG

P4) ATCGATAACTCCATGGTAACGATTCAATAGCTTGTTTTG

P5) AGATCTTCGGACTAGTAAGAAAGTGCATTCAATTTATATG

P6) CAATGGCCCCTTTCCGCGGTTAAAATGTCATTCTATGATGTG

P7) AATGGTTTGATACATGATCTC

P8) TTAGTATATTACCATTTTCTTCTC

P9) CCAATAGATAAAATTTGTAGAG

P10) GCACCATATGCGGTGTGAAATAC

P11) TTAGCTTATGTCAACTCTATCAATAG

A.8 Supplementary Movie Legends

Supplementary movies are available for viewing online (https://www.nature.com/articles/s41564-019-0524-4).

Supplementary Movie A.1: Animation of MD simulation *Pf*PA28.
The apical loops extend from the cap and undergo dynamic motions while individual monomers within the cap undergo more subtle relaxations from the starting crystal structure.

Supplementary Movie A.2: Single-capped complex – eigenvectors 1 to 3.
Movie showing the reconstructed multibody-refined densities repositioning along eigenvectors 1 to 3 shows a pivoting motion of the *Pf*PA28 cap on *Pf*20S. Top and side views.

Supplementary Movie A.3: Double-capped complex – eigenvectors 1 to 3.
Movie showing the reconstructed multibody-refined densities repositioning along eigenvectors 1 to 3 shows a pivoting motion of the *Pf*PA28 caps on *Pf*20S. Top and side views.

References

1 Camus, A. *The Myth of Sisyphus*. (Penguin, 2000).

2 Akdis, M. *et al.* Interleukins, from 1 to 37, and interferon-γ: Receptors, functions, and roles in diseases. *Journal of Allergy and Clinical Immunology* **127**, 701-721.e770, doi:10.1016/j.jaci.2010.11.050 (2011).

3 Isaacs, J. & Lindemann, A. Virus Interference: I. The interferon. *Proceedings of the Royal Society of London, Series B, Biological Sciences* **147**, 258-267 (1957).

4 Dinarello, C. A. Historical insights into cytokines. *European Journal of Immunology* **37**, 34-45, doi:10.1002/eji.200737772 (2007).

5 Paul, S. R. *et al.* Molecular cloning of a cDNA encoding interleukin 11, a stromal cell-derived lymphopoietic and hematopoietic cytokine. *Proceedings of the National Academy of Sciences* **87**, 7512-7516, doi:10.1073/pnas.87.19.7512 (1990).

6 Nicola, N. A. A (selective) history of Australian involvement in cytokine biology. *Cytokine and Growth Factor Reviews* **24**, 179-187, doi:10.1016/j.cytogfr.2013.03.004 (2013).

7 Stark, G. R. & Darnell, J. E. The JAK-STAT Pathway at Twenty. *Immunity* **36**, 503-514, doi:10.1016/j.immuni.2012.03.013 (2012).

8 O'Shea, J. J., Gadina, M. & Kanno, Y. Cytokine Signaling: Birth of a Pathway. *Journal of Immunology* **187**, 5475-5478, doi:10.4049/jimmunol.1102913 (2011).

9 Bradley, T. R. & Metcalf, D. The growth of mouse bone marrow cells in vitro. *Australian Journal of Experimental Biology and Medical Science* **44**, 287-299 (1966).

10 Burgess, A. W., Camakaris, J. & Metcalf, D. Purification and Properties of Colony-stimulating from Mouse Lung-conditioned Medium. *Journal of Biological Chemistry* **252**, 1998-2003 (1977).

11 Sparrow, L. G., Metcalf, D., Hunkapiller, M. W., Hood, L. E. & Burgess, A. W. Purification and partial amino acid sequence of asialo murine granulocyte-macrophage colony stimulating factor. *Proceedings of the National Academy of Sciences* **82**, 292-296, doi:10.1073/pnas.82.2.292 (1985).

12 Morgan; DA. Ruscetti, F. G., R. Selective in vitro Growth of T Lymphocytes from Normal Human Bone Marrows. *Science* **193**, 1007-1008 (1976).

13 Gillis, S., Ferm, M. M., Ou, W. & Smith, K. A. T cell growth factor: parameters of production and a quantitative microassay for activity. *Journal of Immunology* **120**, 2027-2032 (1978).

14 Johnson, G. R. Colony formation in agar by adult bone marrow multipotential hemopoietic cells. *Journal of Cellular Physiology* **103**, 371-383, doi:10.1002/jcp.1041030302 (1980).

15 Ihle, J. N. *et al.* Biologic properties of homogeneous interleukin 3. I. Demonstration of WEHI-3 growth factor activity, mast cell growth factor activity, p cell-stimulating factor activity, colony-stimulating factor activity, and histamine-producing cell-stimulating factor *Journal of Immunology* **131**, 282-287 (1983).

16 Cohen, S., Bigazzi, P. E. & Yoshida, T. Similarities of T cell function in cell-mediated immunity and antibody production. *Cellular Immunology* **12**, 150-159, doi:10.1016/0008-8749(74)90066-5 (1974).
17 Arden, L. A. *et al.* Revised Nomenclature for Antigen-Nonspecific T Cell Proliferation and Helper Factors. *Journal of Immunology* **123**, 2928-2929 (1979).
18 Branca, A. A. & Baglioni, C. Evidence that types I and II interferons have different receptors. *Nature* **294**, 768-770, doi:10.1038/294768a0 (1981).
19 Walker, F., Nicola, N. A., Metcalf, D. & Burgess, A. W. Hierarchical down-modulation of hemopoietic growth factor receptors. *Cell* **43**, 269-276, doi:10.1016/0092-8674(85)90032-7 (1985).
20 Walker, F. & Burgess, A. W. Specific binding of radioiodinated granulocyte-macrophage colony-stimulating factor to hemopoietic cells. *The EMBO Journal* **4**, 933-939, doi:10.1002/j.1460-2075.1985.tb03721.x (1985).
21 Schindler, C., Fu, X. Y., Improta, T., Aebersold, R. & Darnell, J. E. Proteins of transcription factor ISGF-3: one gene encodes the 91-and 84-kDa ISGF-3 proteins that are activated by interferon alpha. *Proceedings of the National Academy of Sciences* **89**, 7836-7839, doi:10.1073/pnas.89.16.7836 (1992).
22 Fu, X. Y., Kessler, D. S., Veals, S. A., Levy, D. E. & Darnell, J. E. ISGF3, the transcriptional activator induced by interferon alpha, consists of multiple interacting polypeptide chains. *Proceedings of the National Academy of Sciences* **87**, 8555-8559, doi:10.1073/pnas.87.21.8555 (1990).
23 Zhong, Z., Wen, Z. & Darnell Jr., J. E. Stat3: A STAT Family Member Activated by Tyrosine Phosphorylation in Response to Epidermal Growth Factor and Interleukin-6. *Science* **264**, 95-98 (1994).
24 Zhong, Z., Wen, Z. & Darnell, J. E. Stat3 and Stat4: Members of the family of signal transducers and activators of transcription. *Proceedings of the National Academy of Sciences* **91**, 4806-4810 (1994).
25 Shuai, K., Stark, G. R., Kerr, M. & Jr, J. E. D. A Single Phosphotyrosine Residue of Stat91 Required for Gene Activation by Interferon-γ. *Science* **261**, 1744-1746 (1993).
26 Schindler, C., Shuai, K., Prezioso, V. R. & Darnell, J. E. Interferon-Dependent Tyrosine Phosphorylation of a Latent Cytoplasmic Transcription Factor. *Science* **257**, 809-813 (1992).
27 Wilks, A. F. Two putative protein-tyrosine kinases identified by application of the polymerase chain reaction. *Proceedings of the National Academy of Sciences* **86**, 1603-1607, doi:10.1073/pnas.86.5.1603 (1989).
28 Wilks, A. F. *et al.* Two novel protein-tyrosine kinases, each with a second phosphotransferase-related catalytic domain, define a new class of protein kinase. *Molecular and Cellular Biology* **11**, 2057-2065, doi:10.1128/mcb.11.4.2057 (1991).
29 Velazquez, L., Fellous, M., Stark, G. R. & Pellegrini, S. A protein tyrosine kinase in the interferon α/β signaling pathway. *Cell* **70**, 313-322, doi:10.1016/0092-8674(92)90105-L (1992).
30 Johnston, J. A. *et al.* Phosphorylation and activation of the Jak-3 Janus kinase in response to interleukin-2. *Nature* **370**, 151-153, doi:10.1038/370151a0 (1994).

31 Nicholson, S. E. *et al.* Tyrosine kinase JAK1 is associated with the granulocyte-colony-stimulating factor receptor and both become tyrosine-phosphorylated after receptor activation. *Proceedings of the National Academy of Sciences* **91**, 2985-2988, doi:10.1073/pnas.91.8.2985 (1994).
32 Muller, M. *et al.* The protein tyrosine kinase JAK1 complements defects in interferon-alpha/beta and -gamma signal transduction. *Nature* **366**, 0-129 (1993).
33 Starr, R. *et al.* A family of cytokine-inducible inhibitors of signalling. *Nature* **387**, 917-921 (1997).
34 Yoshimura, A. *et al.* A new protein containing an SH2 domain that inhibits JAK kinases. *Nature* **387**, 921-924, doi:10.1038/43213 (1997).
35 Kajita, T. *et al.* Structure and function of a new STAT-induced STAT inhibitor. *Nature* **387**, 924-929, doi:10.1038/43219 (1997).
36 Sprang, S. R. & Bazan, J. F. Cytokine structural taxonomy and mechanisms of receptor engagement. *Current Opinion in Structural Biology* **3**, 815-827, doi:10.1016/0959-440X(93)90144-A (1993).
37 Bazan, J. F. Haemopoietic receptors and helical cytokines. *Immunology Today* **11**, 350-354, doi:10.1016/j.mcn.2016.12.008 (1990).
38 Bazan, J. F. Structural design and molecular evolution of a cytokine receptor superfamily. *Proceedings of the National Academy of Sciences* **87**, 6934-6938, doi:10.1073/pnas.87.18.6934 (1990).
39 Morris, R., Kershaw, N. J. & Babon, J. J. The molecular details of cytokine signaling via the JAK/STAT pathway. *Protein Science* **27**, 1984-2009, doi:10.1002/pro.3519 (2018).
40 Boulanger, M. J. & Garcia, K. C. Shared cytokine signaling receptors: Structural insights from the GP130 system. *Advances in Protein Chemistry* **68**, 107-146, doi:10.1016/S0065-3233(04)68004-1 (2004).
41 Jelkmann, W. Erythropoietin after a century of research: Younger than ever. *European Journal of Haematology* **78**, 183-205, doi:10.1111/j.1600-0609.2007.00818.x (2007).
42 Lindholm, J. Growth hormone: Historical notes. *Pituitary* **9**, 5-10, doi:10.1007/s11102-006-7557-4 (2006).
43 Cosman, D. *et al.* A new cytokine receptor superfamily. *Trends in Biochemistry* **15**, 265 - 270, doi:10.1016/1043-4666(93)90047-9 (1993).
44 D'Andrea, A. D., Fasman, G. D. & Lodish, H. F. Erythropoietin Receptor and Interleukin-2 Receptor β Chain: A New Receptor Family. *Cell* **58**, 1023-1024, doi:10.1519/JSC.0b013e31826ee4e1 (1989).
45 Somers, W., Stahl, M. & Seehra, J. S. 1.9 Å crystal structure of interleukin 6: Implications for a novel mode of receptor dimerization and signaling. *The EMBO Journal* **16**, 989-997, doi:10.1093/emboj/16.5.989 (1997).
46 Redfield, C. *et al.* Analysis of the solution structure of human interleukin-4 determined by heteronuclear three-dimensional nuclear magnetic resonance techniques. *Journal of Molecular Biology* **238**, 23-41, doi:10.1006/jmbi.1994.1265 (1994).
47 Walter, M. R. *et al.* Three-dimensional structure of recombinant human granulocyte-macrophage colony-stimulating factor. *Journal of Molecular Biology* **224**, 1075-1085, doi:10.1016/0022-2836(92)90470-5 (1992).

48 Rickert, M., Wang, X., Boulanger, M. J., Goriatcheva, N. & Garcia, K. C. The structure of interleukin-2 complexed with its alpha receptor. *Science* **308**, 1477-1480, doi:10.1126/science.1109745 (2005).
49 Ring, A. M. *et al.* Mechanistic and structural insight into the functional dichotomy between IL-2 and IL-15. *Nature Immunology* **13**, doi:10.1038/ni.2449 (2012).
50 Hilton, D. J., Watowich, S. S., Katz, L. & Lodish, H. F. Saturation Mutagenesis of the WSXWS Motif of the Erythropoietin Receptor. *Journal of Biological Chemistry* **271**, 4699-4708 (1996).
51 Yoshimura, A. *et al.* Mutations in the Trp-Ser-X-Trp-Ser motif of the erythropoietin receptor abolish processing, ligand binding, and activation of the receptor. *Journal of Biological Chemistry* **267**, 11619-11625 (1992).
52 Duriez, B. *et al.* A naturally occurring growth hormone receptor mutation: in vivo and in vitro evidence for the functional importance of the WS motif common to all members of the cytokine receptor superfamily. *Molecular Endocrinology* **7**, 806-814, doi:10.1210/mend.7.6.8361502 (1993).
53 Hamming, O. J. *et al.* Crystal structure of interleukin-21 receptor (IL-21R) bound to IL-21 reveals that sugar chain interacting with WSXWS motif is integral part of IL-21R. *Journal of Biological Chemistry* **287**, 9454-9460, doi:10.1074/jbc.M111.311084 (2012).
54 Doucey, M. A., Hess, D., Blommers, M. J. J. & Hofsteenge, J. Recombinant human interleukin-12 is the second example of a C-mannosylated protein. *Glycobiology* **9**, 435-441, doi:10.1093/glycob/9.5.435 (1999).
55 Yoon, C. *et al.* Charged residues dominate a unique interlocking topography in the heterodimeric cytokine interleukin-12. *The EMBO Journal* **19**, 3530-3541, doi:10.1093/emboj/19.14.3530 (2000).
56 Beyer, B. M. *et al.* Crystal Structures of the Pro-Inflammatory Cytokine Interleukin-23 and Its Complex with a High-Affinity Neutralizing Antibody. *Journal of Molecular Biology* **382**, 942-955, doi:10.1016/j.jmb.2008.08.001 (2008).
57 Lupardus, P. J. & Garcia, K. C. The Structure of Interleukin-23 Reveals the Molecular Basis of p40 Subunit Sharing with Interleukin-12. *Journal of Molecular Biology* **382**, 931-941, doi:10.1016/j.jmb.2008.07.051 (2008).
58 Dagil, R. *et al.* The WSXWS motif in cytokine receptors is a molecular switch involved in receptor activation: Insight from structures of the prolactin receptor. *Structure* **20**, 270-282, doi:10.1016/j.str.2011.12.010 (2012).
59 Chantalat, L., Jones, N. D., Korber, F., Navaza, J. & Pavlovsky, A. G. The Crystal Structure of Wild-type Growth-Hormone at 2.5 Angstrom Resolution. *Protein Peptide Letters* **2**, 333-340 (1995).
60 Cheetham, J. C. *et al.* NMR structure of human erythropoietin and a comparison with its receptor bound conformation. *Nature Structural Biology* **5**, 861-866, doi:10.1038/2302 (1998).
61 Brown, R. J. *et al.* Model for growth hormone receptor activation based on subunit rotation within a receptor dimer. *Nature Structural and Molecular Biology* **12**, 814-821, doi:10.1038/nsmb977 (2005).
62 De Vos, A., Ultsch, M. & Kossiakoff, A. Human growth hormone and extracellular domain of its receptor: crystal structure of the complex. *Science* **255**, 306-312, doi:10.1126/science.1549776 (1992).

63 Xu, Y. *et al.* Crystal structure of the entire ectodomain of gp130: Insights into the molecular assembly of the tall cytokine receptor complexes. *Journal of Biological Chemistry* **285**, 21214-21218, doi:10.1074/jbc.C110.129502 (2010).
64 Huyton, T. *et al.* An unusual cytokine:Ig-domain interaction revealed in the crystal structure of leukemia inhibitory factor (LIF) in complex with the LIF receptor. *Proceedings of the National Academy of Sciences* **104**, 12737-12742, doi:10.1073/pnas.0705577104 (2007).
65 Vollmer, P., Oppmann, B., Voltz, N., Fischer, M. & Rose-John, S. A role for the immunoglobulin-like domain of the human IL-6 receptor: Intracellular protein transport and shedding. *European Journal of Biochemistry* **263**, 438-446, doi:10.1046/j.1432-1327.1999.00511.x (1999).
66 Davis, S. *et al.* The receptor for ciliary neurotrophic factor. *Science* **253**, 59-63, doi:10.1126/science.1648265 (1991).
67 Paonessa, G. *et al.* Two distinct and independent sites on IL-6 trigger gp 130 dimer formation and signalling. *The EMBO Journal* **14**, 1942-1951, doi:10.1002/j.1460-2075.1995.tb07186.x (1995).
68 Bugge, K. *et al.* A combined computational and structural model of the full-length human prolactin receptor. *Nature Communications* **7**, 1-11, doi:10.1038/ncomms11578 (2016).
69 Bocharov, E. V. *et al.* Structural basis of the signal transduction via transmembrane domain of the human growth hormone receptor. *Biochimica et Biophysica Acta - General Subjects* **1862**, 1410-1420, doi:10.1016/j.bbagen.2018.03.022 (2018).
70 Schmidt, T. *et al.* A conserved ectodomain-transmembrane domain linker motif tunes the allosteric regulation of cell surface receptors. *Journal of Biological Chemistry* **291**, 17536-17546, doi:10.1074/jbc.M116.733683 (2016).
71 Skiniotis, G., Lupardus, P. J., Martick, M., Walz, T. & Garcia, K. C. Structural Organization of a Full-Length gp130/LIF-R Cytokine Receptor Transmembrane Complex. *Molecular Cell* **31**, 737-748, doi:10.1016/j.molcel.2008.08.011 (2008).
72 Haxholm, G. W. *et al.* Intrinsically disordered cytoplasmic domains of two cytokine receptors mediate conserved interactions with membranes. *Biochemical Journal* **468**, 495-506, doi:10.1042/BJ20141243 (2015).
73 Chow, D., He, X., Snow, a. L., Rose-John, S. & Garcia, K. C. Structure of an extracellular gp130 cytokine receptor signaling complex. *Science* **291**, 2150-2155, doi:10.1126/science.1058308 (2001).
74 Boulanger, M. J., Chow, D.-c., Brevnova, E. E. & Garcia, K. C. Hexameric structure and assembly of the interleukin-6/IL-6 alpha-receptor/gp130 complex. *Science* **300**, 2101-2104, doi:10.1126/science.1083901 (2003).
75 Hansen, G. *et al.* The Structure of the GM-CSF Receptor Complex Reveals a Distinct Mode of Cytokine Receptor Activation. *Cell* **134**, 496-507, doi:10.1016/j.cell.2008.05.053 (2008).
76 Lupardus, P. J. *et al.* Structural snapshots of full-length Jak1, a transmembrane gp130/IL-6/IL-6Rα cytokine receptor complex, and the receptor-Jak1 holocomplex. *Structure* **19**, 45-55, doi:10.1016/j.str.2010.10.010 (2011).

77 Broughton, S. E. *et al.* The βc receptor family - Structural insights and their functional implications. *Cytokine* **74**, 247-258, doi:10.1016/j.cyto.2015.02.005 (2015).
78 LaPorte, S. L. *et al.* Molecular and Structural Basis of Cytokine Receptor Pleiotropy in the Interleukin-4/13 System. *Cell* **132**, 259-272, doi:10.1016/j.cell.2007.12.030 (2008).
79 Rose-John, S., Scheller, J. & Schaper, F. "Family reunion" – A structured view on the composition of the receptor complexes of interleukin-6-type and interleukin-12-type cytokines. *Cytokine and Growth Factor Reviews* **1**, 10-13, doi:10.1016/j.cytogfr.2015.07.011 (2015).
80 Boulanger, M. J., Bankovich, A. J., Kortemme, T., Baker, D. & Garcia, K. C. Convergent mechanisms for recognition of divergent cytokines by the shared signaling receptor gp130. *Molecular Cell* **12**, 577-589, doi:10.1016/S1097-2765(03)00365-4 (2003).
81 Lupardus, P. J. *et al.* Structure of the pseudokinase-kinase domains from protein kinase TYK2 reveals a mechanism for Janus kinase (JAK) autoinhibition. *Proceedings of the National Academy of Sciences* **111**, 8025-8030, doi:10.1073/pnas.1401180111 (2014).
82 Ferrao, R. *et al.* The Structural Basis for Class II Cytokine Receptor Recognition by JAK1. *Structure* **24**, 897-905, doi:10.1016/j.str.2016.03.023 (2016).
83 Wallweber, H. J. A., Tam, C., Franke, Y., Starovasnik, M. A. & Lupardus, P. J. Structural basis of recognition of interferon-α receptor by tyrosine kinase 2. *Nature Structural and Molecular Biology* **21**, 443-448, doi:10.1038/nsmb.2807 (2014).
84 Tanner, J. W., Chen, W., Young, R. L., Longmore, G. D. & Shaw, S. The conserved box 1 motif of cytokine receptors is required for association with JAK kinases. *Journal of Biological Chemistry* **270**, 6523-6530, doi:10.1074/jbc.270.12.6523 (1995).
85 Kershaw, N. J., Laktyushin, A., Nicola, N. A. & Babon, J. J. Reconstruction of an active SOCS3-based E3 ubiquitin ligase complex in vitro : identification of the active components and JAK2 and gp130 as substrates. *Growth Factors* **32**, 1-10, doi:10.3109/08977194.2013.877005 (2014).
86 Babon, J. J., Sabo, J. K., Zhang, J. G., Nicola, N. A. & Norton, R. S. The SOCS Box Encodes a Hierarchy of Affinities for Cullin5: Implications for Ubiquitin Ligase Formation and Cytokine Signalling Suppression. *Journal of Molecular Biology* **387**, 162-174, doi:10.1016/j.jmb.2009.01.024 (2009).
87 Liau, N. P. D. *et al.* The molecular basis of JAK/STAT inhibition by SOCS1. *Nature Communications* **9**, 1-14, doi:10.1038/s41467-018-04013-1 (2018).
88 Kershaw, N. J. *et al.* SOCS3 binds specific receptor-JAK complexes to control cytokine signaling by direct kinase inhibition. *Nature Structural and Molecular Biology* **20**, 469-476, doi:10.1038/nsmb.2519 (2013).
89 Shuai, K. & Liu, B. Regulation of gene-activation pathways by pias proteins in the immune system. *Nature Reviews Immunology* **5**, 593-605, doi:10.1038/nri1667 (2005).
90 Chung, C. D. *et al.* PIAS3 Specific Inhibition of Stat3 Signal Transduction by PIAS3. *Science* **278**, 1803-1805 (1997).

91 Alicea-Velázquez, N. L., Jakoncic, J. & Boggon, T. J. Structure-guided studies of the SHP-1/JAK1 interaction provide new insights into phosphatase catalytic domain substrate recognition. *Journal of Structural Biology* **181**, 243-251, doi:10.1016/j.jsb.2012.12.009 (2013).
92 David, M., Chen, H. E., Goelz, S., Larner, A. C. & Neel, B. G. Differential regulation of the alpha/beta interferon-stimulated Jak/Stat pathway by the SH2 domain-containing tyrosine phosphatase SHPTP1. *Molecular and Cellular Biology* **15**, 7050-7058, doi:10.1128/mcb.15.12.7050 (1995).
93 Myers, M. P. *et al.* TYK2 and JAK2 Are Substrates of Protein-tyrosine Phosphatase 1B. *Journal of Biological Chemistry* **276**, 47771-47774, doi:10.1074/jbc.C100583200 (2001).
94 Tong, W., Zhang, J. & Lodish, H. F. Lnk inhibits erythropoiesis and Epo-dependent JAK2 activation and downstream signaling pathways. *Blood* **105**, 4604-4612, doi:10.1182/blood-2004-10-4093 (2005).
95 Hercus, T. R. *et al.* Signalling by the βc family of cytokines. *Cytokine and Growth Factor Reviews* **24**, 189-201, doi:10.1016/j.cytogfr.2013.03.002 (2013).
96 Salmond, R. J. & Alexander, D. R. SHP2 forecast for the immune system: Fog gradually clearing. *Trends in Immunology* **27**, 154-160, doi:10.1016/j.it.2006.01.007 (2006).
97 Goeddel, V. *et al.* Rational Design of Potent Antagonists to the Human Growth Hormone Receptor. *Science* **256**, 1677-1680 (1992).
98 Brooks, A. *et al.* Mechanism of Activation of Protein Kinase JAK2 by the Growth Hormone Receptor. *Science* **344**, 703-704, doi:10.1126/science.1254799 (2014).
99 Livnah, O. *et al.* Crystallographic evidence for preformed dimers of erythropoietin receptor before ligand activation. *Science* **283**, 987-990, doi:10.1126/science.283.5404.987 (1999).
100 Giese, B. *et al.* Dimerization of the cytokine receptors gp130 and LIFR analysed in single cells. *Journal of Cell Science* **118**, 5129-5140, doi:10.1242/jcs.02628 (2005).
101 Tenhumberg, S. *et al.* gp130 dimerization in the absence of ligand: Preformed cytokine receptor complexes. *Biochemical and Biophysical Research Communications* **346**, 649-657, doi:10.1016/j.bbrc.2006.05.173 (2006).
102 Seubert, N. *et al.* Active and inactive orientations of the transmembrane and cytosolic domains of the erythropoietin receptor dimer. *Molecular Cell* **12**, 1239-1250, doi:10.1016/S1097-2765(03)00389-7 (2003).
103 Fagerberg, L. *et al.* Analysis of the Human Tissue-specific Expression by Genome-wide Integration of Transcriptomics and Antibody-based Proteomics. *Molecular and Cellular Proteomics* **13**, 397-406, doi:10.1074/mcp.m113.035600 (2014).
104 Schuster, B. *et al.* Signaling of human ciliary neurotrophic factor (CNTF) revisited: The interleukin-6 receptor can serve as an α-receptor for CNTF. *Journal of Biological Chemistry* **278**, 9528-9535, doi:10.1074/jbc.M210044200 (2003).
105 Crabé, S. *et al.* The IL-27 p28 Subunit Binds Cytokine-Like Factor 1 to Form a Cytokine Regulating NK and T Cell Activities Requiring IL-6R for Signaling.

Journal of Immunology **183**, 7692-7702, doi:10.4049/jimmunol.0901464 (2009).
106 Garbers, C. *et al.* An Interleukin-6 receptor-dependent molecular switch mediates signal transduction of the IL-27 cytokine subunit p28 (IL-30) via a gp130 protein receptor homodimer. *Journal of Biological Chemistry* **288**, 4346-4354, doi:10.1074/jbc.M112.432955 (2013).
107 Boulanger, M. J. *et al.* Molecular Mechanisms for Viral Mimicry of a Human Cytokine: Activation of gp130 by HHV-8 Interleukin-6. *Journal of Molecular Biology* **335**, 641-654, doi:10.1016/j.jmb.2003.10.070 (2004).
108 Neipel, F. *et al.* Human herpesvirus 8 encodes a homolog of interleukin-6. *Journal of Virology* **71**, 839-842 (1997).
109 Putoczki, T. L., Dobson, R. C. J. & Griffin, M. D. W. The structure of human interleukin-11 reveals receptor-binding site features and structural differences from interleukin-6. *Acta Crystallogr D* **3**, 2277-2285, doi:10.1107/S1399004714012267 (2014).
110 Robinson, R. C. *et al.* The crystal structure and biological function of leukemia inhibitory factor: Implications for receptor binding. *Cell* **77**, 1101-1116, doi:10.1016/0092-8674(94)90449-9 (1994).
111 Deller, M. C. *et al.* Crystal structure and functional dissection of the cytostatic cytokine oncostatin M. *Structure* **8**, 863-874 (2000).
112 Kishimoto, T. The Biology of Interleukin-6. *Blood* **71**, 1-10 (1988).
113 Hirano, T. *et al.* Complementary DNA for a novel human interleukin (BSF-2) that induces B lymphocytes to produce immunoglobulin. *Nature* **324**, 73-76 (1986).
114 van Damme, J. *et al.* Hybridoma / Plasmacytoma Growth Factor Induced By Interleukin 1 and Tumor Necrosis Factor. *Journal of Experimental Medicine* **165**, 914-919 (1987).
115 Gauldie, J., Richards, C., Harnish, D., Lansdorp, P. & Baumann, H. Interferon beta 2/B-cell stimulatory factor type 2 shares identity with monocyte-derived hepatocyte-stimulating factor and regulates the major acute phase protein response in liver cells. *Proceedings of the National Academy of Sciences* **84**, 7251-7255, doi:10.1073/pnas.84.20.7251 (1987).
116 Xu, G. Y. *et al.* Solution structure of recombinant human interleukin-6. *Journal of Molecular Biology* **268**, 468-481, doi:10.1006/jmbi.1997.0933 (1997).
117 Varghese, J. *et al.* Structure of the extracellular domains of the human interleukin-6 receptor α-chain. *Proceedings of the National Academy of Sciences* **99**, 15959-15964, doi:10.1073/pnas.232432399 (2002).
118 Lokau, J. & Garbers, C. The length of the interleukin-11 receptor stalk determines its capacity for classic signaling. *Journal of Biological Chemistry* **293**, 6398-6409, doi:10.1074/jbc.RA118.001879 (2018).
119 Baran, P., Nitz, R., Grotzinger, J., Scheller, J. & Garbers, C. Minimal Interleukin 6 (IL-6) receptor stalk composition for IL-6 receptor shedding and IL-6 classic signaling. *Journal of Biological Chemistry* **288**, 14756-14768, doi:10.1074/jbc.M113.466169 (2013).
120 Nitz, R., Lokau, J., Aparicio-Siegmund, S., Scheller, J. & Garbers, C. Modular organization of Interleukin-6 and Interleukin-11 α-receptors. *Biochimie* **119**, 175-182, doi:10.1016/j.biochi.2015.11.005 (2015).

121 Taga, T. *et al.* Interleukin-6 triggers the association of its receptor with a possible signal transducer, gp130. *Cell* **58**, 573-581, doi:10.1016/0092-8674(89)90438-8 (1989).
122 Hibi, M. *et al.* Molecular cloning and expression of an IL-6 signal transducer, gp130. *Cell* **63**, 1149-1157, doi:10.1016/0092-8674(90)90411-7 (1990).
123 Hilton, D. J. *et al.* Cloning of a murine IL-11 receptor alpha-chain; requirement for gp130 for high affinity binding and signal transduction. *The EMBO Journal* **13**, 4765-4775, doi:10.1002/j.1460-2075.1994.tb06802.x (1994).
124 Gimpel, S. D. *et al.* The IL-6 Signal Transducer , gp130: An Oncostatin M Receptor and Affinity Converter for the LIF Receptor. *Science* **255**, 1434-1437 (1992).
125 Ip, N. Y. *et al.* CNTF and LIF act on neuronal cells via shared signaling pathways that involve the IL-6 signal transducing receptor component gp130. *Cell* **69**, 1121-1132, doi:10.1016/0092-8674(92)90634-O (1992).
126 Bravo, J., Staunton, D., Heath, J. K. & Yvonne Jones, E. Crystal structure of a cytokine-binding region of gp130. *The EMBO Journal* **17**, 1665-1674, doi:10.1093/emboj/17.6.1665 (1998).
127 Spannbauer, M. M. & Trautwein, C. Frequent in-frame somatic deletions activate gp130 in inflammatory hepatocellular tumors. *Nature* **49**, 1387-1389, doi:10.1002/hep.22902 (2009).
128 Schütt, A. *et al.* gp130 activation is regulated by D2-D3 interdomain connectivity. *Biochemical Journal* **450**, 487-496, doi:10.1042/BJ20121660 (2013).
129 Timmermann, A., Küster, A., Kurth, I., Heinrich, P. C. & Müller-Newen, G. A functional role of the membrane-proximal extracellular domains of the signal transducer gp130 in heterodimerization with the leukemia inhibitory factor receptor. *European Journal of Biochemistry* **269**, 2716-2726, doi:10.1046/j.1432-1033.2002.02941.x (2002).
130 Matadeen, R., Hon, W. C., Heath, J. K., Jones, E. Y. & Fuller, S. The Dynamics of Signal Triggering in a gp130-Receptor Complex. *Structure* **15**, 441-448, doi:10.1016/j.str.2007.02.006 (2007).
131 Hemmann, U. *et al.* Differential Activation of Acute Phase Response Factor/Stat3 and Stat1 via the Cytoplasmic Domain of the Interleukin 6 Signal Transducer gp130. *Journal of Biological Chemistry* **271**, 12999-13007, doi:10.1074/jbc.271.22.12999 (2002).
132 Stahl, N. *et al.* Choice of STATs and other substrates specified by modular tyrosine-based motifs in cytokine receptors. *Science* **267**, 1349-1353, doi:10.1126/science.7871433 (1995).
133 Schmitz, J. *et al.* The Cytoplasmic Tyrosine Motifs in Full-Length Glycoprotein 130 Have Different Roles in IL-6 Signal Transduction. *Journal of Immunology* **164**, 848-854, doi:10.4049/jimmunol.164.2.848 (2000).
134 Garbers, C., Heink, S., Korn, T. & Rose-John, S. Interleukin-6: Designing specific therapeutics for a complex cytokine. *Nature Reviews Drug Discovery* **17**, 395-412, doi:10.1038/nrd.2018.45 (2018).
135 Anhuf, D. *et al.* Signal Transduction of IL-6, Leukemia-Inhibitory Factor, and Oncostatin M: Structural Receptor Requirements for Signal Attenuation.

Journal of Immunology **165**, 2535-2543, doi:10.4049/jimmunol.165.5.2535 (2000).
136 Heinrich, P. C. *et al.* Principles of interleukin (IL)-6-type cytokine signalling and its regulation. *Biochemical Journal* **374**, 1-20, doi:10.1042/BJ20030407 (2003).
137 Ward, L. D. *et al.* High affinity interleukin-6 receptor is a hexameric complex consisting of two molecules each of interleukin-6, interleukin-6 receptor, and gp-130. *Journal of Biological Chemistry* **269**, 23286-23289 (1994).
138 Chow, D.-c., Ho, J., Nguyen Pham, T. L., Rose-John, S. & Garcia, K. C. In Vitro Reconstitution of Recognition and Activation Complexes between Interleukin-6 and gp130. *Biochemistry* **40**, 7593-7603, doi:10.1021/bi010192q (2001).
139 Wang, X., Lupardus, P., Laporte, S. L. & Garcia, K. C. Structural biology of shared cytokine receptors. *Annual review of immunology* **27**, 29-60, doi:10.1146/annurev.immunol.24.021605.090616 (2009).
140 Thilakasiri, P. *et al.* Repurposing the selective estrogen receptor modulator *bazedoxifene* to suppress gastrointestinal cancer growth. *EMBO Molecular Medicine*, e9539, doi:10.15252/emmm.201809539 (2019).
141 Kurth, I. *et al.* Activation of the signal transducer glycoprotein 130 by both IL-6 and IL-11 requires two distinct binding epitopes. *Journal of immunology* **162**, 1480-1487 (1999).
142 Wijdenes, J. *et al.* Interleukin-6 signal transducer gp130 has specific binding sites for different cytokines as determined by antagonistic and agonistic anti-gp130 monoclonal antibodies. *European Journal of Immunology* **25**, 3474-3481 (1995).
143 Skiniotis, G., Boulanger, M. J., Garcia, K. C. & Walz, T. Signaling conformations of the tall cytokine receptor gp130 when in complex with IL-6 and IL-6 receptor. *Nature Structural and Molecular Biology* **12**, 545-551, doi:10.1038/nsmb941 (2005).
144 Grötzinger, J., Kernebeck, T., Kallen, K. J. & Rose-John, S. IL-6 type cytokine receptor complexes: Hexamer, tetramer or both? *Biological Chemistry* **380**, 803-813, doi:10.1515/BC.1999.100 (1999).
145 Grötzinger, J., Kurapkat, G., Wollmer, A., Kalai, M. & Rose-John, S. The family of the IL-6-type cytokines: Specificity and promiscuity of the receptor complexes. *Proteins: Structure, Function and Genetics* **27**, 96-109, doi:10.1002/(SICI)1097-0134(199701)27:1<96::AID-PROT10>3.0.CO;2-D (1997).
146 Pflanz, S., Kurth, I., Grötzinger, J., Heinrich, P. C. & Müller-Newen, G. Two Different Epitopes of the Signal Transducer gp130 Sequentially Cooperate on IL-6-Induced Receptor Activation. *Journal of Immunology* **165**, 7042-7049, doi:10.4049/jimmunol.165.12.7042 (2000).
147 Chalaris, A., Garbers, C., Rabe, B., Rose-John, S. & Scheller, J. The soluble Interleukin 6 receptor: Generation and role in inflammation and cancer. *European Journal of Cell Biology* **90**, 484-494, doi:10.1016/j.ejcb.2010.10.007 (2011).
148 Jostock, T. *et al.* Soluble gp130 is the natural inhibitor of soluble interleukin-6 receptor transsignaling responses. *European Journal of Biochemistry* **268**, 160-167 (2001).

149 Heink, S. *et al.* Trans-presentation of IL-6 by dendritic cells is required for the priming of pathogenic TH17 cells. *Nature Immunology* **18**, doi:10.1038/ni.3632 (2016).
150 Lamertz, L. *et al.* Soluble gp130 prevents interleukin-6 and interleukin-11 cluster signaling but not intracellular autocrine responses. *Science Signaling* **11**, eaar7388, doi:10.1074/jbc.M407382200 (2018).
151 Wuest, S. C. *et al.* A role for interleukin-2 trans-presentation in dendritic cell-mediated T cell activation in humans, as revealed by daclizumab therapy. *Nature Medicine* **17**, 604-609, doi:10.1038/nm.2365 (2011).
152 Dubois, S., Mariner, J., Waldmann, T. A. & Tagaya, Y. IL-15Rα Recycles and Presents IL-15 In trans to Neighboring Cells. *Immunity* **17**, 537-547 (2002).
153 Wang, X., Rickert, M. & Garcia, K. C. Structure of the quaternary complex of interleukin-2 with its α, β, and γc receptors. *Science* **310**, 1159-1163, doi:10.1126/science.1117893 (2005).
154 Brown, S., Hu, N. & Hombría, J. C. G. Identification of the first invertebrate interleukin JAK/STAT receptor, the Drosophila gene domeless. *Current Biology* **11**, 1700-1705, doi:10.1016/S0960-9822(01)00524-3 (2001).
155 Jones, S. A. & Jenkins, B. J. Recent insights into targeting the IL-6 cytokine family in inflammatory diseases and cancer. *Nature Reviews Immunology* **18**, 773-789, doi:10.1038/s41577-018-0066-7 (2018).
156 Harrison, D. a., Mccoon, P. E., Binari, R., Gilman, M. & Perrimon, N. Drosophila unpaired encodes a secreted protein that activates the Drosophila unpaired encodes a secreted protein that activates the JAK signaling pathway. 3252-3263, doi:10.1101/gad.12.20.3252 (1998).
157 Zeidler, M. P. & Bausek, N. The Drosophila JAK-STAT pathway. *Jak-Stat* **2**, e25353, doi:10.4161/jkst.25353 (2013).
158 Agaisse, H., Petersen, U. M., Boutros, M., Mathey-Prevot, B. & Perrimon, N. Signaling role of hemocytes in Drosophila JAK/STAT-dependent response to septic injury. *Developmental Cell* **5**, 441-450, doi:10.1016/S1534-5807(03)00244-2 (2003).
159 Luo, H., Hanratty, W. P. & Dearolf, C. R. An amino acid substitution in the Drosophila hopTum-l Jak kinase causes leukemia-like hematopoietic defects. *The EMBO Journal* **14**, 1412-1420, doi:10.1002/j.1460-2075.1995.tb07127.x (1995).
160 Wang, H., Chen, X., He, T., Zhou, Y. & Luo, H. Evidence for tissue-specific JAK/STAT target genes in Drosophila optic lobe development. *Genetics* **195**, 1291-1306, doi:10.1534/genetics.113.155945 (2013).
161 Perrimon, N. & Mahowald, A. P. l(1)hopscotch, a larval-pupal zygotic lethal with a specific maternal effect on segmentation in Drosophila. *Developmental Biology* **118**, 28-41, doi:10.1016/0012-1606(86)90070-9 (1986).
162 Oldefest, M. *et al.* Upd3 - An ancestor of the four-helix bundle cytokines. *Biochemical and Biophysical Research Communications* **436**, 66-72, doi:10.1016/j.bbrc.2013.04.107 (2013).
163 Liongue, C. & Ward, A. C. Evolution of Class I cytokine receptors. *BMC Evolutionary Biology* **7**, 120, doi:10.1186/1471-2148-7-120 (2007).
164 Liongue, C., Sertori, R. & Ward, A. C. Evolution of Cytokine Receptor Signaling. *Journal of Immunology* **197**, 11-18, doi:10.4049/jimmunol.1600372 (2016).

165 Rose-John, S., Scheller, J. & Schaper, F. "Family reunion" - A structured view on the composition of the receptor complexes of interleukin-6-type and interleukin-12-type cytokines. *Cytokine and Growth Factor Reviews* **26**, 471-474, doi:10.1016/j.cytogfr.2015.07.011 (2015).
166 Chérel, M. *et al.* Molecular cloning of two isoforms of a receptor for the human hematopoietic cytokine interleukin-11. *Blood* **86**, 2534-2540 (1995).
167 Barton, V., Hall, M., Hudson, K. R. & Heath, J. K. Interleukin-11 signals through the formation of a hexameric receptor complex. *Journal of Biological Chemistry* **275**, 36197-36203, doi:10.1074/jbc.M004648200 (2000).
168 Barton, V., Hudson, K. R. & Heath, J. K. Identification of three distinct receptor binding sites of murine interleukin-11. *Journal of Biological Chemistry* **274**, 5755-5761, doi:10.1074/jbc.274.9.5755 (1999).
169 Tacken, I. *et al.* Definition of receptor binding sites on human interleukin-11 by molecular modeling-guided mutagenesis. *European Journal of Biochemistry* **265**, 645-655, doi:10.1046/j.1432-1327.1999.00755.x (1999).
170 Czupryn, M. *et al.* Alanine-scanning mutagenesis of human interleukin-11: identification of regions important for biological activity. *Annals of the New York Academy of Sciences* **762**, 152-164 (1995).
171 Nguyen, P. M., Abdirahman, S. M. & Putoczki, T. L. Emerging roles for Interleukin-11 in disease. *Growth Factors* **37**, 1-11, doi:10.1080/08977194.2019.1620227 (2019).
172 Keller, D. C., Du, X. X., Srour, E. F., Hoffman, R. & Williams, D. A. Interleukin-11 Inhibits Adipogenesis and Stimulates Myelopoiesis in Human Long-Term Marrow Cultures. *Blood* **82**, 1428-1435 (1993).
173 Kawashima, I. *et al.* Molecular cloning of cDNA encoding adipogenesis inhibitory factor and identity with interleukin-11. *FEBS Journal* **283**, 199-202 (1991).
174 Teramura, M., Kobayashi, S., Hoshino, S., Oshimi, K. & Mizoguchi, H. Interleukin-11 enhances human megakaryocytopoiesis in vitro. *Blood* **79**, 327-331 (1992).
175 Musashi, M. *et al.* Direct and synergistic effects of interleukin 11 on murine hemopoiesis in culture. *Proceedings of the National Academy of Sciences* **88**, 765-769, doi:10.1073/pnas.88.3.765 (1991).
176 Musashi, M., Clark, S. C., Sudo, T., Urdal, D. L. & Ogawa, M. Synergistic interactions between interleukin-11 and interleukin-4 in support of proliferation of primitive hematopoietic progenitors of mice. *Blood* **78**, 1448-1451 (1991).
177 Leonard, J. P., Quinto, C. M., Kozitza, M. K., Neben, T. Y. & Goldman, S. J. Recombinant human interleukin-11 stimulates multilineage hematopoietic recovery in mice after a myelosuppressive regimen of sublethal irradiation and carboplatin. *Blood* **83**, 1499-1506 (1994).
178 Wilde, M. I. & Faulds, D. Oprelvekin: A review of its pharmacology and therapeutic potential in chemotherapy-induced thrombocytopenia. *BioDrugs* **10**, 159-171, doi:10.2165/00063030-199810020-00006 (1998).
179 Du, X. & Williams, D. Interleukin-11: Review of Molecular, Cell Biology, and Clinical Use. *Blood* **89**, 3897-3908 (1997).
180 Anderson, K. C. *et al.* Interleukin-11 promotes accessory cell-dependent B-cell differentiation in humans. *Blood* **80**, 2797-2804 (1992).

181 Quesniaux, V. F. J., Clark, S. C., Turner, K. & Fagg, B. Interleukin-11 stimulates multiple phases of erythropoiesis in vitro. *Blood* **80**, 1218-1223 (1992).
182 Cairo, M. S., Plunkett, J. M., Nguyen, A., Schendel, P. & Van De Ven, C. Effect of interleukin-11 with and without granulocyte colony-stimulating factor on in vivo neonatal rat hematopoiesis: Induction of neonatal thrombocytosis by interleukin-11 and synergistic enhancement of neutrophilia by interleukin-11 + granulocyte colony-stimulating factor. *Pediatric Research* **34**, 56-61, doi:10.1203/00006450-199307000-00014 (1993).
183 Sims, N. A. Cell-specific paracrine actions of IL-6 family cytokines from bone, marrow and muscle that control bone formation and resorption. *International Journal of Biochemistry and Cell Biology* **79**, 14-23, doi:10.1016/j.biocel.2016.08.003 (2016).
184 Johnson, R. W. *et al.* Glycoprotein130 (Gp130)/interleukin-6 (IL-6) signalling in osteoclasts promotes bone formation in periosteal and trabecular bone. *Bone* **81**, 343-351, doi:10.1016/j.bone.2015.08.005 (2015).
185 Sims, N. A. *et al.* Interleukin-11 receptor signaling is required for normal bone remodeling. *Journal of Bone and Mineral Research* **20**, 1093-1102, doi:10.1359/JBMR.050209 (2005).
186 Takeuchi, Y. *et al.* Interleukin-11 as a Stimulatory Factor for Bone Formation Prevents Bone Loss with Advancing Age in Mice. *Journal of Biological Chemistry* **277**, 49011-49018, doi:10.1074/jbc.M207804200 (2002).
187 Marouli, E. *et al.* Rare and low-frequency coding variants alter human adult height. *Nature* **542**, 186-190, doi:10.1038/nature21039 (2017).
188 Lanktree, M. B. *et al.* Meta-analysis of dense genecentric association studies reveals common and uncommon variants associated with height. *American Journal of Human Genetics* **88**, 6-18, doi:10.1016/j.ajhg.2010.11.007 (2011).
189 Styrkarsdottir, U. *et al.* Meta-analysis of Icelandic and UK data sets identifies missense variants in SMO, IL11, COL11A1 and 13 more new loci associated with osteoarthritis. *Nature Genetics* **50**, 1681-1687, doi:10.1038/s41588-018-0247-0 (2018).
190 Lokau, J. *et al.* The SNP rs4252548 (R112H) which is associated with reduced human height compromises the stability of IL-11. *Biochimica et Biophysica Acta - Molecular Cell Research* **4252548**, doi:10.1016/j.bbamcr.2017.12.003 (2017).
191 Nieminen, P. *et al.* Inactivation of IL11 signaling causes craniosynostosis, delayed tooth eruption, and supernumerary teeth. *American Journal of Human Genetics* **89**, 67-81, doi:10.1016/j.ajhg.2011.05.024 (2011).
192 Neveling, K. *et al.* Mutations in the interleukin receptor IL11RA cause autosomal recessive Crouzon-like craniosynostosis. *Molecular Genetics and Genomic Medicine* **1**, 223-237, doi:10.1002/mgg3.28 (2013).
193 Brischoux-Boucher, E. *et al.* IL11RA-related Crouzon-like autosomal recessive craniosynostosis in 10 new patients: Resemblances and differences. *Clinical Genetics* **94**, 373-380, doi:10.1111/cge.13409 (2018).
194 Agthe, M. *et al.* Mutations in Craniosynostosis Patients Cause Defective Interleukin-11 Receptor Maturation and Drive Craniosynostosis-like Disease in Mice. *Cell Reports*, 10-18, doi:10.1016/j.celrep.2018.09.005 (2018).

195 Einarsson, O., Geba, G. P., Zhu, Z., Landry, M. & Elias, J. a. Interleukin-11: Stimulation in vivo and in vitro by respiratory viruses and induction of airways hyperresponsiveness. *Journal of Clinical Investigation* **97**, 915-924, doi:10.1172/JCI118514 (1996).
196 Tang, W. *et al.* Targeted expression of IL-11 in the murine airway causes lymphocytic inflammation, bronchial remodeling, and airways obstruction. *Journal of Clinical Investigation* **98**, 2845-2853, doi:10.1172/JCI119113 (1996).
197 Chen, Q. *et al.* IL-11 Receptor α in the Pathogenesis of IL-13-Induced Inflammation and Remodeling. *Journal of Immunology* **174**, 2305-2313, doi:10.4049/jimmunol.174.4.2305 (2005).
198 Chun, G. L. *et al.* Endogenous IL-11 signaling is essential in Th2- and IL-13-induced inflammation and mucus production. *American Journal of Respiratory Cell and Molecular Biology* **39**, 739-746, doi:10.1165/rcmb.2008-0053OC (2008).
199 Kapina, M. a. *et al.* Interleukin-11 drives early lung inflammation during mycobacterium tuberculosis infection in genetically susceptible mice. *PLoS ONE* **6**, e21878, doi:10.1371/journal.pone.0021878 (2011).
200 Winship, A., Menkhorst, E., Van Sinderen, M. & Dimitriadis, E. Interleukin 11: Similar or opposite roles in female reproduction and reproductive cancer? *Reproduction, Fertility and Development* **28**, 395-405, doi:10.1071/RD14128 (2016).
201 Robb, L. *et al.* Infertility in female mice lacking the receptor for interleukin 11 is due to a defective uterine response to implantation. *Nature Medicine* **4**, 303-308, doi:10.1038/nm0398-303 (1998).
202 Dimitriadis, E. *et al.* IL-11 and IL-11Rα immunolocalisation at primate implantation sites suports a role for IL-11 in placentation and fetal development. *Reproductive Biology and Endocrinology* **1**, 1-10, doi:10.1186/1477-7827-1-34 (2003).
203 Menkhorst, E., Salamonsen, L., Robb, L. & Dimitriadis, E. IL11 Antagonist Inhibits Uterine Stromal Differentiation, Causing Pregnancy Failure in Mice. *Biology of Reproduction* **80**, 920-927, doi:10.1095/biolreprod.108.073601 (2009).
204 Chen, H. F. *et al.* Defective production of interleukin-11 by decidua and chorionic villi in human anembryonic pregnancy. *Journal of Clinical Endocrinology and Metabolism* **87**, 2320-2328, doi:10.1210/jcem.87.5.8478 (2002).
205 Winship, A. L. *et al.* Interleukin-11 alters placentation and causes preeclampsia features in mice. *Proceedings of the National Academy of Sciences* **112**, 15928-15933, doi:10.1073/pnas.1515076112 (2015).
206 Paiva, P. *et al.* Interleukin-11 promotes migration, but not proliferation, of human trophoblast cells, implying a role in placentation. *Endocrinology* **148**, 5566-5572, doi:10.1210/en.2007-0517 (2007).
207 Paiva, P., Salamonsen, L. A., Manuelpillai, U. & Dimitriadis, E. Interleukin 11 Inhibits Human Trophoblast Invasion Indicating a Likely Role in the Decidual Restraint of Trophoblast Invasion During Placentation1. *Biology of Reproduction* **80**, 302-310, doi:10.1095/biolreprod.108.071415 (2008).

208 Putoczki, T. *et al.* Interleukin-11 is the dominant Il-6 family cytokine during gastrointestinal tumorigenesis and can be targeted therapeutically. *Cancer Cell* **24**, 257-271, doi:10.1016/j.ccr.2013.06.017 (2013).
209 Ernst, M. *et al.* STAT3 and STAT1 mediate IL-11-dependent and inflammation-associated gastric tumorigenesis in gp130 receptor mutant mice. *Journal of Clinical Investigation* **118**, 1727-1738, doi:10.1172/JCI34944 (2008).
210 Johnstone, C. N., Chand, A., Putoczki, T. L. & Ernst, M. Emerging roles for IL-11 signaling in cancer development and progression: focus on breast cancer. *Cytokine and Growth Factor Reviews* **26**, 489-498, doi:10.1016/j.cytogfr.2015.07.015 (2015).
211 Hanahan, D. & Weinberg, R. A. Hallmarks of cancer: The next generation. *Cell* **144**, 646-674, doi:10.1016/j.cell.2011.02.013 (2011).
212 Hanahan, D. & Weinberg, R. A. The hallmarks of cancer. *Cell* **100**, 57-70, doi:10.1007/s00262-010-0968-0 (2000).
213 Ren, L., Wang, X., Dong, Z., Liu, J. & Zhang, S. Bone metastasis from breast cancer involves elevated IL-11 expression and the gp130/STAT3 pathway. *Medical Oncology* **30**, doi:10.1007/s12032-013-0634-4 (2013).
214 Yap, J., Salamonsen, L. A., Jobling, T., Nicholls, P. K. & Dimitriadis, E. Interleukin 11 is upregulated in uterine lavage and endometrial cancer cells in women with endometrial carcinoma. *Reproductive Biology and Endocrinology* **8**, 1-11, doi:10.1186/1477-7827-8-63 (2010).
215 Putoczki, T. & Ernst, M. IL-11 signalling as a therapeutic target for cancer. *Immunotherapy* **7**, 441-453 (2015).
216 Bellone, G. *et al.* Cytokine expression profile in human pancreatic carcinoma cells and in surgical specimens: Implications for survival. *Cancer Immunology, Immunotherapy* **55**, 684-698, doi:10.1007/s00262-005-0047-0 (2006).
217 Paglia, D., Oran, A., Sauder, D. N., Mckenzie, R. C. & Kerbel, R. S. Expression of Leukemia Inhibitory Factor and Interleukin-11 by Human Melanoma Cell Lines: LIF, IL-6, and IL-11 Are Not Coregulated. *Journal of Interferon and Cytokine Research* **15**, 455-460, doi:10.1089/jir.1995.15.455 (1995).
218 Elias, J. A., Tang, W. & Horowitz, M. C. Cytokine and hormonal stimulation of human osteosarcoma interleukin-11 production. *Endocrinology* **136**, 489-498, doi:10.1210/endo.136.2.7835281 (1995).
219 Putoczki, T. & Ernst, M. More than a sidekick: the IL-6 family cytokine IL-11 links inflammation to cancer. *Journal of Leukocyte biology* **88**, 1109-1117, doi:10.1189/jlb.0410226 (2010).
220 Lokau, J. *et al.* Proteolytic Cleavage Governs Interleukin-11 Trans-signaling. *Cell Reports* **14**, 1761-1773, doi:10.1016/j.celrep.2016.01.053 (2016).
221 Balic, J. J., Garbers, C., Rose-John, S., Yu, L. & Jenkins, B. J. Interleukin-11-driven gastric tumourigenesis is independent of trans-signalling. *Cytokine* **92**, 118-123, doi:10.1016/j.cyto.2017.01.015 (2017).
222 Agthe, M., Garbers, Y., Putoczki, T. & Garbers, C. Interleukin-11 classic but not trans-signaling is essential for fertility in mice. *Placenta* **57**, 13-16, doi:10.1016/j.placenta.2017.05.015 (2017).

223 Leng, S. X. & Elias, J. A. Interleukin-11 inhibits macrophage interleukin-12 production. *Journal of Immunology* **159**, 2161-2168 (1997).
224 Trepicchio, W. L., Bozza, M., Pedneault, G. & Dorner, A. J. Recombinant Human IL-11 Attenuates the Inflammatory Response Through Down-Regulation of Proinflammatory Cytokine Release and Nitric Oxide Production. *Journal of Immunology* **157**, 3627-3634 (1996).
225 Trepicchio, W. L., Wang, L., Bozza, M. & Dorner, A. J. IL-11 regulates macrophage effector function through the inhibition of nuclear factor-κB. *Journal of Immunology* **159**, 5661-5670 (1997).
226 Hermann, J. A., Hall, M. A., Maini, R. N., Feldmann, M. & Brennan, F. M. Important immunoregulatory role of interleukin-11 in the inflammatory process in rheumatoid arthritis. *Arthritis and Rheumatism* **41**, 1388-1397, doi:10.1002/1529-0131(199808)41:8<1388::AID-ART7>3.0.CO;2-F (1998).
227 Anguita, J., Barthold, Stephen W., Samanta, S., Ryan, J. & Fikrig, E. Selective Anti-Inflammatory Action of Interleukin-11 in Murine Lyme Disease: Arthritis Decreases while Carditis Persists. *The Journal of Infectious Diseases* **179**, 734-737, doi:10.1086/314613 (1999).
228 Orner, A. N. J. D. & Repicchio, W. I. L. T. Interleukin-11 Reduces T-Cell – Dependent Experimental Liver Injury in Mice. *Hepatology* **30**, 1441-1447 (1999).
229 Klein, W. *et al.* A polymorphism in the IL11 gene is associated with ulcerative colitis. *Genes and Immunity* **3**, 494-496, doi:10.1038/sj.gene.6363897 (2002).
230 Schafer, S. *et al.* IL-11 is a crucial determinant of cardiovascular fibrosis. *Nature* **552**, 110-115, doi:10.1038/nature24676 (2017).
231 Widjaja, A. A. *et al.* Inhibiting Interleukin 11 Signaling Reduces Hepatocyte Death and Liver Fibrosis, Inflammation, and Steatosis in Mouse Models of Nonalcoholic Steatohepatitis. *Gastroenterology* **157**, 777-792.e714, doi:10.1053/j.gastro.2019.05.002 (2019).
232 Strikoudis, A. *et al.* Modeling of Fibrotic Lung Disease Using 3D Organoids Derived from Human Pluripotent Stem Cells. *Cell Reports*, 3709-3723, doi:10.1016/j.celrep.2019.05.077 (2019).
233 Ng, B. *et al.* IL-11 Is a Therapeutic Target in Idiopathic Pulmonary Fibrosis. *Science Translational Medicine* **11**, eaaw1237, doi:10.1126/scitranslmed.aaw1237
(2019).
234 Obana, M. *et al.* Therapeutic activation of signal transducer and activator of transcription 3 by interleukin-11 ameliorates cardiac fibrosis after myocardial infarction. *Circulation* **121**, 684-691, doi:10.1161/CIRCULATIONAHA.109.893677 (2010).
235 Schwartz, D. M. *et al.* JAK inhibition as a therapeutic strategy for immune and inflammatory diseases. *Nature Reviews Drug Discovery* **16**, 843-862, doi:10.1038/nrd.2017.201 (2017).
236 Mesa, R. A., Yasothan, U. & Kirkpatrick, P. Ruxolitinib. *Nature Reviews Drug Discovery* **11**, 103-104, doi:10.1038/nrd3652 (2012).
237 Fleischmann, R. *et al.* Placebo-Controlled Trial of Tofacitinib Monotherapy in Rheumatoid Arthritis. *New England Journal of Medicine* **367**, 495-507, doi:10.1056/nejmoa1109071 (2012).

238 Mogul, A., Corsi, K. & McAuliffe, L. Baricitinib: The Second FDA-Approved JAK Inhibitor for the Treatment of Rheumatoid Arthritis. *Annals of Pharmacotherapy*, doi:10.1177/1060028019839650 (2019).
239 Fragoulis, G. E., Mcinnes, I. B. & Siebert, S. JAK-inhibitors. New players in the field of immune-mediated diseases, beyond rheumatoid arthritis. *Rheumatology* **58**, i43-i54, doi:10.1093/rheumatology/key276 (2019).
240 Strand, V. *et al.* Systematic review and meta-analysis of serious infections with tofacitinib and biologic disease-modifying antirheumatic drug treatment in rheumatoid arthritis clinical trials. *Arthritis Research and Therapy* **17**, 1-9, doi:10.1186/s13075-015-0880-2 (2015).
241 Vincenti, F. *et al.* Randomized phase 2b trial of tofacitinib (CP-690,550) in de novo kidney transplant patients: Efficacy, renal function and safety at 1 year. *American Journal of Transplantation* **12**, 2446-2456, doi:10.1111/j.1600-6143.2012.04127.x (2012).
242 Wollenhaupt, J. *et al.* Safety and efficacy of tofacitinib, an oral janus kinase inhibitor, for the treatment of rheumatoid arthritis in open-Label, longterm extension studies. *Journal of Rheumatology* **41**, 837-852, doi:10.3899/jrheum.130683 (2014).
243 Miklossy, G., Hilliard, T. S. & Turkson, J. Therapeutic modulators of STAT signalling for human diseases. *Nature Reviews Drug Discovery* **12**, 611-629, doi:10.1038/nrd4088 (2013).
244 Song, H., Wang, R., Wang, S. & Lin, J. A low-molecular-weight compound discovered through virtual database screening inhibits Stat3 function in breast cancer cells. *Proceedings of the National Academy of Sciences* **102**, 4700-4705, doi:10.1073/pnas.0409894102 (2005).
245 Turkson, J. *et al.* Phosphotyrosyl Peptides Block Stat3-mediated DNA Binding Activity, Gene Regulation, and Cell Transformation. *Journal of Biological Chemistry* **276**, 45443-45455, doi:10.1074/jbc.M107527200 (2001).
246 Hong, D. *et al.* AZD9150, a next-generation antisense oligonucleotide inhibitor of STAT3 with early evidence of clinical activity in lymphoma and lung cancer. *Science Translational Medicine* **7**, doi:10.1126/scitranslmed.aac5272 (2015).
247 Reilley, M. J. *et al.* STAT3 antisense oligonucleotide AZD9150 in a subset of patients with heavily pretreated lymphoma: results of a phase 1b trial. *Journal for Immunotherapy of C*
ancer **6**, 119, doi:10.1186/s40425-018-0436-5 (2018).
248 Wong, A. L. *et al.* Phase I and biomarker study of OPB-51602, a novel signal transducer and activator of transcription (STAT) 3 inhibitor, in patients with refractory solid malignancies. *Annals of Oncology* **26**, 998-1005, doi:10.1093/annonc/mdv026 (2015).
249 Bai, L. *et al.* A Potent and Selective Small-Molecule Degrader of STAT3 Achieves Complete Tumor Regression In Vivo. *Cancer Cell* **36**, 498-511.e417, doi:10.1016/j.ccell.2019.10.002 (2019).
250 Wong, A. L. A. *et al.* Do STAT3 inhibitors have potential in the future for cancer therapy? *Expert Opinion on Investigational Drugs* **26**, 883-887, doi:10.1080/13543784.2017.1351941 (2017).

251 Nero, T. L., Morton, C. J., Holien, J. K., Wielens, J. & Parker, M. W. Oncogenic protein interfaces: small molecules, big challenges. *Nature Reviews Cancer* **14**, 248-262, doi:10.1038/nrc3690 (2014).
252 Õmura, S., Hayashi, M. & Tomoda, H. Recent progress of the research on novel microbial metabolites. *Pure and Applied Chemistry* **71**, 1673-1681, doi:10.1351/pac199971091673 (1999).
253 Hayashi, M. *et al.* Suppression of bone resorption by madindoline A, a novel nonpeptide antagonist to gp130. *Proceedings of the National Academy of Sciences* **99**, 14728-14733, doi:10.1073/pnas.232562799 (2002).
254 Saleh, A. Z. M., Greenman, K. L., Billings, S., Van Vranken, D. L. & Krolewski, J. J. Binding of madindoline A to the extracellular domain of gp130. *Biochemistry* **44**, 10822-10827, doi:10.1021/bi050439+ (2005).
255 Sunazuka, T. *et al.* Total synthesis of (+)-madindoline A and (-)-madindoline B, potent, selective inhibitors of interleukin 6. Determination of the relative and absolute configurations. *Journal of the American Chemical Society* **122**, 2122-2123, doi:10.1021/ja9938074 (2000).
256 Hong, S.-S. *et al.* A Novel Small-Molecule Inhibitor Targeting the IL-6 Receptor β Subunit, Glycoprotein 130. *Journal of Immunology* **195**, 237-245, doi:10.4049/jimmunol.1402908 (2015).
257 Singh, S. *et al.* Structure-activity relationship study of a series of novel oxazolidinone derivatives as IL-6 signaling blockers. *Bioorganic and Medicinal Chemistry Letters* **26**, 1282-1286, doi:10.1016/j.bmcl.2016.01.016 (2016).
258 Grande, F. *et al.* Synthesis and antitumor activities of a series of novel quinoxalinhydrazides. *Bioorganic and Medicinal Chemistry* **15**, 288-294, doi:10.1016/j.bmc.2006.09.073 (2007).
259 Xu, S., Grande, F., Garofalo, A. & Neamati, N. Discovery of a novel orally active small-molecule gp130 inhibitor for the treatment of ovarian cancer. *Molecular Cancer Therapeutics* **12**, 937-949, doi:10.1158/1535-7163.MCT-12-1082 (2013).
260 Li, H. *et al.* Drug design targeting protein-protein interactions (PPIs) using multiple ligand simultaneous docking (MLSD) and drug repositioning: Discovery of raloxifene and bazedoxifene as novel inhibitors of IL-6/GP130 interface. *Journal of Medicinal Chemistry* **57**, 632-641, doi:10.1021/jm401144z (2014).
261 Biskobing, D. M. Update on bazedoxifene: A novel selective estrogen receptor modulator. *Clinical Interventions in Aging* **2**, 299-303 (2007).
262 Xiao, H. *et al.* Repositioning Bazedoxifene as a novel IL-6/GP130 signaling antagonist for human rhabdomyosarcoma therapy. *PLoS ONE* **12**, 1-19, doi:10.1371/journal.pone.0180297 (2017).
263 Yadav, A. & Kumar, B. Bazedoxifene enhances the anti-tumor effects of cisplatin and radiation treatment by blocking IL-6 signaling in head and neck cancer. *Oncotarget* **8**, 66912-66924 (2016).
264 Tian, J. *et al.* Bazedoxifene is a novel IL-6/GP130 inhibitor for treating triple-negative breast cancer. *Breast Cancer Research and Treatment* **175**, 553-566, doi:10.1007/s10549-019-05183-2 (2019).

265 Wilson, C. G. M. & Arkin, M. R. in *Small-Molecule Inhibitors of Protein-Protein Interactions* (eds Lyubomir Vassilev & David Fry) 25-59 (Springer Berlin Heidelberg, 2011).
266 Escamilla, R. F. & Bennett, L. Pituitary Infantilism treated with purified growth hormone, thyroid and sublingual methyltestosterone: A case report. *Journal of Clinical Endocrinology and Metabolism* **11**, 221-228 (1951).
267 Raben, M. S. Treatment of a pituitary dwarf with human growth hormone. *Journal of Clinical Endocrinology and Metabolism* **18**, 901-903 (1958).
268 Cronin, M. J. Pioneering recombinant growth hormone manufacturing: Pounds produced per mile of height. *Journal of Pediatrics* **131**, 5-7 (1997).
269 Tamura, Y., Kohno, H., Mohri, T., Fujio, Y. & Matsumiya, G. The cardioprotective effect of interleukin-11 against ischemia-reperfusion injury in a heart donor model. *Annals of Cardiothoracic Surgery* **7**, 99-105, doi:10.21037/acs.2017.09.11 (2018).
270 McCullough, P. A. *et al.* Cardiovascular toxicity of epoetin-alfa in patients with chronic kidney disease. *American Journal of Nephrology* **37**, 549-558, doi:10.1159/000351175 (2013).
271 Morstyn, G. *et al.* Effect of Granulocyte Colony Stimulating Factor on Neutropenia Induced By Cytotoxic Chemotherapy. *The Lancet* **331**, 667-672, doi:10.1016/S0140-6736(88)91475-4 (1988).
272 Lyman, G. H. *et al.* The impact of the granulocyte colony-stimulating factor on chemotherapy dose intensity and cancer survival: A systematic review and meta-analysisof randomized controlled trials. *Annals of Oncology* **24**, 2475-2484, doi:10.1093/annonc/mdt226 (2013).
273 De Groot, A. S. & Scott, D. W. Immunogenicity of protein therapeutics. *Trends in Immunology* **28**, 482-490, doi:10.1016/j.it.2007.07.011 (2007).
274 Eckardt, K. U. & Casadevall, N. Pure red-cell aplasia due to anti-erythropoietin antibodies. *Nephrology Dialysis Transplantation* **18**, 865-869, doi:10.1093/ndt/gfg182 (2003).
275 Baldo, B. A. Side Effects of Cytokines Approved for Therapy. *Drug Safety* **37**, 921-943, doi:10.1007/s40264-014-0226-z (2014).
276 Tepler, I. *et al.* A randomized placebo-controlled trial of recombinant human interleukin-11 in cancer patients with severe thrombocytopenia due to chemotherapy. *Blood* **87**, 3607-3614 (1996).
277 Kaye, J. A. FDA Licensure of Neumega to Prevent Severe Chemotherapy-Induced Thrombocytopenia. *Stem Cells* **16**, 207-223 (1998).
278 Montero, A. J. *et al.* Phase II study of low-dose interleukin-11 in patients with myelodysplastic syndrome. *Leukemia and Lymphoma* **47**, 2049-2054, doi:10.1080/10428190600758058 (2006).
279 Cantor, S. B., Elting, L. S., Hudson, D. V. & Rubenstein, E. B. Pharmacoeconomic analysis of oprelvekin (recombinant human interleukin-11) for secondary prophylaxis of thrombocytopenia in solid tumor patients receiving chemotherapy. *Cancer* **97**, 3099-3106, doi:10.1002/cncr.11447 (2003).
280 Bussel, J. B., Mukherjee, R. & Stone, A. J. A pilot study of rhuIL-11 treatment of refractory ITP. *American Journal of Hematology* **66**, 172-177, doi:10.1002/1096-8652(200103)66:3<172::AID-AJH1041>3.0.CO;2-Q (2001).

281 Milman, E. *et al.* Periostitis secondary to interleukin-11 (Oprelvekin, Neumega). Treatment for thrombocytopenia in pediatric patients. *Pediatric Radiology* **33**, 450-452, doi:10.1007/s00247-003-0893-x (2003).
282 Tsimberidou, A. M. *et al.* Low-dose interleukin-11 in patients with bone marrow failure: Update of the M. D. Anderson Cancer Center experience. *Annals of Oncology* **16**, 139-145, doi:10.1093/annonc/mdi007 (2005).
283 Sands, B. E. *et al.* Preliminary evaluation of safety and activity of recombinant human interleukin 11 in patients with active Crohn's disease. *Gastroenterology* **117**, 58-64, doi:10.1016/S0016-5085(99)70550-0 (1999).
284 Moreland, L. *et al.* Results of a phase-I/II randomized, masked, placebo-controlled trial of recombinant human interleukin-11 (rhIL-11) in the treatment of subjects with active rheumatoid arthritis. *Arthritis Research* **3**, 247-252, doi:10.1186/ar309 (2001).
285 Kaplon, H. & Reichert, J. M. Antibodies to watch in 2019. *mAbs* **11**, 219-238, doi:10.1080/19420862.2018.1556465 (2019).
286 Chapman, T. M. & Keating, G. M. Basiliximab: A Review of its Use as Induction Therapy in Renal Transplantation. *Drugs* **63**, 2803-2835, doi:10.2165/00003495-200363240-00009 (2003).
287 Segal, B. M. *et al.* Repeated subcutaneous injections of IL12/23 p40 neutralising antibody, ustekinumab, in patients with relapsing-remitting multiple sclerosis: a phase II, double-blind, placebo-controlled, randomised, dose-ranging study. *The Lancet Neurology* **7**, 796-804, doi:10.1016/S1474-4422(08)70173-X (2008).
288 Reich, K. *et al.* Risankizumab compared with adalimumab in patients with moderate-to-severe plaque psoriasis (IMMvent): a randomised, double-blind, active-comparator-controlled phase 3 trial. *The Lancet* **6736**, doi:10.1016/S0140-6736(19)30952-3 (2019).
289 Kang, S., Tanaka, T., Narazaki, M. & Kishimoto, T. Targeting Interleukin-6 Signaling in Clinic. *Immunity* **50**, 1007-1023, doi:10.1016/j.immuni.2019.03.026 (2019).
290 Burmester, G. R. *et al.* Tocilizumab in early progressive rheumatoid arthritis: FUNCTION, a randomised controlled trial. *Annals of the Rheumatic Diseases* **75**, 1081-1091, doi:10.1136/annrheumdis-2015-207628 (2016).
291 Lamb, Y. N. & Deeks, E. D. Sarilumab: A Review in Moderate to Severe Rheumatoid Arthritis. *Drugs* **78**, 929-940, doi:10.1007/s40265-018-0929-z (2018).
292 Rossi, J. F. *et al.* A phase I/II study of siltuximab (CNTO 328), an anti-interleukin-6 monoclonal antibody, in metastatic renal cell cancer. *British Journal of Cancer* **103**, 1154-1162, doi:10.1038/sj.bjc.6605872 (2010).
293 Grupp, S. A. *et al.* Chimeric antigen receptor-modified T cells for acute lymphoid leukemia. *New England Journal of Medicine* **368**, 1509-1518, doi:10.1056/NEJMoa1215134 (2013).
294 Tanaka, T., Narazaki, M. & Kishimoto, T. IL-6 in Inflammation, Immunity, and Disease. *Cold Spring Harbor Perspectives in Biology* **6**, a016295 (2014).
295 Liu, Q., Zhou, Y. H. & Yang, Z. Q. The cytokine storm of severe influenza and development of immunomodulatory therapy. *Cellular and Molecular Immunology* **13**, 3-10, doi:10.1038/cmi.2015.74 (2016).

296 Zhang, Y. *et al.* Analysis of serum cytokines in patients with severe acute respiratory syndrome. *Infection and Immunity* **72**, 4410-4415, doi:10.1128/IAI.72.8.4410-4415.2004 (2004).
297 Lau, S. K. P. *et al.* Delayed induction of proinflammatory cytokines and suppression of innate antiviral response by the novel Middle East respiratory syndrome coronavirus: Implications for pathogenesis and treatment. *Journal of General Virology* **94**, 2679-2690, doi:10.1099/vir.0.055533-0 (2013).
298 Mehta, P. *et al.* COVID-19: consider cytokine storm syndromes and immunosuppression. *The Lancet* **6736**, 19-20, doi:10.1016/S0140-6736(20)30628-0 (2020).
299 Zhou, P. *et al.* A pneumonia outbreak associated with a new coronavirus of probable bat origin. *Nature* **579**, doi:10.1038/s41586-020-2012-7 (2020).
300 Müller-Newen, G., Küster, A., Wijdenes, J., Schaper, F. & Heinrich, P. C. Studies on the interleukin-6-type cytokine signal transducer gp130 reveal a novel mechanism of receptor activation by monoclonal antibodies. *Journal of Biological Chemistry* **275**, 4579-4586, doi:10.1074/jbc.275.7.4579 (2000).
301 Deguchi, Y. *et al.* Generation of and characterization of anti-IL-11 antibodies using newly established Il11-deficient mice. *Biochemical and Biophysical Research Communications* **505**, 453-459, doi:10.1016/j.bbrc.2018.09.128 (2018).
302 Blanc, C. *et al.* Monoclonal antibodies against the human interleukin-11 receptor alpha-chain (IL-11Rα) and their use in studies of human mononuclear cells. *Journal of Immunological Methods* **241**, 43-59 (2000).
303 Winship, A. L., Van Sinderen, M., Donoghue, J., Rainczuk, K. & Dimitriadis, E. Targeting interleukin-11 receptor-α impairs human endometrial cancer cell proliferation and invasion in vitro and reduces tumor growth and metastasis in vivo. *Molecular Cancer Therapeutics* **15**, 720-730, doi:10.1158/1535-7163.MCT-15-0677 (2016).
304 Du, J. *et al.* Structural Basis for the Blockage of IL-2 Signaling by Therapeutic Antibody Basiliximab. *Journal of Immunology* **184**, 1361-1368, doi:10.4049/jimmunol.0903178 (2010).
305 Arenas-Ramirez, N. *et al.* Improved cancer immunotherapy by a CD25-mimobody conferring selectivity to human interleukin-2. *Science Translational Medicine* **8**, 1-13, doi:10.1126/scitranslmed.aag3187 (2016).
306 Trotta, E. *et al.* A human anti-IL-2 antibody that potentiates regulatory T cells by a structure-based mechanism. *Nature Medicine* **24**, 1005-1014, doi:10.1038/s41591-018-0070-2 (2018).
307 Boyman, O., Kovar, M., Rubinstein, M. P., Surh, C. D. & Sprent, J. Selective Stimulation of T Cell Subsets with Antibody-Cytokine Immune Complexes. *Science* **311**, 1924-1927 (2006).
308 Bloch, Y. *et al.* Structural Activation of Pro-inflammatory Human Cytokine IL-23 by Cognate IL-23 Receptor Enables Recruitment of the Shared Receptor IL-12Rβ1. *Immunity*, 45-58, doi:10.1016/j.immuni.2017.12.008 (2017).
309 Broughton, S. E. *et al.* Dual Mechanism of Interleukin-3 Receptor Blockade by an Anti-Cancer Antibody. *Cell Reports* **8**, 410-419, doi:10.1016/j.celrep.2014.06.038 (2014).
310 Panousis, C. *et al.* CSL311, a novel, potent, therapeutic monoclonal antibody for the treatment of diseases mediated by the common β chain of the IL-3,

GM-CSF and IL-5 receptors. *mAbs* **8**, 436-453, doi:10.1080/19420862.2015.1119352 (2016).
311 Hoge, J. *et al.* IL-6 Controls the Innate Immune Response against Listeria monocytogenes via Classical IL-6 Signaling *Journal of Immunology* **190**, 703-711, doi:10.4049/jimmunol.1201044 (2013).
312 Lesina, M. *et al.* Stat3/Socs3 Activation by IL-6 Transsignaling Promotes Progression of Pancreatic Intraepithelial Neoplasia and Development of Pancreatic Cancer. *Cancer Cell* **19**, 456-469, doi:10.1016/j.ccr.2011.03.009 (2011).
313 Bergmann, J. *et al.* IL-6 trans-signaling is essential for the development of hepatocellular carcinoma in mice. *Hepatology* **65**, 89-103, doi:10.1002/hep.28874 (2017).
314 Richards, P. J. *et al.* Functional characterization of a soluble gp130 isoform and its therapeutic capacity in an experimental model of inflammatory arthritis. *Arthritis and Rheumatism* **54**, 1662-1672, doi:10.1002/art.21818 (2006).
315 Nowell, M. A. *et al.* Soluble IL-6 Receptor Governs IL-6 Activity in Experimental Arthritis: Blockade of Arthritis Severity by Soluble Glycoprotein 130. *Journal of Immunology* **171**, 3202-3209, doi:10.4049/jimmunol.171.6.3202 (2003).
316 Mitsuyama, K. *et al.* STAT3 activation via interleukin 6 trans-signalling contributes to ileitis in SAMP1/Yit mice. *Gut* **55**, 1263-1269, doi:10.1136/gut.2005.079343 (2006).
317 Atreya, R. *et al.* Blockade of interleukin 6 trans signaling suppresses T-cell resistance against apoptosis in chronic intestinal inflammation: Evidence in Crohn disease and experimental colitis in vivo. *Nature Medicine* **6**, 583-588, doi:10.1038/75068 (2000).
318 Zhang, H. *et al.* IL-6 trans-signaling promotes pancreatitis- associated lung injury and lethality. *Journal of Clinical Investigation* **123**, 1019-1031, doi:10.1172/JCI64931.in (2013).
319 Adams, R. *et al.* Discovery of a junctional epitope antibody that stabilizes IL-6 and gp80 protein:protein interaction and modulates its downstream signaling. *Scientific Reports* **7**, 37716, doi:10.1038/srep37716 (2017).
320 Fairlie, W. D. *et al.* Affinity Maturation of Leukemia Inhibitory Factor and Conversion to Potent Antagonists of Signaling. *Journal of Biological Chemistry* **279**, 2125-2134, doi:10.1074/jbc.M310103200 (2004).
321 de Hon, F. D. *et al.* Development of an interleukin (IL) 6 receptor antagonist that inhibits IL-6-dependent growth of human myeloma cells. *Journal of Experimental Medicine* **180**, 2395-2400, doi:10.1084/jem.180.6.2395 (1994).
322 Moraga, I. *et al.* Tuning cytokine receptor signaling by re-orienting dimer geometry with surrogate ligands. *Cell* **160**, 1196-1208, doi:10.1016/j.cell.2015.02.011 (2015).
323 Mohan, K. *et al.* Topological control of cytokine receptor signaling induces differential effects in hematopoiesis. *Science* **364**, doi:10.1126/science.aav7532 (2019).
324 Liao, W., Lin, J. X. & Leonard, W. J. Interleukin-2 at the Crossroads of Effector Responses, Tolerance, and Immunotherapy. *Immunity* **38**, 13-25, doi:10.1016/j.immuni.2013.01.004 (2013).

325 Mitra, S. & Leonard, W. J. Biology of IL-2 and its therapeutic modulation: Mechanisms and strategies. *Journal of Leukocyte Biology* **103**, 643-655, doi:10.1002/JLB.2RI0717-278R (2018).
326 Arkin, M. R. *et al.* Binding of small molecules to an adaptive protein-protein interface. *Proceedings of the National Academy of Sciences* **100**, 1603-1608, doi:10.1073/pnas.252756299 (2003).
327 Krissinel, E. & Henrick, K. Inference of Macromolecular Assemblies from Crystalline State. *Journal of Molecular Biology* **372**, 774-797, doi:10.1016/j.jmb.2007.05.022 (2007).
328 Spangler, J. B. *et al.* Antibodies to Interleukin-2 Elicit Selective T Cell Subset Potentiation through Distinct Conformational Mechanisms. *Immunity* **42**, 815-825, doi:10.1016/j.immuni.2015.04.015 (2015).
329 Boyman, O. & Sprent, J. The role of interleukin-2 during homeostasis and activation of the immune system. *Nature Reviews Immunology* **12**, 180-190, doi:10.1038/nri3156 (2012).
330 Noble, S. & Goa, K. L. Aldesleukin. *BioDrugs* **7**, 394-422 (1997).
331 Rosenberg, S. A. Raising the bar: The curative potential of human cancer immunotherapy. *Science Translational Medicine* **4**, 1-6, doi:10.1126/scitranslmed.3003634 (2012).
332 Klapper, J. A. *et al.* High-dose interleukin-2 for the treatment of metastatic renal cell carcinoma: A retrospective analysis of response and survival in patients treated in the Surgery Branch at the National Cancer Institute between 1986 and 2006. *Cancer* **113**, 293-301, doi:10.1002/cncr.23552 (2008).
333 Nakagawa, K. *et al.* Mechanisms of interleukin-2-induced hepatic toxicity. *Cancer Research* **56**, 507-510 (1996).
334 Baluna, R. & Vitetta, E. S. Vascular leak syndrome: A side effect of immunotherapy. *Immunopharmacology* **37**, 117-132, doi:10.1016/S0162-3109(97)00041-6 (1997).
335 Krieg, C., Létourneau, S., Pantaleo, G. & Boyman, O. Improved IL-2 immunotherapy by selective stimulation of IL-2 receptors on lymphocytes and endothelial cells. *Proceedings of the National Academy of Sciences* **107**, 11906-11911, doi:10.1073/pnas.1119897109 (2010).
336 Prummer, O. Treatment-induced antibodies to interleukin-2. *Biotherapy* **10**, 15-24 (1997).
337 Brandhuber, B. J., Boone, T. O. M., Kenney, W. C. & Mckay, D. B. Three-Dimensional Structure of Interleukin-2. *Science* **3151**, 1985-1988 (1987).
338 Mckay, D. B. Response: Unravelling the Structure of IL-2. *Science* **257**, 412-413 (1992).
339 Mott, H. R. *et al.* The Solution Structure of the F42A Mutant of Human Interleukin 2. *Journal of Molecular Biology* **247**, 979-994, doi:10.1006/jmbi.1994.0194 (1995).
340 Stauber, D., Debler, E., Horton, P., Smith, K. & Wilson, I. Crystal structure of the interleukin-2 signaling complex: paradigm for a heterotrimeric cytokine receptor. *Proceedings of the National Academy of Sciences* **103**, 2788-2793 (2005).

341 Tilley, J. W. *et al.* Identification of a small moleucle inhibitor of the IL-2/IL-2Rα receptor interaction which binds to IL-2. *Journal of the American Chemical Society* **119**, 7589-7590, doi:10.1021/ja970702x (1997).
342 Emerson, S. D. *et al.* NMR characterization of interleukin-2 in complexes with the IL-2Ralpha receptor component, and with low molecular weight compounds that inhibit the IL-2/IL-Ralpha interaction. *Protein Science* **12**, 811-822, doi:10.1110/ps.0232803 (2003).
343 Rickert, M. *et al.* The Structure of Interleukin-2 Complexed with Its Alpha Receptor. *Science* **308**, 1477-1481, doi:10.1126/science.1109745 (2005).
344 Thanos, C. D., Randal, M. & Wells, J. a. Potent Small-Molecule Binding to a Dynamic Hot Spot on IL-2. *Journal of the American Chemical Society* **125**, 15280-15281, doi:10.1021/ja0382617 (2003).
345 Raimundo, B. C. *et al.* Integrating fragment assembly and biophysical methods in the chemical advancement of small-molecule antagonists of IL-2: An approach for inhibiting protein-protein interactions. *Journal of Medicinal Chemistry* **47**, 3111-3130, doi:10.1021/jm049967u (2004).
346 Braisted, A. C. *et al.* Discovery of a potent small molecule IL-2 inhibitor through fragment assembly. *Journal of the American Chemical Society* **125**, 3714-3715, doi:10.1021/ja034247i (2003).
347 Shanafelt, A. B. *et al.* A T-cell-selective interleukin 2 mutein exhibits potent antitumor activity and is well tolerated in vivo. *Nature Biotechnology* **18**, 1197-1202, doi:10.1038/82454 (2000).
348 Chen, X. *et al.* A novel human IL-2 mutein with minimal systemic toxicity exerts greater antitumor efficacy than wild-type IL-2. *Cell Death and Disease* **9**, doi:10.1038/s41419-018-1047-2 (2018).
349 Levin, A. M. *et al.* Exploiting a natural conformational switch to engineer an interleukin-2 'superkine'. *Nature* **484**, 529-533, doi:10.1038/nature10975 (2012).
350 Silva, D.-A. *et al.* De novo design of potent and selective mimics of IL-2 and IL-15. *Nature* **565**, 186-191, doi:10.1038/s41586-018-0830-7 (2019).
351 Mitra, S. *et al.* Interleukin-2 Activity Can Be Fine Tuned with Engineered Receptor Signaling Clamps. *Immunity* **42**, 826-838, doi:10.1016/j.immuni.2015.04.018 (2015).
352 Underhill-Day, N. *et al.* Functional characterization of W147A: A high-affinity interleukin-11 antagonist. *Endocrinology* **144**, 3406-3414, doi:10.1210/en.2002-0144 (2003).
353 Harmegnies, D. *et al.* Characterization of a potent human interleukin-11 agonist. *Biochemical Journal* **375**, 23-32, doi:10.1042/BJ20030459 (2003).
354 Xie, S. C. *et al.* The structure of the PA28–20S proteasome complex from Plasmodium falciparum and implications for proteostasis. *Nature Microbiology*, 1990–2000, doi:10.1038/s41564-019-0524-4 (2019).
355 LaVallie, E. R. *et al.* A thioredoxin gene fusion expression system that circumvents inclusion body formation in the E. coli cytoplasm. *Bio/technology* **11**, 187-193, doi:10.1038/nbt0293-187 (1993).
356 Yanaka, S. *et al.* Non-core region modulates interleukin-11 signaling activity: Generation of agonist and antagonist variants. *Journal of Biological Chemistry* **286**, 8085-8093, doi:10.1074/jbc.M110.152561 (2011).

357 Kapust, R. B. & Waugh, D. S. Escherichia coli maltose-binding protein is uncommonly effective at promoting the solubility of polypeptides to which it is fused. *Protein Science* **8**, 1668-1674, doi:10.1110/ps.8.8.1668 (1999).
358 Weir, M. P. & Sparks, J. Purification and renaturation of recombinant human interleukin-2. *Biochemical Journal* **245**, 85-91, doi:10.1042/bj2450085 (1987).
359 Arcone, R. *et al.* Single-step purification and structural characterization of human interleukin-6 produced in Escherichia coli from a T7 RNA polymerase expression vector. *European Journal of Biochemistry* **198**, 541-547, doi:10.1111/j.1432-1033.1991.tb16048.x (1991).
360 Lubkowski, J. *et al.* Crystal Structure of the Labile Complex of IL-24 with the Extracellular Domains of IL-22R1 and IL-20R2. *Journal of Immunology* **201**, 2082-2093, doi:10.4049/jimmunol.1800726 (2018).
361 Bracken, C., Marley, J. & Lu, M. A method for efficient isotopic labeling of recombinant proteins. *Journal of Biomolecular NMR* **20**, 71-75 (2001).
362 Schleinkofer, K. *et al.* Identification of the domain in the human interleukin-11 receptor that mediates ligand binding. *Journal of Molecular Biology* **306**, 263-274, doi:10.1006/jmbi.2000.4387 (2001).
363 Van Den Berg, S., Löfdahl, P. Å., Härd, T. & Berglund, H. Improved solubility of TEV protease by directed evolution. *Journal of Biotechnology* **121**, 291-298, doi:10.1016/j.jbiotec.2005.08.006 (2006).
364 Cabrita, L. D. *et al.* Enhancing the stability and solubility of TEV protease using in silico design. *Protein Science* **16**, 2360-2367, doi:10.1110/ps.072822507 (2007).
365 Kapust, R. B. *et al.* Tobacco etch virus protease: mechanism of autolysis and rational design of stable mutants with wild-type catalytic proficiency. *Protein Engineering* **14**, 993-1000, doi:10.1093/protein/14.12.993 (2001).
366 Gasteiger, E. *et al.* in *The Proteomics Protocols Handbook* 571-608 (2005).
367 Tyler, R. C. *et al.* Auto-induction medium for the production of [U-15N]- and [U-13C, U-15N]-labeled proteins for NMR screening and structure determination. *Protein expression and purification* **40**, 268-278, doi:10.1016/j.pep.2004.12.024 (2005).
368 Heim, R., Prashert, D. C., Tsien, R. Y. & Kandel, E. R. Wavelength mutations and posttranslational autoxidation of green fluorescent protein (Aequorea victoria/blue fluorescent protein/Escherichia coli/imidazolidinone). *Proceedings of the National Academy of Sciences* **91**, 12501-12504 (1994).
369 Bartkiewicz, M. *et al.* Non–fluorescent mutant of green fluorescent protein sheds light on the mechanism of chromophore formation. *FEBS Letters* **592**, 1516-1523, doi:10.1002/1873-3468.13051 (2018).
370 Yong, K. J. & Scott, D. J. Rapid directed evolution of stabilized proteins with cellular high-throughput encapsulation solubilization and screening (CHESS). *Biotechnology and Bioengineering* **112**, 438-446, doi:10.1002/bit.25451 (2015).
371 Geoghegan, K. F. *et al.* Spontaneous α-N-6-phosphogluconoylation of a 'His tag' in Escherichia coli: The cause of extra mass of 258 or 178 Da in fusion proteins. *Analytical Biochemistry* **267**, 169-184, doi:10.1006/abio.1998.2990 (1999).
372 Laemmli, U. K. Cleavage of Structural Proteins during the Assembly of the Head of Bacteriophage T4. *Nature* **227**, 680-685 (1970).

373 Ladner, C. L., Yang, J., Turner, R. J. & Edwards, R. A. Visible fluorescent detection of proteins in polyacrylamide gels without staining. *Analytical Biochemistry* **326**, 13-20, doi:10.1016/j.ab.2003.10.047 (2004).
374 Freeby, S., Liu, N., McDonald, K., Palus, A. & Posch, A. Stain Free Protein Quantification and Normalization. doi:10.1016/j.(73) (2017).
375 Candiano, G. *et al.* Blue silver: A very sensitive colloidal Coomassie G-250 staining for proteome analysis. *Electrophoresis* **25**, 1327-1333, doi:10.1002/elps.200305844 (2004).
376 Taga, T. & Kishimoto, T. Gp130 and the interleukin-6 family of cytokines. *Annual review of immunology* **15**, 797-819, doi:10.1146/annurev.immunol.15.1.797 (1997).
377 Ortega, A., Amorós, D. & García De La Torre, J. Prediction of hydrodynamic and other solution properties of rigid proteins from atomic- and residue-level models. *Biophysical Journal* **101**, 892-898, doi:10.1016/j.bpj.2011.06.046 (2011).
378 Bork, P., Holm, L. & Sander, C. The Immunoglobulin Fold. *Journal of Molecular Biology* **242**, 309-320, doi:10.1006/jmbi.1994.1582 (1994).
379 Seabrook, S. & Newman, J. High-throughput thermal scanning for protein stability: Making a good technique more robust. *ACS Combinatorial Science* **15**, 387-392, doi:10.1021/co400013v (2013).
380 Wang, X.-m. *et al.* Engineering and use of 32 P-labeled human recombinant interleukin-11 for receptor binding studies. *Construction* **68**, 61-68 (2002).
381 Jung, Y. *et al.* Improvement of biological and pharmacokinetic features of human interleukin-11 by site-directed mutagenesis. *Biochemical and Biophysical Research Communications* **405**, 399-404, doi:10.1016/j.bbrc.2011.01.041 (2011).
382 Bobby, R. *et al.* Functional implications of large backbone amplitude motions of the glycoprotein 130-binding epitope of interleukin-6. *FEBS Journal* **281**, 2471-2483, doi:10.1111/febs.12800 (2014).
383 Yao, S. *et al.* Backbone dynamics measurements on leukemia inhibitory factor, a rigid four-helical bundle cytokine. *Protein Science* **9**, 671-682, doi:10.1110/ps.9.4.671 (2000).
384 Zhao, H., Mayer, M. L. & Schuck, P. Analysis of Protein Interactions with Picomolar Binding Affinity by Fluorescence-Detected Sedimentation Velocity. *Analytical Chemistry* **86**, 3181-3187 (2014).
385 Scott, D. J. *et al.* A Novel Ultra-Stable, Monomeric Green Fluorescent Protein For Direct Volumetric Imaging of Whole Organs Using CLARITY. *Scientific Reports* **8**, 667, doi:10.1038/s41598-017-18045-y (2018).
386 Rickert, M., Boulanger, M. J., Goriatcheva, N. & Garcia, K. C. Compensatory energetic mechanisms mediating the assembly of signaling complexes between interleukin-2 and its α, β, and γc receptors. *Journal of Molecular Biology* **339**, 1115-1128, doi:10.1016/j.jmb.2004.04.038 (2004).
387 McElroy, C. A., Dohm, J. A. & Walsh, S. T. R. Structural and Biophysical Studies of the Human IL-7/IL-7Rα Complex. *Structure* **17**, 54-65, doi:10.1016/j.str.2008.10.019 (2009).
388 Zacharias, D. A., Violin, J. D., Newton, A. C. & Tsien, R. Y. Partitioning of Lipid-Modified Monomeric GFPs into Membrane Microdomains of Live Cells. *Science* **296**, 913-916, doi:10.1126/science.1068539 (2002).

389 Zhao, H., Lomash, S., Glasser, C., Mayer, M. L. & Schuck, P. Analysis of high affinity self-association by fluorescence optical sedimentation velocity analytical ultracentrifugation of labeled proteins: Opportunities and limitations. *PLoS ONE* **8**, doi:10.1371/journal.pone.0083439 (2013).
390 Murphy, K. P., Xie, D., Garcia, K. C., Amzel, L. M. & Freire, E. Structural energetics of peptide recognition: Angiotensin II/antibody binding. *Proteins: Structure, Function, and Bioinformatics* **15**, 113-120, doi:10.1002/prot.340150203 (1993).
391 Freire, E. & Gómez, J. Thermodynamic Mapping of the Inhibitor Site of the Aspartic Protease Endothiapepsin. *Journal of Molecular Biology* **252**, 337-350 (1995).
392 Murphy, K. P. & Freire, E. Thermodynamics of structural stability and cooperative folding behavior in proteins. *Advances in Protein Chemistry* **43**, 313-361 (1992).
393 Lyskov, S. & Gray, J. J. The RosettaDock server for local protein-protein docking. *Nucleic Acids Research* **36**, 233-238, doi:10.1093/nar/gkn216 (2008).
394 Lyskov, S. *et al.* Serverification of Molecular Modeling Applications: The Rosetta Online Server That Includes Everyone (ROSIE). *PLoS ONE* **8**, 5-7, doi:10.1371/journal.pone.0063906 (2013).
395 Luft, J. R. & DeTitta, G. T. A method to produce microseed stock for use in the crystallization of biological macromolecules. *Acta Crystallographica Section D: Biological Crystallography* **55**, 988-993, doi:10.1107/S0907444999002085 (1999).
396 Aragão, D. *et al.* MX2: a high-flux undulator microfocus beamline serving both the chemical and macromolecular crystallography communities at the Australian Synchrotron. *Journal of Synchrotron Radiation* **25**, 885-891, doi:10.1107/s1600577518003120 (2018).
397 Kabsch, W. Xds. *Acta Crystallographica Section D: Biological Crystallography* **66**, 125-132, doi:10.1107/S0907444909047337 (2010).
398 Evans, P. Scaling and assessment of data quality. *Acta Crystallographica Section D: Biological Crystallography* **62**, 72-82, doi:10.1107/S0907444905036693 (2006).
399 Evans, P. R. & Murshudov, G. N. How good are my data and what is the resolution? *Acta Crystallographica Section D: Biological Crystallography* **69**, 1204-1214, doi:10.1107/S0907444913000061 (2013).
400 McCoy, A. J. *et al.* Phaser crystallographic software *Journal of Applied Crystallography* **40**, 658-674, doi:10.1107/s0021889807021206 (2007).
401 Afonine, P. V. *et al.* Towards automated crystallographic structure refinement with phenix.refine. *Acta Crystallographica Section D: Biological Crystallography* **68**, 352-367, doi:10.1107/S0907444912001308 (2012).
402 Emsley, P., Lohkamp, B., Scott, W. G. & Cowtan, K. Features and development of Coot. *Acta Crystallographica Section D: Biological Crystallography* **66**, 486-501, doi:10.1107/S0907444910007493 (2010).
403 Schuck, P. Size-distribution analysis of macromolecules by sedimentation velocity ultracentrifugation and lamm equation modeling. *Biophysical Journal* **78**, 1606-1619, doi:10.1016/S0006-3495(00)76713-0 (2000).

404 Laue, T. M., Shah, B. D., Ridgeway, T. M. & Pelletier, S. L. *Analytical Ultracentrifugation in Biochemistry and Polymer Science*. 90-125 (Cambridge: Royal Society of Chemistry, 1992).
405 Zhao, H. & Schuck, P. Combining biophysical methods for the analysis of protein complex stoichiometry and affinity in SEDPHAT. *Acta Crystallographica Section D: Biological Crystallography* **71**, 3-14, doi:10.1107/S1399004714010372 (2015).
406 Kirby, N. M. *et al.* A low-background-intensity focusing small-angle X-ray scattering undulator beamline. *Journal of Applied Crystallography* **46**, 1670-1680, doi:10.1107/S002188981302774X (2013).
407 Kirby, N. *et al.* Improved radiation dose efficiency in solution SAXS using a sheath flow sample environment. *Acta Crystallographica Section D Structural Biology* **72**, 1254-1266, doi:10.1107/S2059798316017174 (2016).
408 Ryan, T. M. *et al.* An optimized SEC-SAXS system enabling high X-ray dose for rapid SAXS assessment with correlated UV measurements for biomolecular structure analysis:. *Journal of Applied Crystallography* **51**, 97-111, doi:10.1107/S1600576717017101 (2018).
409 Panjkovich, A. & Svergun, D. I. CHROMIXS: automatic and interactive analysis of chromatography-coupled small-angle X-ray scattering data. *Bioinformatics* **34**, 1944-1946
, doi:10.1093/bioinformatics/btx846 (2017).
410 Franke, D. *et al.* ATSAS 2.8: A comprehensive data analysis suite for small-angle scattering from macromolecular solutions. *Journal of Applied Crystallography* **50**, 1212-1225, doi:10.1107/S1600576717007786 (2017).
411 Barberato, C. & Koch, M. H. J. CRYSOL - a Program to Evaluate X-ray Solution Scattering of Biological Macromolecules from Atomic Coordinates. *Journal of Applied Crystallography* **28**, 768-773, doi:10.1107/S0021889895007047 (1995).
412 Franke, D. & Svergun, D. I. DAMMIF, a program for rapid ab-initio shape determination in small-angle scattering. *Journal of Applied Crystallography* **42**, 342-346, doi:10.1107/S0021889809000338 (2009).
413 Volkov, V. V. & Svergun, D. I. Uniqueness of ab initio shape determination in small-angle scattering. *Journal of Applied Crystallography* **36**, 860-864, doi:10.1107/S0021889803000268 (2003).
414 Svergun, D. Restoring low resolution structure of biological macromolecules from solution scattering using simulated annealing. *Biophysical Journal* **76**, 2879-2886 (1999).
415 Phillips, J. C. *et al.* Scalable molecular dynamics with NAMD. *Journal of Computational Chemistry* **26**, 1781-1802, doi:10.1002/jcc.20289 (2005).
416 Brooks, B. R. *et al.* CHARMM: The Biomolecular Simulation Program. *Journal of Computational Chemistry* **20**, 1545-1614, doi:10.1002/jcc (2009).
417 Humphrey, W., Dalke, A. & Schulten, K. VMD: Visual Molecular Dynamics. *Journal of Molecular Graphics* **7855**, 33-38, doi:10.1016/0263-7855(96)00018-5 (1996).
418 Kelly, L. A., Mezulis, S., Yates, C., Wass, M. & Sternberg, M. The Phyre2 web portal for protein modelling, prediction, and analysis. *Nature Protocols* **10**, 845-858, doi:10.1038/nprot.2015-053 (2015).

419 Brautigam, C. A., Zhao, H., Vargas, C., Keller, S. & Schuck, P. Integration and global analysis of isothermal titration calorimetry data for studying macromolecular interactions. *Nature Protocols* **11**, 882-894, doi:10.1038/nprot.2016.044 (2016).
420 Keller, S. *et al.* High-Precision Isothermal Titration Calorimetry with Automated Peak Shape Analysis. *Analytical Chemistry* **84**, 5066-5073, doi:10.1021/ac3007522 (2012).
421 Chaudhury, S. *et al.* Benchmarking and analysis of protein docking performance in Rosetta v3.2. *PLoS ONE* **6**, doi:10.1371/journal.pone.0022477 (2011).
422 Rambo, R. P. & Tainer, J. A. Accurate assessment of mass, models and resolution by small-angle scattering. *Nature* **496**, 477-481, doi:10.1038/nature12070 (2013).
423 Tuukkanen, A. T., Kleywegt, G. J. & Svergun, D. I. Resolution of ab initio shapes determined from small-angle scattering *IUCrJ* **3**, 440-447, doi:10.1107/s2052252516016018 (2016).
424 Tickle, I. J. *et al. STARANISO*, <http://staraniso.globalphasing.org/cgi-bin/staraniso.cgi> (2018).
425 Kimanius, D., Forsberg, B. O., Scheres, S. H. & Lindahl, E. Accelerated cryo-EM structure determination with parallelisation using GPUs in RELION-2. *Elife* **5**, doi:10.7554/eLife.18722 (2016).
426 Scheres, S. H. Semi-automated selection of cryo-EM particles in RELION-1.3. *J Struct Biol* **189**, 114-122, doi:10.1016/j.jsb.2014.11.010 (2015).
427 Punjani, A., Rubinstein, J. L., Fleet, D. J. & Brubaker, M. A. CryoSPARC: Algorithms for rapid unsupervised cryo-EM structure determination. *Nature Methods* **14**, 290-296, doi:10.1038/nmeth.4169 (2017).
428 Terwilliger, T. C., Sobolev, O. V., Afonine, P. V. & Adams, P. D. Automated map sharpening by maximization of detail and connectivity. *Acta Crystallographica Section D Structural Biology* **74**, 545-559, doi:10.1107/S2059798318004655 (2018).
429 Emsley, P., Lohkamp, B., Scott, W. G. & Cowtan, K. Features and development of Coot. *Acta Crystallogr D* **66**, 486-501, doi:Doi 10.1107/S0907444910007493 (2010).
430 Afonine, P. V. *et al.* Real-space refinement in Phenix for cryo-EM and crystallography. *Acta Crystallographica Section D Structural Biology* **74**, 531-544, doi:10.1101/249607 (2018).
431 Pettersen, E. F. *et al.* UCSF Chimera--a visualization system for exploratory research and analysis. *J Comput Chem* **25**, 1605-1612, doi:10.1002/jcc.20084 (2004).
432 Barad, B. A. *et al.* EMRinger: side chain–directed model and map validation for 3D cryo-electron microscopy. *Nature Methods* **12**, 943-946, doi:10.1038/nmeth.3541 (2015).
433 Williams, C. J. *et al.* MolProbity: More and better reference data for improved all-atom structure validation. *Protein Science* **27**, 293-315, doi:10.1002/pro.3330 (2018).
434 Shindyalov, I. N. & Bourne, P. E. Protein structure alignment by incremental combinatorial extension (CE) of the optimal path. *Protein Engineering* **11**, 739-747 (1998).

435 Moraga, I. *et al.* Instructive roles for cytokine-receptor binding parameters in determining signaling and functional potency. *Science Signaling* **8**, ra114-ra114, doi:10.1126/scisignal.aab2677 (2015).
436 Kim, A. R. *et al.* Functional Selectivity in Cytokine Signaling Revealed Through a Pathogenic EPO Mutation Article Functional Selectivity in Cytokine Signaling Revealed Through a Pathogenic EPO Mutation. *Cell* **168**, 1053-1064.e1015, doi:10.1016/j.cell.2017.02.026 (2017).
437 Hinds, M. G., Maurer, T., Zhang, J. G., Nicola, N. A. & Norton, R. S. Solution structure of leukemia inhibitory factor. *Journal of Biological Chemistry* **273**, 13738-13745 (1998).
438 Scanlon, M. J. & Norton, R. S. Multiple conformations of the sea anemone polypeptide anthopleurin-A in solution. *Protein Science* **3**, 1121-1124, doi:10.1002/pro.5560030717 (1994).
439 Xu, G. Y. *et al.* Complete 1H, 15N and 13C assignments, secondary structure, and topology of recombinant human interleukin-6. *Journal of Biomolecular NMR* **8**, 123-135, doi:10.1007/BF00211159 (1996).
440 Keeler, C., Dannies, P. S. & Hodsdon, M. E. The tertiary structure and backbone dynamics of human prolactin. *Journal of Molecular Biology* **328**, 1105-1121, doi:10.1016/S0022-2836(03)00367-X (2003).
441 Hoffman, R. C. *et al.* Resonance assignments for Oncostatin M, a 24-kDa alpha-helical protein. *Journal of Biomolecular NMR* **7**, 273-282 (1996).
442 Feng, Y., Klein, B. K., Vu, L., Aykent, S. & McWherter, C. a. 1H, 13C, and 15N NMR resonance assignments, secondary structure, and backbone topology of a variant of human interleukin-3. *Biochemistry* **34**, 6540-6551 (1995).
443 Sattler, M. & Fesik, S. W. Use of deuterium labeling in NMR: Overcoming a sizeable problem. *Structure* **4**, 1245-1249, doi:10.1016/S0969-2126(96)00133-5 (1996).
444 Marsh, J. A., Singh, V. K., Jia, Z. & Forman-Kay, J. D. Sensitivity of secondary structure propensities to sequence differences between α- and γ-synuclein: Implications for fibrillation. *Protein Science* **15**, 2795-2804, doi:10.1110/ps.062465306 (2006).
445 Schubert, M., Labudde, D., Oschkinat, H. & Schmieder, P. A software tool for the prediction of Xaa-Pro peptide bond conformations in proteins based on 13 C chemical shift statistics. *Journal of Biomolecular NMR* **24**, 149-154, doi:10.1023/A:1020997118364 (2002).
446 Kleckner, I. R. & Foster, M. P. An introduction to NMR-based approaches for measuring protein dynamics. *Biochimica et Biophysica Acta* **1814**, 942-968, doi:10.1016/j.bbapap.2010.10.012 (2011).
447 Kasimova, M. R. *et al.* NMR studies of the backbone flexibility and structure of human growth hormone: A comparison of high and low pH conformations. *Journal of Molecular Biology* **318**, 679-695, doi:10.1016/S0022-2836(02)00137-7 (2002).
448 Duff, A. P., Wilde, K. L., Rekas, A., Lake, V. & Holden, P. J. Robust High-Yield Methodologies for 2H and 2H/15N/13C Labeling of Proteins for Structural Investigations Using Neutron Scattering and NMR. *Methods in Enzymology* **565**, 3-25, doi:10.1016/bs.mie.2015.06.014 (2015).

449 Scheuermann, T. H., Padrick, S. B., Gardner, K. H. & Brautigam, C. A. On the acquisition and analysis of microscale thermophoresis data. *Analytical Biochemistry* **496**, 79-83, doi:10.1016/j.ab.2015.12.013 (2016).
450 Delaglio, F. *et al.* NMRPipe: A multidimensional spectral processing system based on UNIX pipes. *Journal of Biomolecular NMR* **6**, 277-293, doi:10.1007/BF00197809 (1995).
451 Kazimierczuk, K. & Orekhov, V. Y. Accelerated NMR spectroscopy by using compressed sensing. *Angewandte Chemie - International Edition* **50**, 5556-5559, doi:10.1002/anie.201100370 (2011).
452 Lee, W., Tonelli, M. & Markley, J. L. NMRFAM-SPARKY: enhanced software for biomolecular NMR spectroscopy. *Bioinformatics* **31**, 1325-1327, doi:10.1093/bioinformatics/btu830 (2014).
453 Pervushin, K., Riek, R., Wider, G. & Wüthrich, K. Attenuated T2 relaxation by mutual cancellation of dipole-dipole coupling and chemical shift anisotropy indicates an avenue to NMR structures of very large biological macromolecules in solution. *Proceedings of the National Academy of Sciences* **94**, 12366-12371, doi:10.1073/pnas.94.23.12366 (1997).
454 Bahrami, A., Assadi, A. H., Markley, J. L. & Eghbalnia, H. R. Probabilistic interaction network of evidence algorithm and its application to complete labeling of peak lists from protein NMR spectroscopy. *PLoS Computational Biology* **5**, doi:10.1371/journal.pcbi.1000307 (2009).
455 Zhang, H., Neal, S. & Wishart, D. S. RefDB: A database of uniformly referenced protein chemical shifts. *Journal of Biomolecular NMR* **25**, 173-195, doi:10.1023/A:1022836027055 (2003).
456 Zhu, G., Xia, Y., Nicholson, L. K. & Sze, K. H. Protein dynamics measurements by TROSY-based NMR experiments. *Journal of Magnetic Resonance* **143**, 423-426, doi:10.1006/jmre.2000.2022 (2000).
457 Farrow, N. A. *et al.* Backbone dynamics of a free and phosphopeptide-complexed Src homology 2 domain studied by 15N NMR relaxation. *Biochemistry* **33**, 5984-6003, doi:10.1021/bi00185a040 (1994).
458 Bieri, M., d'Auvergne, E. J. & Gooley, P. R. relaxGUI: a new software for fast and simple NMR relaxation data analysis and calculation of ps-ns and μs motion of proteins. *Journal of Biomolecular NMR* **50**, 147-155, doi:10.1007/s10858-011-9509-1 (2011).
459 d'Auvergne, E. J. & Gooley, P. R. Optimisation of NMR dynamic models I. Minimisation algorithms and their performance within the model-free and Brownian rotational diffusion spaces. *Journal of Biomolecular NMR* **40**, 107-119, doi:10.1007/s10858-007-9214-2 (2008).
460 d'Auvergne, E. J. & Gooley, P. R. Optimisation of NMR dynamic models II. A new methodology for the dual optimisation of the model-free parameters and the Brownian rotational diffusion tensor. *Journal of Biomolecular NMR* **40**, 121-133, doi:10.1007/s10858-007-9213-3 (2008).
461 Stone, M. J. *et al.* Backbone dynamics of the Bacillus subtilis glucose permease IIA domain determined from 15N NMR relaxation measurements. *Biochemistry* **31**, 4394-4406, doi:10.1021/bi00133a003 (1992).
462 Tate, J. G. *et al.* COSMIC: The Catalogue Of Somatic Mutations In Cancer. *Nucleic Acids Research* **47**, D941-D947, doi:10.1093/nar/gky1015 (2019).

463 Kuhlbrandt, W. The resolution revolution. *Science* **343**, 1443-1445, doi:10.1007/s12551-019-00558-7 (2014).
464 De la Peña, A. H., Goodall, E. A., Gates, S. N., Lander, G. C. & Martin, A. Substrate-engaged 26S proteasome structures reveal mechanisms for ATP-hydrolysis–driven translocation. *Science* **362**, doi:10.1126/science.aav0725 (2018).
465 Zhang, X. *et al.* Structure of the human activated spliceosome in three conformational states. *Cell Research* **28**, 307-322, doi:10.1038/cr.2018.14 (2018).
466 Liao, M., Cao, E., Julius, D. & Cheng, Y. Structure of the TRPV1 ion channel determined by electron cryo-microscopy. *Nature* **504**, 107-112, doi:10.1038/nature12822 (2013).
467 Wong, W. *et al.* Cryo-EM structure of the Plasmodium falciparum 80S ribosome bound to the anti-protozoan drug emetine. *eLife* **2014**, 1-20, doi:10.7554/eLife.03080 (2014).
468 Draper-Joyce, C. J. *et al.* Structure of the adenosine-bound human adenosine A1 receptor – Gi complex. *Nature* **558**, 559-563, doi:10.1038/s41586-018-0236-6 (2018).
469 Li, H. *et al.* Structure and function based design of Plasmodium-selective proteasome inhibitors. *Nature* **530**, 233–236 (2016).
470 Wu, Z. *et al.* Cryo-EM structures and dynamics of substrate-engaged human 26S proteasome. *Nature* **565**, 49-55, doi:10.1038/s41586-018-0736-4 (2018).
471 Fitzpatrick, A. W. P. *et al.* Cryo-EM structures of tau filaments from Alzheimer's disease. *Nature* **547**, 185-190, doi:10.1038/nature23002 (2017).
472 Falcon, B. *et al.* Novel tau filament fold in chronic traumatic encephalopathy encloses hydrophobic molecules. *Nature* **568**, 420-423, doi:10.1038/s41586-019-1026-5 (2019).
473 Wong, W. *et al.* Structure of Plasmodium falciparum Rh5–CyRPA–Ripr invasion complex. *Nature* **565**, 118-121, doi:10.1038/s41586-018-0779-6 (2019).
474 Zhou, B.-R. *et al.* Atomic resolution cryo-EM structure of a native-like CENP-A nucleosome aided by an antibody fragment. *Nature Communications* **10**, 2301, doi:10.1038/s41467-019-10247-4 (2019).
475 Mendoza, J. L. *et al.* Structure of the IFNγ receptor complex guides design of biased agonists. *Nature* **567**, 56-60, doi:10.1038/s41586-019-0988-7 (2019).
476 Manglik, A. *et al.* Structural Insights into the Dynamic Process of β2-Adrenergic Receptor Signaling. *Cell* **161**, 1101-1111, doi:10.1016/j.cell.2015.04.043 (2015).
477 Kato, H. E. *et al.* Conformational transitions of a neurotensin receptor 1–Gi1 complex. *Nature*, doi:10.1038/s41586-019-1337-6 (2019).
478 Scapin, G. *et al.* Structure of the insulin receptor-insulin complex by single-particle cryo-EM analysis. *Nature* **556**, 122-125, doi:10.1038/nature26153 (2018).
479 Weis, F. *et al.* The signalling conformation of the insulin receptor ectodomain. *Nature Communications* **9**, 1-10, doi:10.1038/s41467-018-06826-6 (2018).
480 Uchikawa, E., Choi, E., Shang, G., Yu, H. & Bai, X.-c. Activation mechanism of the insulin receptor revealed by cryo-EM structure of the fully liganded receptor–ligand complex. *eLife* **8**, 1-23, doi:10.7554/elife.48630 (2019).

481 Garbers, C. & Scheller, J. Interleukin-6 and interleukin-11: Same same but different. *Biological Chemistry* **394**, 1145-1161, doi:10.1515/hsz-2013-0166 (2013).
482 Lin, J. X. & Leonard, W. J. The common cytokine receptor γ chain family of cytokines. *Cold Spring Harbor Perspectives in Biology* **10**, doi:10.1101/cshperspect.a028449 (2018).
483 Findeisen, M. *et al.* Treatment of type 2 diabetes with the designer cytokine IC7Fc. *Nature* **574**, 63-68, doi:10.1038/s41586-019-1601-9 (2019).
484 Moraga, I. *et al.* Synthekines are surrogate cytokine and growth factor agonists that compel signaling through non-natural receptor dimers. *eLife* **6**, 1-22, doi:10.7554/eLife.22882 (2017).
485 Pleiner, T. *et al.* Nanobodies: Site-specific labeling for super-resolution imaging, rapid epitope- mapping and native protein complex isolation. *eLife* **4**, 1-21, doi:10.7554/eLife.11349 (2015).
486 Virant, D. *et al.* A peptide tag-specific nanobody enables high-quality labeling for dSTORM imaging. *Nature Communications* **9**, 1-14, doi:10.1038/s41467-018-03191-2 (2018).
487 Götzke, H. *et al.* A rationally designed and highly versatile epitope tag for nanobody-based purification, detection and manipulation of proteins. *bioRxiv*, 640771, doi:10.1101/640771 (2019).
488 Thanos, C. D., DeLano, W. L. & Wells, J. A. Hot-spot mimicry of a cytokine receptor by a small molecule. *Proceedings of the National Academy of Sciences* **103**, 15422-15427, doi:10.1073/pnas.0607058103 (2006).
489 Mukherjee, S. *The emperor of all maladies: a biography of cancer*. (Scribner, 2010).
490 Druker, B. J. Perspectives on the development of a molecularly targeted agent. *Cancer Cell* **1**, 31-36, doi:10.1016/S1535-6108(02)00025-9 (2002).
491 Jordan, V. C. Tamoxifen: A most unlikely pioneering medicine. *Nature Reviews Drug Discovery* **2**, 205-213, doi:10.1038/nrd1031 (2003).
492 Cho, H.-S. *et al.* Structure of the extracellular region of HER2 alone and in complex with the Herceptin Fab. *Nature* **421**, 756-760, doi:10.1038/nature01392 (2003).
493 Kish-Trier, E. & Hill, C. P. Structural Biology of the Proteasome. *Annual Review of Biophysics* **42**, 29-49, doi:10.1146/annurev-biophys-083012-130417 (2013).
494 Stadtmueller, B. M. & Hill, C. P. Proteasome Activators. *Molecular Cell* **41**, 8-19, doi:10.1016/j.molcel.2010.12.020 (2011).
495 Morris, E. P. & Da Fonseca, P. C. A. High-resolution cryo-EM proteasome structures in drug development. *Acta Crystallographica Section D: Structural Biology* **73**, 522-533, doi:10.1107/S2059798317007021 (2017).
496 Xie, S. C., Dick, L. R., Gould, A., Brand, S. & Tilley, L. The proteasome as a target for protozoan parasites. *Expert Opinion on Therapeutic Targets* **23**, 903-914, doi:10.1080/14728222.2019.1685981 (2019).
497 Eisele, M. R. *et al.* Expanded Coverage of the 26S Proteasome Conformational Landscape Reveals Mechanisms of Peptidase Gating. *Cell Reports* **24**, 1301-1315.e1305, doi:10.1016/j.celrep.2018.07.004 (2018).

498 Zhu, Y. *et al.* Structural mechanism for nucleotide-driven remodeling of the AAA-ATPase unfoldase in the activated human 26S proteasome. *Nature Communications* **9**, 1-12, doi:10.1038/s41467-018-03785-w (2018).
499 Kirkman, L. A. *et al.* Antimalarial proteasome inhibitor reveals collateral sensitivity from intersubunit interactions and fitness cost of resistance. *Proceedings of the National Academy of Sciences* **115**, E6863-E6870, doi:10.1073/pnas.1806109115 (2018).
500 Yoo, E. *et al.* Defining the determinants of specificity of *Plasmodium* proteasome inhibitors. *Journal of the American Chemical Society* **140**, 11424-11437, doi:10.1021/jacs.8b06656 (2018).
501 Dogovski, C. *et al.* Targeting the cell stress response of *Plasmodium falciparum* to overcome artemisinin resistance. *PLoS biology* **13**, e1002132, doi:10.1371/journal.pbio.1002132 (2015).
502 Bridgford, J. L. *et al.* Artemisinin kills malaria parasites by damaging proteins and inhibiting the proteasome. *Nature Communications* **9**, 3801, doi:10.1038/s41467-018-06221-1 (2018).
503 Harshbarger, W., Miller, C., Diedrich, C. & Sacchettini, J. Crystal structure of the human 20S proteasome in complex with carfilzomib. *Structure* **23**, 418-424, doi:10.1016/j.str.2014.11.017 (2015).
504 Huber, E. M. *et al.* Immuno- and constitutive proteasome crystal structures reveal differences in substrate and inhibitor specificity. *Cell* **148**, 727-738, doi:10.1016/j.cell.2011.12.030 (2012).
505 Lin, G. *et al.* Inhibitors selective for mycobacterial versus human proteasomes. *Nature* **461**, 621-626, doi:10.1038/nature08357 (2009).
506 Löwe, J. *et al.* Crystal structure of the 20s proteasome from the archaeon T. acidophilum at 3.4 angstrom resolution. *Science* **268**, 533-539 (1995).
507 Groll, M. *et al.* Structure of 20S proteasome from yeast at 2.4 A resolution. *Nature* **386**, 463-471, doi:10.1038/386463a0 (1997).
508 Choi, W. H. *et al.* Open-gate mutants of the mammalian proteasome show enhanced ubiquitin-conjugate degradation. *Nature Communications* **7**, 1-12, doi:10.1038/ncomms10963 (2016).
509 Groll, M. *et al.* A gated channel into the proteasome core particle. *Nature Structural Biology* **7**, 1062-1067, doi:10.1038/80992 (2000).
510 Voges, D., Zwickl, P. & Baumeister, W. The 26S proteasome: a molecular machine designed for controlled proteolysis. *Annual Review of Biochemistry* **68**, 1015-1068, doi:10.1146/annurev.biochem.68.1.1015 (1999).
511 Mott, J. D. *et al.* PA28, an activator of the 20 S proteasome, is composed of two nonidentical but homologous subunits. *Journal of Biological Chemistry* **269**, 31466-31471 (1994).
512 Respondek, D. *et al.* PA28 modulates antigen processing and viral replication during coxsackievirus B3 infection. *PLoS ONE* **12**, e0173259, doi:10.1371/journal.pone.0173259 (2017).
513 Huang, L., Haratake, K., Miyahara, H. & Chiba, T. Proteasome activators, PA28gamma and PA200, play indispensable roles in male fertility. *Scientific Reports* **6**, 23171, doi:10.1038/srep23171 (2016).
514 Li, J., Powell, S. R. & Wang, X. Enhancement of proteasome function by PA28 alpha; overexpression protects against oxidative stress. *The FASEB Journal* **25**, 883-893, doi:10.1096/fj.10-160895 (2011).

515 Pickering, A. M. *et al.* The immunoproteasome, the 20S proteasome and the PA28alphabeta proteasome regulator are oxidative-stress-adaptive proteolytic complexes. *Biochemical Journal* **432**, 585-594, doi:10.1042/BJ20100878 (2010).
516 Seifert, U. *et al.* Immunoproteasomes preserve protein homeostasis upon interferon-induced oxidative stress. *Cell* **142**, 613-624, doi:10.1016/j.cell.2010.07.036 (2010).
517 Tanahashi, N. *et al.* Hybrid proteasomes. Induction by interferon-gamma and contribution to ATP-dependent proteolysis. *Journal of Biological Chemistry* **275**, 14336-14345 (2000).
518 Cascio, P., Call, M., Petre, B. M., Walz, T. & Goldberg, A. L. Properties of the hybrid form of the 26S proteasome containing both 19S and PA28 complexes. *The EMBO Journal* **21**, 2636-2645, doi:10.1093/emboj/21.11.2636 (2002).
519 Sugiyama, M. *et al.* Spatial arrangement and functional role of alpha subunits of proteasome activator PA28 in hetero-oligomeric form. *Biochemical and Biophysical Research Communications* **432**, 141-145, doi:10.1016/j.bbrc.2013.01.071 (2013).
520 Li, H. *et al.* Validation of the proteasome as a therapeutic target in *Plasmodium* using an epoxyketone inhibitor with parasite-specific toxicity. *Chemistry and Biology* **19**, 1535-1545, doi:10.1016/j.chembiol.2012.09.019 (2012).
521 Boice, J. A. & Fairman, R. Structural characterization of the tumor suppressor p16, an ankyrin-like repeat protein. *Protein Science* **5**, 1776-1784, doi:10.1002/pro.5560050903 (1996).
522 Ben-Saadon, R. *et al.* The tumor suppressor protein p16(INK4a) and the human papillomavirus oncoprotein-58 E7 are naturally occurring lysine-less proteins that are degraded by the ubiquitin system. Direct evidence for ubiquitination at the N-terminal residue. *Journal of Biological Chemistry* **279**, 41414-41421, doi:10.1074/jbc.M407201200 (2004).
523 Chen, X., Barton, L. F., Chi, Y., Clurman, B. E. & Roberts, J. M. Ubiquitin-independent degradation of cell-cycle inhibitors by the REGgamma proteasome. *Molecular Cell* **26**, 843-852, doi:10.1016/j.molcel.2007.05.022 (2007).
524 Kobayashi, T., Wang, J., Al-Ahmadie, H. & Abate-Shen, C. ARF regulates the stability of p16 protein via REGgamma-dependent proteasome degradation. *Molecular Cancer Research* **11**, 828-833, doi:10.1158/1541-7786.MCR-13-0207 (2013).
525 Forster, A., Masters, E. I., Whitby, F. G., Robinson, H. & Hill, C. P. The 1.9 A structure of a proteasome-11S activator complex and implications for proteasome-PAN/PA700 interactions. *Molecular Cell* **18**, 589-599, doi:10.1016/j.molcel.2005.04.016 (2005).
526 Zhang, Z. *et al.* Identification of an activation region in the proteasome activator REGalpha. *Proceedings of the National Academy of Sciences* **95**, 2807-2811, doi:10.1073/pnas.95.6.2807 (1998).
527 Knowlton, J. R. *et al.* Structure of the proteasome activator REGalpha (PA28alpha). *Nature* **390**, 639-643, doi:10.1038/37670 (1997).

528 Petoukhov, M. V. *et al.* New developments in the ATSAS program package for small-angle scattering data analysis. *Journal of Applied Crystallography* **45**, 342-350, doi:10.1107/S0021889812007662 (2012).
529 Svergun, D. I., Petoukhov, M. V. & Koch, M. H. Determination of domain structure of proteins from X-ray solution scattering. *Biophysical Journal* **80**, 2946-2953, doi:10.1016/S0006-3495(01)76260-1 (2001).
530 Speed, M. A., Wang, D. I. & King, J. Specific aggregation of partially folded polypeptide chains: the molecular basis of inclusion body composition. *Nature Biotechnology* **14**, 1283-1287, doi:10.1038/nbt1096-1283 (1996).
531 Santner, A. A. *et al.* Sweeping away protein aggregation with entropic bristles: intrinsically disordered protein fusions enhance soluble expression. *Biochemistry* **51**, 7250-7262, doi:10.1021/bi300653m (2012).
532 Blees, A. *et al.* Structure of the human MHC-I peptide-loading complex. *Nature* **551**, 525, doi:10.1038/nature24627 (2017).
533 Liu, X., Li, M., Xia, X., Li, X. & Chen, Z. Mechanism of chromatin remodelling revealed by the Snf2-nucleosome structure. *Nature* **544**, 440, doi:10.1038/nature22036 (2017).
534 Li, N. *et al.* Structure of the origin recognition complex bound to DNA replication origin. *Nature* **559**, 217-222, doi:10.1038/s41586-018-0293-x (2018).
535 Martino, F. *et al.* RPAP3 provides a flexible scaffold for coupling HSP90 to the human R2TP co-chaperone complex. *Nature Communications* **9**, 1501, doi:10.1038/s41467-018-03942-1 (2018).
536 Forster, A., Whitby, F. G. & Hill, C. P. The pore of activated 20S proteasomes has an ordered 7-fold symmetric conformation. *The EMBO Journal* **22**, 4356-4364, doi:10.1093/emboj/cdg436 (2003).
537 Whitby, F. G. *et al.* Structural basis for the activation of 20S proteasomes by 11S regulators. *Nature* **408**, 115-120, doi:10.1038/35040607 (2000).
538 Smith, D. M. *et al.* Docking of the Proteasomal ATPases' Carboxyl Termini in the 20S Proteasome's α Ring Opens the Gate for Substrate Entry. *Molecular Cell* **27**, 731-744, doi:10.1016/j.molcel.2007.06.033 (2007).
539 Nakane, T., Kimanius, D., Lindahl, E. & Scheres, S. H. Characterisation of molecular motions in cryo-EM single-particle data by multi-body refinement in RELION. *eLife* **7**, doi:10.7554/eLife.36861 (2018).
540 Nakane, T., Kimanius, D., Lindahl, E. & Scheres, S. H. W. Characterisation of molecular motions in cryo-EM single-particle data by multi-body refinement in RELION. *eLife* **7**, e36861, doi:10.1101/286856 (2018).
541 Tian, G. *et al.* An asymmetric interface between the regulatory and core particles of the proteasome. *Nature Structural and Molecular Biology* **18**, 1259-1267, doi:10.1038/nsmb.2147 (2011).
542 da Fonseca, P. C., He, J. & Morris, E. P. Molecular model of the human 26S proteasome. *Molecular Cell* **46**, 54-66, doi:10.1016/j.molcel.2012.03.026 (2012).
543 Labun, K., Montague, T. G., Gagnon, J. A., Thyme, S. B. & Valen, E. CHOPCHOP v2: a web tool for the next generation of CRISPR genome engineering. *Nucleic Acids Research* **44**, W272-276, doi:10.1093/nar/gkw398 (2016).

544 Spillman, N. J., Beck, J. R., Ganesan, S. M., Niles, J. C. & Goldberg, D. E. The chaperonin TRiC forms an oligomeric complex in the malaria parasite cytosol. *Cellular Microbiology* **19**, doi:10.1111/cmi.12719 (2017).
545 Ganesan, S. M. *et al.* Yeast dihydroorotate dehydrogenase as a new selectable marker for *Plasmodium falciparum* transfection. *Molecular and Biochemical Parasitology* **177**, 29-34, doi:10.1016/j.molbiopara.2011.01.004 (2011).
546 Spillman, N. J., Dalmia, V. K. & Goldberg, D. E. Exported epoxide hydrolases modulate erythrocyte vasoactive lipids during *Plasmodium falciparum* infection. *MBio* **7**, doi:10.1128/mBio.01538-16 (2016).
547 Xie, S. C. *et al.* Target validation and identification of novel boronate inhibitors of the *Plasmodium falciparum* proteasome. *Journal of Medicinal Chemistry* **61**, 10053-10066, doi:10.1021/acs.jmedchem.8b01161 (2018).
548 Schuck, P. & Rossmanith, P. Determination of the sedimentation coefficient distribution by least-squares boundary modeling. *Biopolymers* **54**, 328-341 (2000).
549 Winn, M. D. *et al.* Overview of the CCP4 suite and current developments. *Acta Crystallographica Section D Biological Crystallography* **67**, 235-242, doi:10.1107/S0907444910045749 (2011).
550 Cowtan, K. Recent developments in classical density modification. *Acta Crystallographica Section D: Biological Crystallography* **66**, 470-478, doi:10.1107/S090744490903947X (2010).
551 Cowtan, K. The Buccaneer software for automated model building. 1. Tracing protein chains. *Acta Crystallographica Section D: Biological Crystallography* **62**, 1002-1011, doi:10.1107/S0907444906022116 (2006).
552 Adams, P. D. *et al.* PHENIX: A comprehensive Python-based system for macromolecular structure solution. *Acta Crystallographica Section D: Biological Crystallography* **66**, 213-221, doi:10.1107/S0907444909052925 (2010).
553 Baker, N. A., Sept, D., Joseph, S., Holst, M. J. & McCammon, J. A. Electrostatics of nanosystems: Application to microtubules and the ribosome. *Proceedings of the National Academy of Sciences* **98**, 10037-10041, doi:DOI 10.1073/pnas.181342398 (2001).
554 Headd, J. J. *et al.* Use of knowledge-based restraints in phenix.refine to improve macromolecular refinement at low resolution. *Acta Crystallographica Section D: Biological Crystallography* **68**, 381-390, doi:10.1107/S0907444911047834 (2012).
555 Sali, A. & Blundell, T. L. Comparative protein modelling by satisfaction of spatial restraints. *Journal of Molecular Biology* **234**, 779-815 (1993).
556 Buchan, D. W., Minneci, F., Nugent, T. C., Bryson, K. & Jones, D. T. Scalable web services for the PSIPRED protein analysis workbench. *Nucleic Acids Research* **41**, W349-357, doi:10.1093/nar/gkt381 (2013).